SOME ASPECTS OF THE CRASHWORTHINESS OF RAIL VEHICLES : VOLUME II

Lik-Beng Lim, *BEng.*

A thesis submitted for the degree of

Doctor of Philosophy at the University of Sheffield

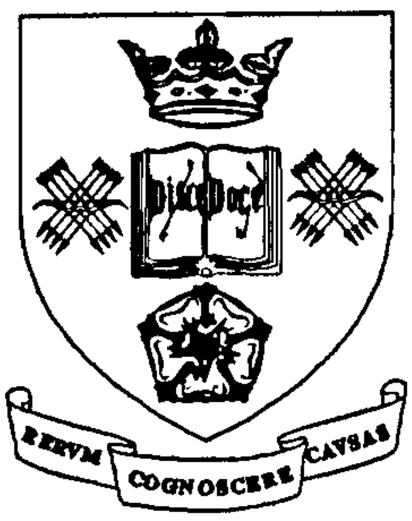

Department of Mechanical and Process Engineering

January, 1996

Contents

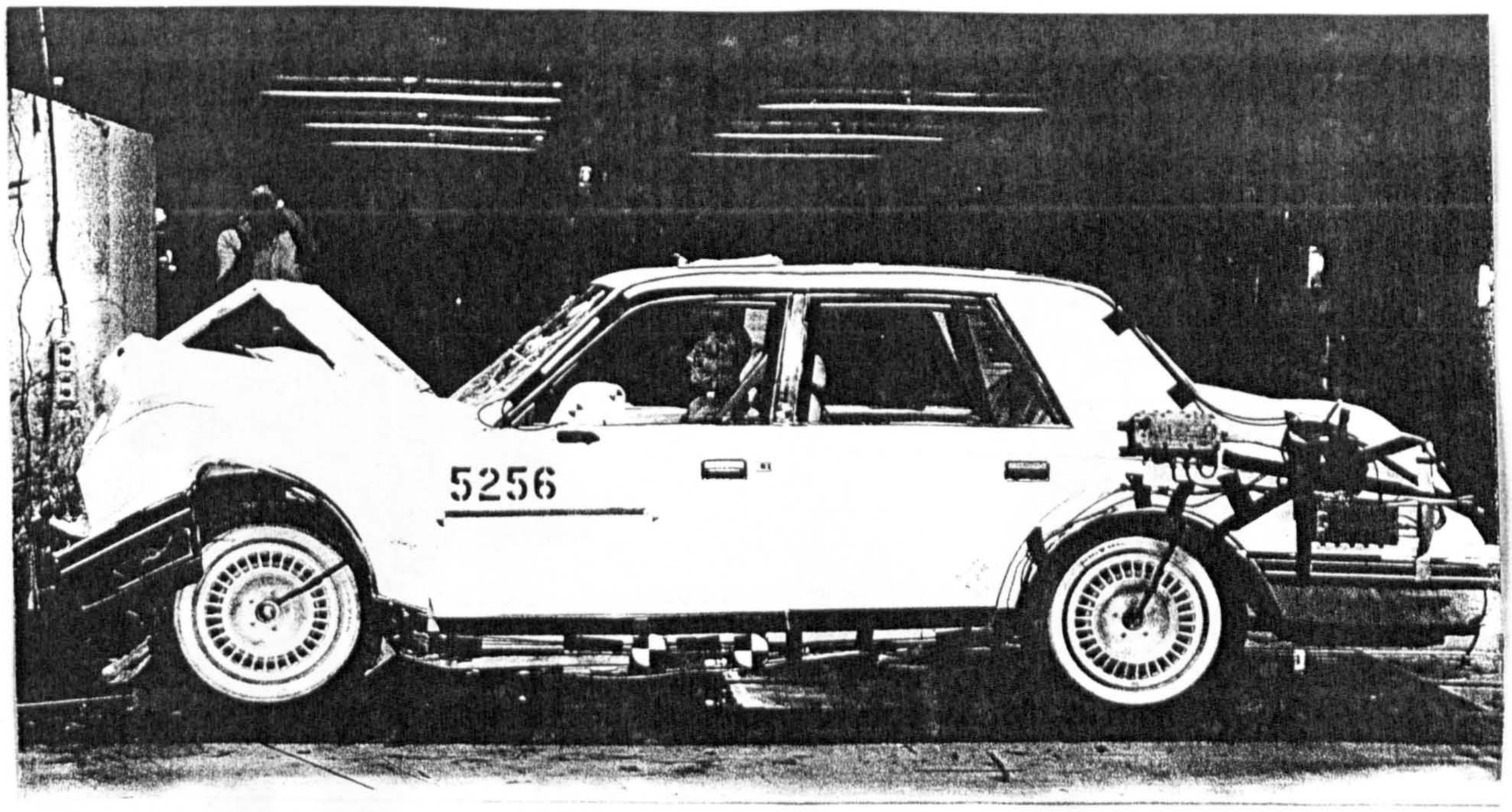

Figure 1.1 : A crush zone situated well away from the passenger compartment provides the necessary survival space for the passengers [3].

Figure 1.2 : The Volvo dummy family [7].

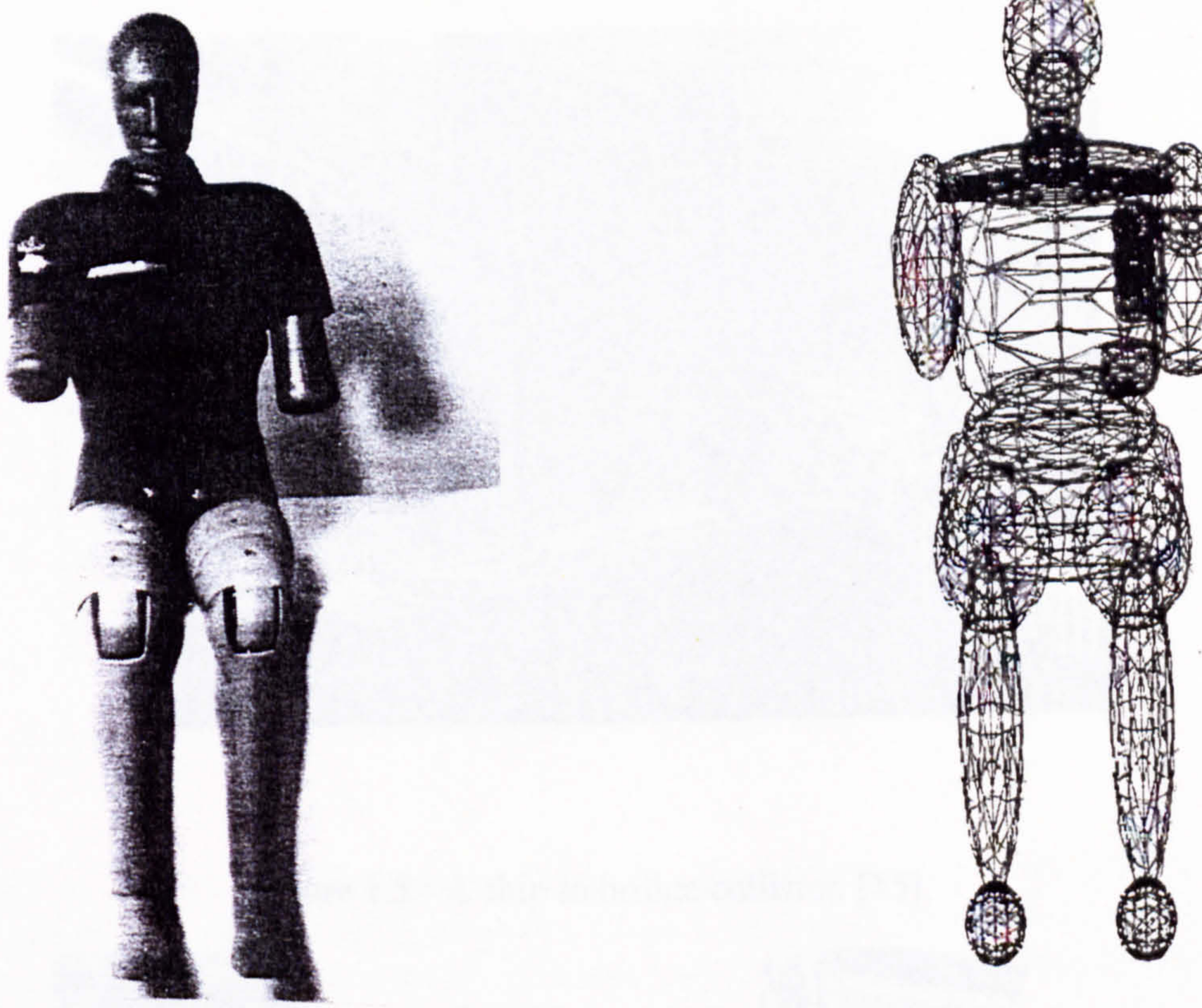

Figure 1.3 : EUROSID --- Actual dummy and its F.E. model [6].

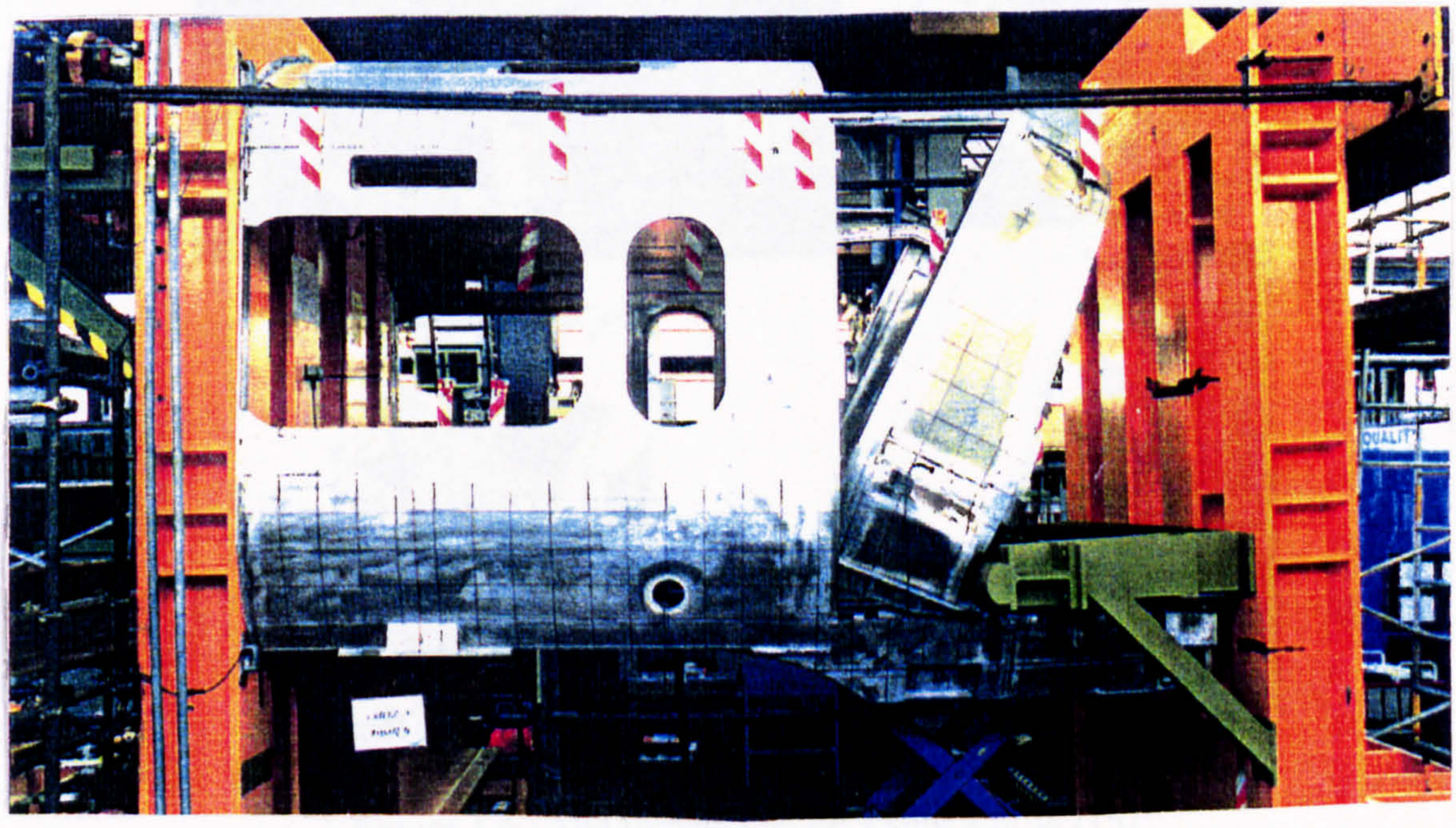

Figure 1.4 : BR static crush test on vehicle end structure [9].

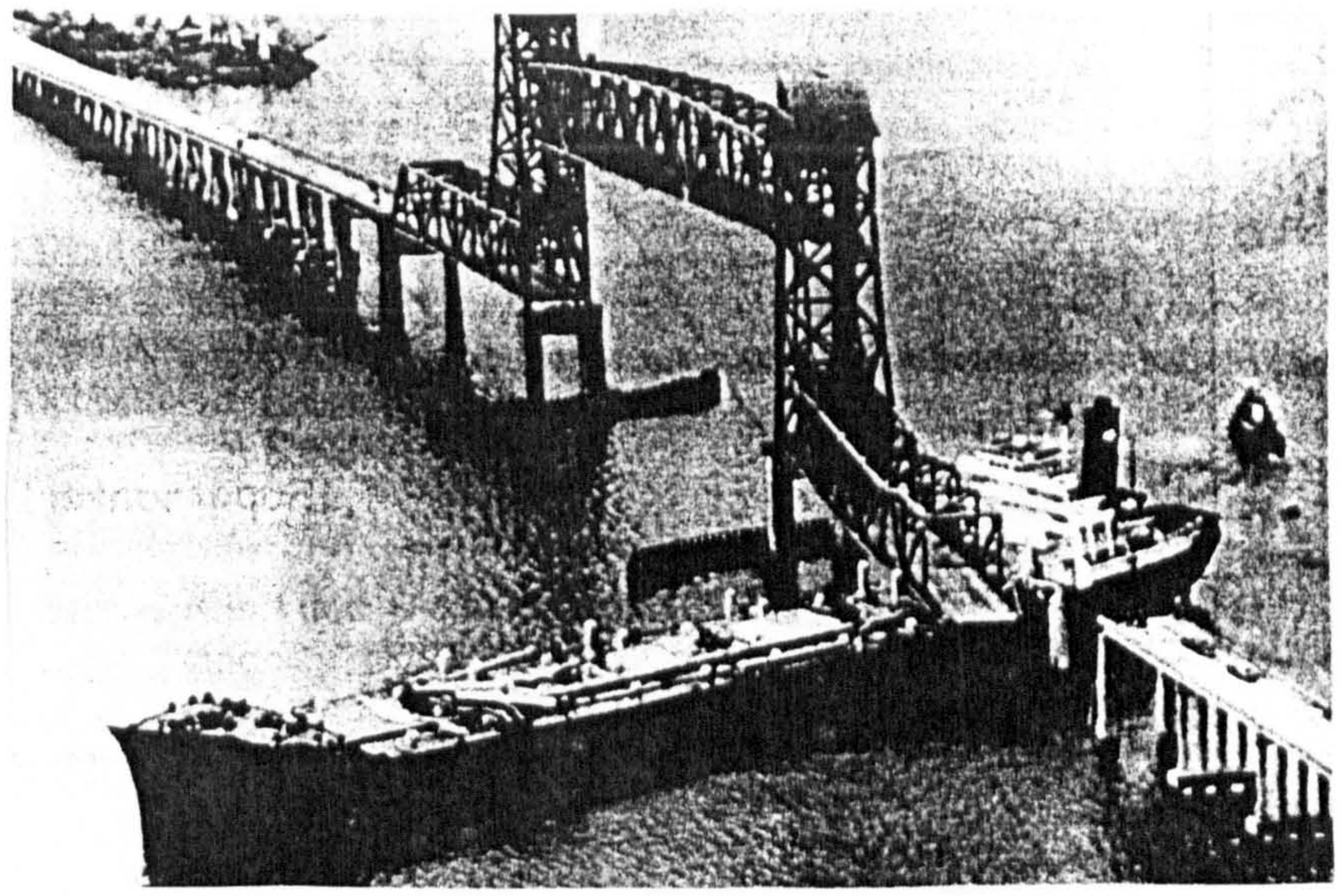

Figure 1.5 : A ship to bridge collision [15].

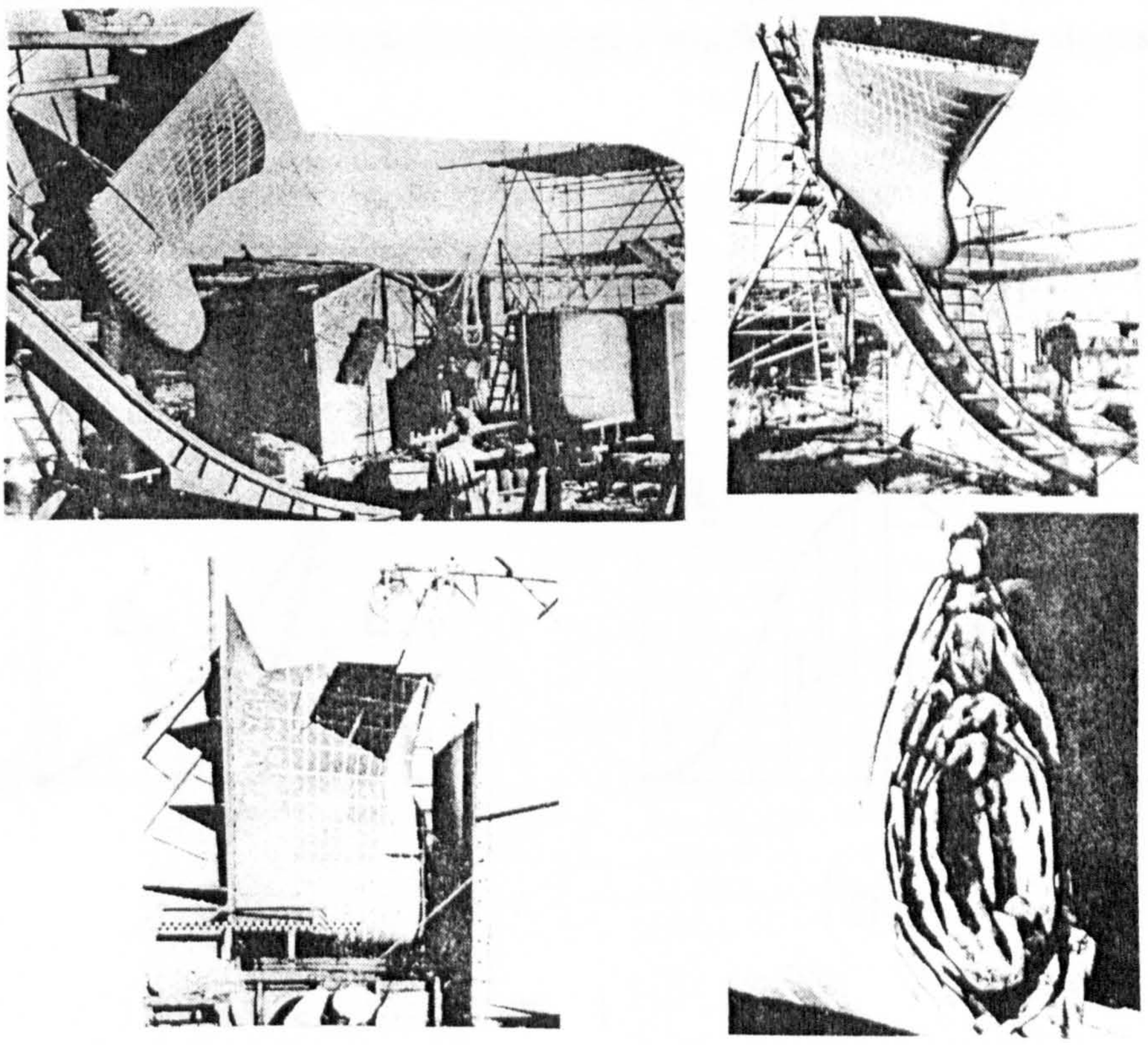

Figure 1.6 : The impact test on a ship's bow [15].

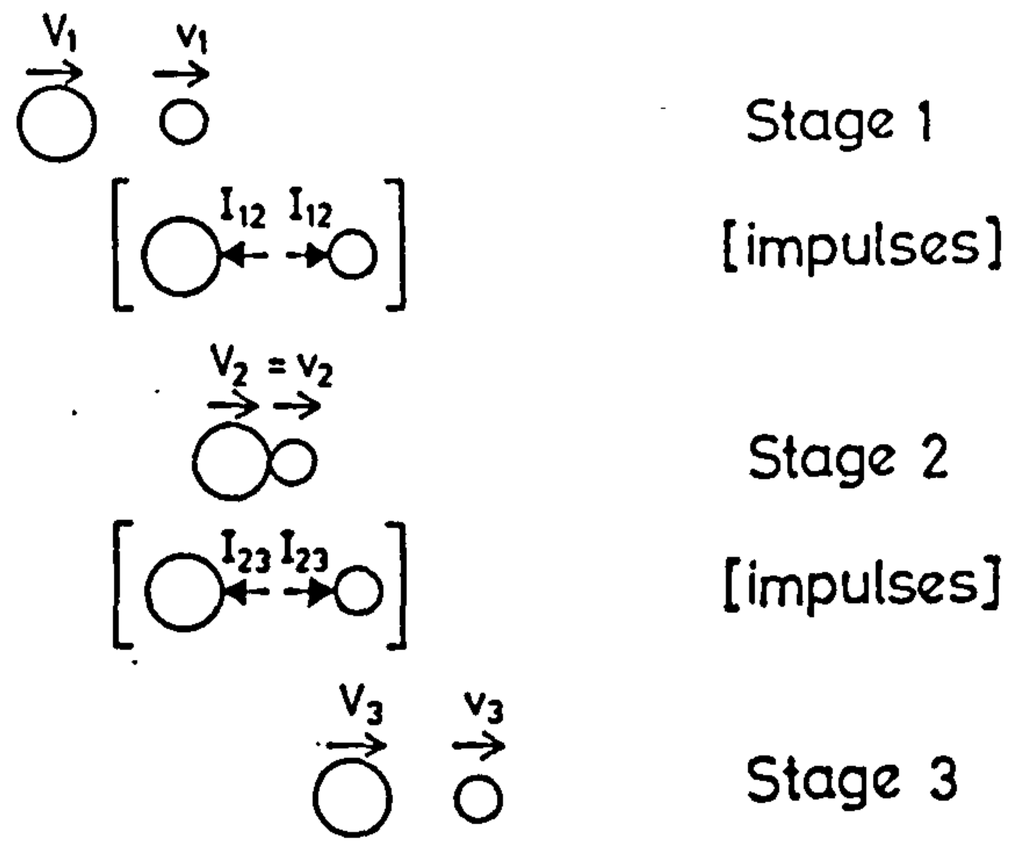

Figure 2.1 : Stage 1 is prior to impact. Stage 2 is the instant at which the centroids of *M* and *m* have exactly equal velocities. Stage 3 represents their separation. The intermediate diagrams show the impulses *I* which act between the stages [9].

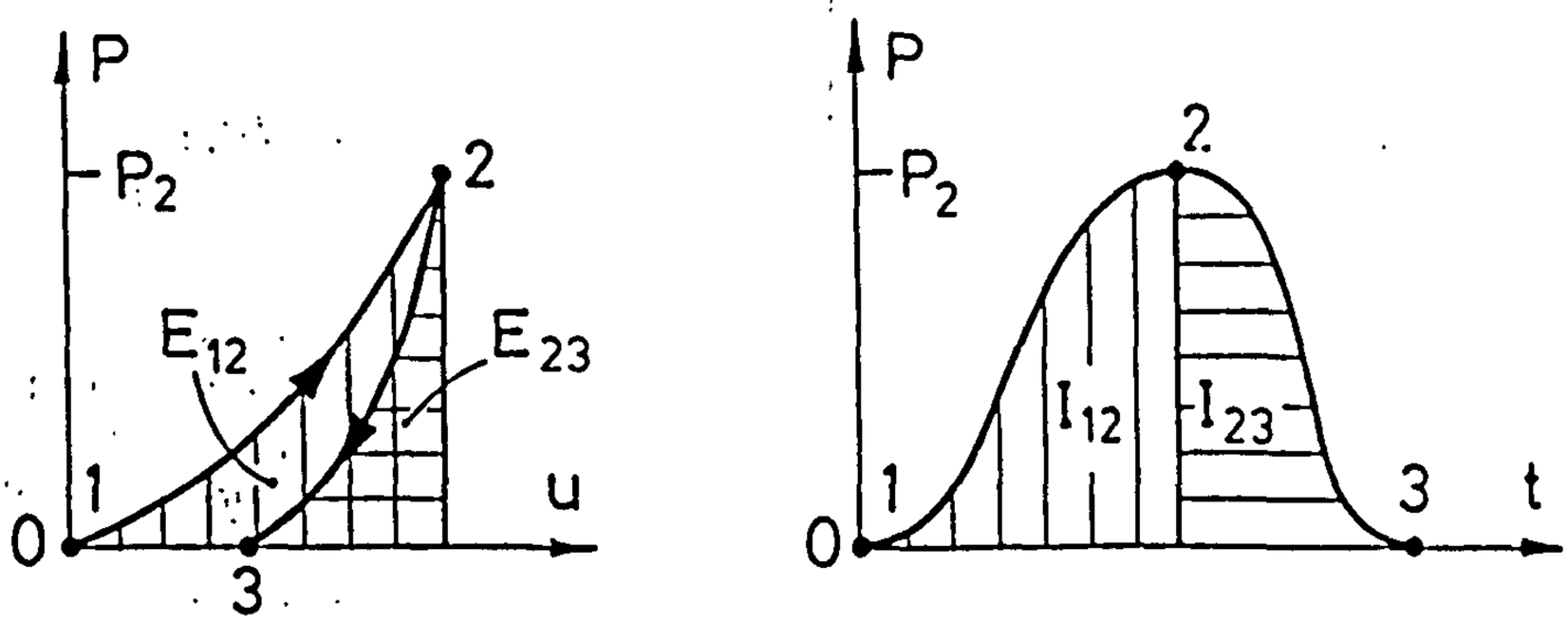

Figure 2.2 : (a) Load-deflection curves of typical loading and unloading path for the contact region. (b) Force-time plot corresponding to (a). After [9].

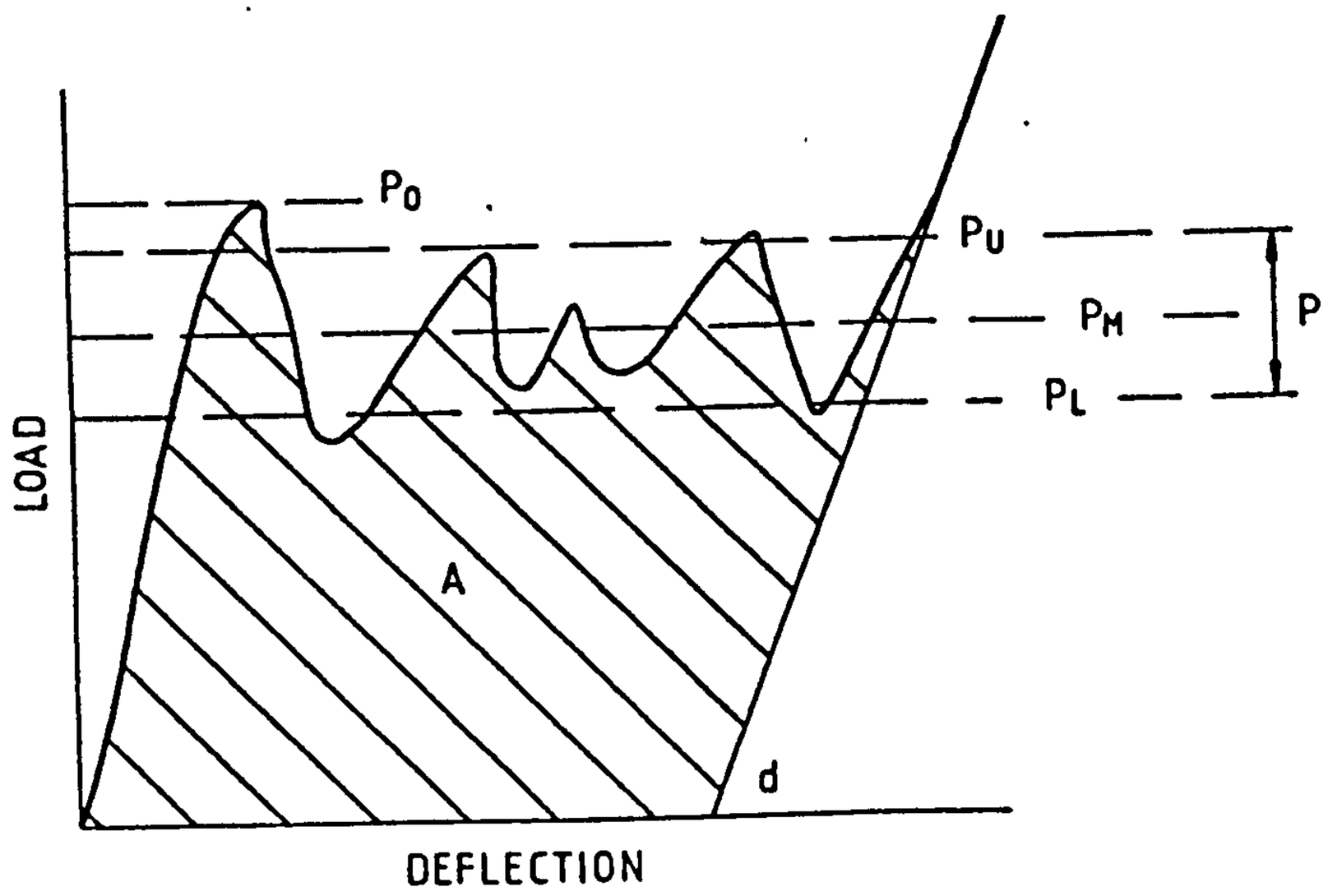

Figure 2.3 : Measures of energy absorption efficiency [10].

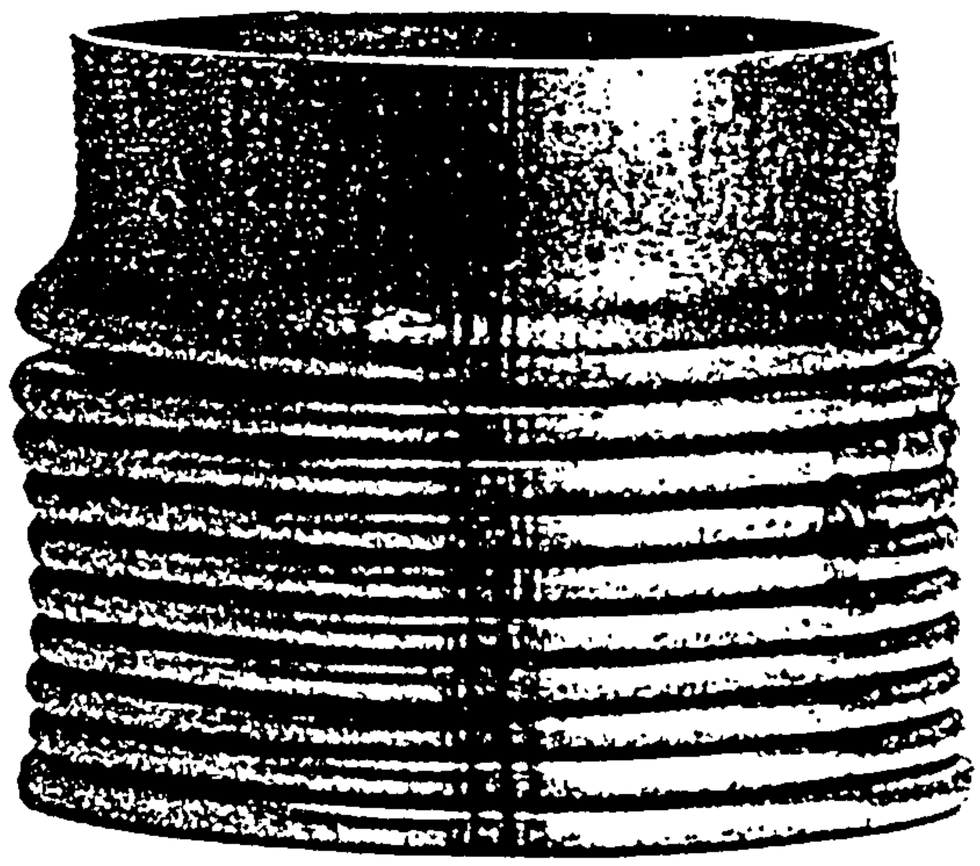

Figure 2.4 : Axisymmetric buckling mode for tubes [16].

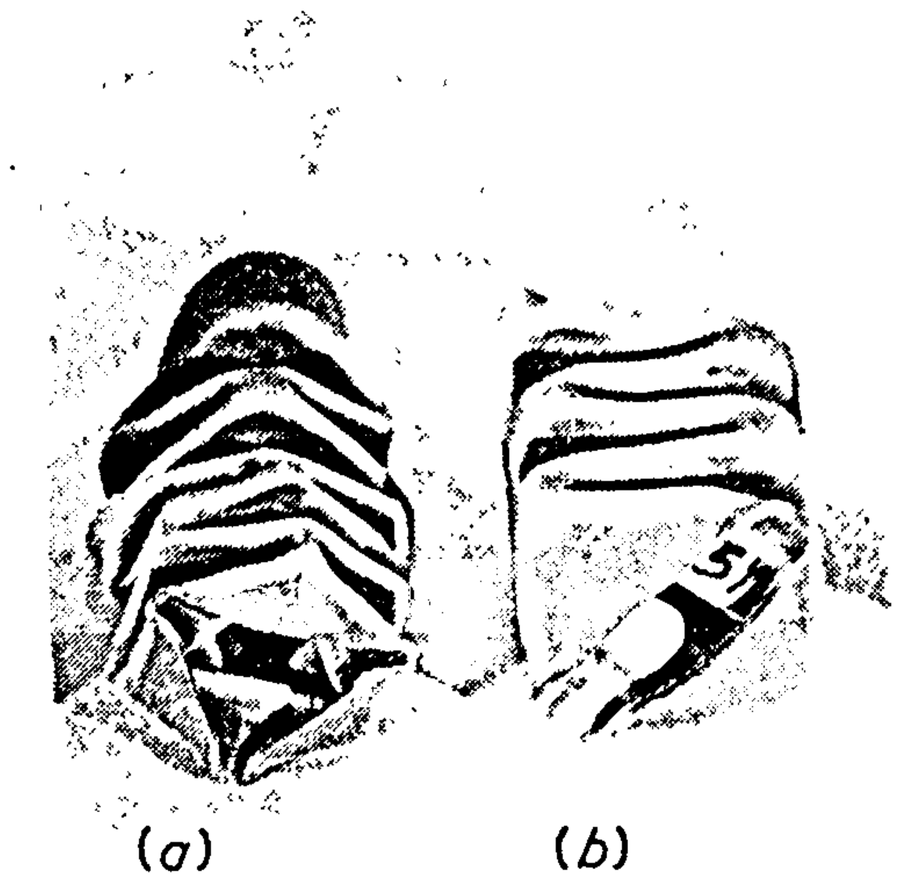

Figure 2.5 : Diamond-lobe buckling mode. Here specimen (a) has a 3 diamond-lobe collapse mode and (b) has a 2 diamond-lobe collapse mode [28].

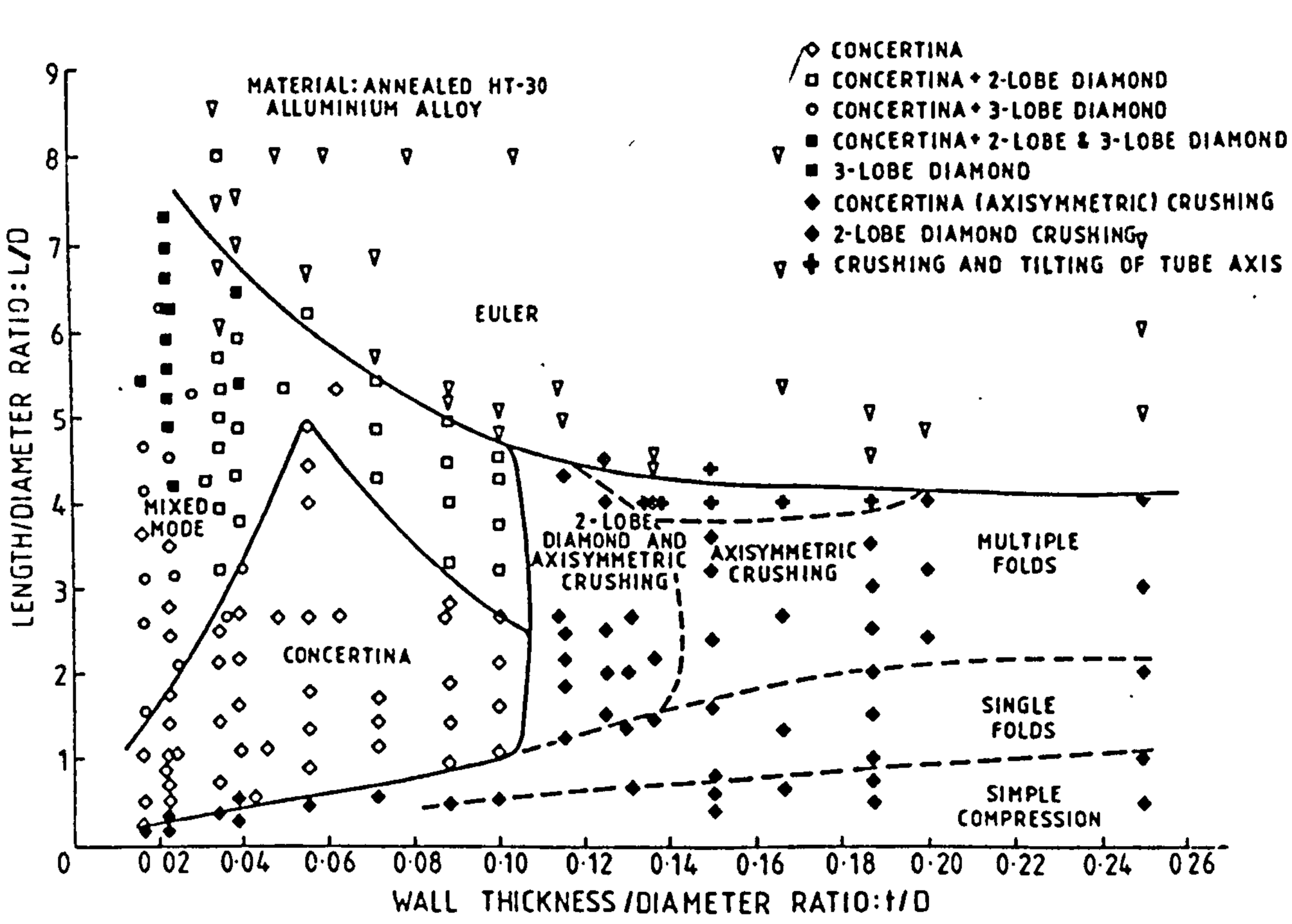

Figure 2.6 : Collapse-mode classification chart for aluminium alloy tubes [20].

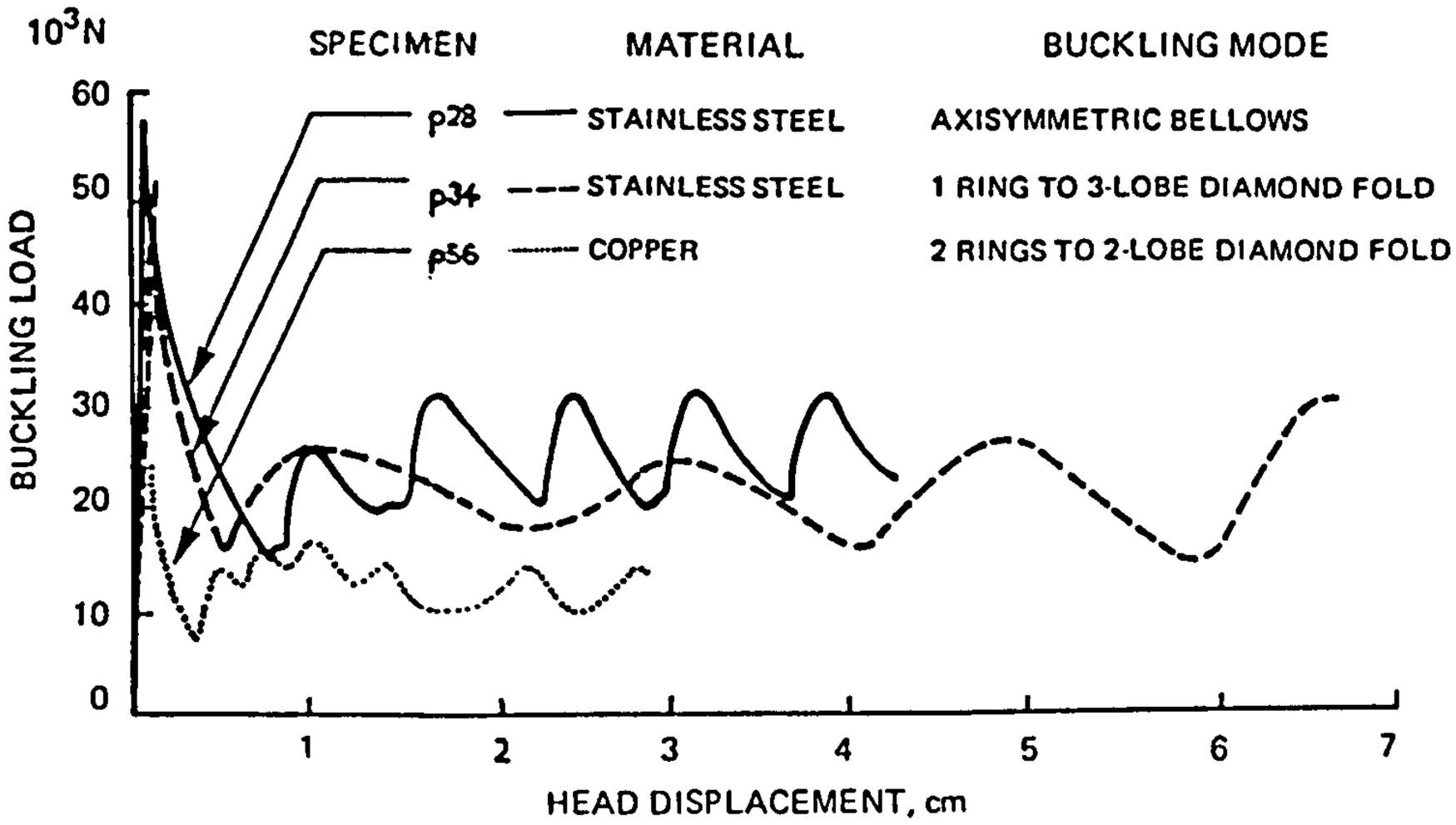

Figure 2.7 : Load-deflection characteristics of axially compressed tubes from reference [19].

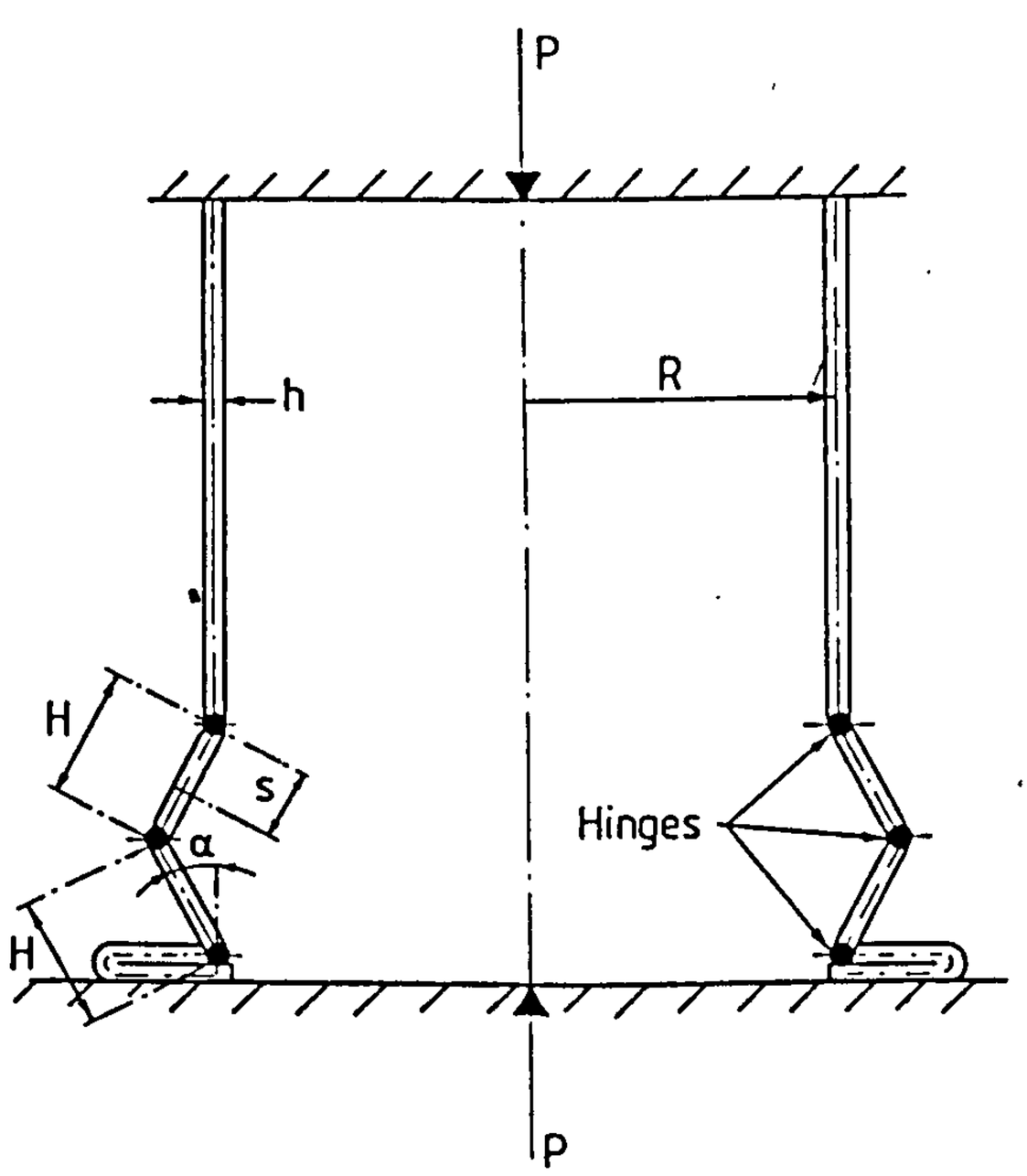

Figure 2.8 : Alexander's idealized axisymmetric collapse mode for cylindrical tubes [24].

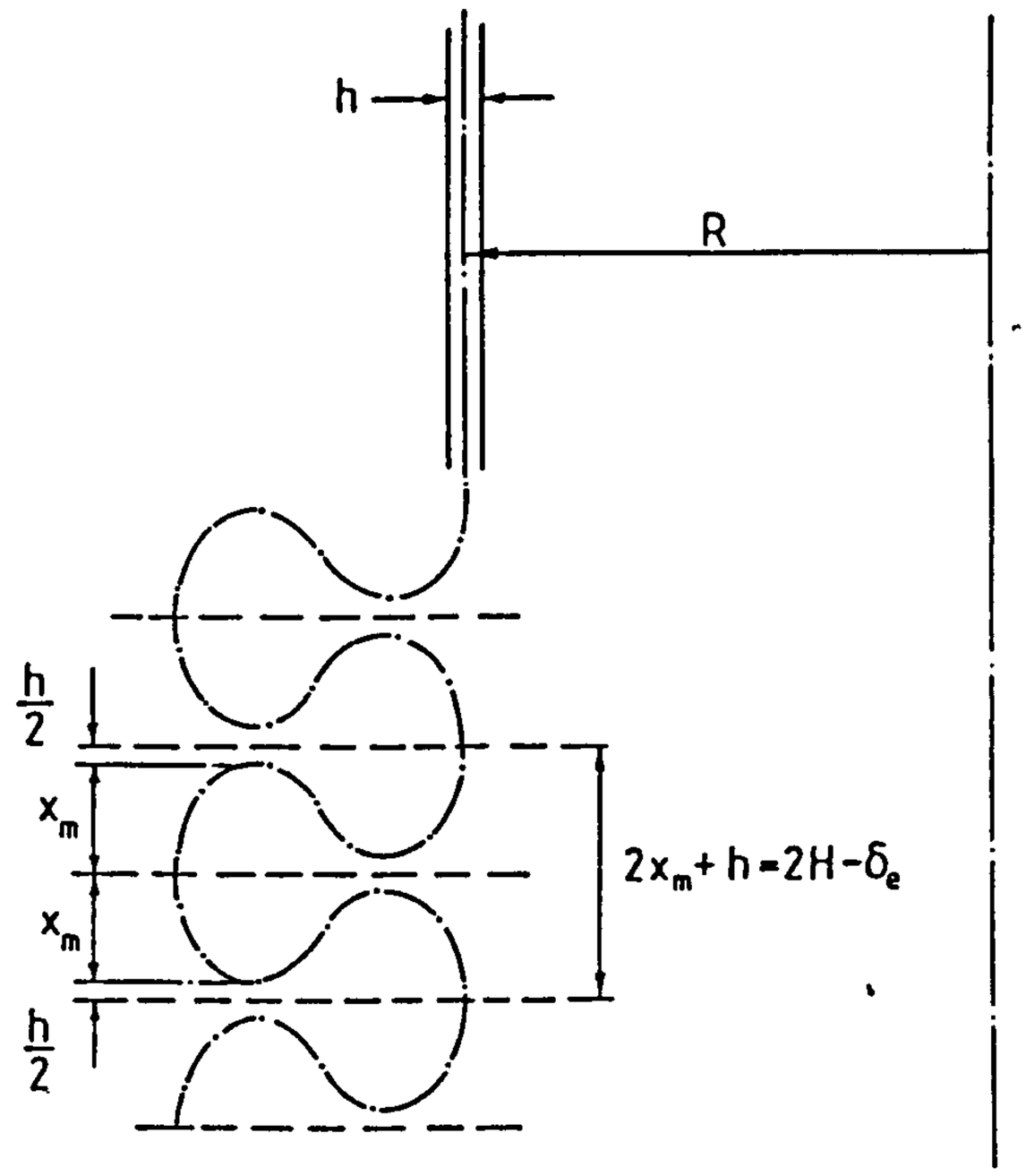

Figure 2.9 : The improved axisymmetric collapse mode. Axial deflection is now governed by an effective crushing stroke [25].

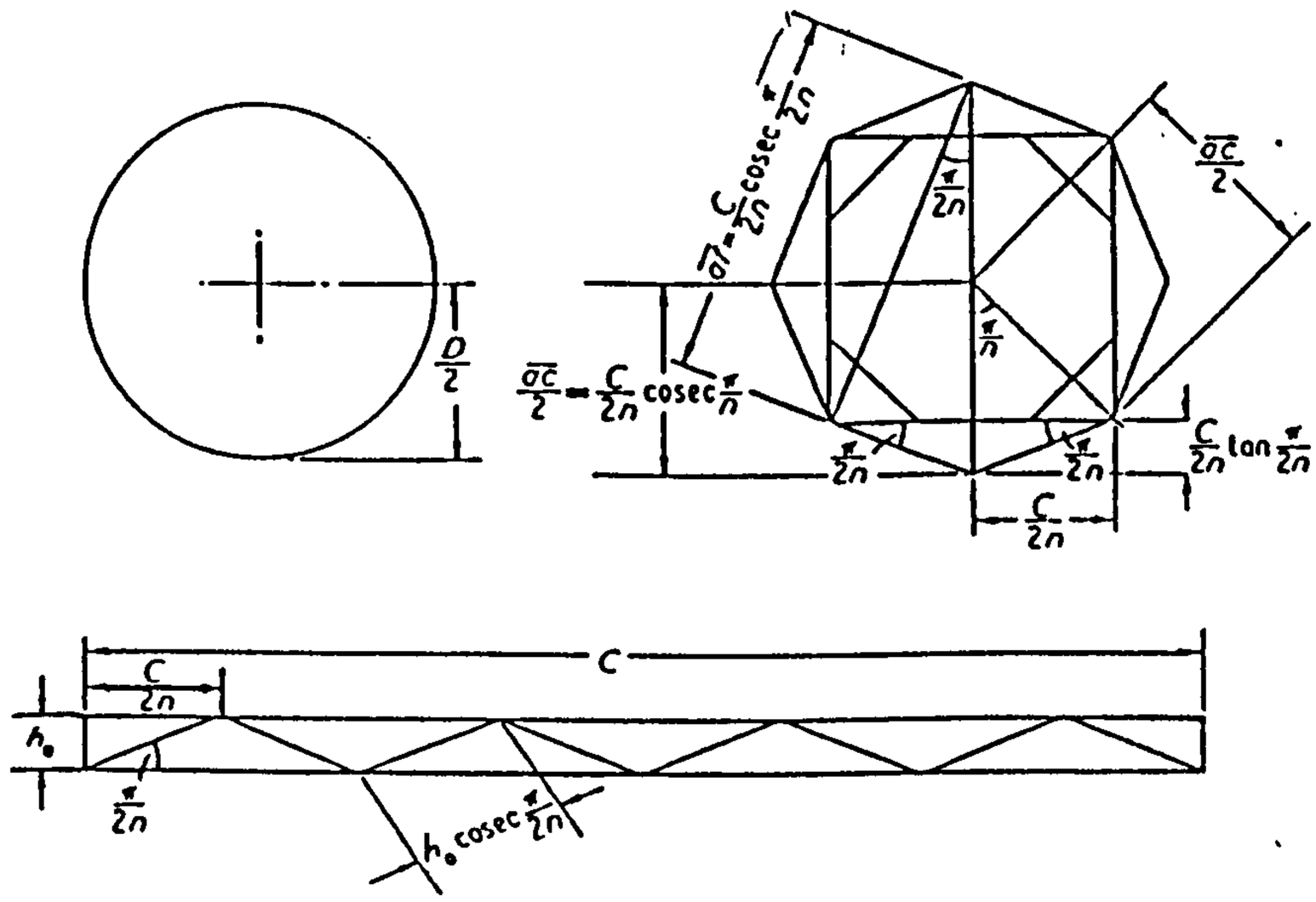

Figure 2.10 : The geometric relationships for diamond collapse modes of PVC tubes as described in [27].

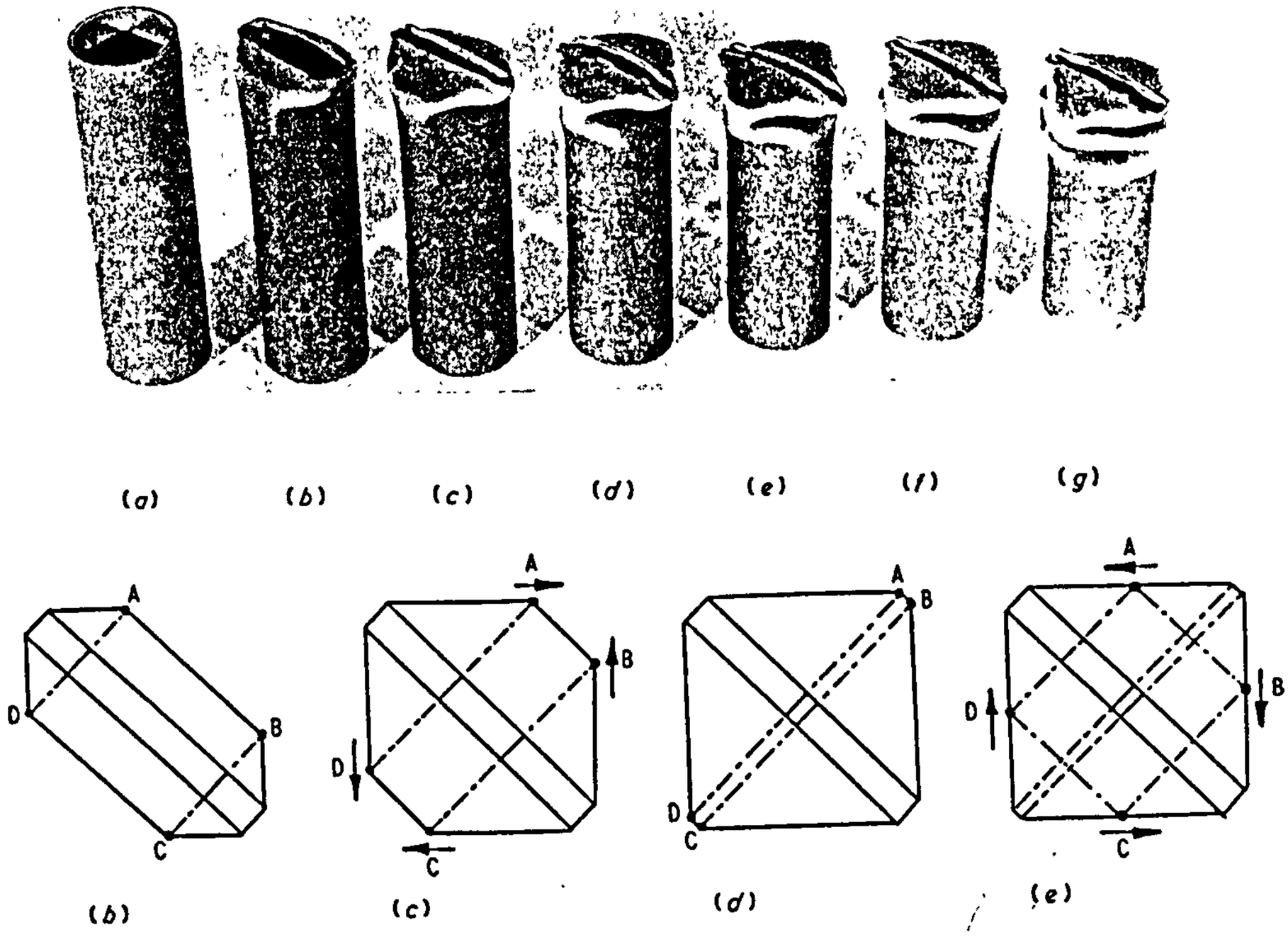

Figure 2.11 : The travelling-hinge mechanism for tubes collapsing in the diamond-lobe mode. [28].

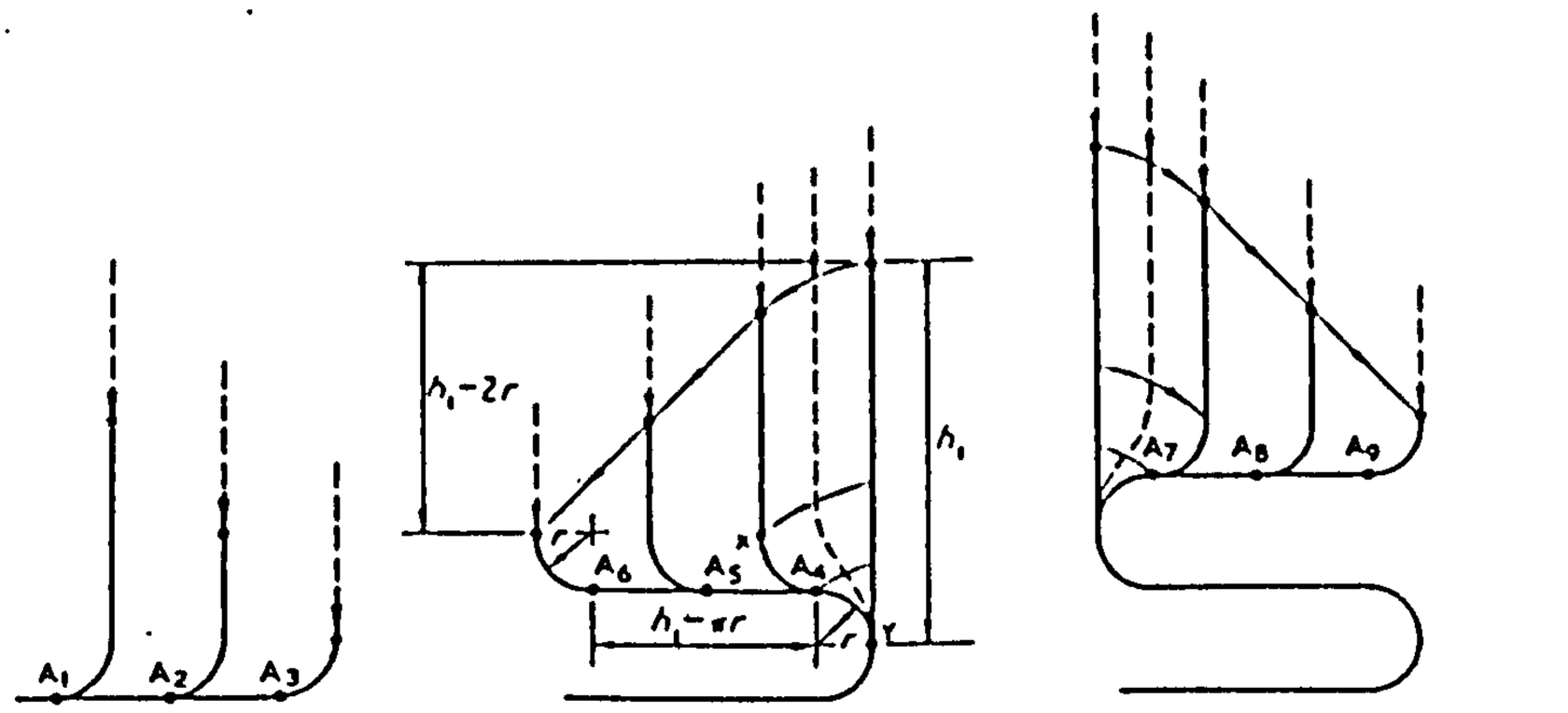

Figure 2.12 : Formation of horizontal hinges in Johnson *et. al.* theory. The radius '*r*' is obtained by minimum energy principle [27].

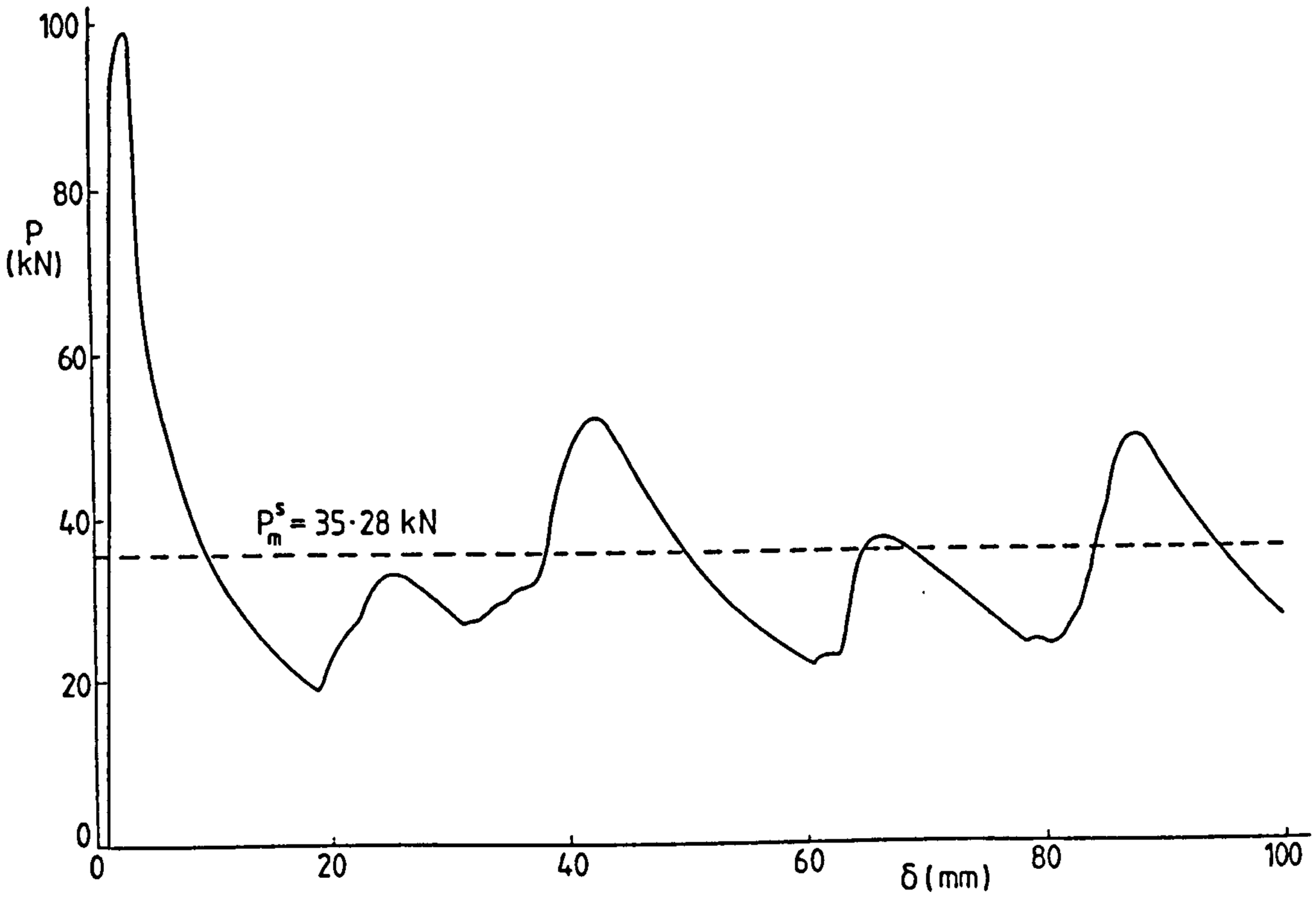

Figure 2.13 : Static axial crushing load versus axial displacement for a square tube of side 49.3mm, wall thickness 1.63mm and tube height 244.1mm [32].

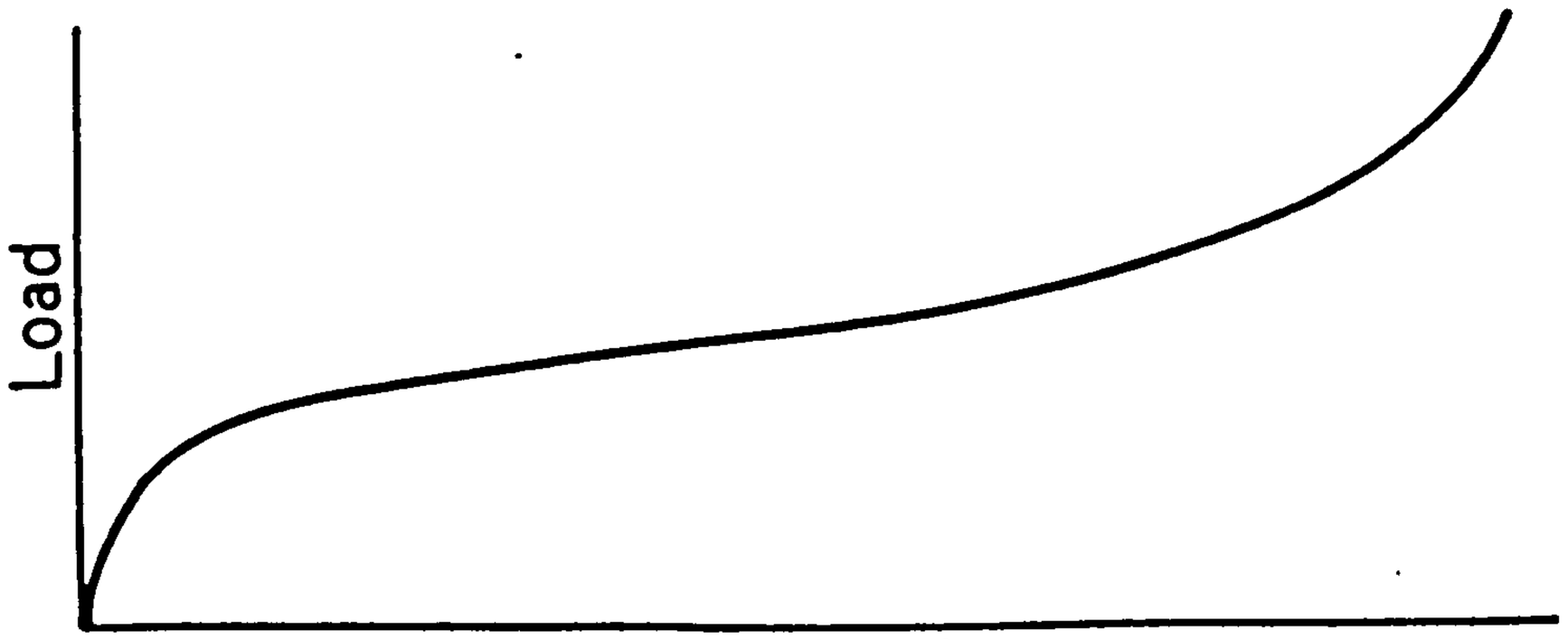

Figure 2.14 : Load-deflection characteristics for a single tube crushed transversely [5].

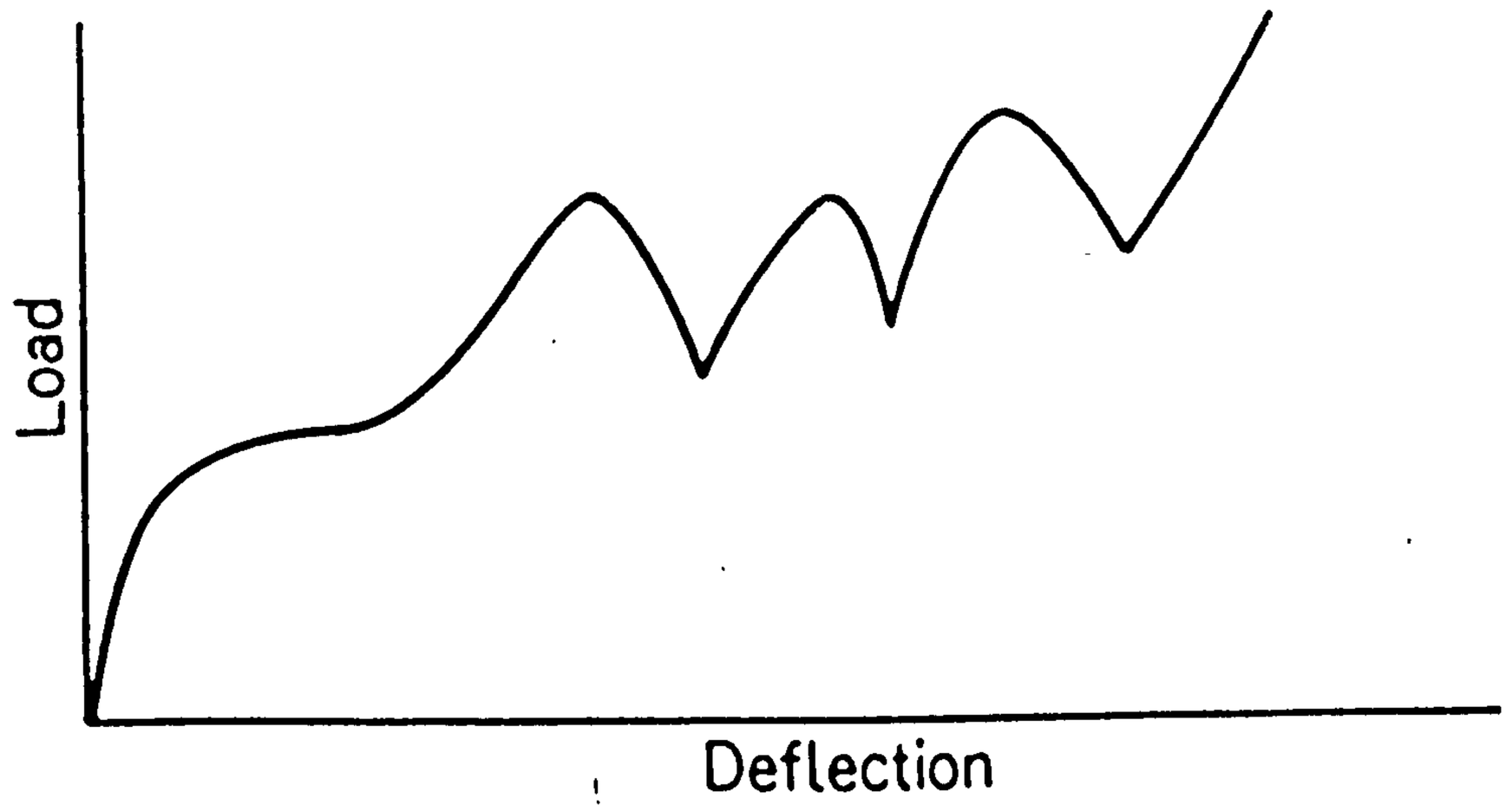

Figure 2.15 : Load-deflection characteristics for three layers of crossed tubes crushed transversely [5].

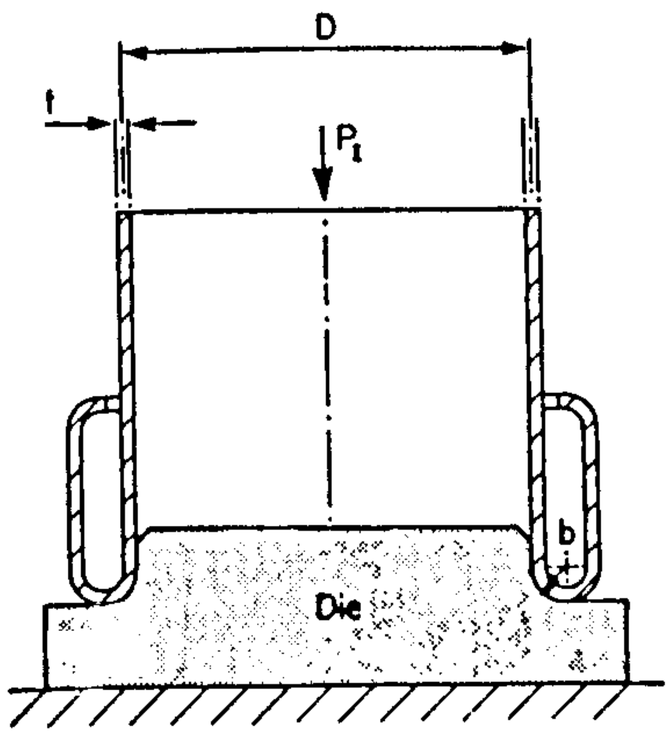

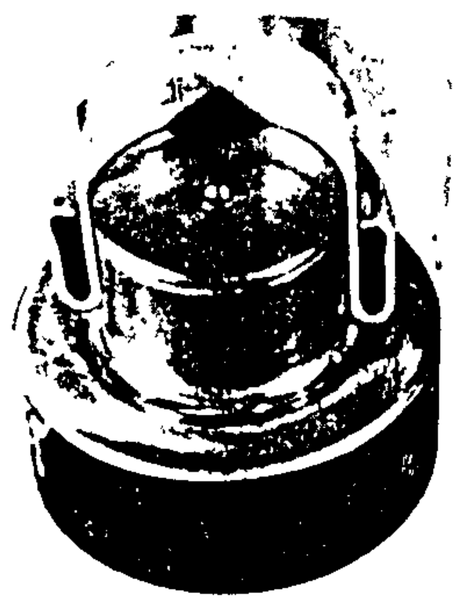

Figure 2.16 : An externally inverted tube [5].

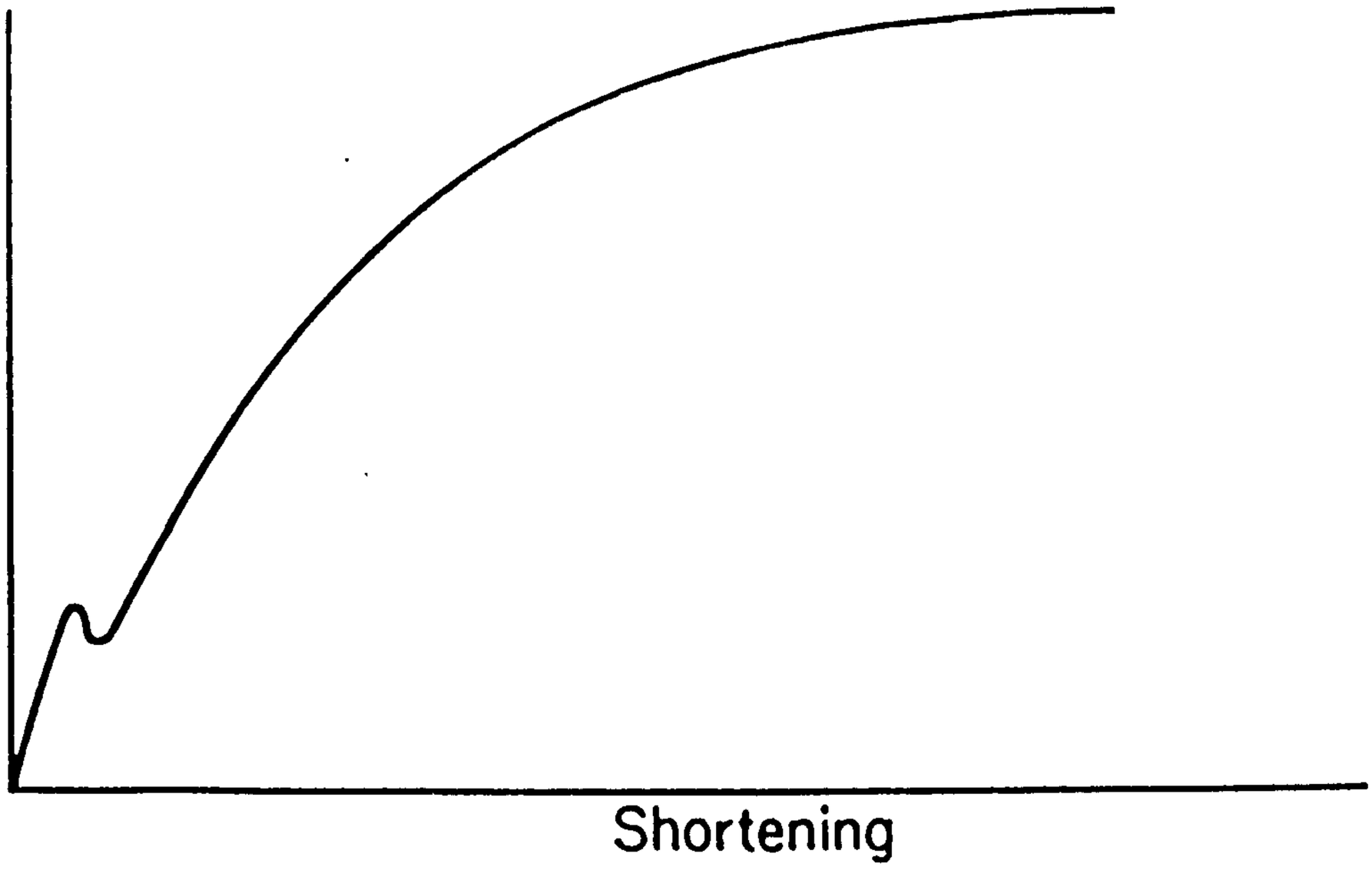

Figure 2.17 : Typical load-deflection characteristics for a tube inverted externally [5].

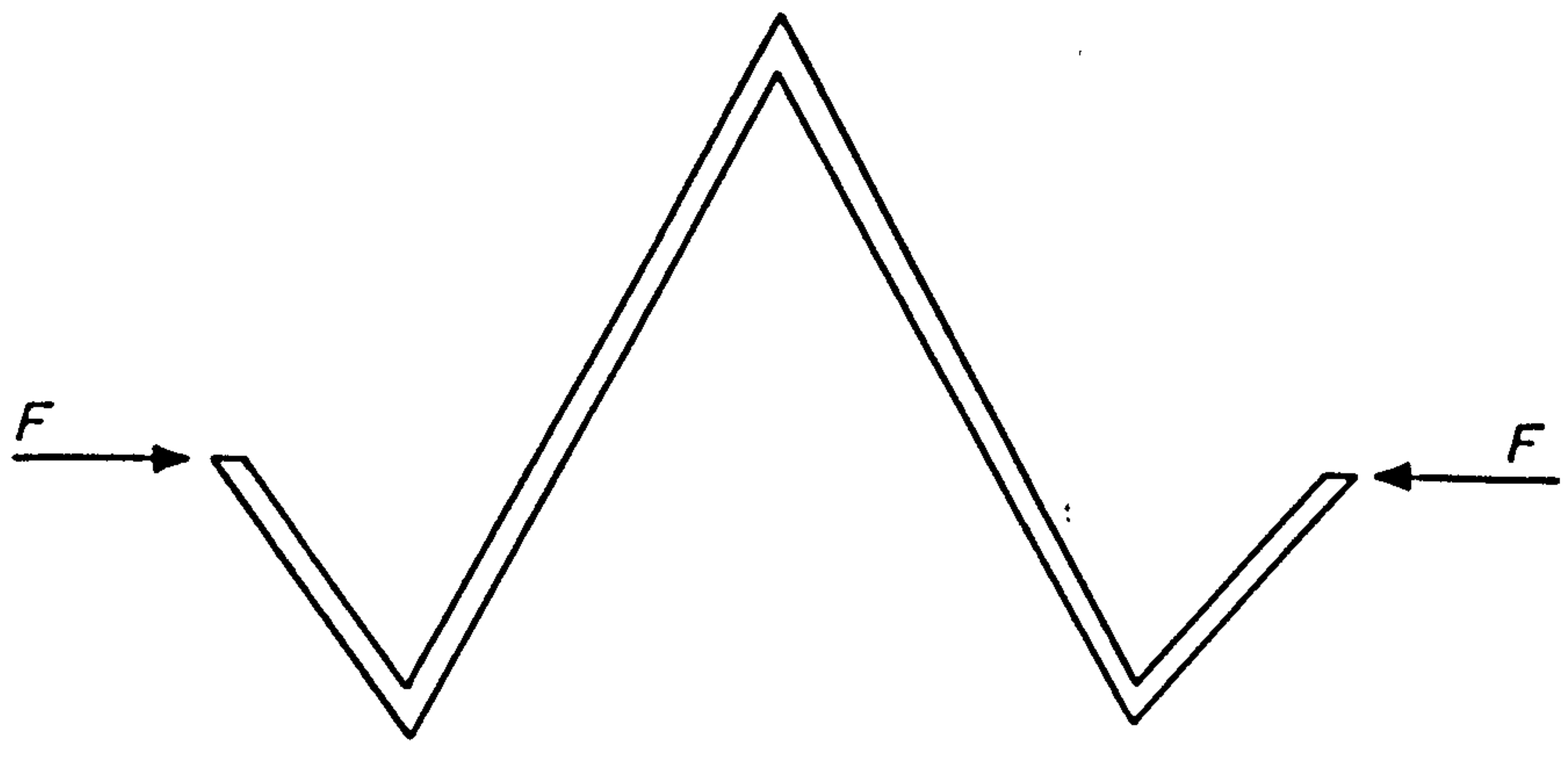

Figure 2.18 : A 'W' frame changing compression into bending [5].

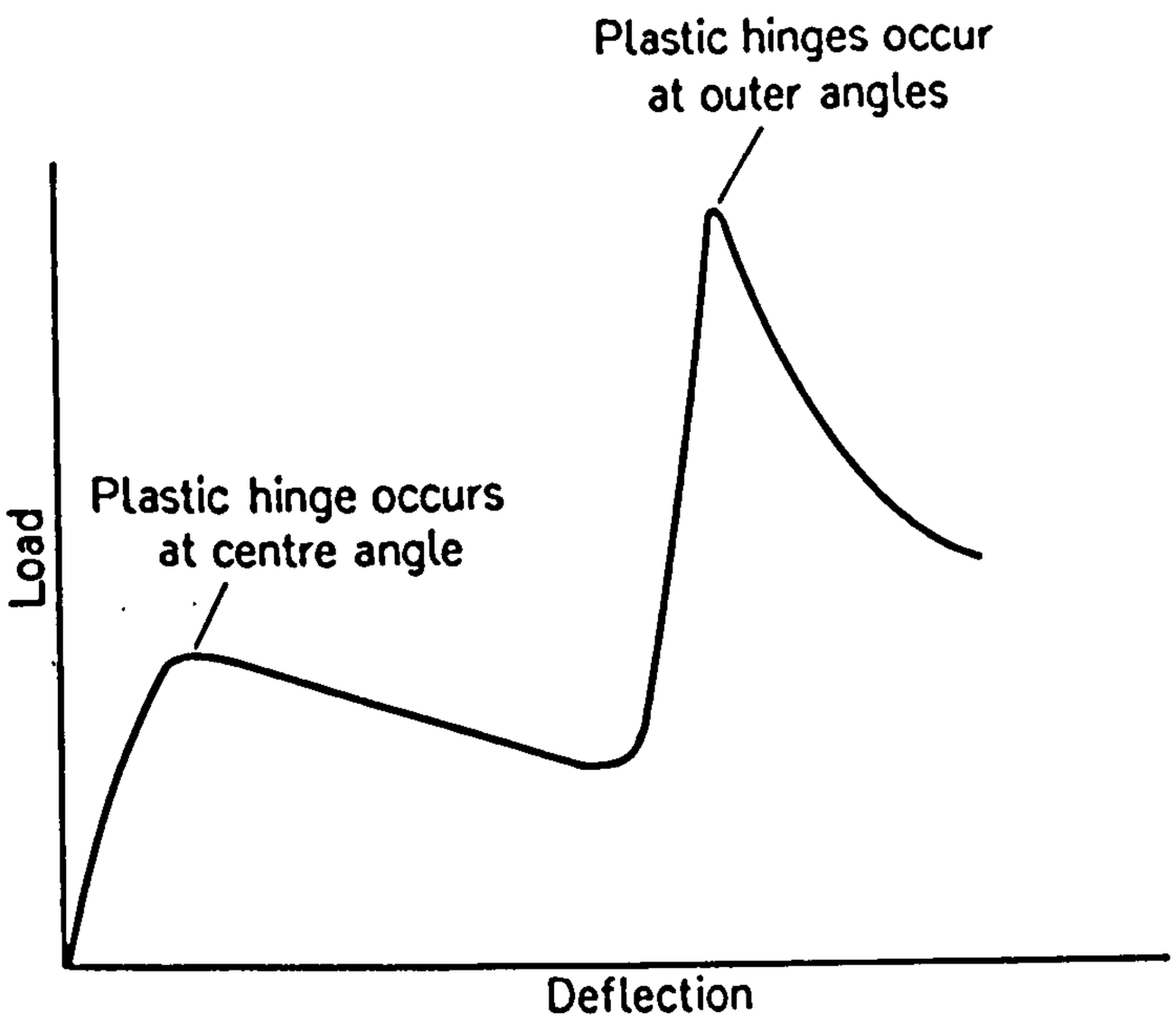

Figure 2.19 : Typical load-deflection characteristics for a 'W' frame [5].

Figure 2.20 : Pulling a wire plastically through four fixed rollers [5].

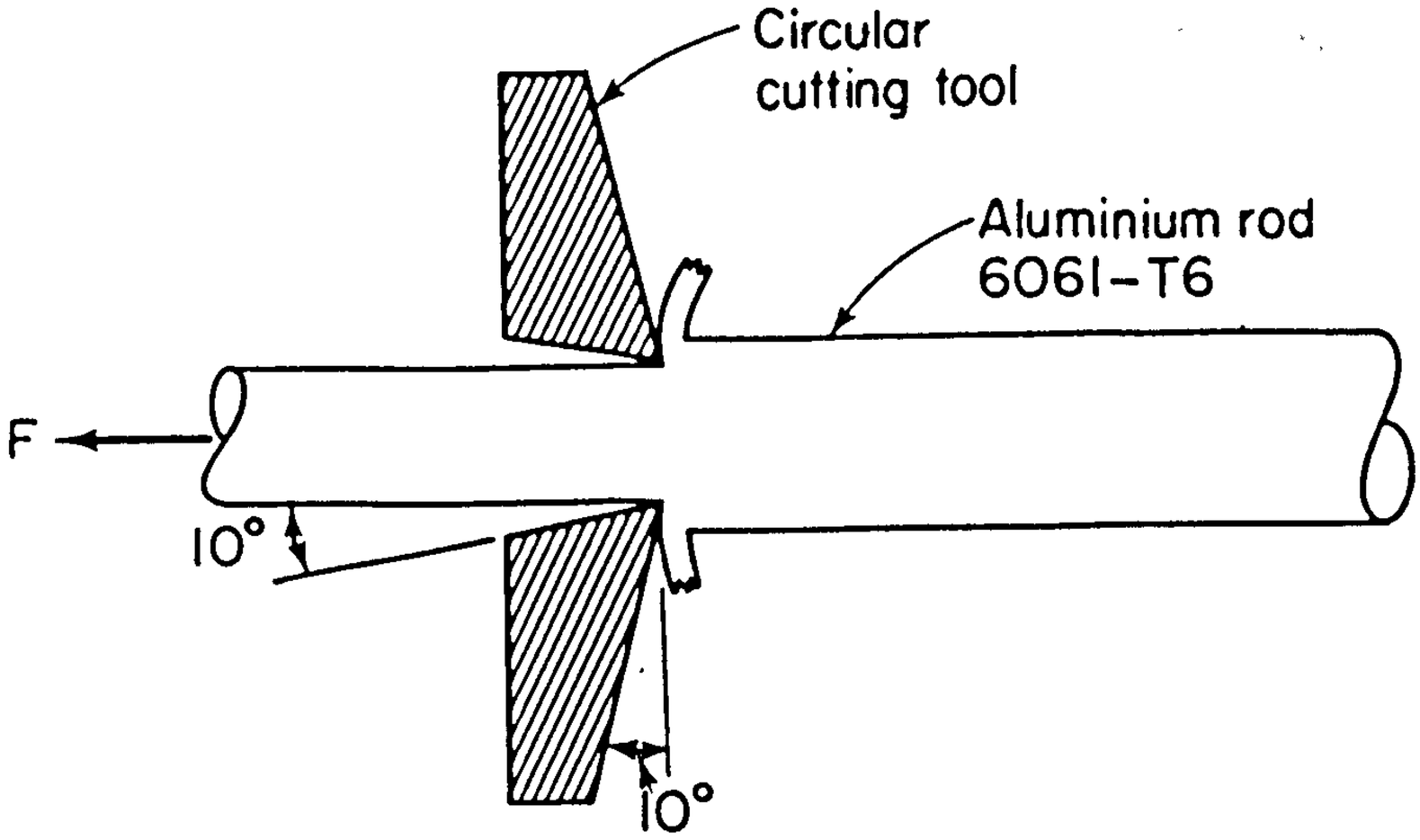

Figure 2.21 : Schematic diagram of a metal skinning device [2].

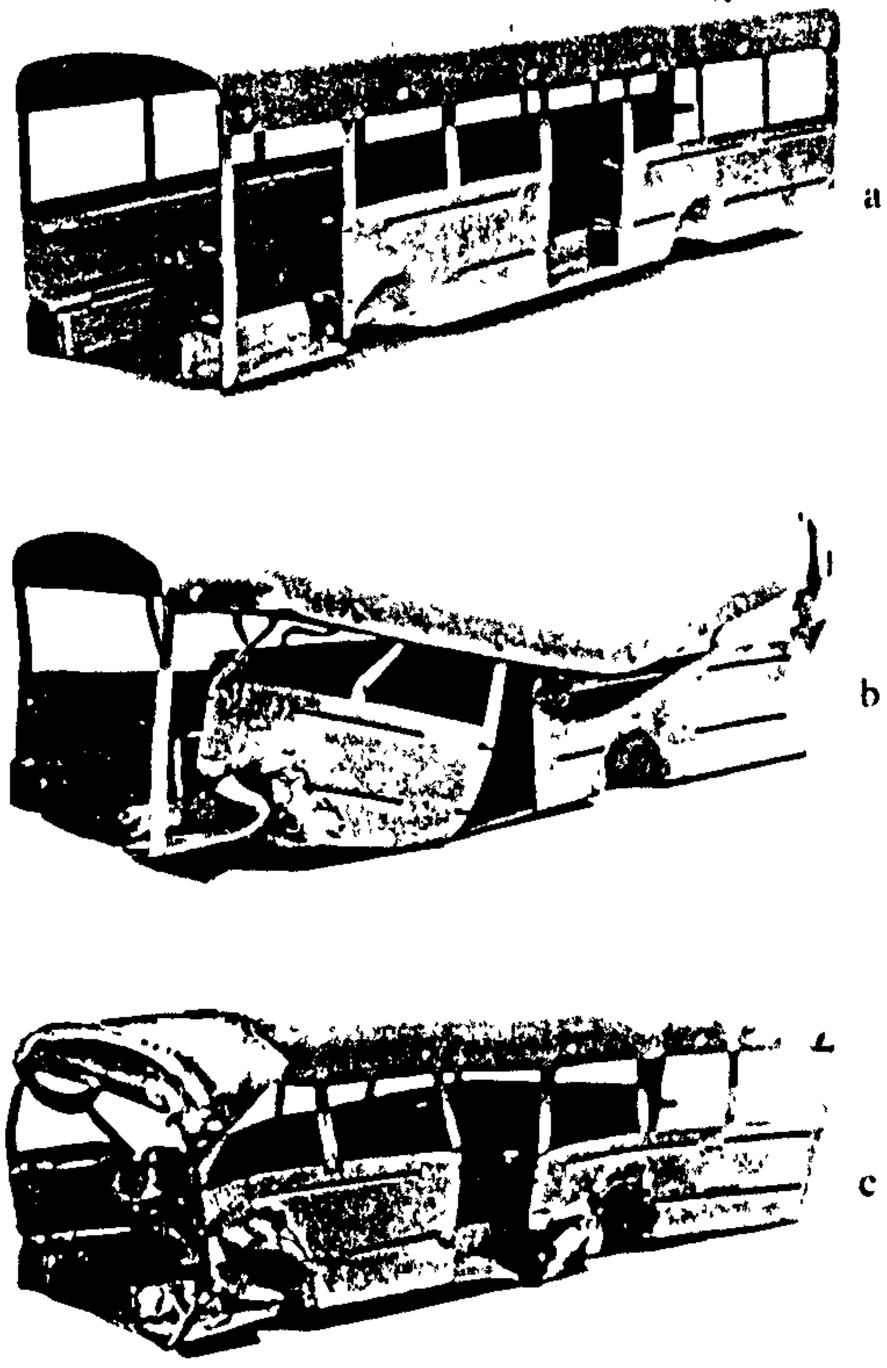

Figure 2.22 : Motor coach models. (a) was the original model, (b) was crushed quasi-statically and (c) was impacted dynamically. [30].

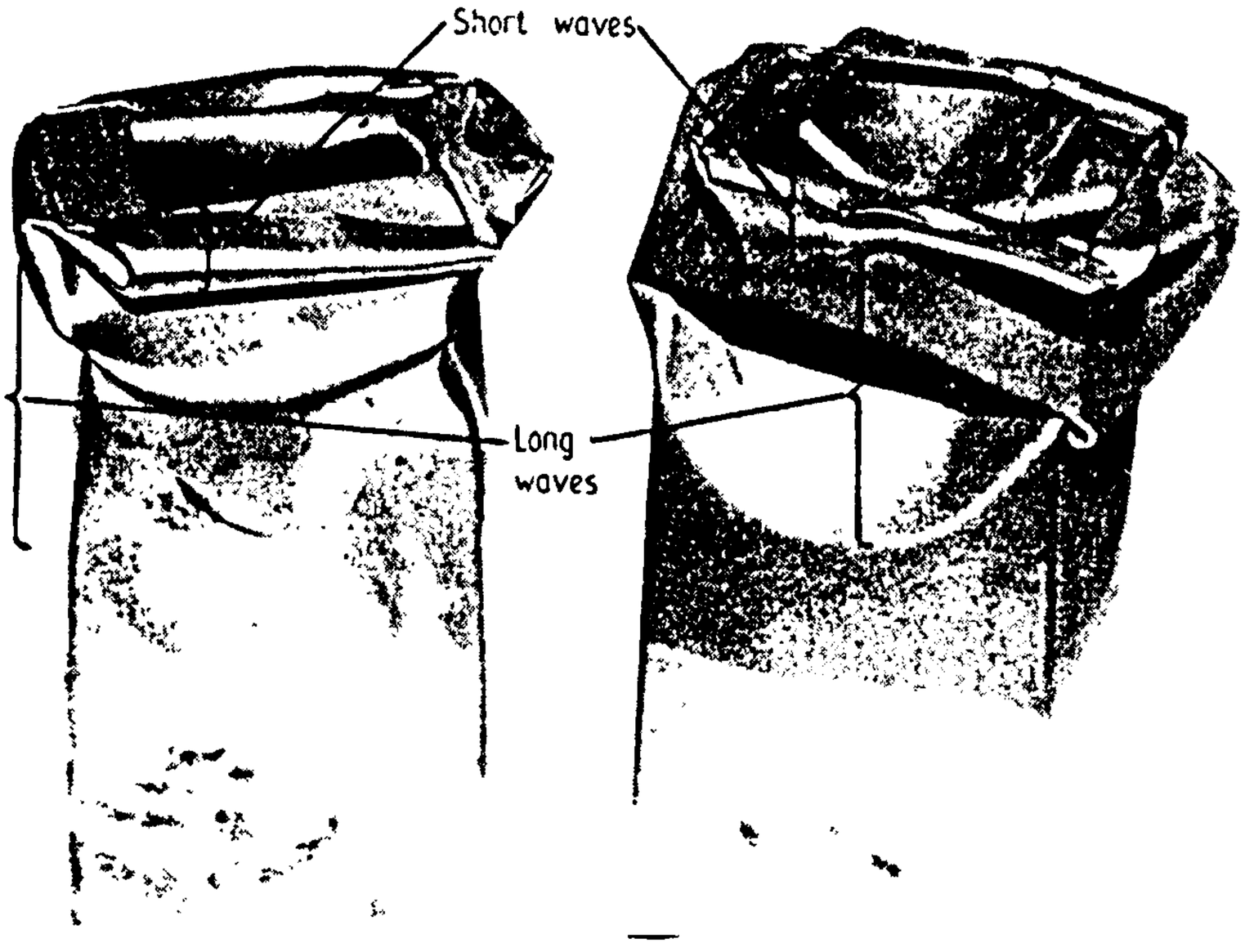

Figure 2.23 : The square tube on the left suffered dynamic crumpling, and the one on the right was crushed quasi-statically [41].

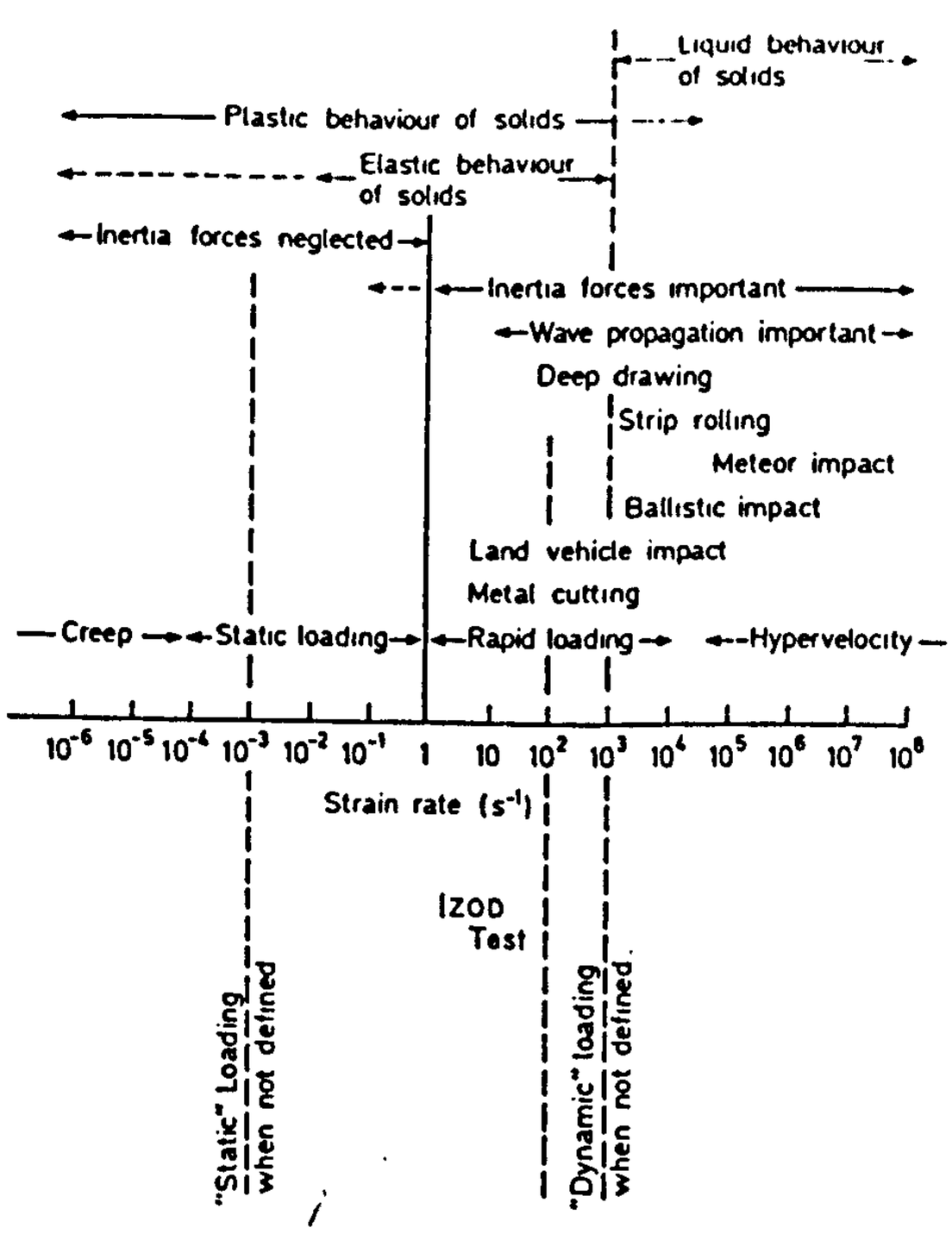

Figure 2.24 : Range of strain rates that are of practical interest [5].

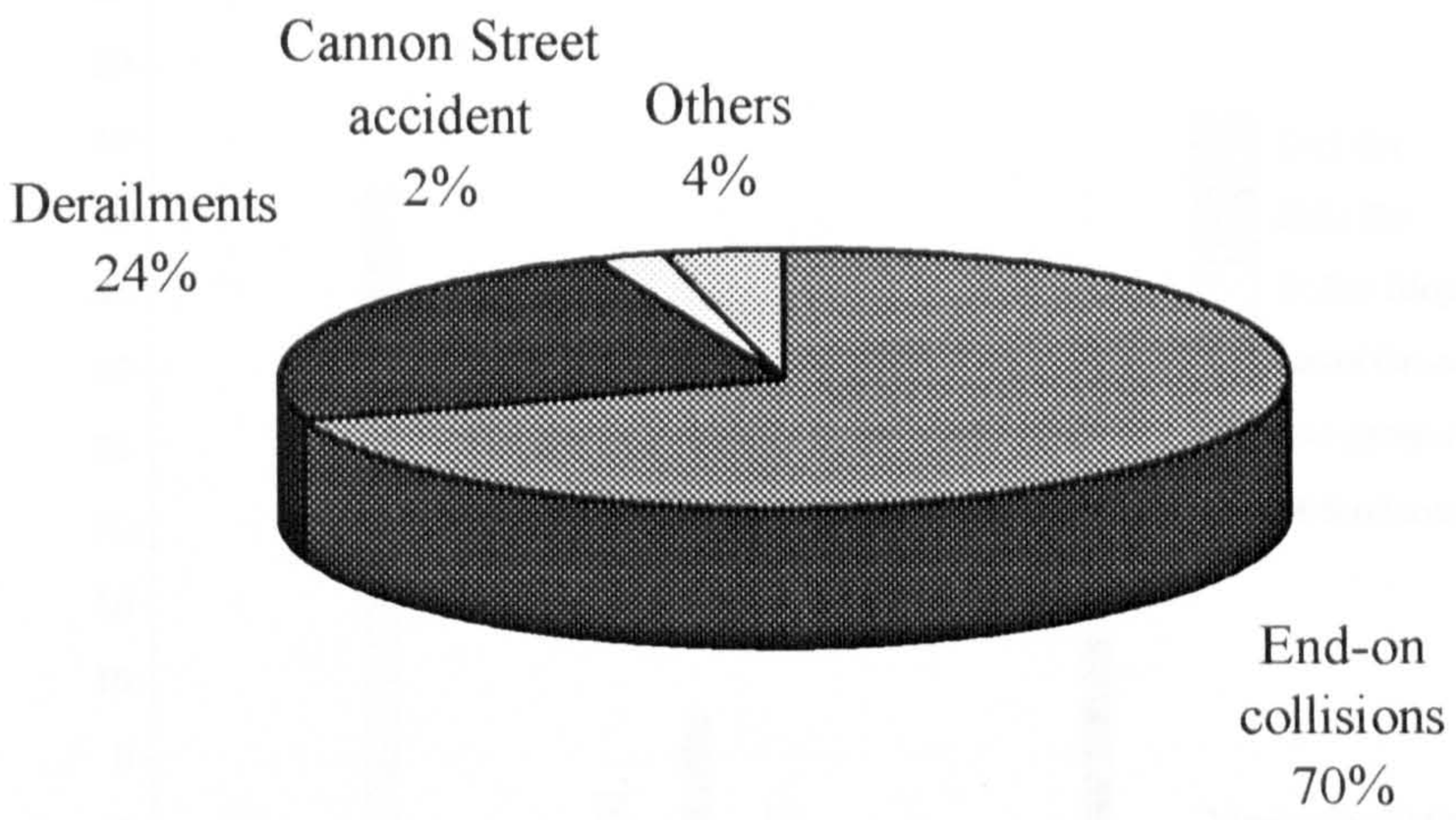

Figure 2.25a : The distribution of past BR accident fatalities according to the type of collisions [47].

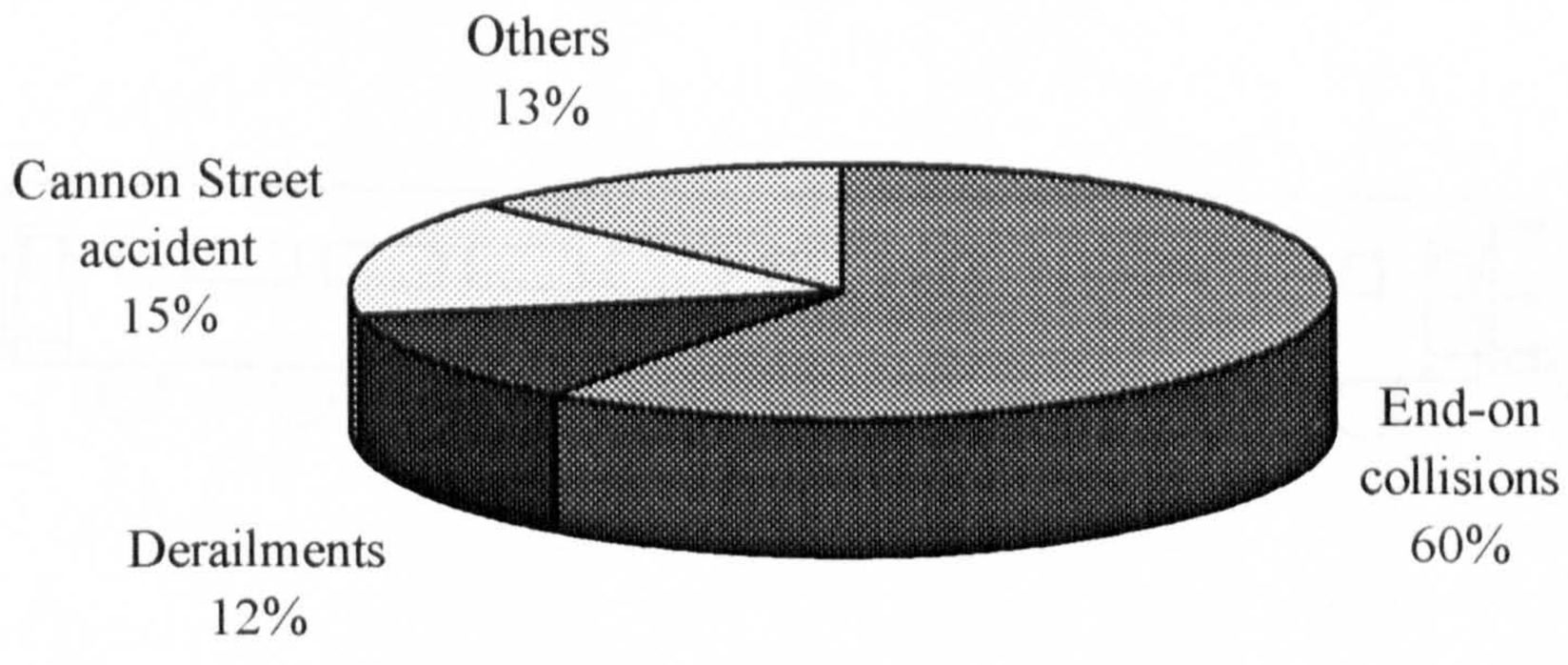

Figure 2.25b : The distribution of past BR accident serious injuries according to the type of collisions [47].

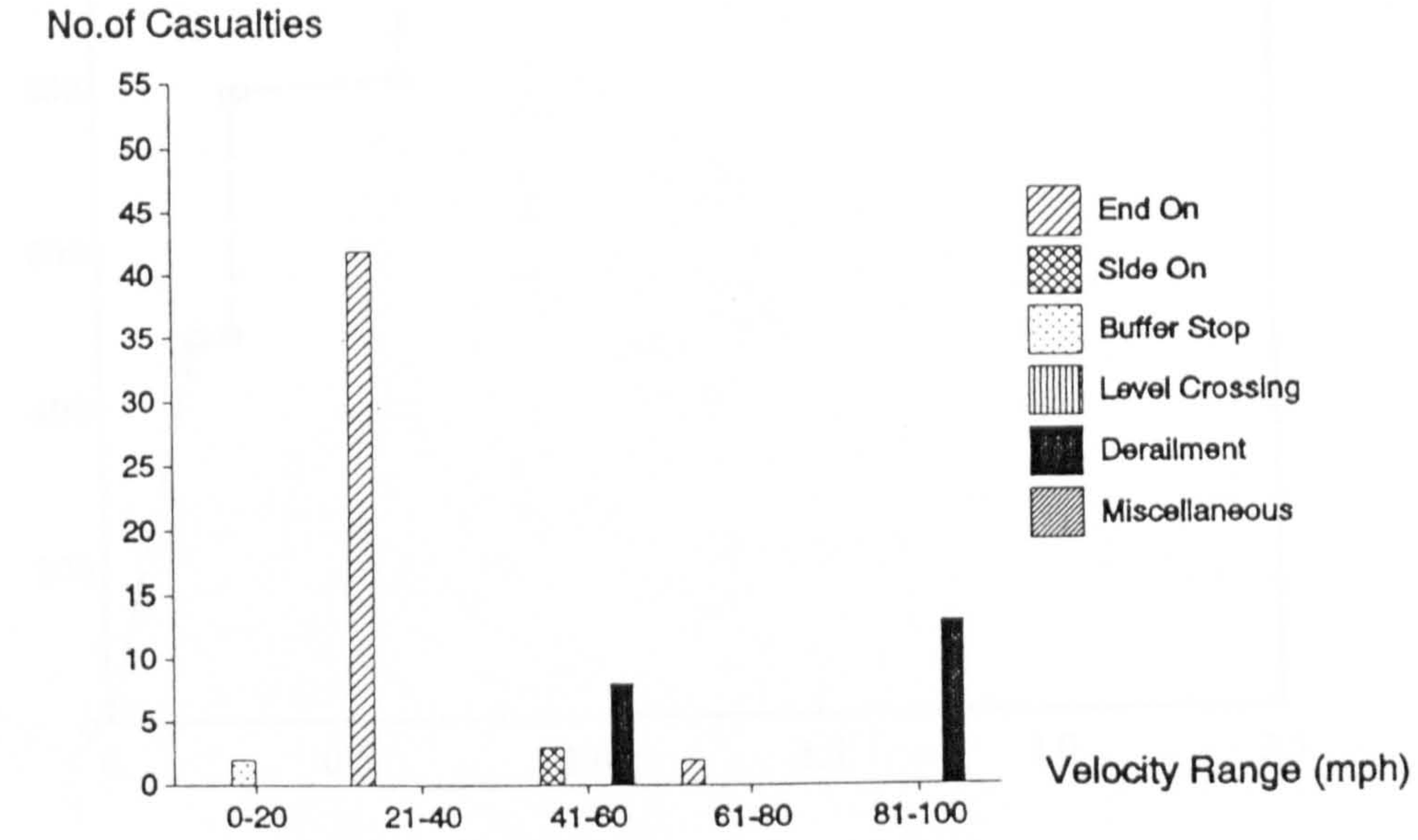

Figure 2.26 : Distribution of passenger fatalities according to velocity and accident type. This chart suggests that derailment is a high speed phenomena [47].

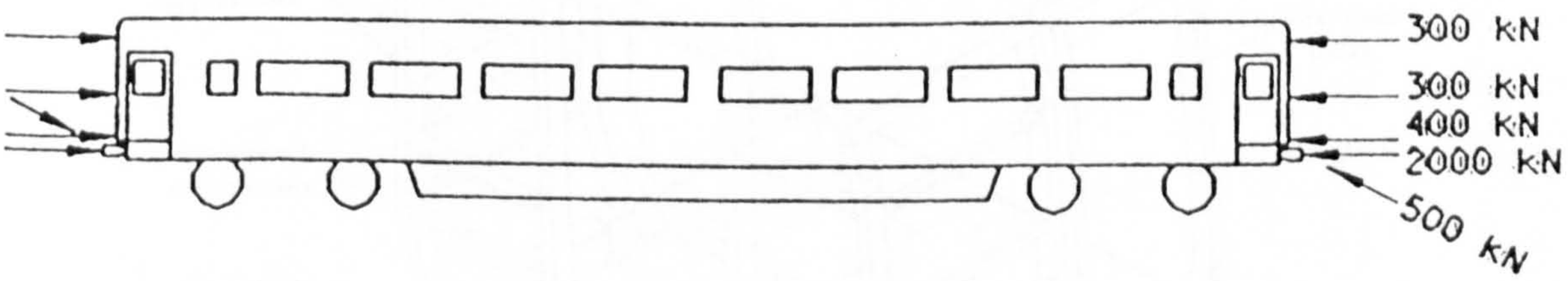

Figure 2.27 : UIC longitudinal loading specification [48].

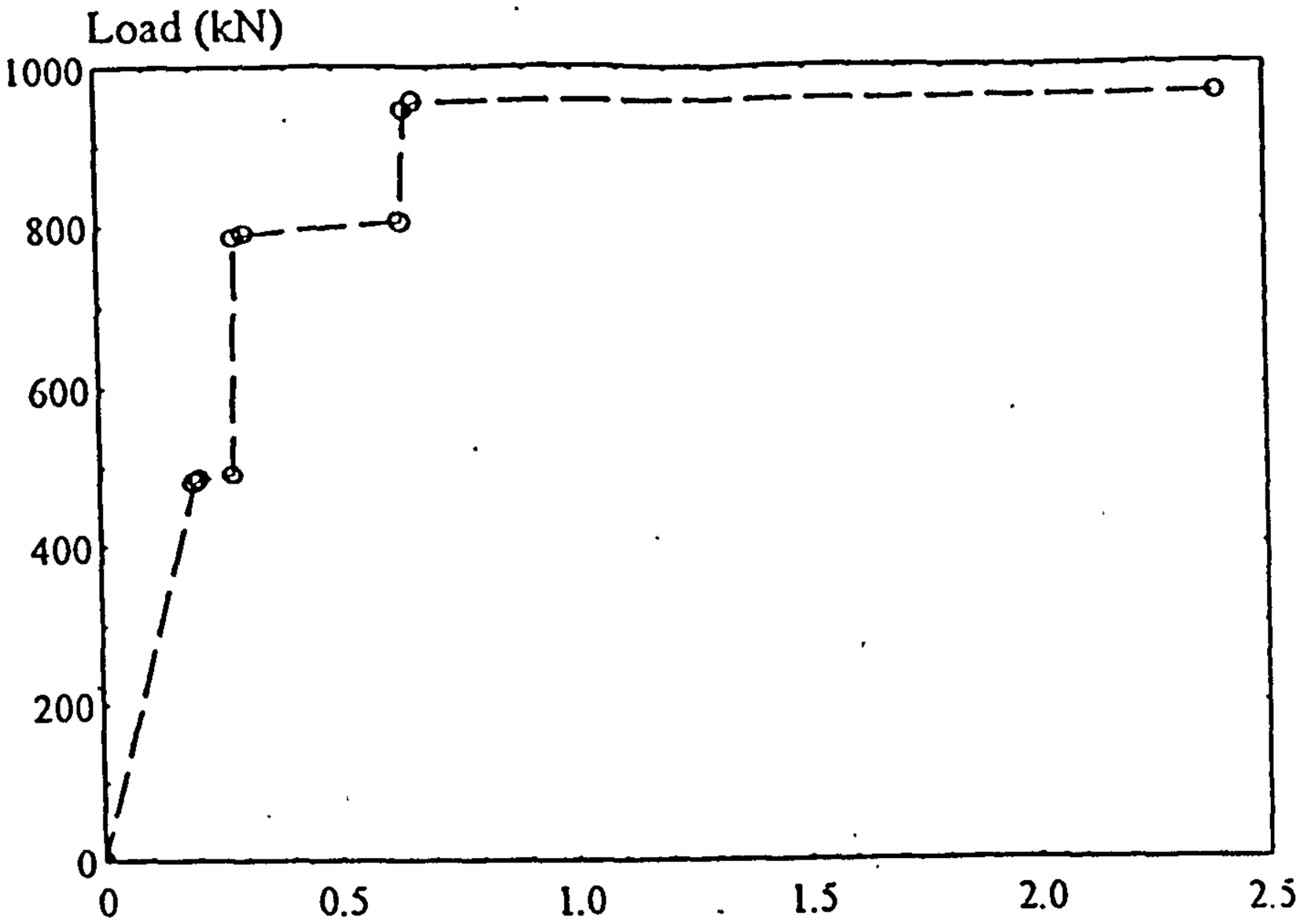

Figure 2.28a : The load-deflection characteristics of the crashworthy coach end-structure as mentioned in reference [50].

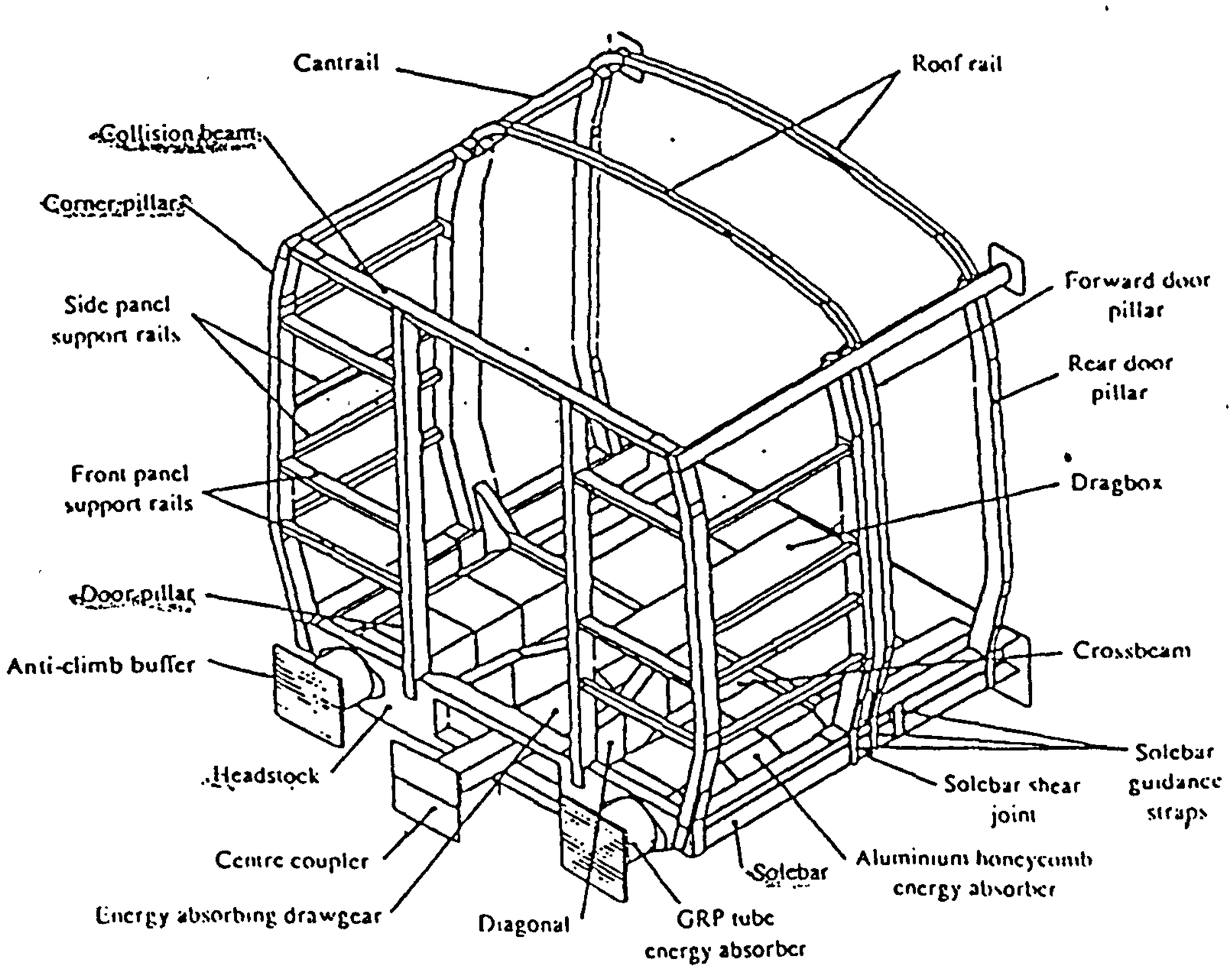

Figure 2.28b : The prototype of the crashworthy coach end-structure as mentioned in reference [50].

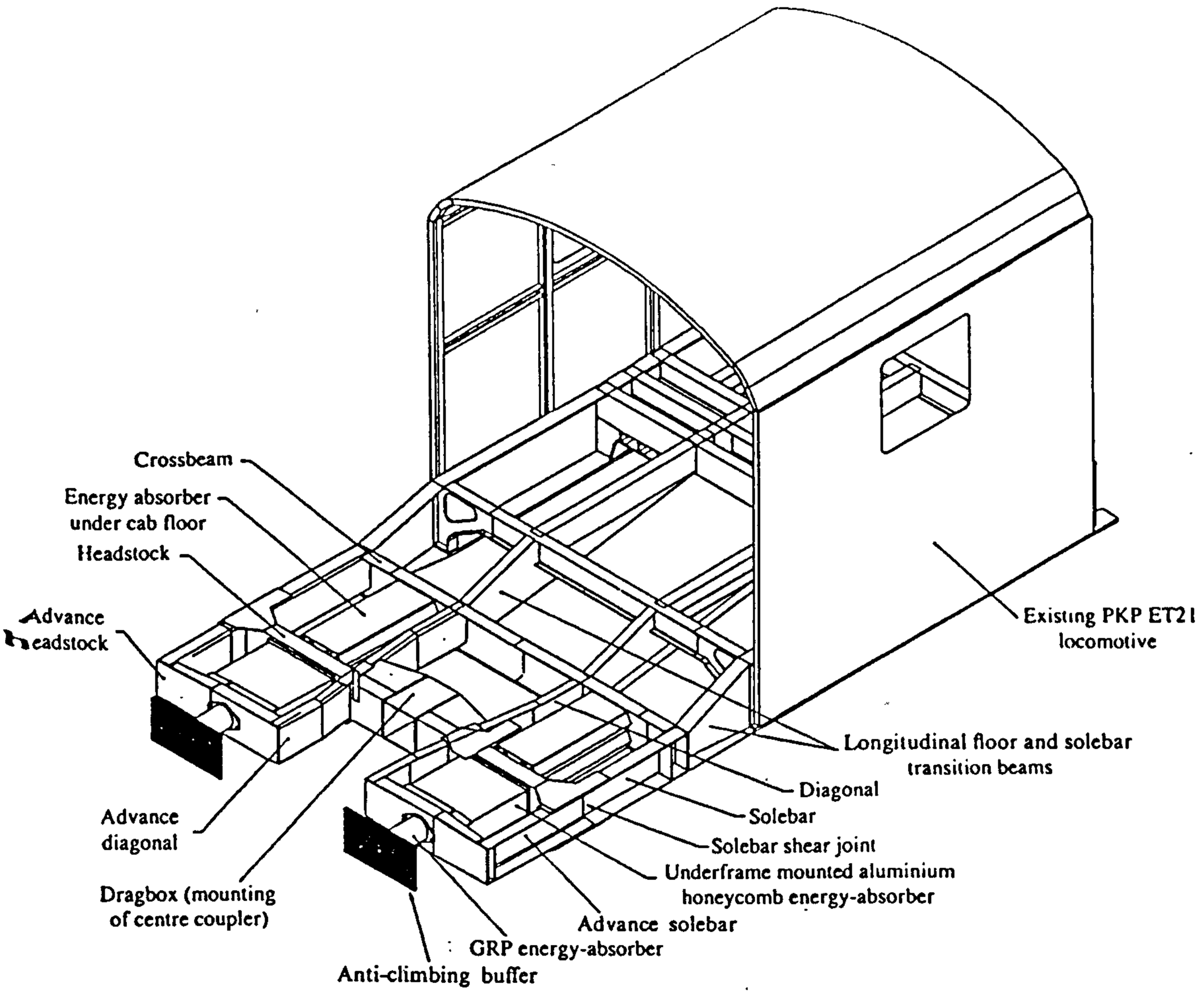

Figure 2.29a : The prototype of the crashworthy coach end-structure used in ORE collision test [50].

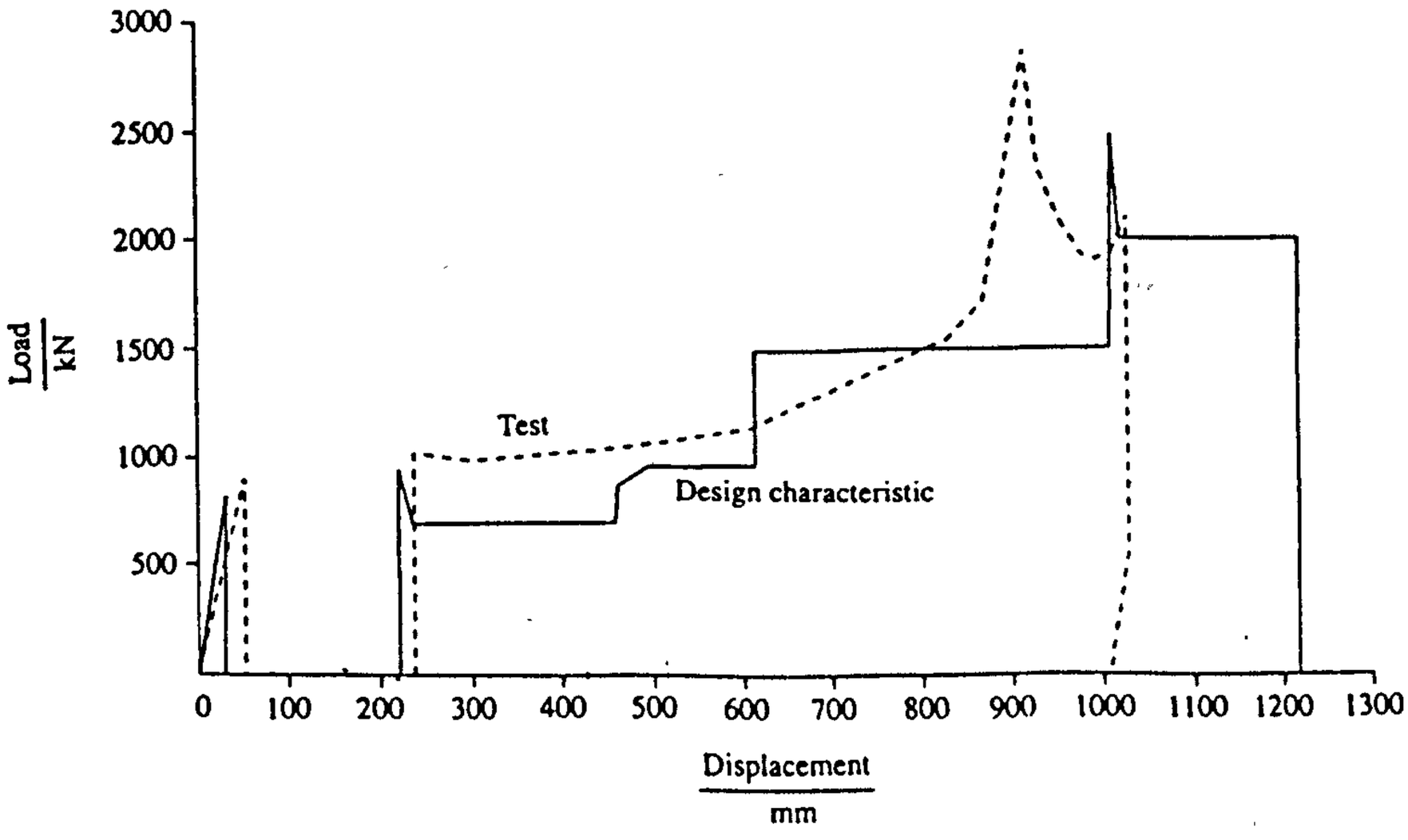

Figure 2.29b : The corresponding load-deflection characteristics of the crashworthy coach end-structure used in ORE collision test [50].

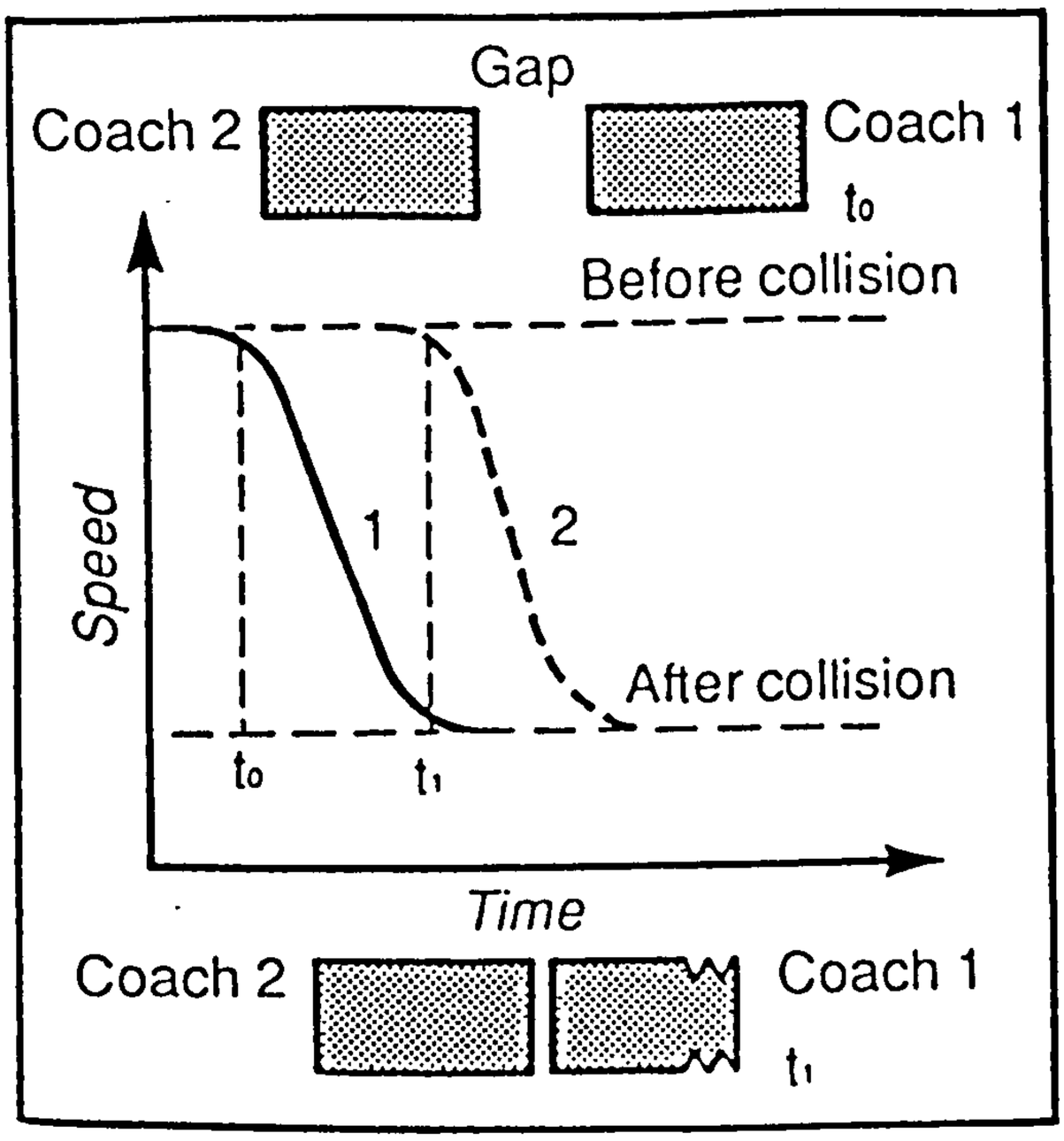

Figure 2.30 : Velocity-time graph showing the concept of energy absorption through sequential collisions along the train [52].

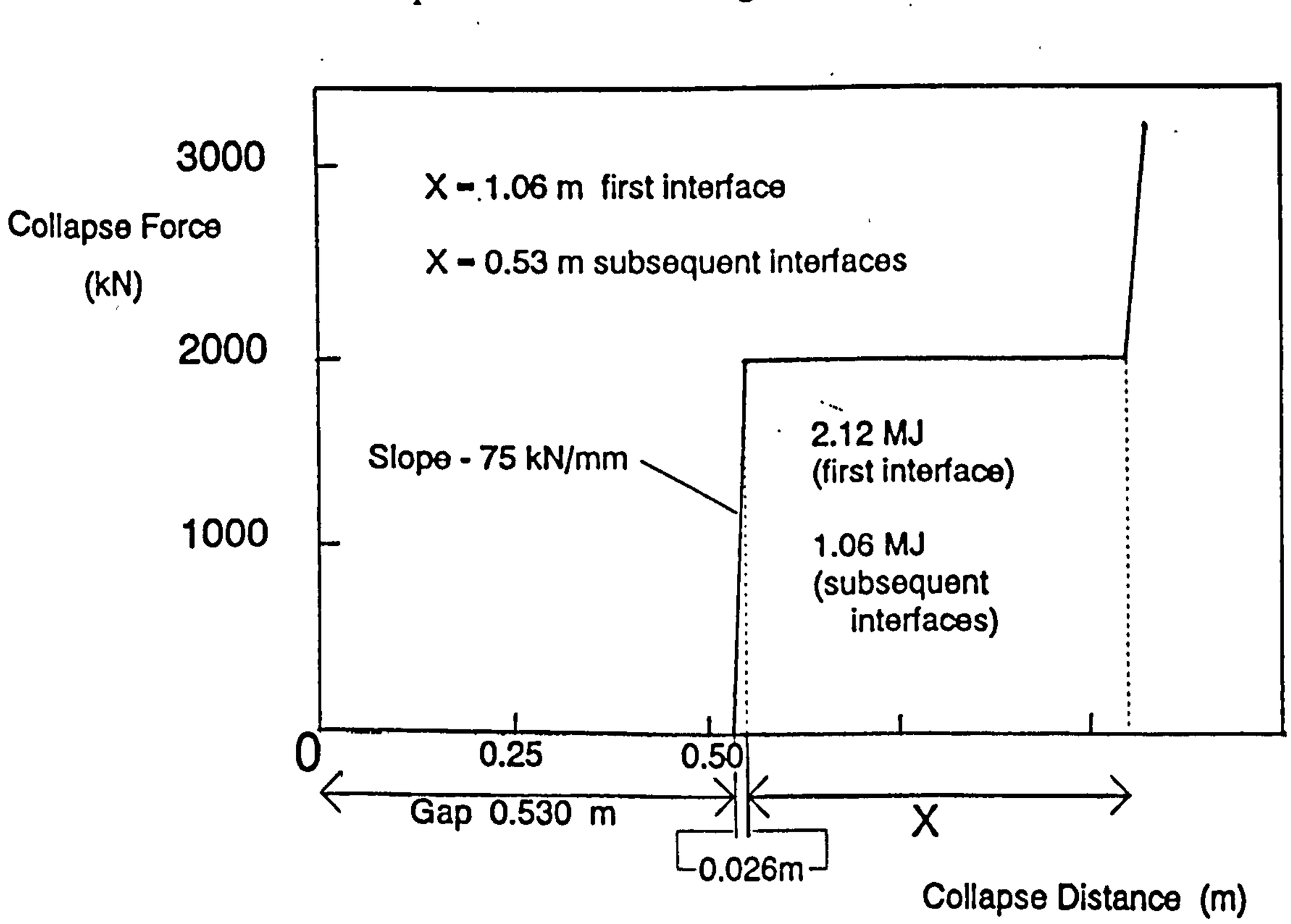

Figure 2.31 : Assumed load-deflection interface characteristic for idealized collisions used in Reference [58].

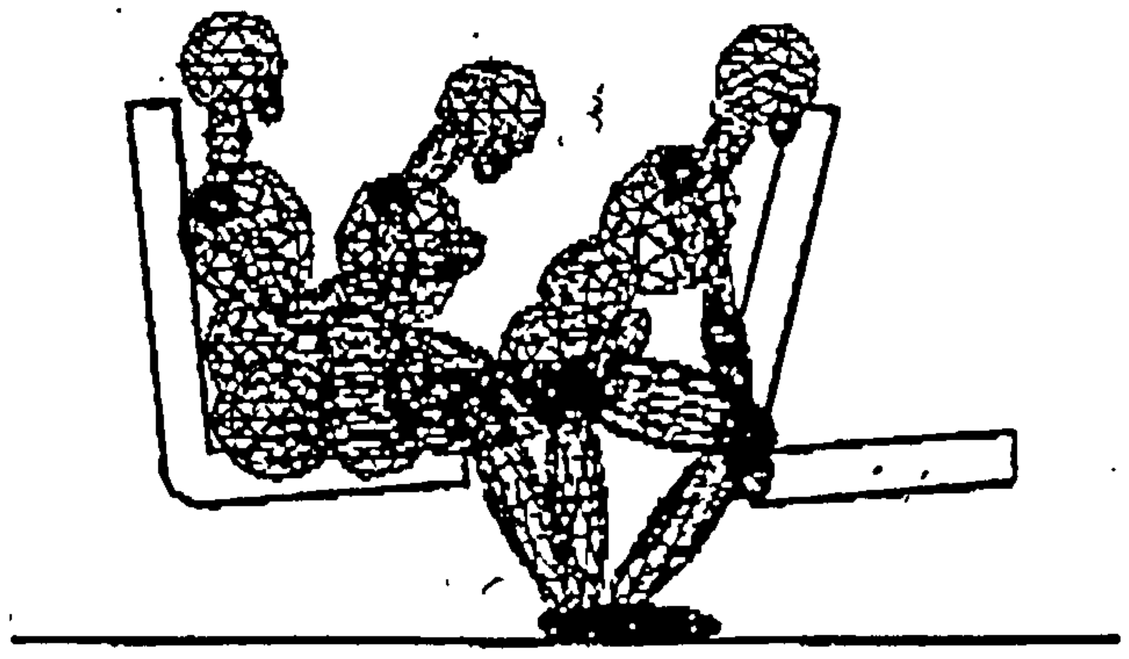

Figure 2.32 : Unrestrained occupant experiencing a secondary collision [60].

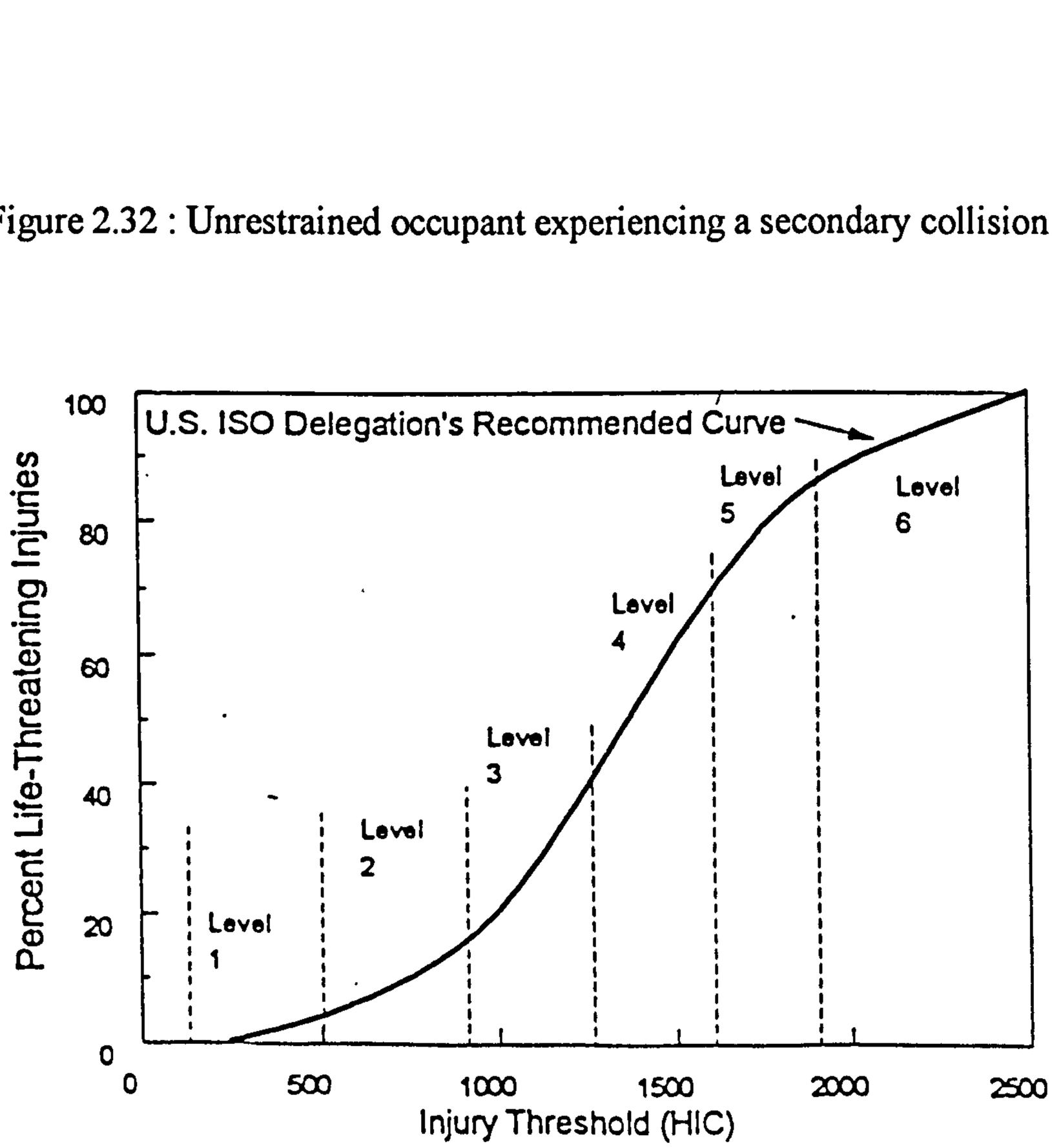

Figure 2.33 : Probability of fatalities as a function of *HIC* [60].

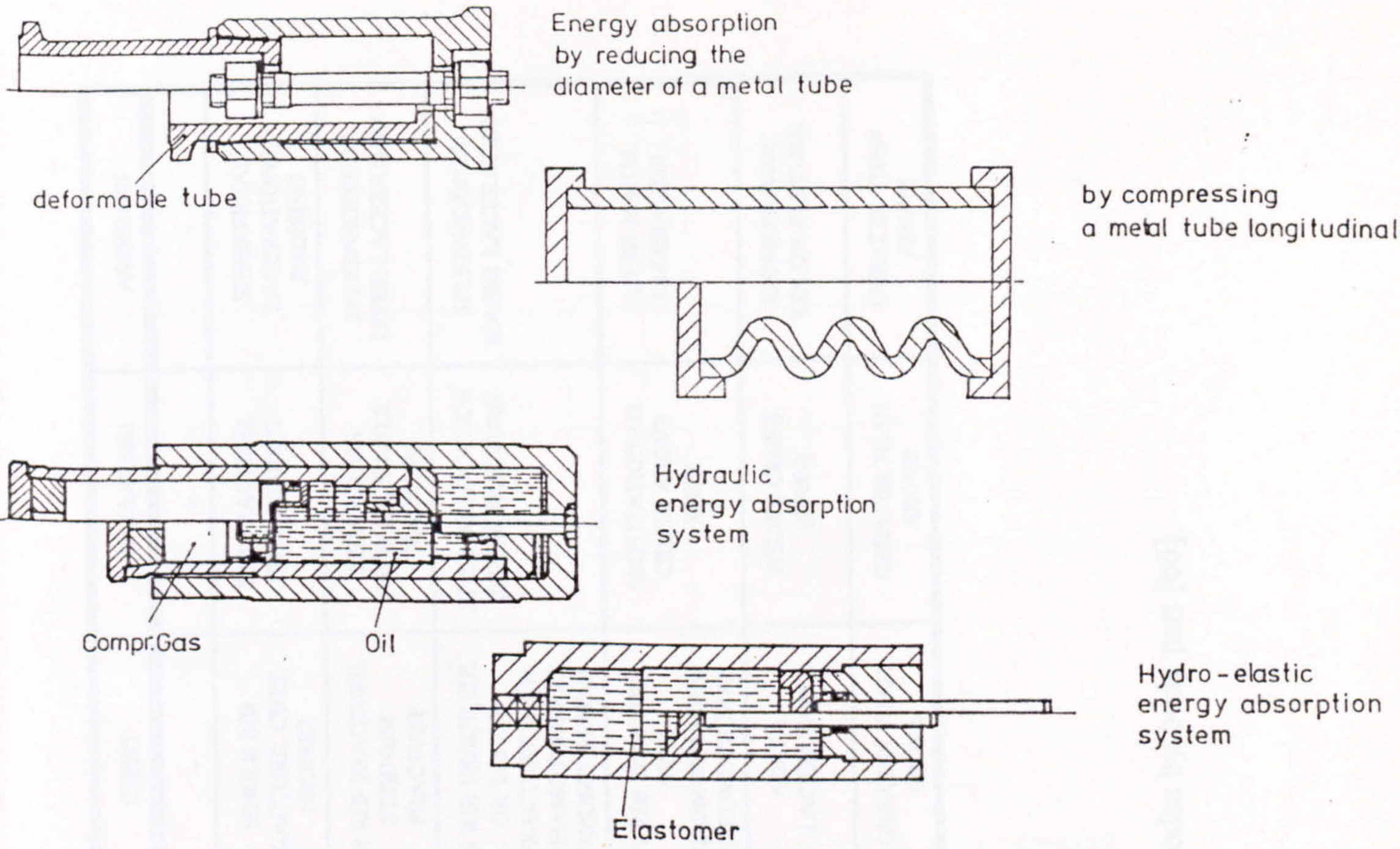

Figure 2.34 : Various type of energy absorbing couplers [61].

Figure 2.35 : A rake of coaches fitted with crashworthy end-structures in pre-test condition [49].

AIS SCORE	GENERAL DESCRIPTION	HEAD	NECK/SPINE	CHEST	LEGS (&ARMS)	ABDOMEN
0	NO INJURY	-	-	-	-	-
1	MINOR INJURY	HEADACHE, CUTS, BRUISES, BROKEN TEETH/NOSE	ACUTE STRAIN, CUTS, BRUISES	SINGLE RIB FRACTURE, CUTS, BRUISES	TOE FRACTURE, CUTS, BRUISES	SUPERFICIAL LACERATIONS, BRUISING
2	MODERATE INJURY	UNCONSCIOUS LESS THAN 1 HOUR, LINEAR FRACTURE	MINOR FRACTURE, NO CORD INVOLVEMENT	2-3 RIB FRACTURE, STERNUM FRACTURE	TIBIA/PELVIS/ PATELLA, SIMPLE FRACTURE	SPLEEN/KIDNEY/ LIVER LACERATION
3	SERIOUS INJURY	UNCONSCIOUS 1-6 HOURS, DEPRESSED FRACTURE	RUPTURED DISC, NERVE ROOT DAMAGE	>3 RIB FRACTURE OR 2-3 RIB FRACTURE WITH HEAMOTHORAX/ PNEUMOTHORAX	KNEE DISLOCATION FEMUR FRACTURE	SPLEEN/KIDNEY MAJOR LACERATION
4	SEVERE INJURY, WITH SIGNIFICANT THREAT TO LIFE	UNCONSCIOUS 6-24 HOURS, OPEN FRACTURE	INCOMPLETE CORD SYNDROME	>3 RIB FRACTURE WITH HAEMOTHORAX/ PNEUMOTHORAX	AMPUTATION OR CRUSH ABOVE KNEE	LIVER MAJOR LACERATION
5	CRITICAL INJURY, WITH MAJOR THREAT TO LIFE	UNCONSCIOUS >24 HOURS, LARGE HEMATOMA	QUADRIPLEGIA	AORTA LACERATION	PELVIS CRUSH (OPEN)	KIDNEY/LIVER/ COLON RUPTURE
6	MAXIMUM, CURRENTLY UNTREATABLE	GREATER THAN ABOVE	GREATER THAN ABOVE	GREATER THAN ABOVE	GREATER THAN ABOVE	GREATER THAN ABOVE

Figure 2.36 : Description and examples of AIS codes by body part [66].

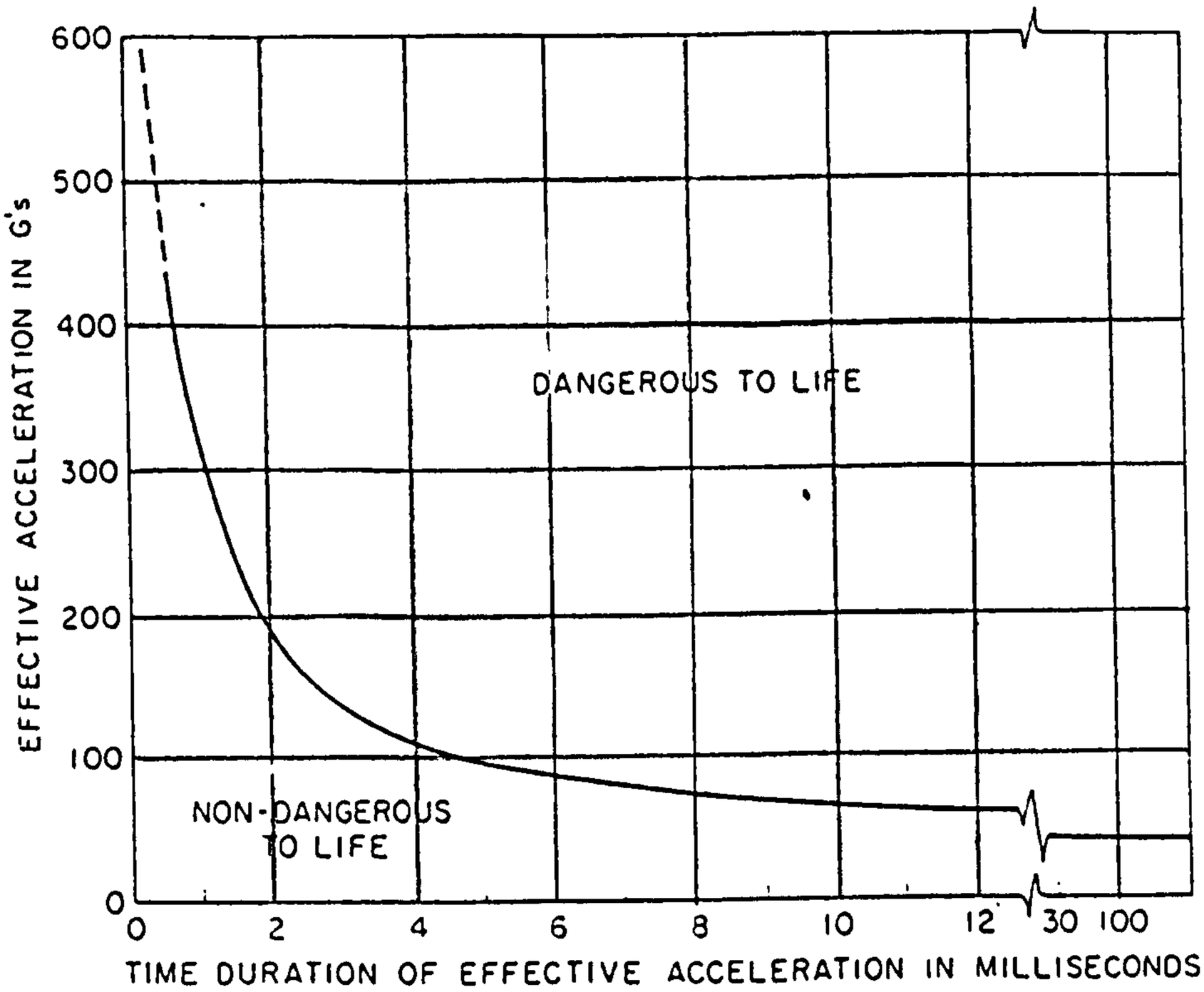

Figure 2.37 : Impact tolerance for human brain in forehead impacts against plane, unyielding surfaces [68].

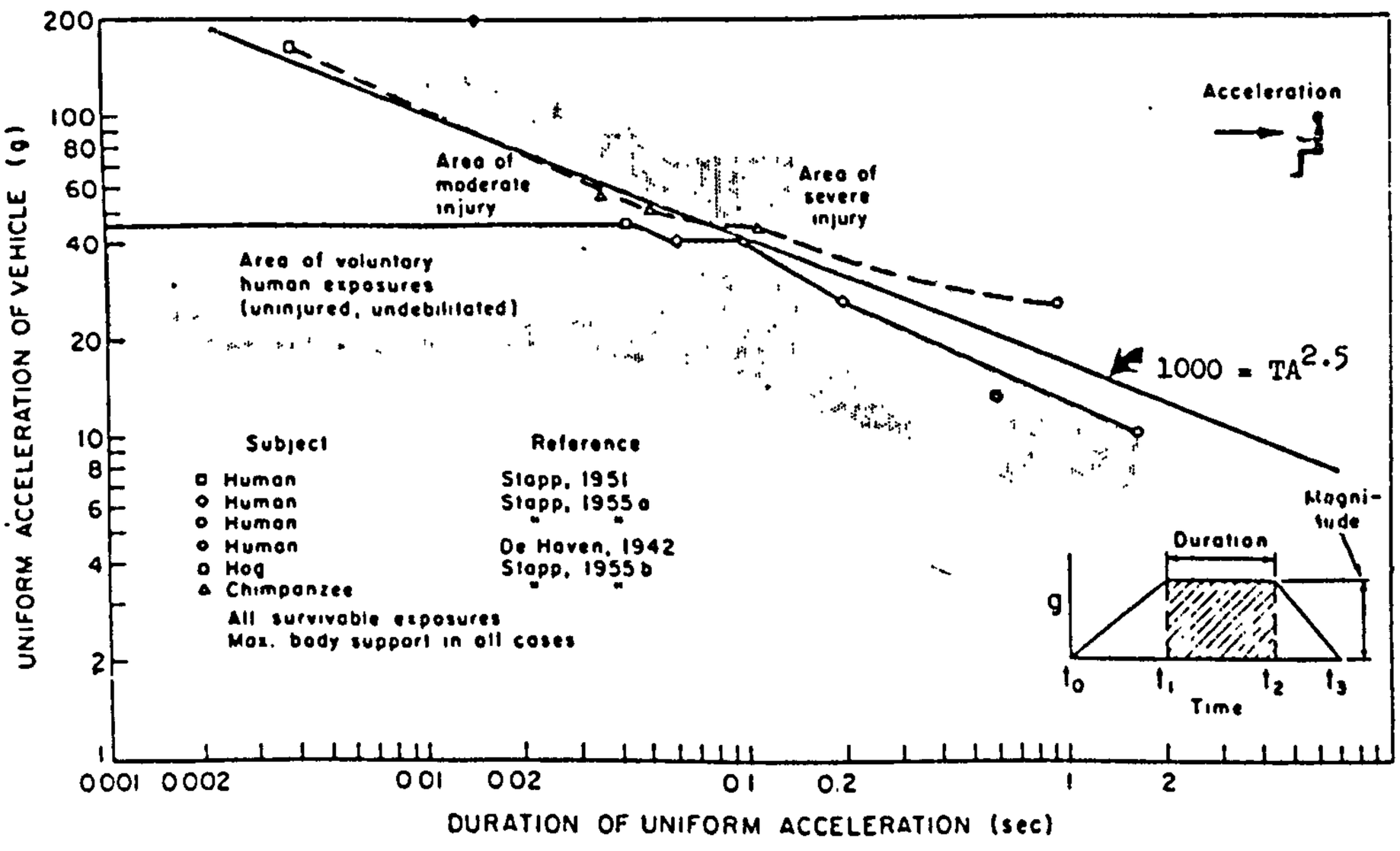

Figure 2.38 : Frontal deceleration versus duration threshold from experimental data. [68].

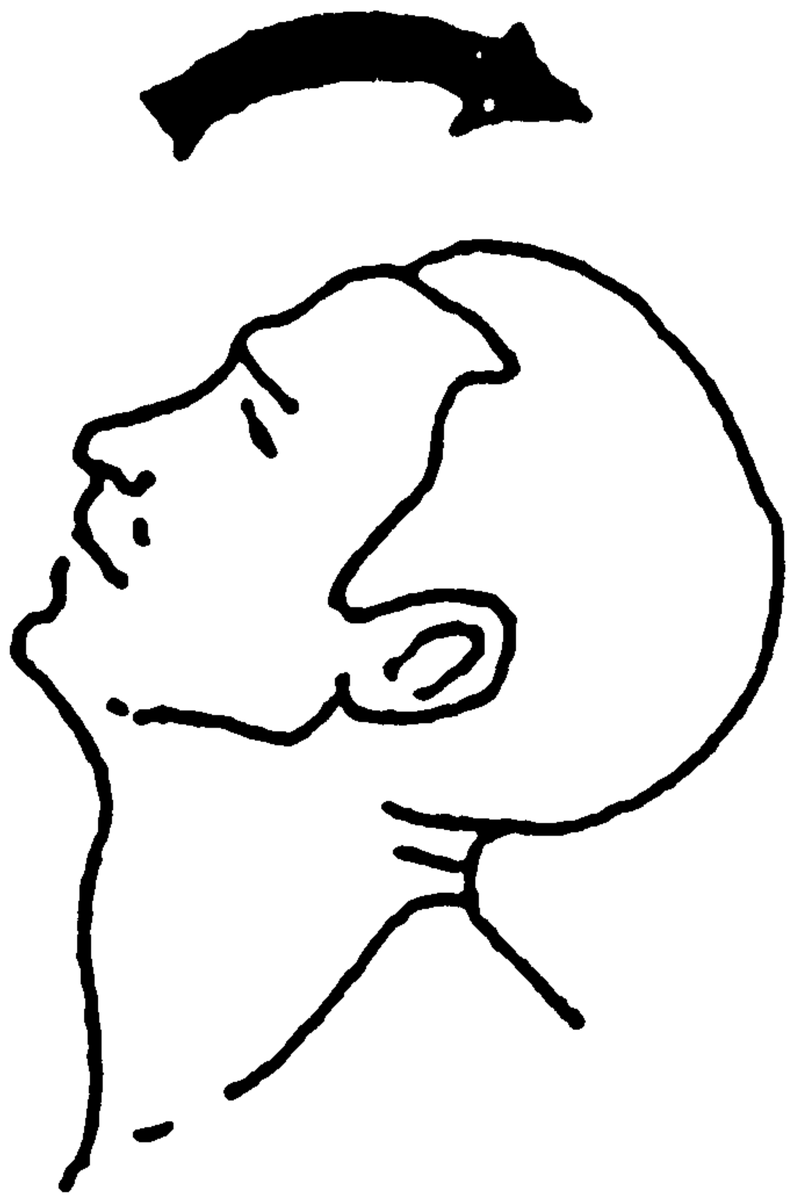

Figure 2.39 : The extension bending mechanism, commonly caused by a low level seat back to a backward facing occupant [65].

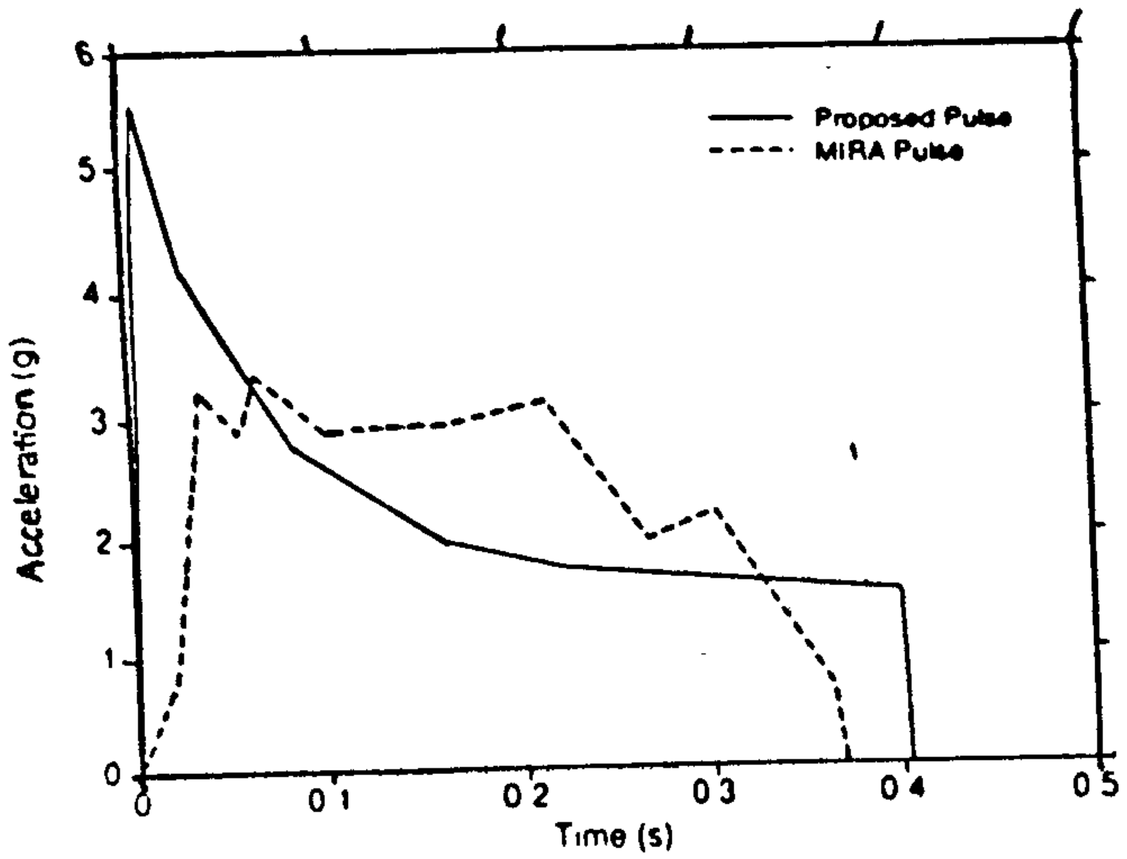

C2 PULSE

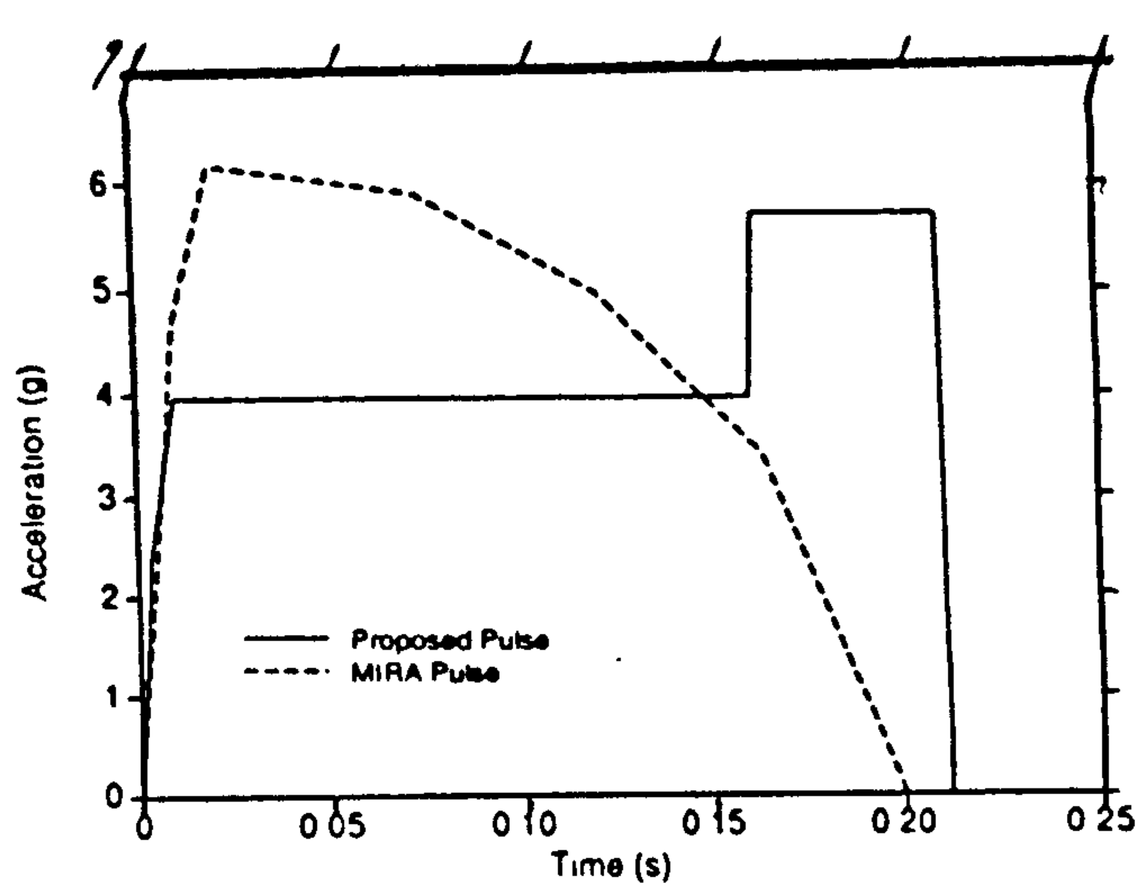

C3PULSE

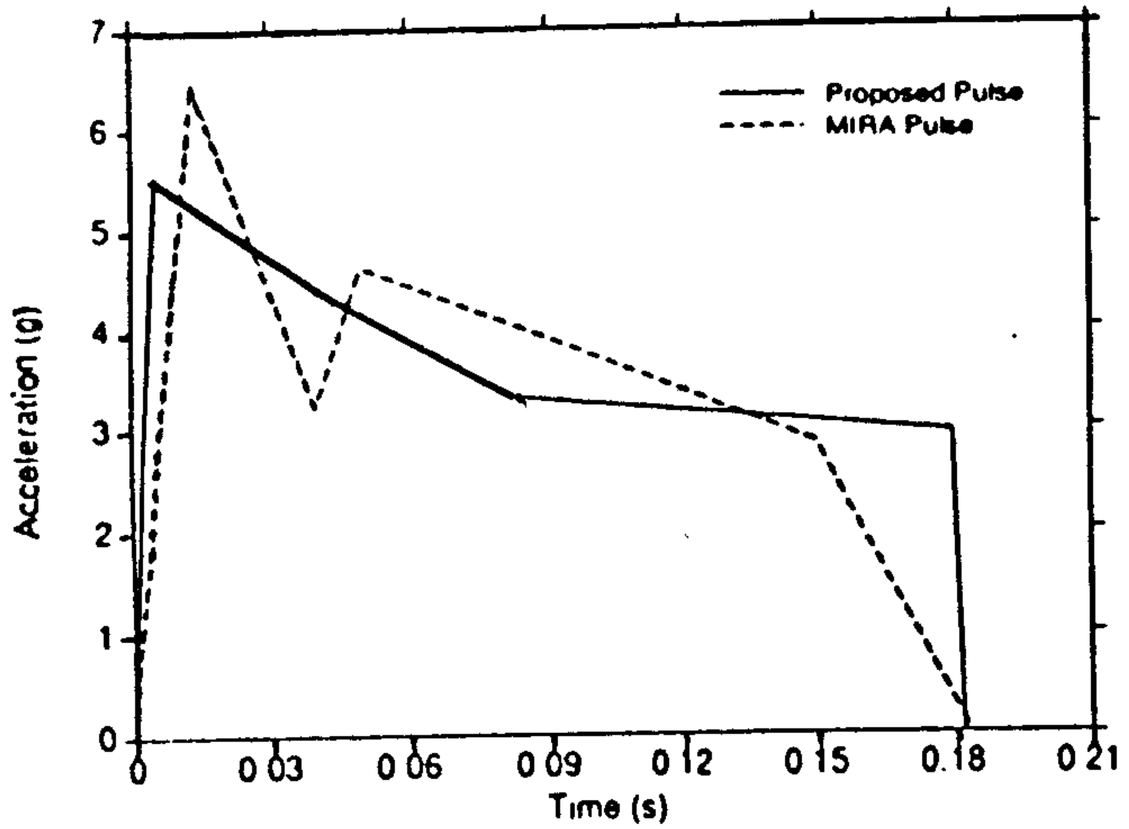

C6 PULSE

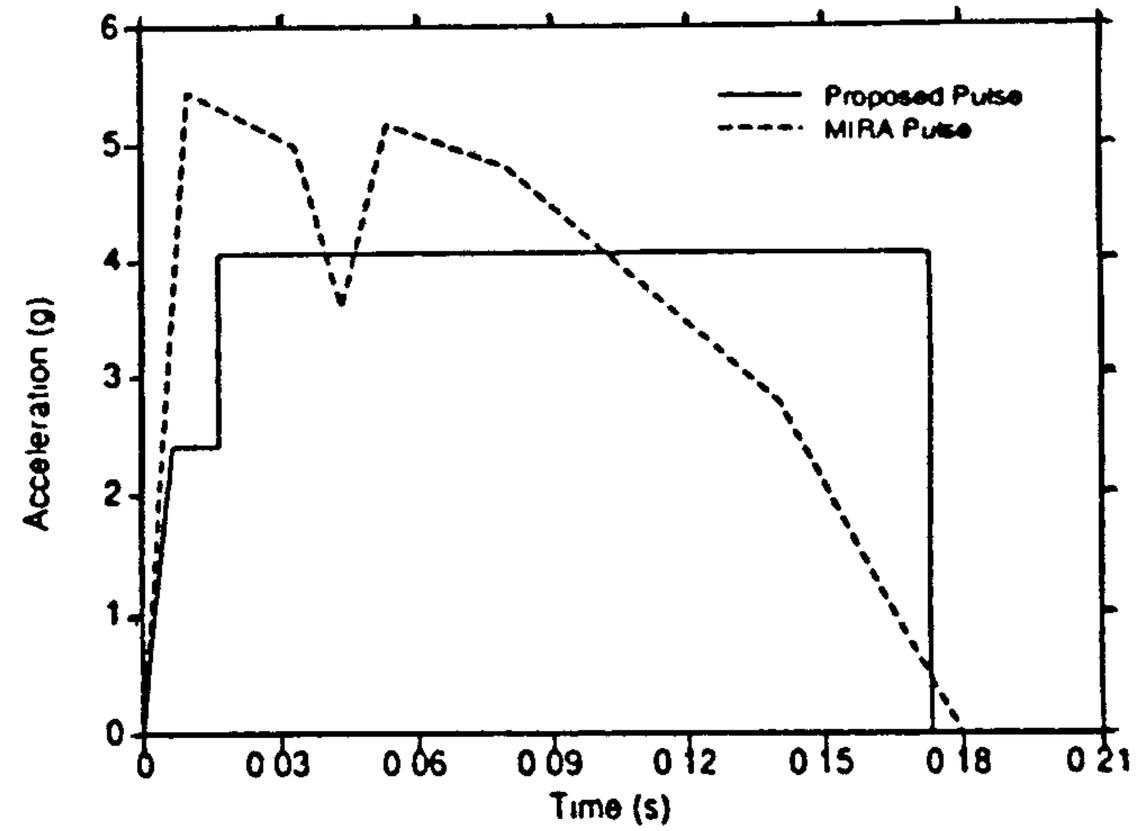

C7 PULSE

Figure 2.40 : Proposed crash pulses and pulses used in MIRA sled tests [71].

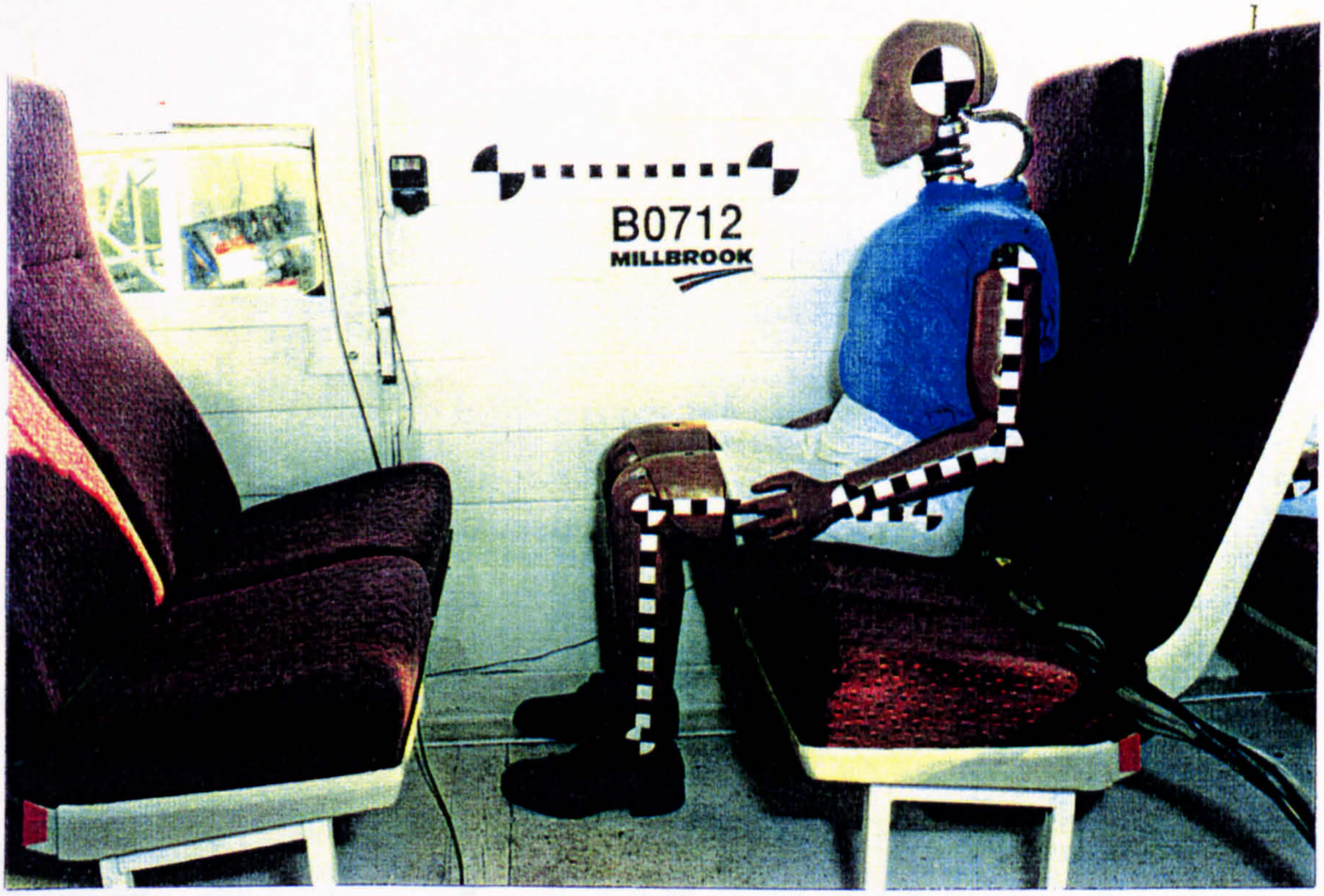

Figure 2.41a : The pre-test position of a forward facing dummy in open-bay seats [75].

Figure 2.41b : The post-test position of the forward facing dummy in open-bay seats [75].

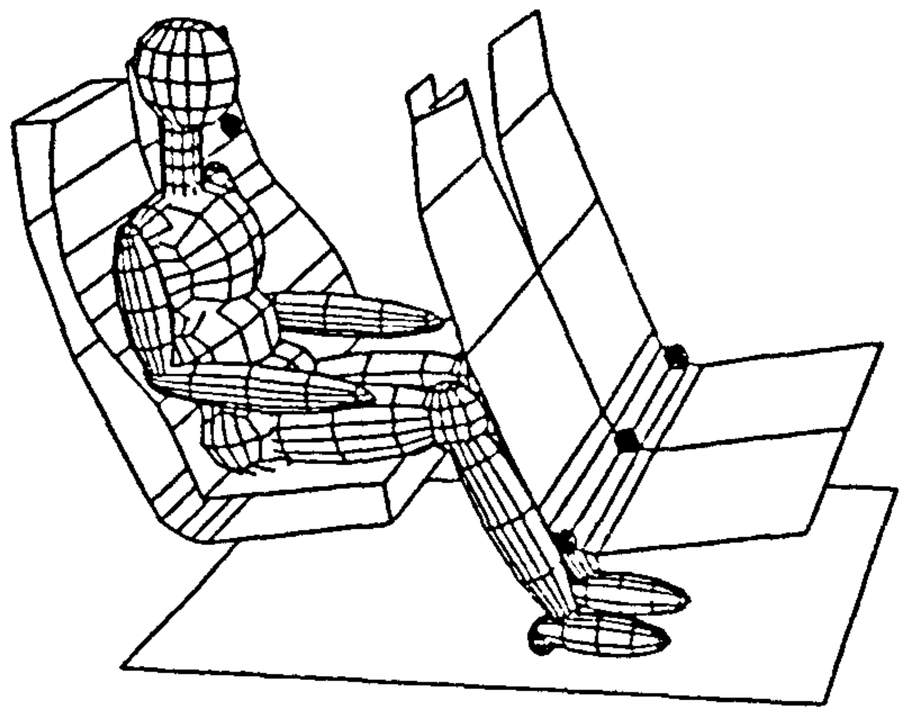

TIME=0ms

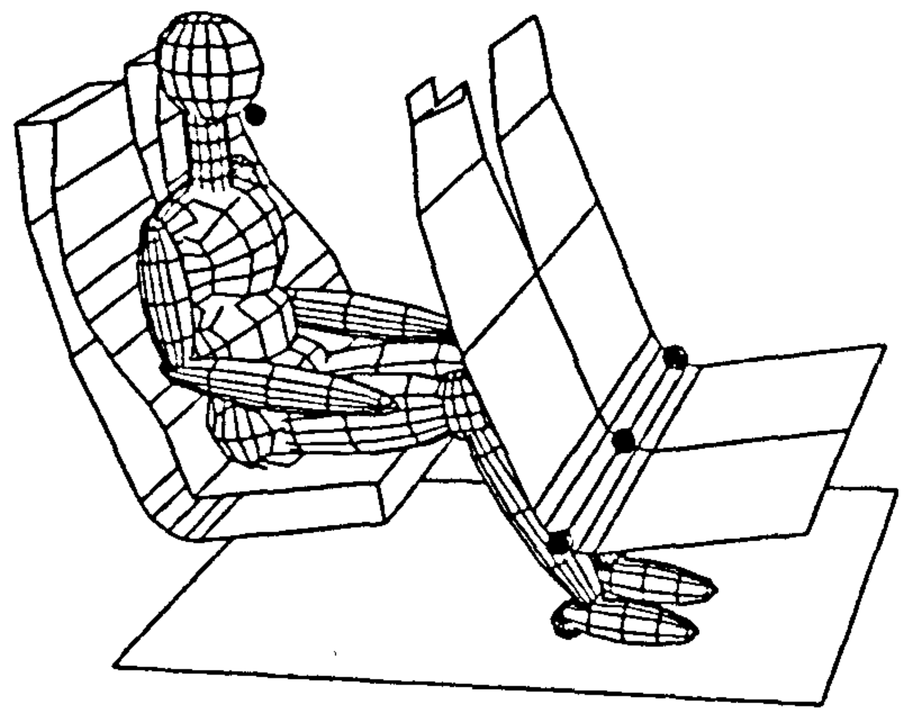

TIME=50ms

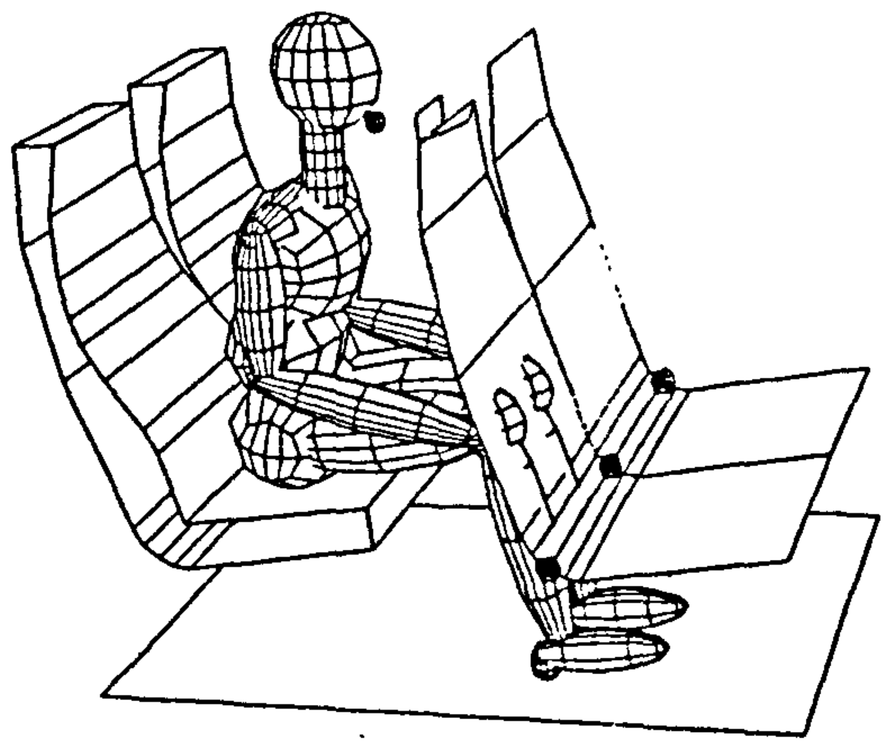

TIME=100ms

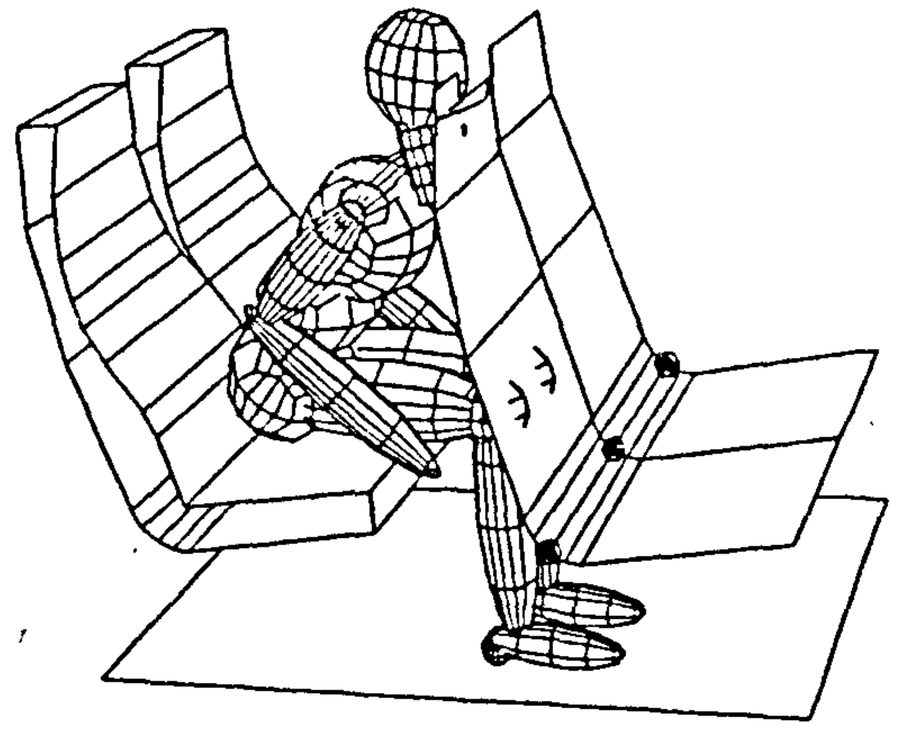

TIME=150ms

Figure 2.42 : The animation of occupant in uni-directional seats (with a grab handle) and subjected to the C3 pulse [72].

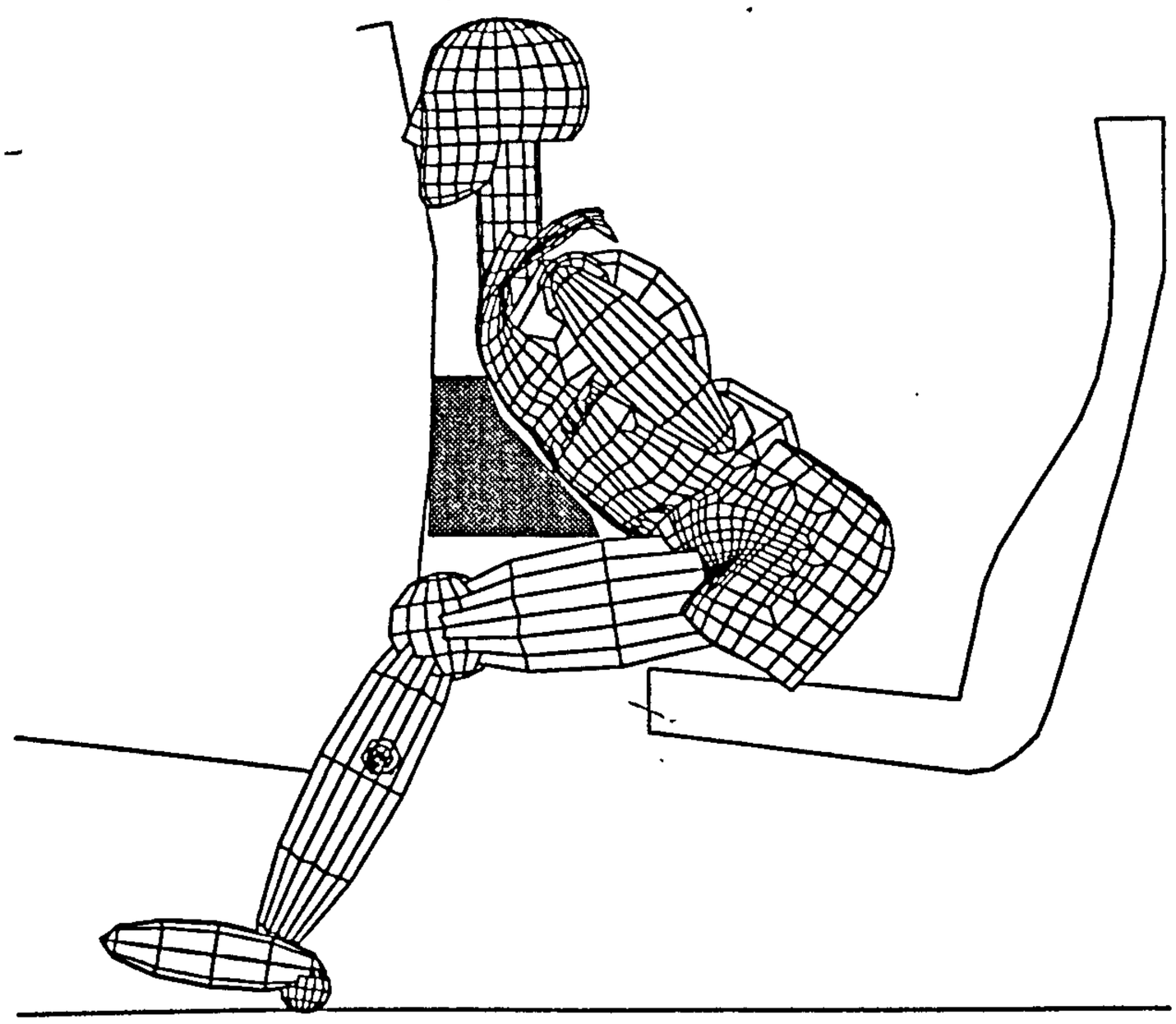

Figure 2.43 : The 'safe' space envelope for mounting a fold-down table at the rear of a unidirectional seat [73].

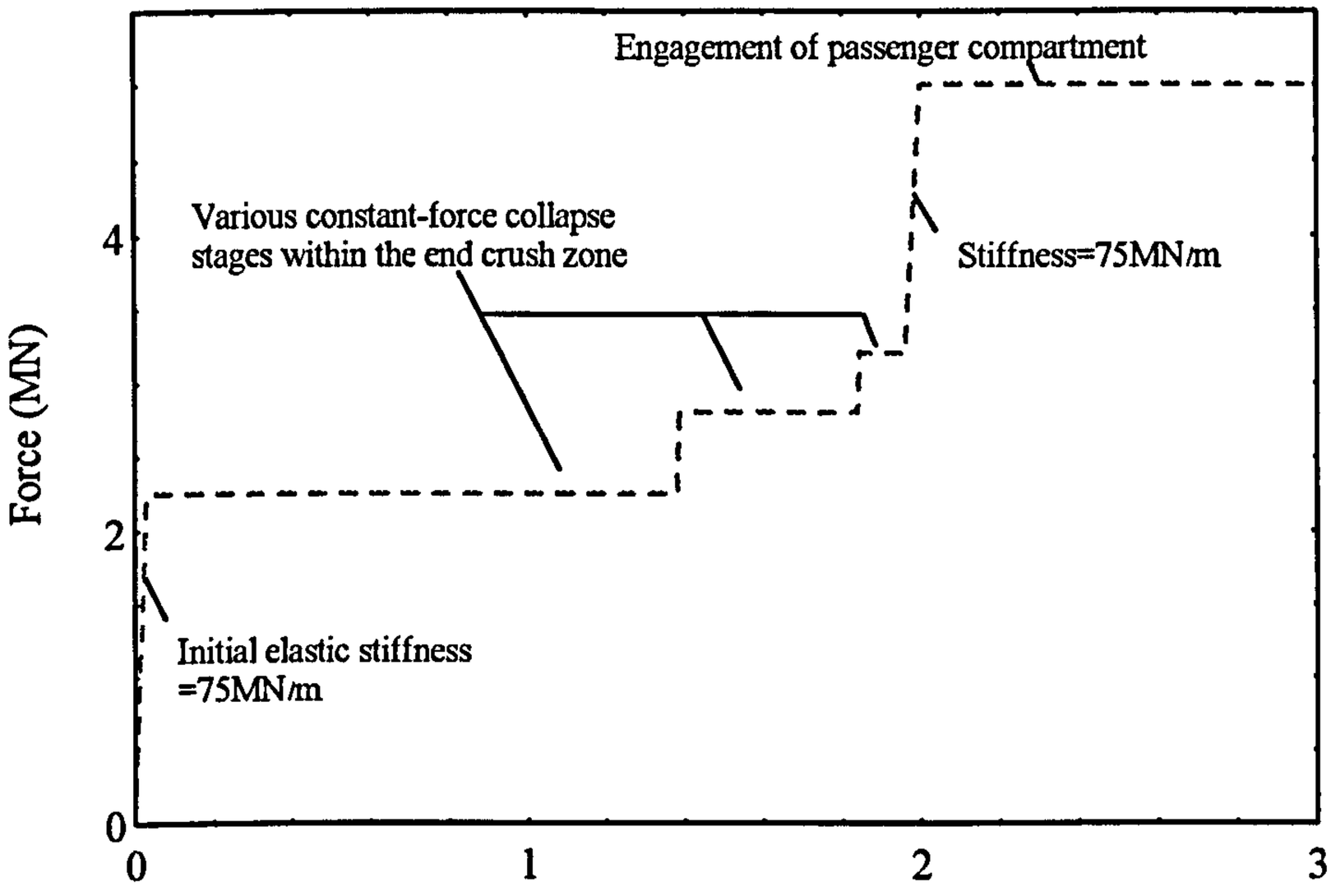

Figure 3.1 : The load-deflection characteristic of a steel crashworthy vehicle end structure designed for a 35tonne coach.

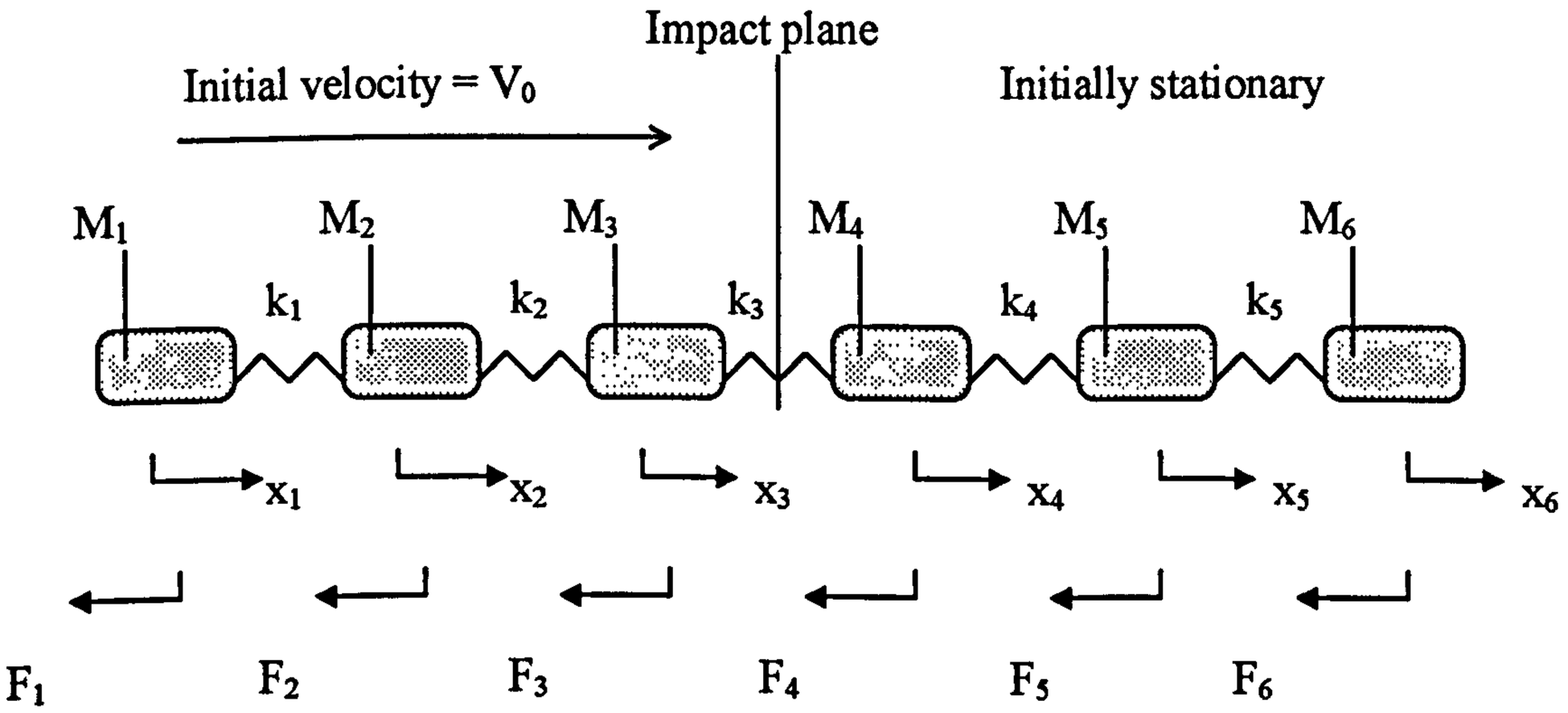

Figure 3.2 : A moving three-coach to a stationary three-coach collision model, including wheel-track friction.

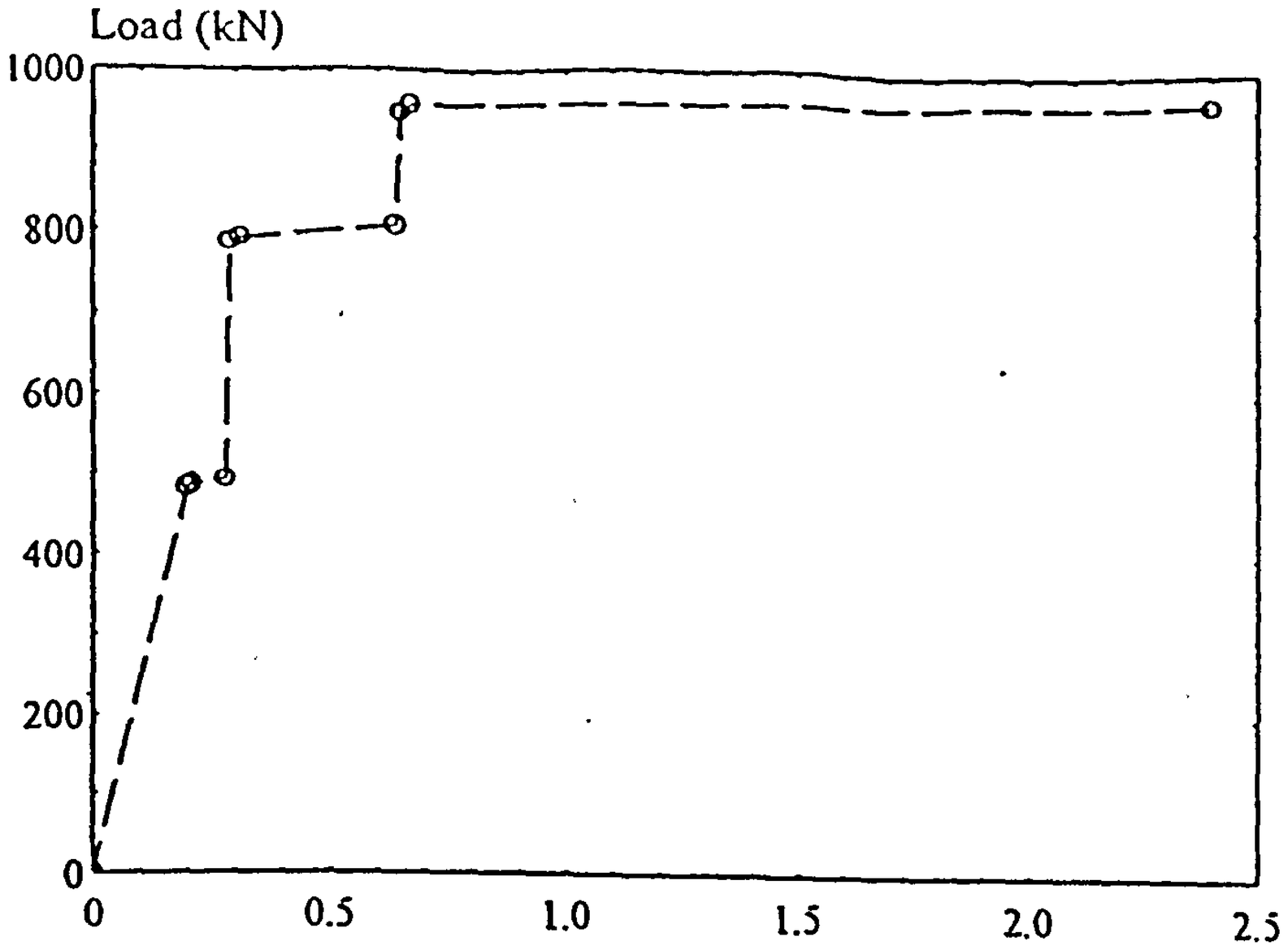

Figure 3.3a : The load-deflection characteristic of the crashworthy coach end-structure as mentioned in reference [2].

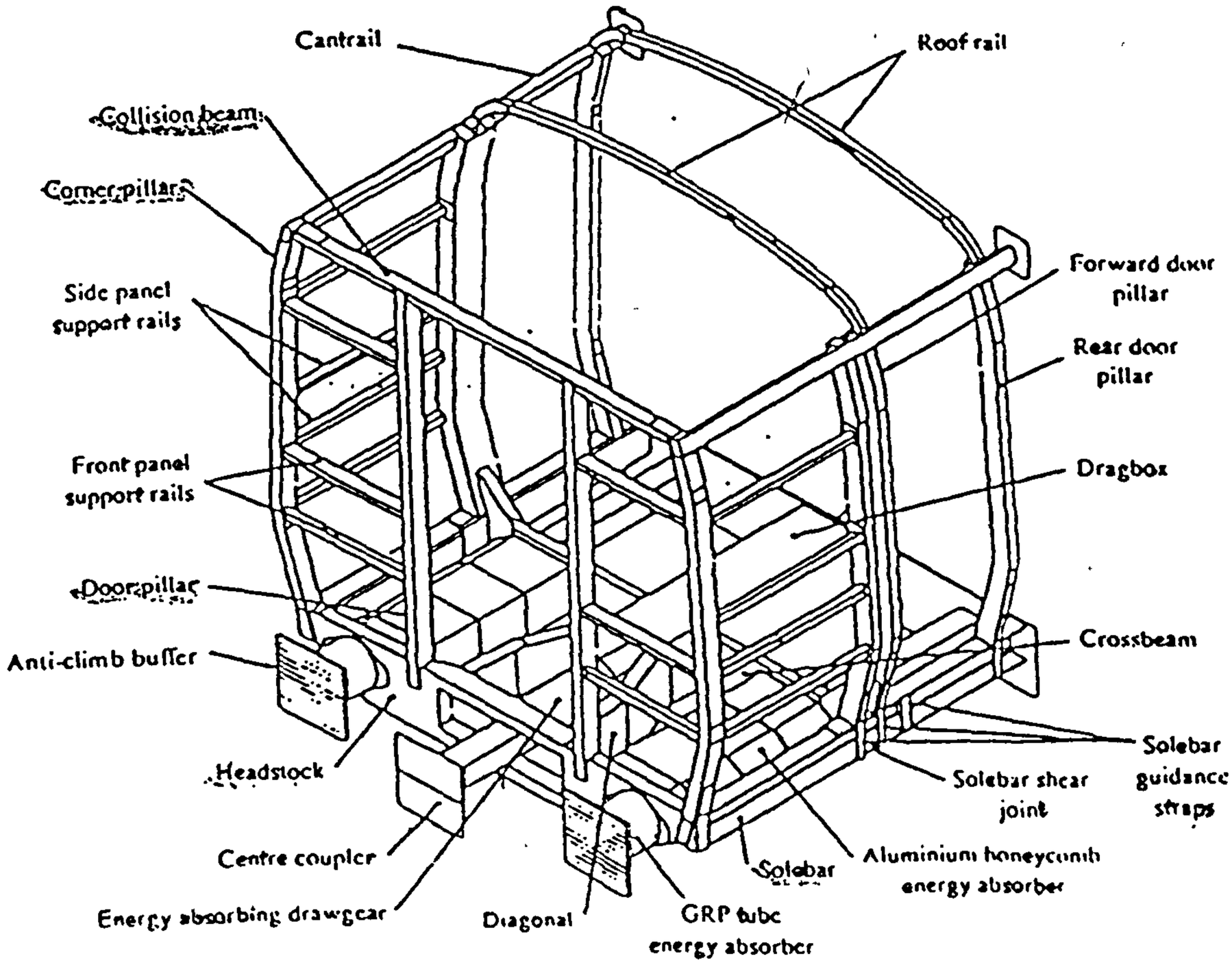

Figure 3.3b : The prototype of the crashworthy coach end-structure as mentioned in reference [2].

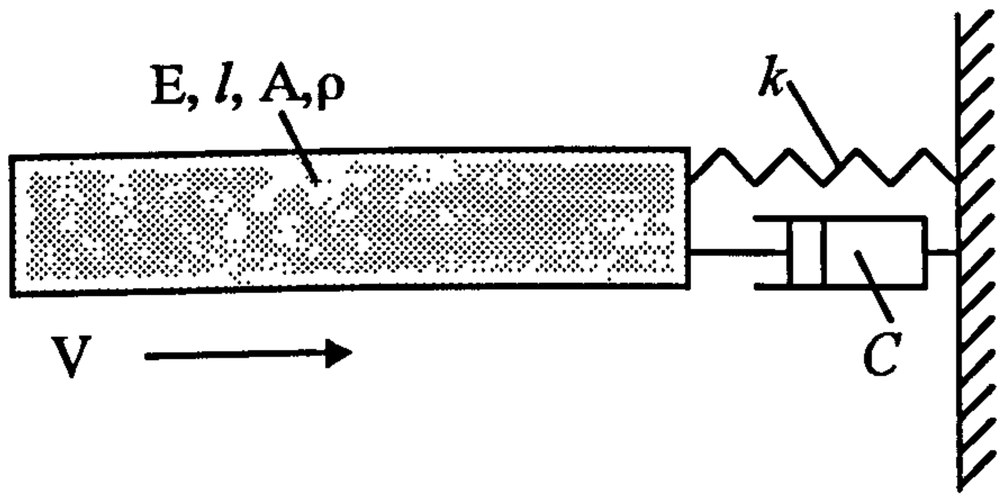

Figure 3.4a : Bar-spring model

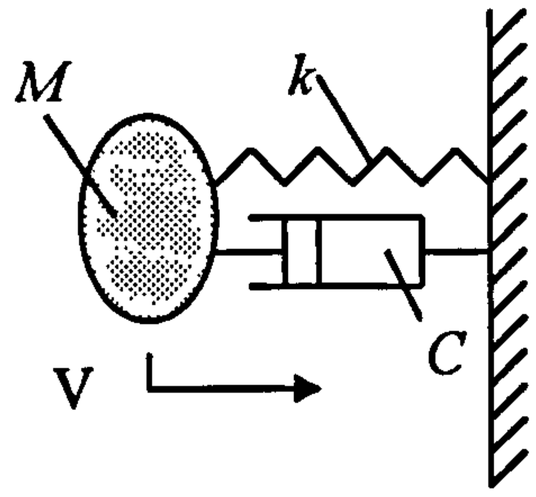

Figure 3.4b : Mass-spring model

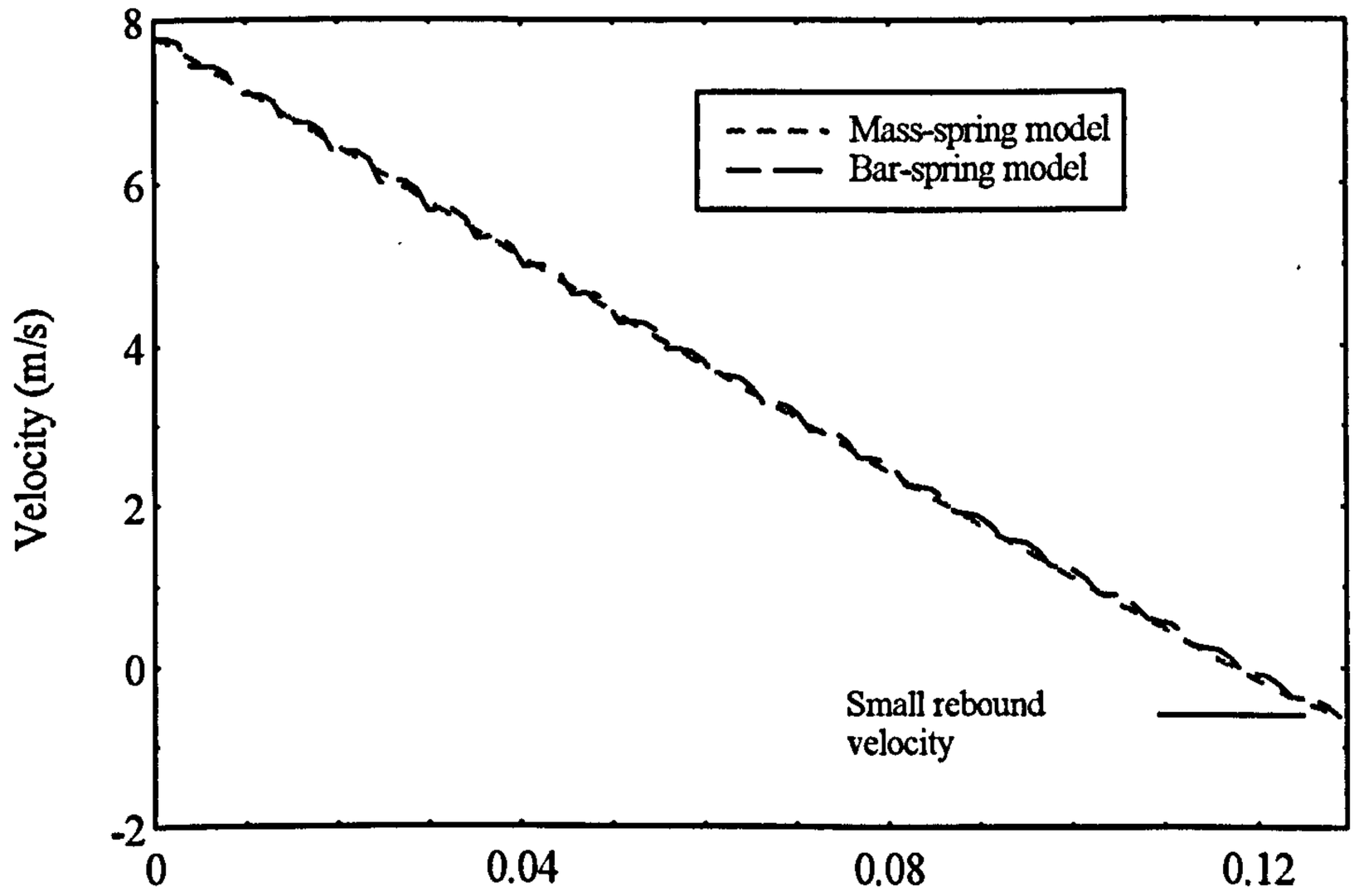

Figure 3.5 : The velocity-time history for the bar-spring & mass-spring models.

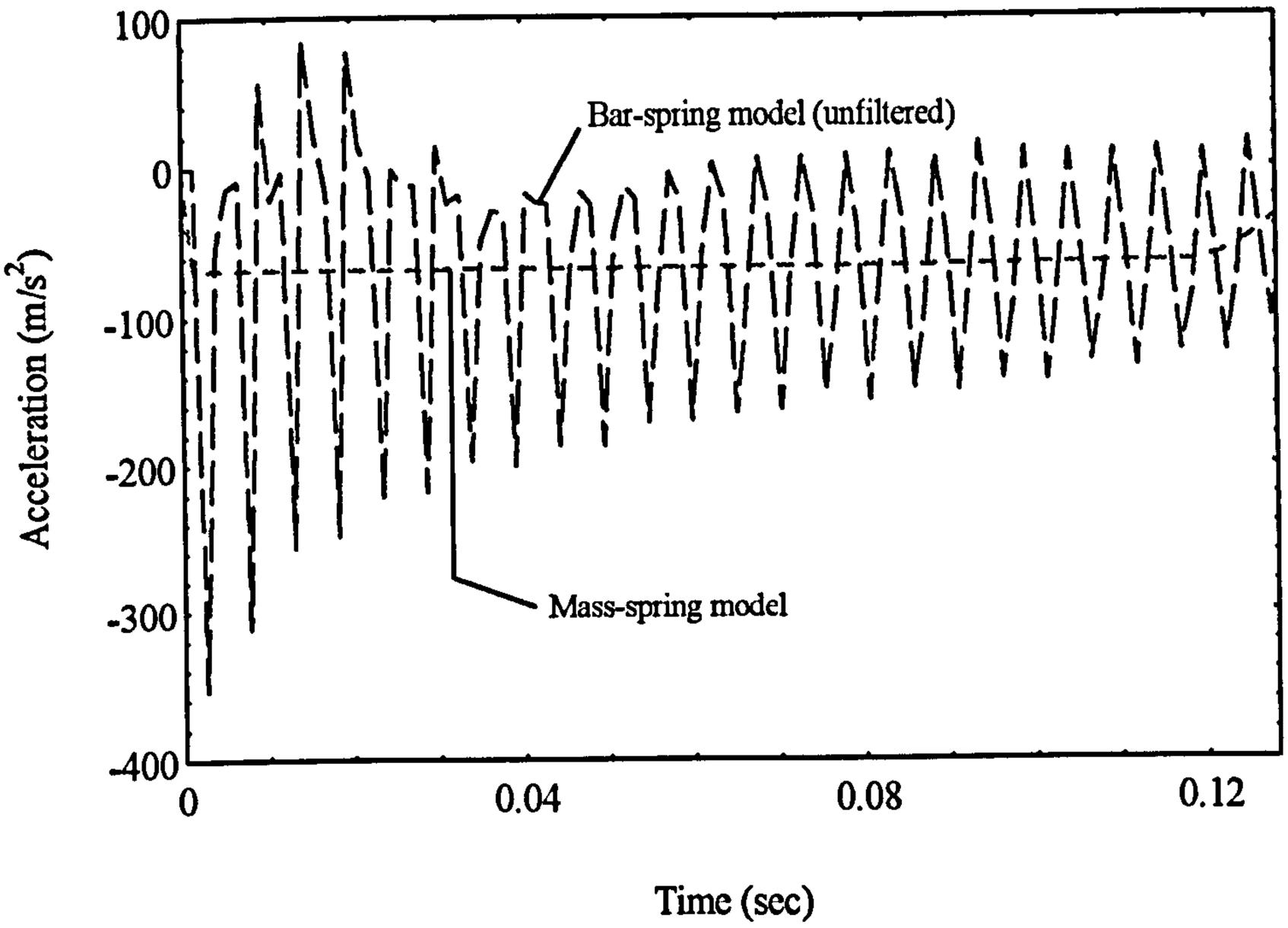

Figure 3.6a : The acceleration-time history for the bar-spring & mass-spring models.

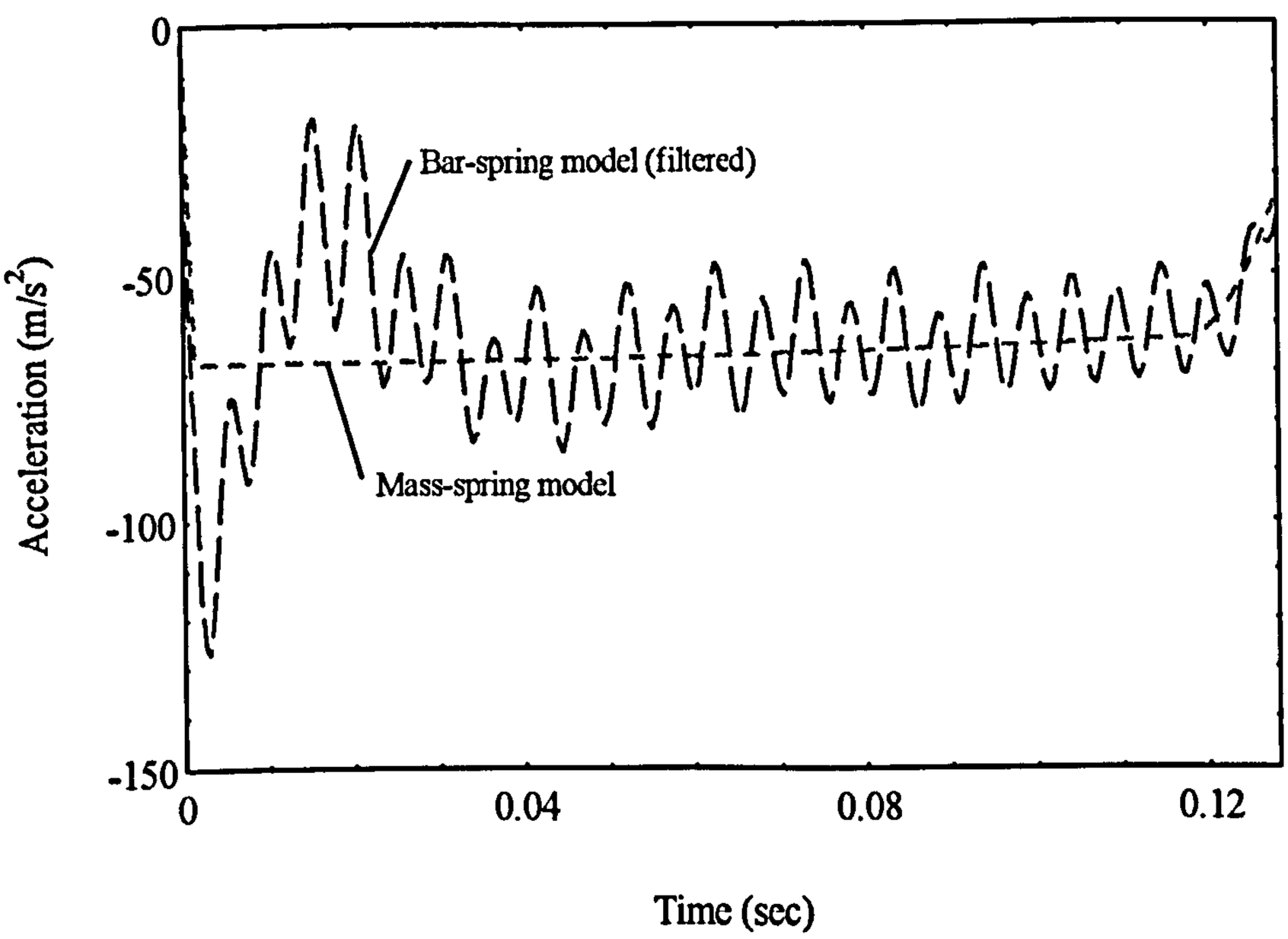

Figure 3.6b : The filtered acceleration-time history for the bar-spring & mass-spring models.

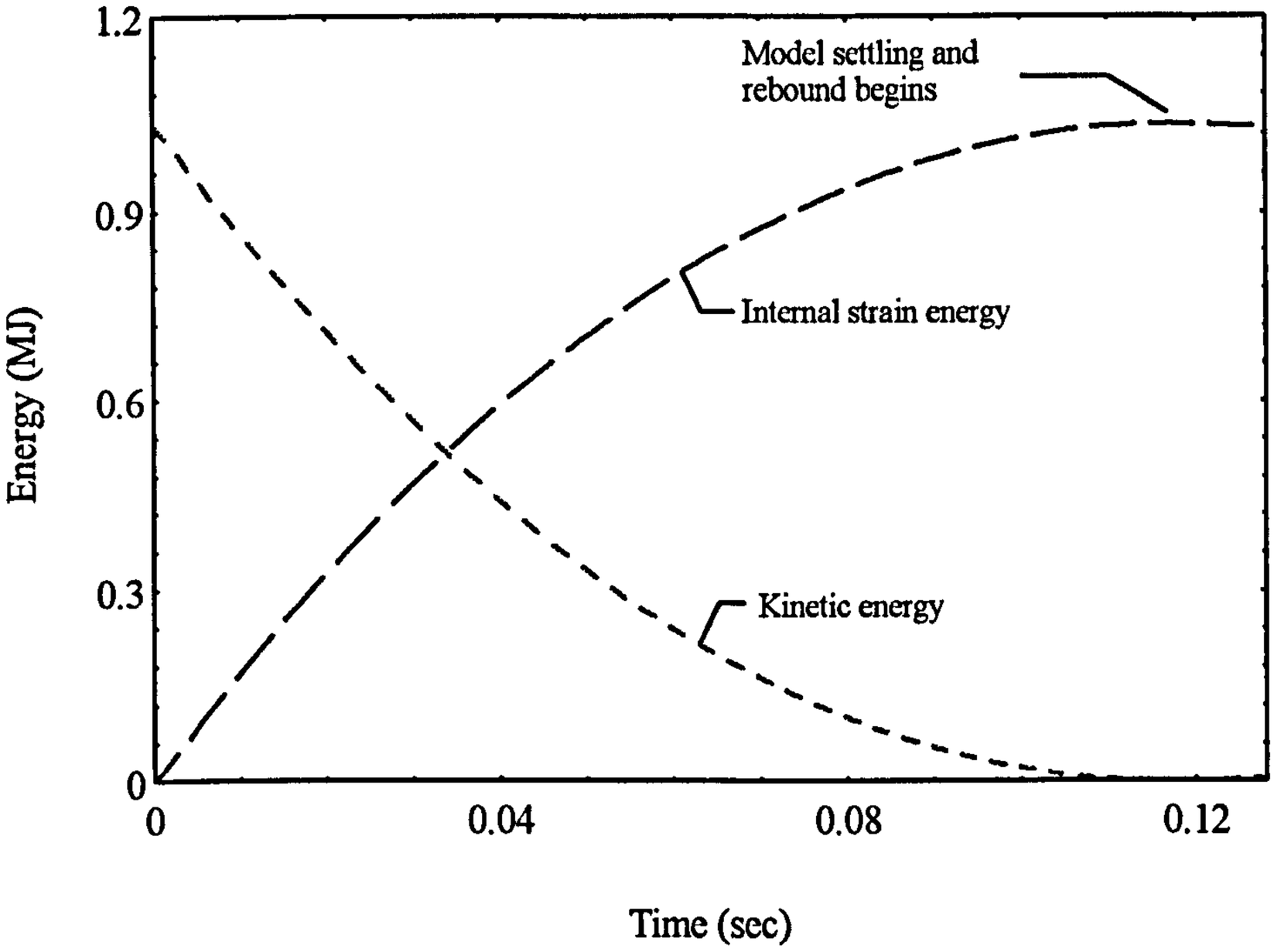

Figure 3.7 : The energy-time history for the mass-spring model.

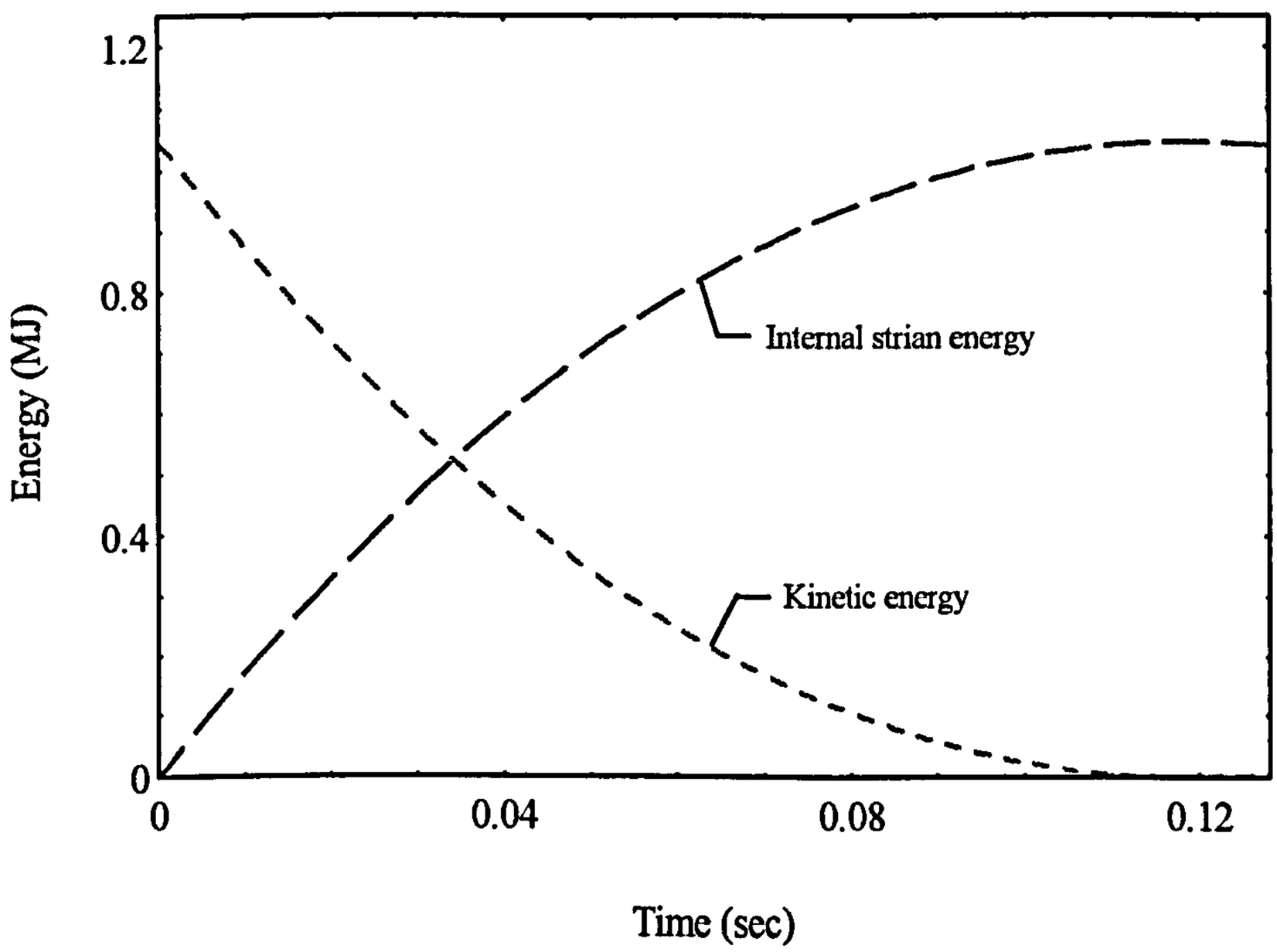

Figure 3.8 : The energy-time history for the bar-spring model.

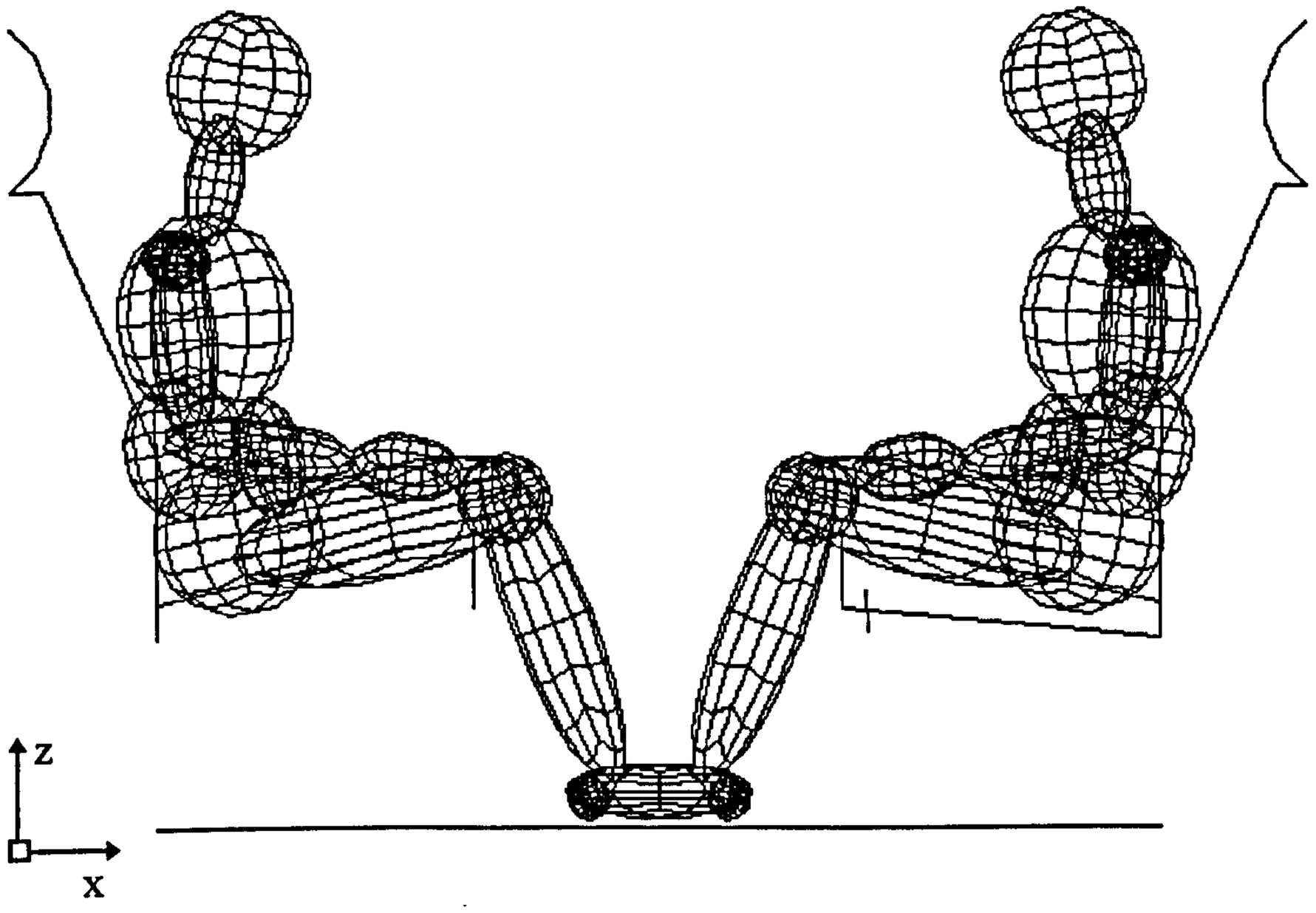

Figure 3.9a : Initial seating position of the occupants.

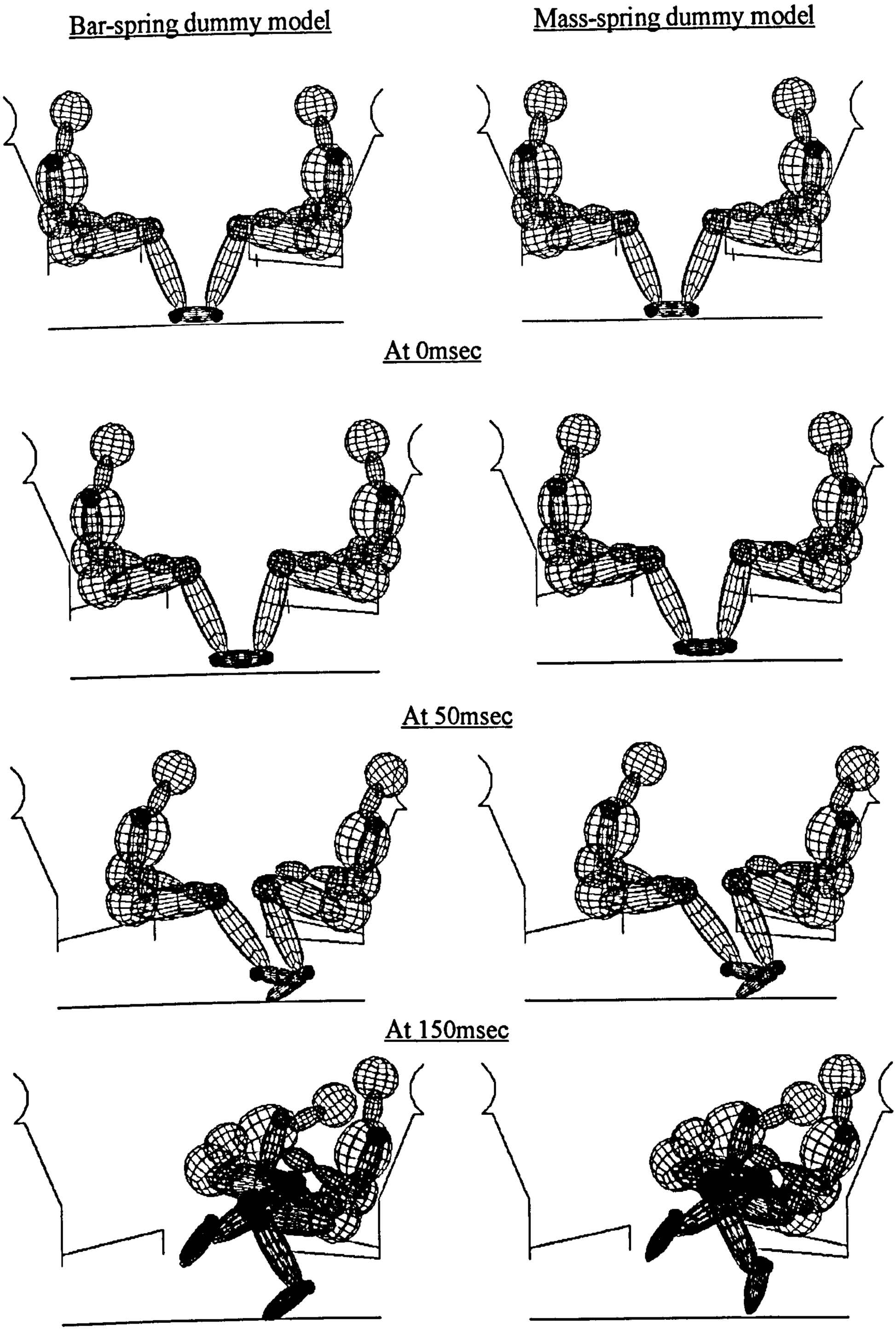

Figure 3.9b : The animation sequence for both dummy models.

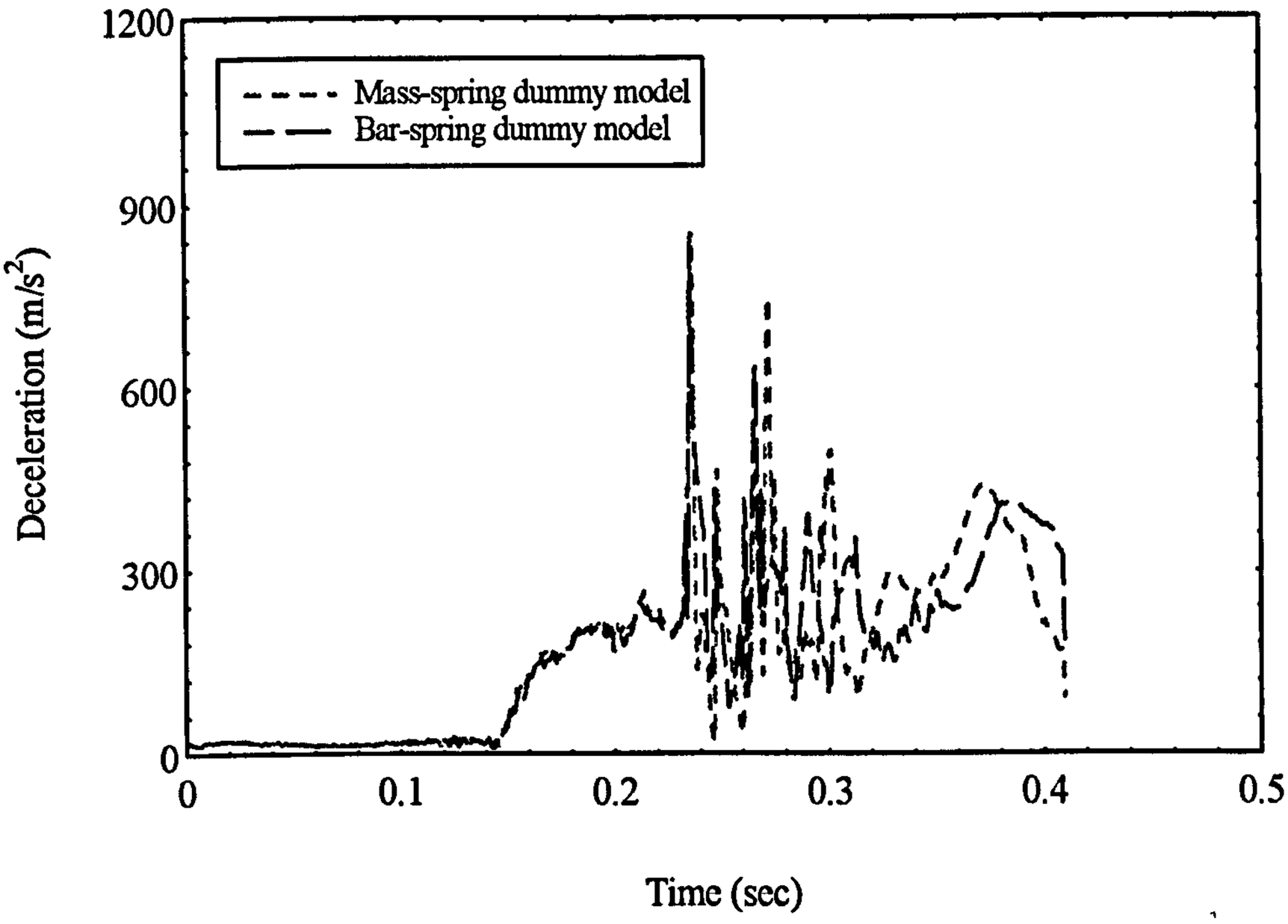

Figure 3.10 : The deceleration-time history for the striking occupants' head.

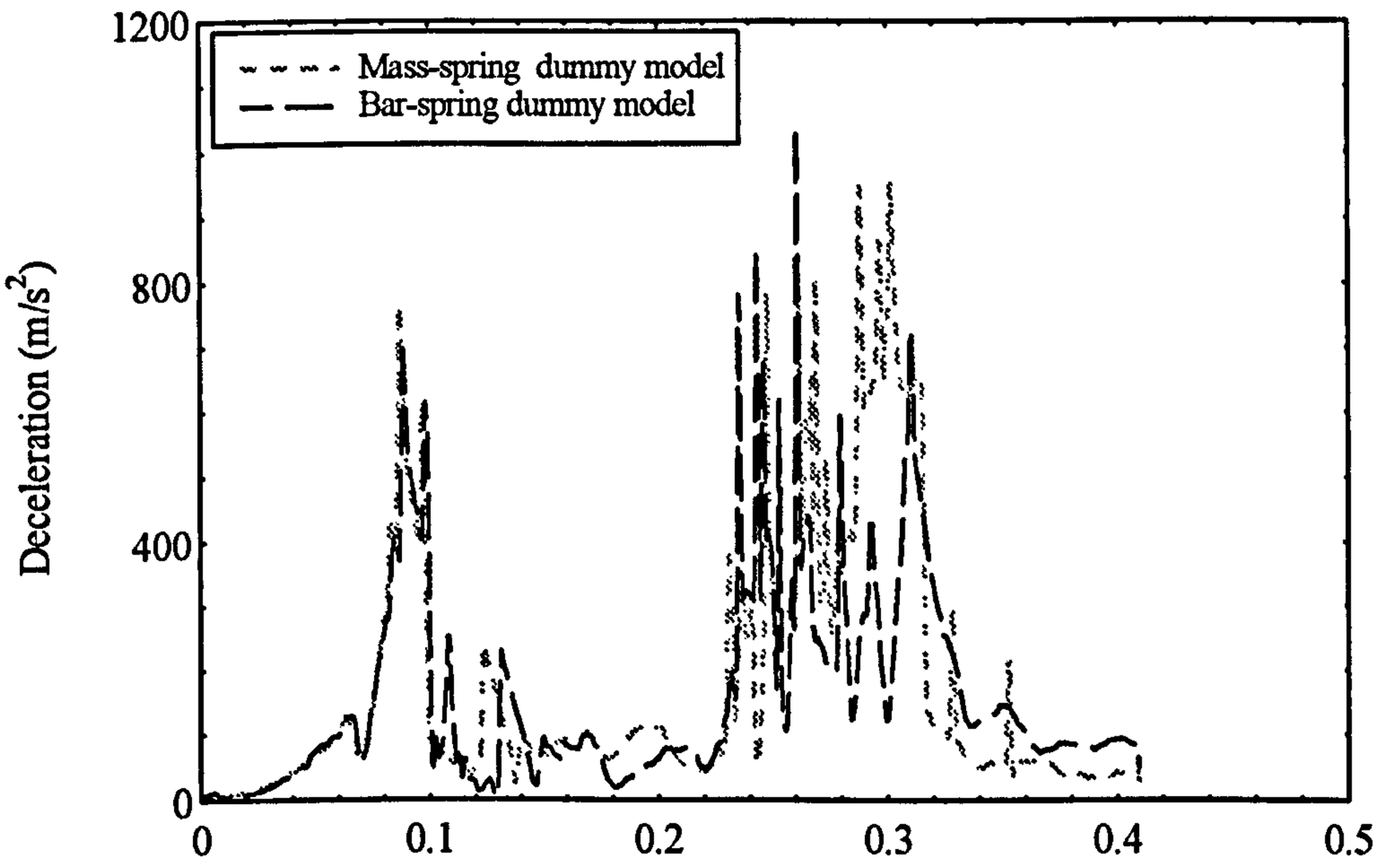

Figure 3.11 : The deceleration-time history for the struck occupants' head.

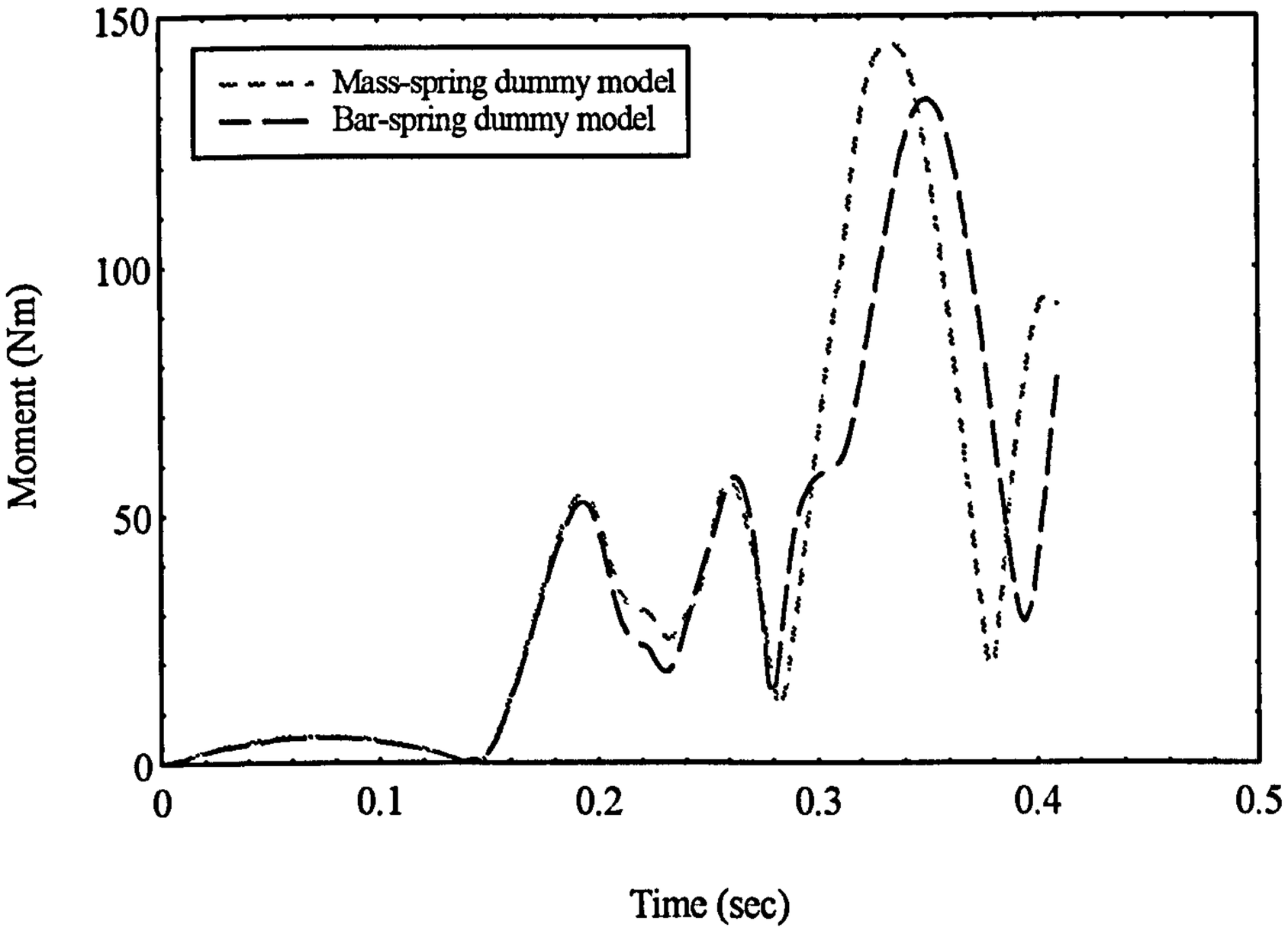

Figure 3.12 : The neck flexion bending moment-time history for the striking occupants.

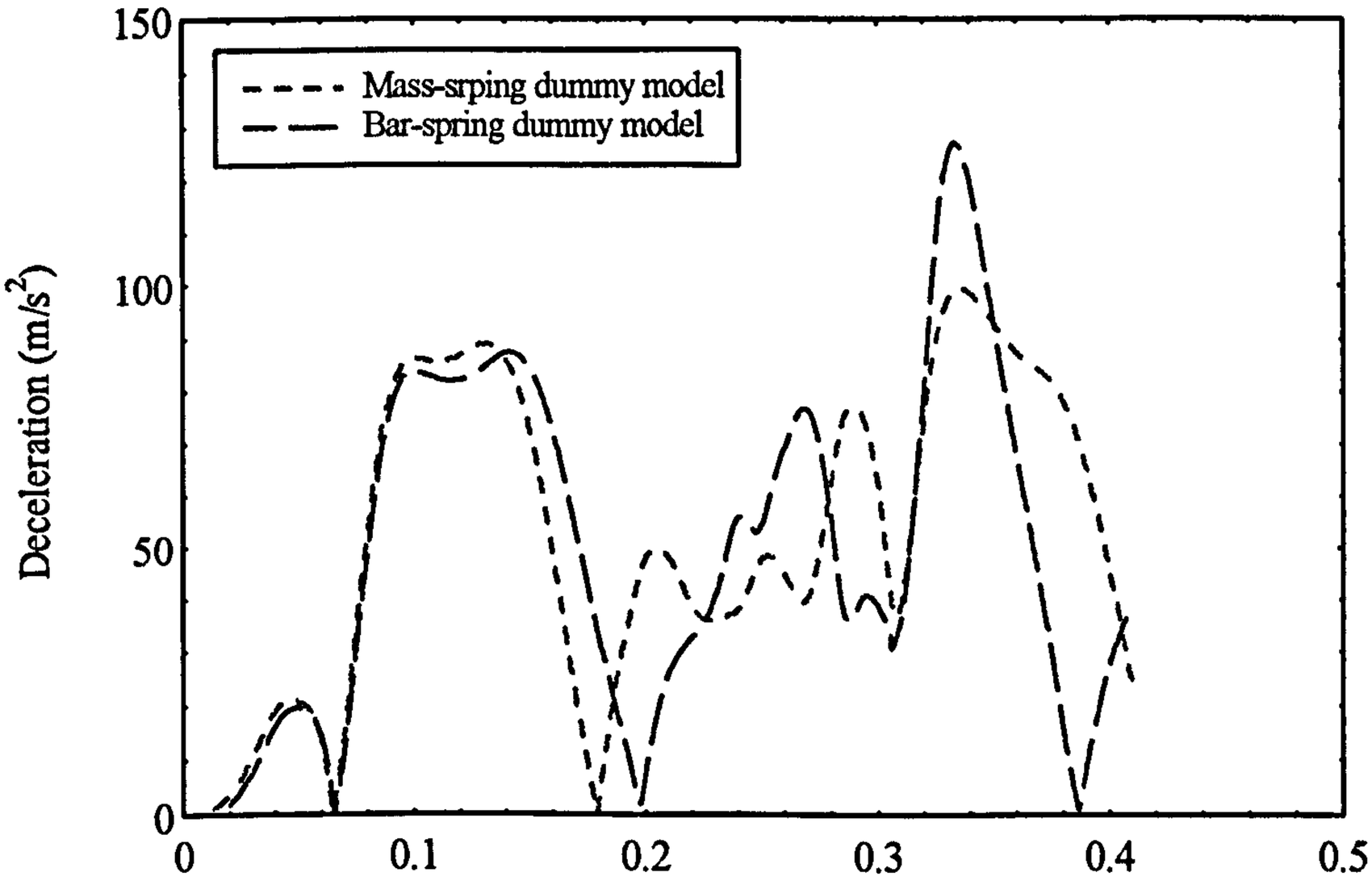

Figure 3.13 : The neck flexion bending moment-time history for the struck occupants.

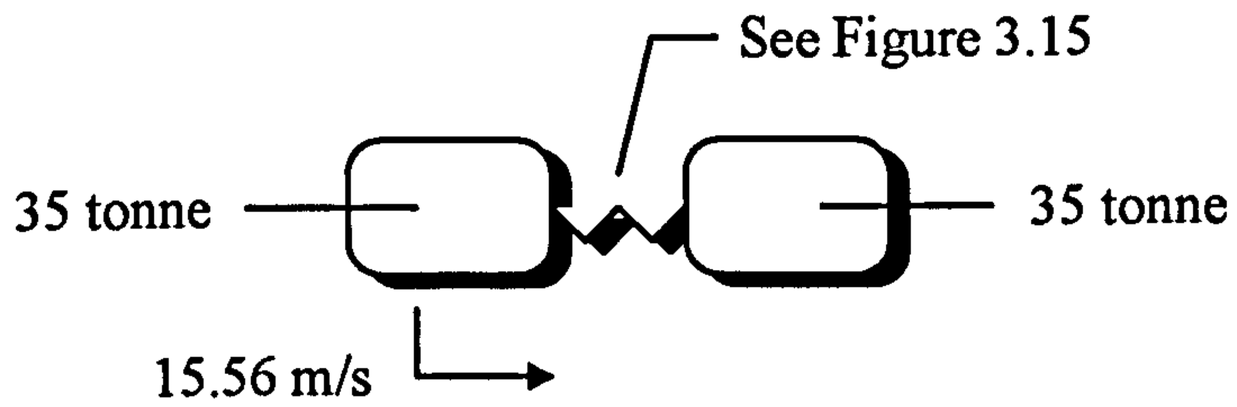

Figure 3.14 : The baseline model used for the parametric study.

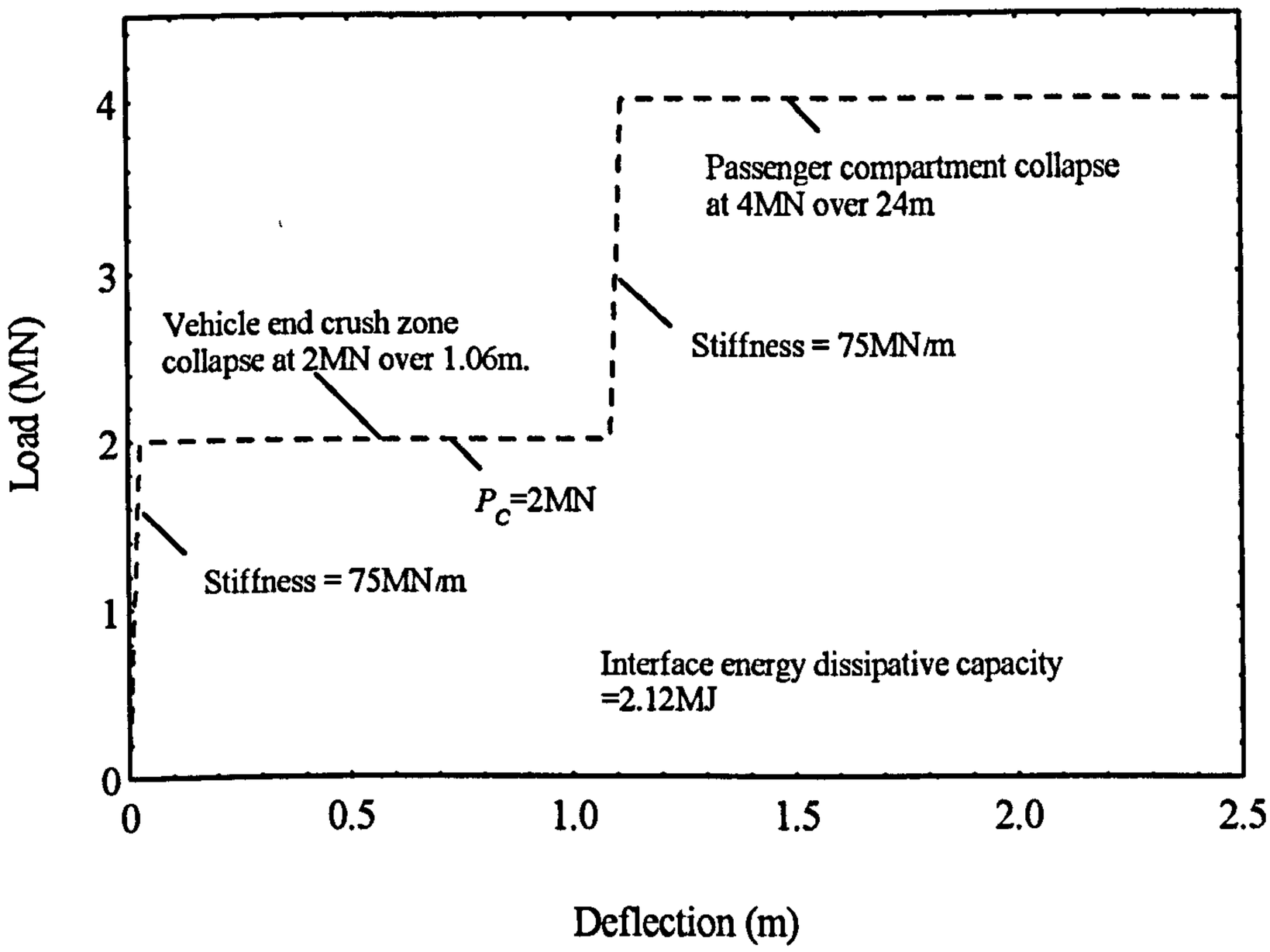

Figure 3.15 : The load-deflection characteristic for the baseline spring.

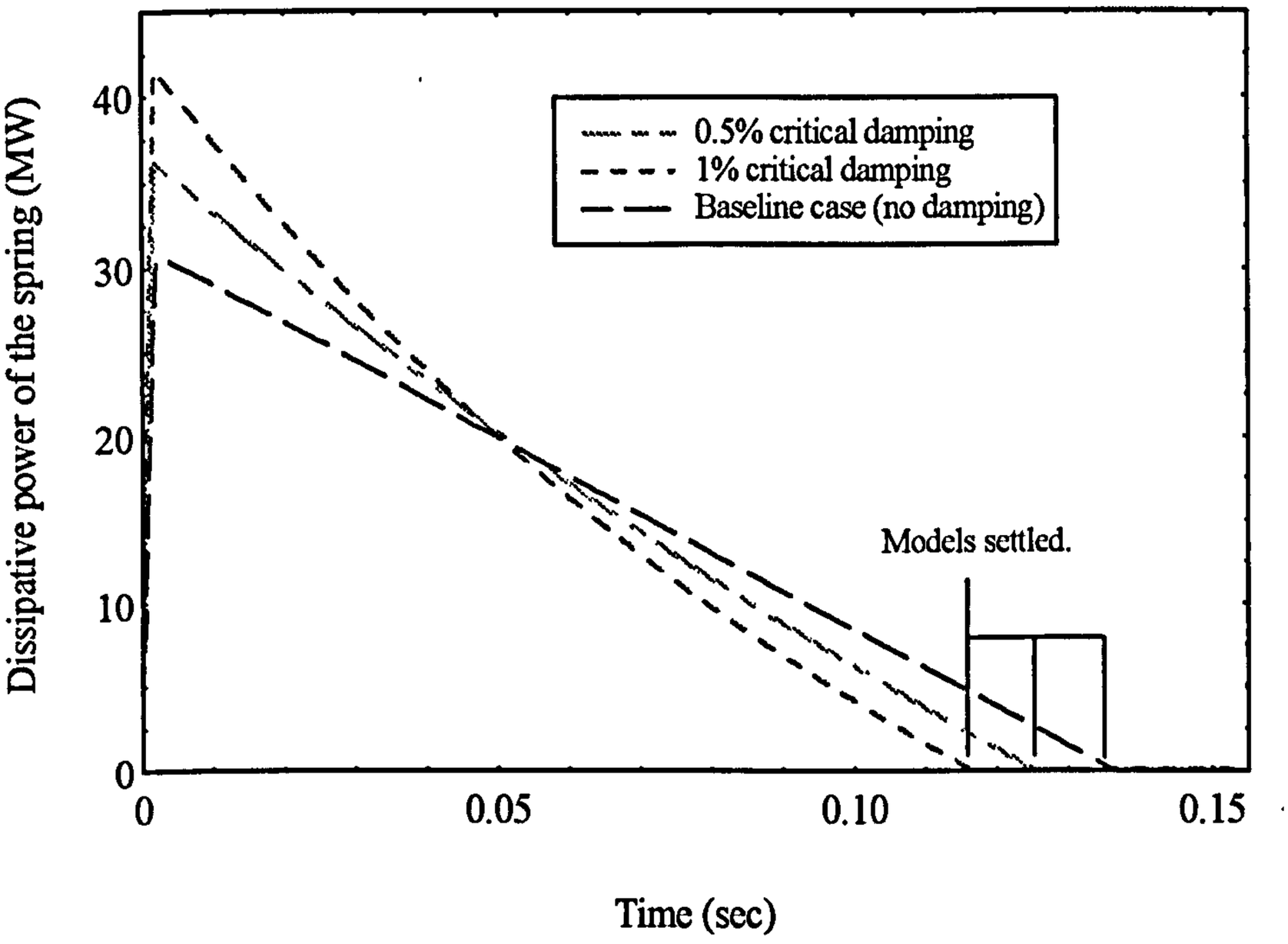

Figure 3.16 : The effects of damping on the energy dissipative power.

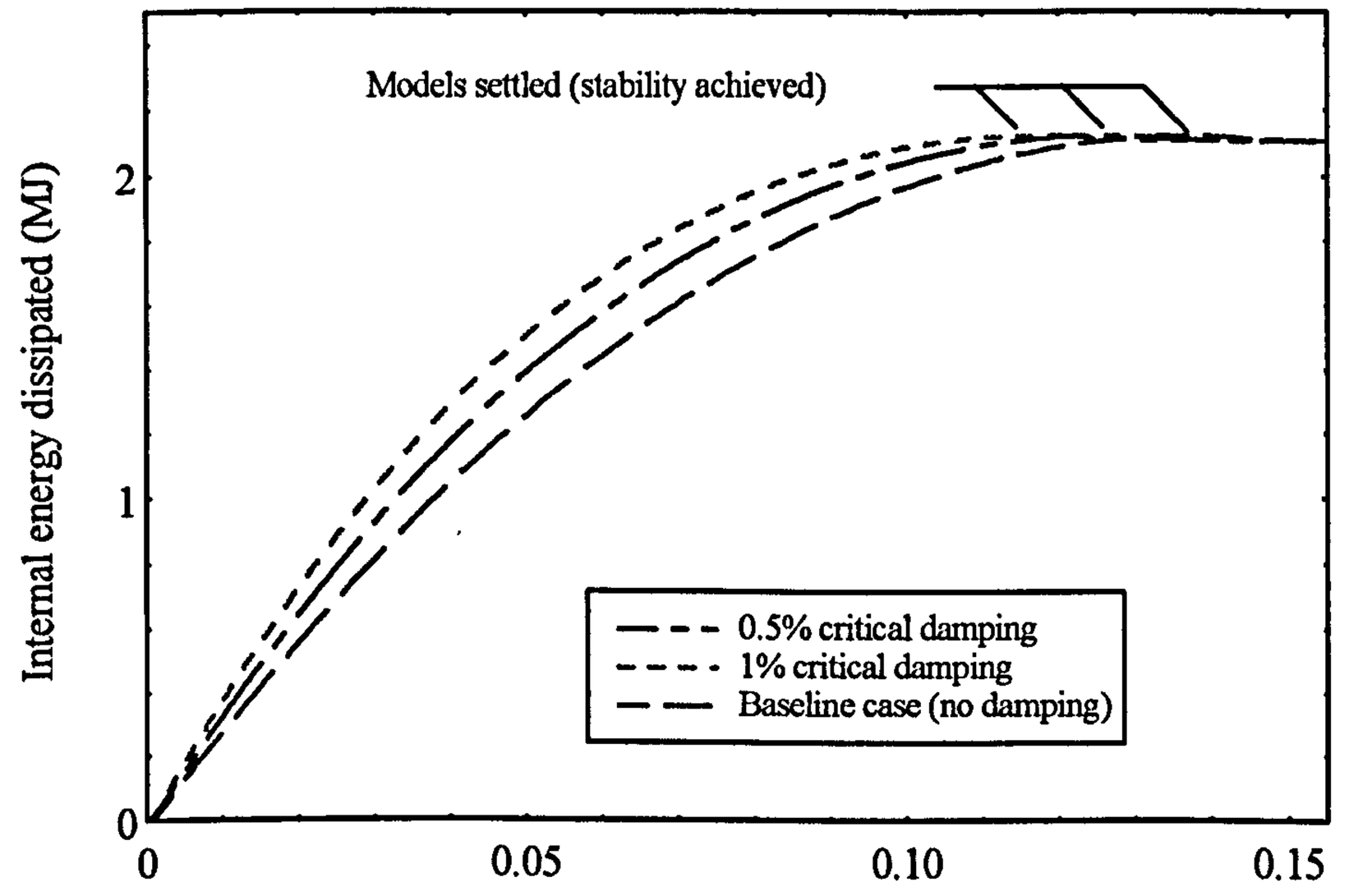

Figure 3.17 : The effects of damping on internal energy dissipation.

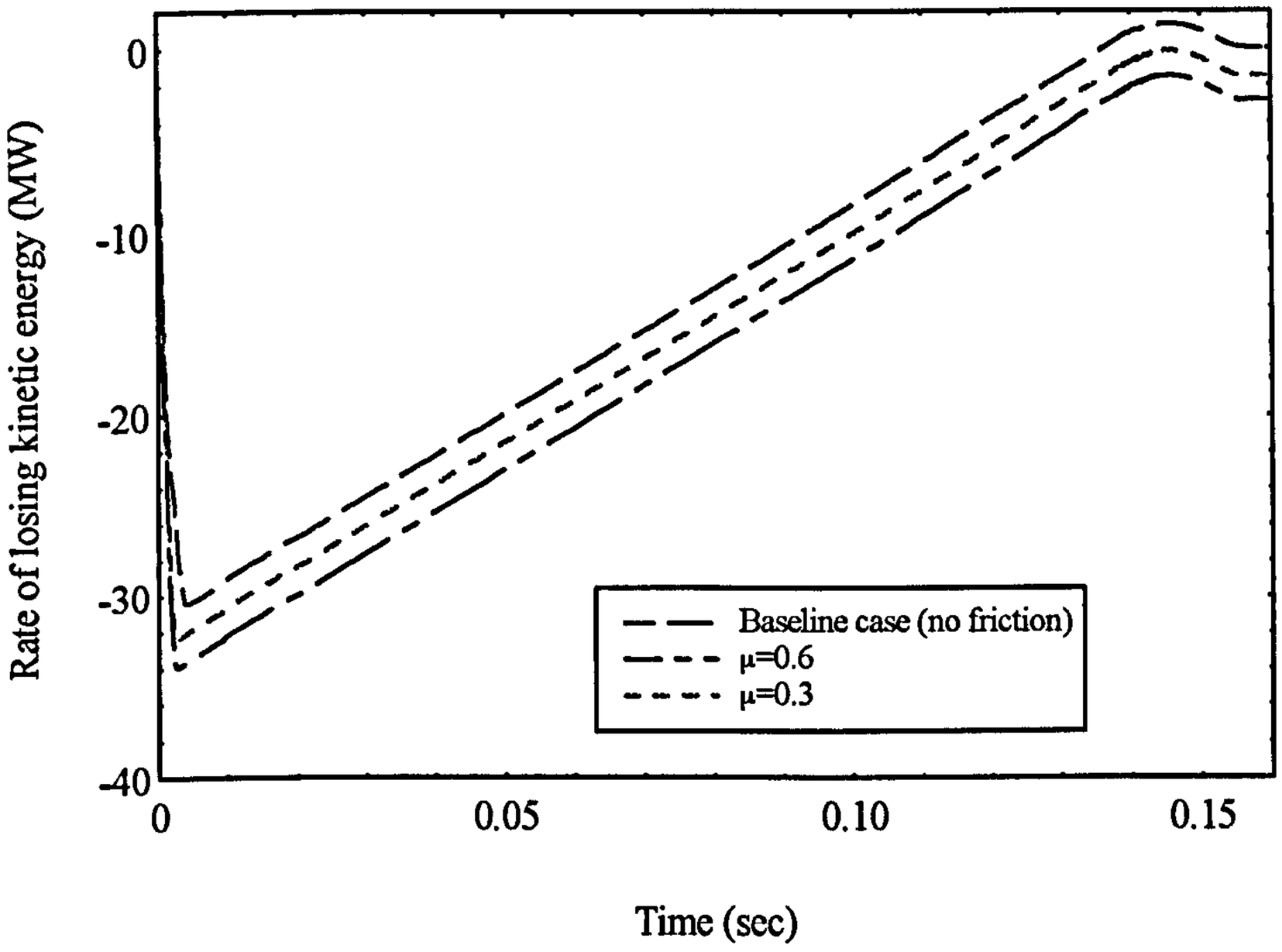

Figure 3.18 : The effects of friction on the total energy dissipative power.

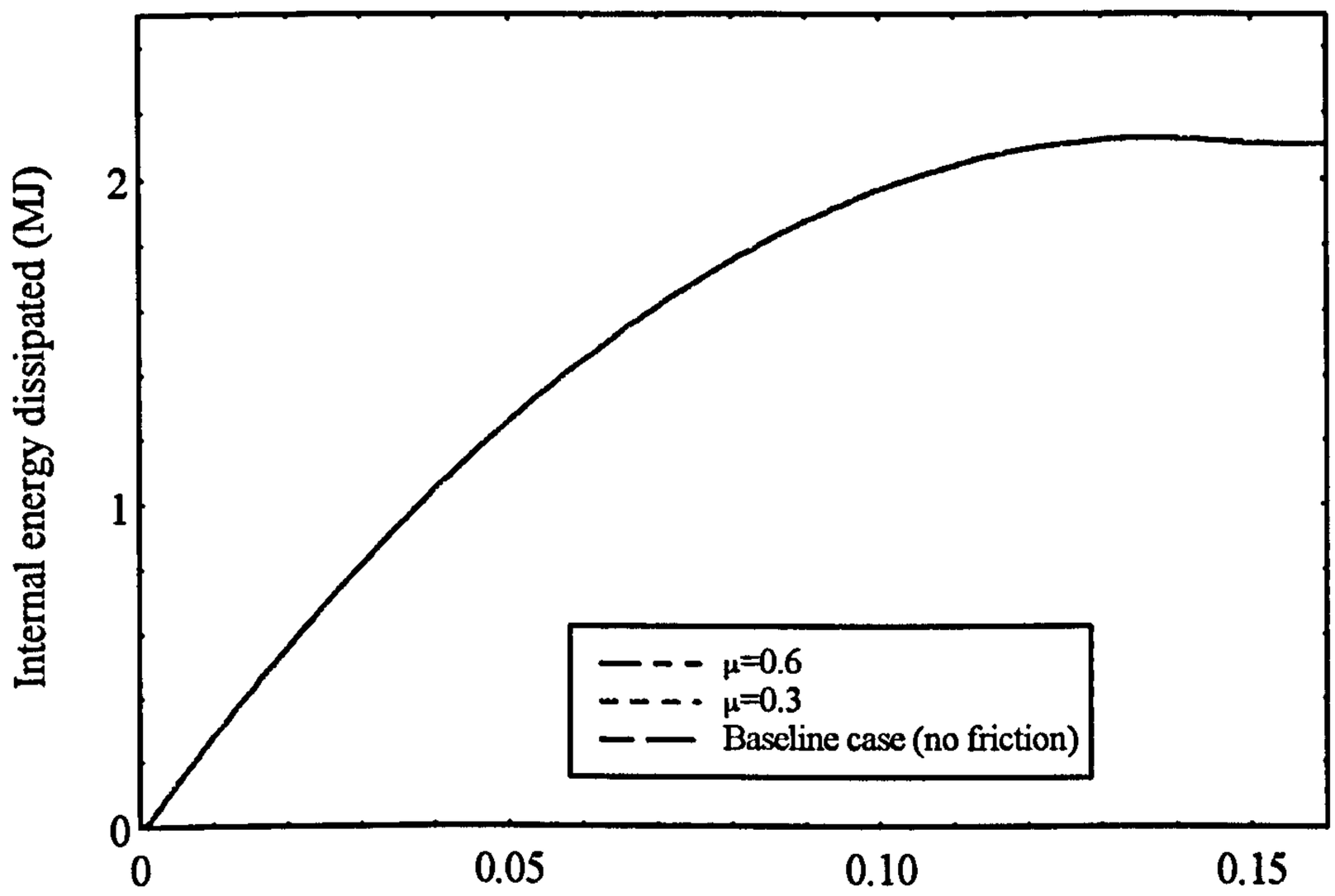

Figure 3.19 : The effects of friction on the dissipated energy.

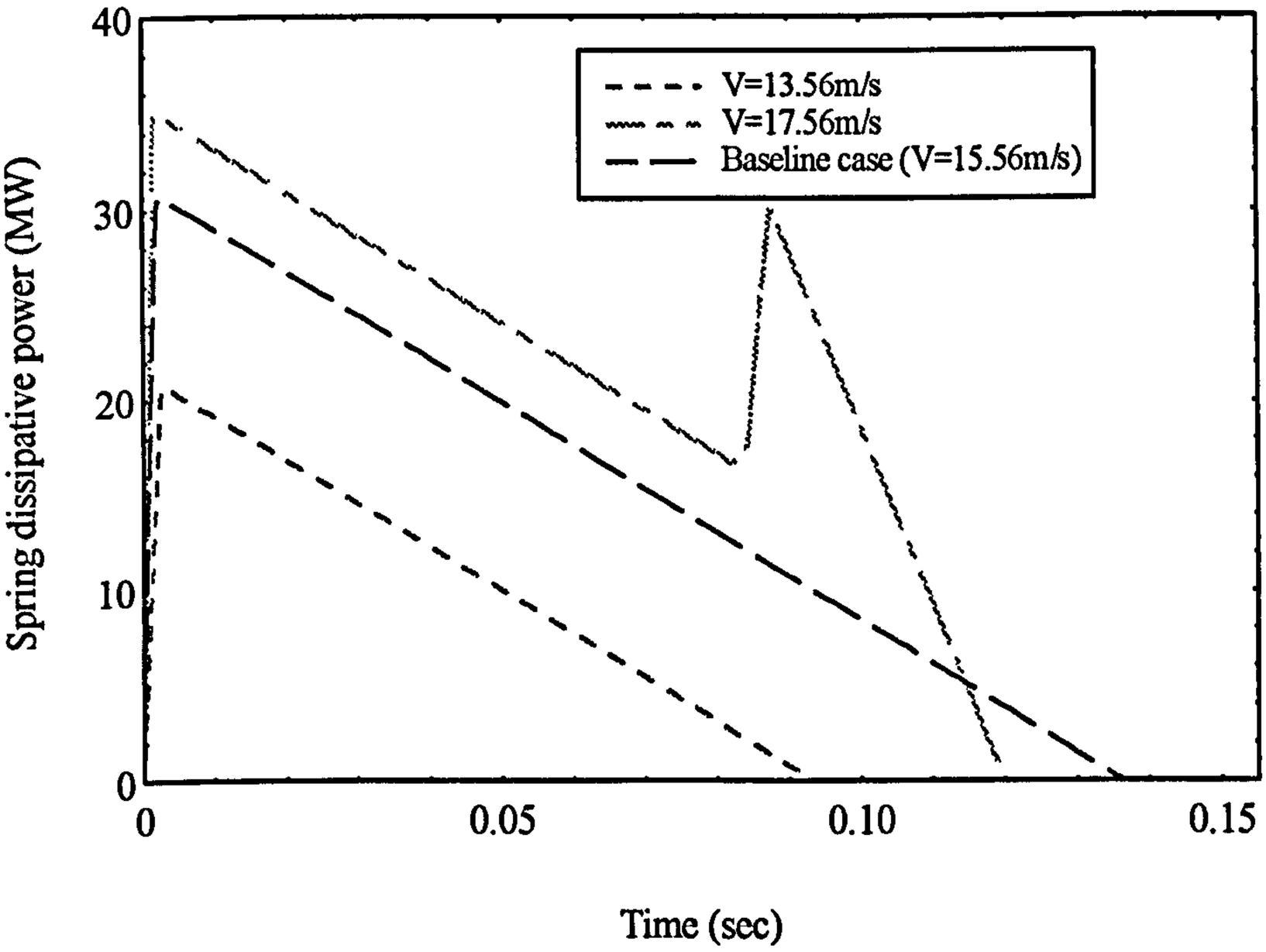

Figure 3.20 : The effects of initial velocity on the spring dissipative power.

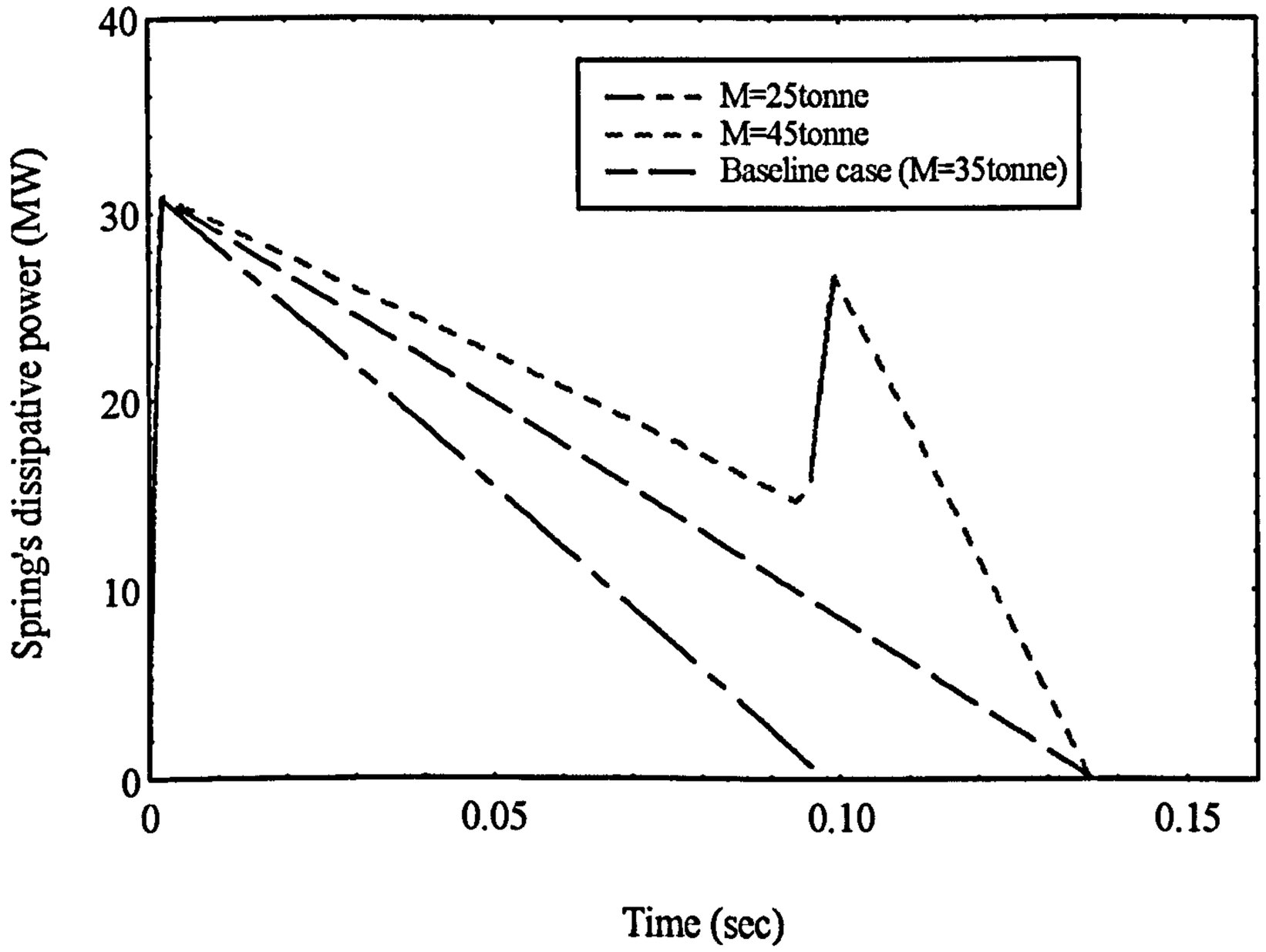

Figure 3.21 : The effects of coach mass on the spring dissipative power.

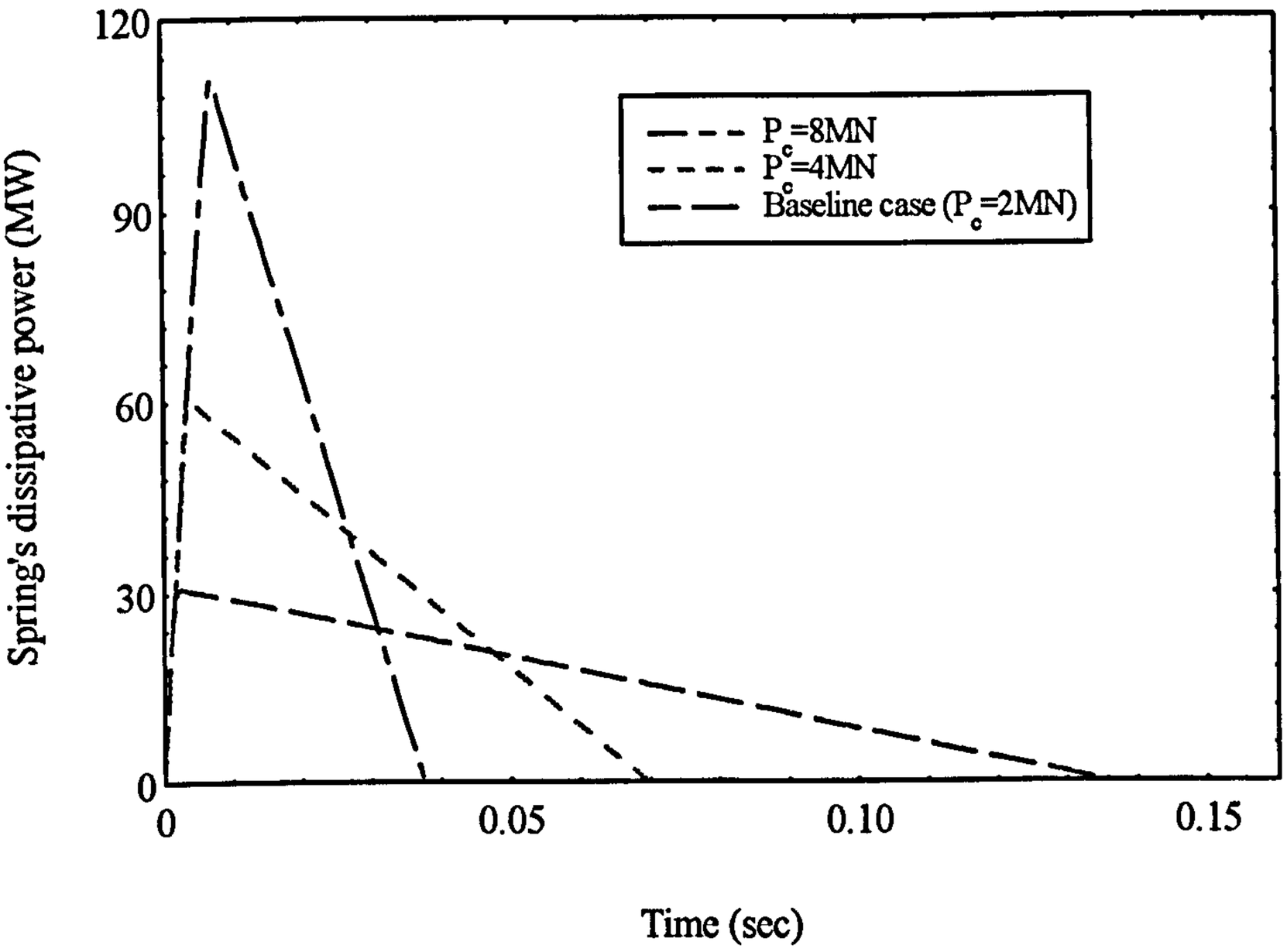

Figure 3.22 : The effects of spring collapse force on its dissipative power.

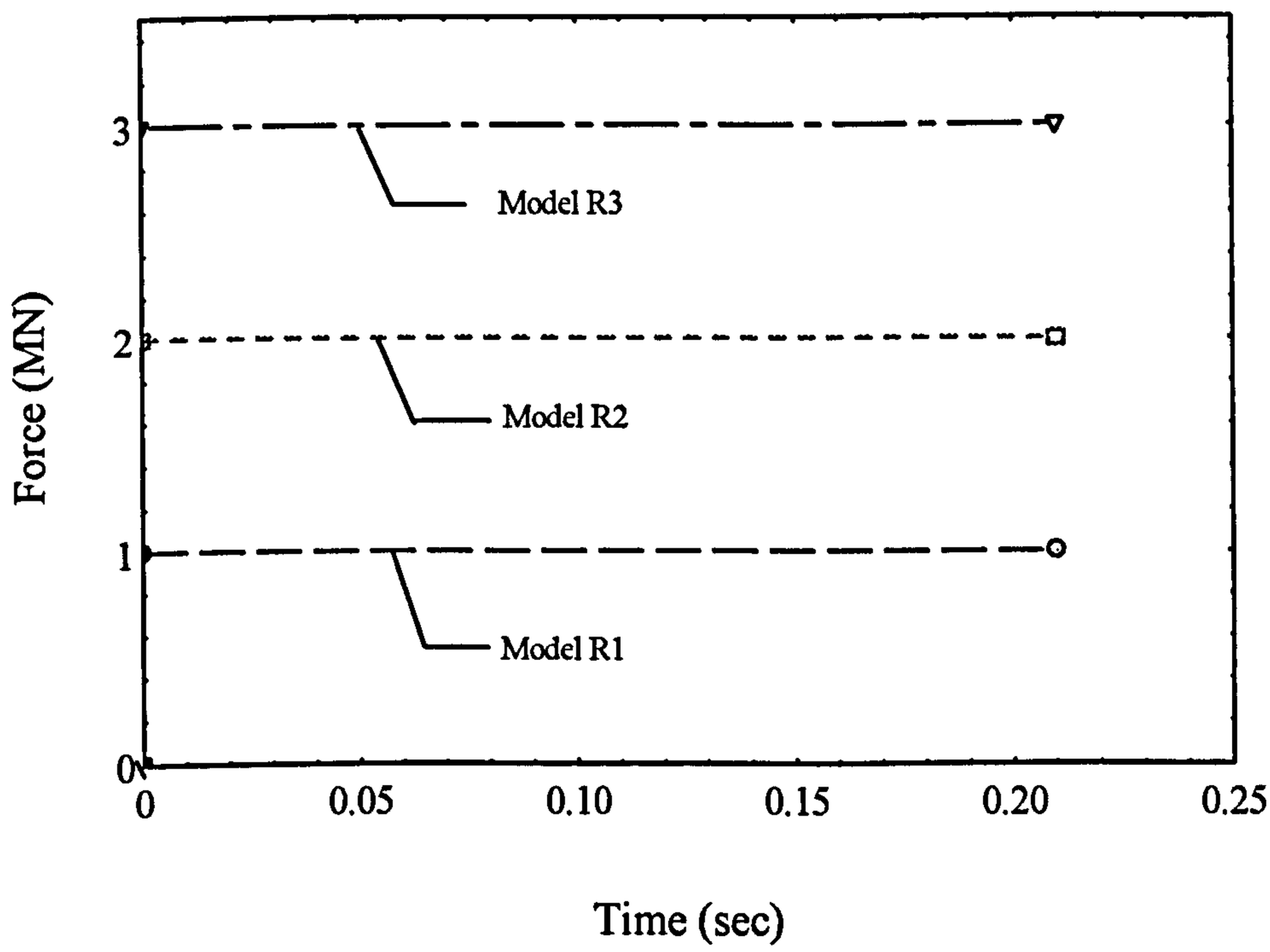

Figure 3.23 : The magnitudes of the external rectangular impulses.

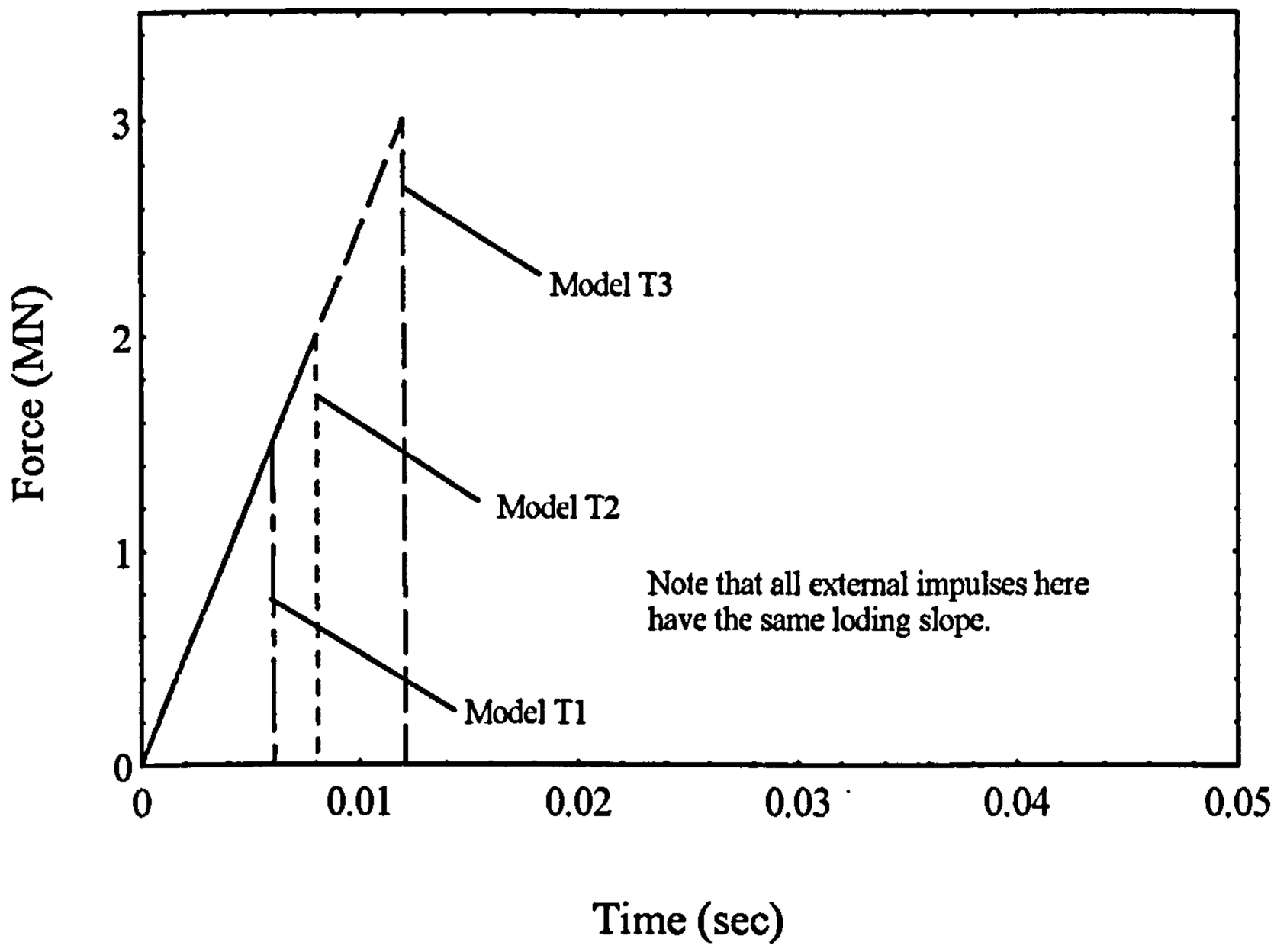

Figure 3.24 : The magnitudes of the external triangular impulses.

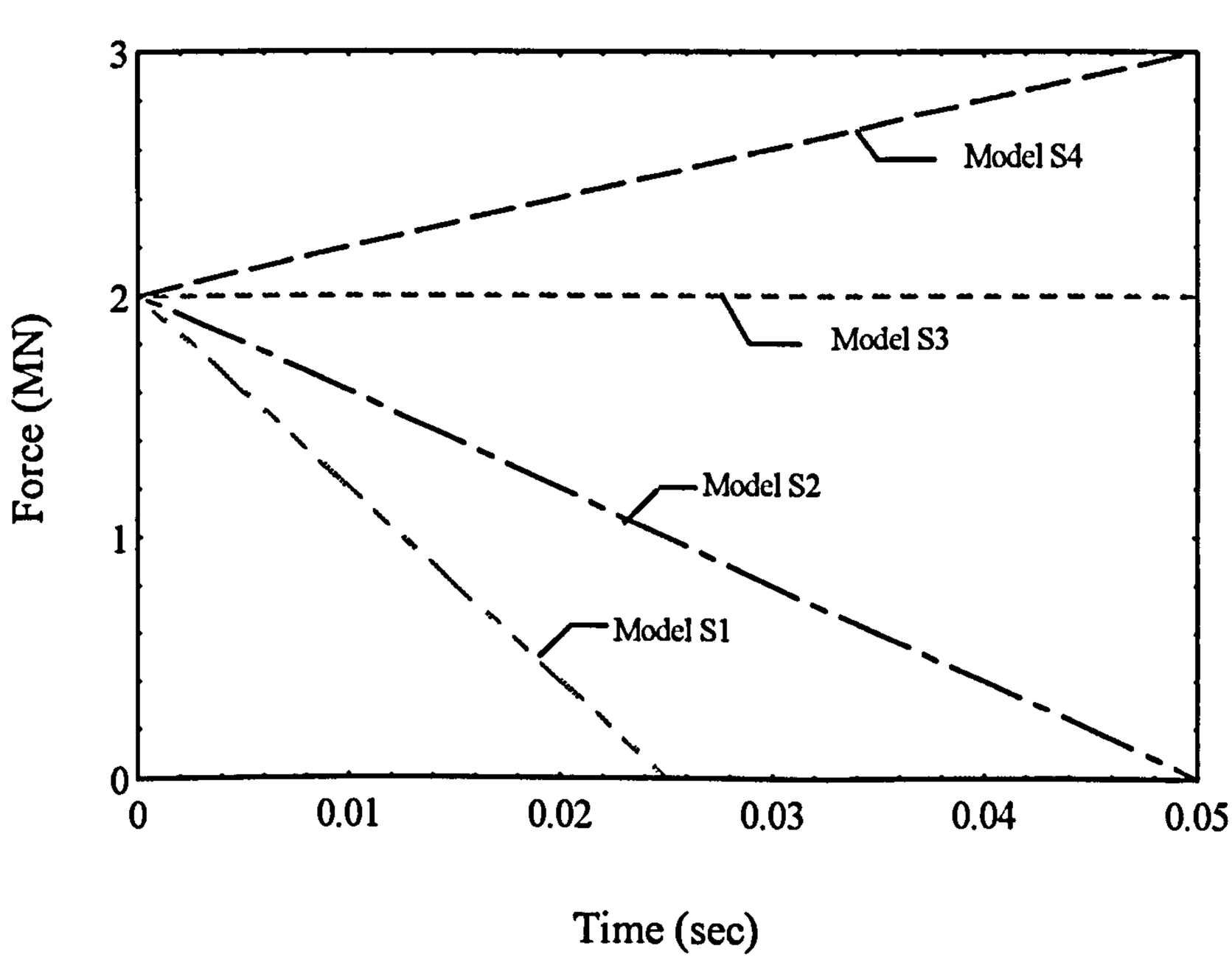

Figure 3.25 : The slopes of the external ramp impulses.

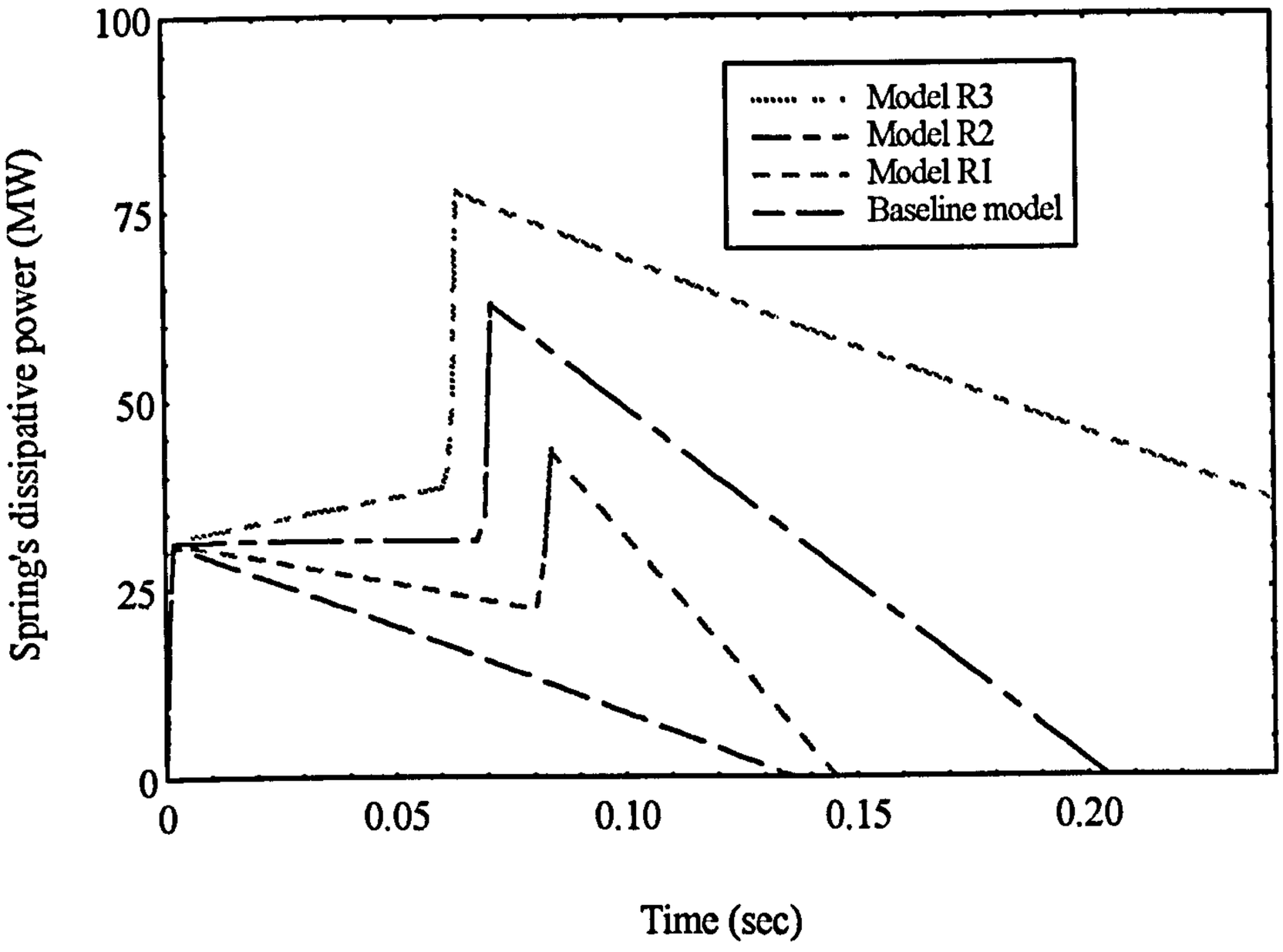

Figure 3.26 : The effects of the magnitude of external rectangular impulses.

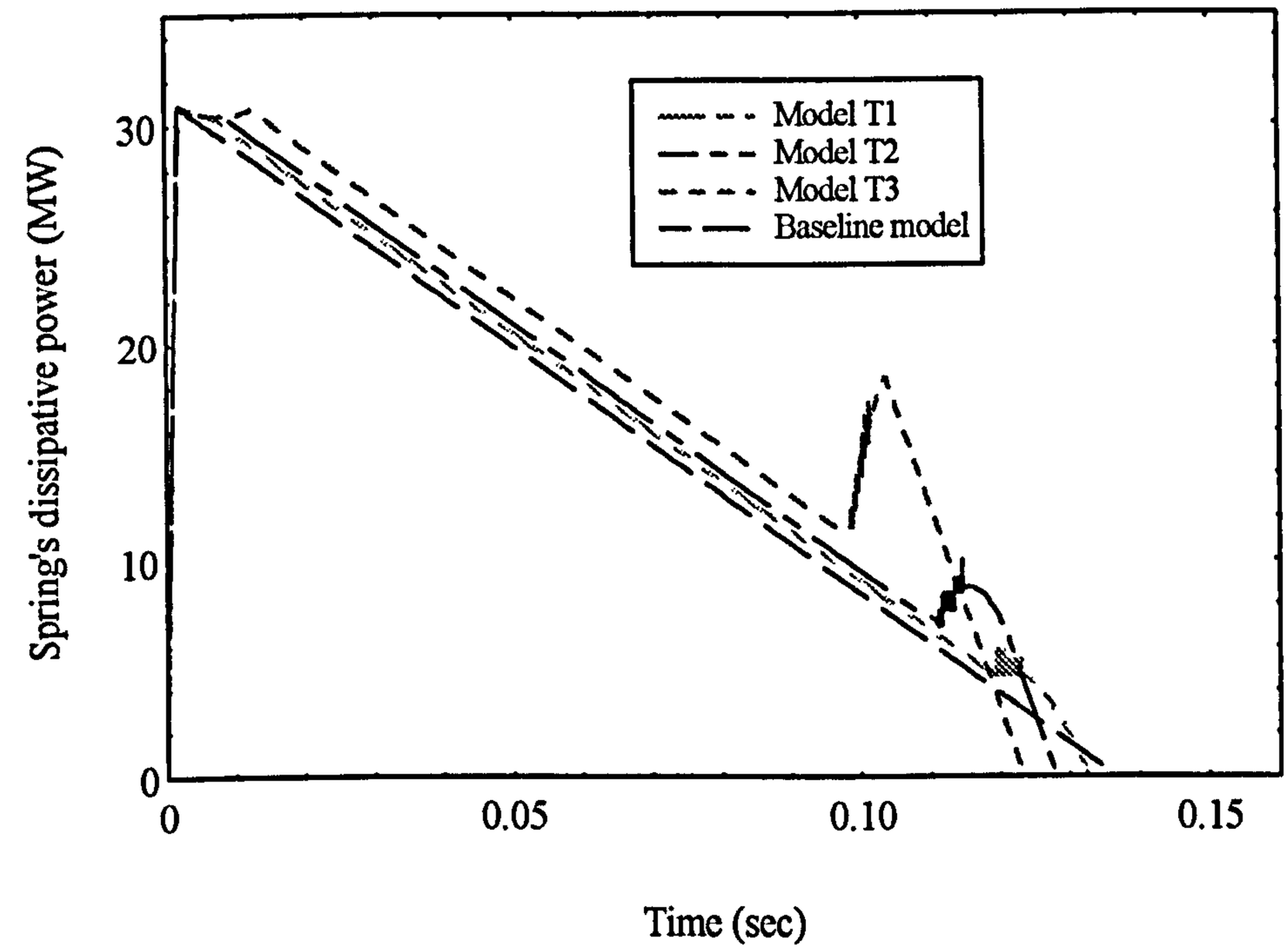

Figure 3.27 : The effects of the magnitude of external triangular impulses.

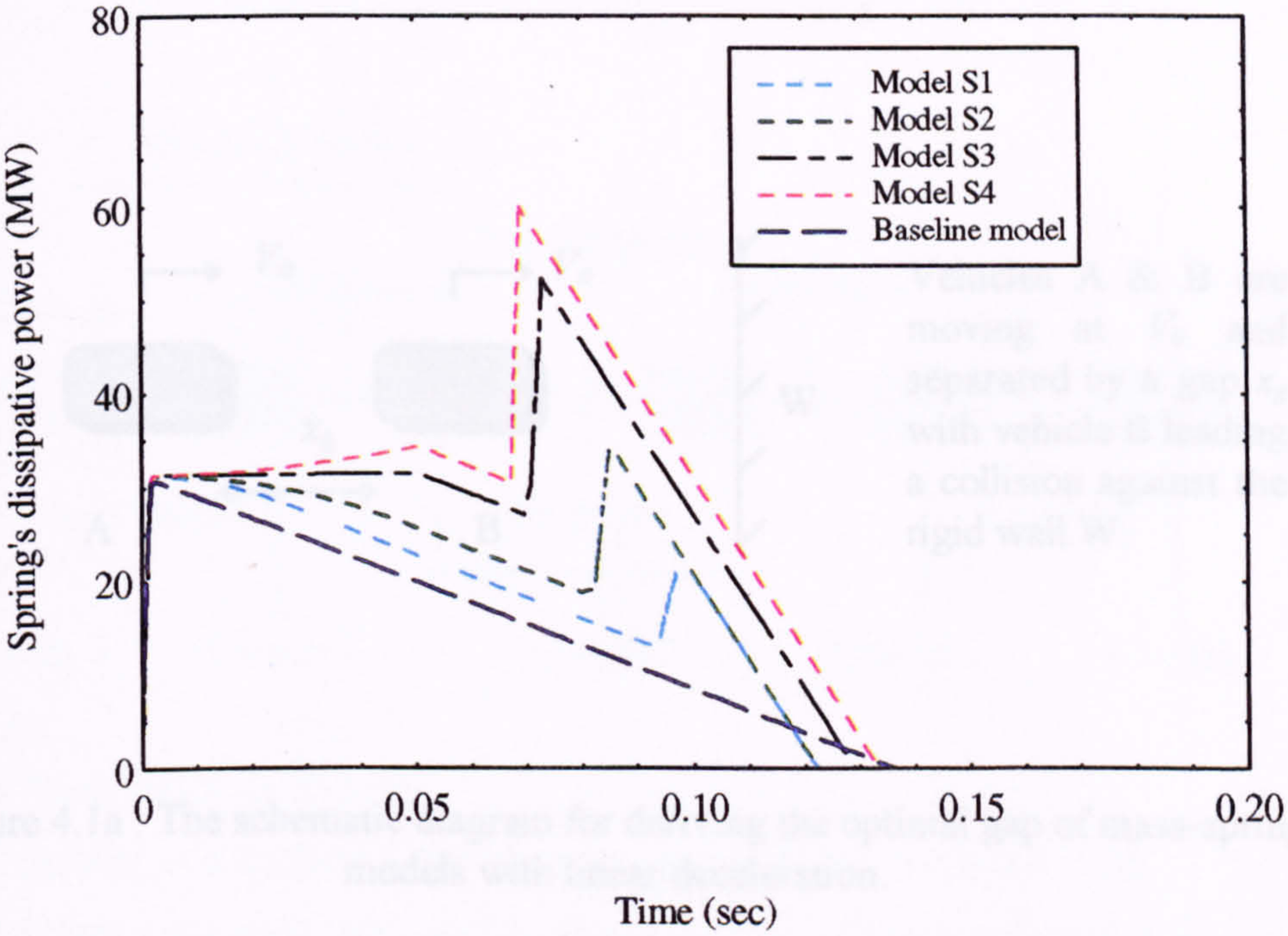

Figure 3.28 : The effects of the slope of external ramp impulses.

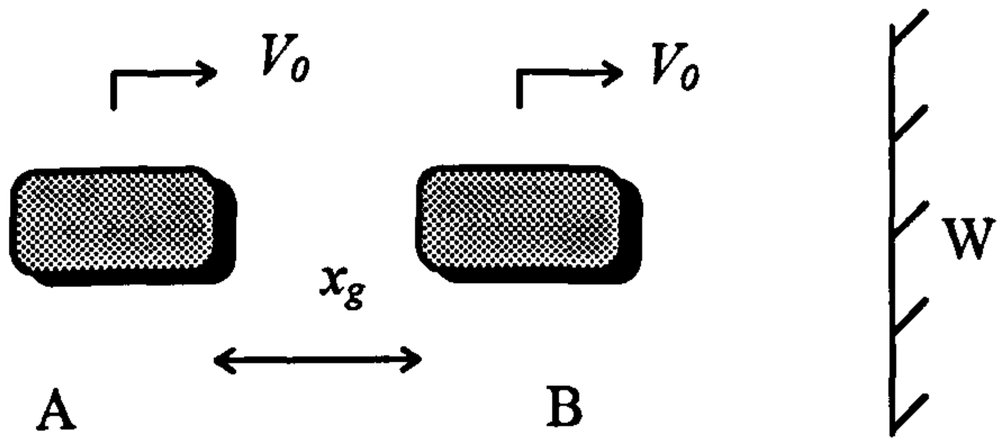

Vehicles A & B are moving at V_0 and separated by a gap x_g with vehicle B leading a collision against the rigid wall W.

Figure 4.1a : The schematic diagram for deriving the optimal gap of mass-spring models with linear deceleration.

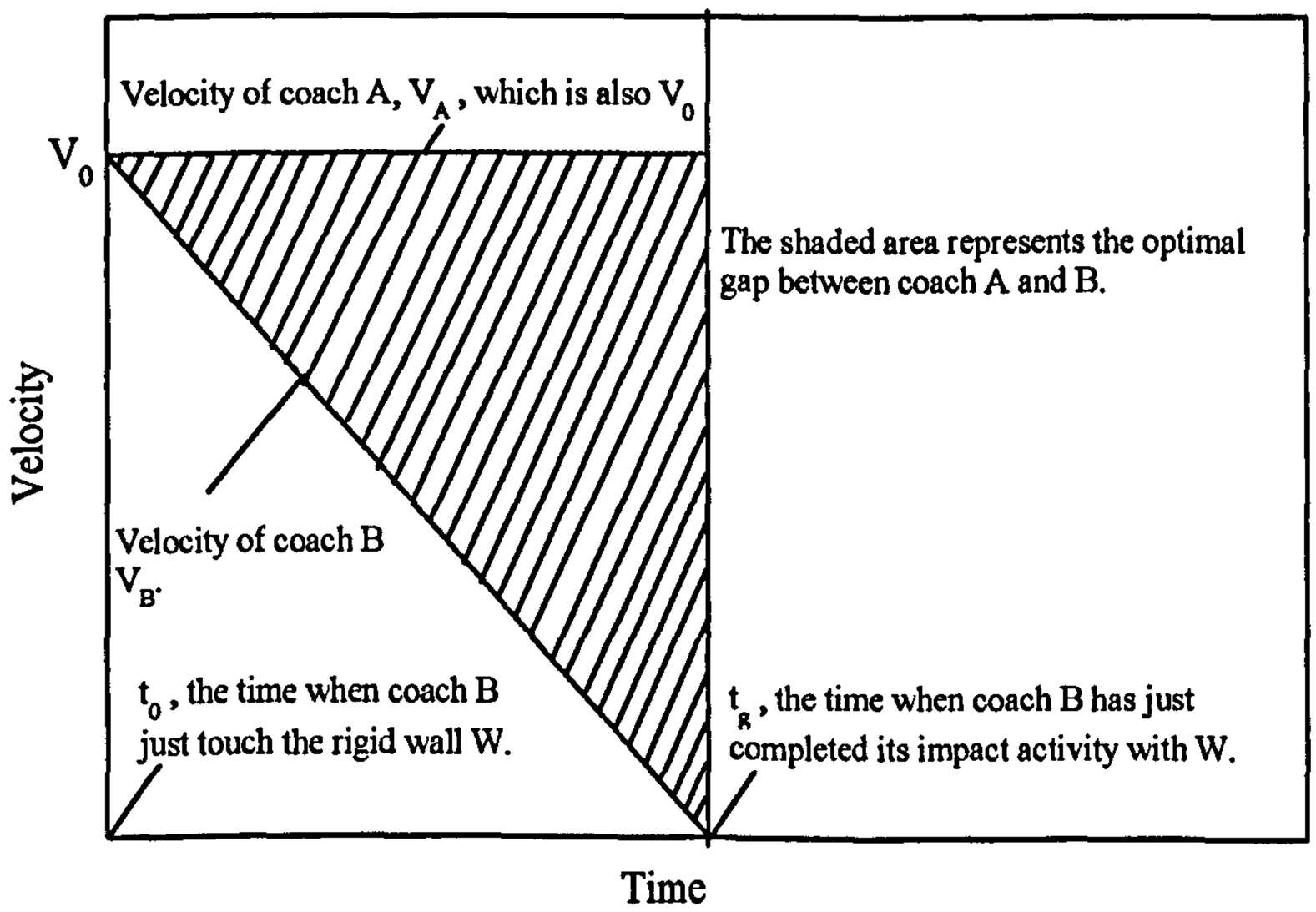

Figure 4.1b : The kinematics graphical interpretation of optimal gap sizes for cases with linear deceleration.

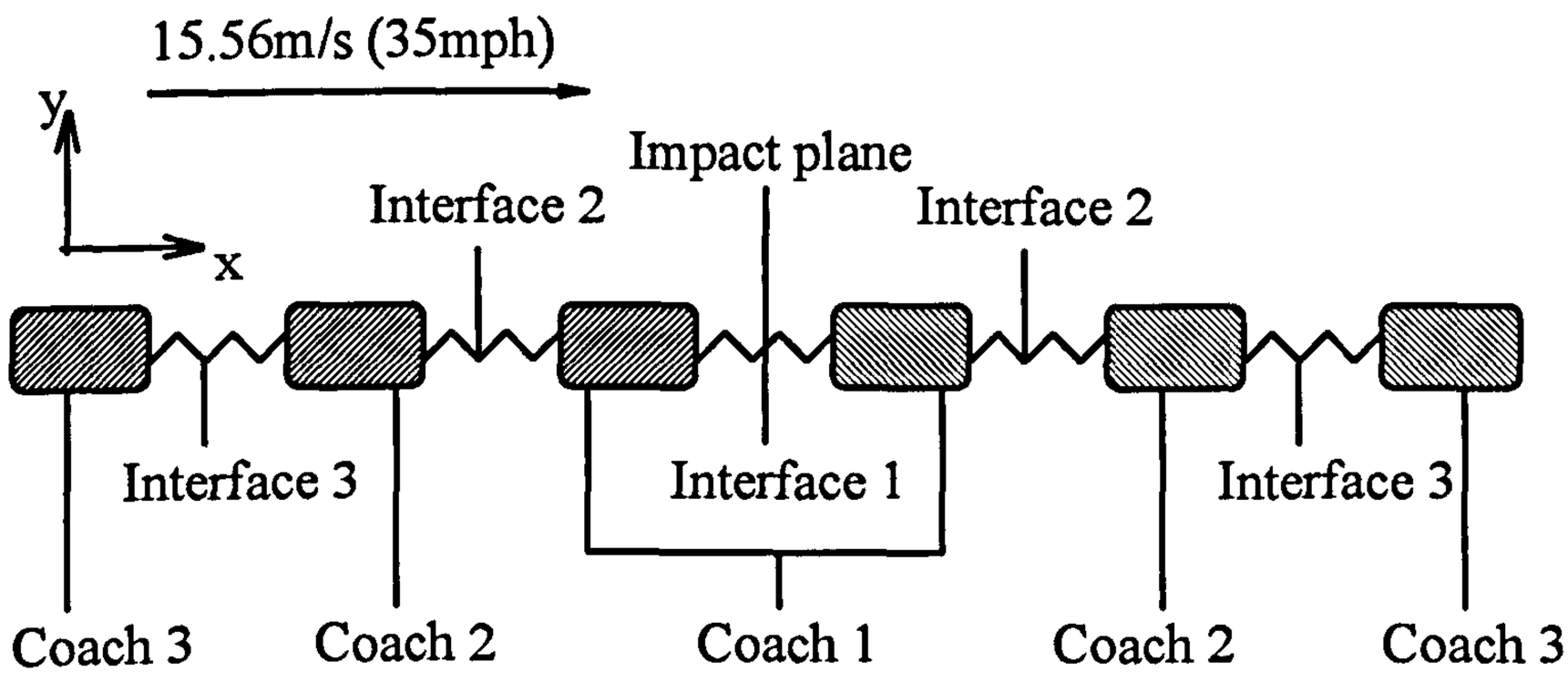

Note:

(1) Each coach is 35tonne.

(2) Spring in interface 1 has characteristics shown in figure 4.3a.

(3) Other interfaces' springs has characteristics shown in figure 4.3b.

Figure 4.2 : The schematic description of the models used in Section 4.2.

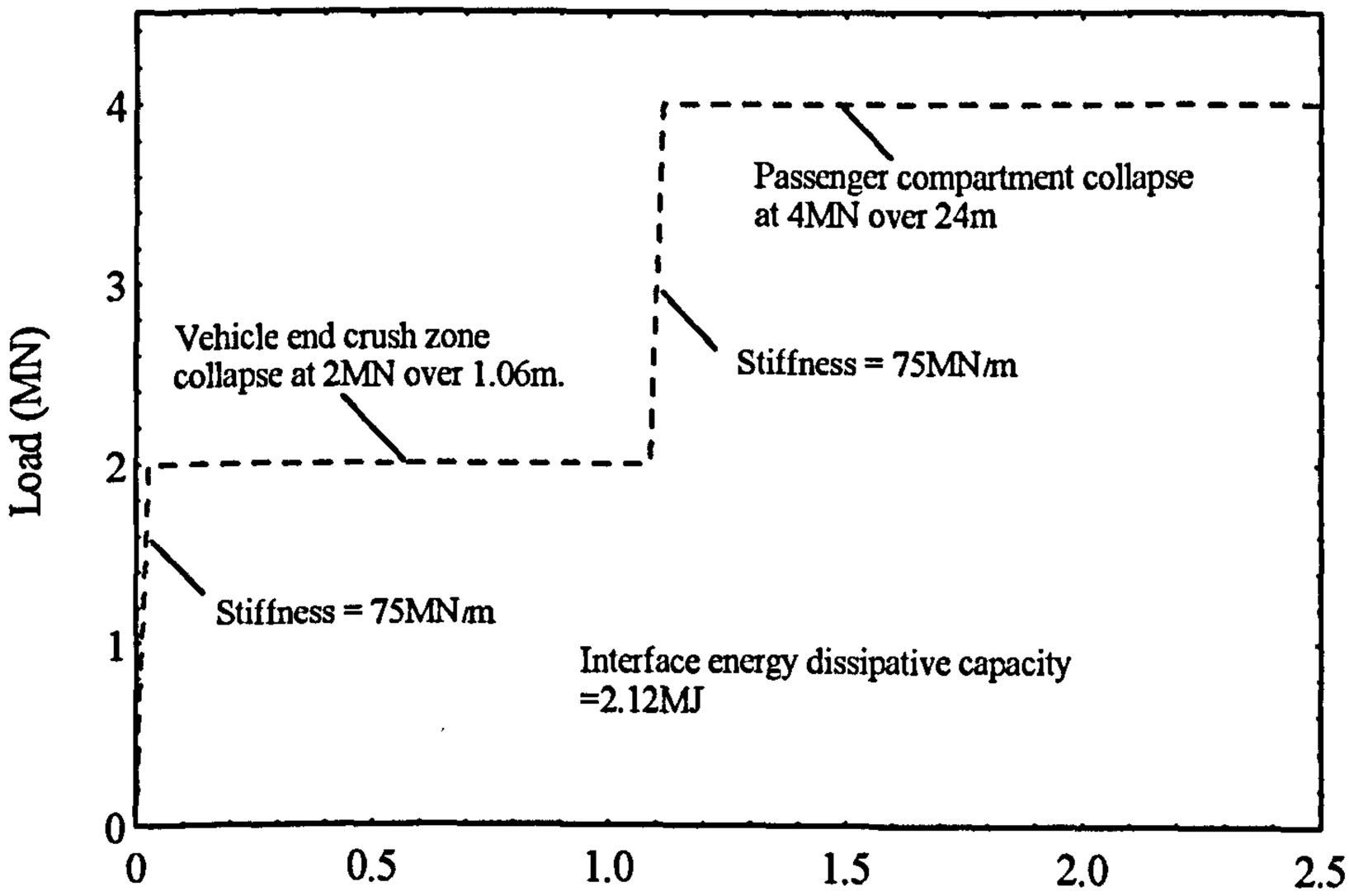

Figure 4.3a : The spring collapse characteristic of impact interface.

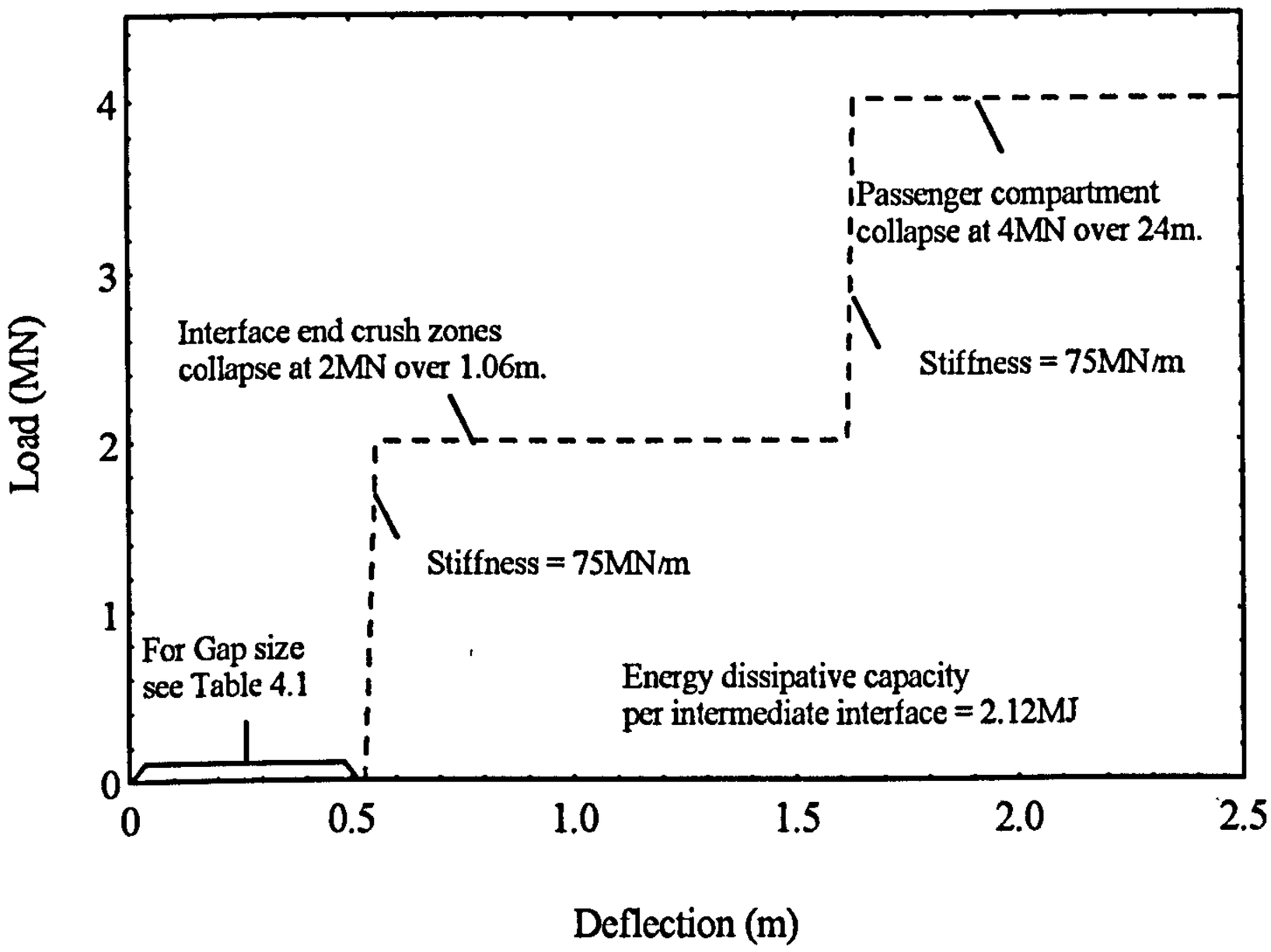

Figure 4.3b : The collapse characteristic for springs in the intermediate interfaces

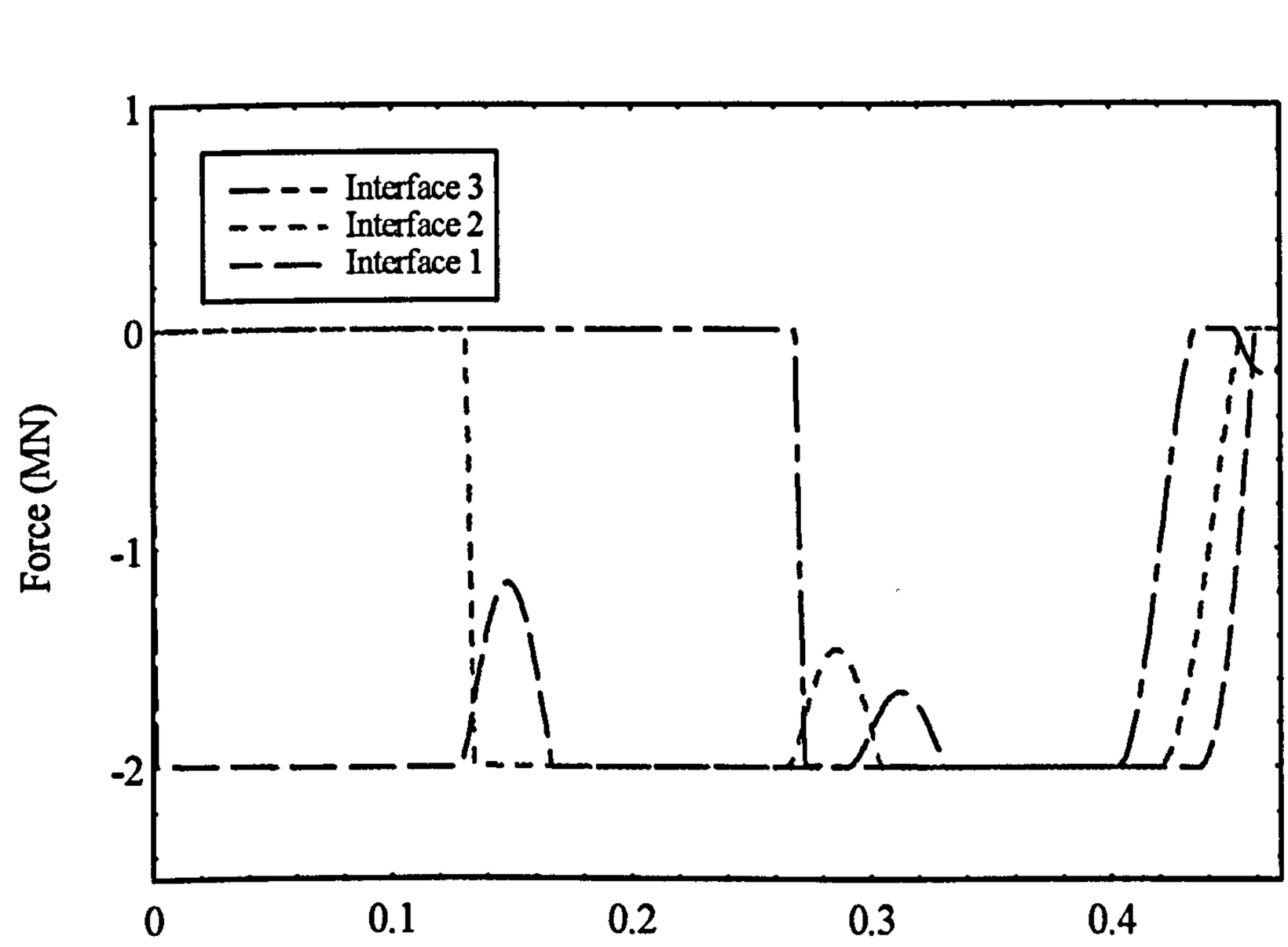

Figure 4.4a : The force-time history of various interfaces for the model Gap3.

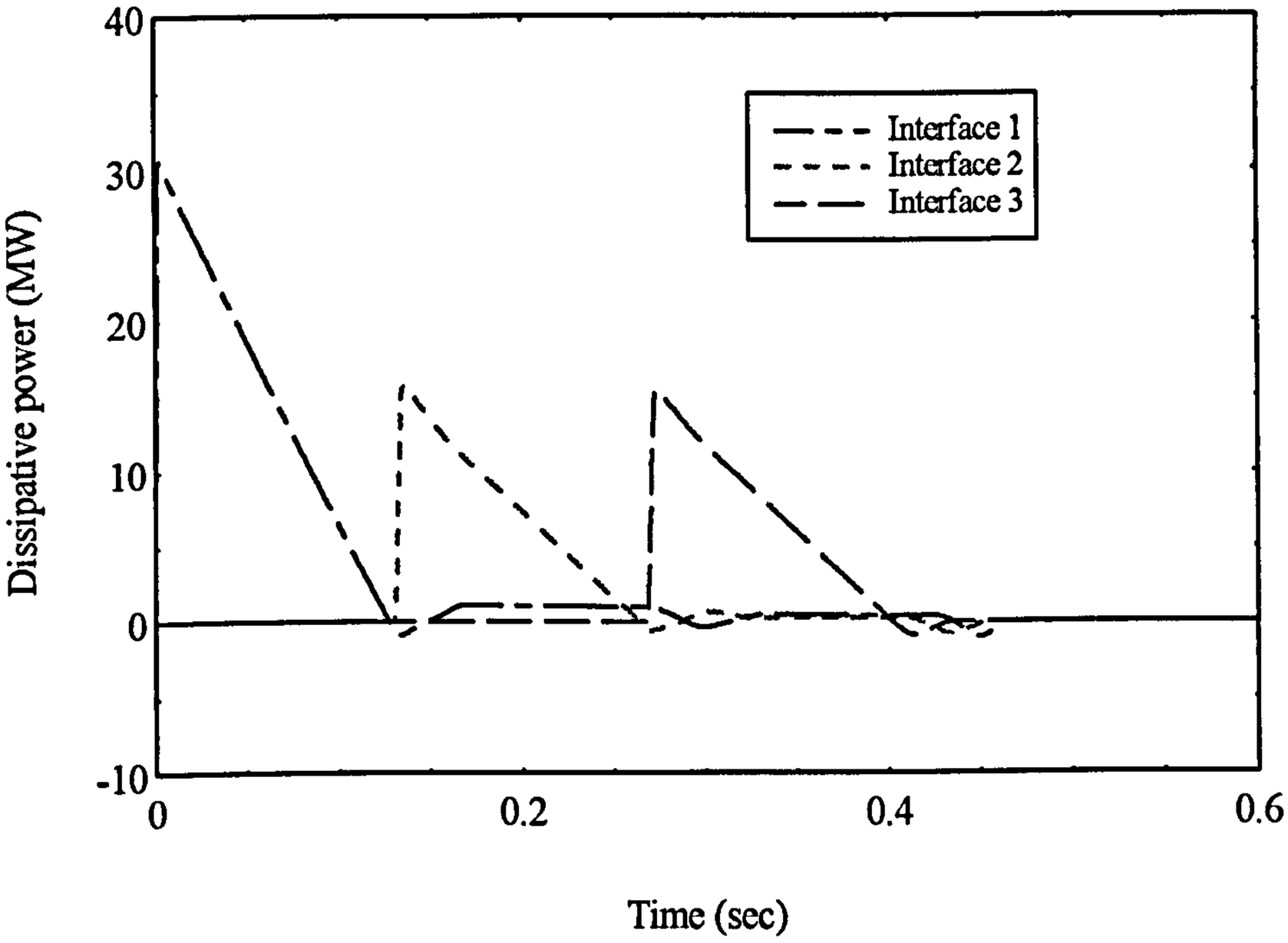

Figure 4.4b : The $\dot{E}$ against t of various interfaces for the model Gap3.

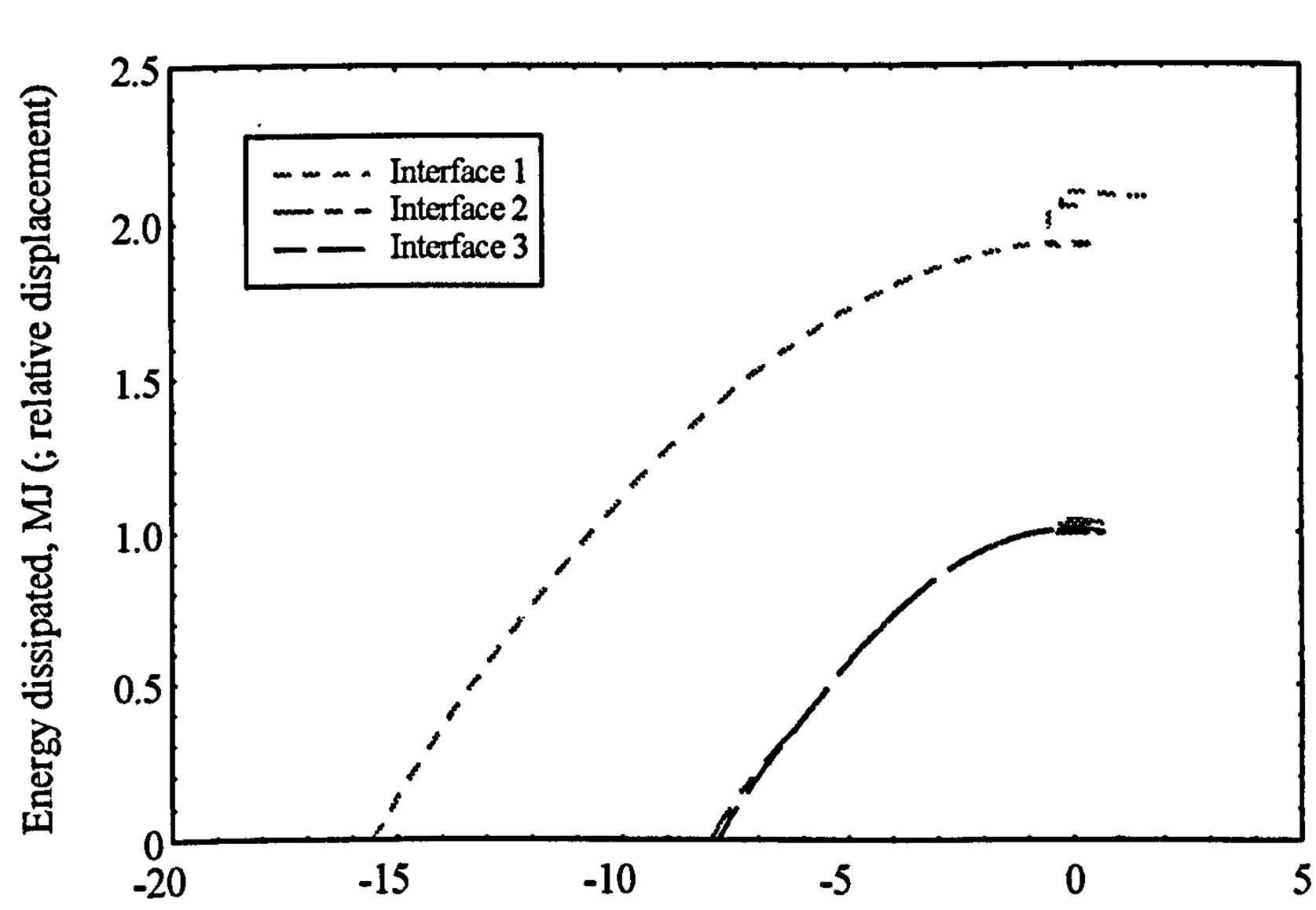

Figure 4.4c : The phase plot of various interfaces for the model Gap3.

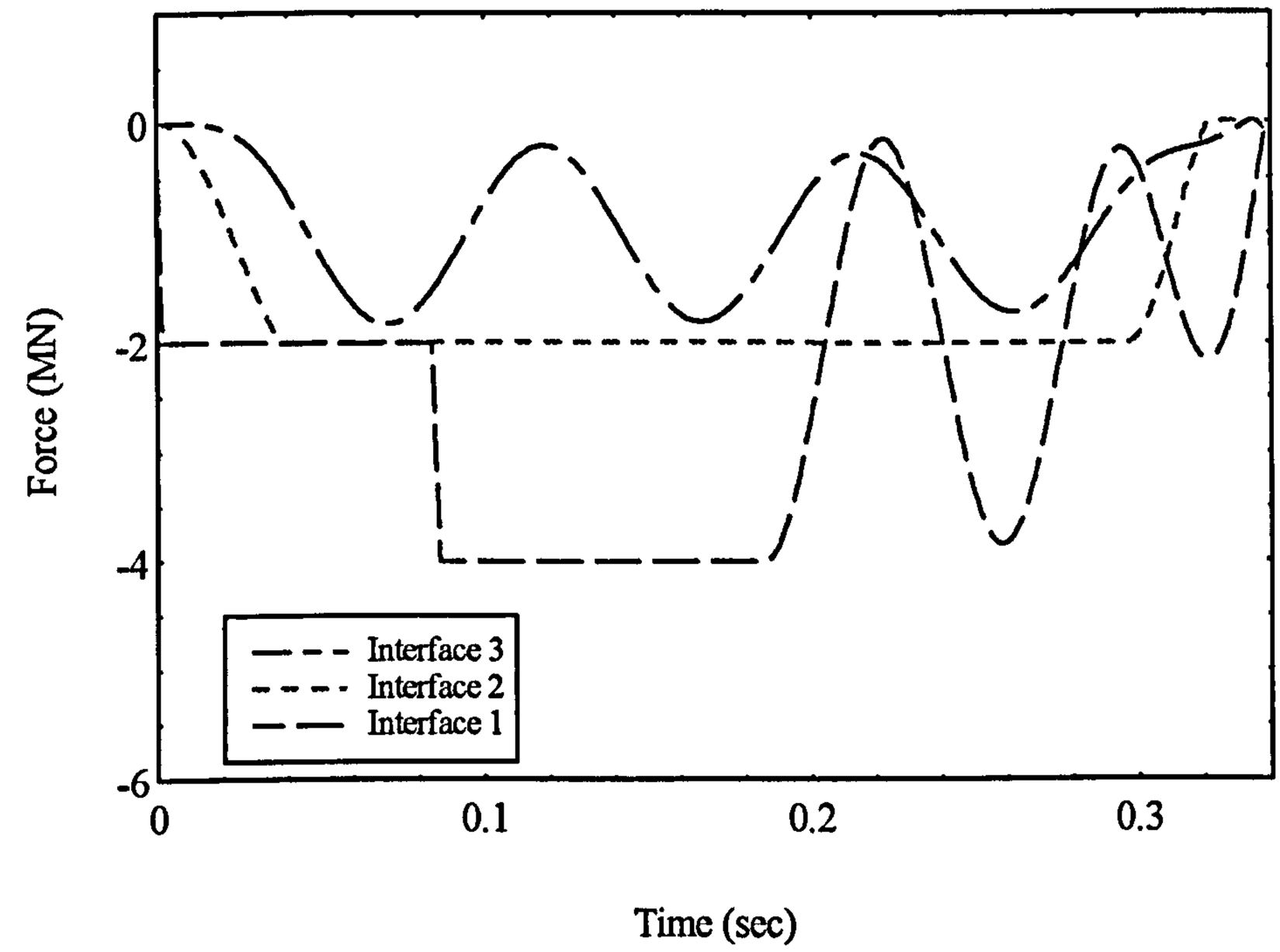

Figure 4.5a : The force-time histories of various interfaces for the model Gap1.

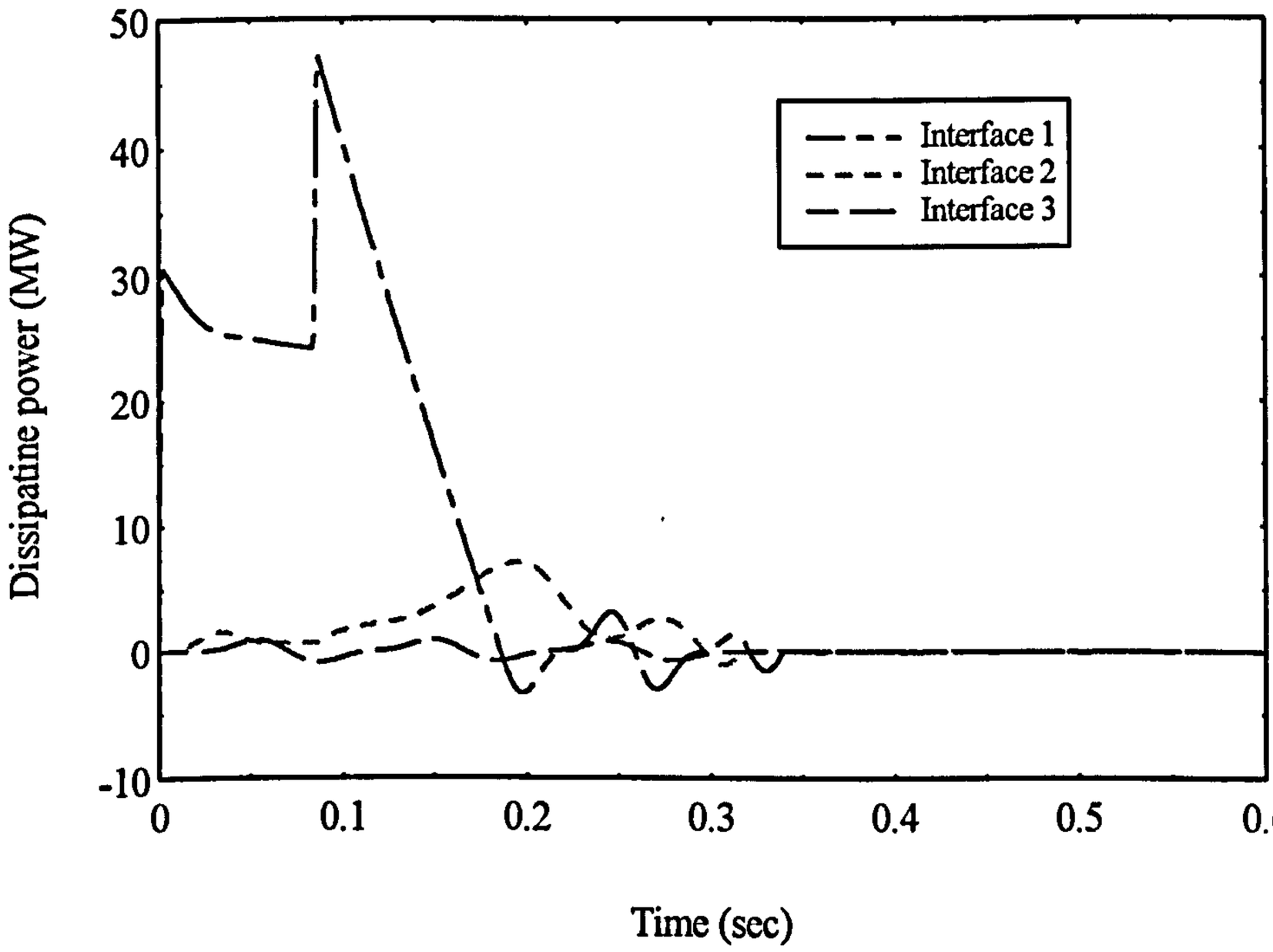

Figure 4.5b : The $\dot{E}$ against t of various interfaces for the model Gap1.

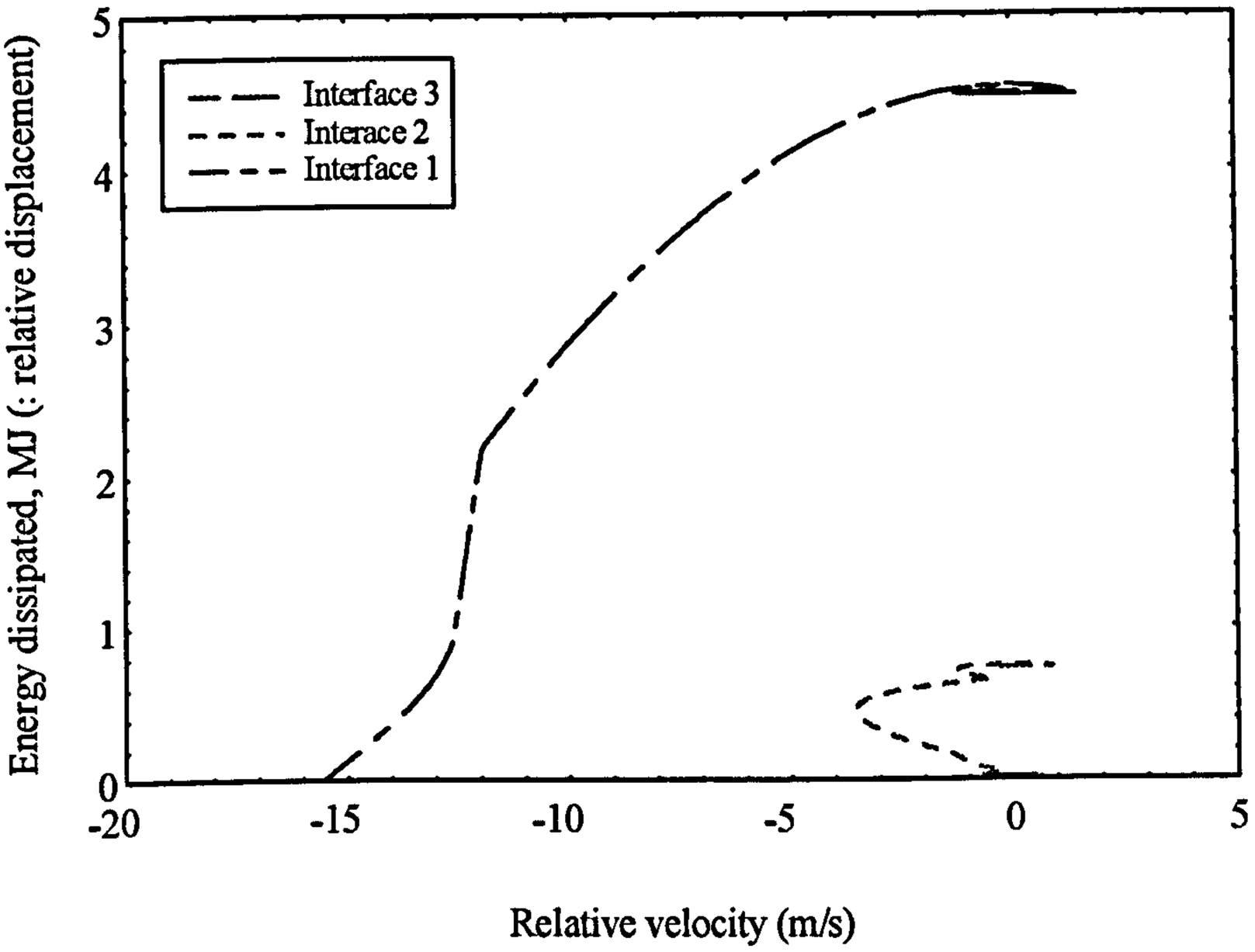

Figure 4.5c : The phase plot of various interfaces for the model Gap1.

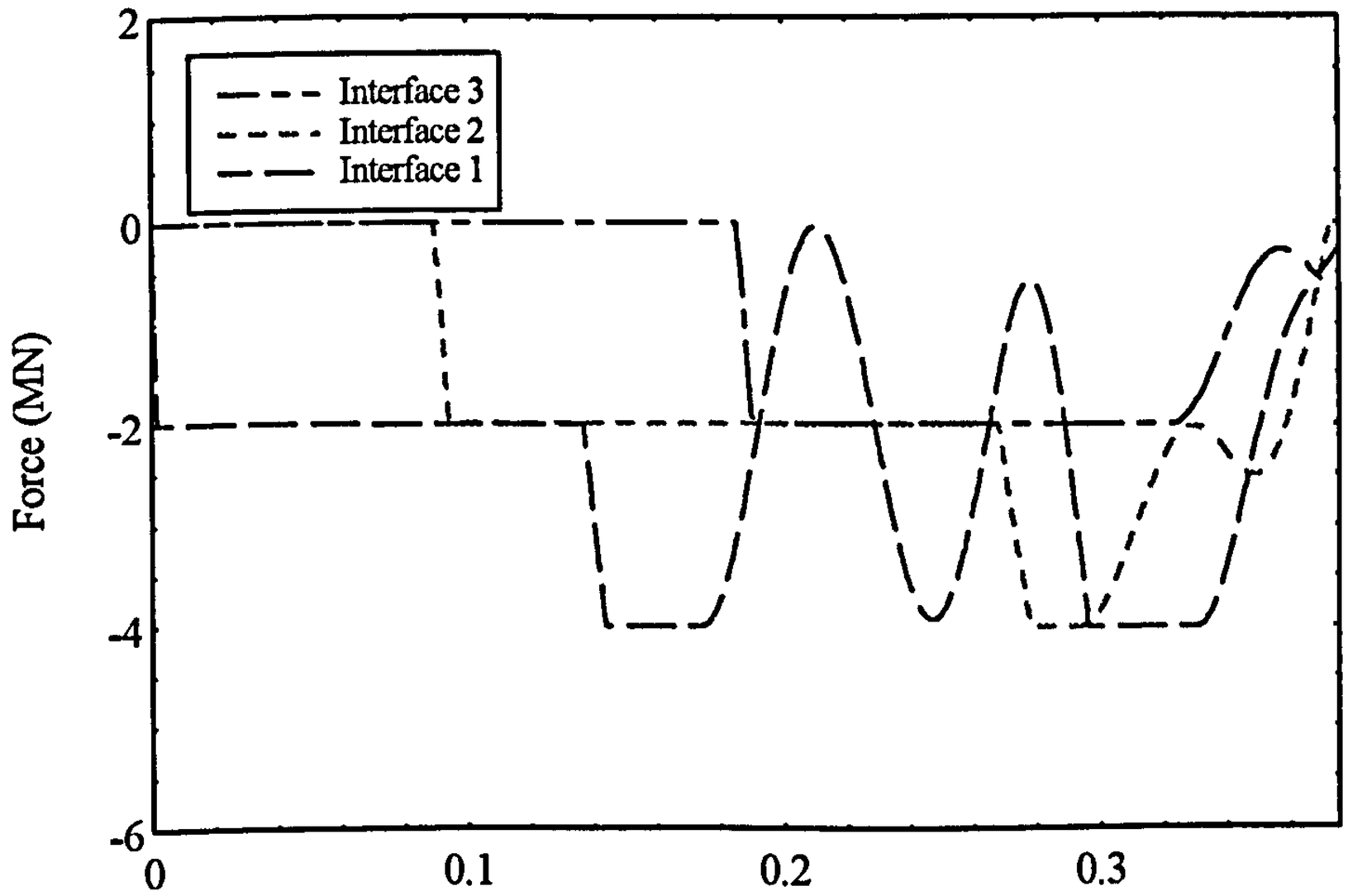

Figure 4.6a : The force-time history of various interfaces for the model Gap2.

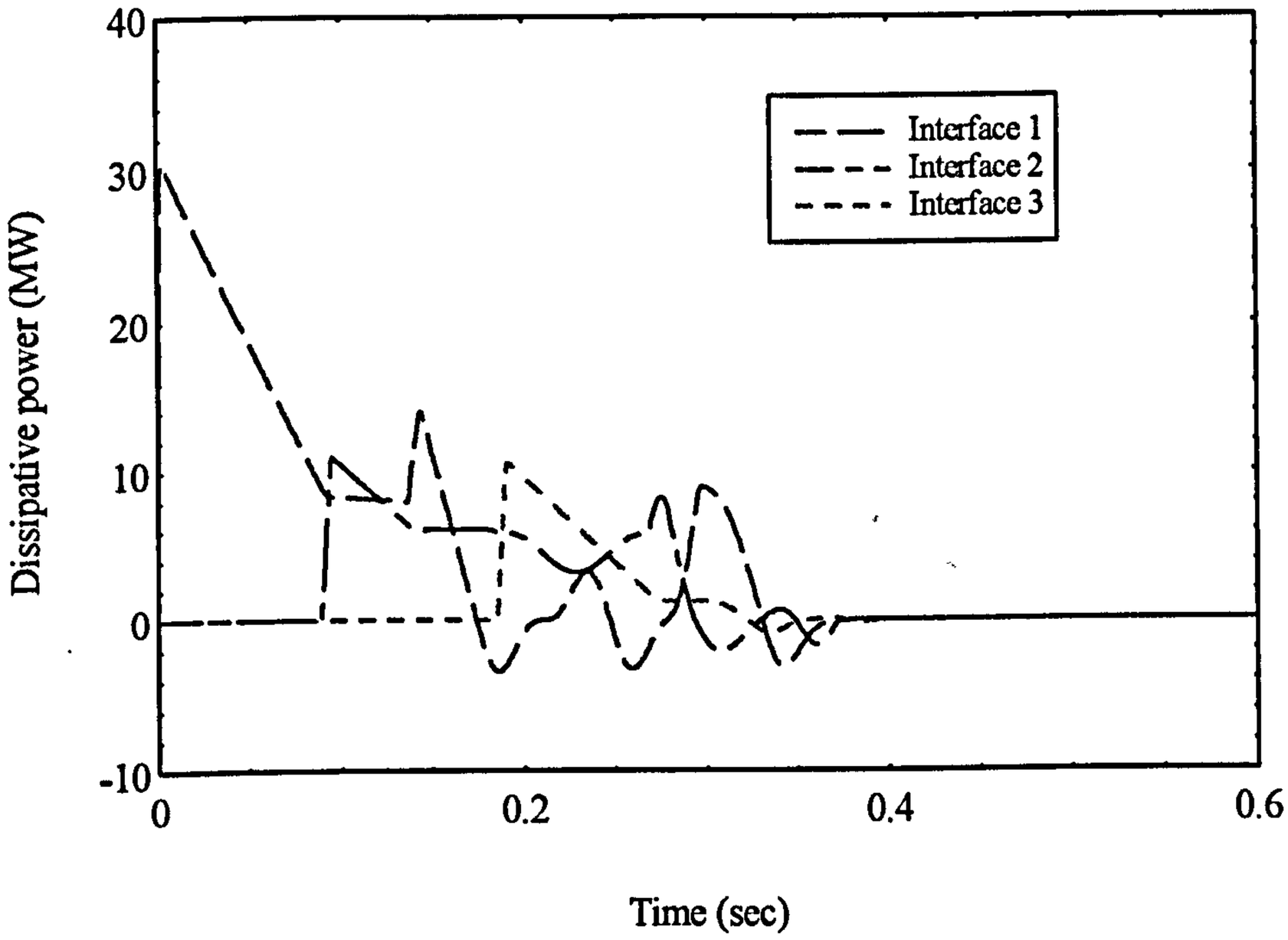

Figure 4.6b : The $\dot{E}$ against t of various interfaces for the model Gap2.

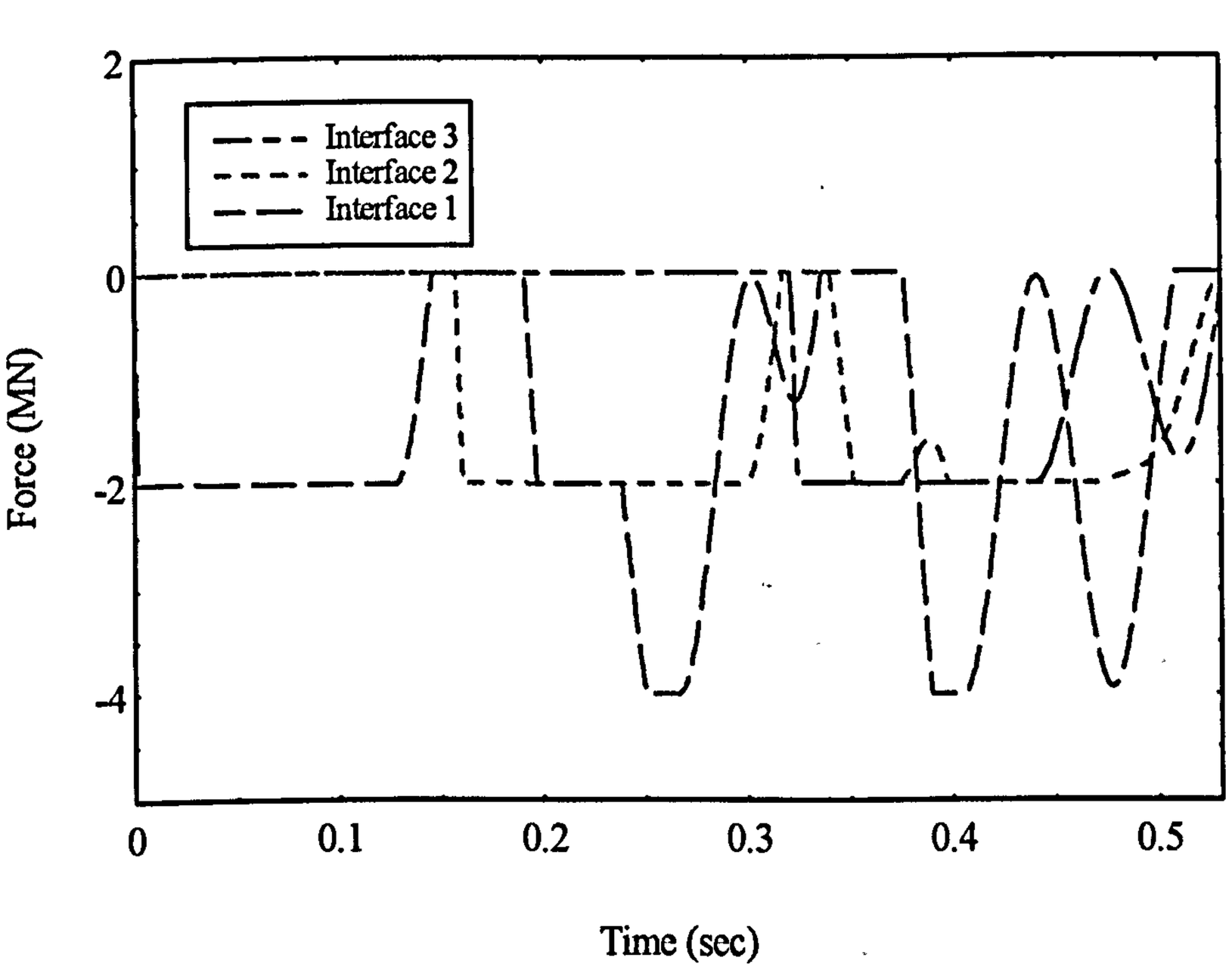

Figure 4.7a : The force-time history of various interfaces for the model Gap4.

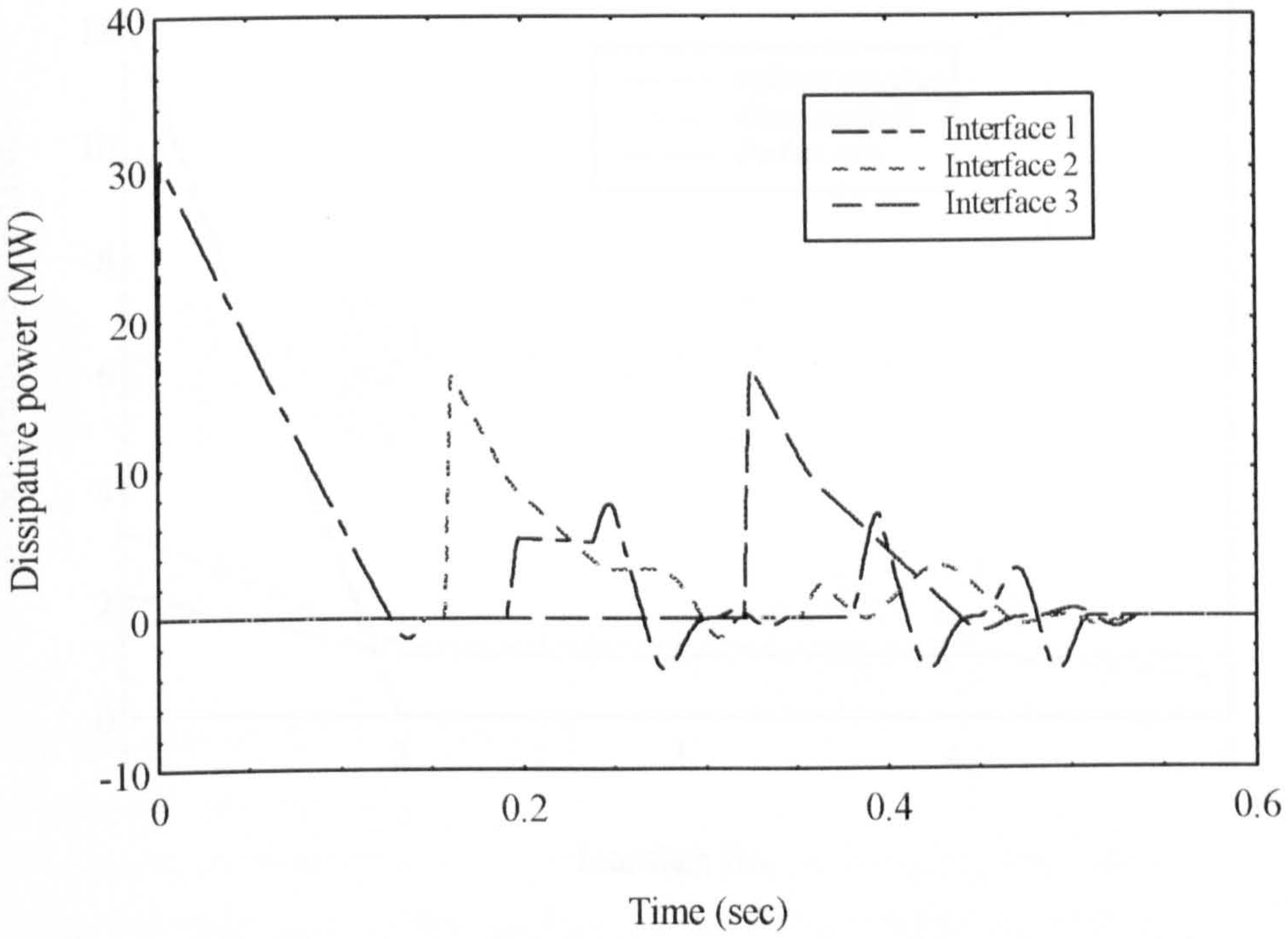

Figure 4.7b : The $\dot{E}$ against t of various interfaces for the model Gap4.

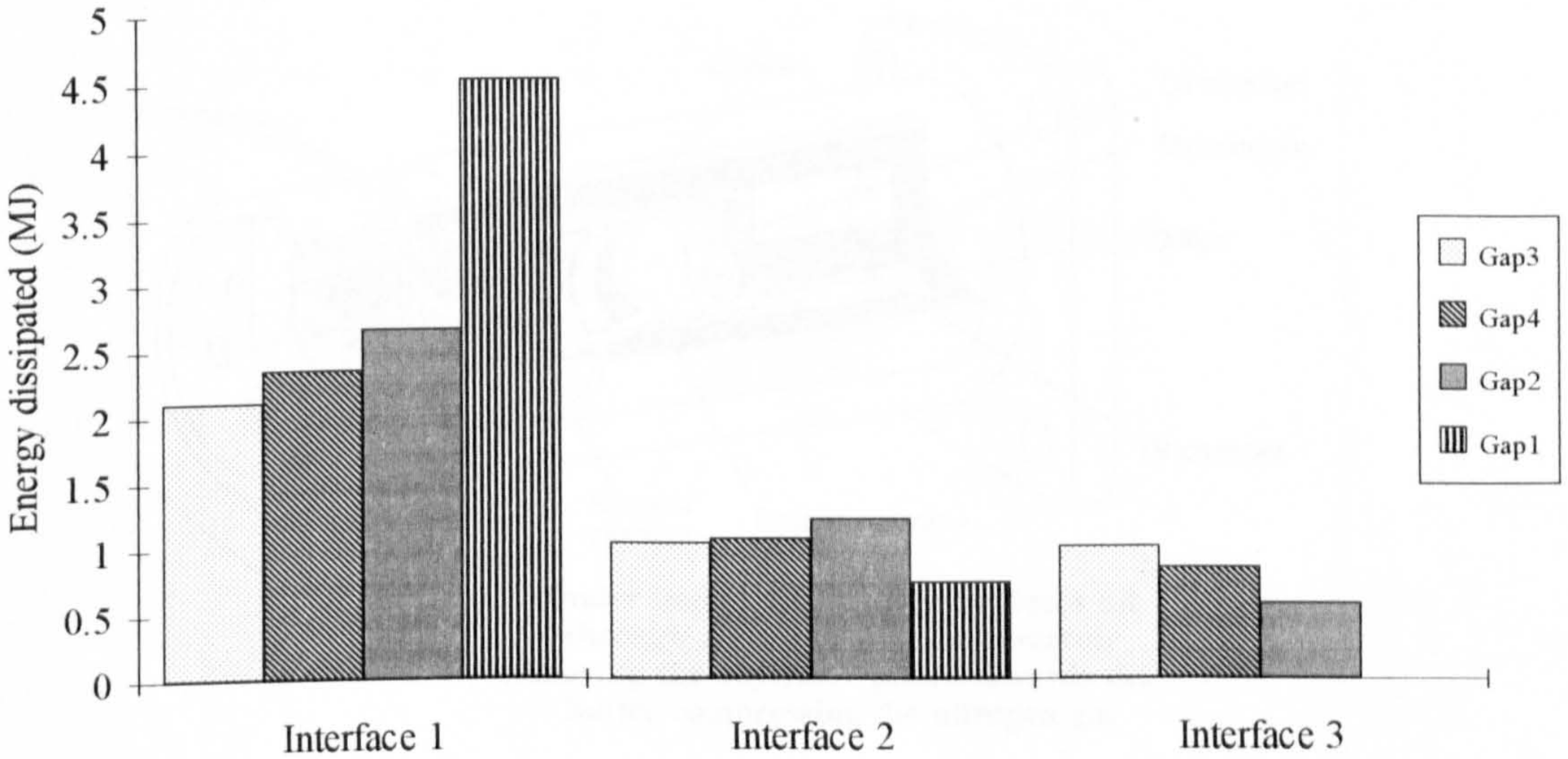

Figure 4.8 : The dissipated energy distribution among the various interfaces of the models.

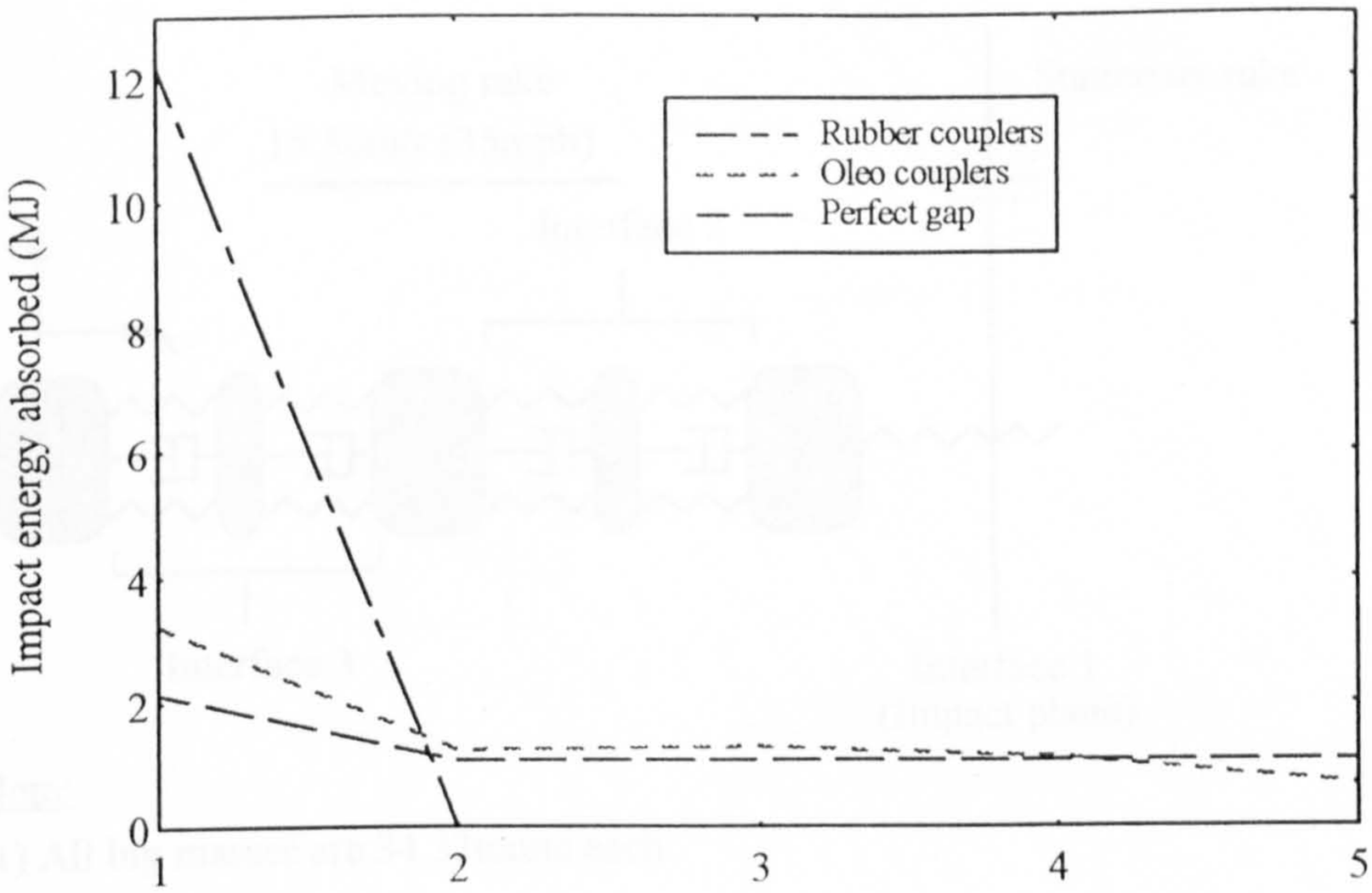

Figure 4.9 : The energy distribution comparison for various coupling arrangement [4].

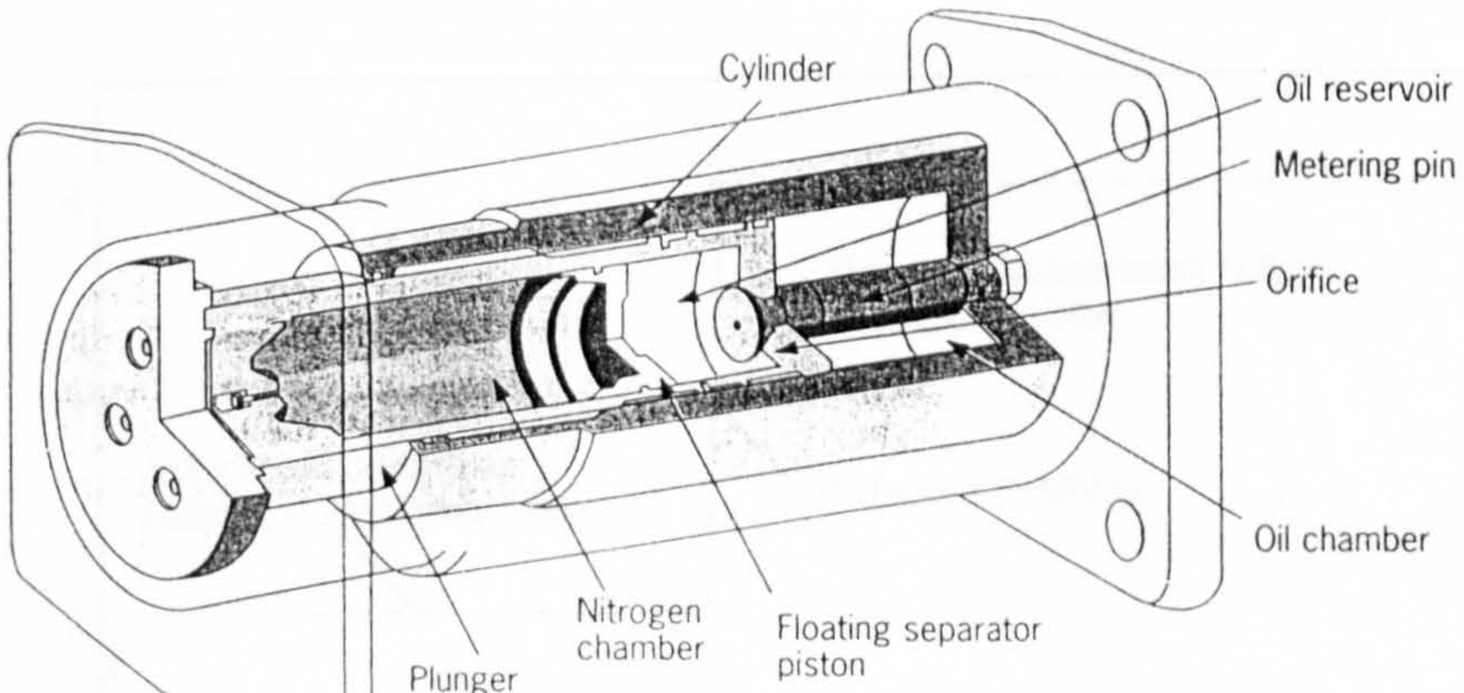

Under impact the plunger displaces oil through an orifice into the reservoir moving the separator piston towards the buffer compressing the nitrogen gas

Figure 4.10 : The detail construction of an Oleo coupler.

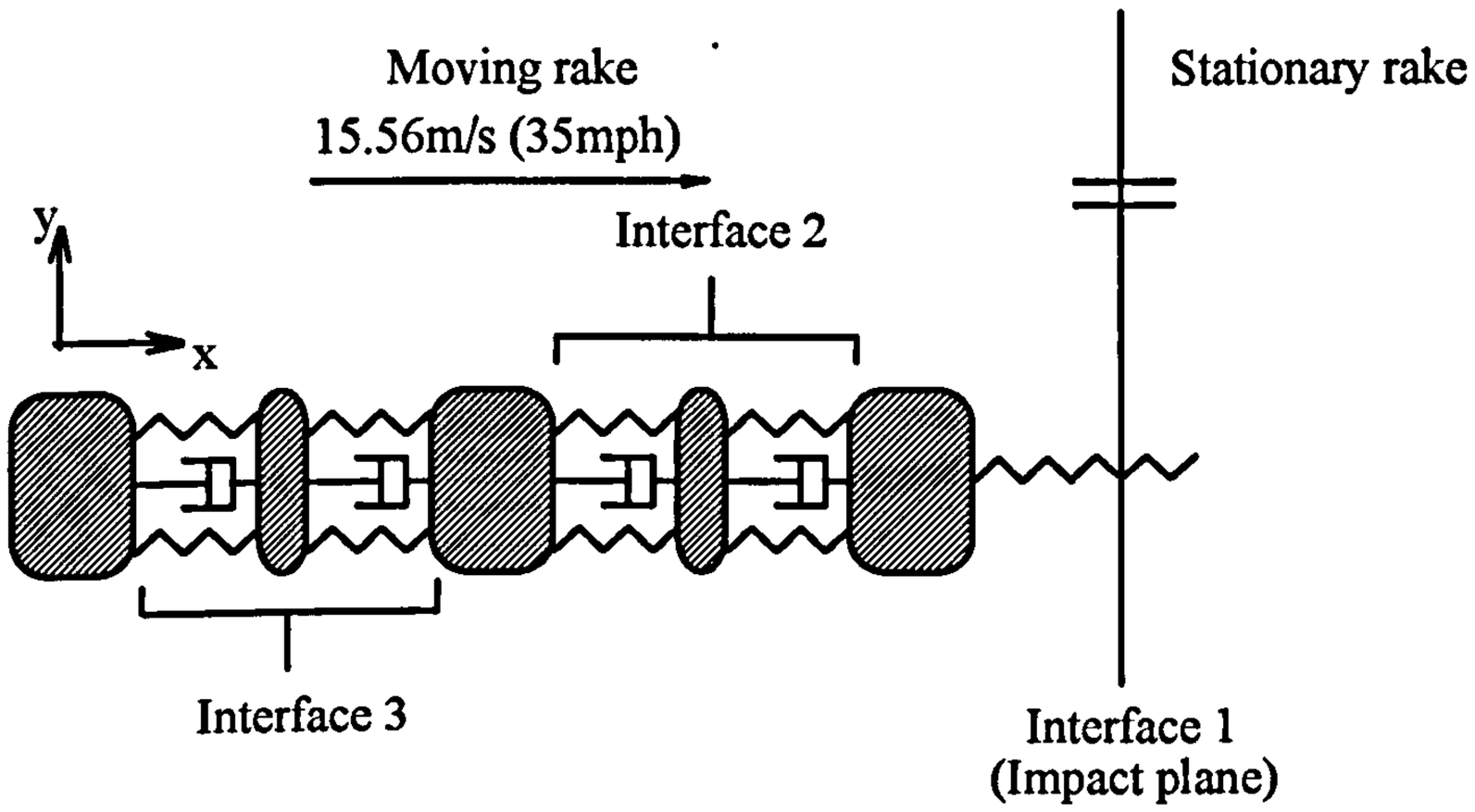

Note:

(1) All big masses are 34.33tonne each.

(2) Each small mass is 1tonne.

(3) The spring in interface 1 has the characteristics shown in figure 4.12a.

(4) Other interfaces' top springs have the characteristics shown in figure 4.12b.

(5) All bottom springs are representations of the hydrogen spring unit in Oleo couplers.

(6) The central dashpot have the characteristics of Oleo hydraulic couplers.

Figure 4.11 : The non-linear mass spring model that includes Oleo hydro-pneumatic couplers.

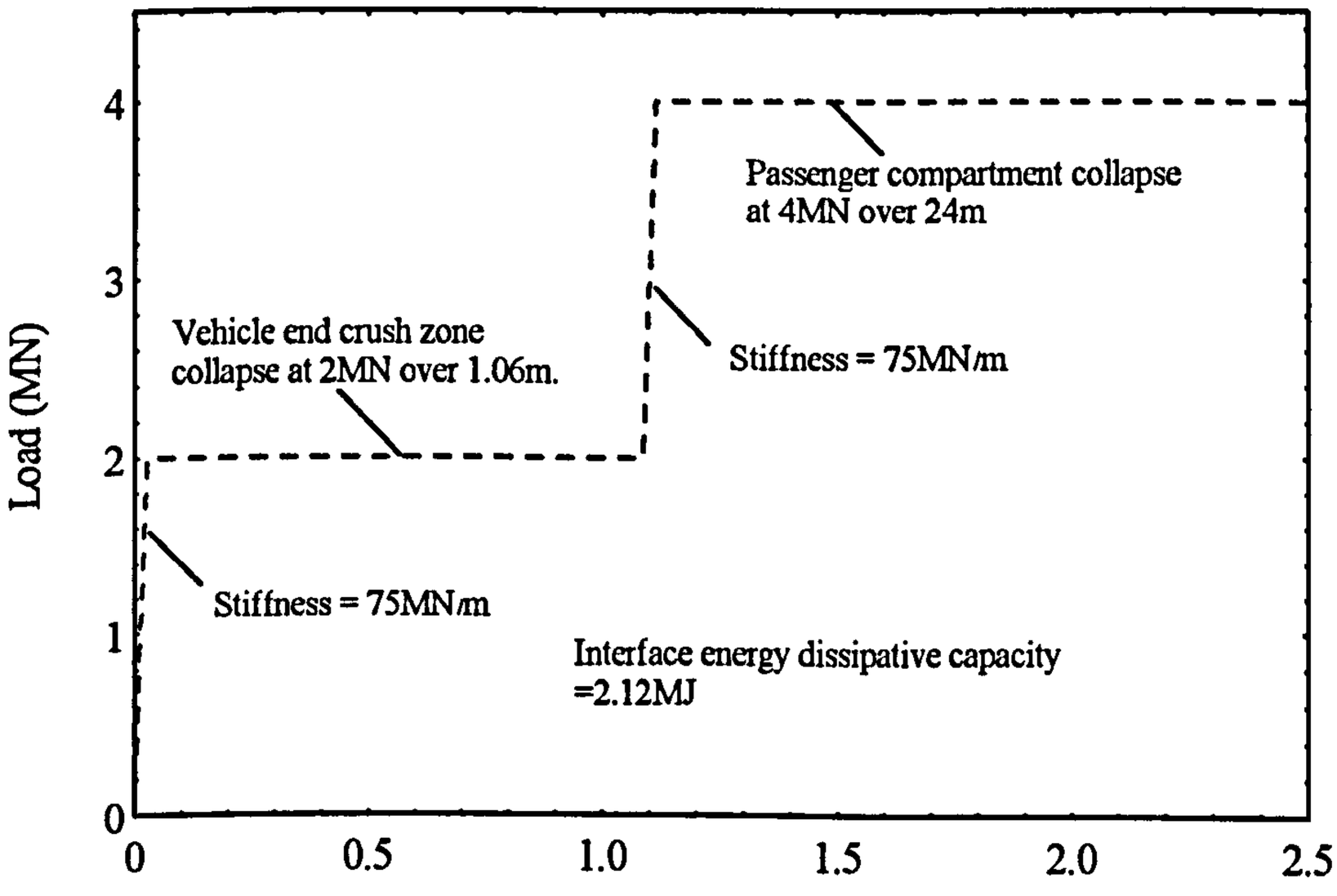

Figure 4.12a : The collapse characteristic of the impact interface spring.

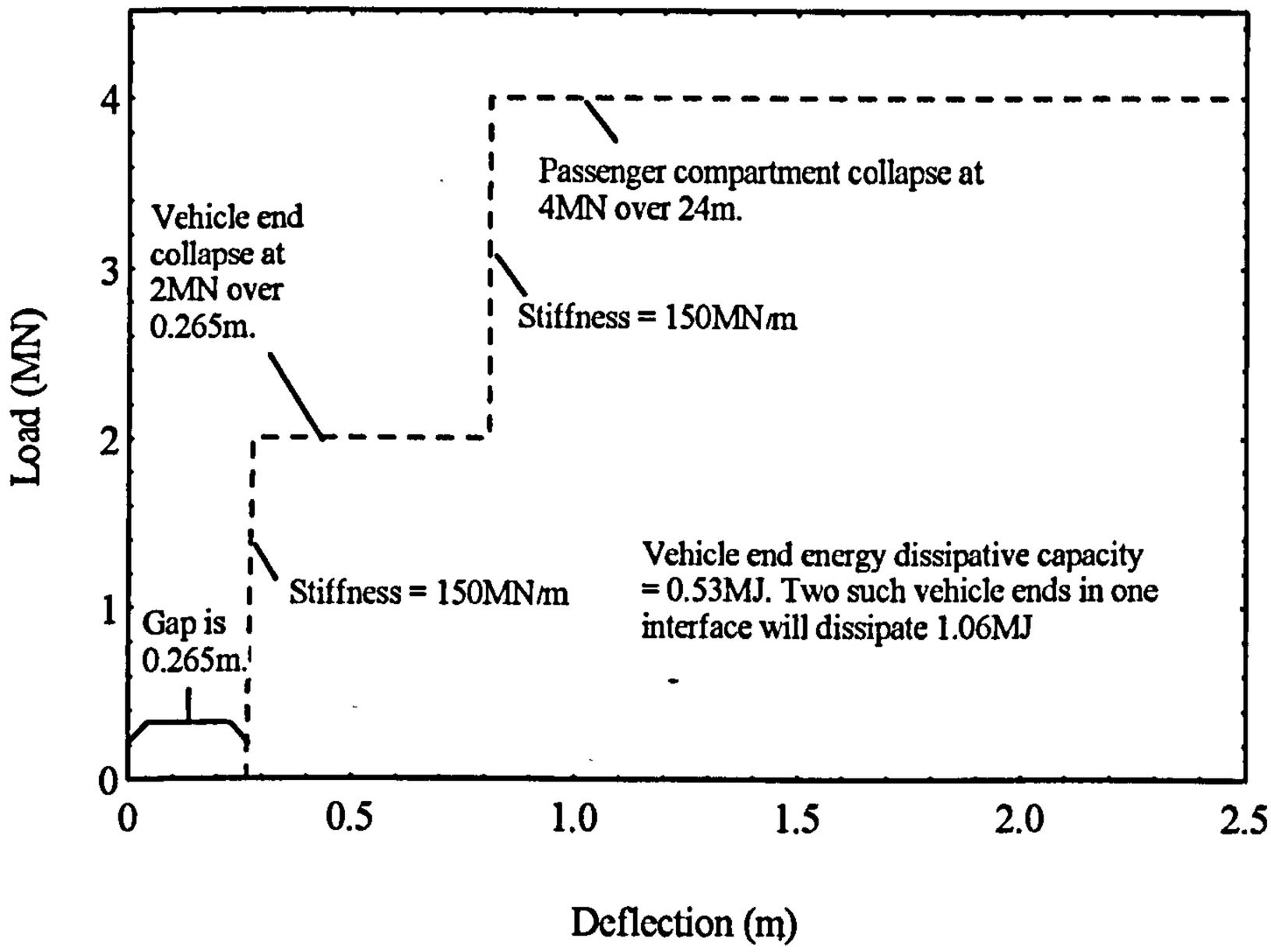

Figure 4.12b : The collapse characteristic of the intermediate springs.

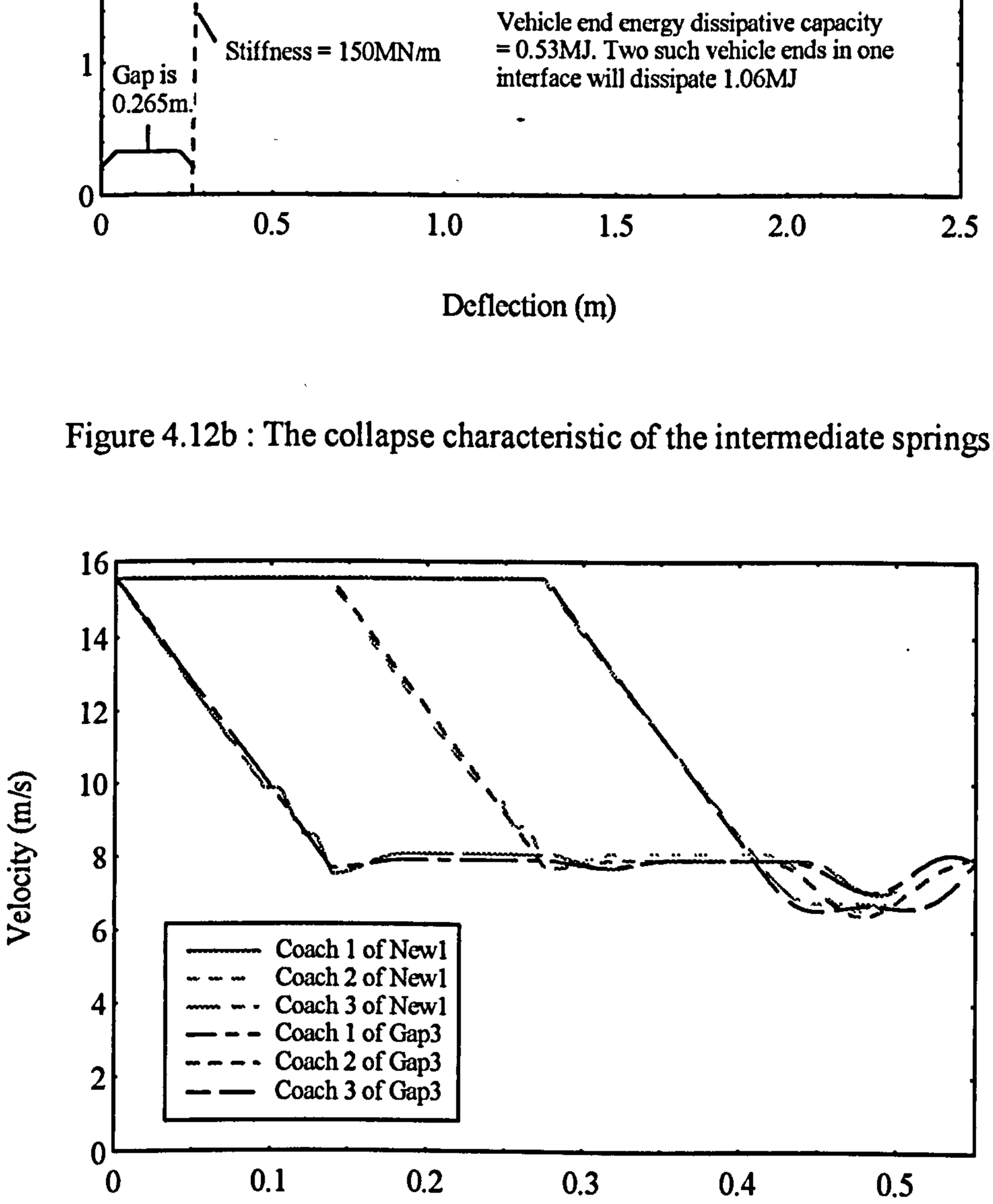

Figure 4.13 : The velocity-time history of various coaches in models New1 and Gap3.

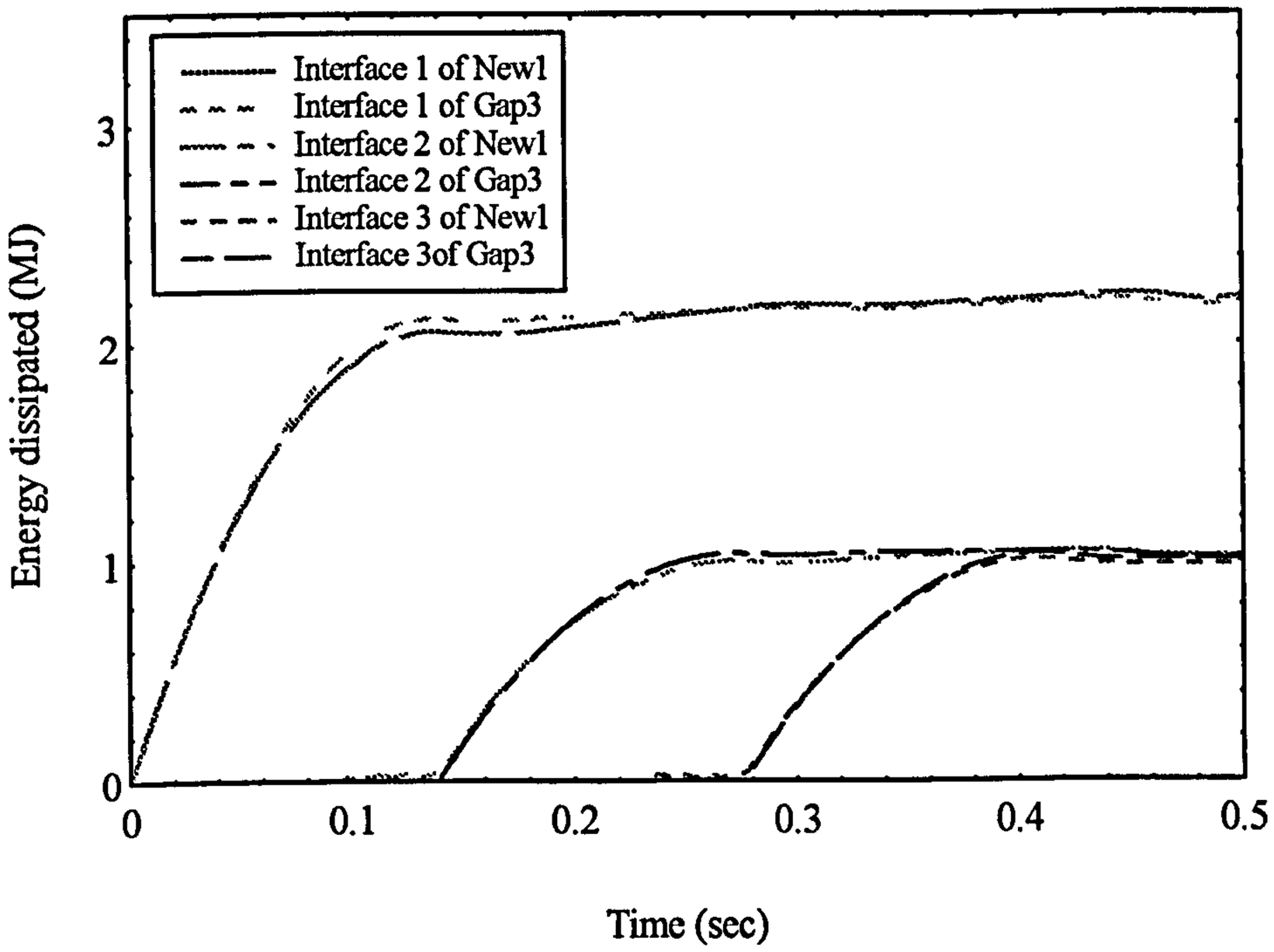

Figure 4.14 : The *E-t* graphs of various interfaces for the models New1 and Gap3.

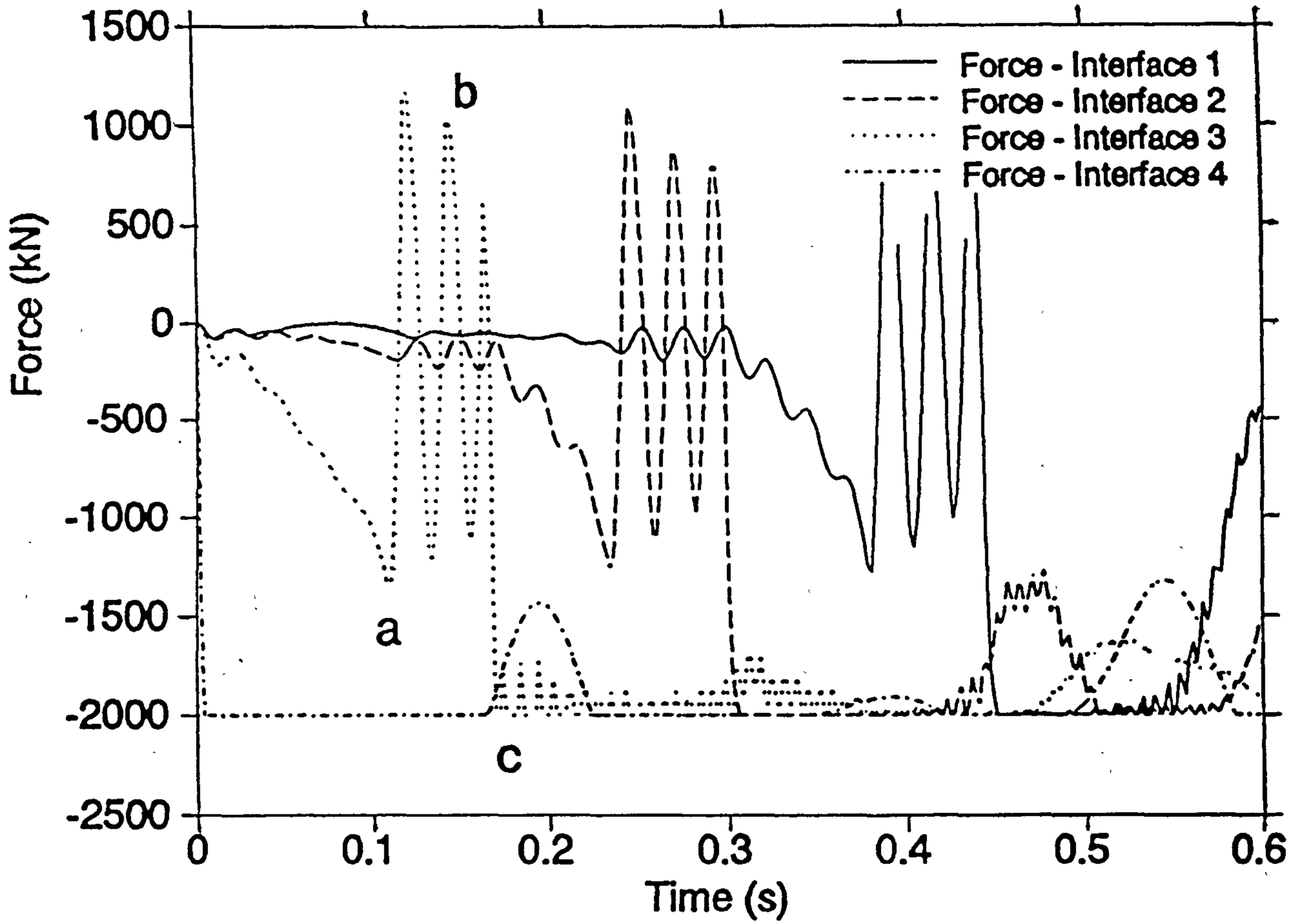

Figure 4.15 : The results produced by the BRR model which simulates a four-to-four (with Oleo couplers) collision [3].

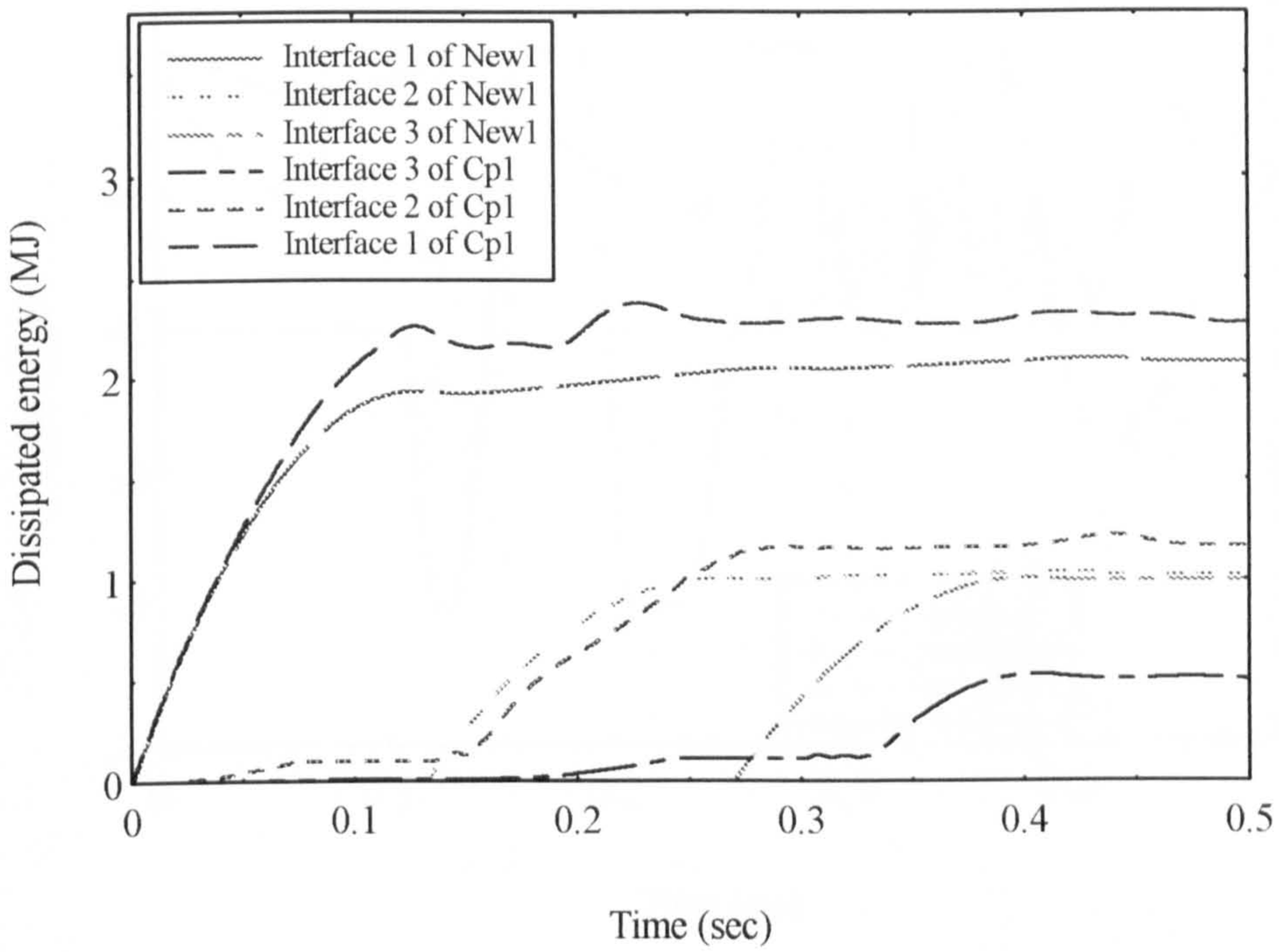

Figure 4.16 : The *E-t* graphs for various interfaces in the models Cp1 and New1.

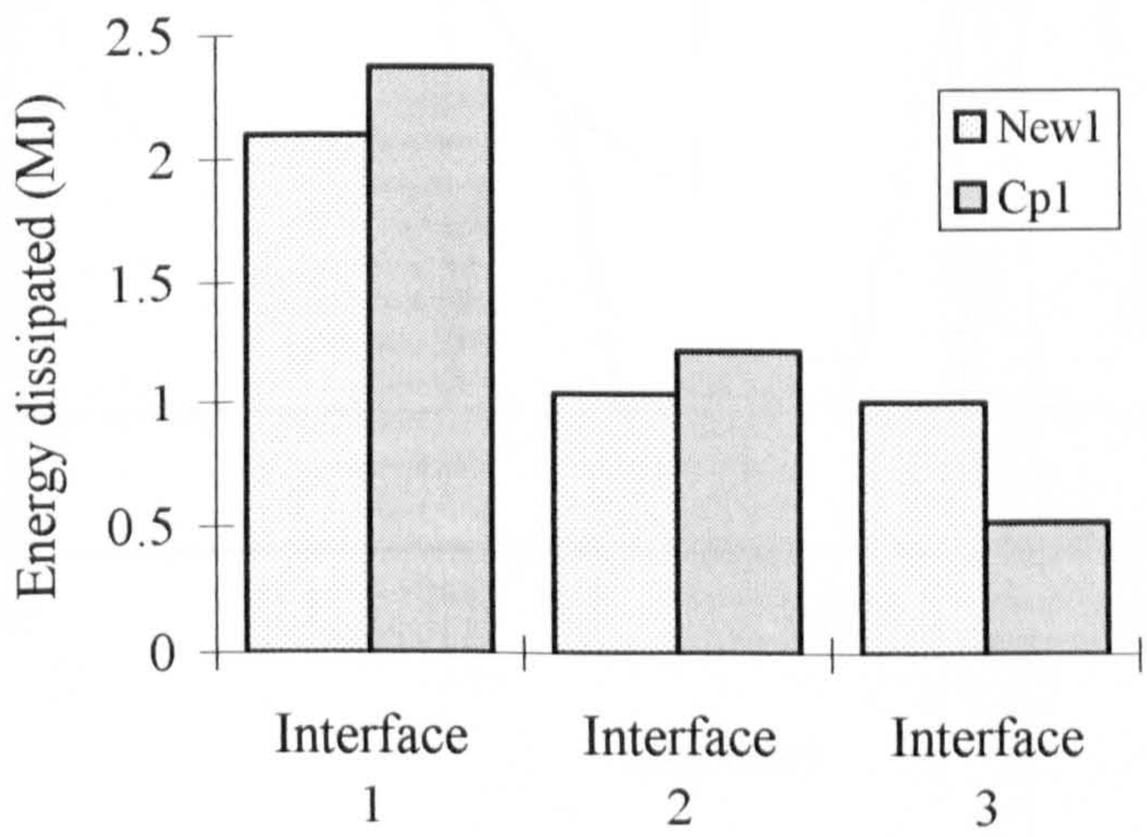

Figure 4.17 : Comparing the energy distribution between Cp1 and New1.

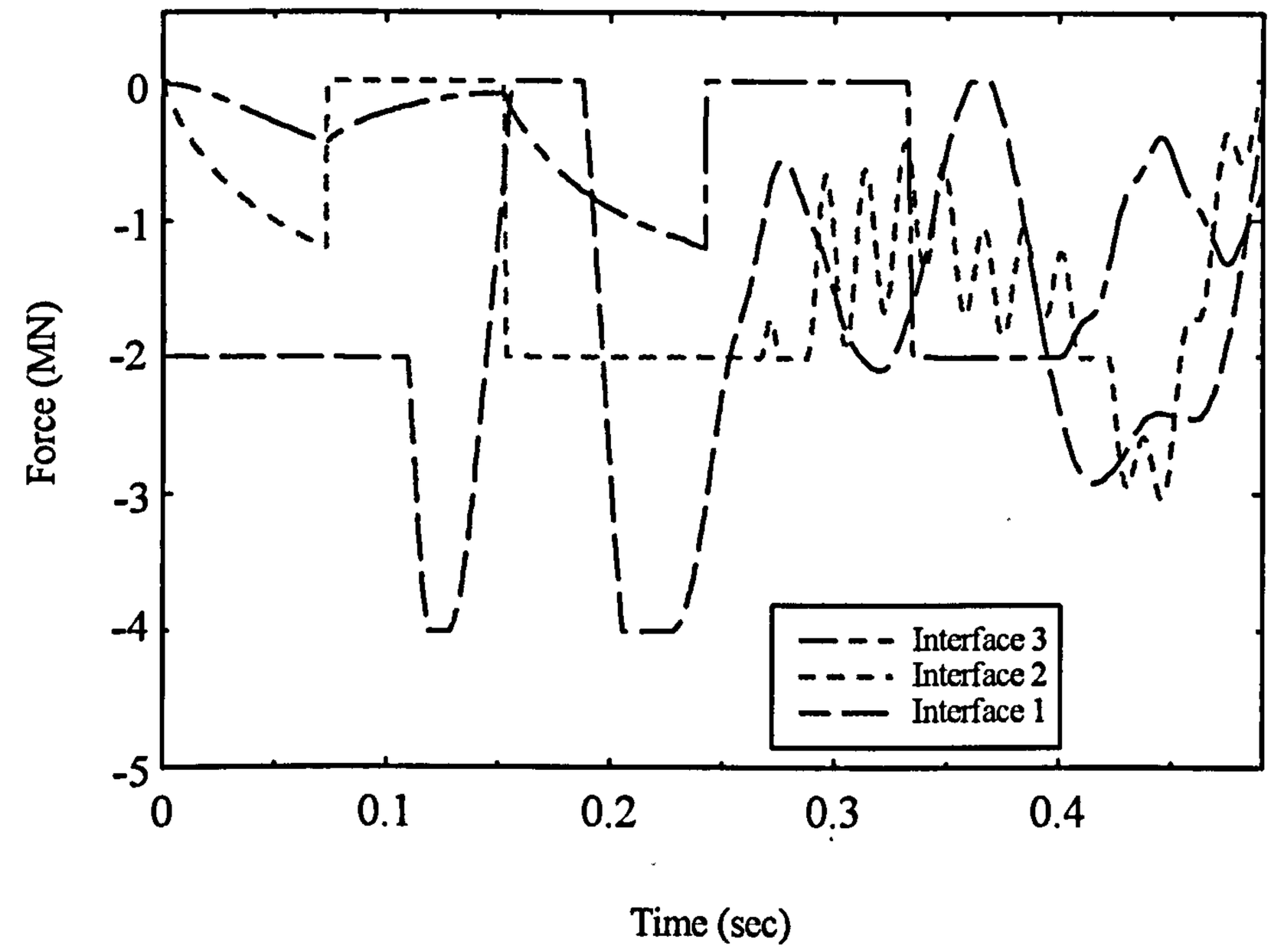

Figure 4.18 : The force-time graphs of various interfaces in the model Cp1.

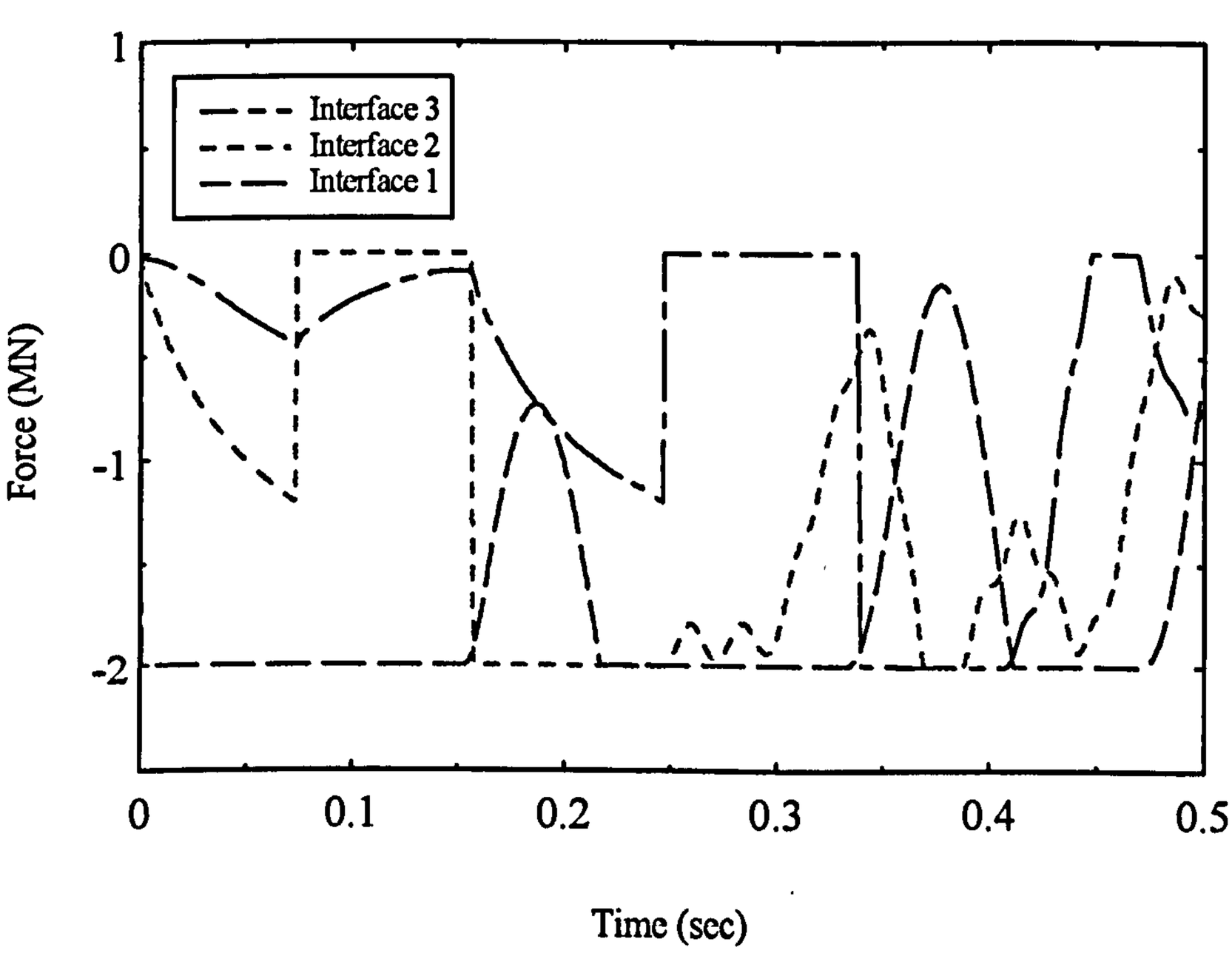

Figure 4.19 : The force-time history of various interfaces for the model Cp2.

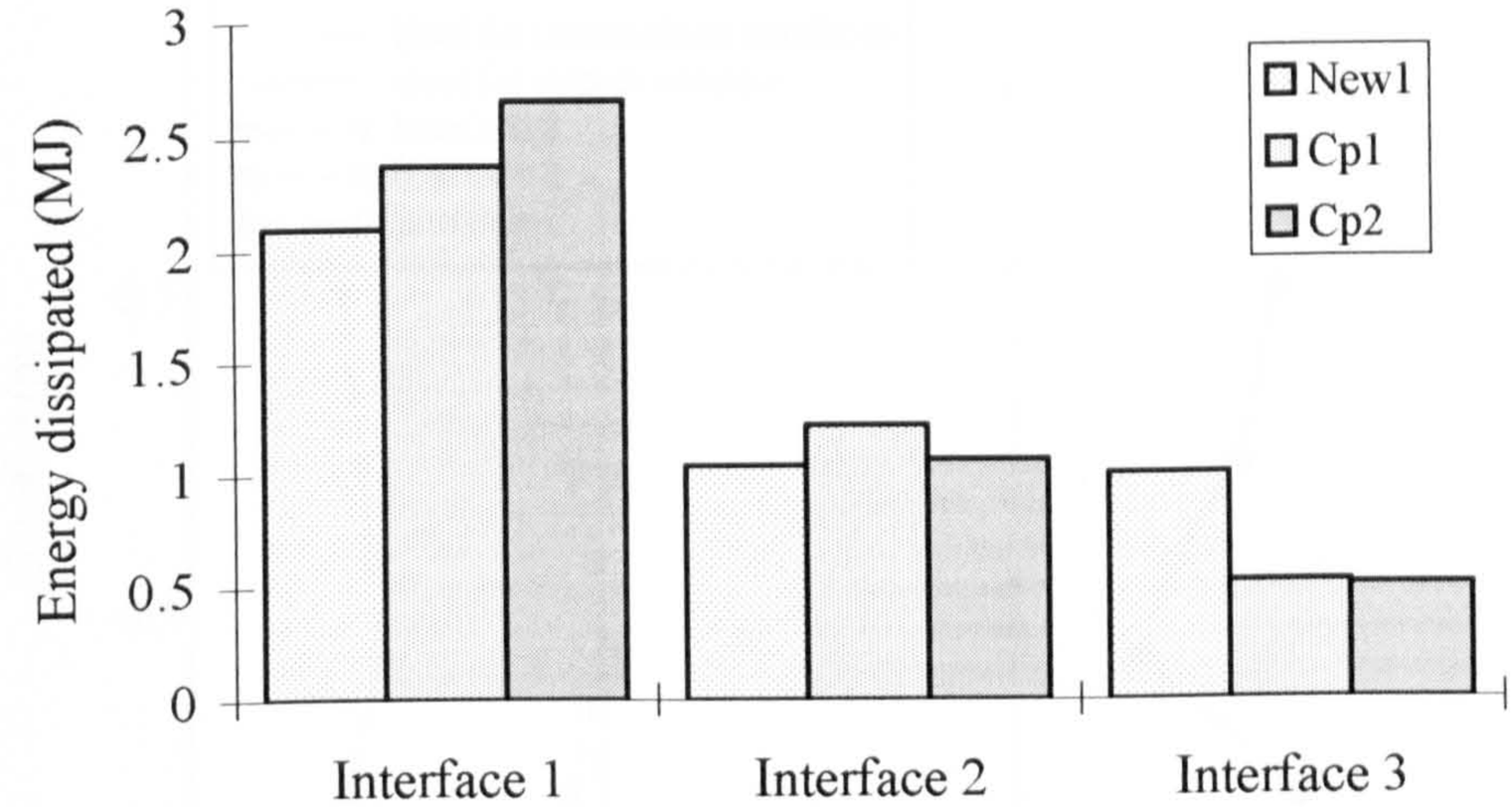

Figure 4.20 : The energy distribution patterns of the three models : New1, Cp1 & Cp2.

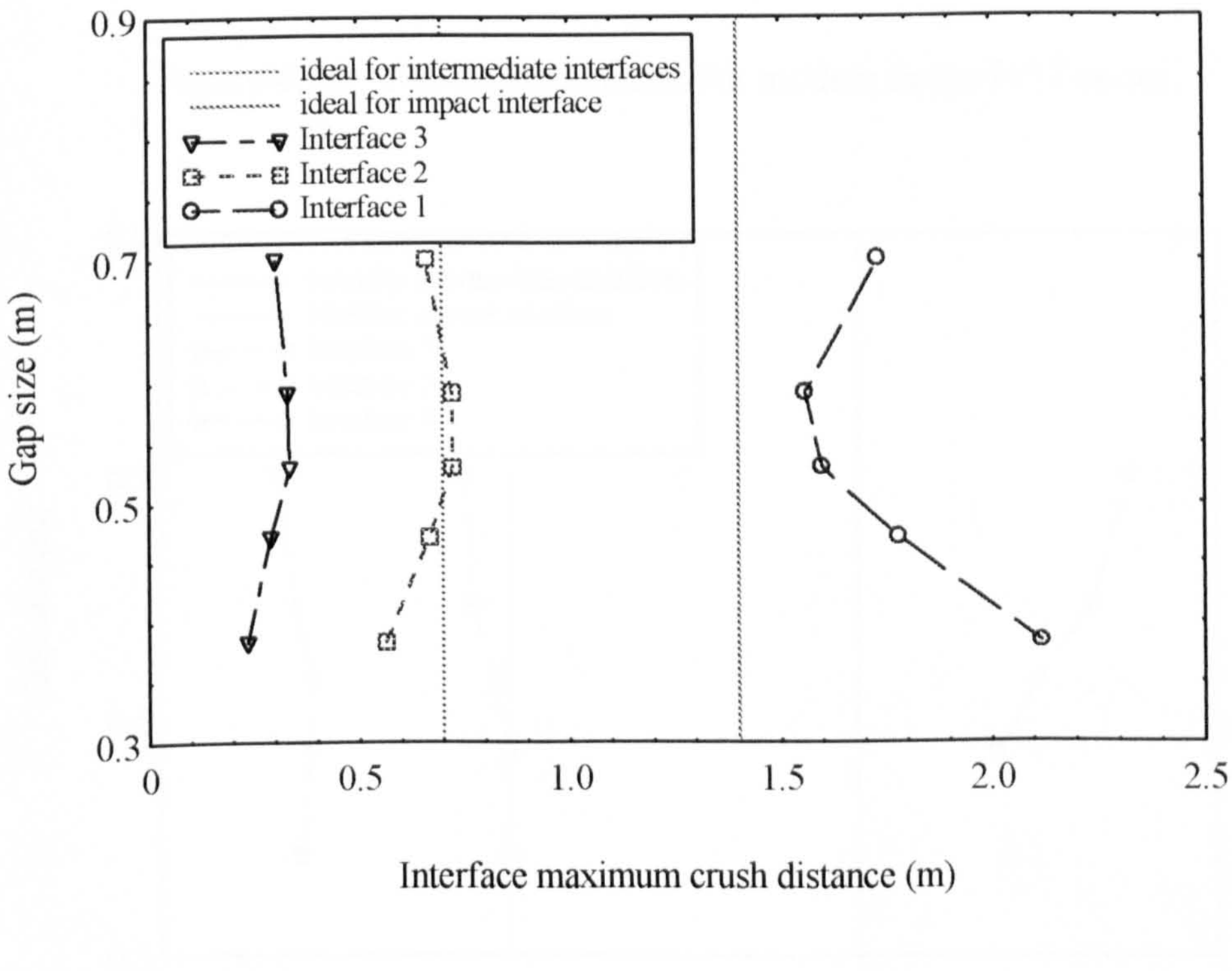

Figure 4.21 : The crush distance for models in the Iv40 series.

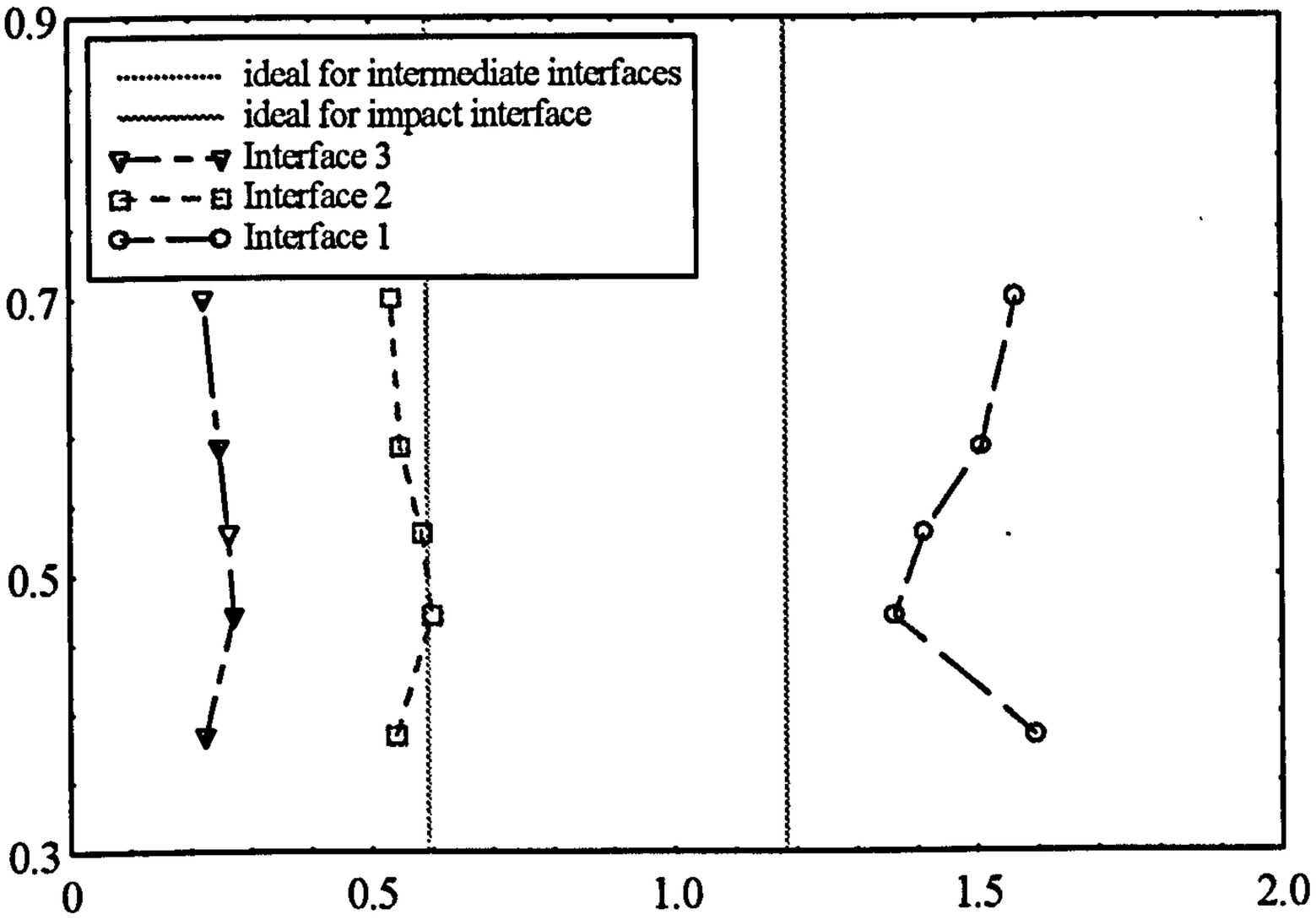

Figure 4.22 : The crush distance for models in the Iv37 series.

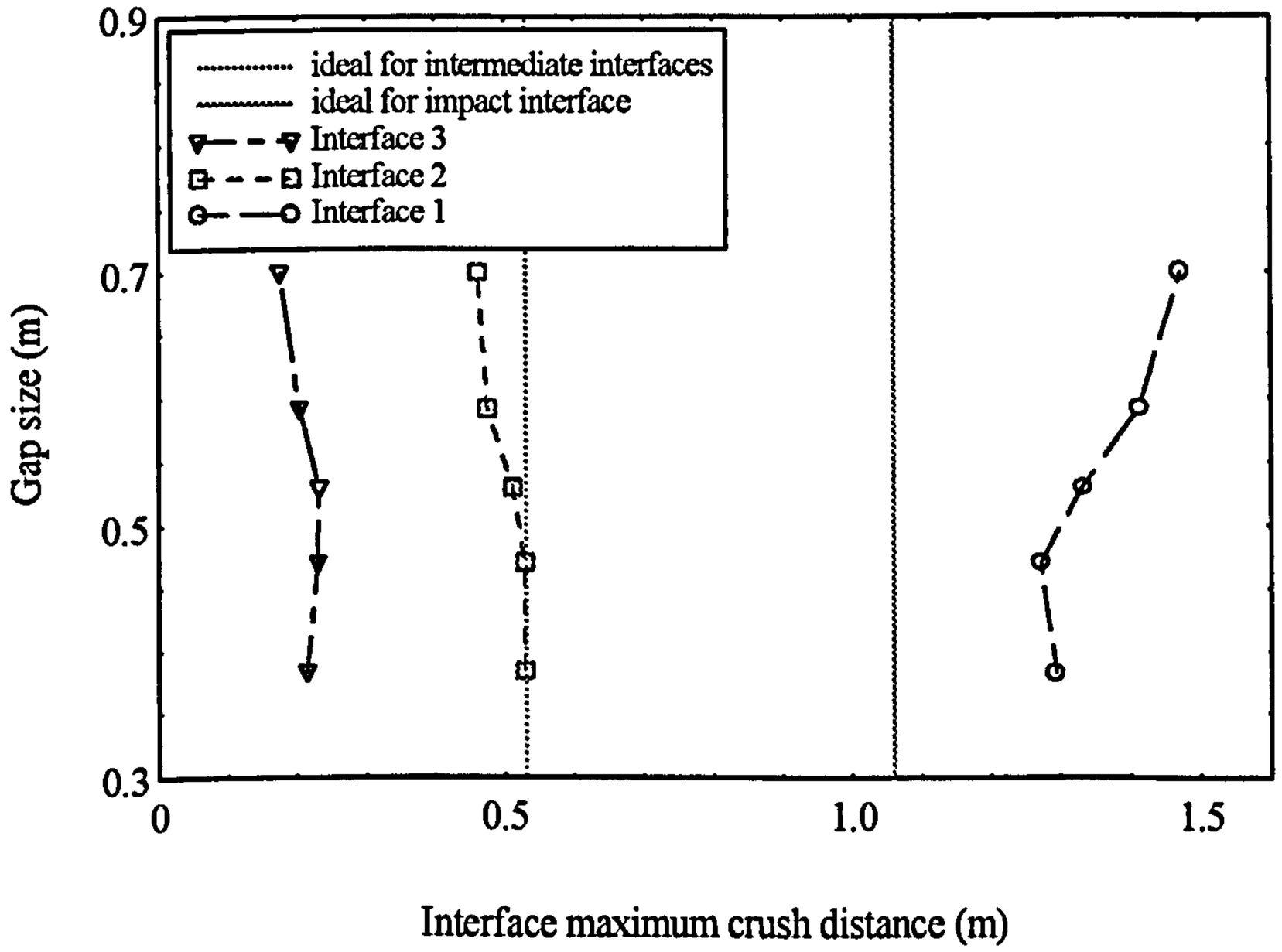

Figure 4.23 : The crush distance for models in the Iv35 series.

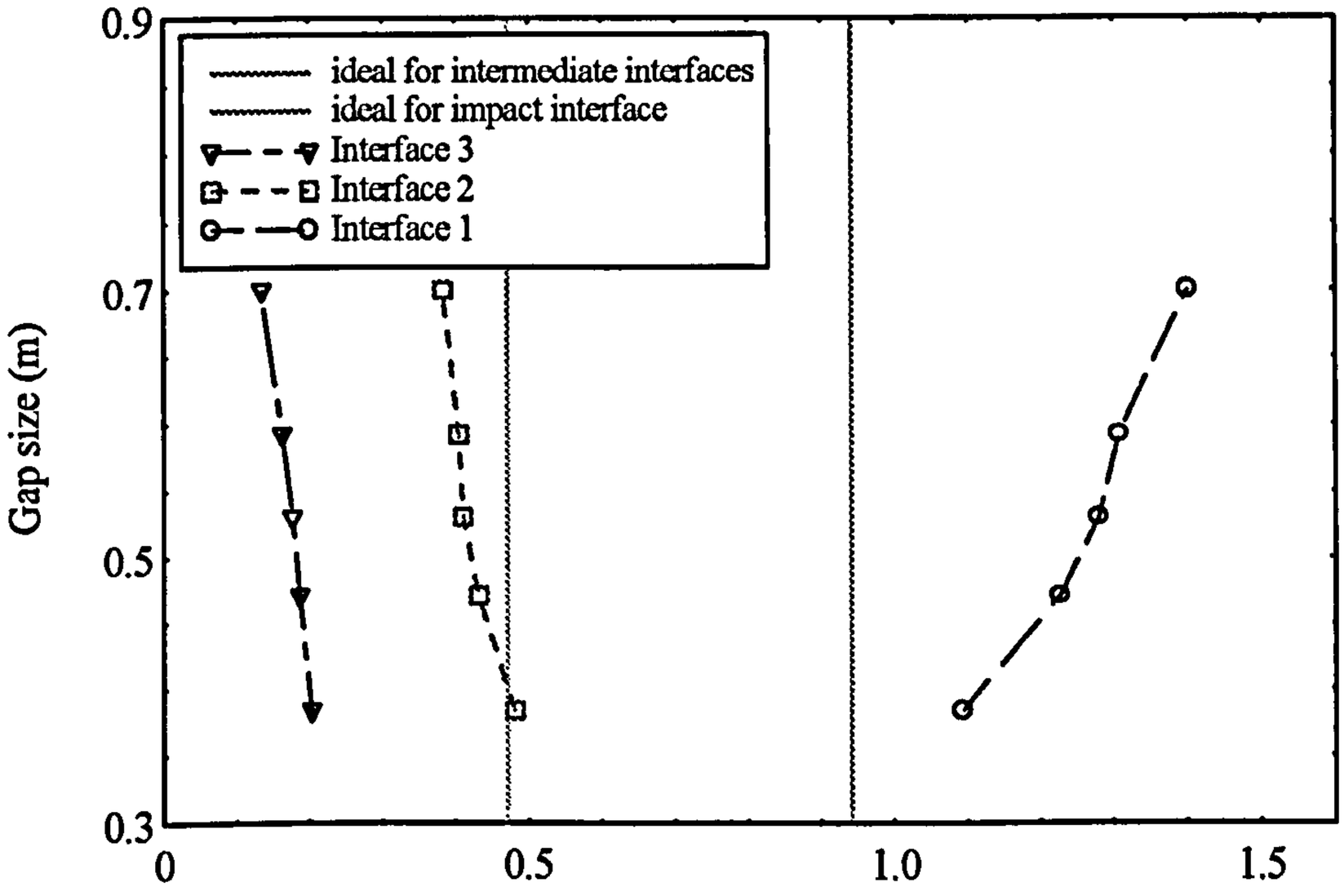

Figure 4.24 : The crush distance for models in the Iv33 series.

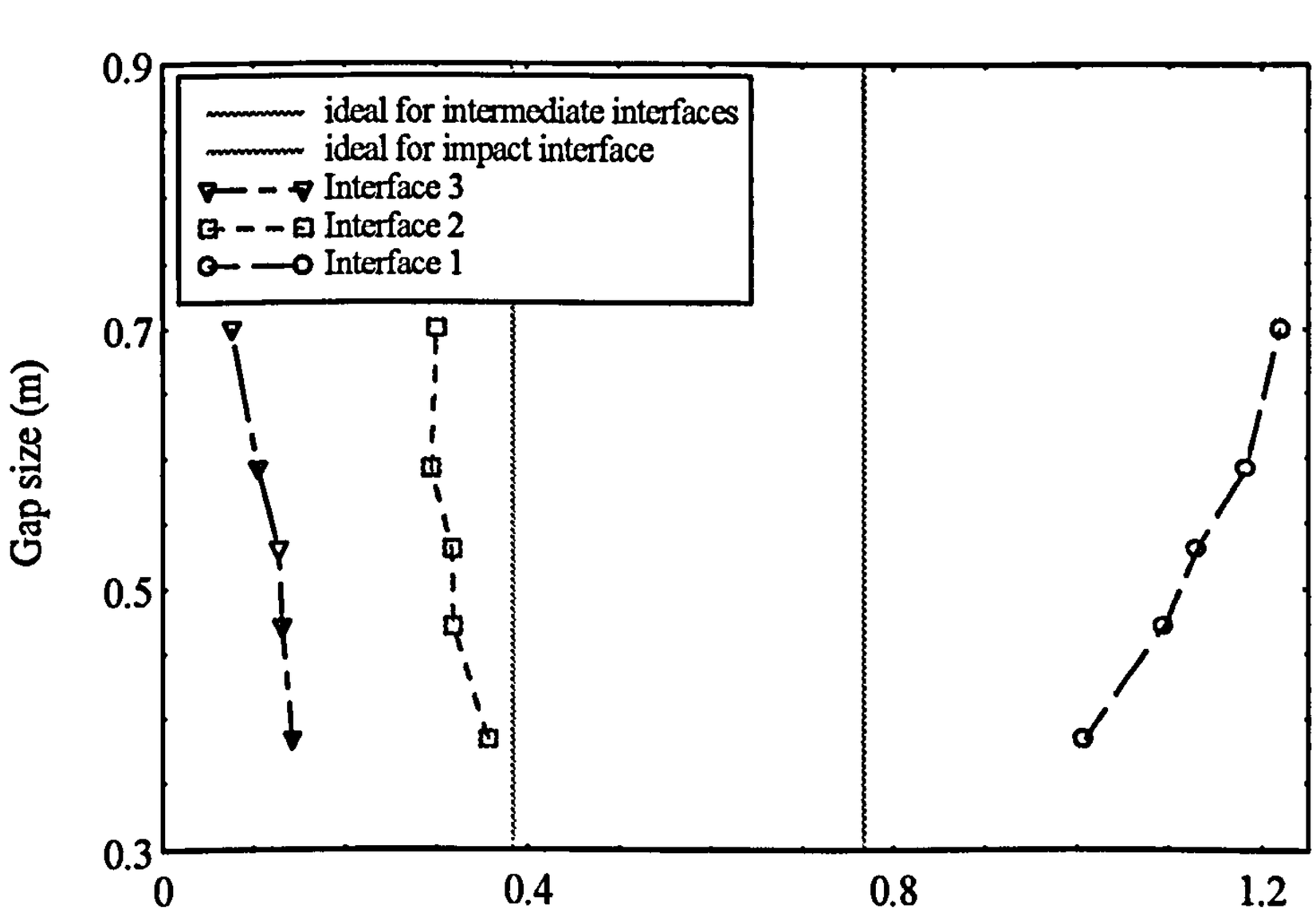

Figure 4.25 : The crush distance for models in the Iv30 series.

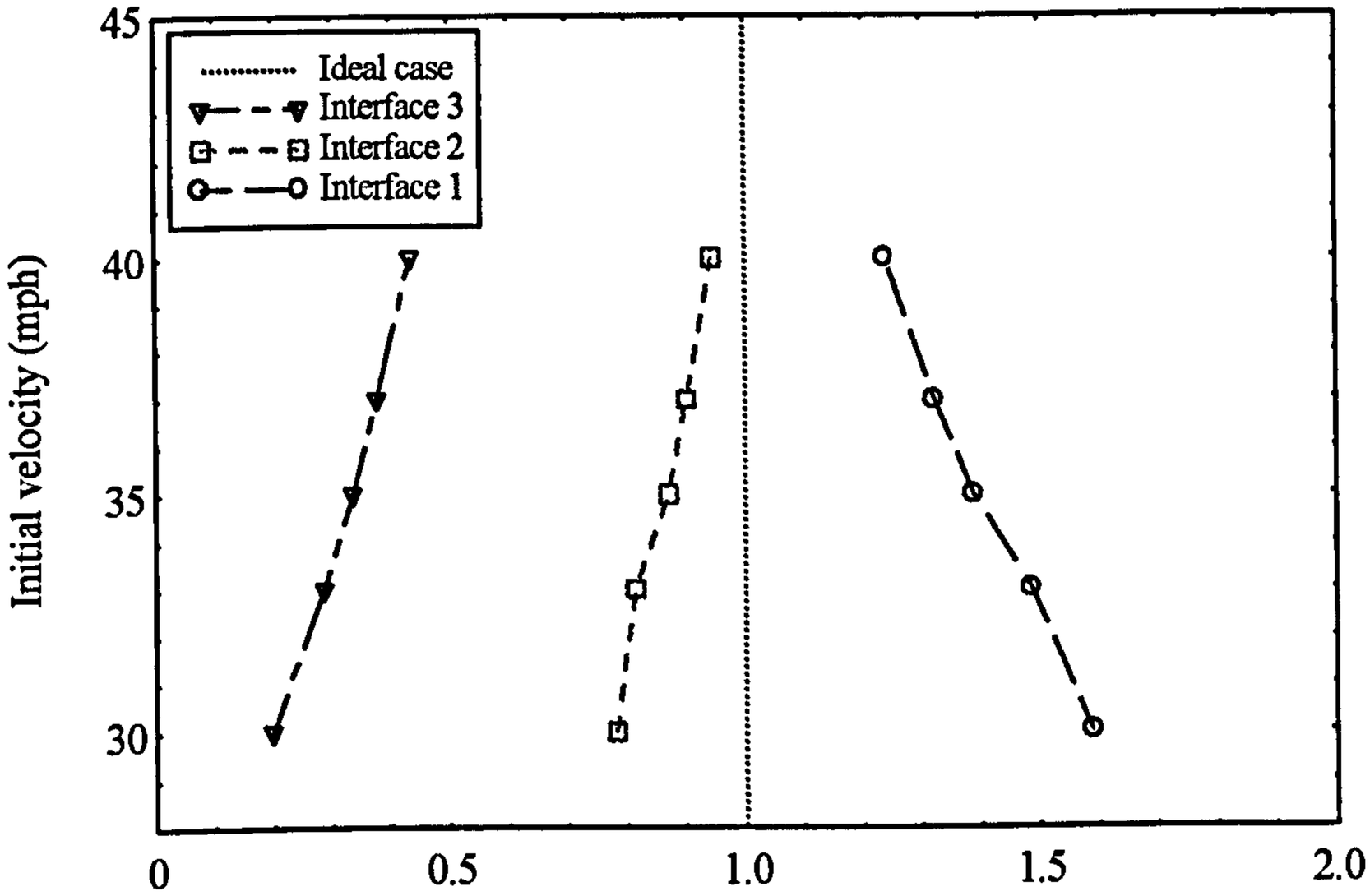

Figure 4.26 : The normalised crush distance for models in the Gp70 series.

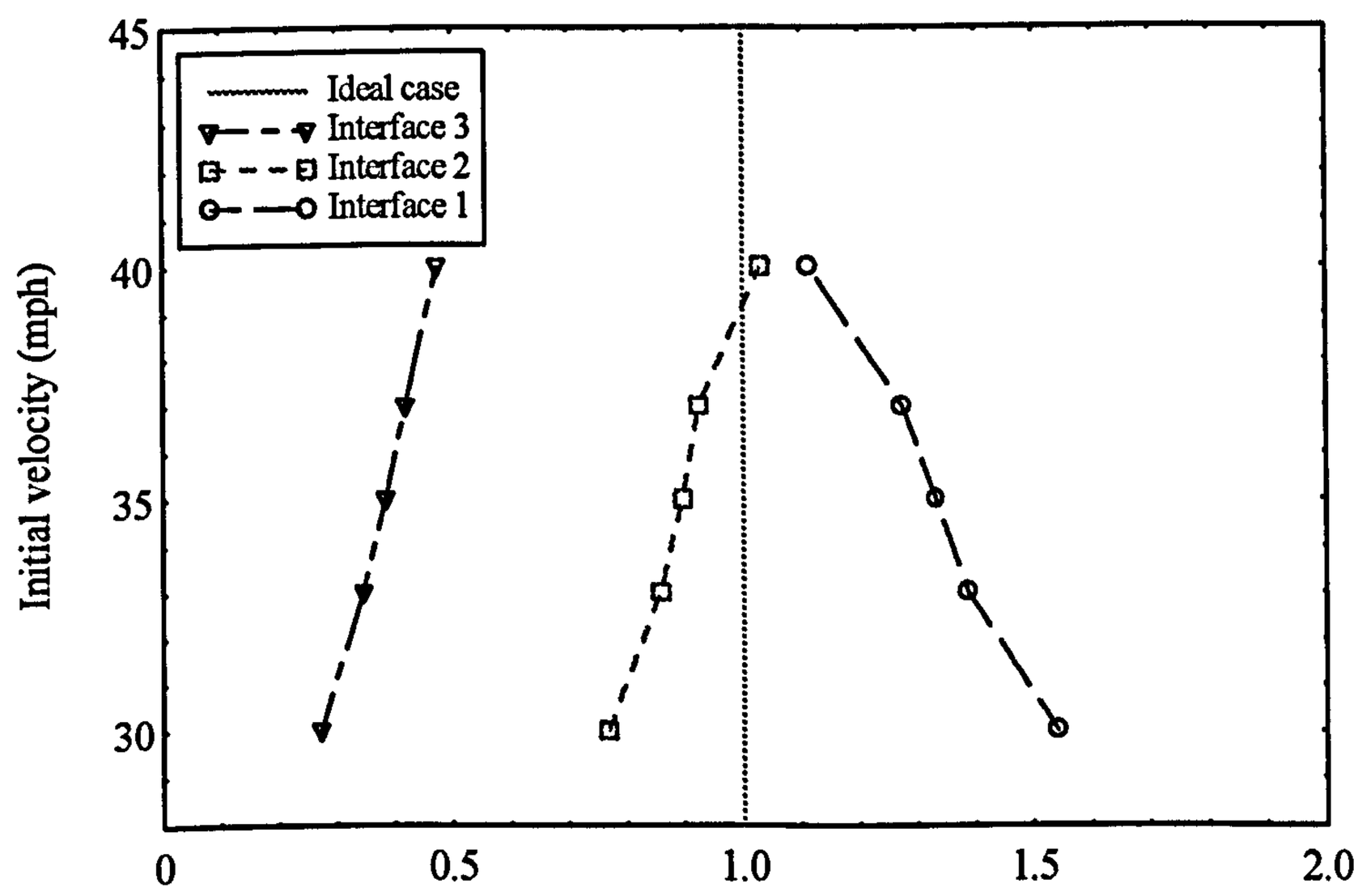

Figure 4.27 : The normalised crush distance for models in the Gp59 series.

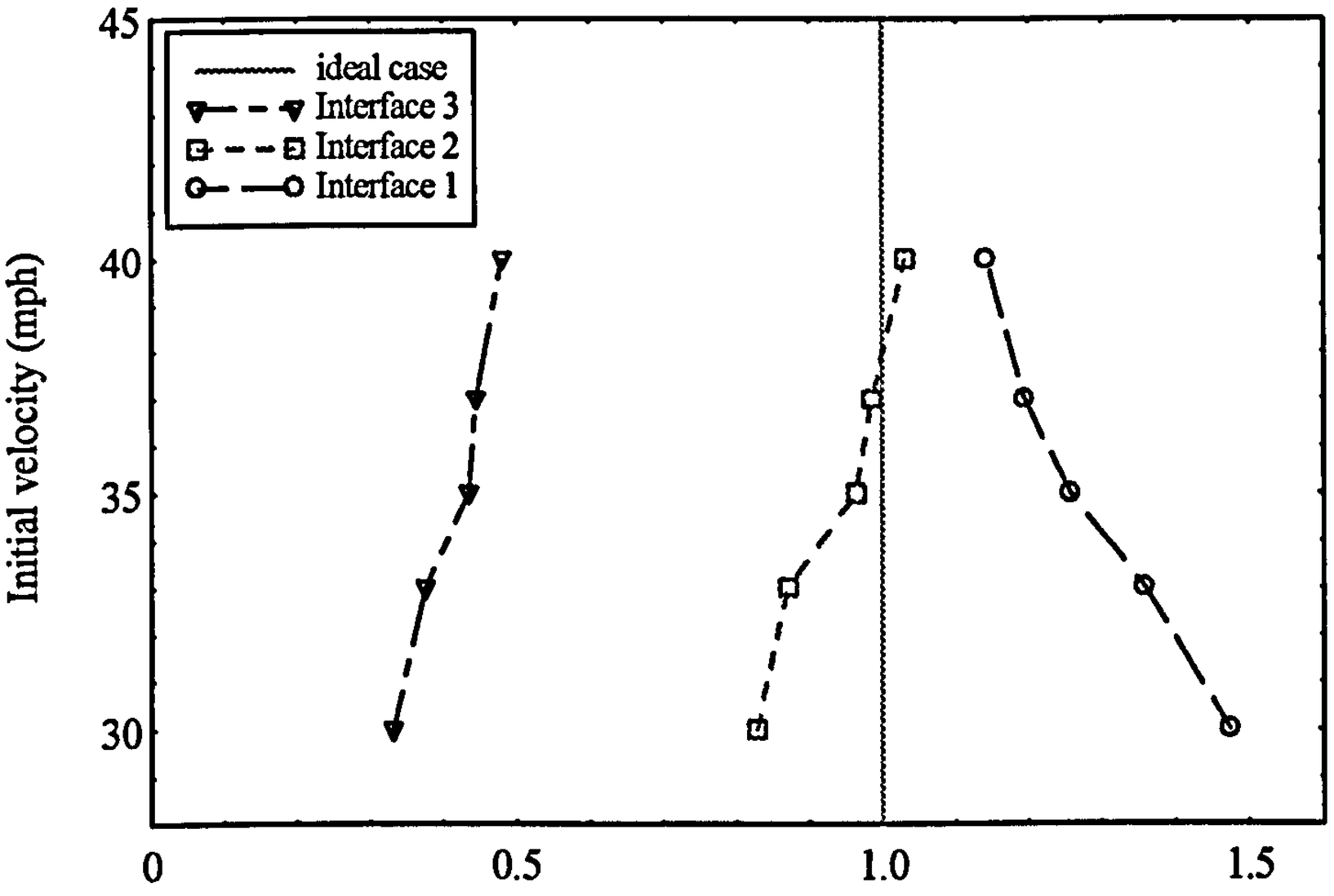

Figure 4.28 : The normalised crush distance for models in the Gp53 series.

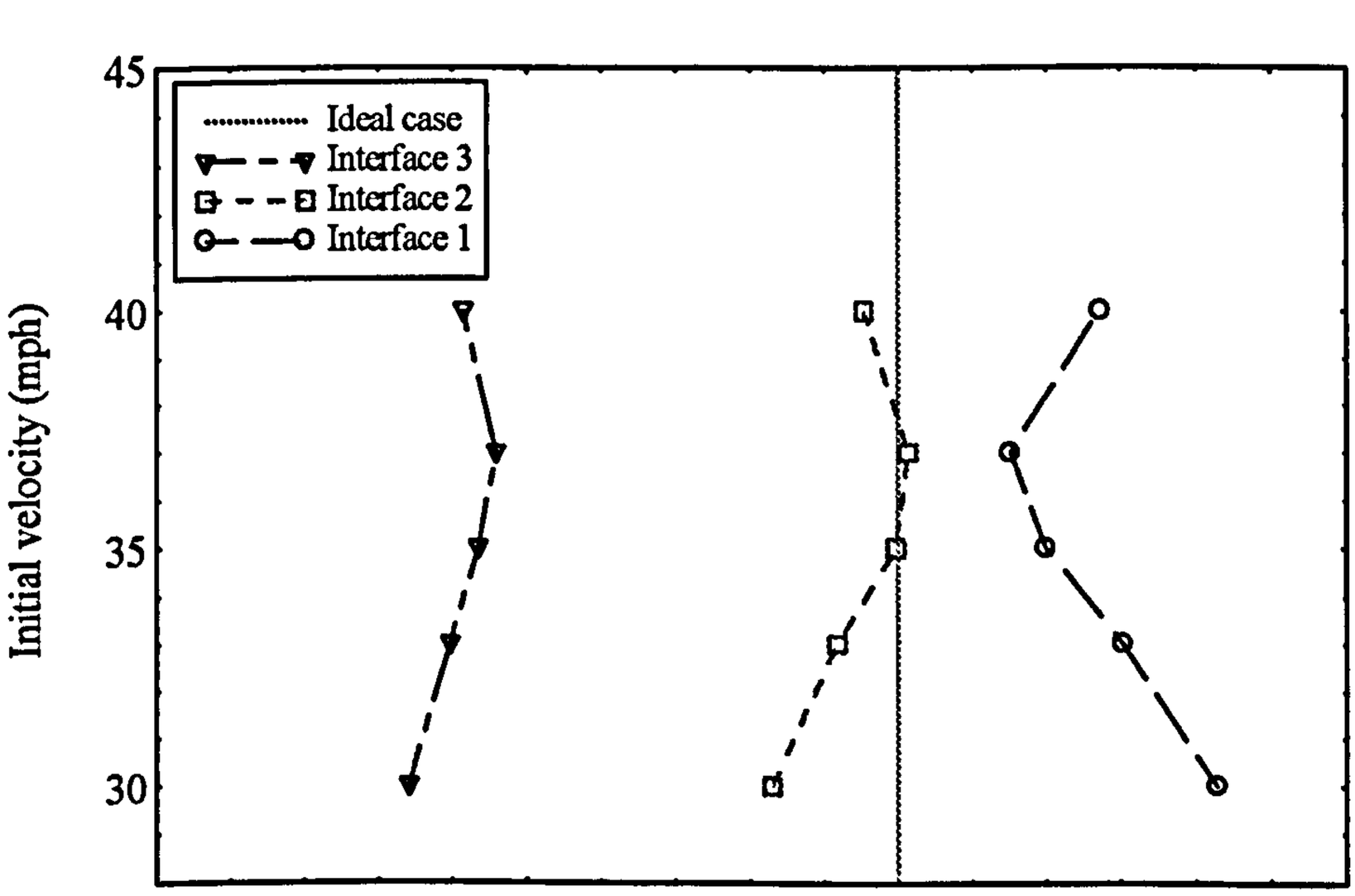

Figure 4.29 : The normalised crush distance for models in the Gp47 series.

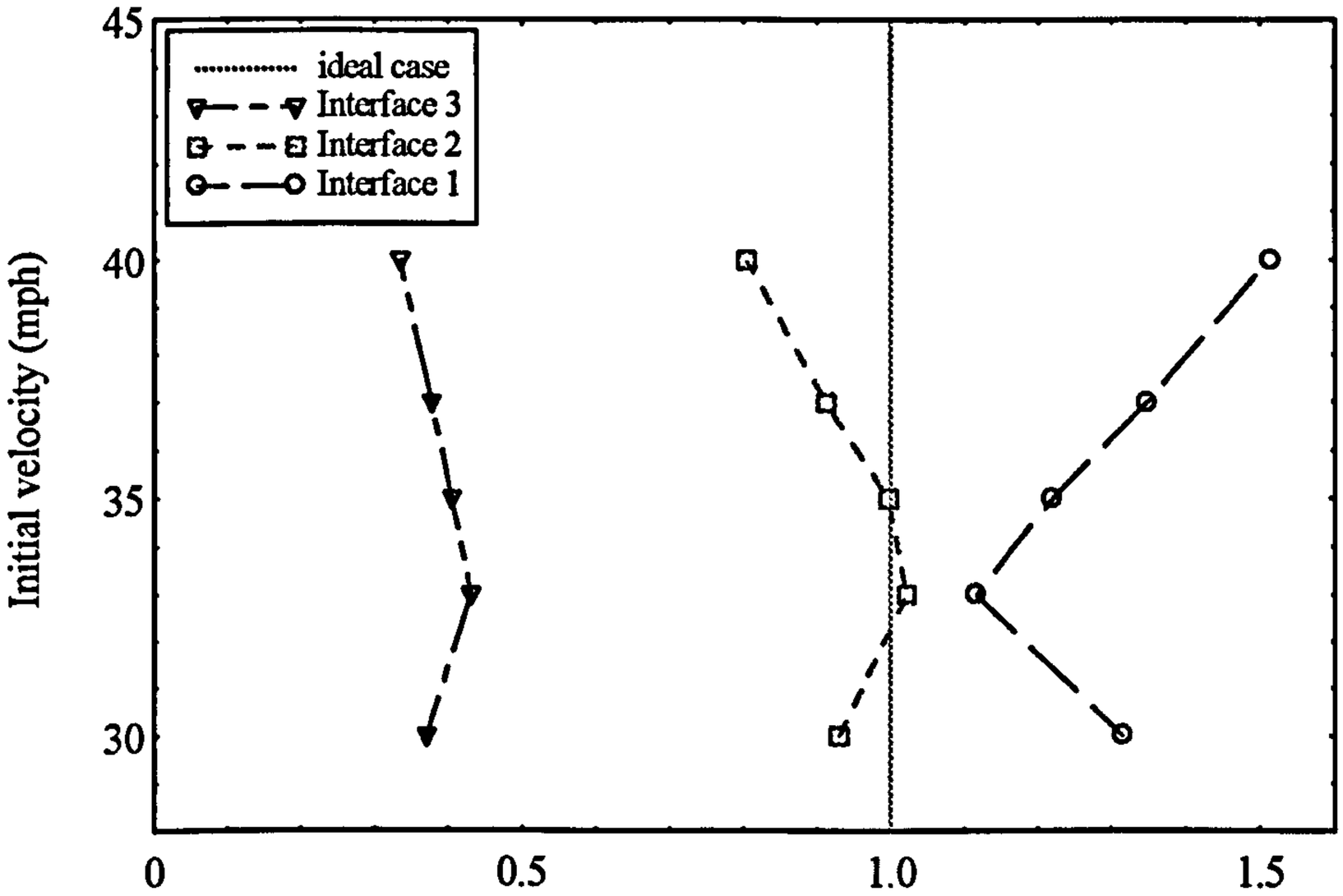

Figure 4.30 : The normalised crush distance for models in the Gp38 series.

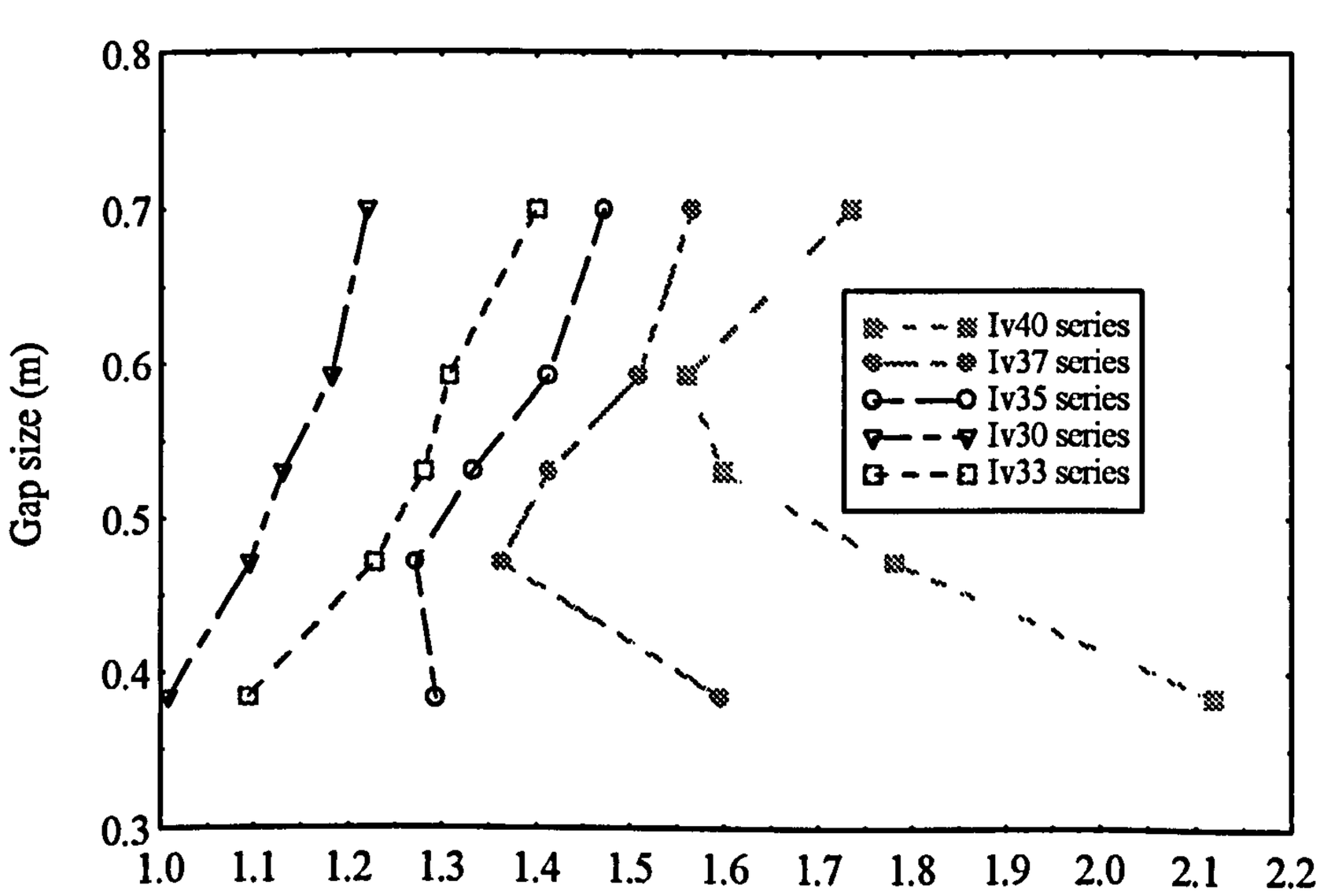

Figure 4.31 : Interface 1 crush distance for various models

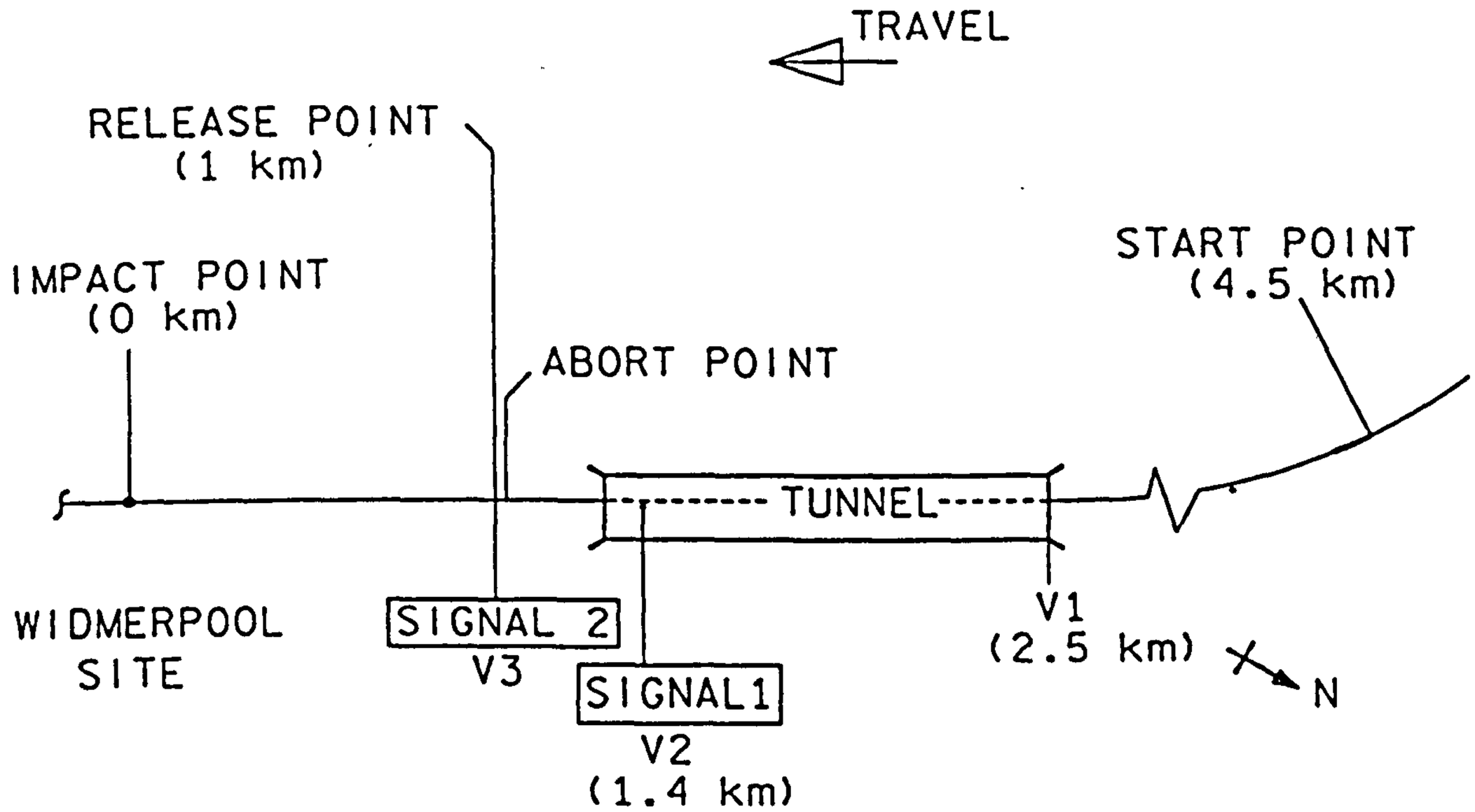

Figure 4.32 : The BR test track for the October 1994 full scale collision test. After [4]

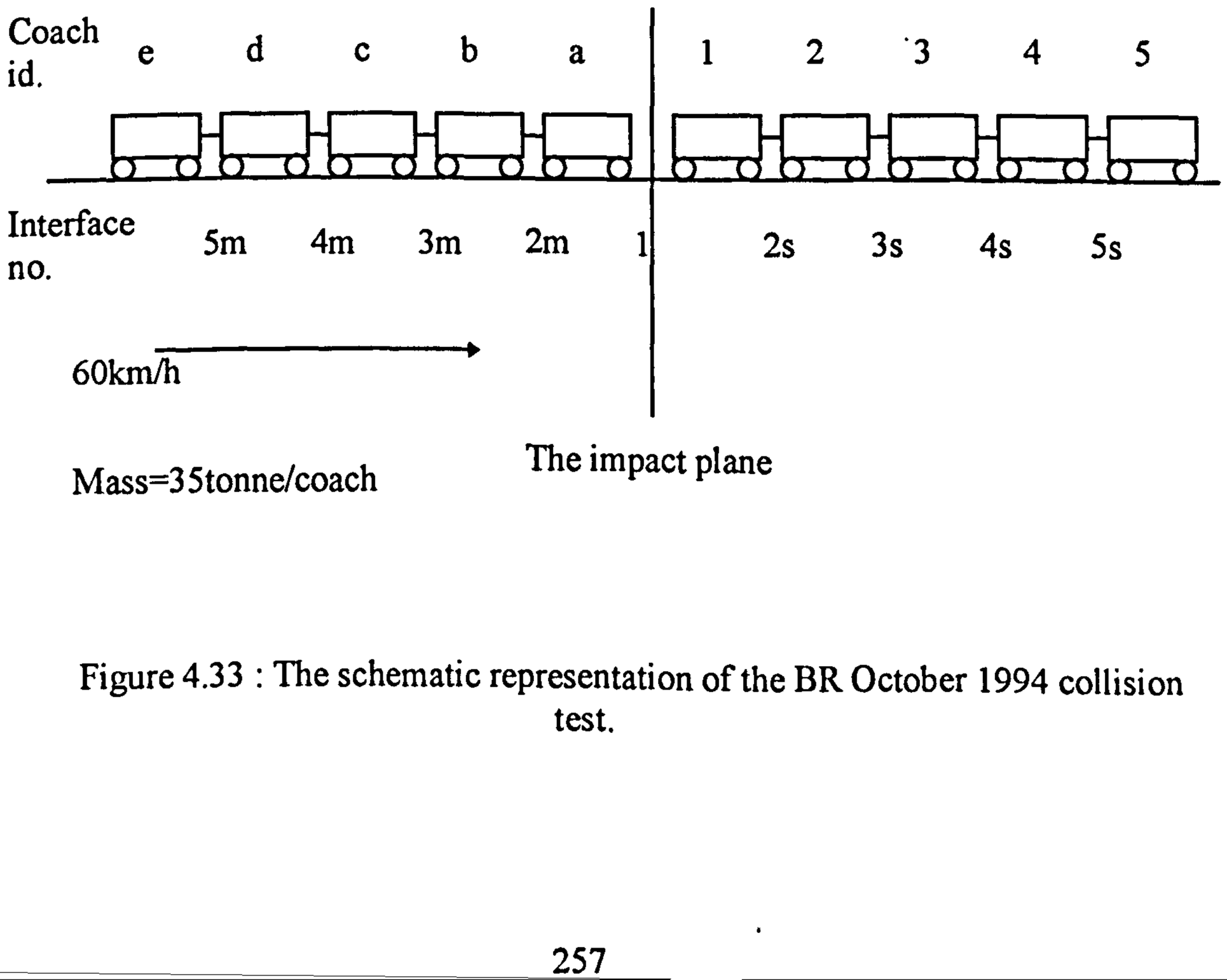

Figure 4.33 : The schematic representation of the BR October 1994 collision test.

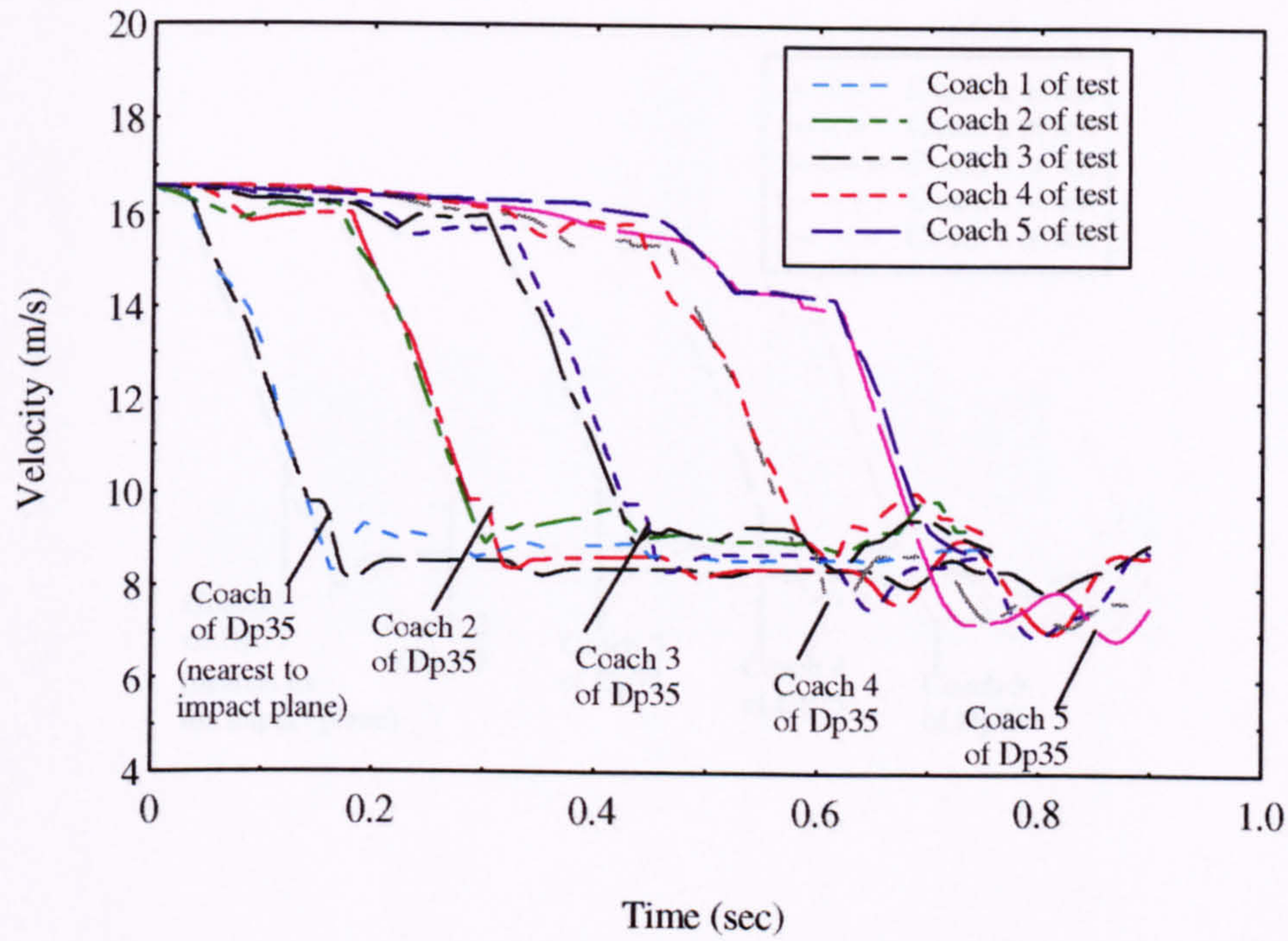

Figure 4.34 : The velocity-time history of various coaches for the test and model Dp35.

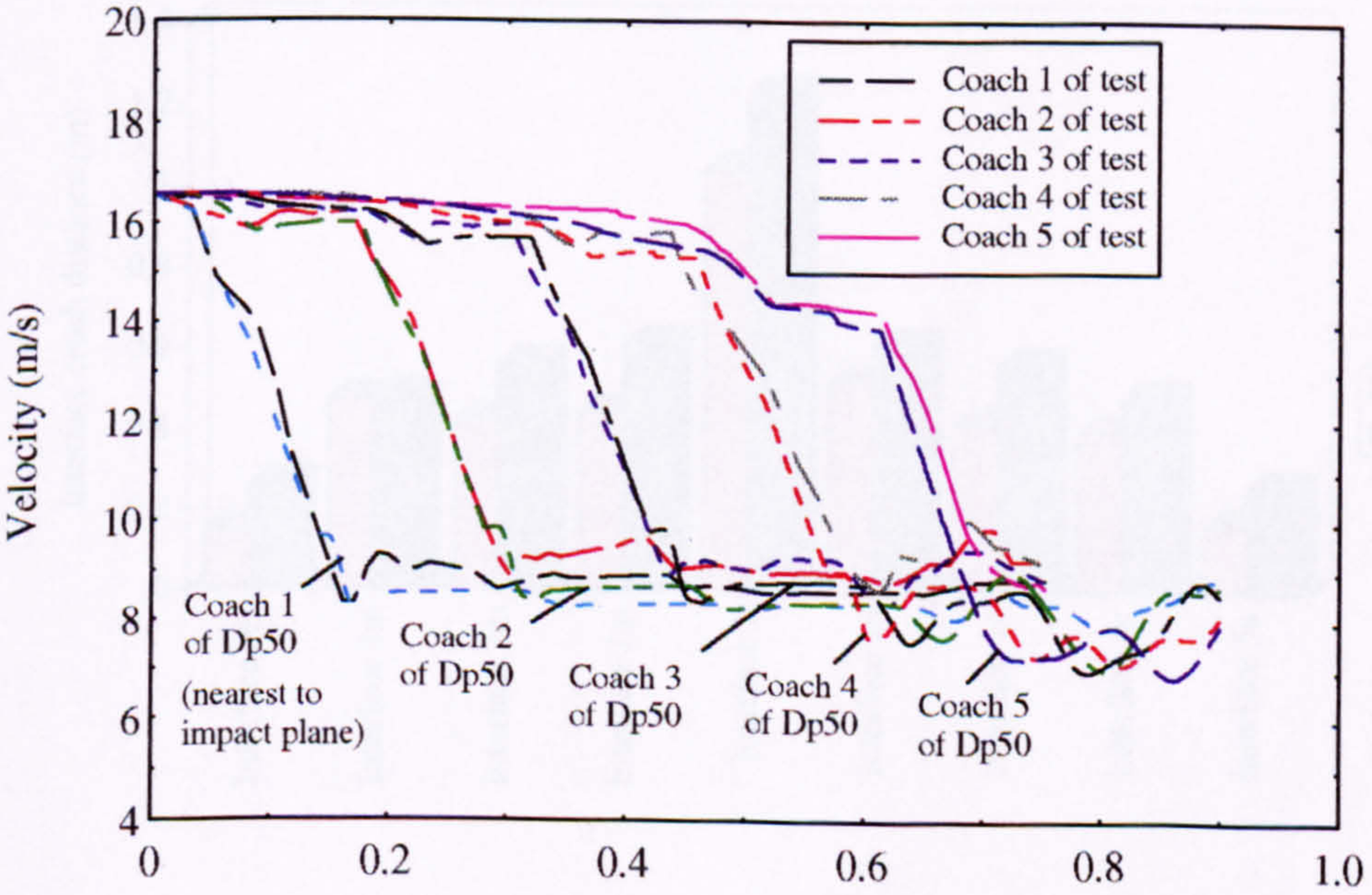

Figure 4.35 : The velocity-time history of various coaches for the test and model Dp50.

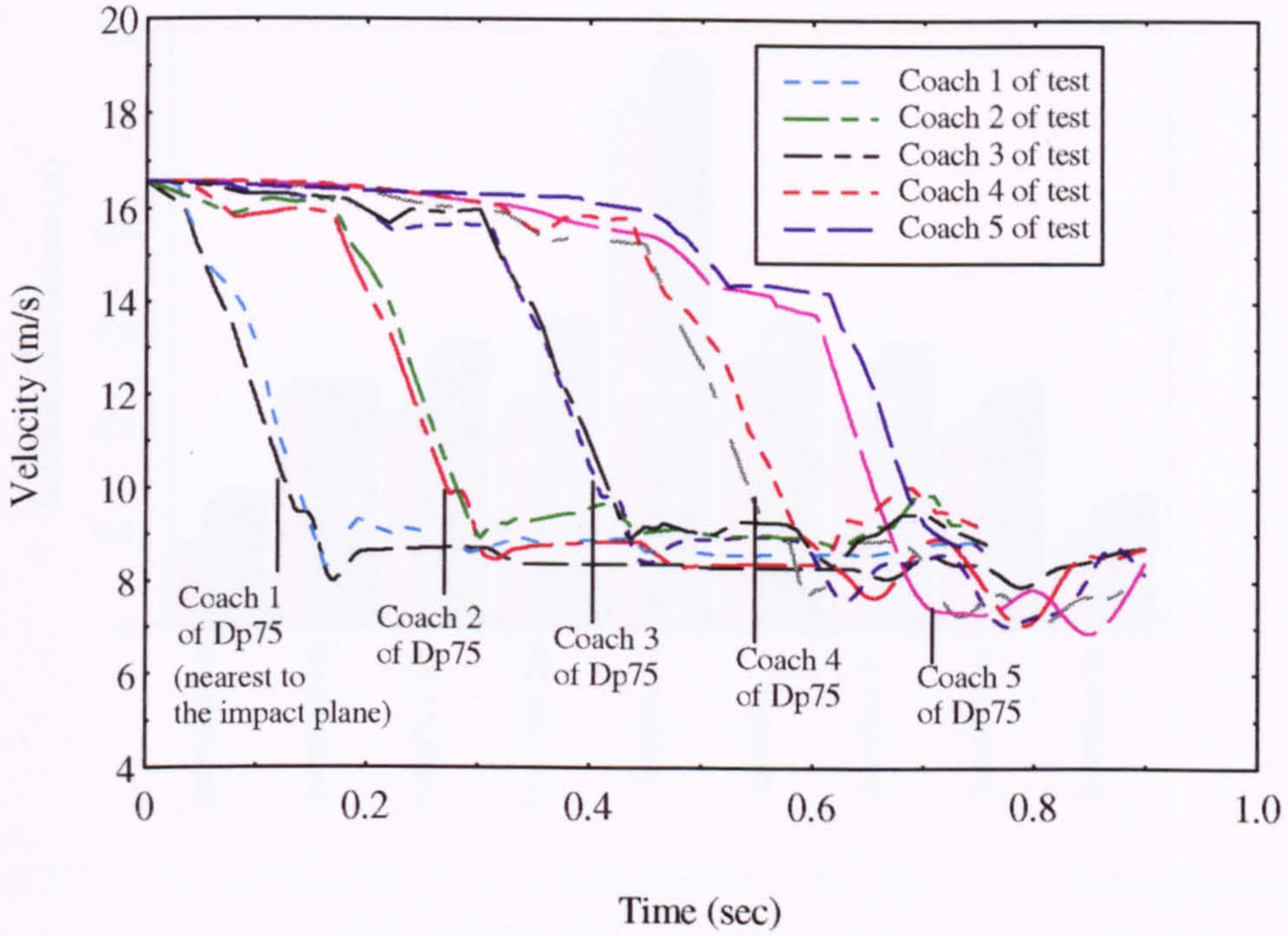

Figure 4.36 : The velocity-time history of various coaches for the test and model Dp75.

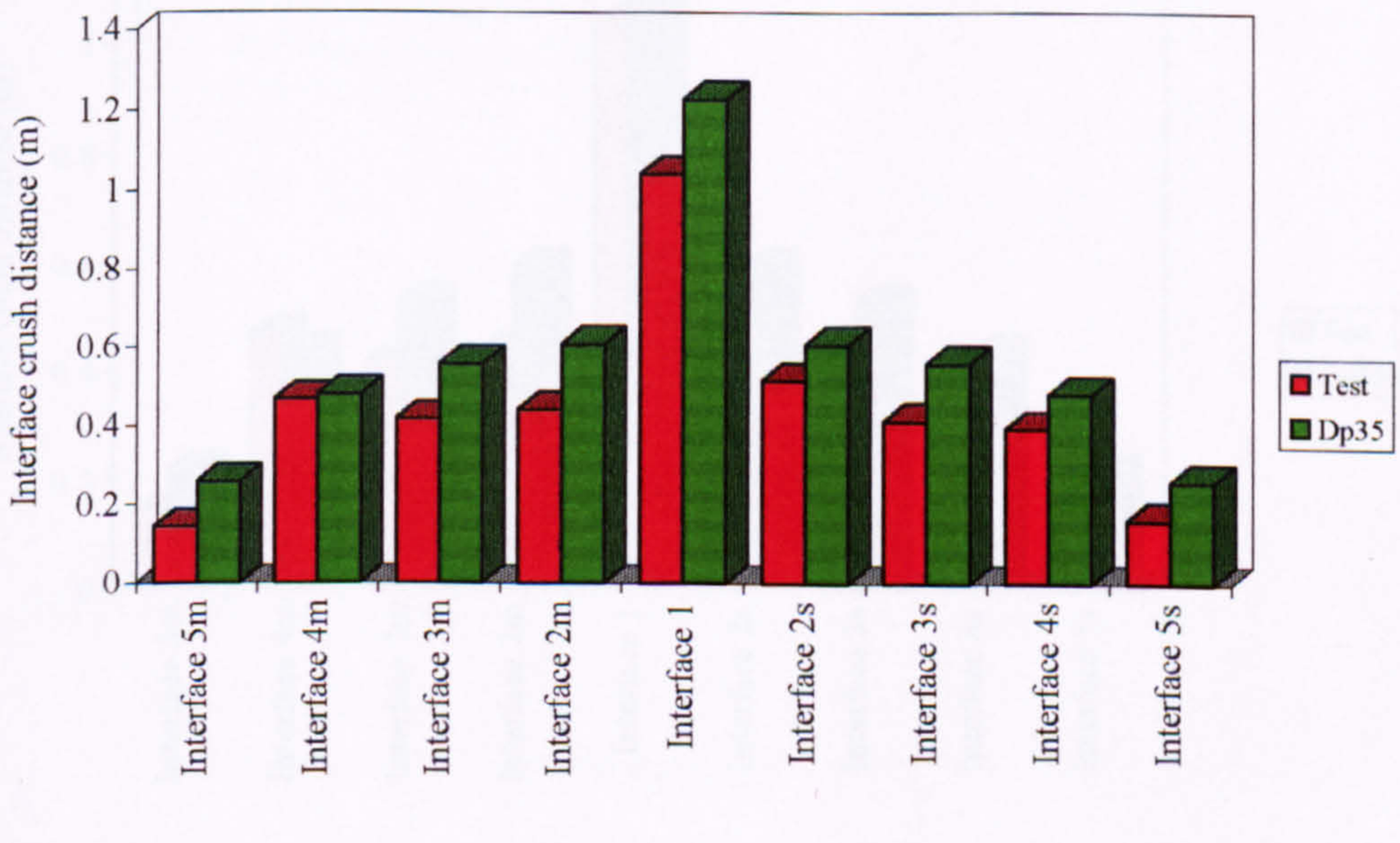

Figure 4.37 : The comparison of various interface crush distance between the test and the model Dp35. Interface 5m-2m are the intermediate interfaces of the moving rake, interface 5s-2s are in the stationary rake, interface 1 is the impact interface.

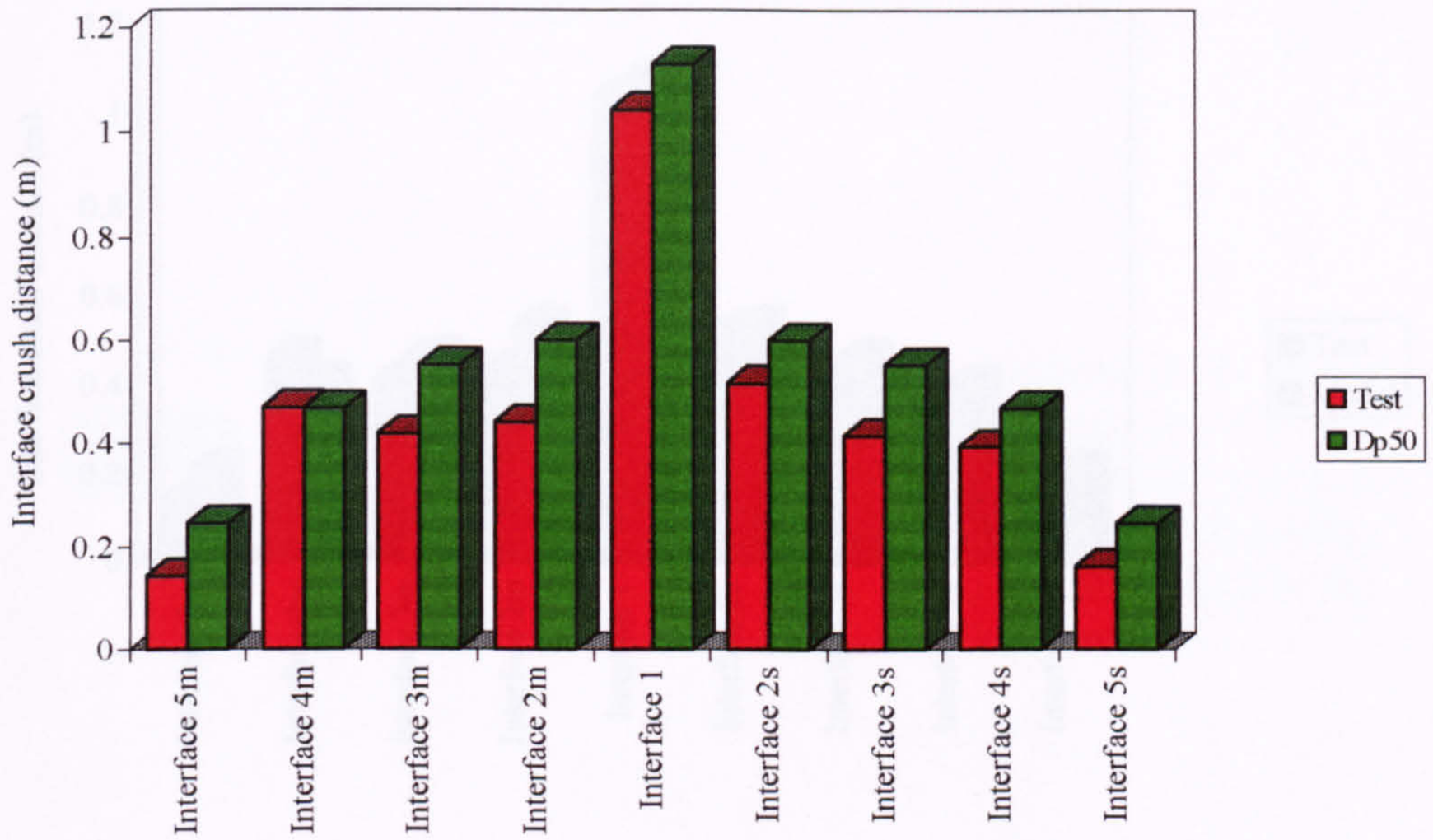

Figure 4.38 : The comparison of various interface crush distance between the test and the model Dp50.

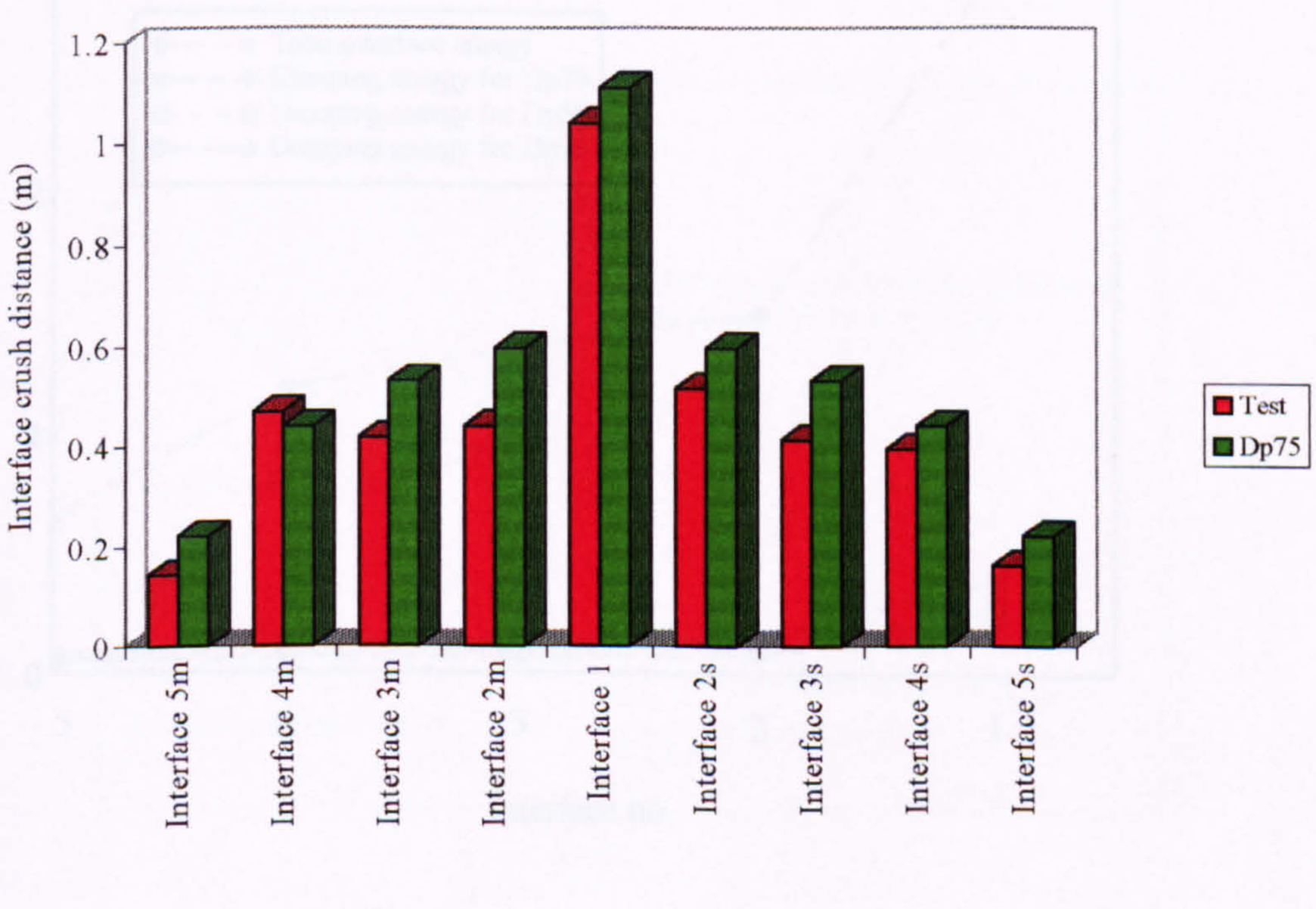

Figure 4.39 : The comparison of various interface crush distance between the test and the model Dp75.

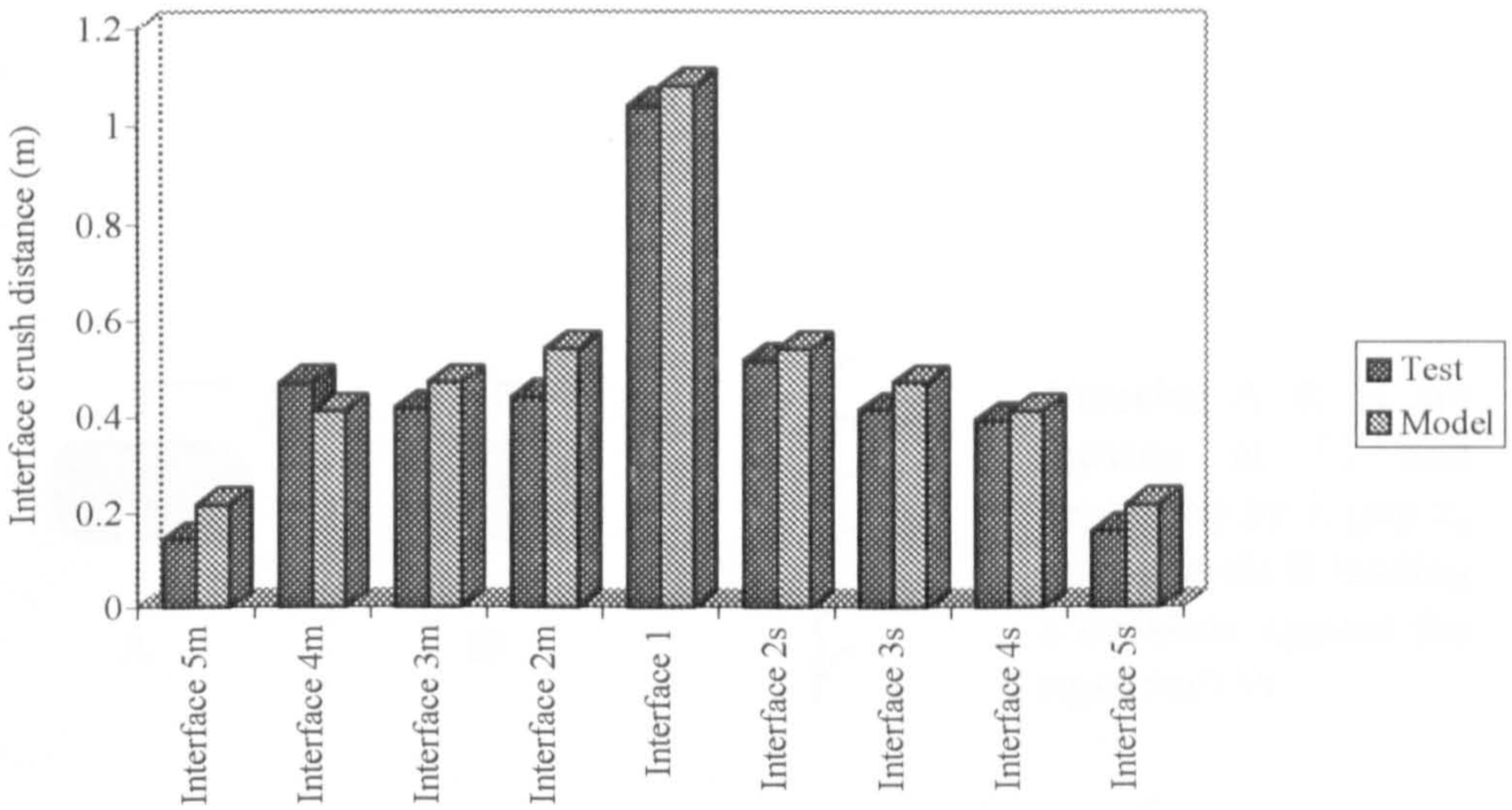

Figure 4.40 : The comparison of various interface crush distance between the test and the dynamically enhanced model.

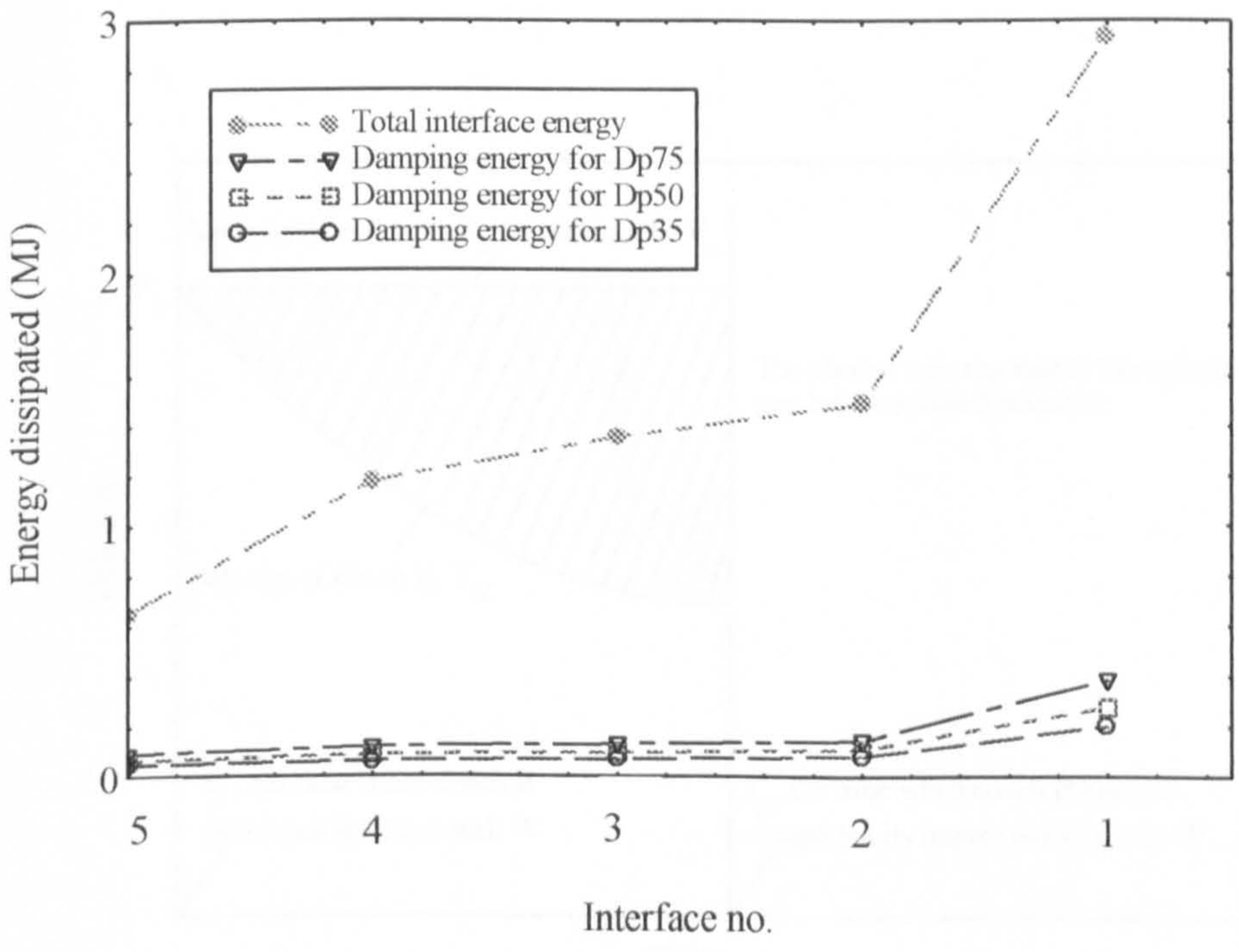

Figure 4.41 : Comparison of the damping energy with the total interface energy in various interfaces for all Dp models.

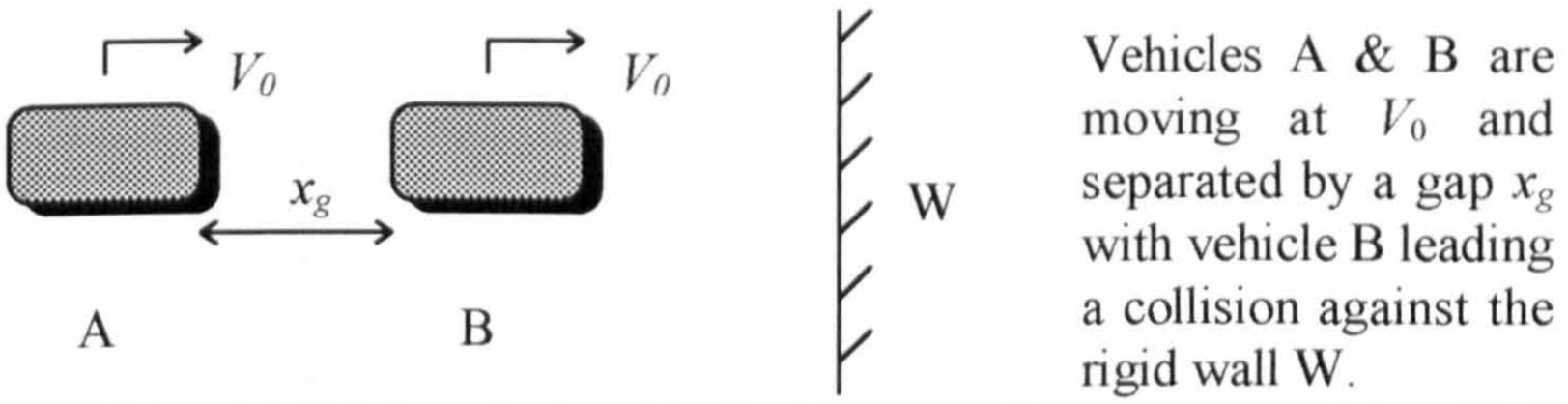

Figure 5.1 : The schematic diagram for deriving the optimal gap of mass-spring models with non-linear deceleration.

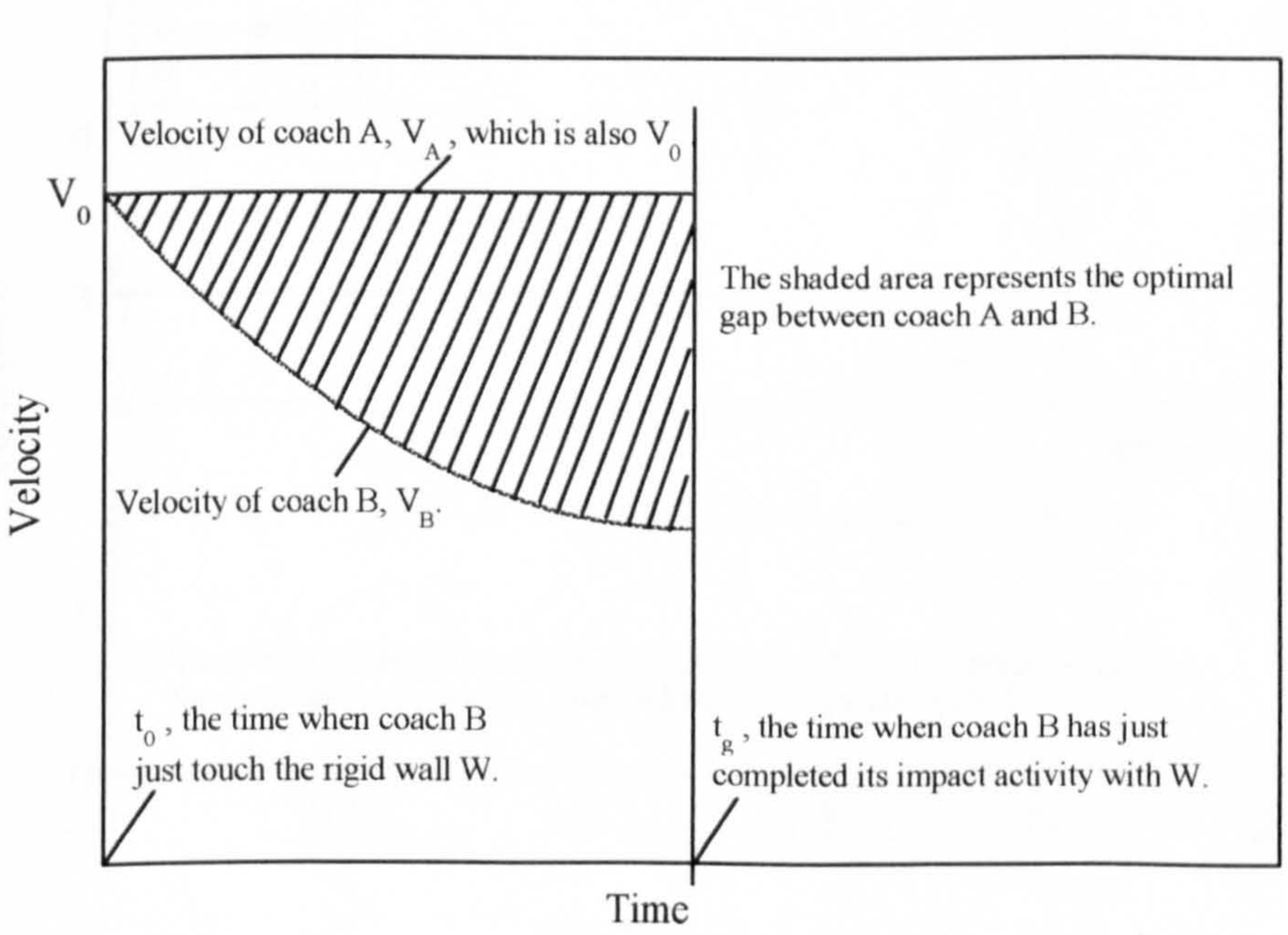

Figure 5.2 : The kinematics graphical interpretation of optimal gap sizes for non-linear deceleration cases.

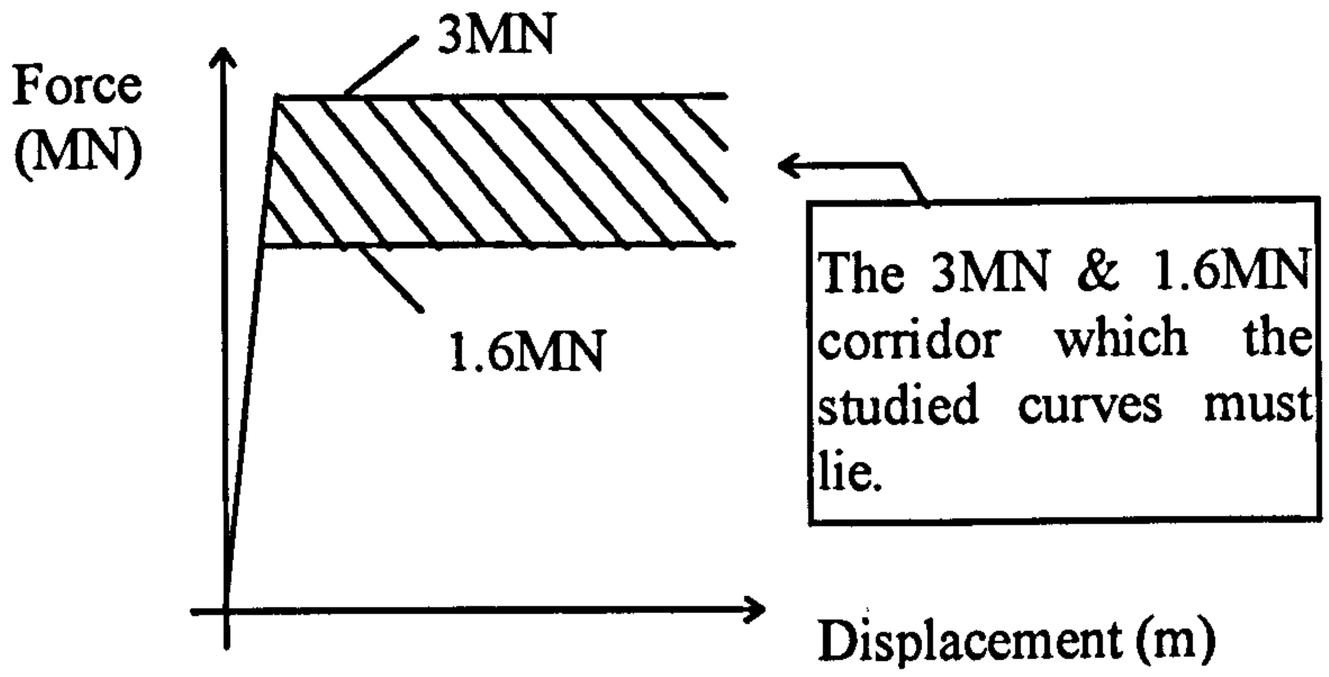

Figure 5.3 : The imposed constraints on the shapes of the spring characteristics.

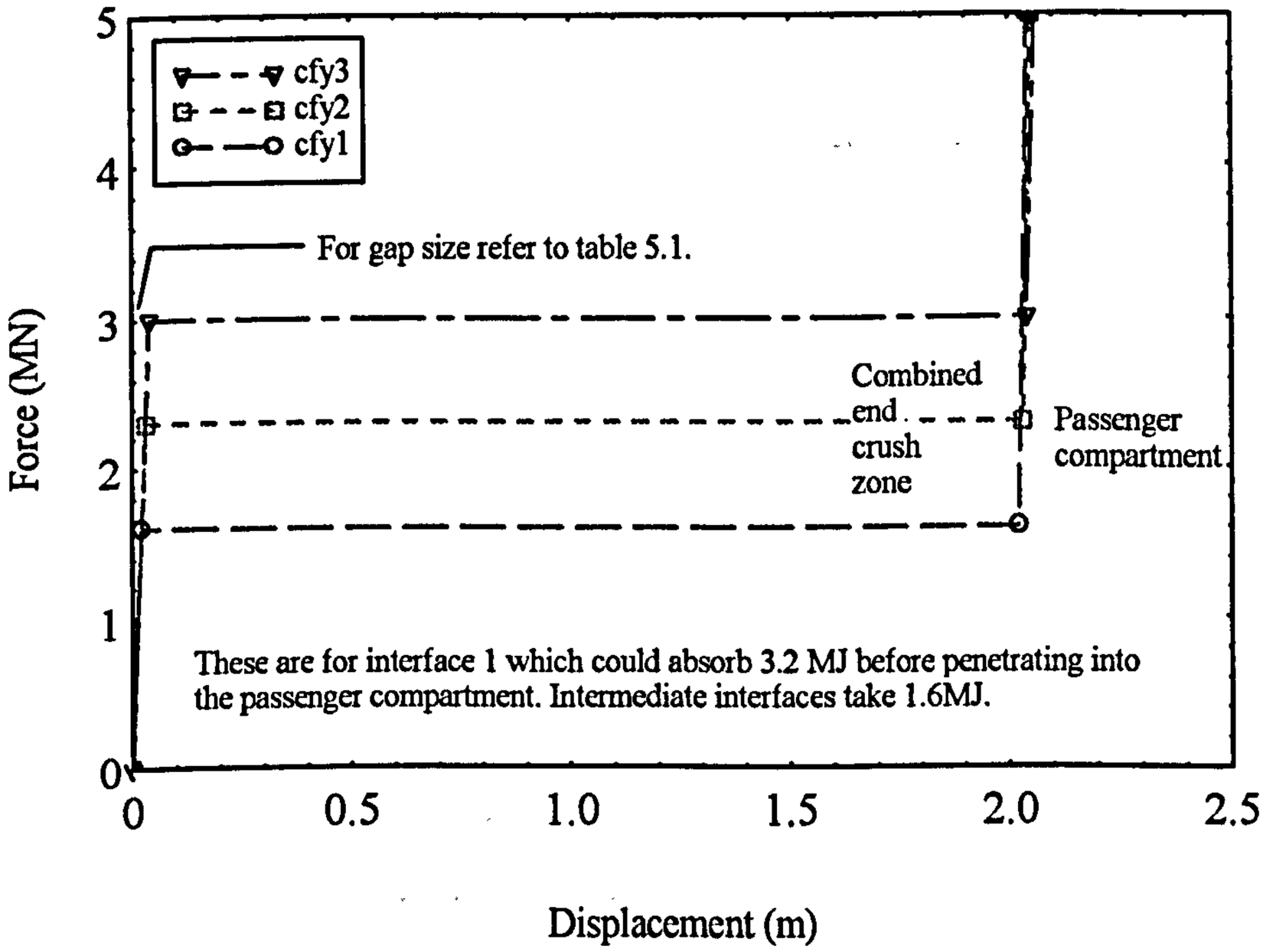

Figure 5.4 : Spring characteristic curves for constant collapse force series.

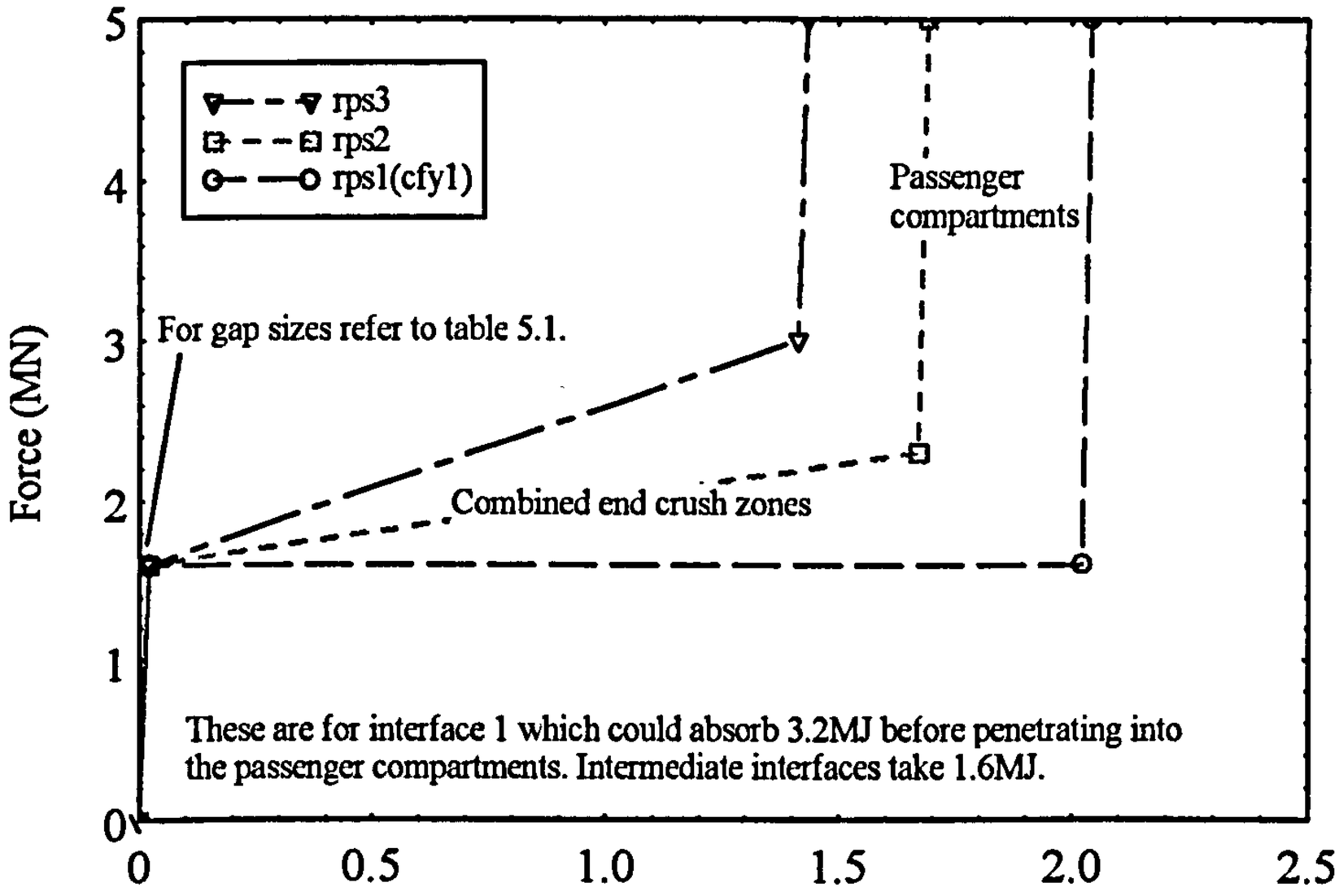

Figure 5.5 : Spring characteristic curves for ramp slope series.

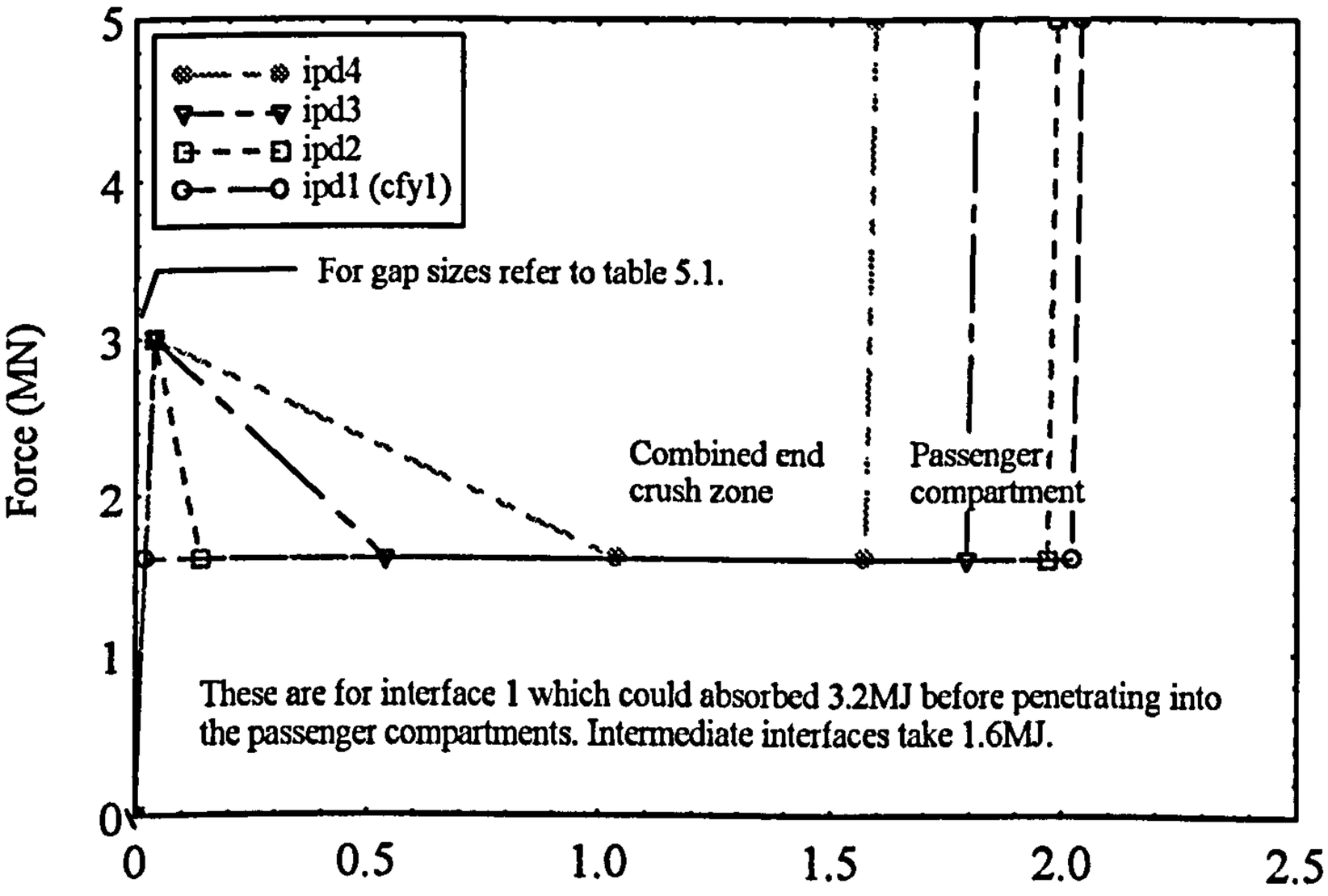

Figure 5.6 : Spring characteristic curves for softening distance series.

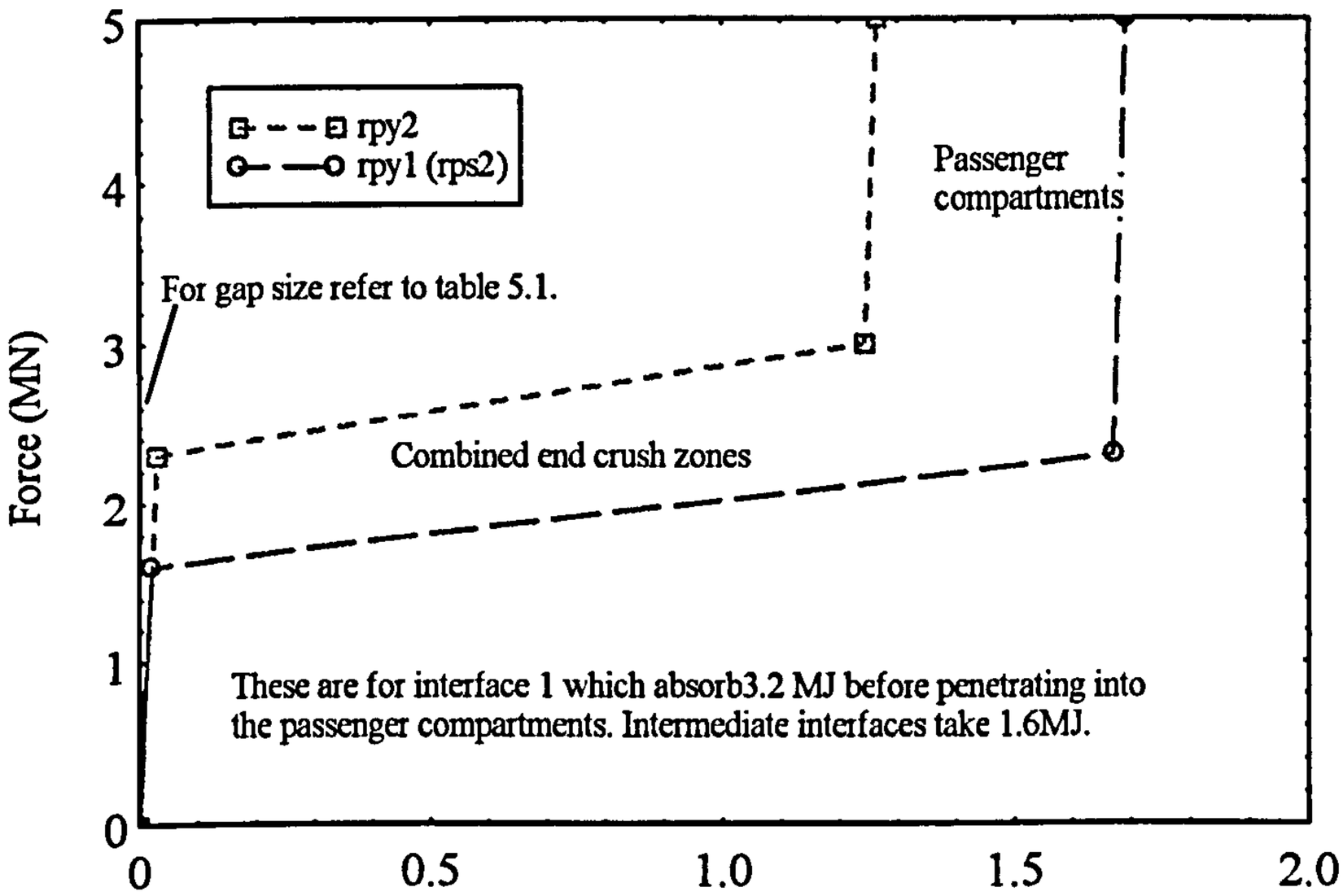

Figure 5.7 : Spring characteristic curves for ramp force series.

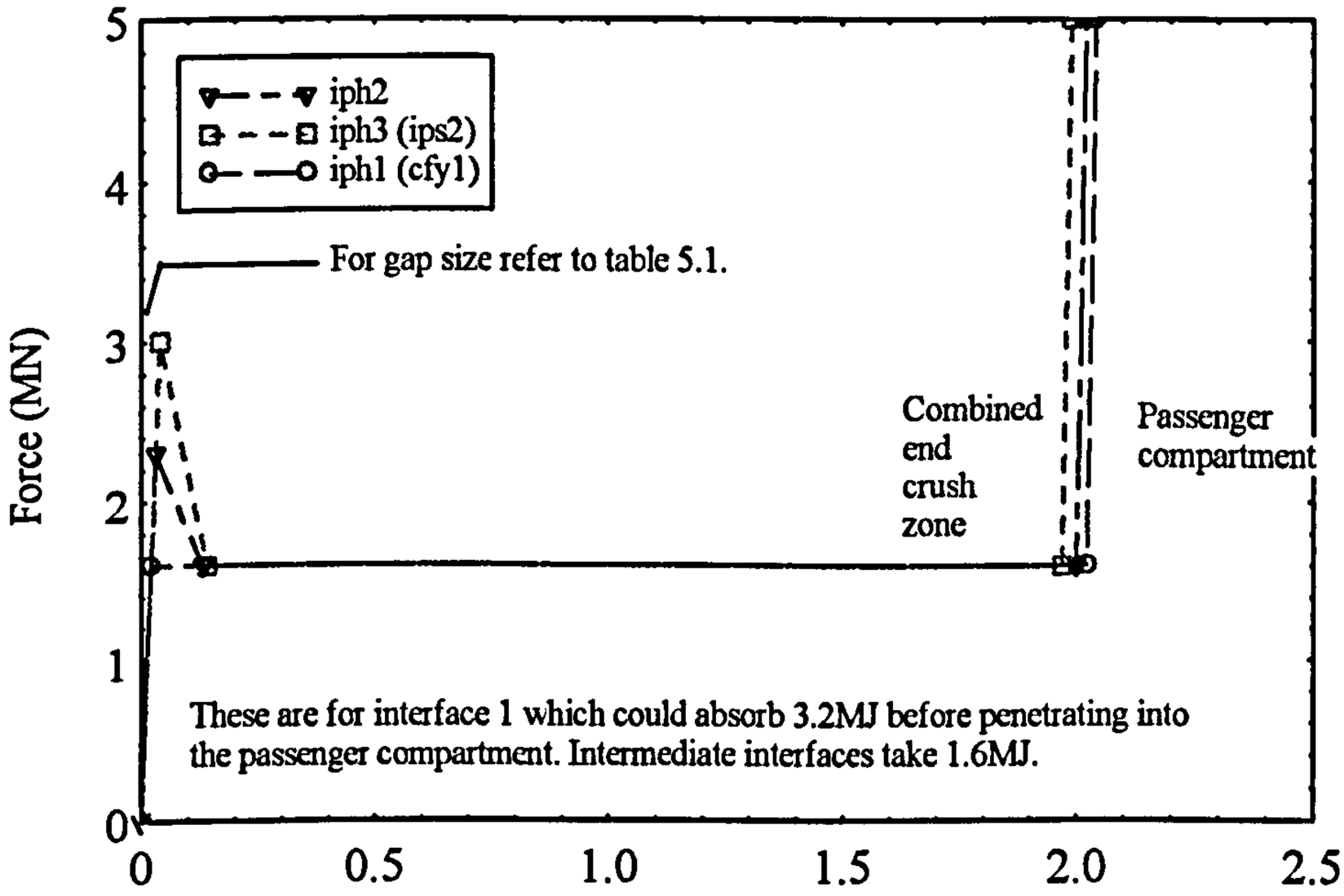

Figure 5.8 : Spring characteristic curves for initial peak force series.

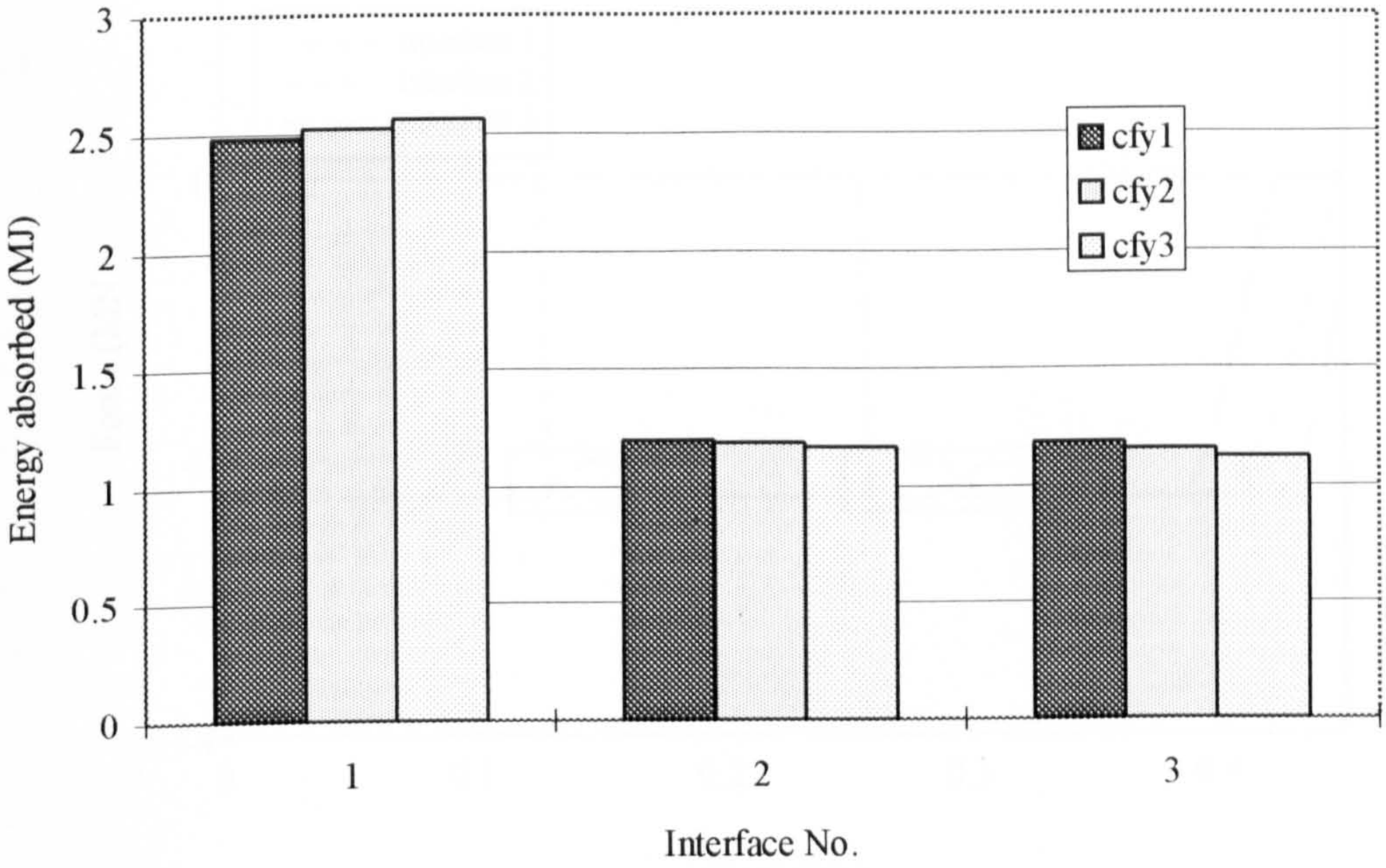

Figure 5.9 : The comparison of interface energy distribution for models in cfy series.

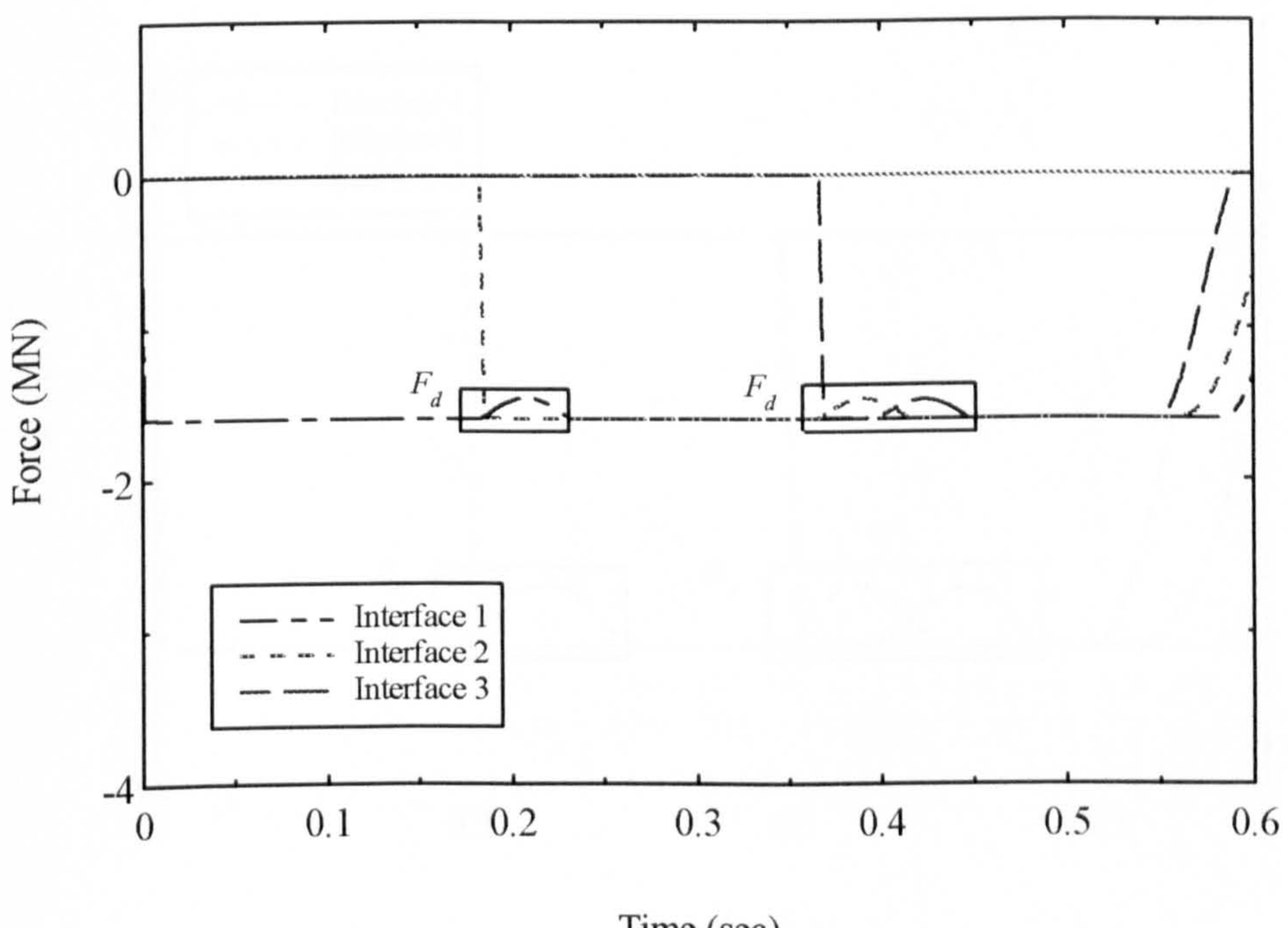

Figure 5.10a : The force-time history of various interfaces in cfy1.

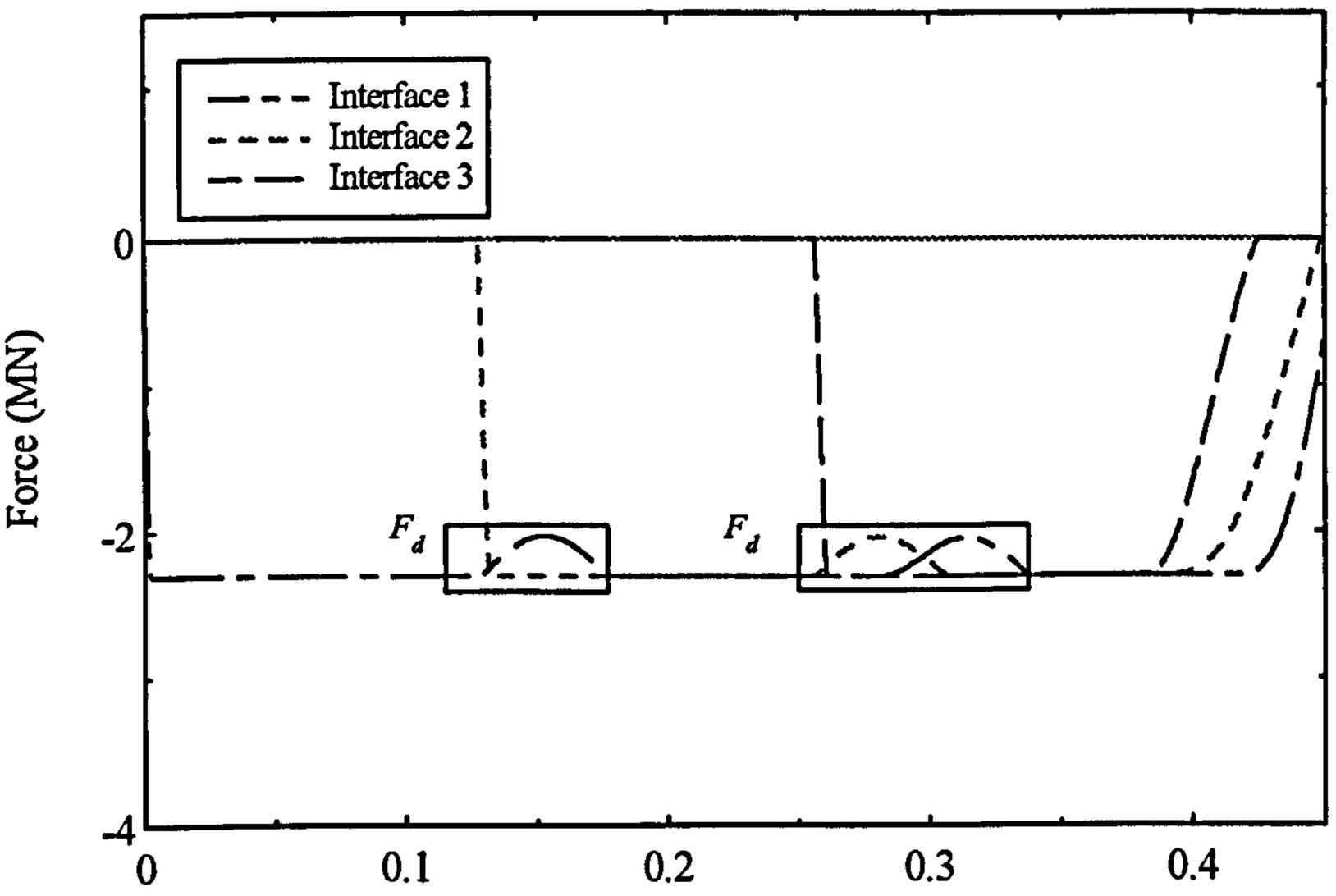

Figure 5.10b : The force-time history of various interfaces in cfy2.

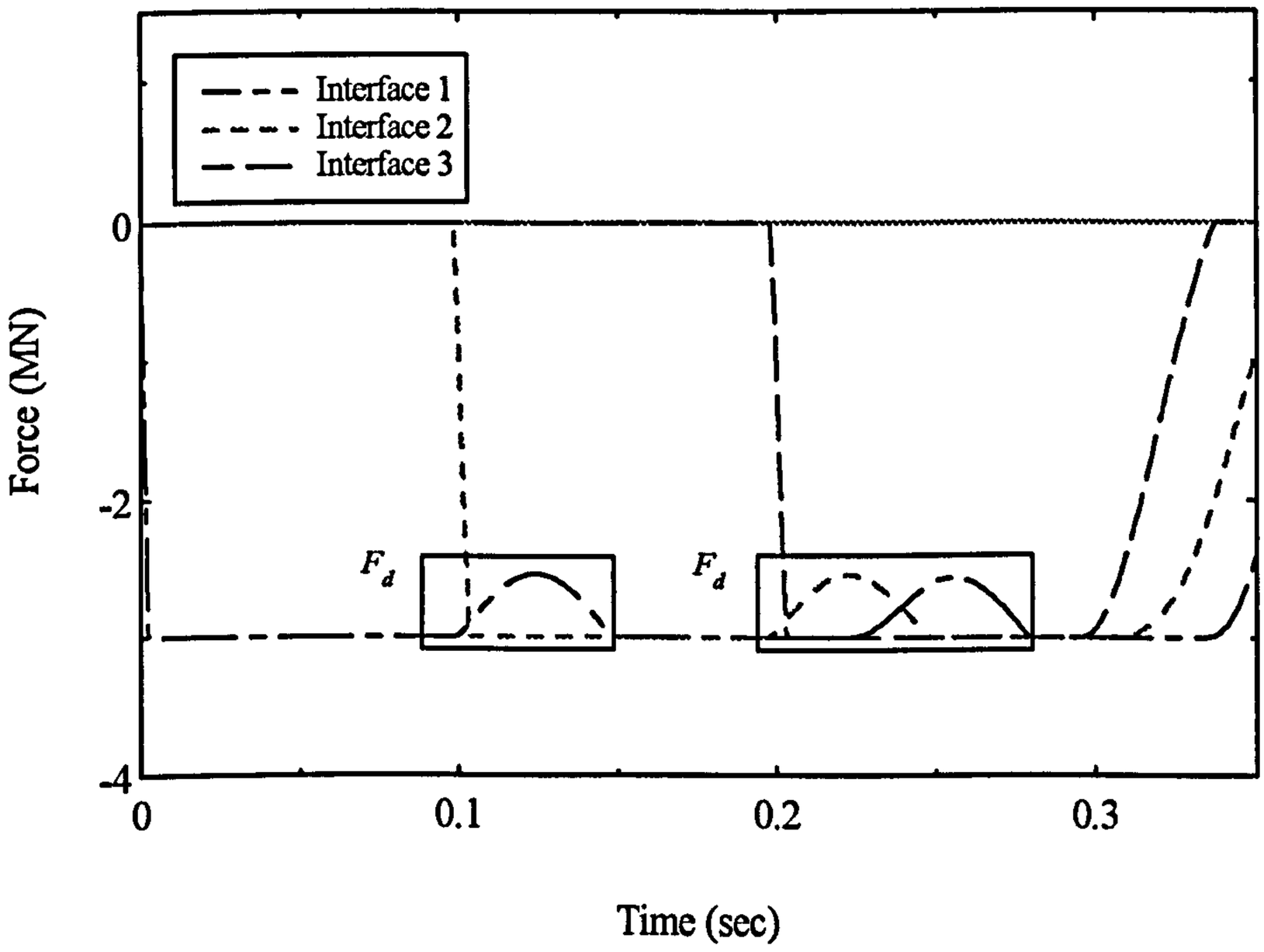

Figure 5.10c : The force-time history of various interfaces in cfy3.

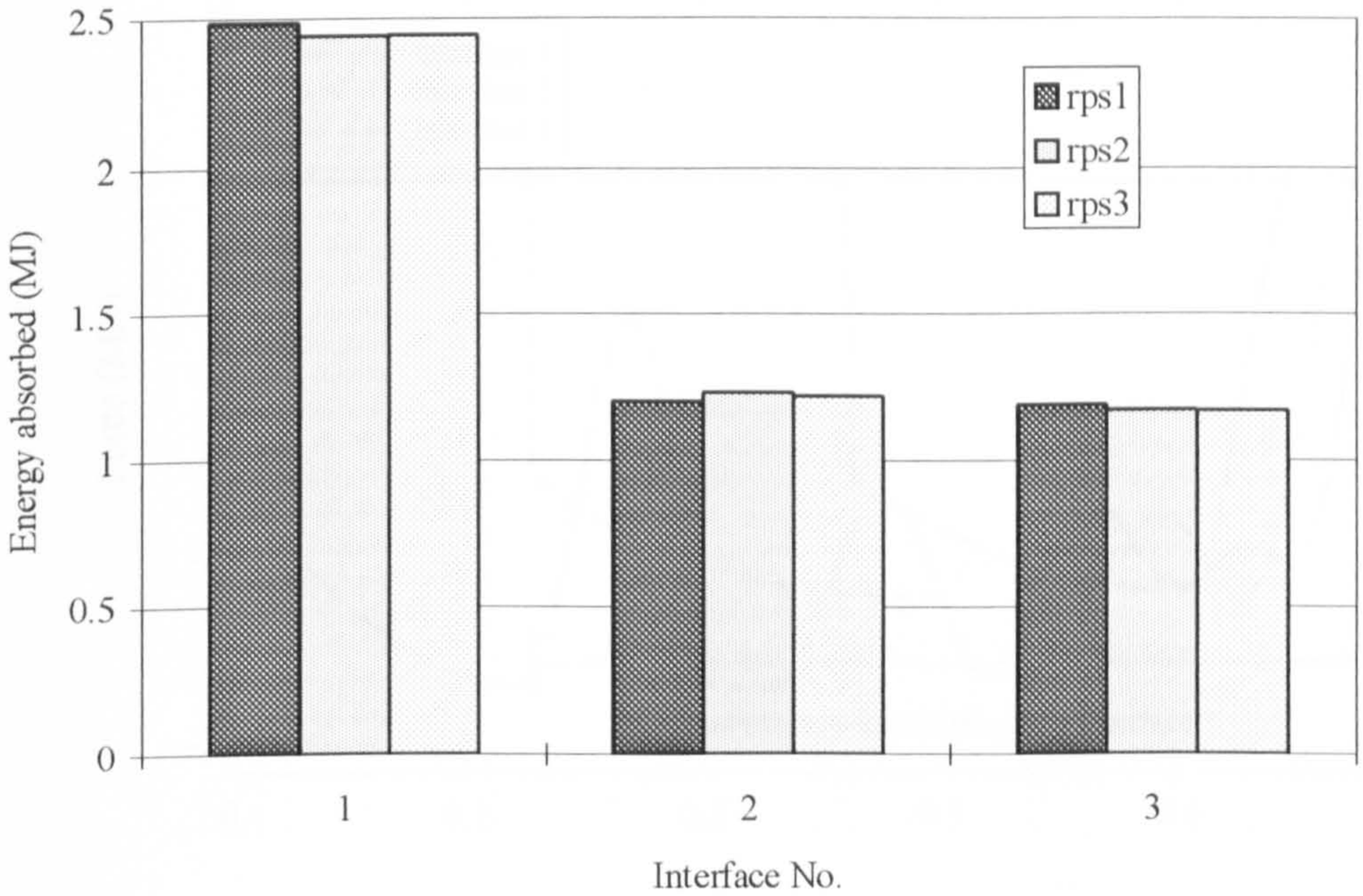

Figure 5.11 : The comparison of interface energy distribution for models in rps series.

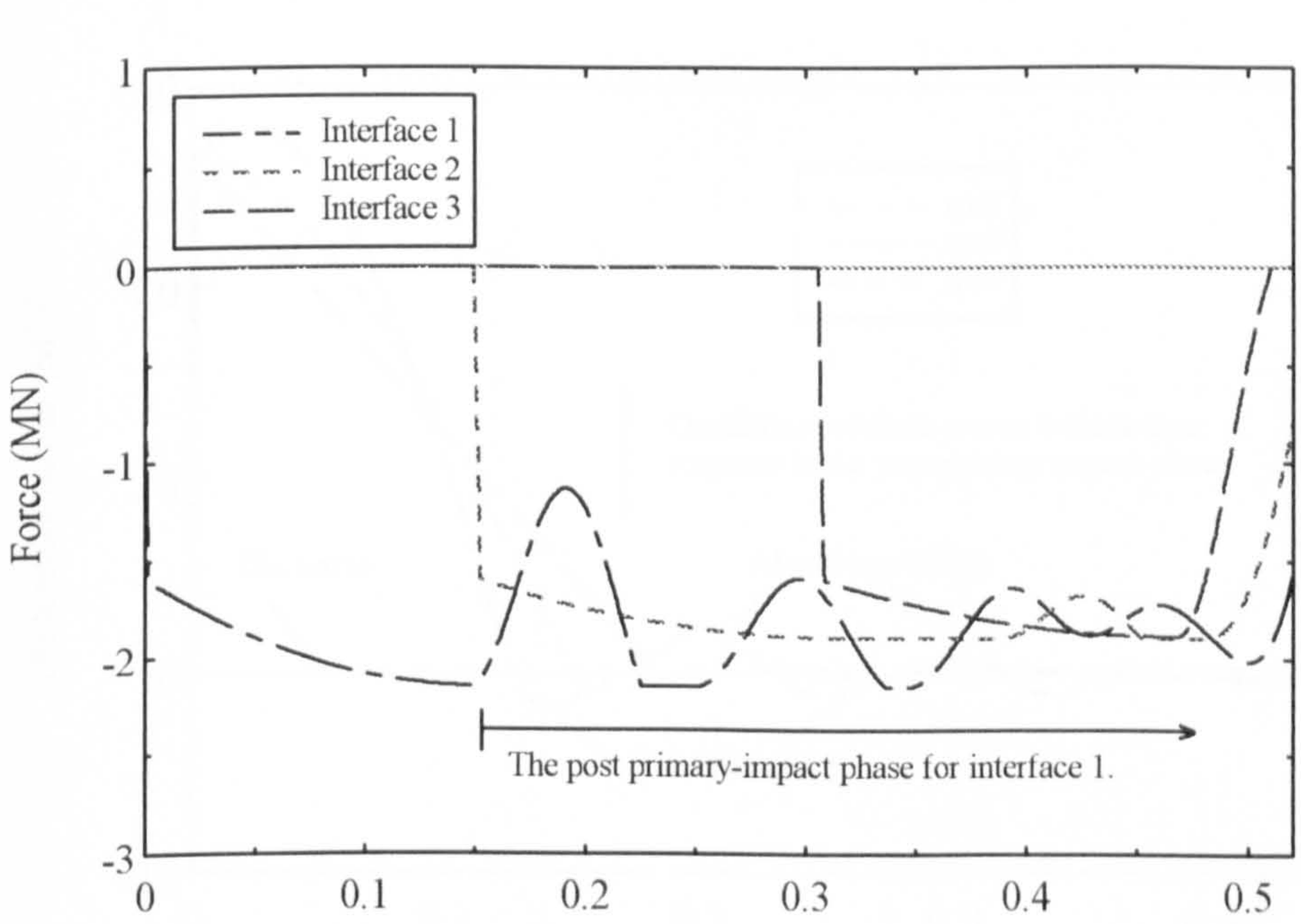

Figure 5.12a : The force-time history of various interfaces in rps2.

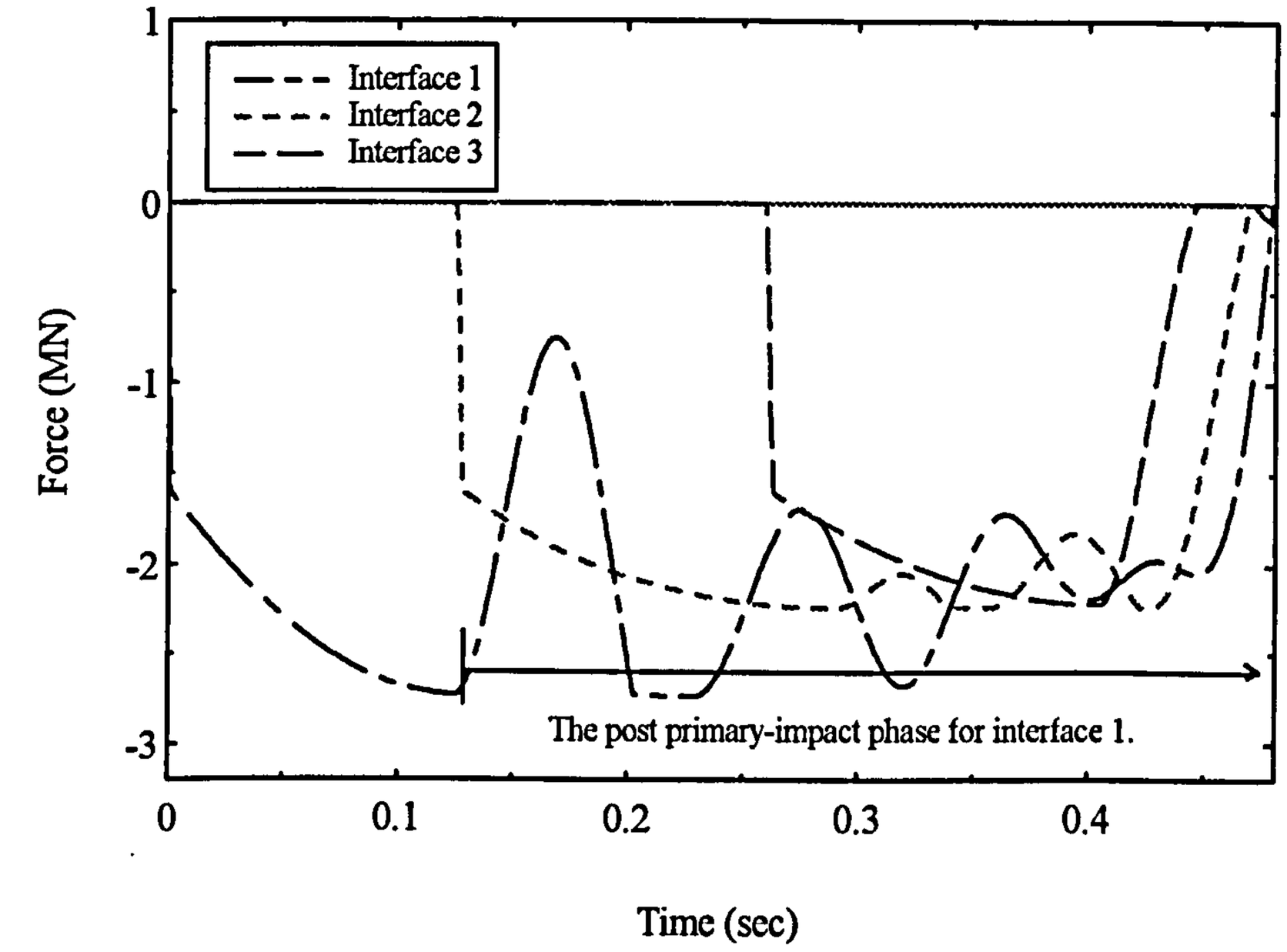

Figure 5.12b : The force-time history of various interfaces in rps3.

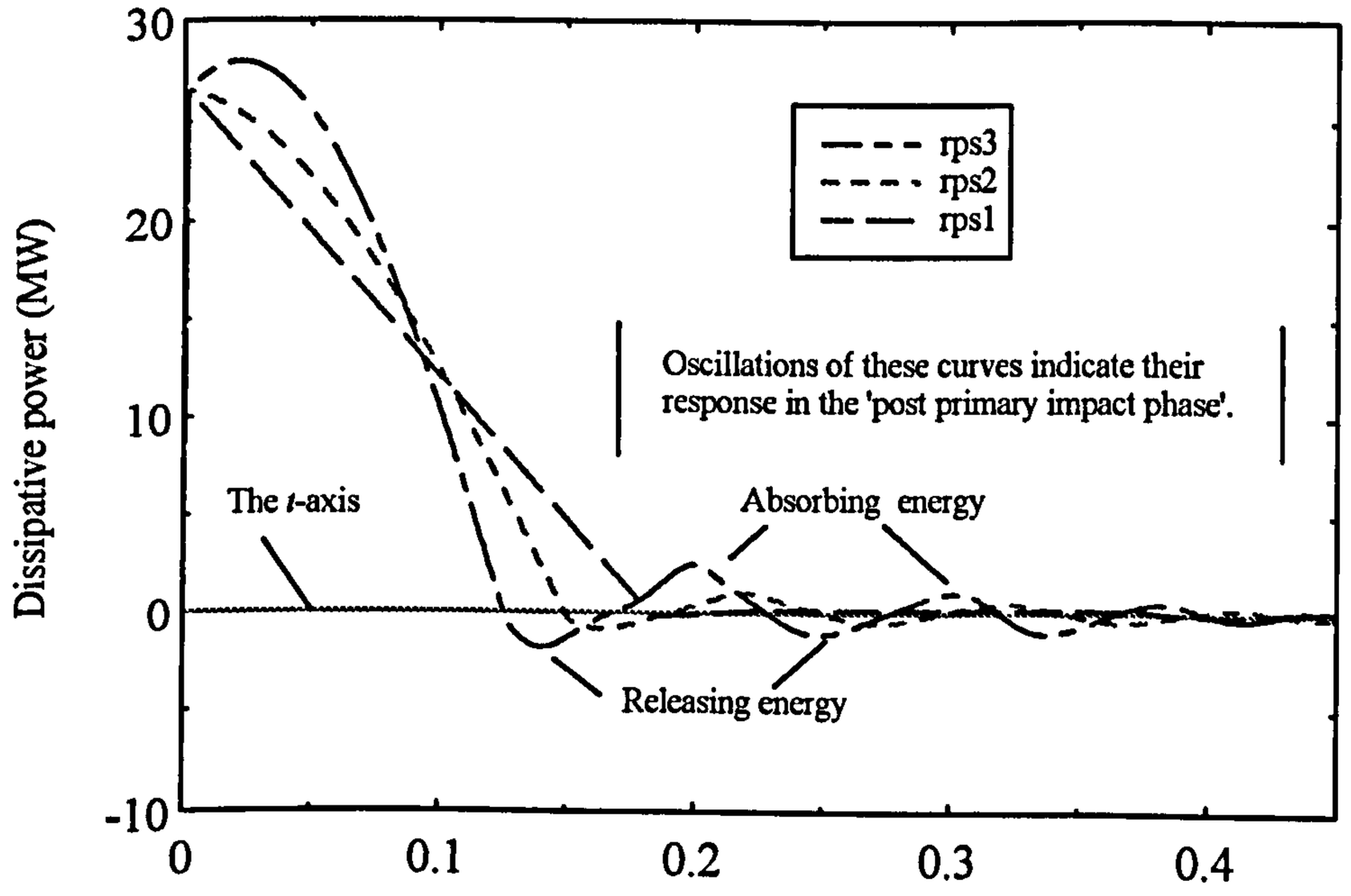

Figure 5.13 : The graph of dissipative power against time for interface 1 of models in the rps series.

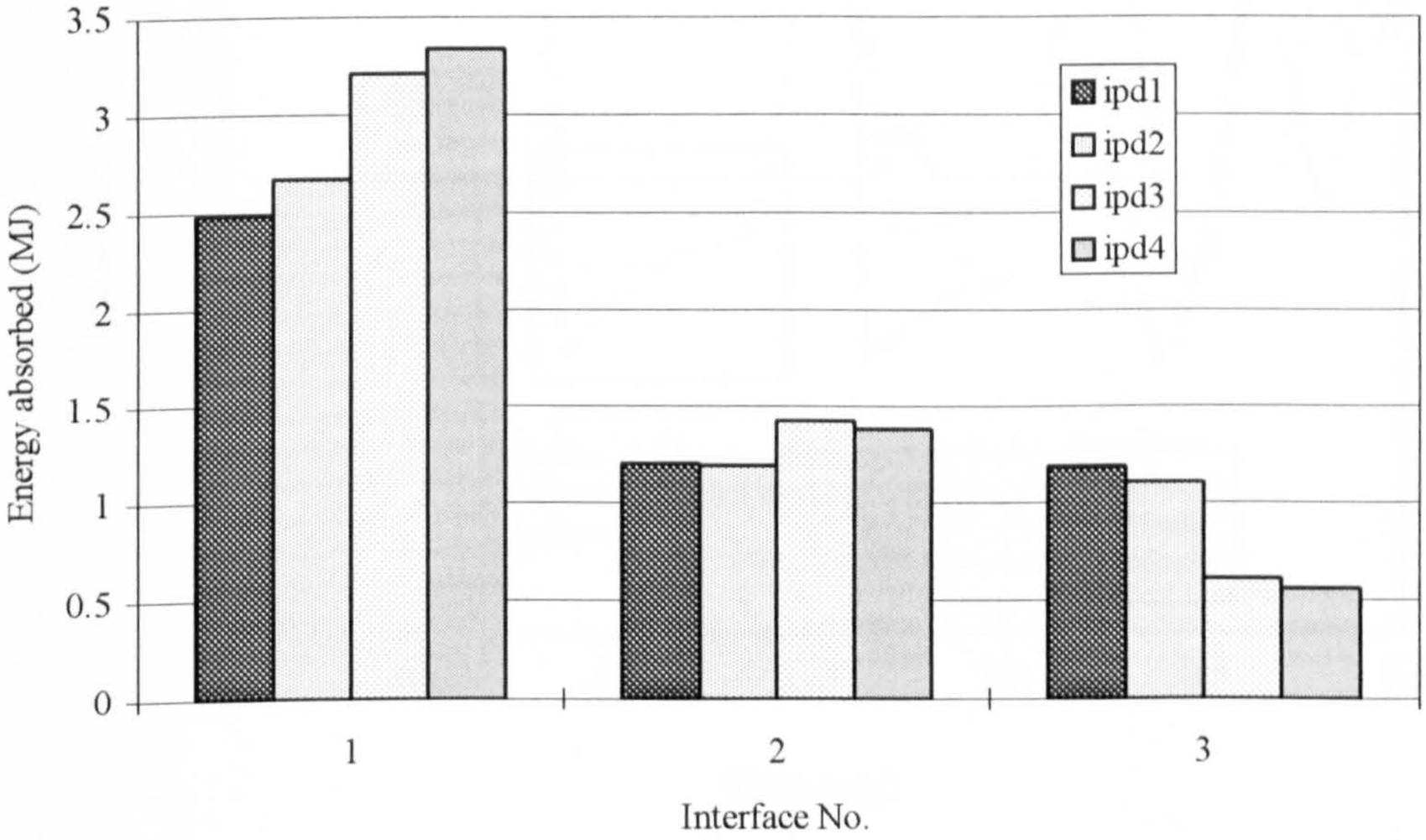

Figure 5.14 : The comparison of interface energy distribution for models in ipd series.

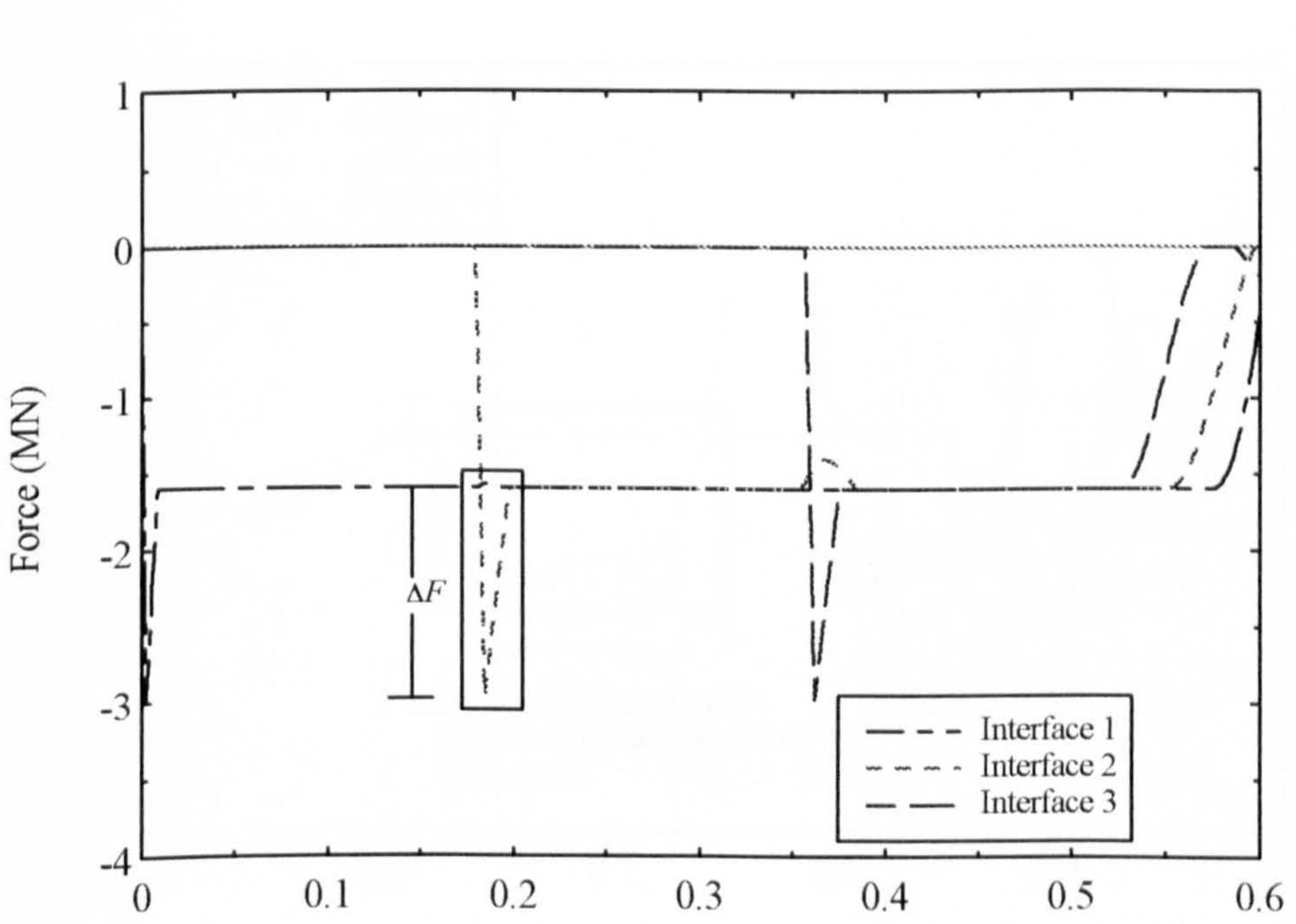

Figure 5.15a : The force-time history of various interfaces in ipd2.

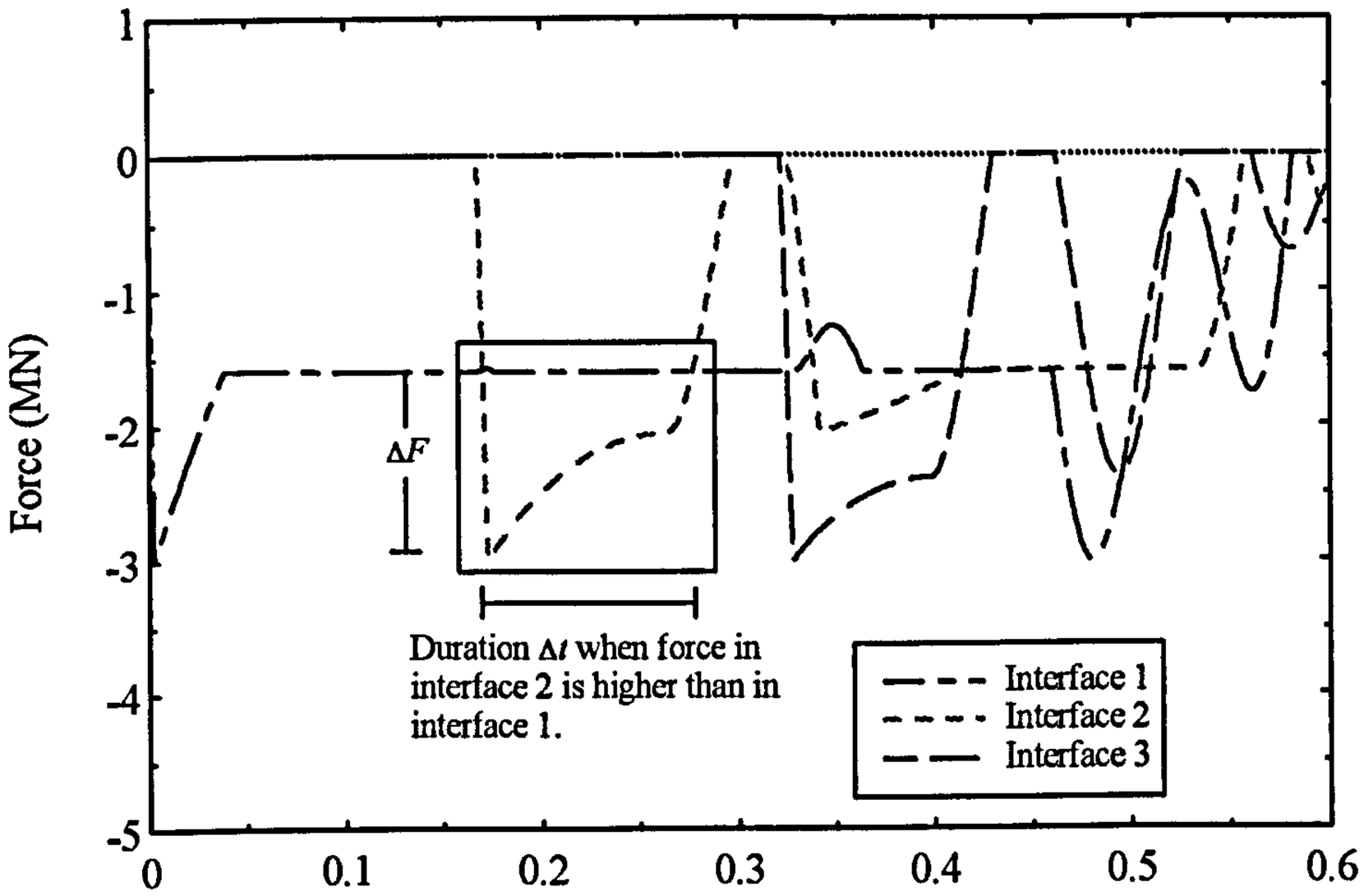

Figure 5.15b : The force-time history of various interfaces in ipd3.

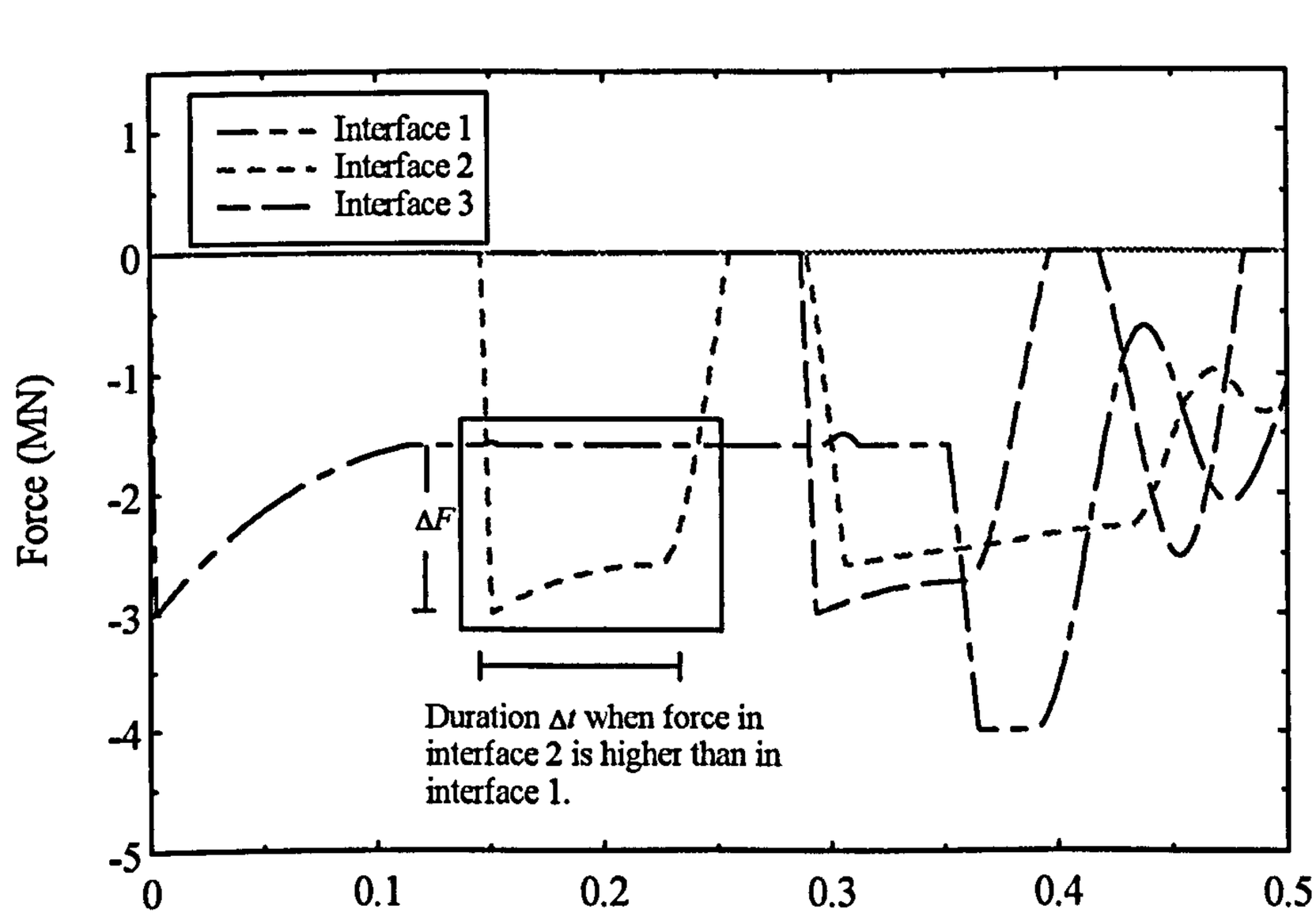

Figure 5.15c : The force-time history of various interfaces in ipd4.

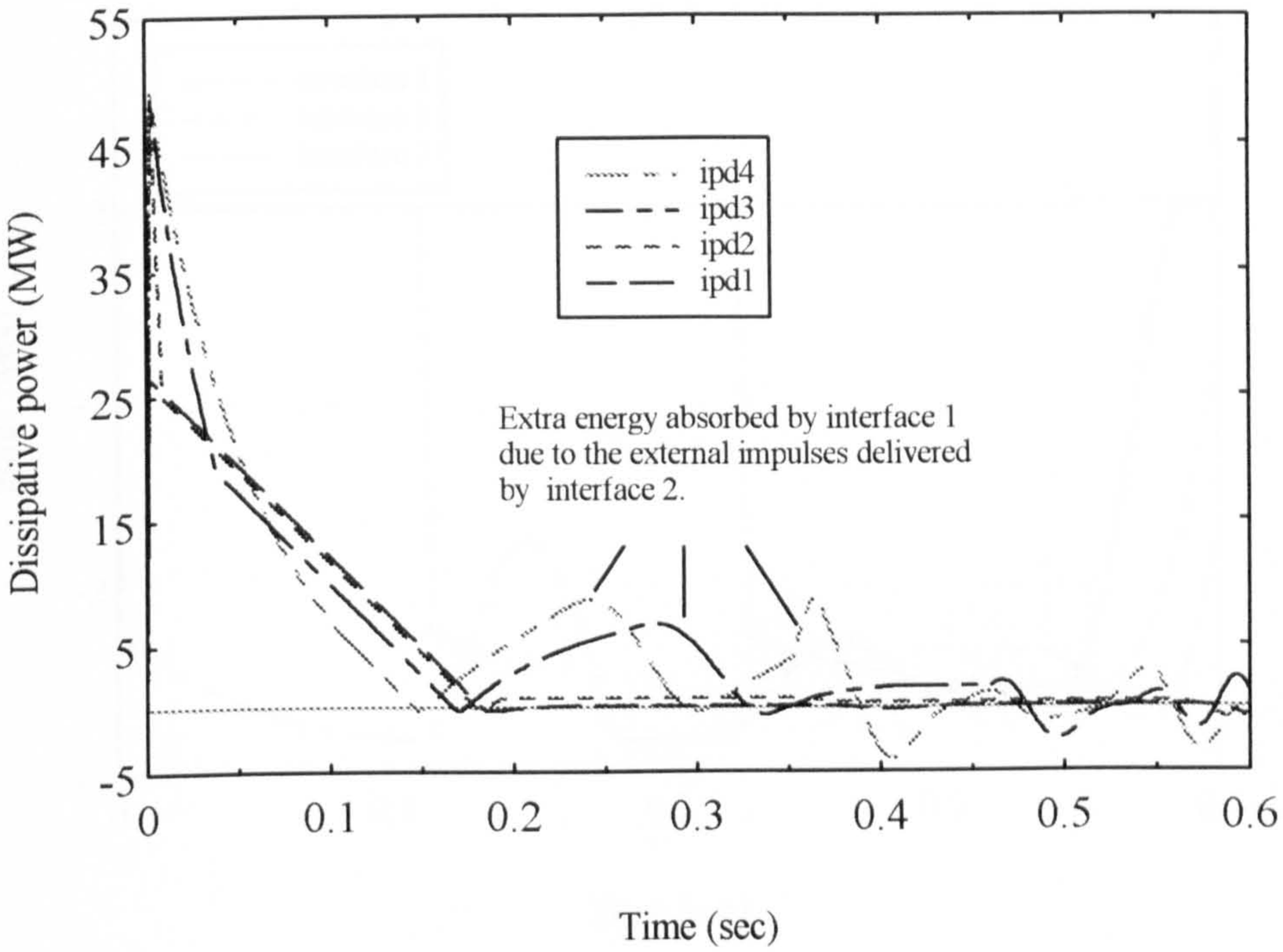

Figure 5.16 : The graph of dissipative power against time for interface 1 of models in the rps series.

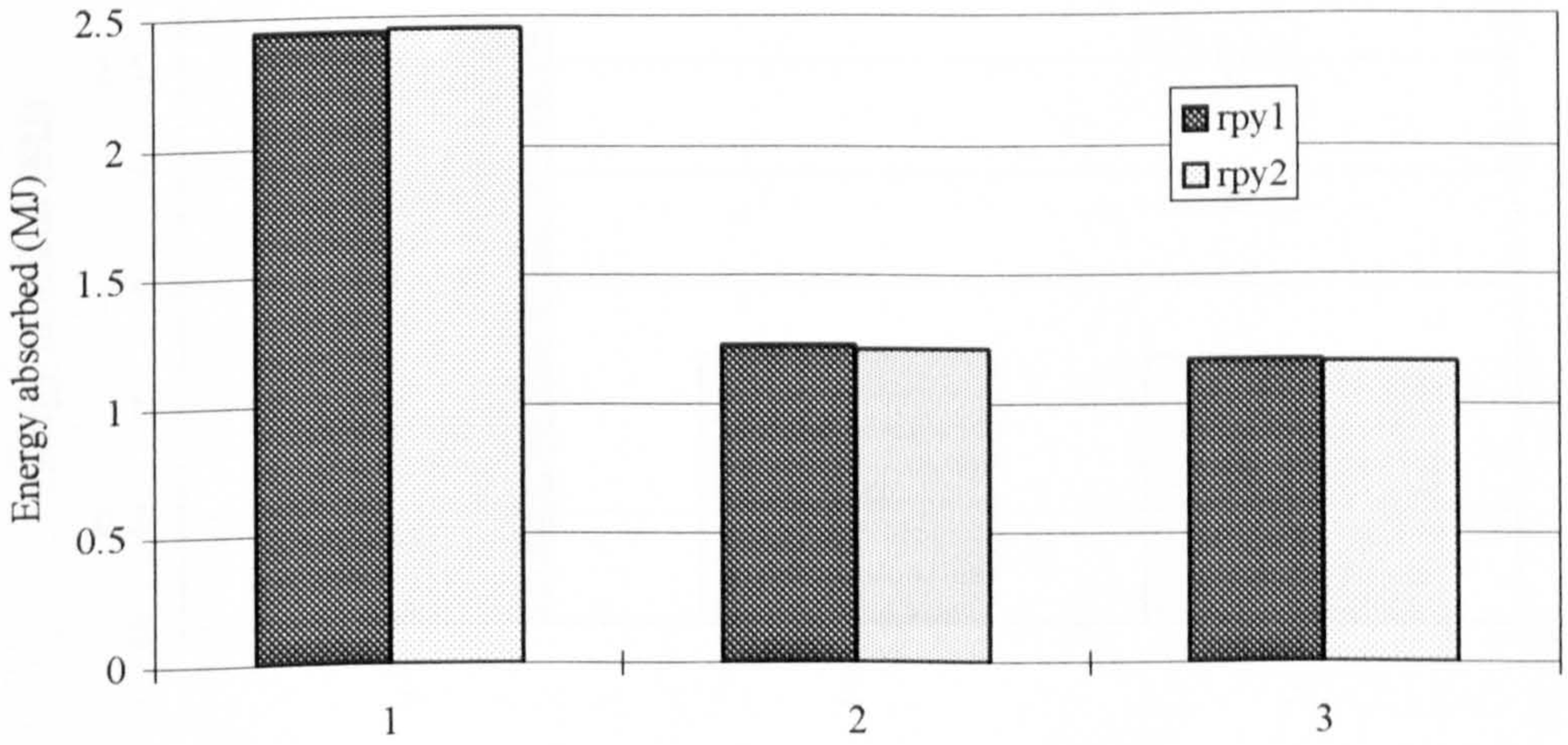

Figure 5.17 : The comparison of interface energy distribution for models in rpy series.

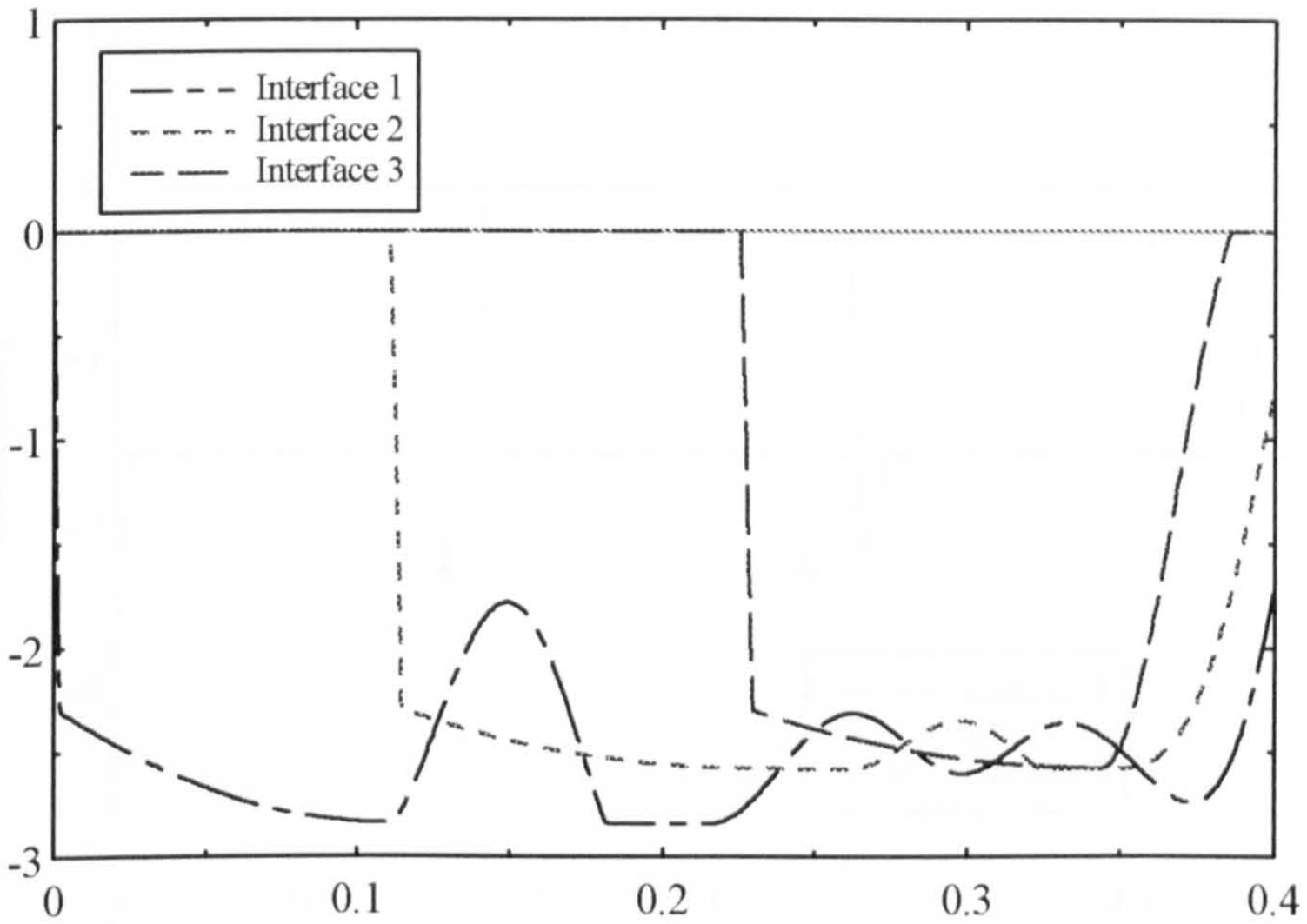

Figure 5.18 : The force-time history of various interfaces in rpy2.

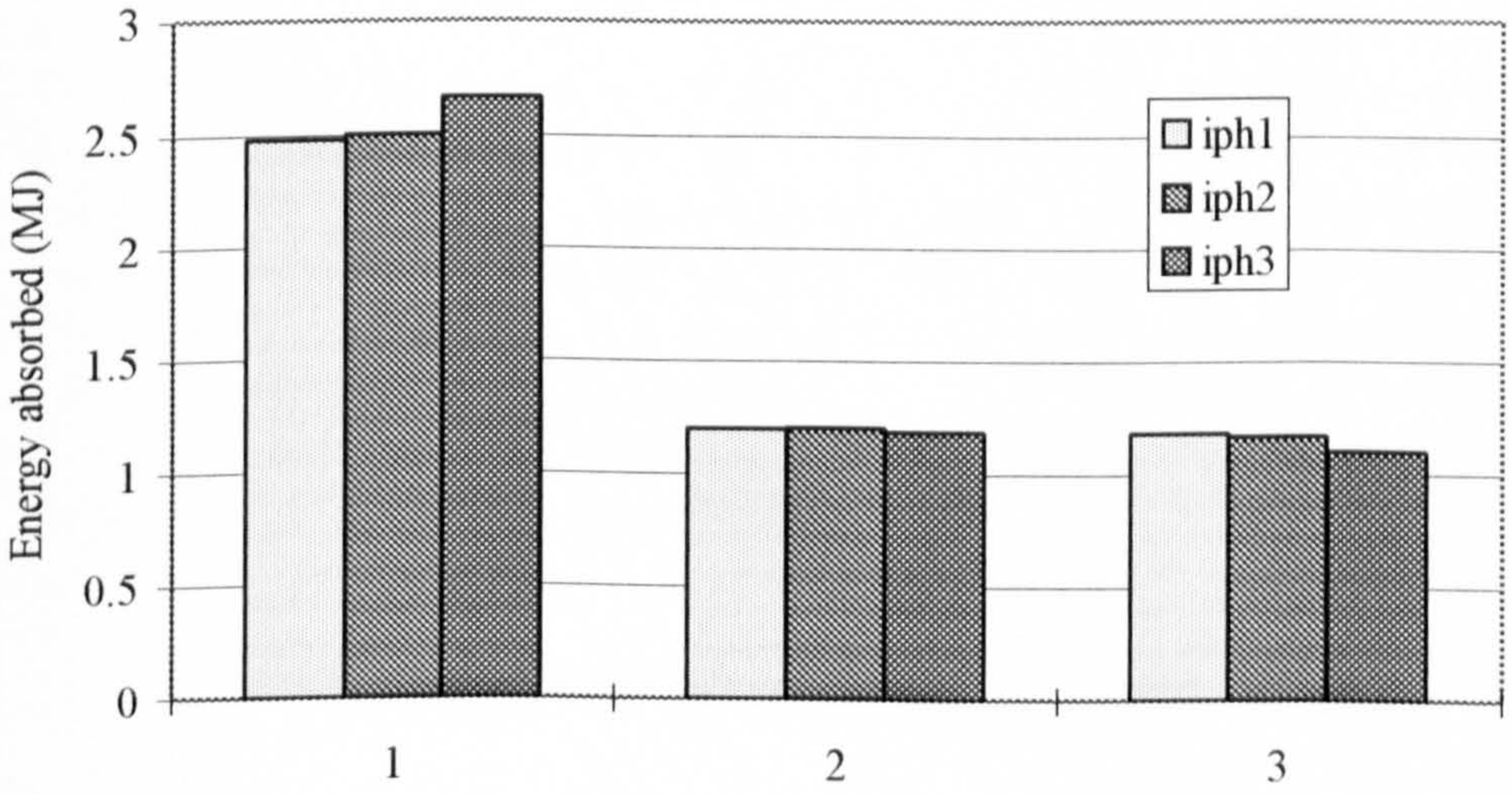

Figure 5.19 : The comparison of interface energy distribution for models in iph series.

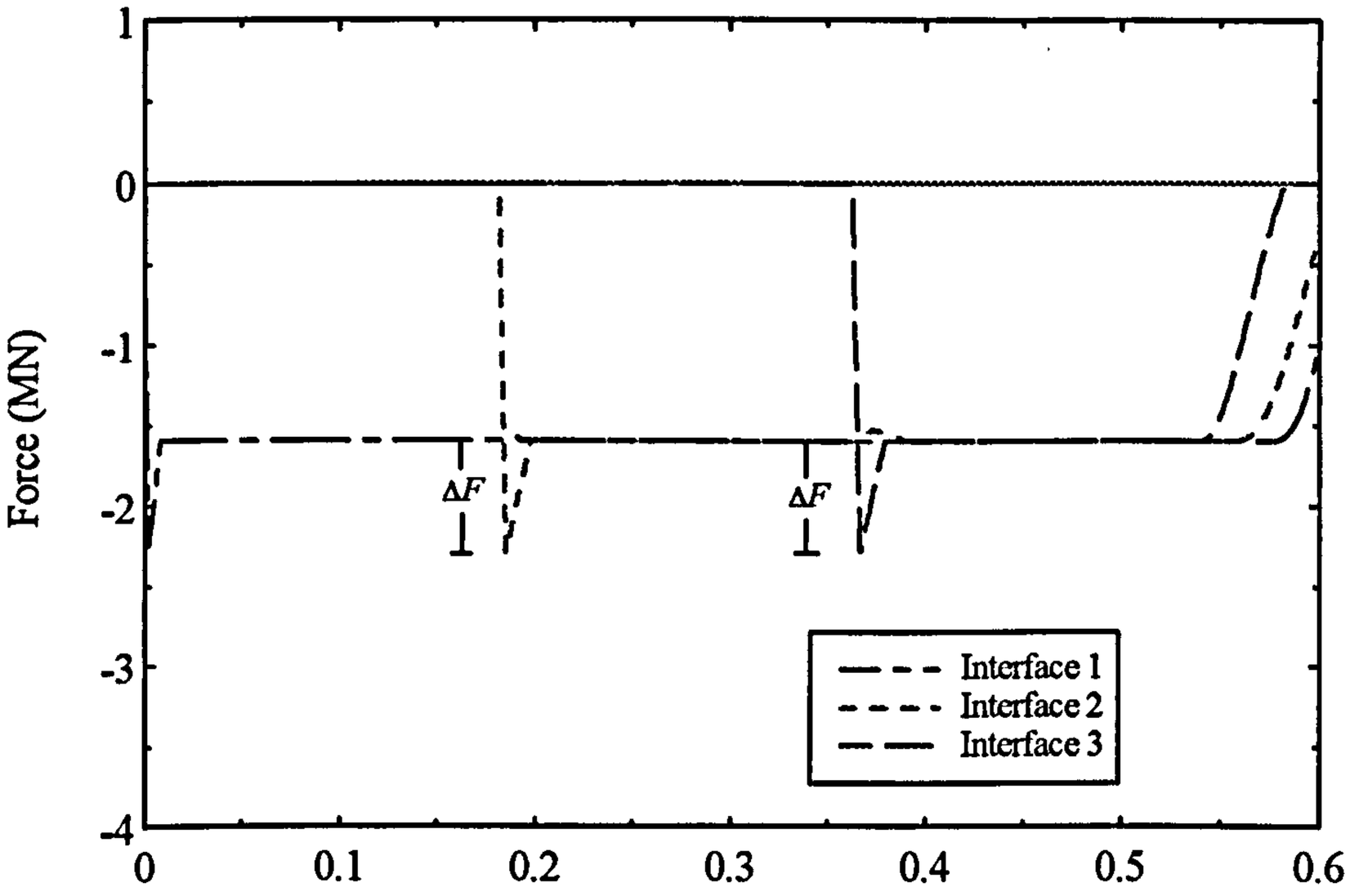

Figure 5.20 : The force-time history of various interfaces in iph3.

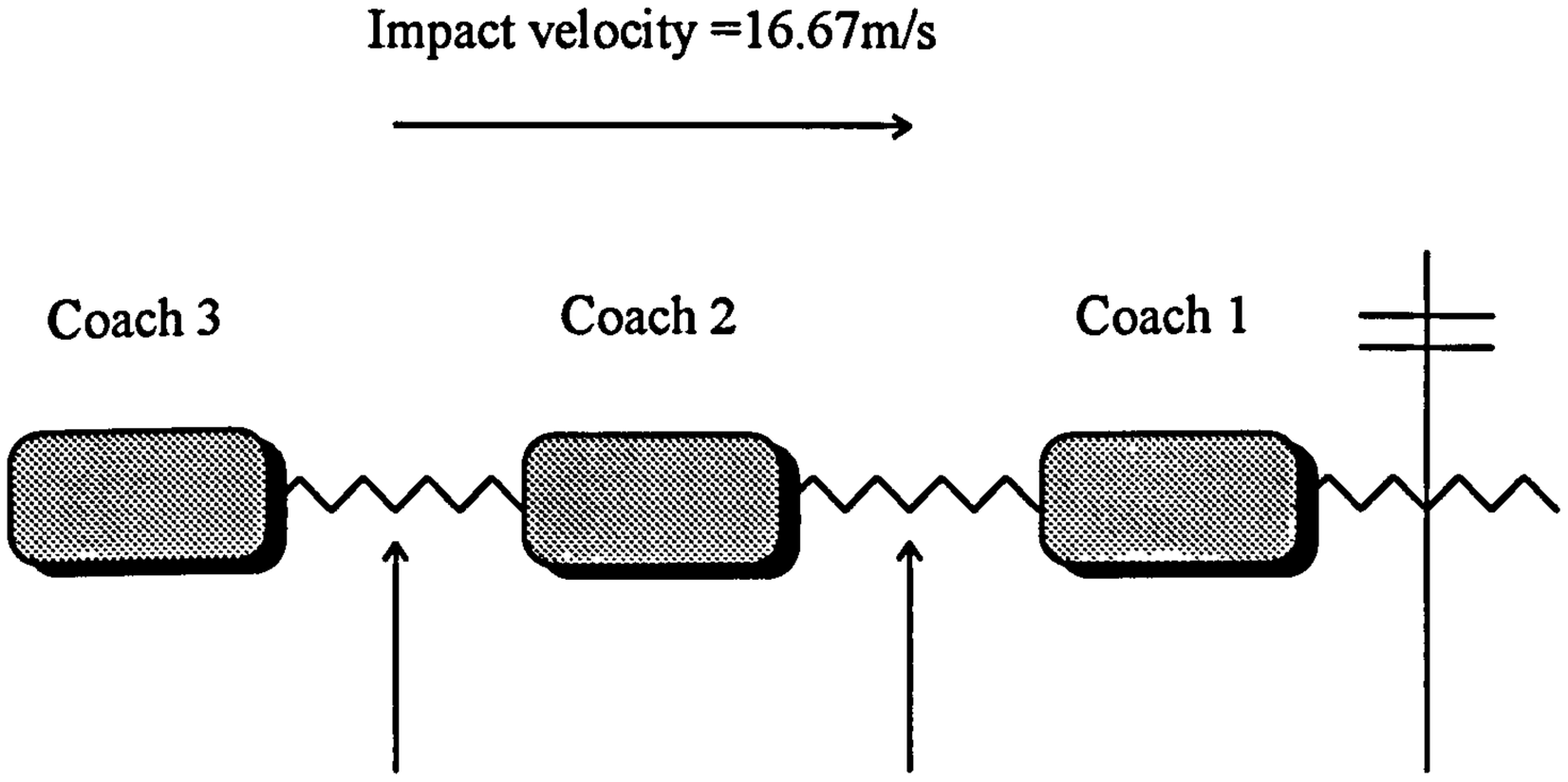

Note :

- The spring in interface 1 is the original spring in ipd4 with no gap since a gap in this interface serves only to delay the collision and not effect the results;
- The spring in interface 2 is taken from cfy1 and the gap is tuned for ipd4 since the leading interface in this case has a iph4 spring;
- The spring in interface 3 is also taken from cfy1 but the gap is tuned to cfy1 since the leading interface has a cfy1 spring;
- By mixing springs in the above model, no trailing interface would exert a load higher than its leading interface during an impact.

Figure 5.21 : The model of modified ipd4 and known as mod4.

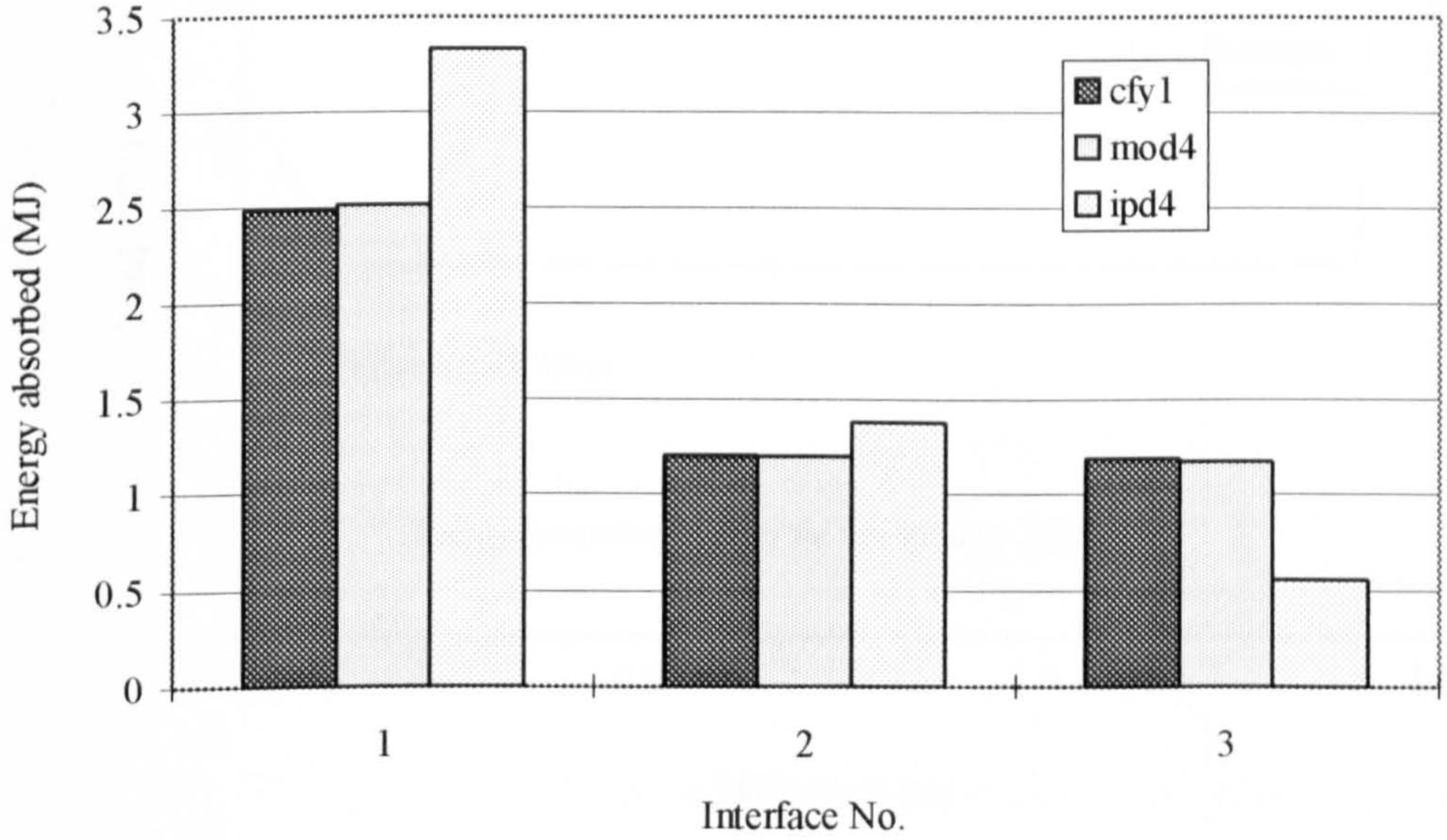

Figure 5.22 : The comparison of interface energy distribution for cfy1, mod4 and ipd4.

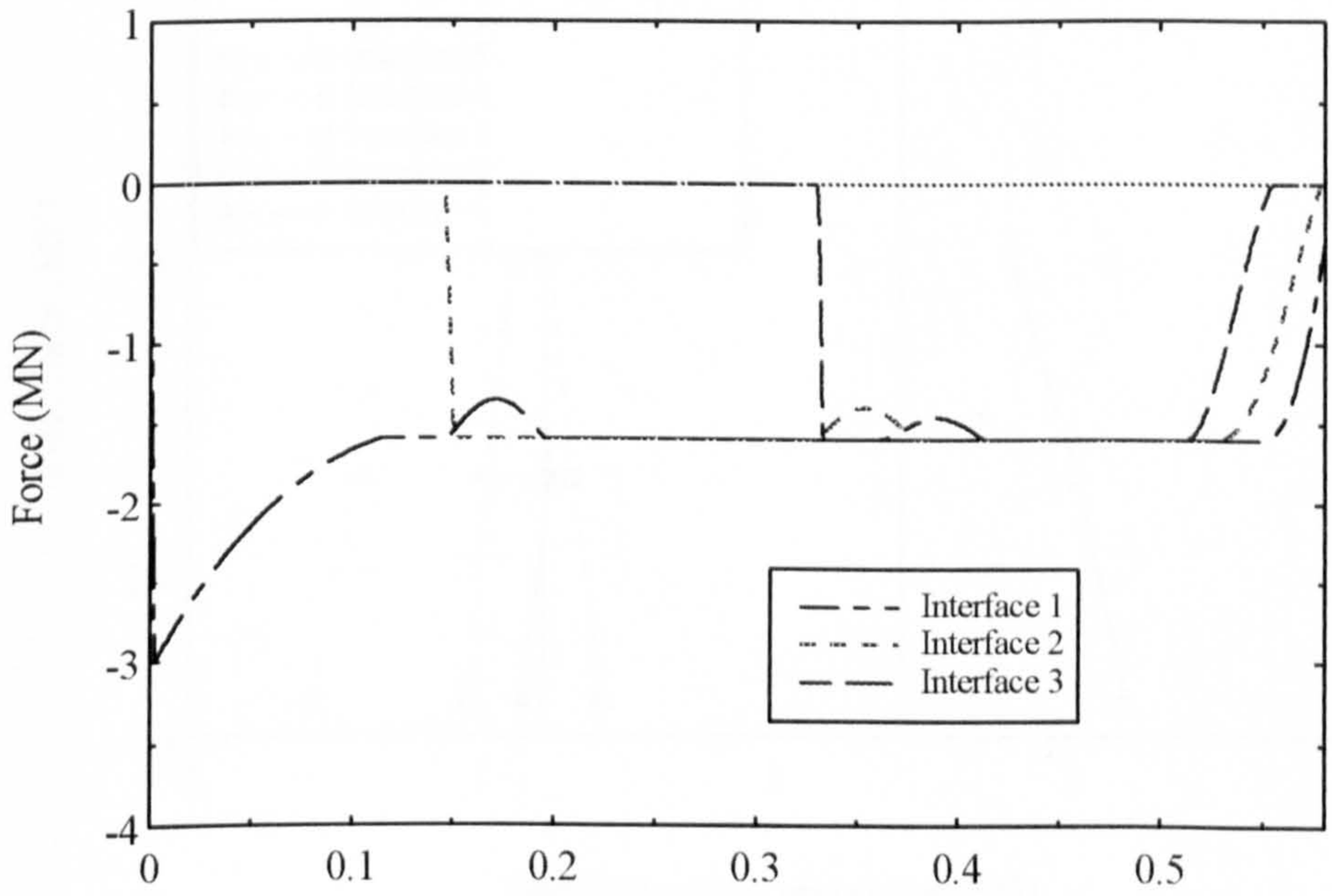

Figure 5.23 : The force-time history of various interfaces in mod4.

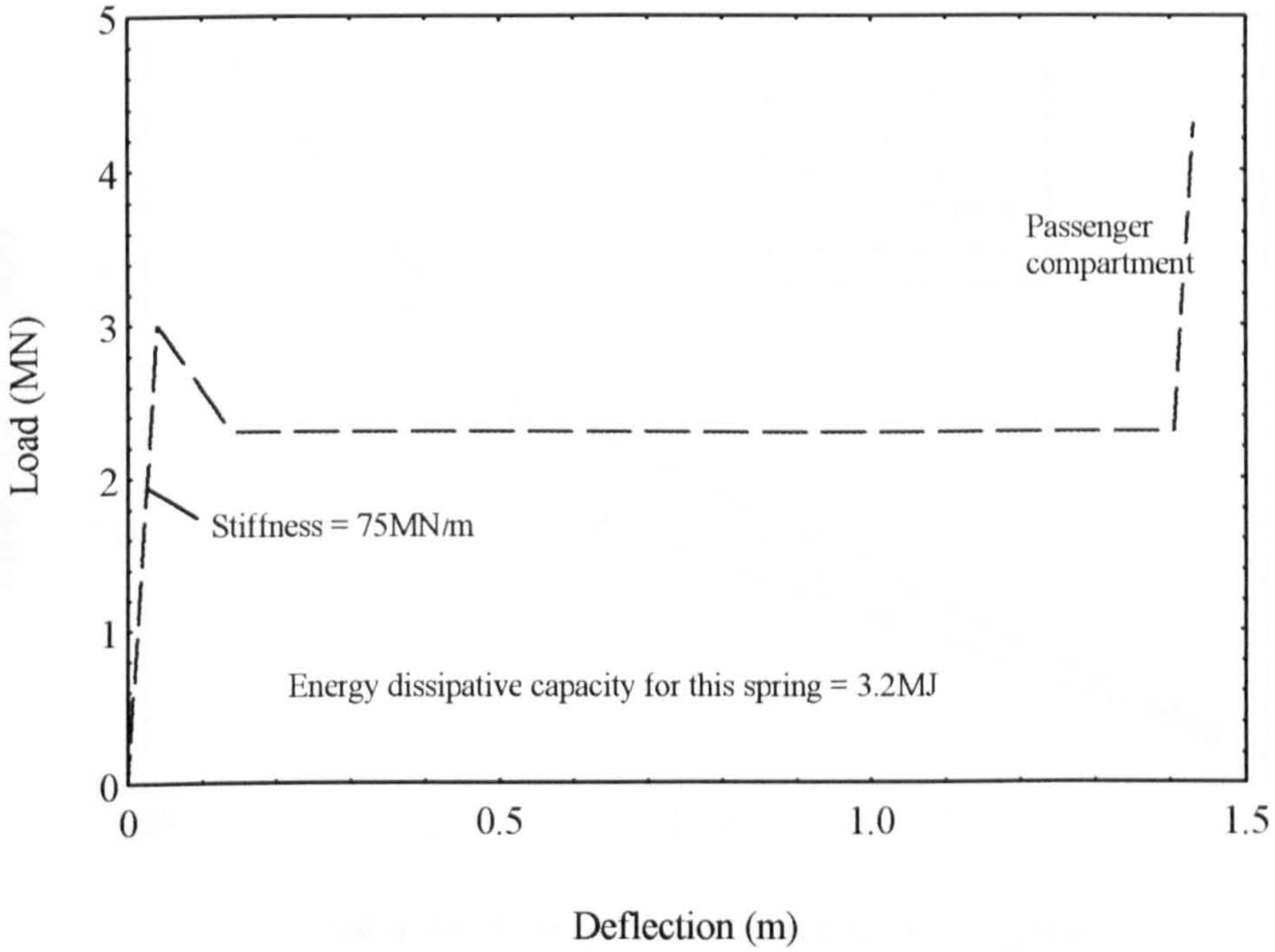

Figure 6.1 : The spring characteristics of the model ip2.33.

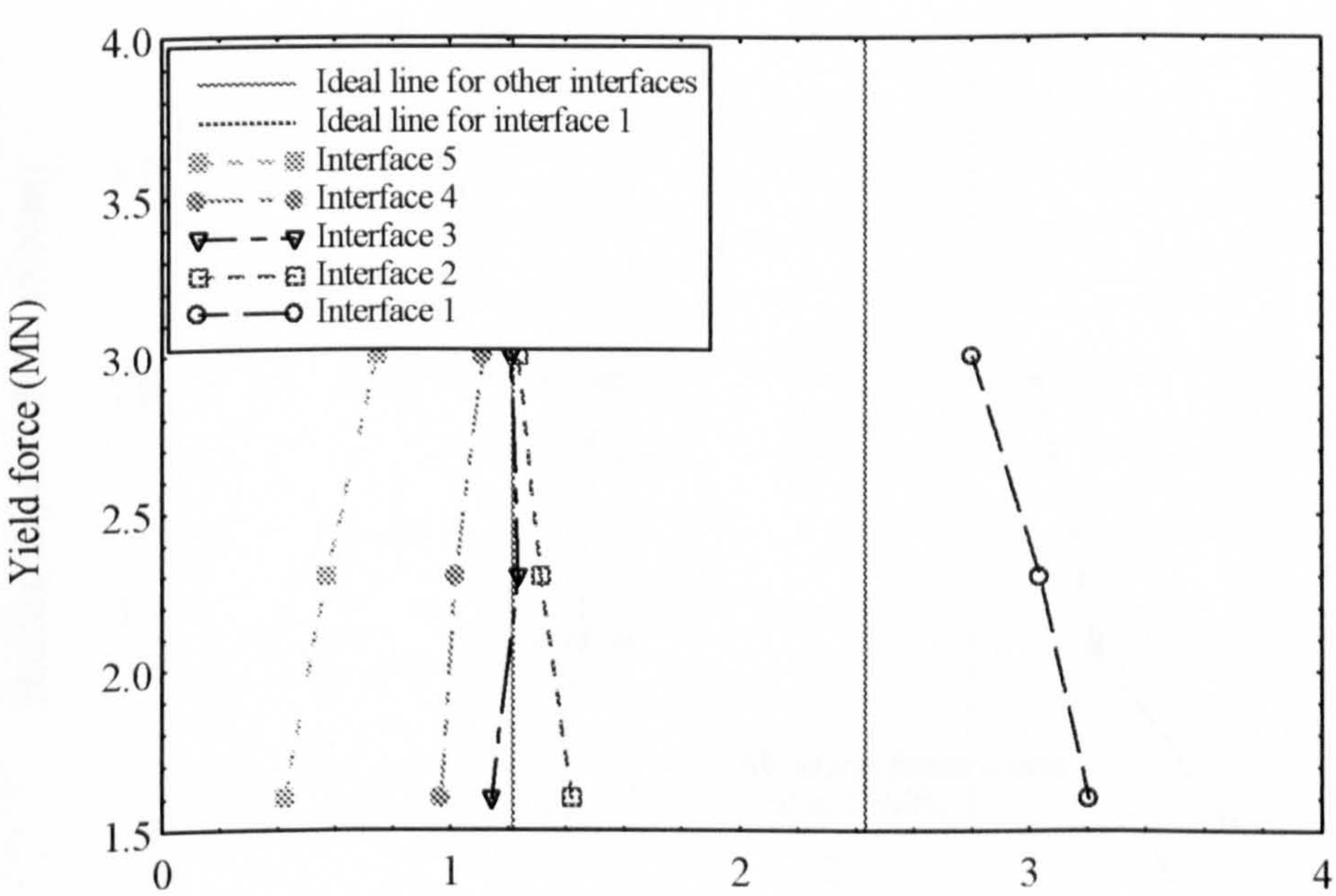

Figure 6.2 : Effect of yield force on interface energy distribution for models in the cfy series.

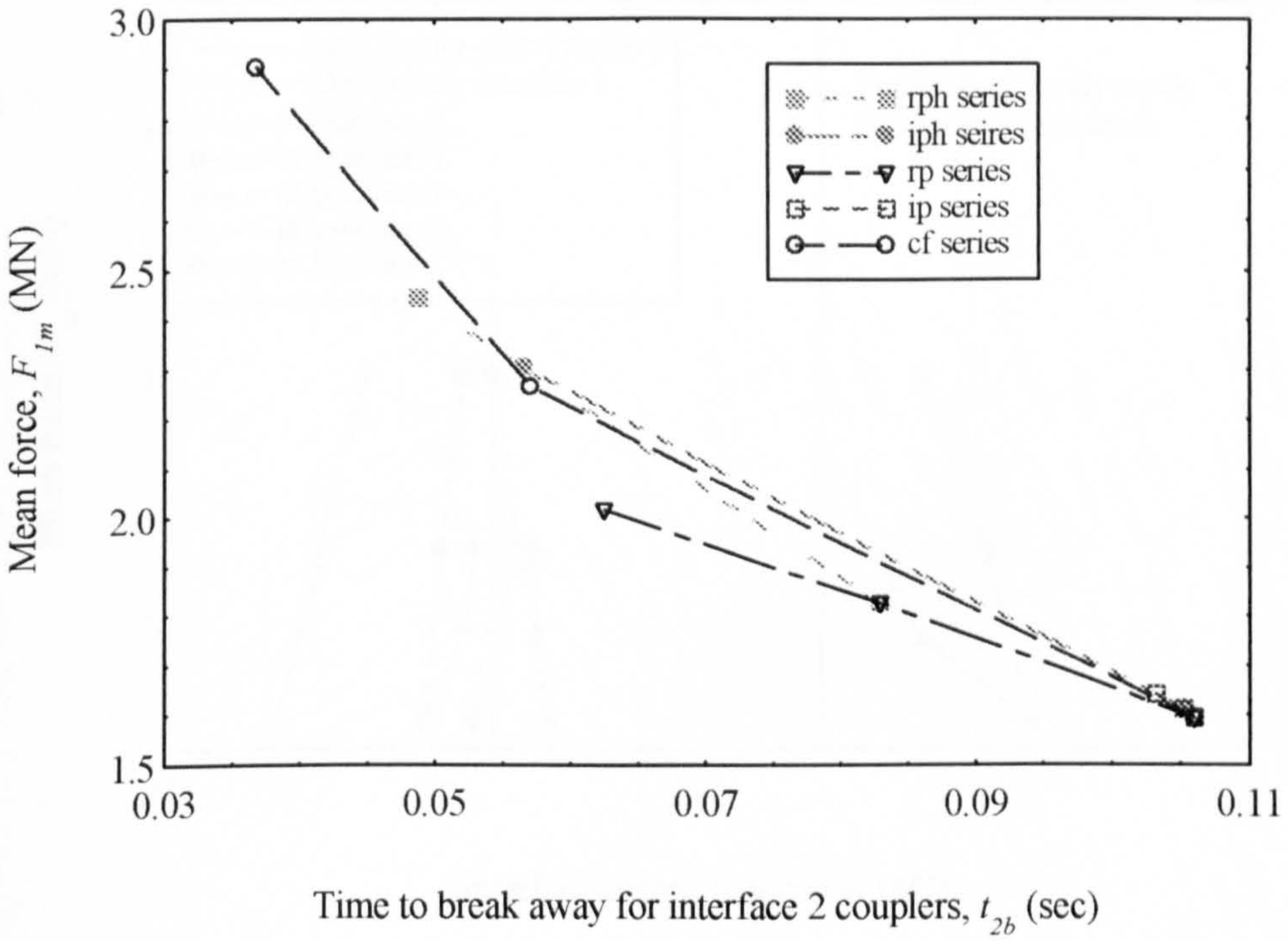

Figure 6.3 : Effects of spring average force on couplers' breakaway time.

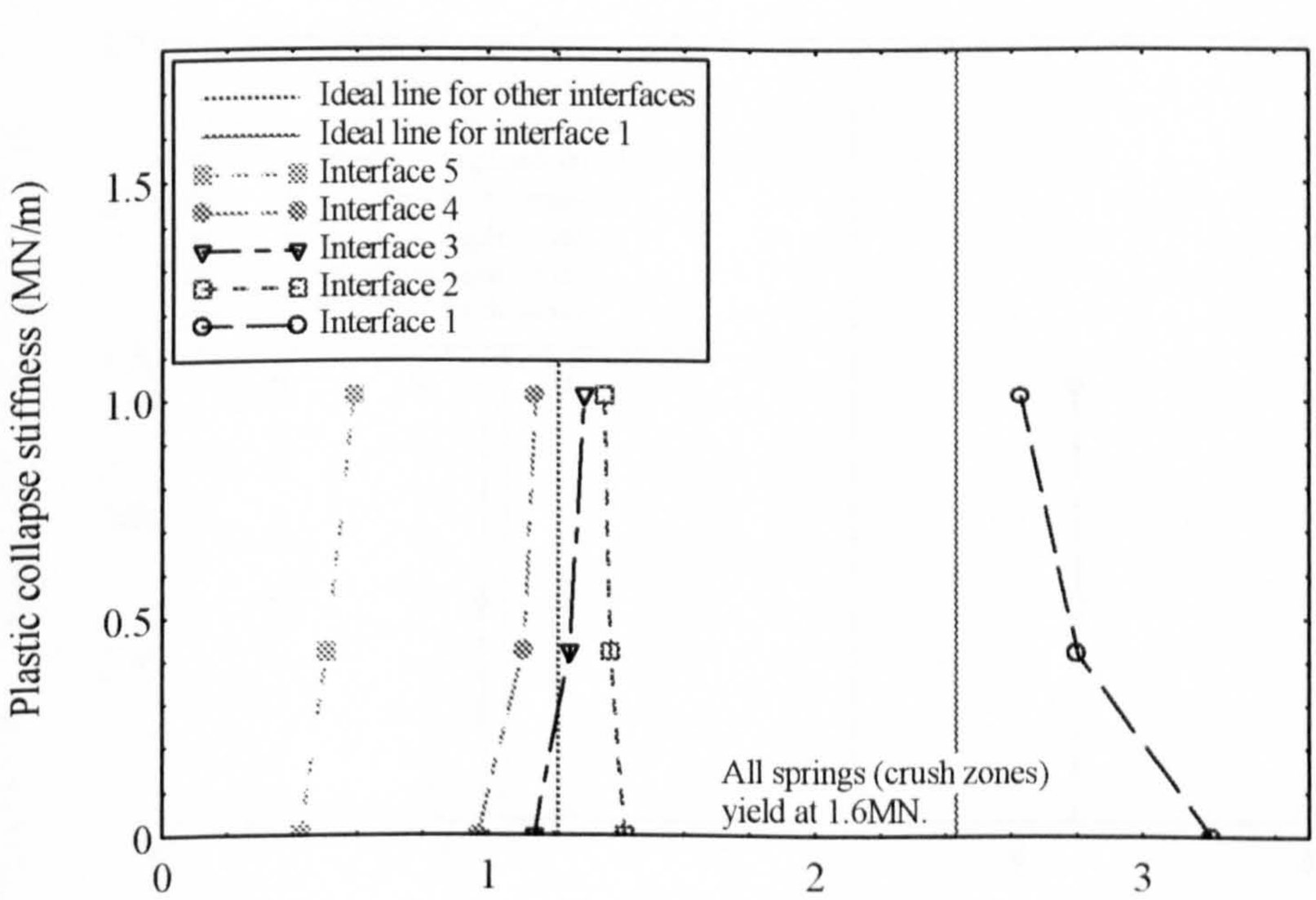

Figure 6.4 : Effects of hardening slope on interface energy distribution for models in the rps series.

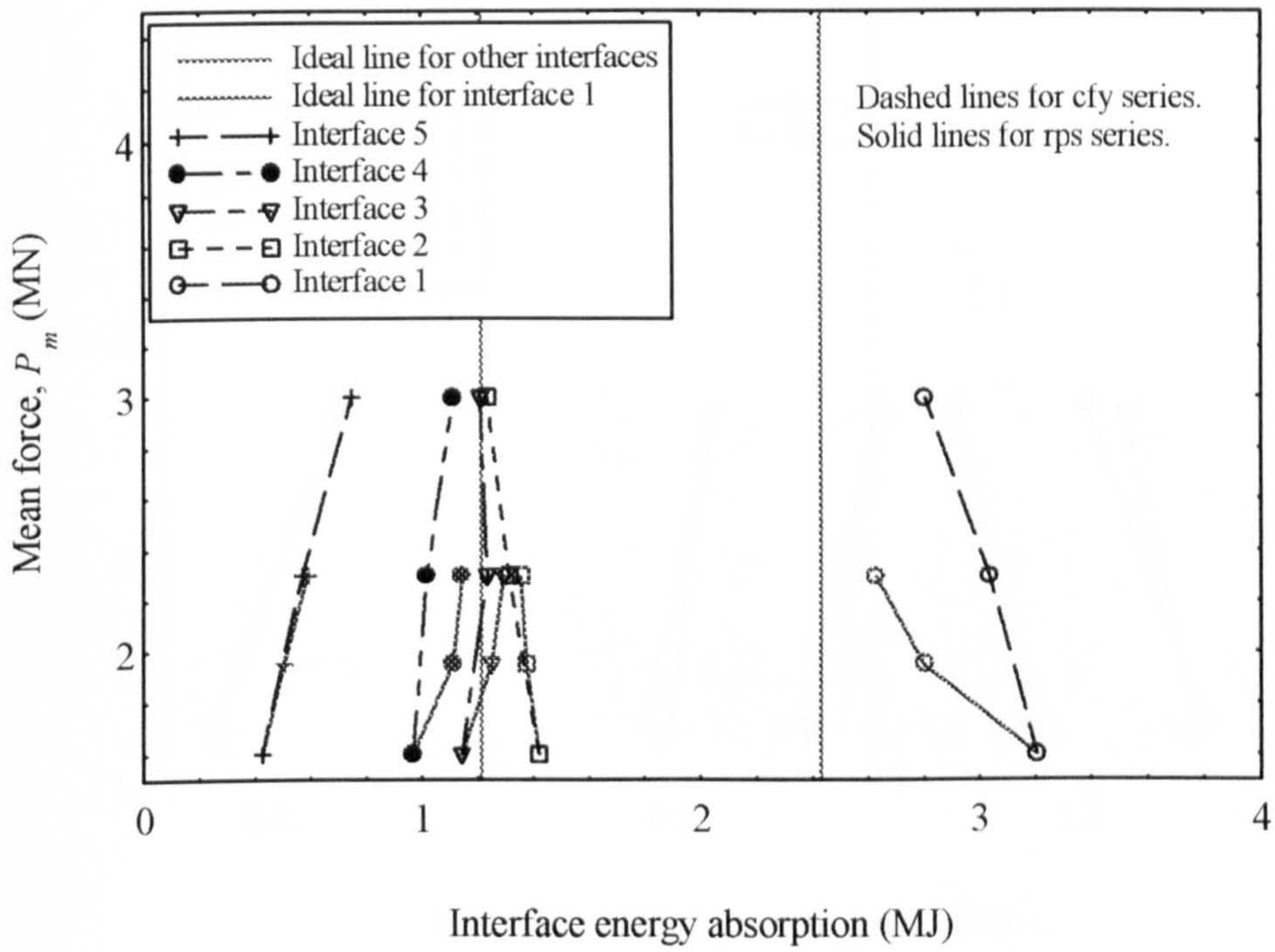

Figure 6.5 : Comparing the energy distribution for models in the cfy and rps series.

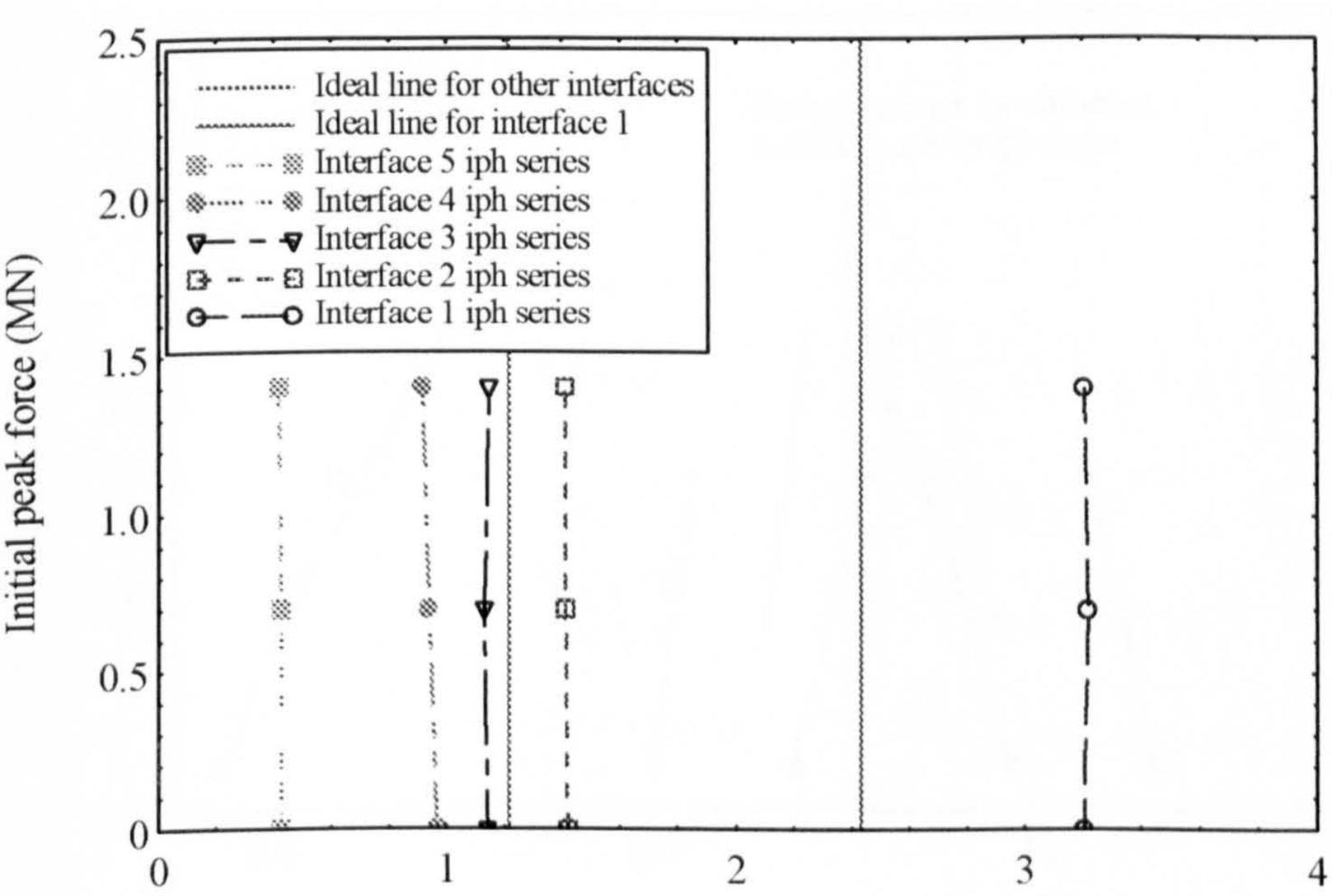

Figure 6.6 : Effects of initial peak force on interface energy distribution for models in the iph series.

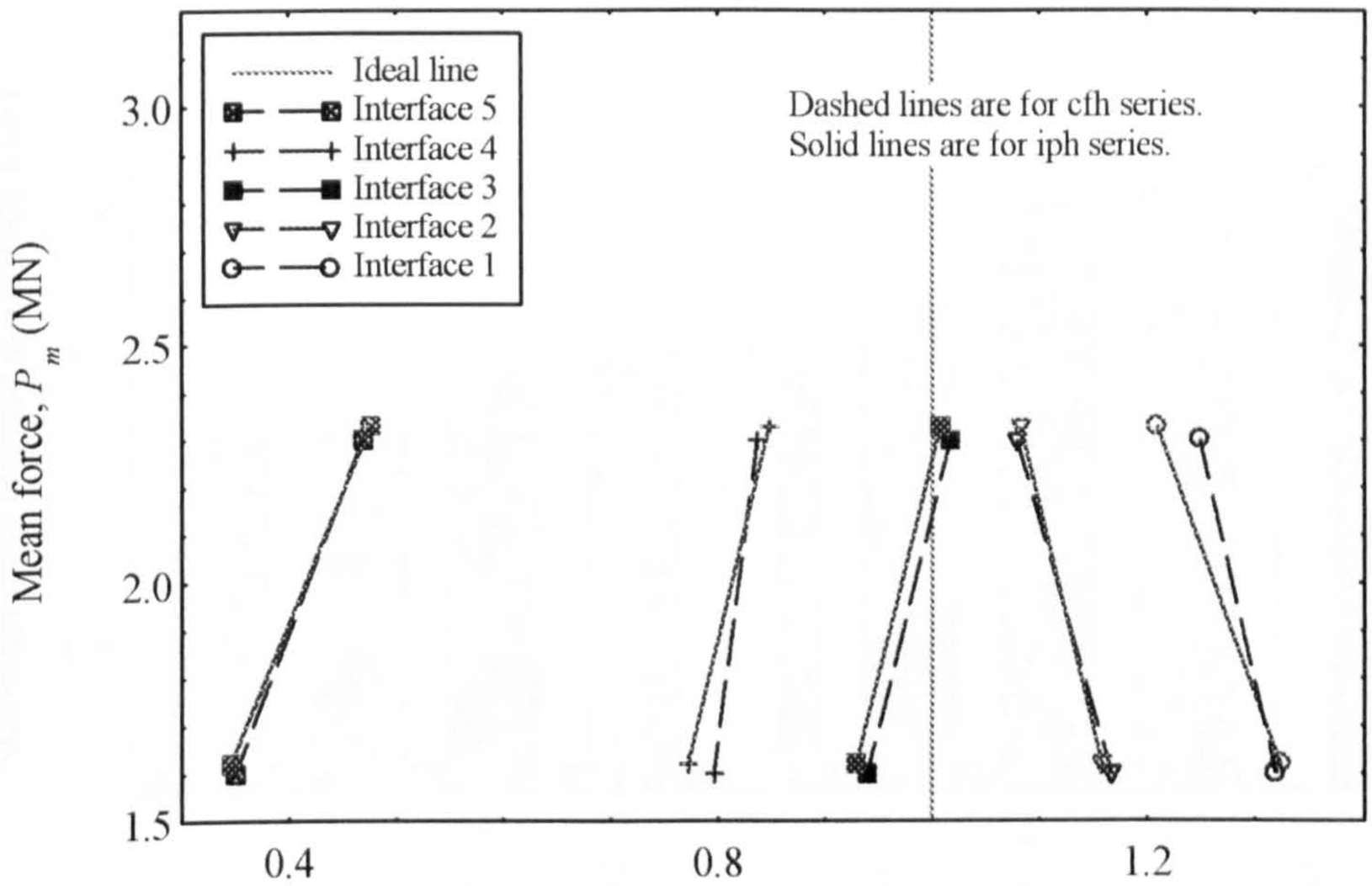

Figure 6.7 : Comparing energy distribution for models in the ipy and cfy series.

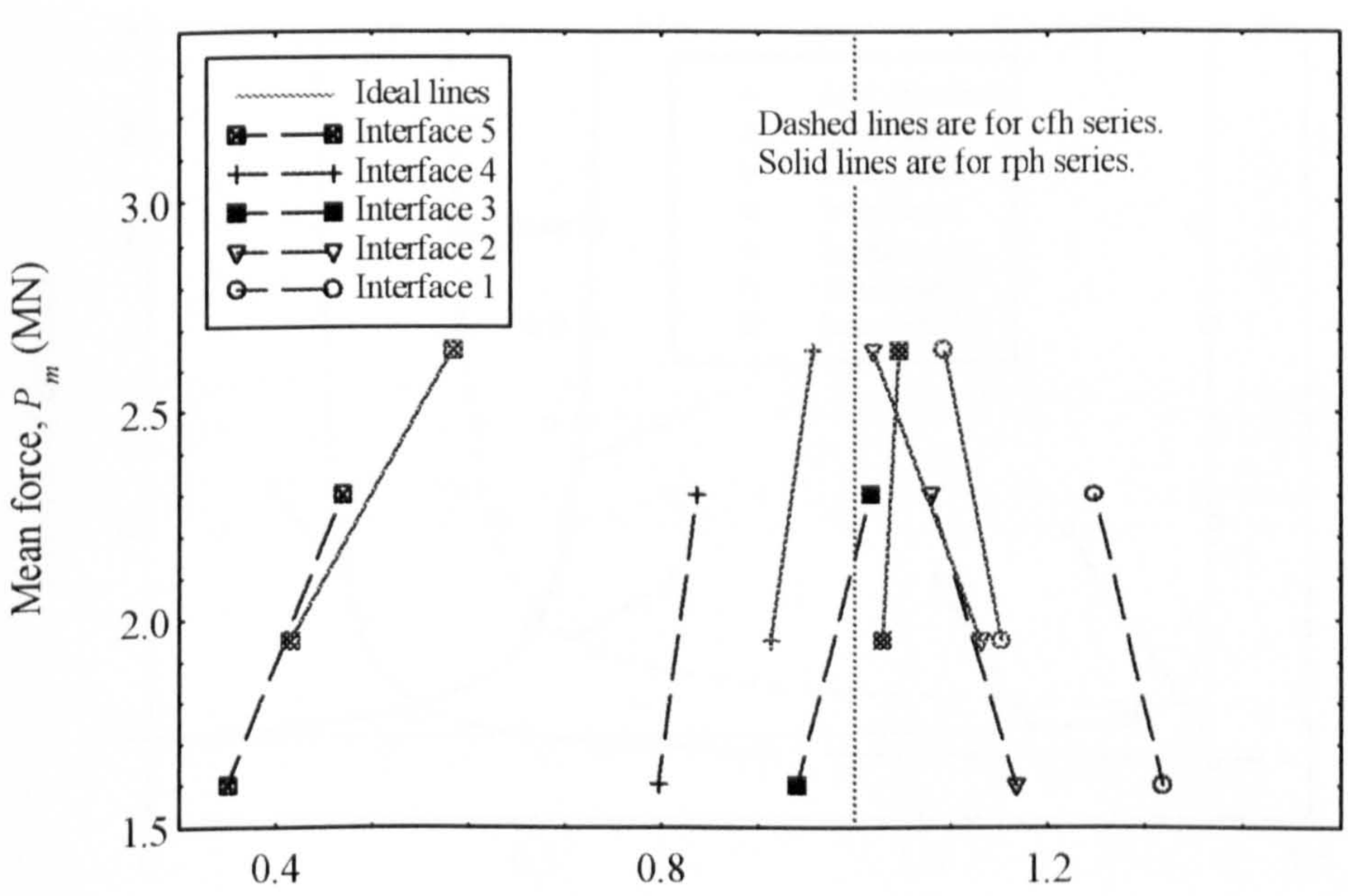

Figure 6.8 : Comparing energy distribution for models in the rpy and cfy series.

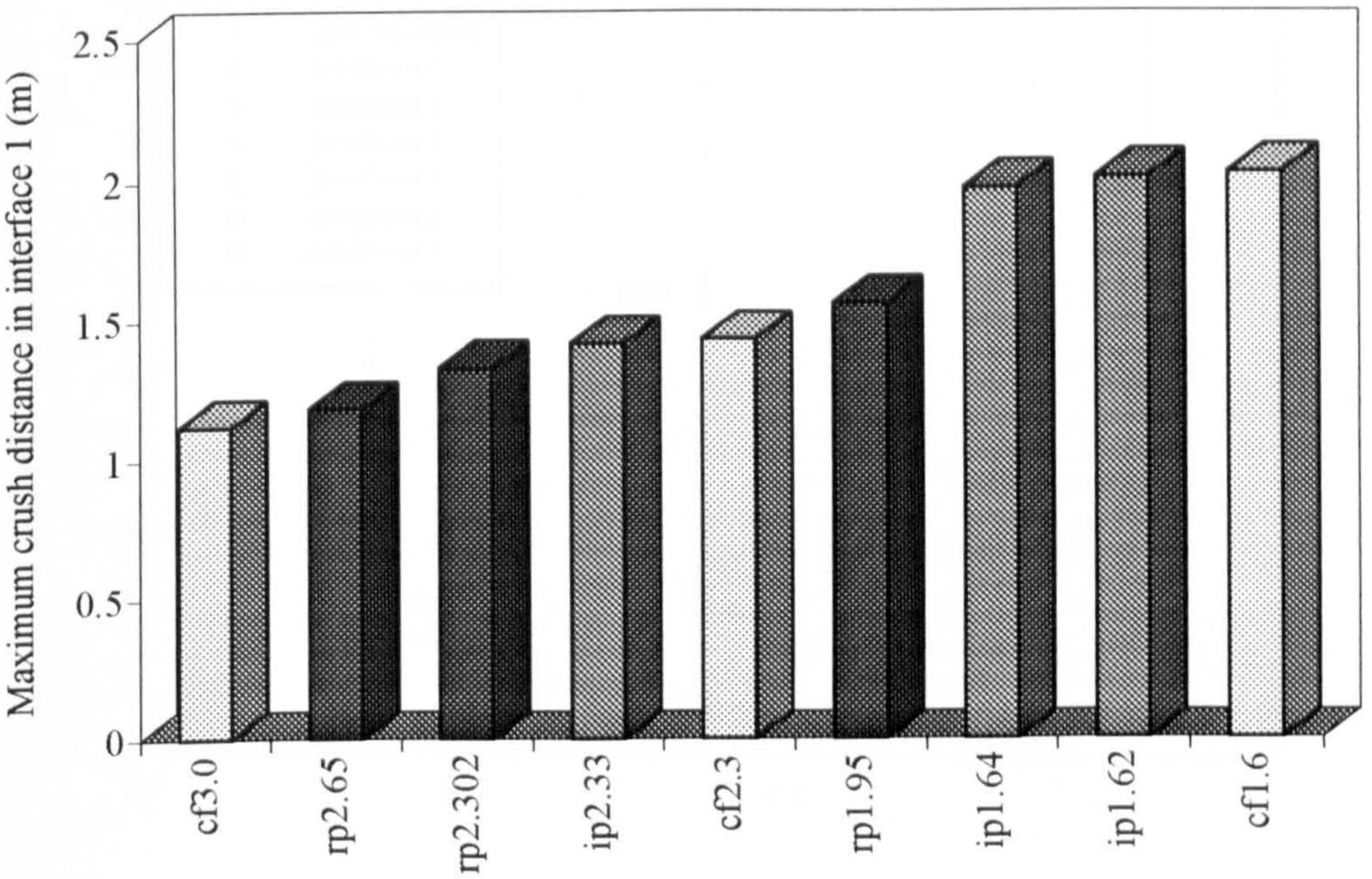

Figure 6.9 : Interface 1 crush distance for various models.

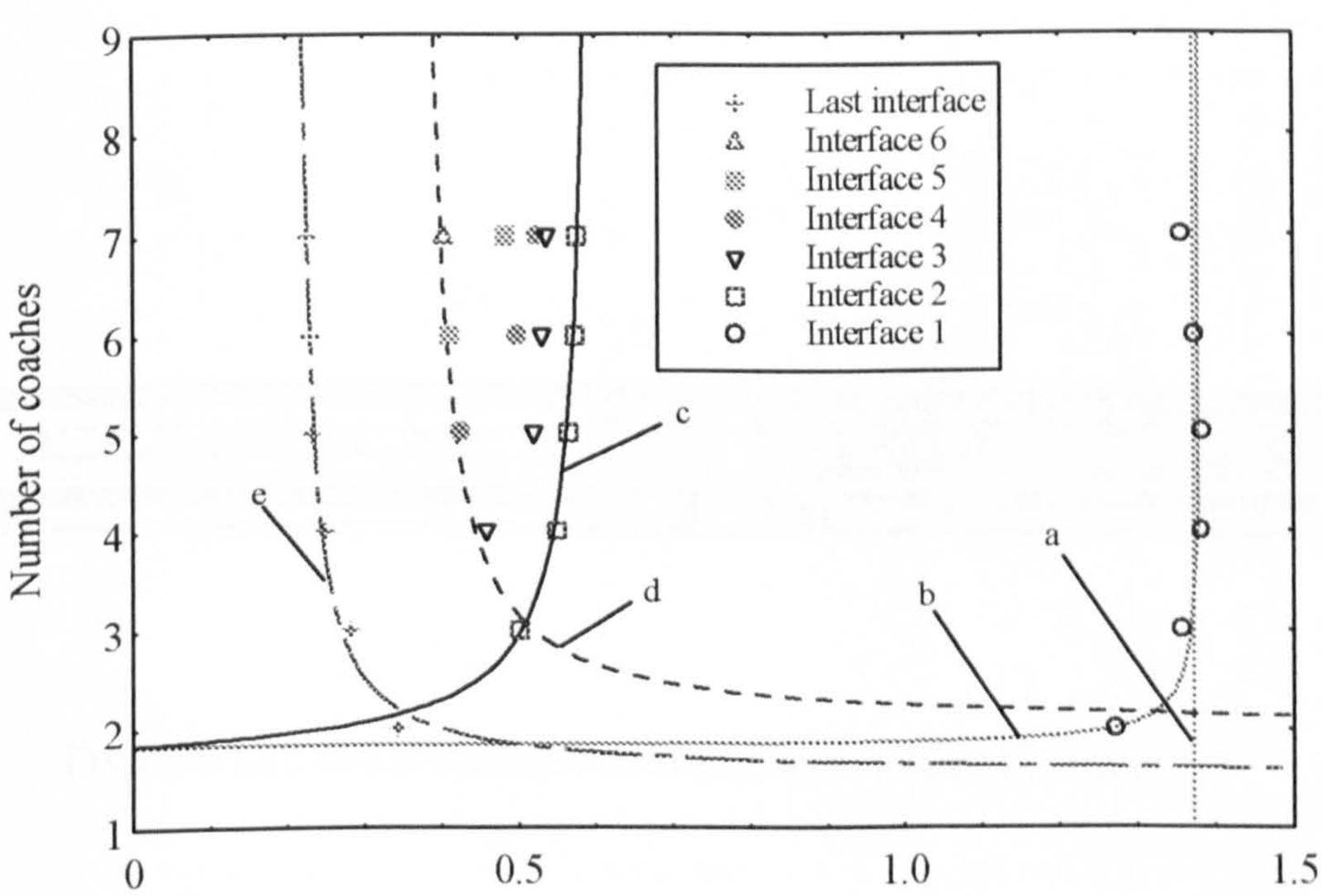

Figure 6.10 : The effects of N on interface crush distribution for models in the cfn series.

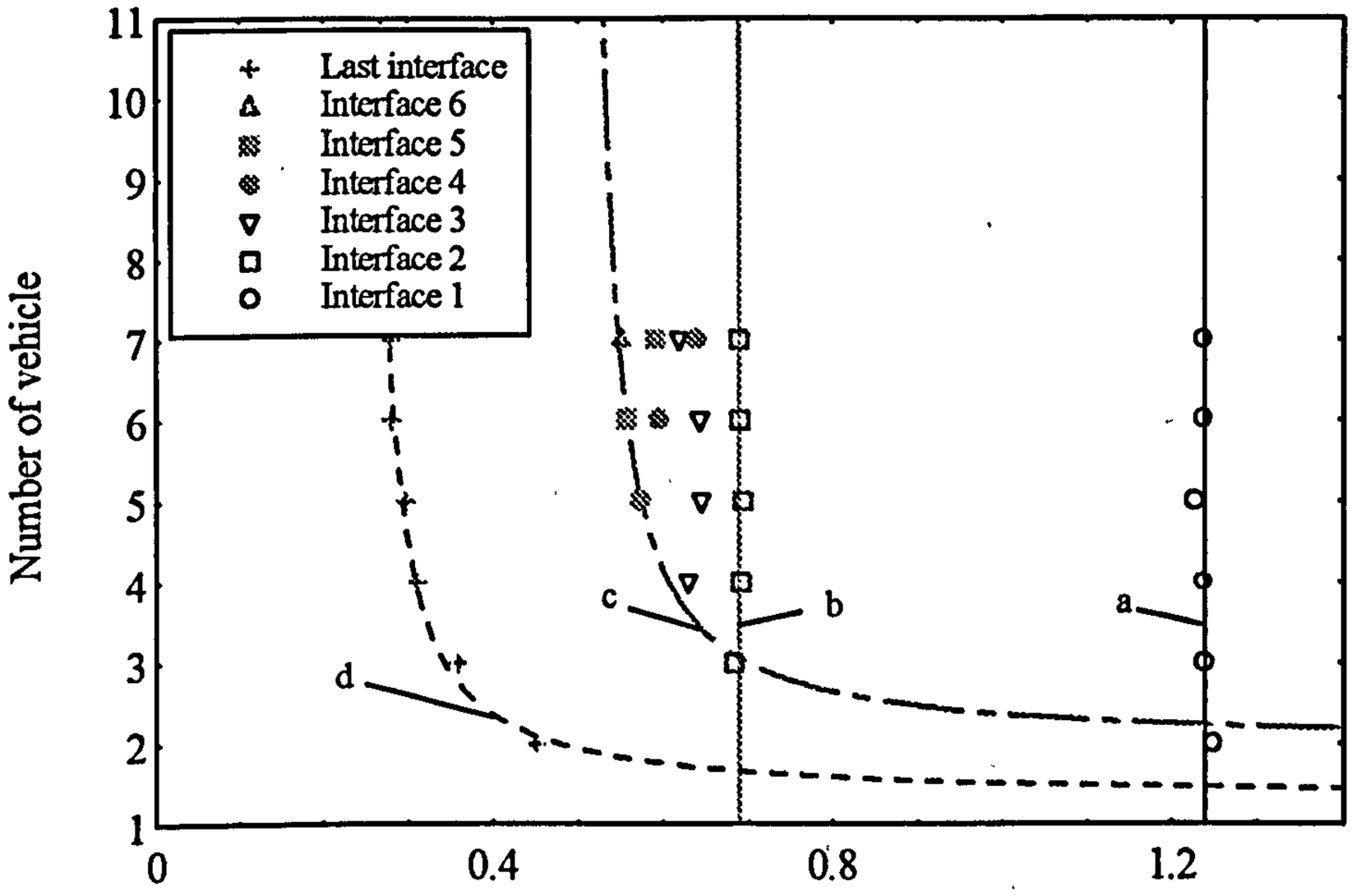

Figure 6.11 : The effects of *N* on interface crush distribution for models in the rpn series.

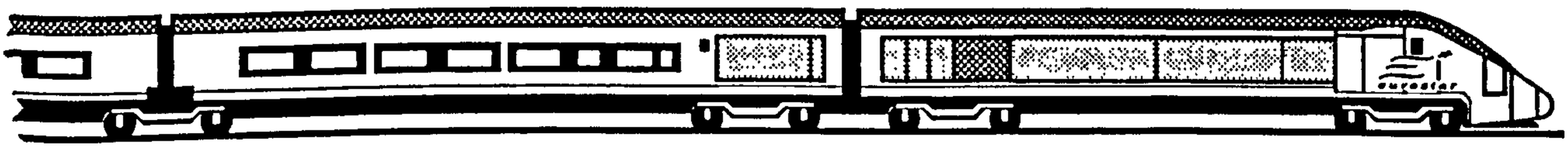

Figure 6.12 : The projected nose heading a rake of Eurostar.

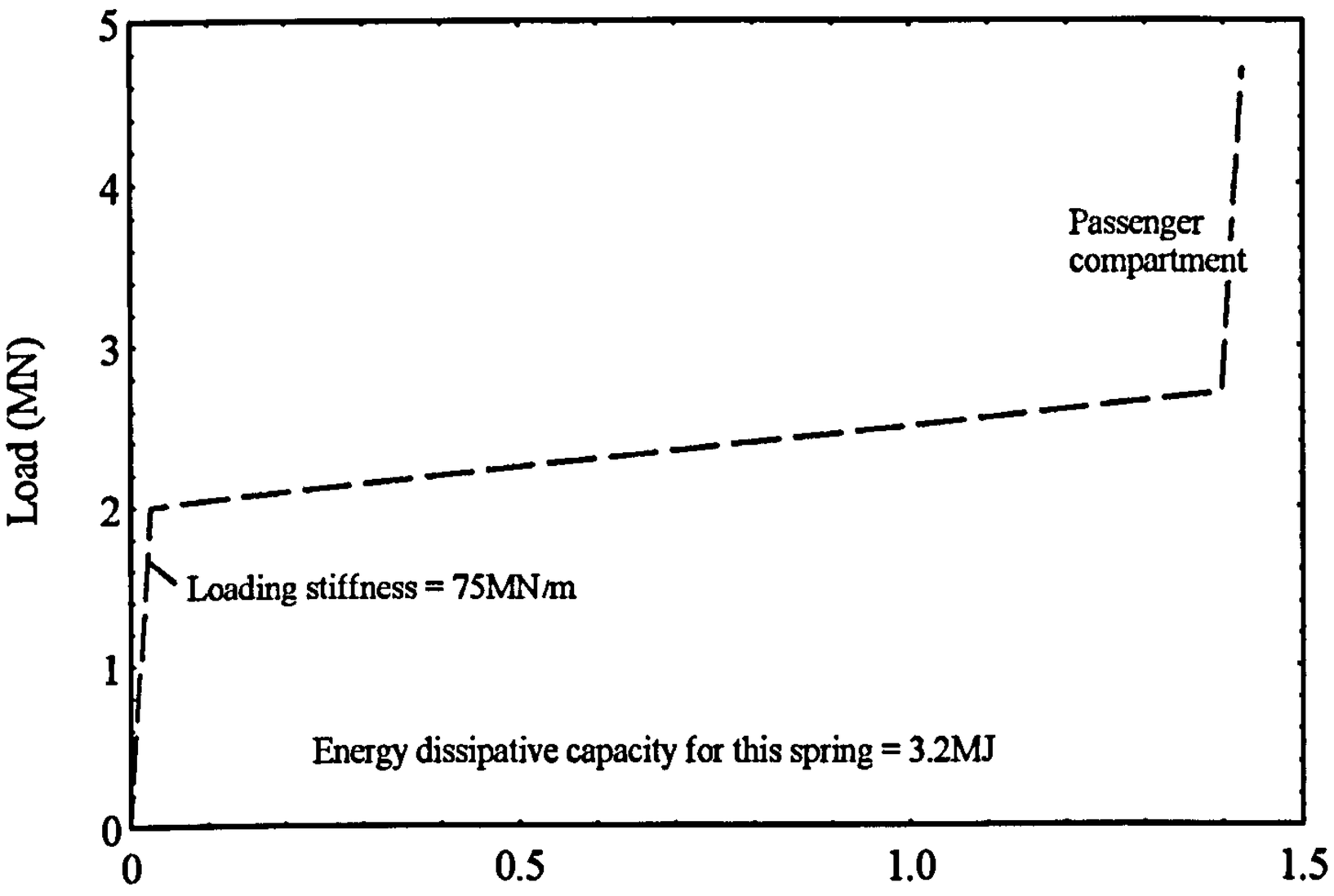

Figure 6.13 : Spring characteristics for interface 1 of mixed-springs models.

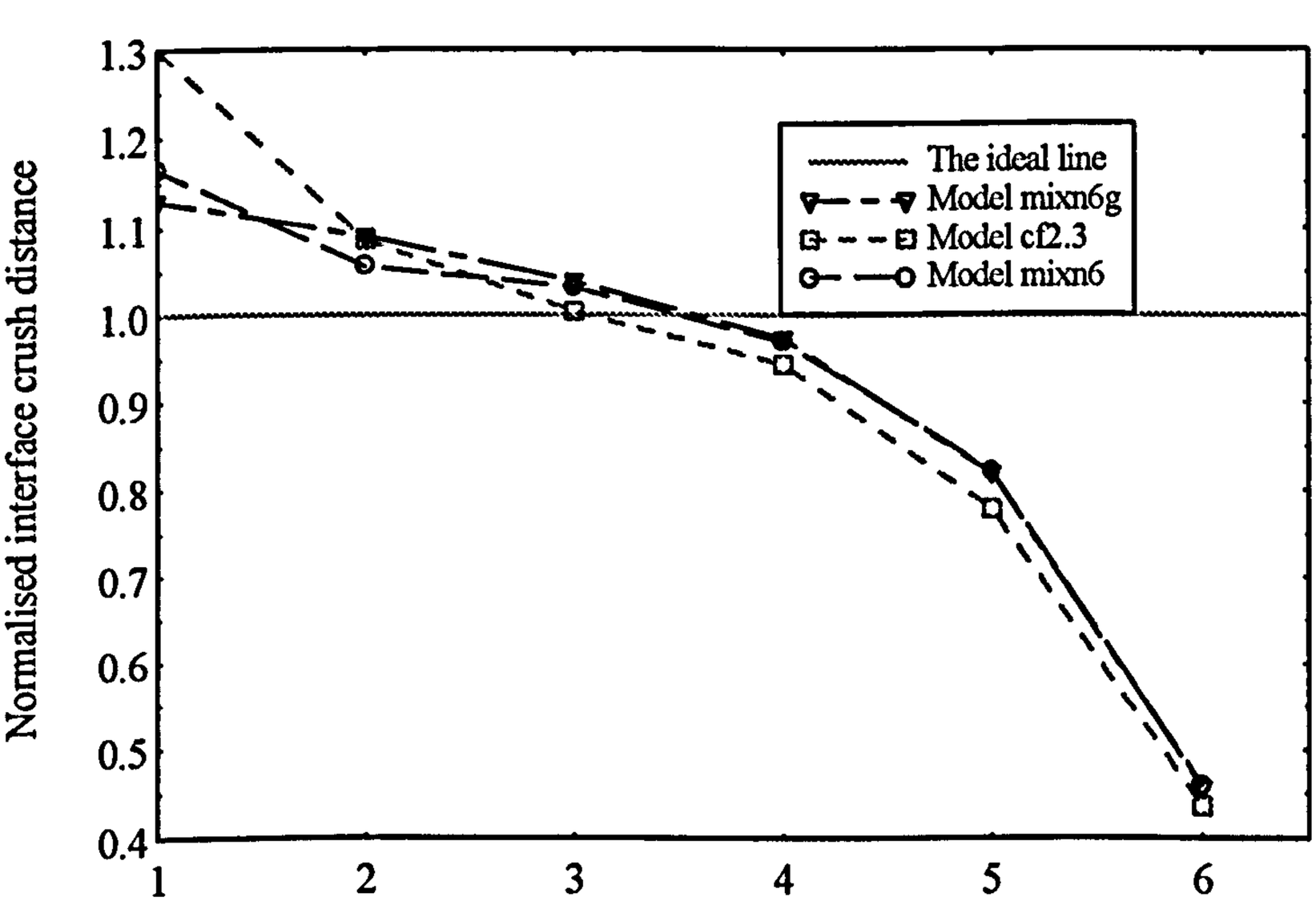

Figure 6.14 : How mixed-springs models modified the crush (energy) distribution of cfn6.

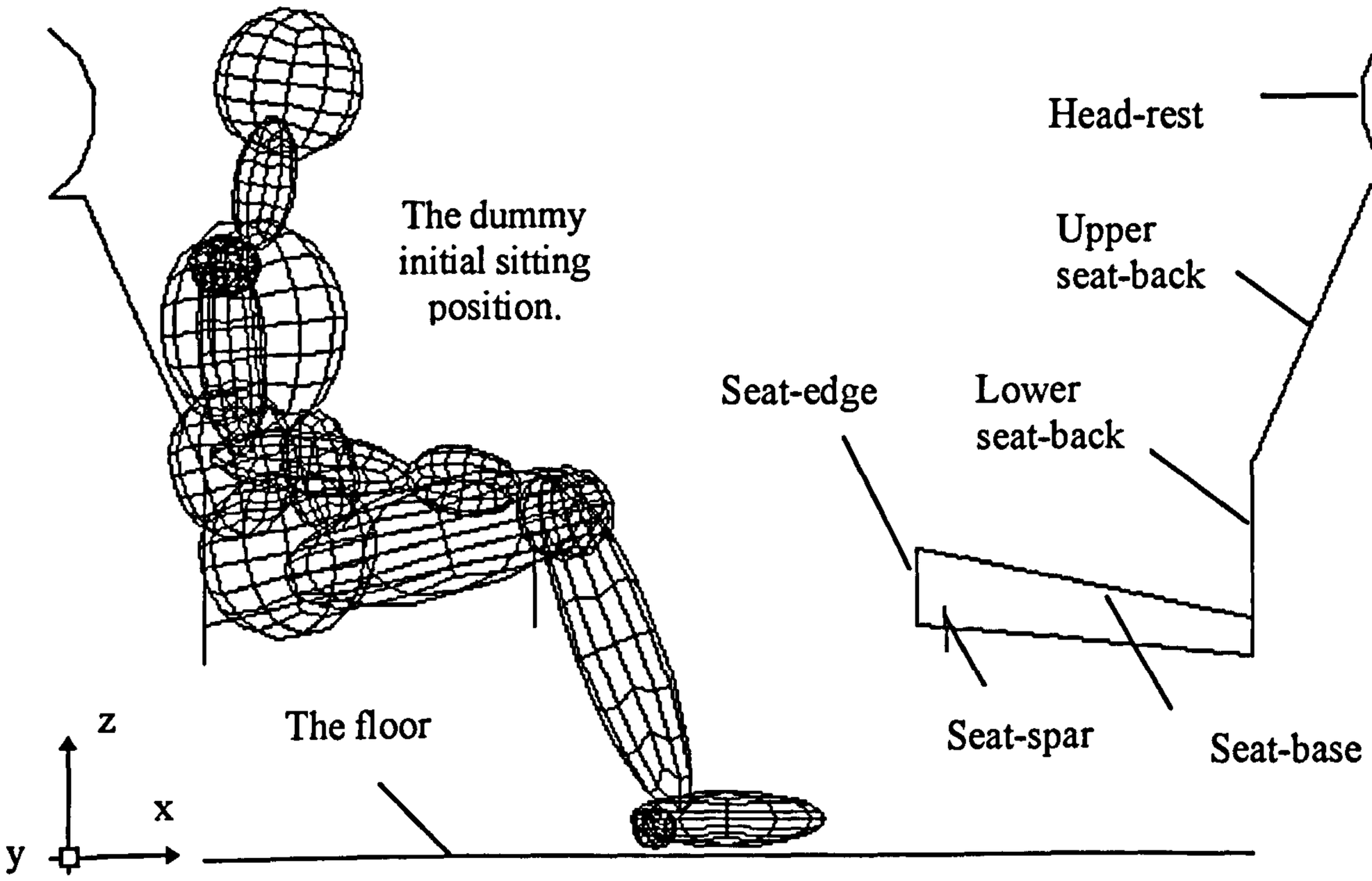

Figure 7.1 : The dummy initial sitting position.

SEAT EDGE CUSHION	SEAT SPAR
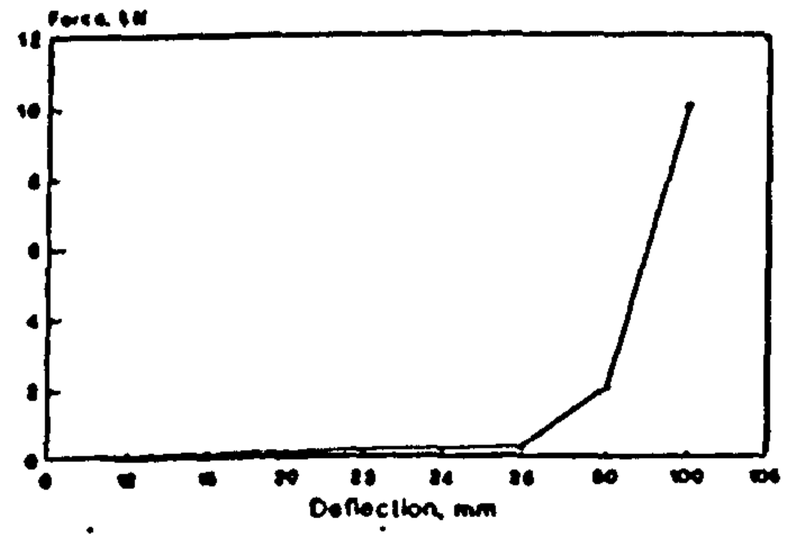	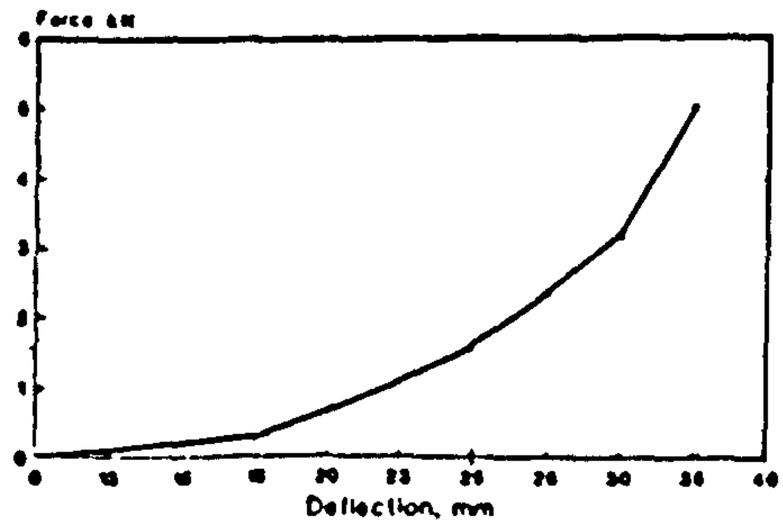
SEAT BACK	**HEADREST**
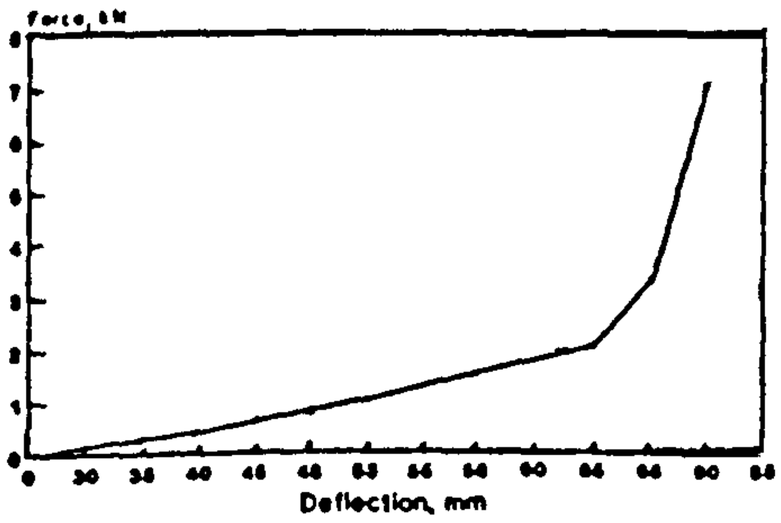	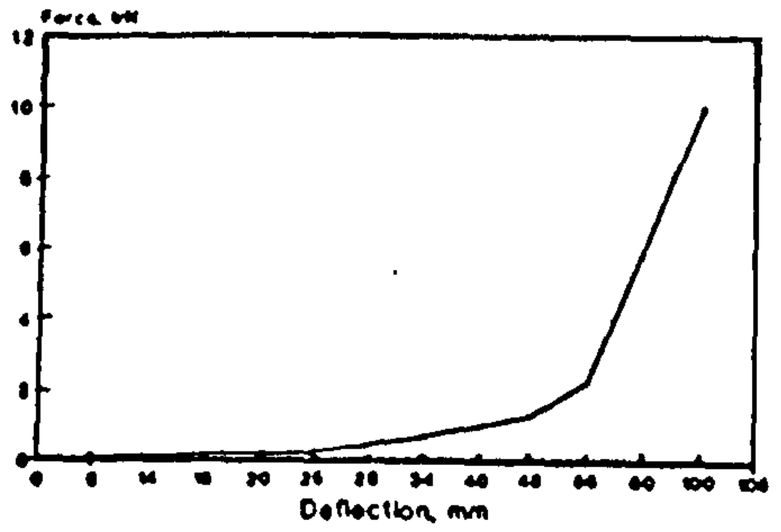
SEAT BASE	
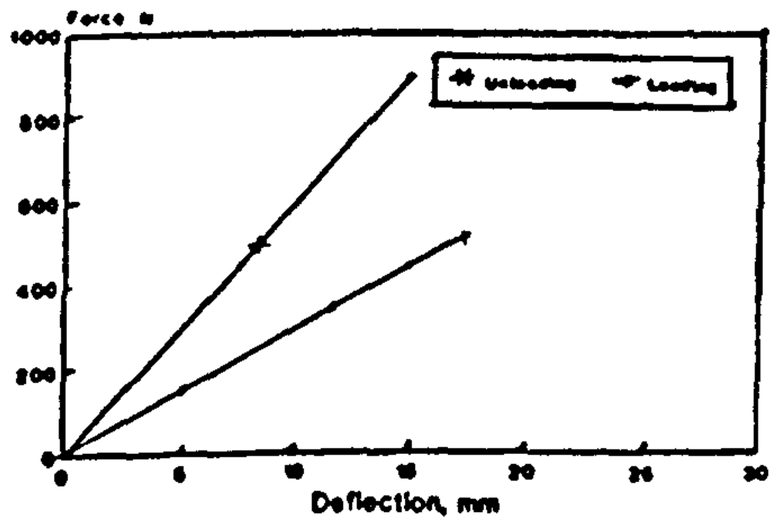	

Figure 7.2 : The contact surface load curves between the dummy and various parts of the seat.

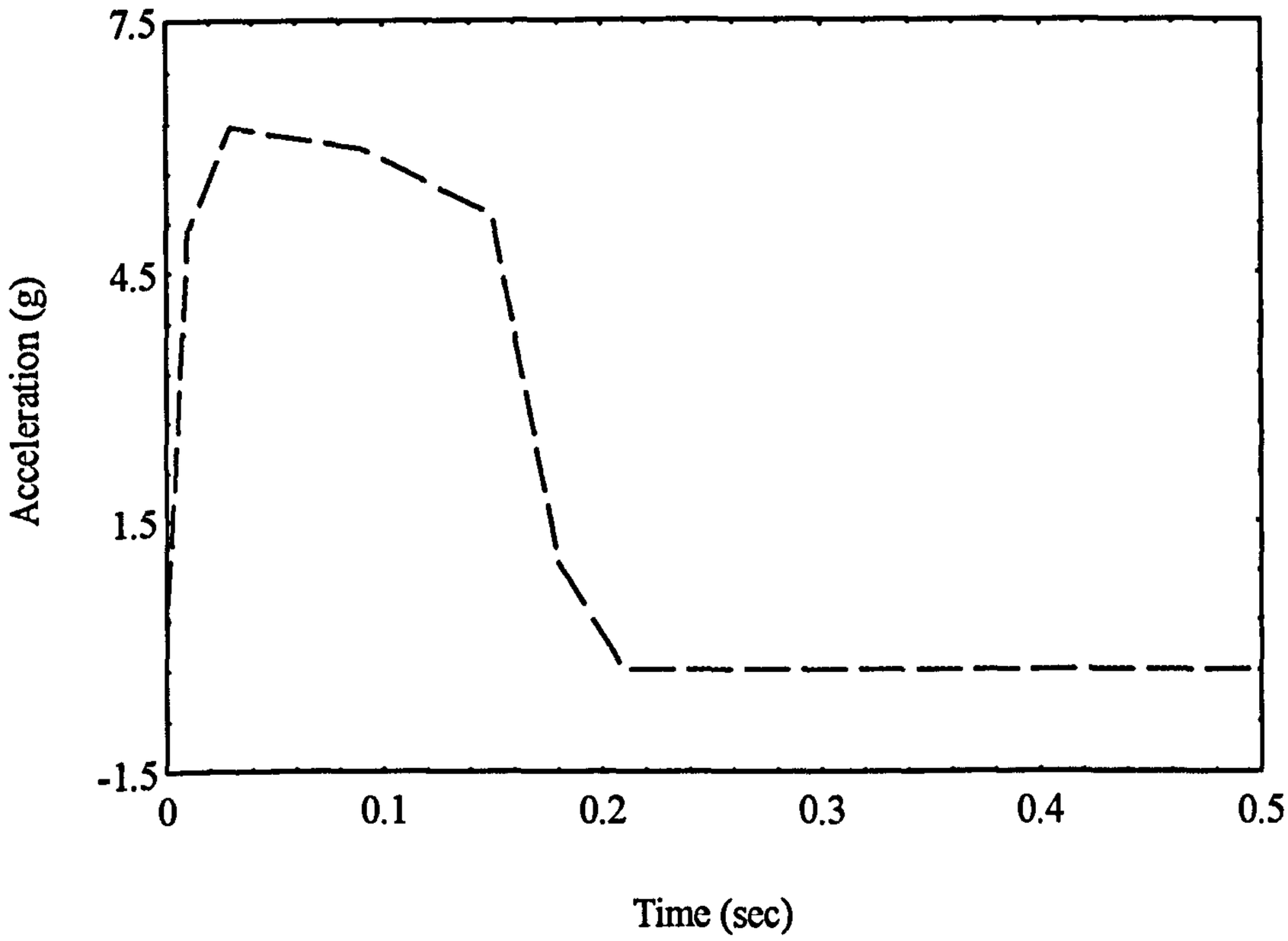

Figure 7.3 : The C3 acceleration pulse used by MIRA.

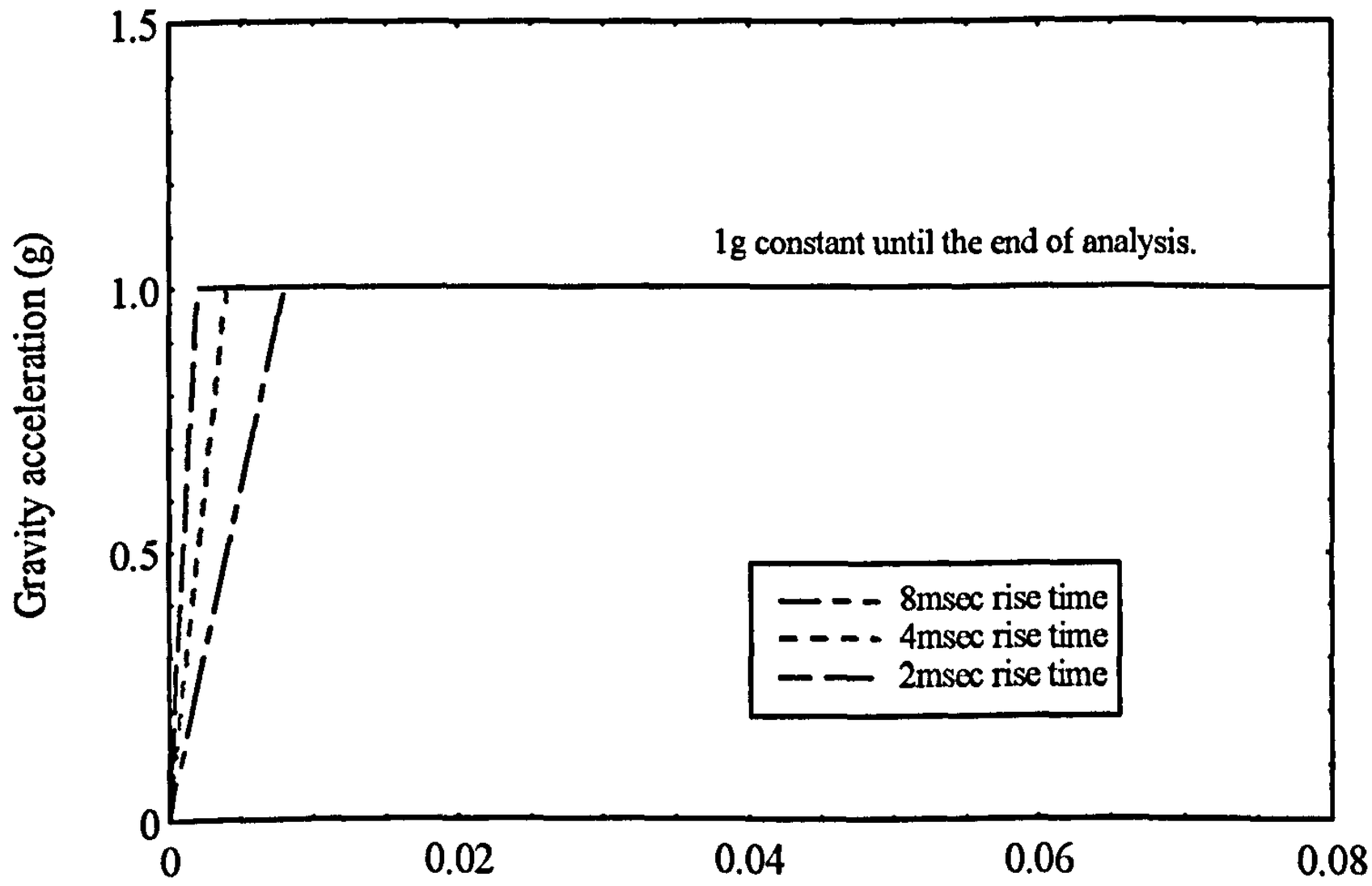

Figure 7.4 : The different rise time for gravity load curves.

PAMCRASH

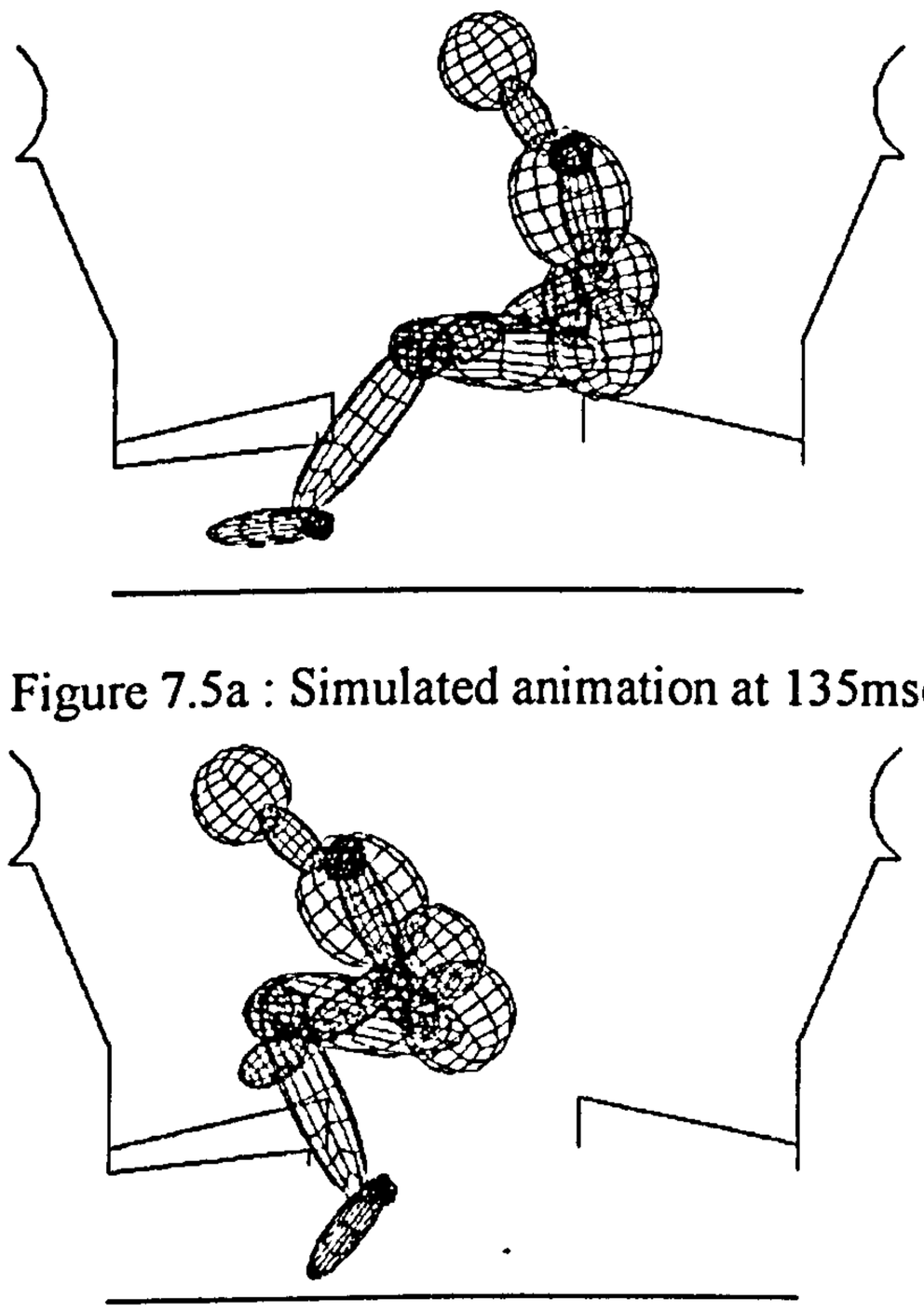

Figure 7.5a : Simulated animation at 135msec

Figure 7.5b : Simulated animation at 200msec

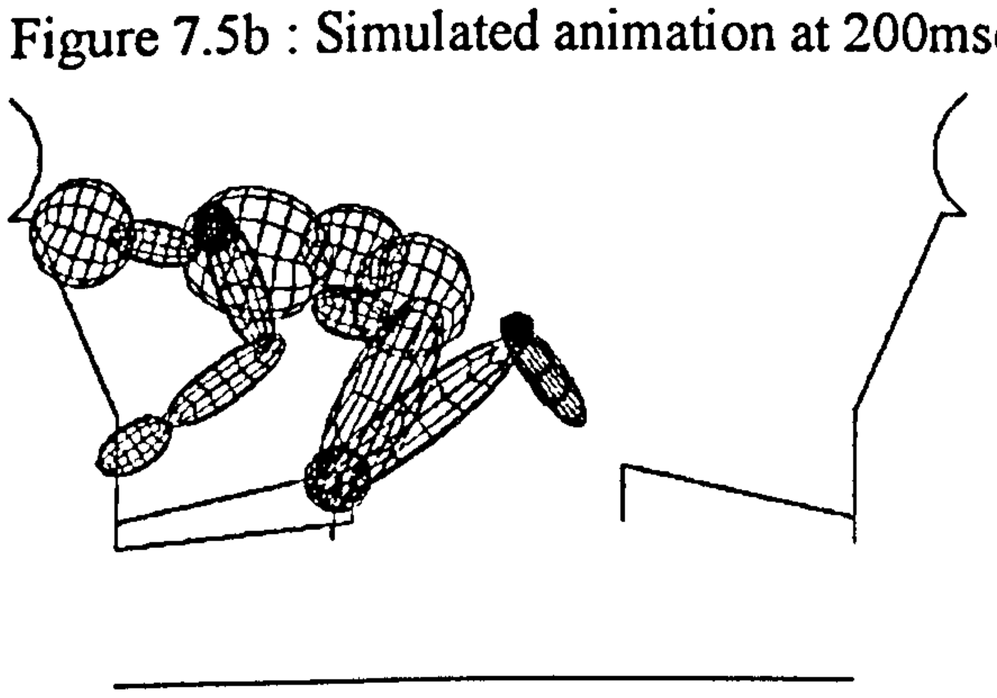

Figure 7.5c : Simulated animation at 240msec

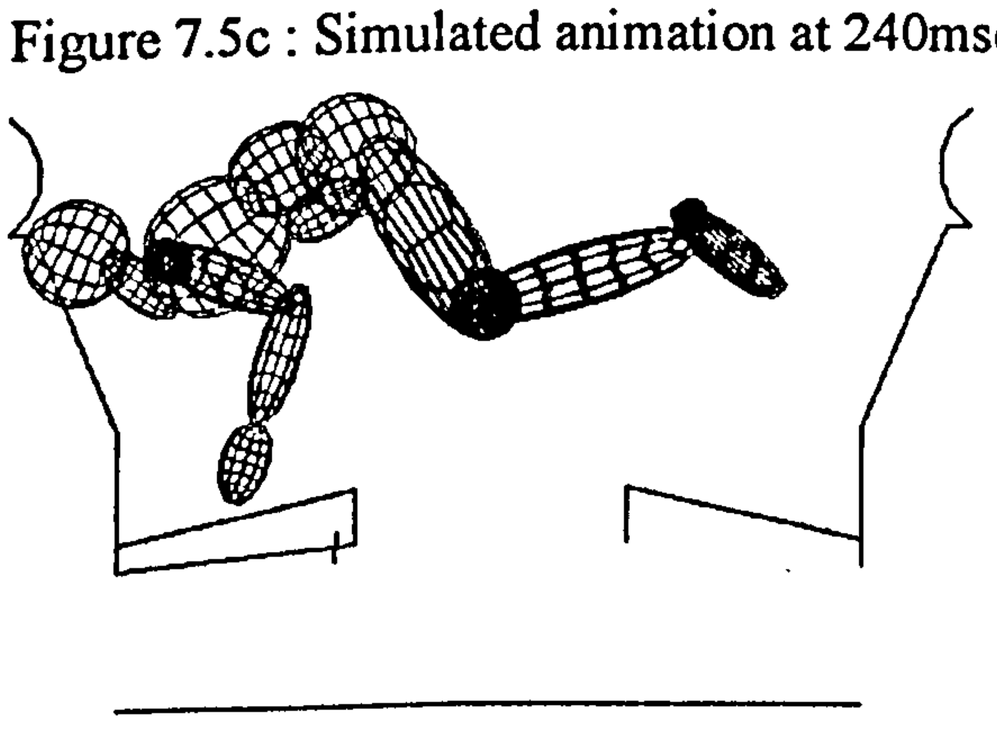

Figure 7.5d : Simulated animation at 290msec

DYNA3D

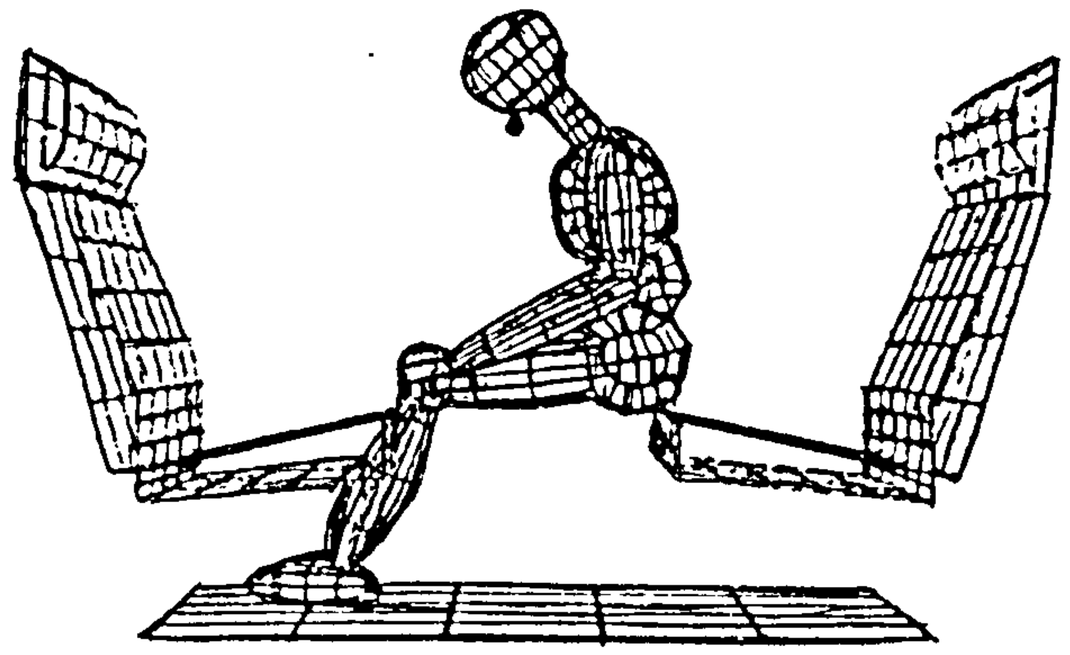

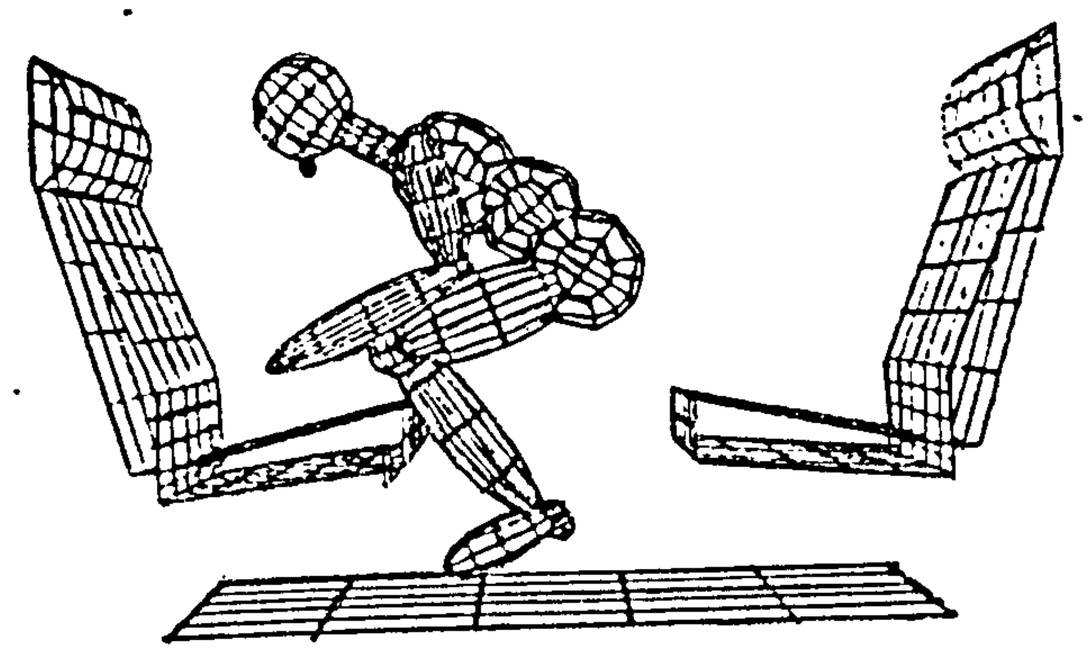

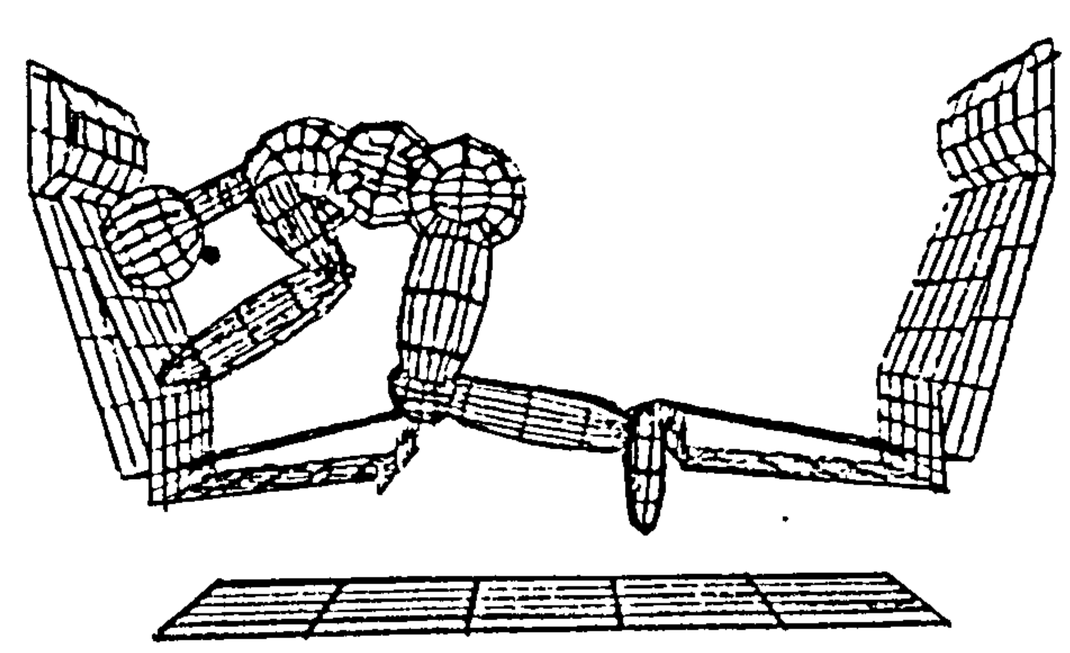

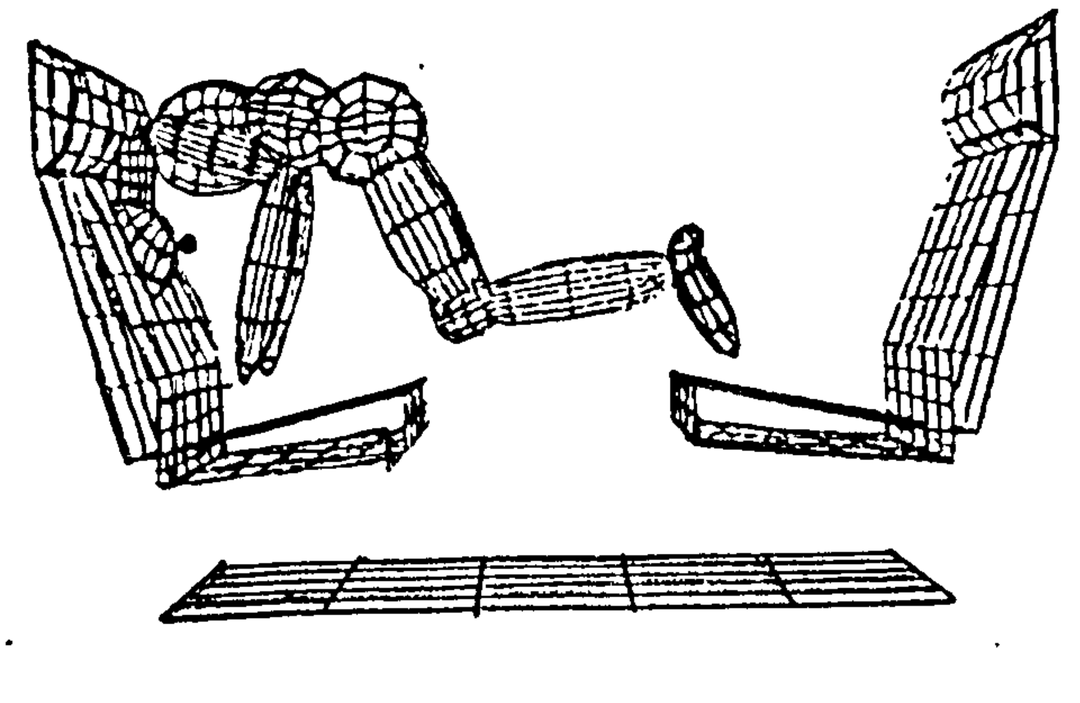

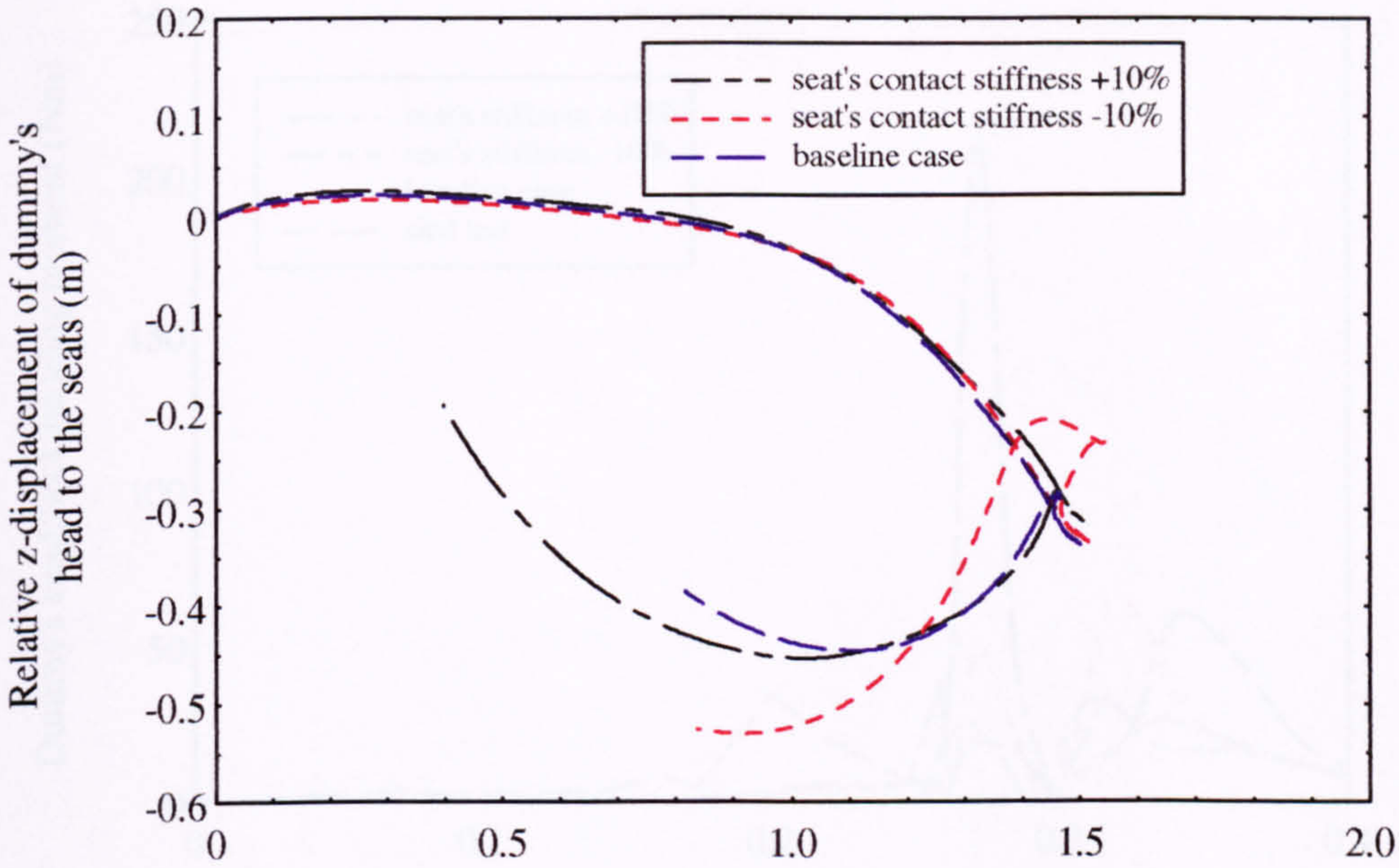

Figure 7.6 : The head's trajectories of the models studying cushion stiffness.

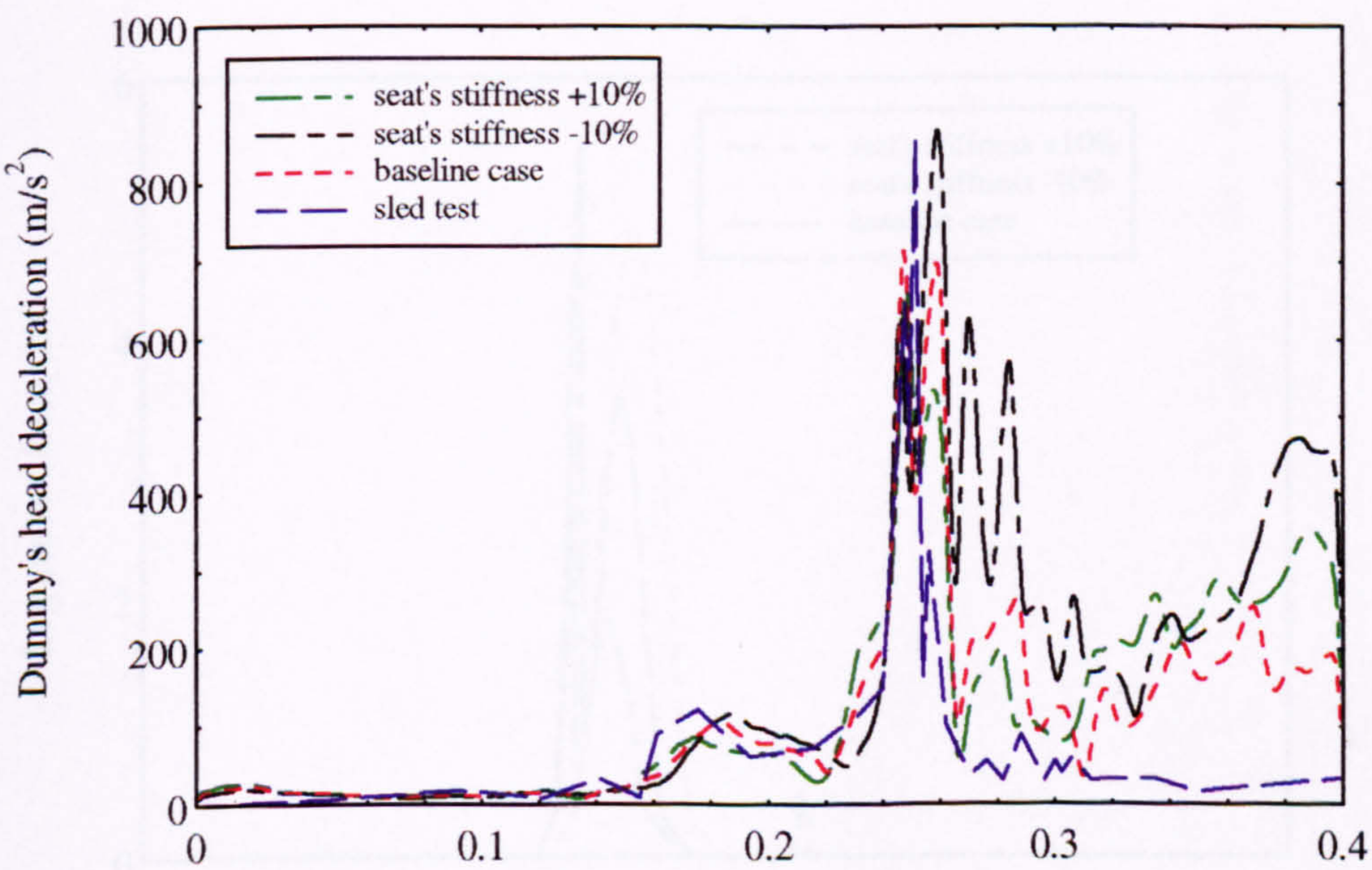

Figure 7.7 : The head's deceleration-time history of the models studying cushion stiffness.

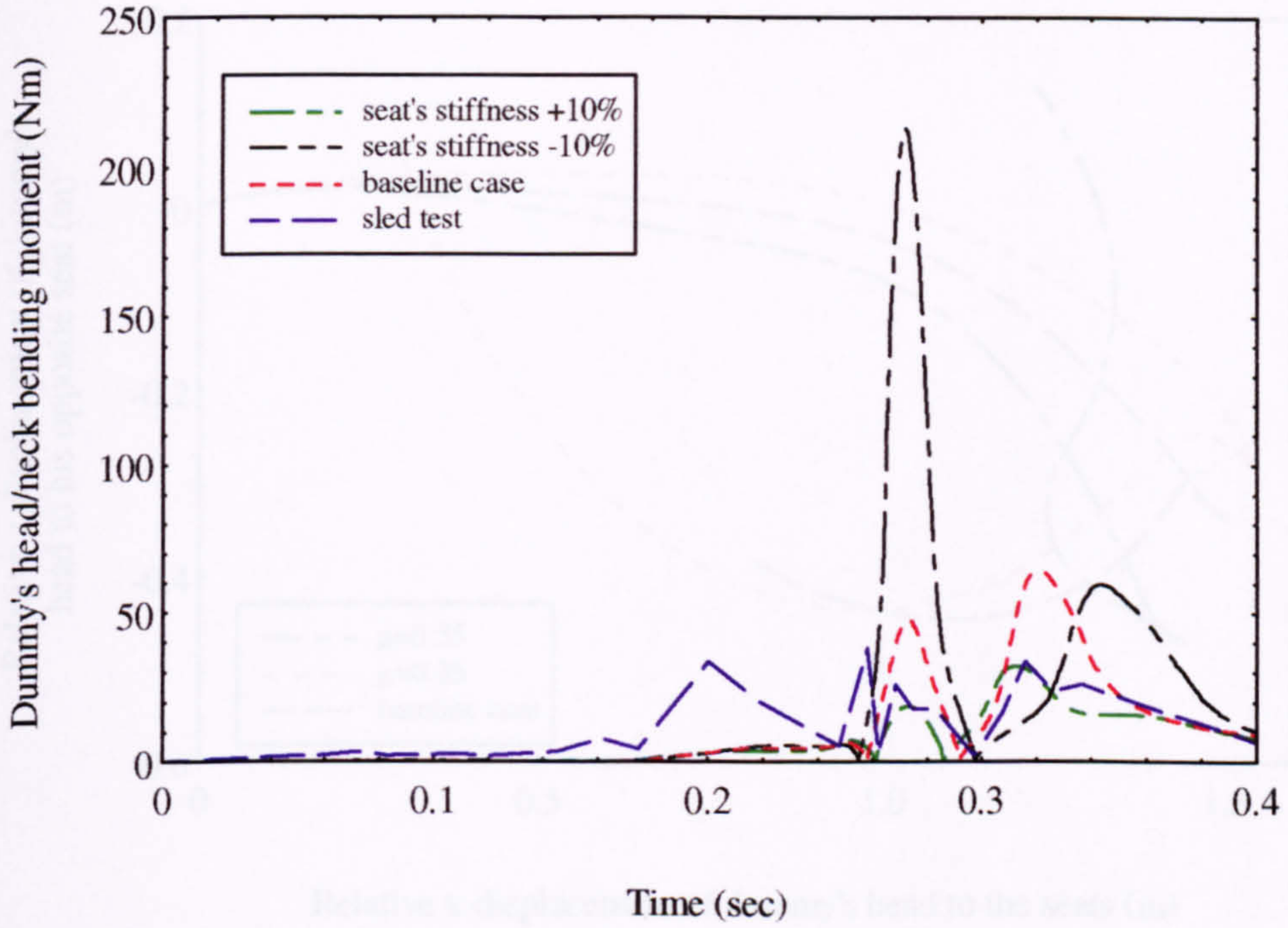

Figure 7.8 : The head/neck moment-time history of the models studying cushion stiffness.

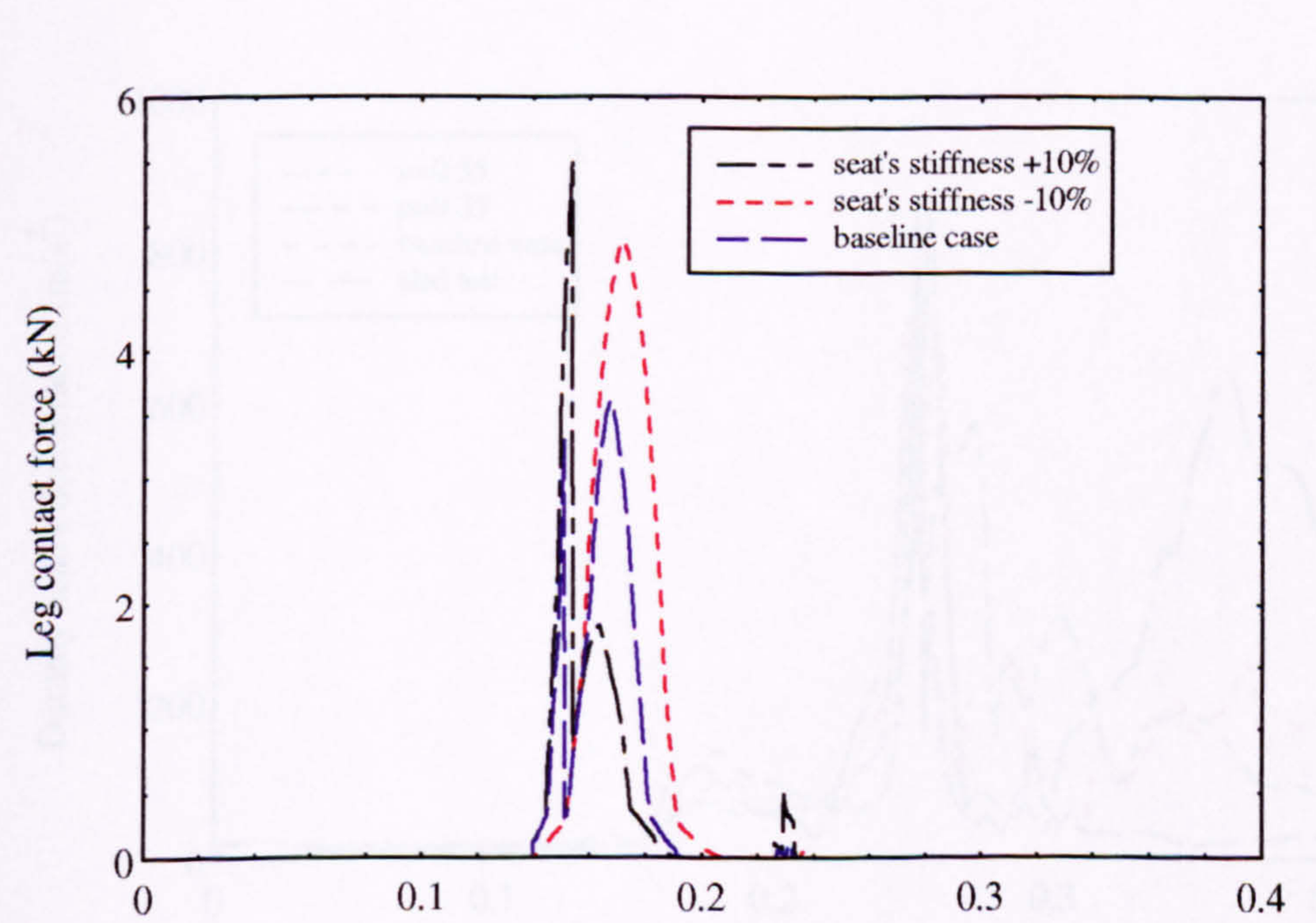

Figure 7.9 : The leg contact force-time history of the models studying cushion stiffness.

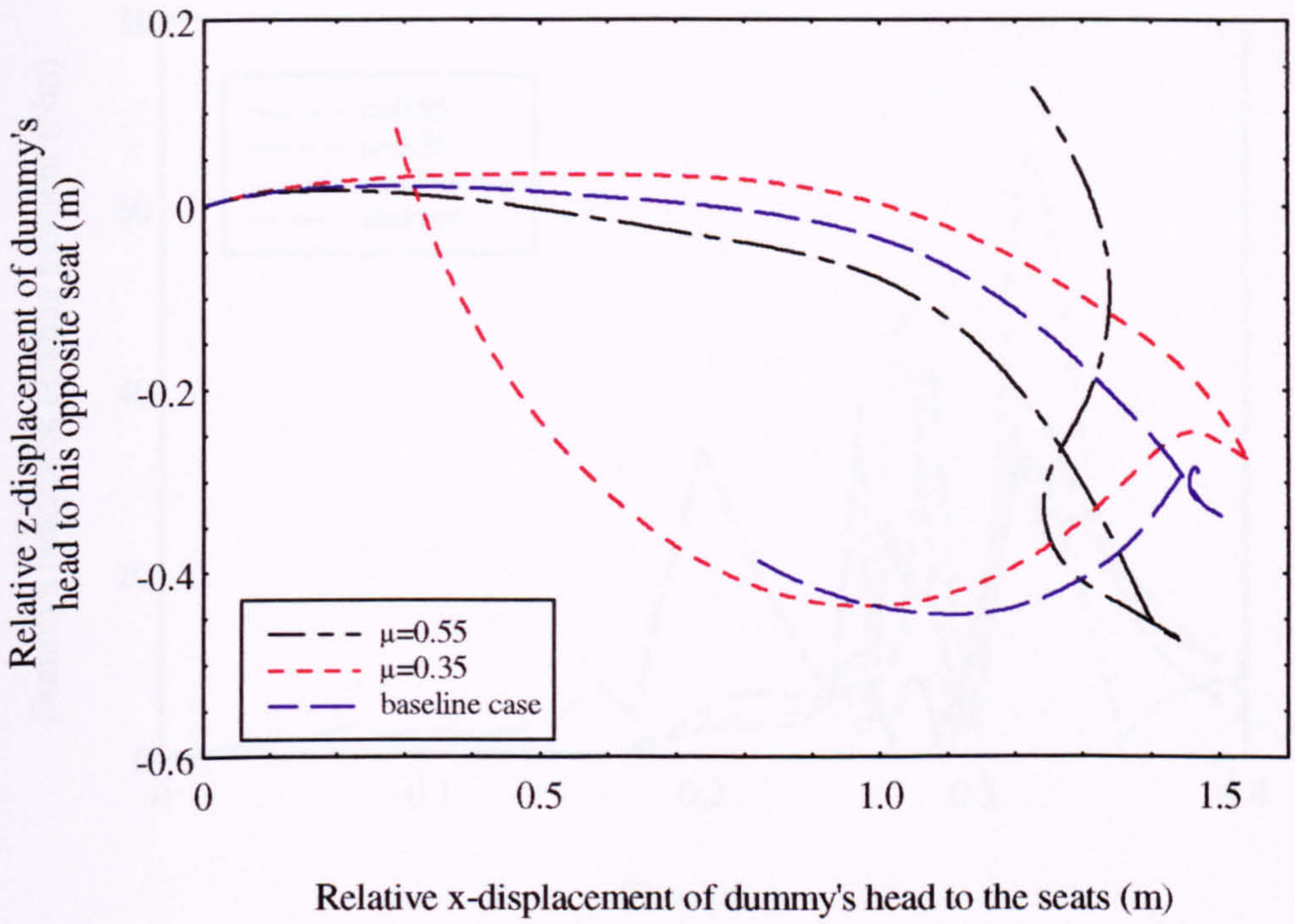

Figure 7.10 : The head's trajectories of the models studying contact friction.

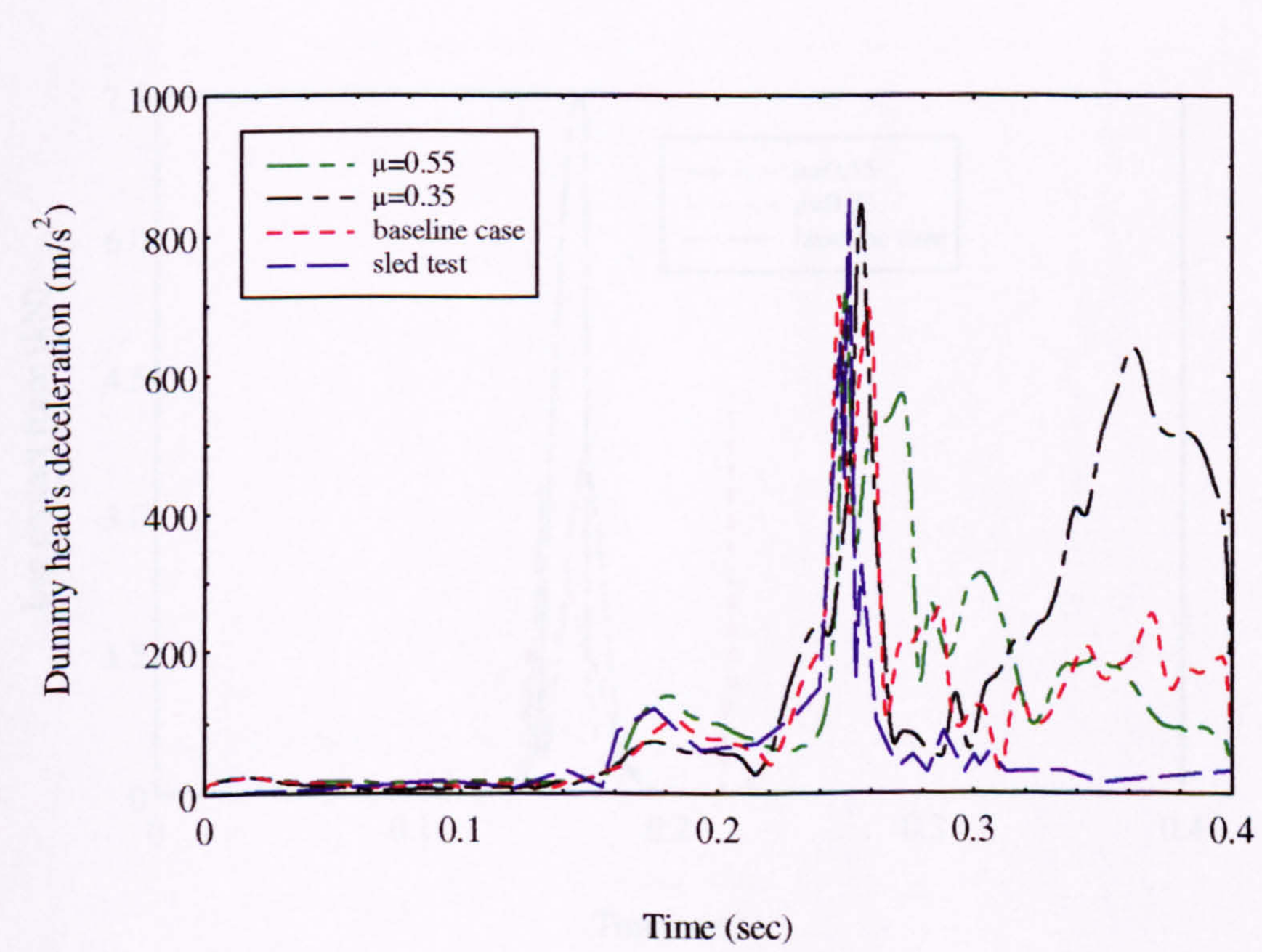

Figure 7.11 : The head's deceleration-time history of the models studying contact friction.

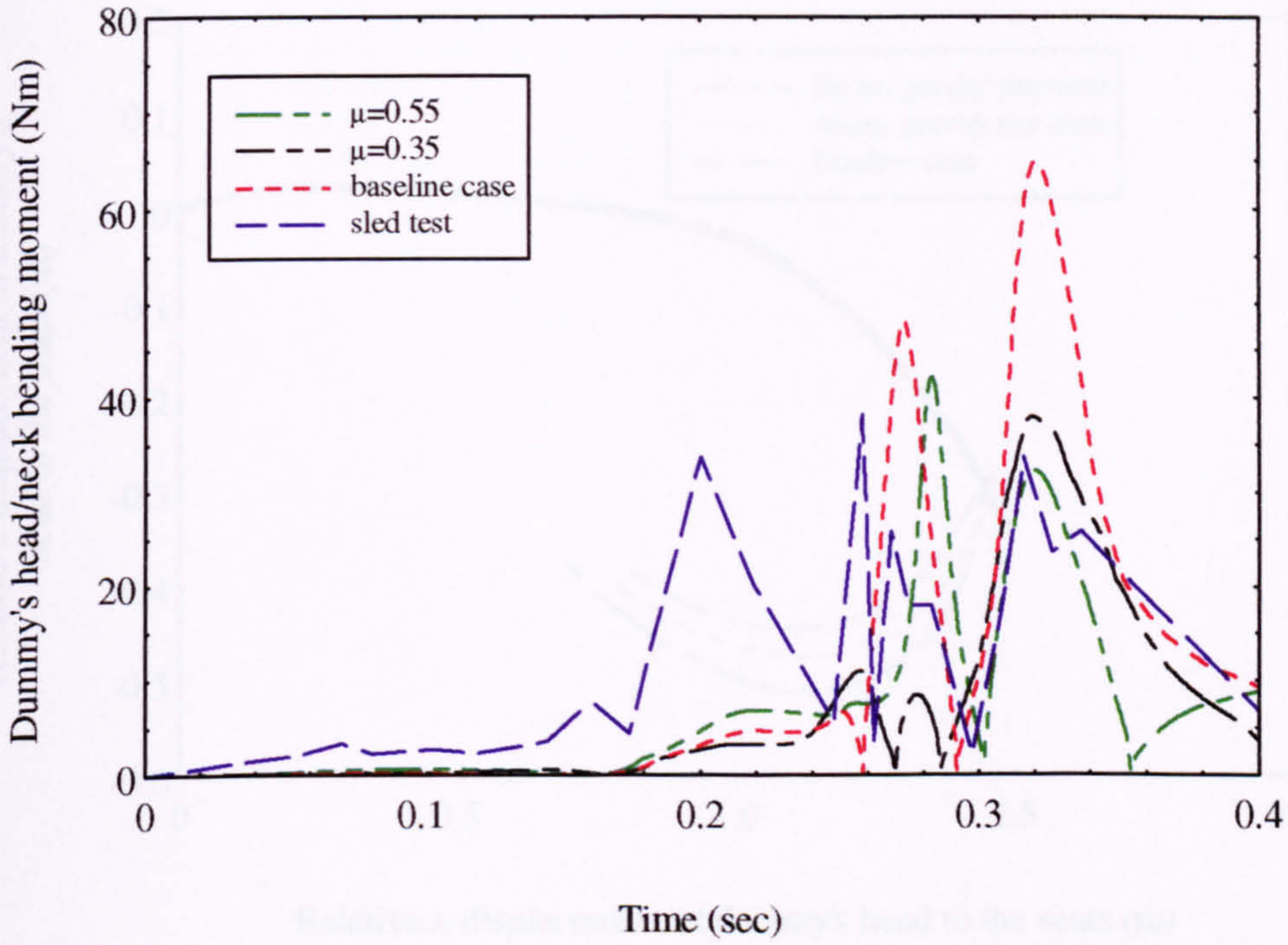

Figure 7.12 : The head/neck moment-time history of the models studying contact friction.

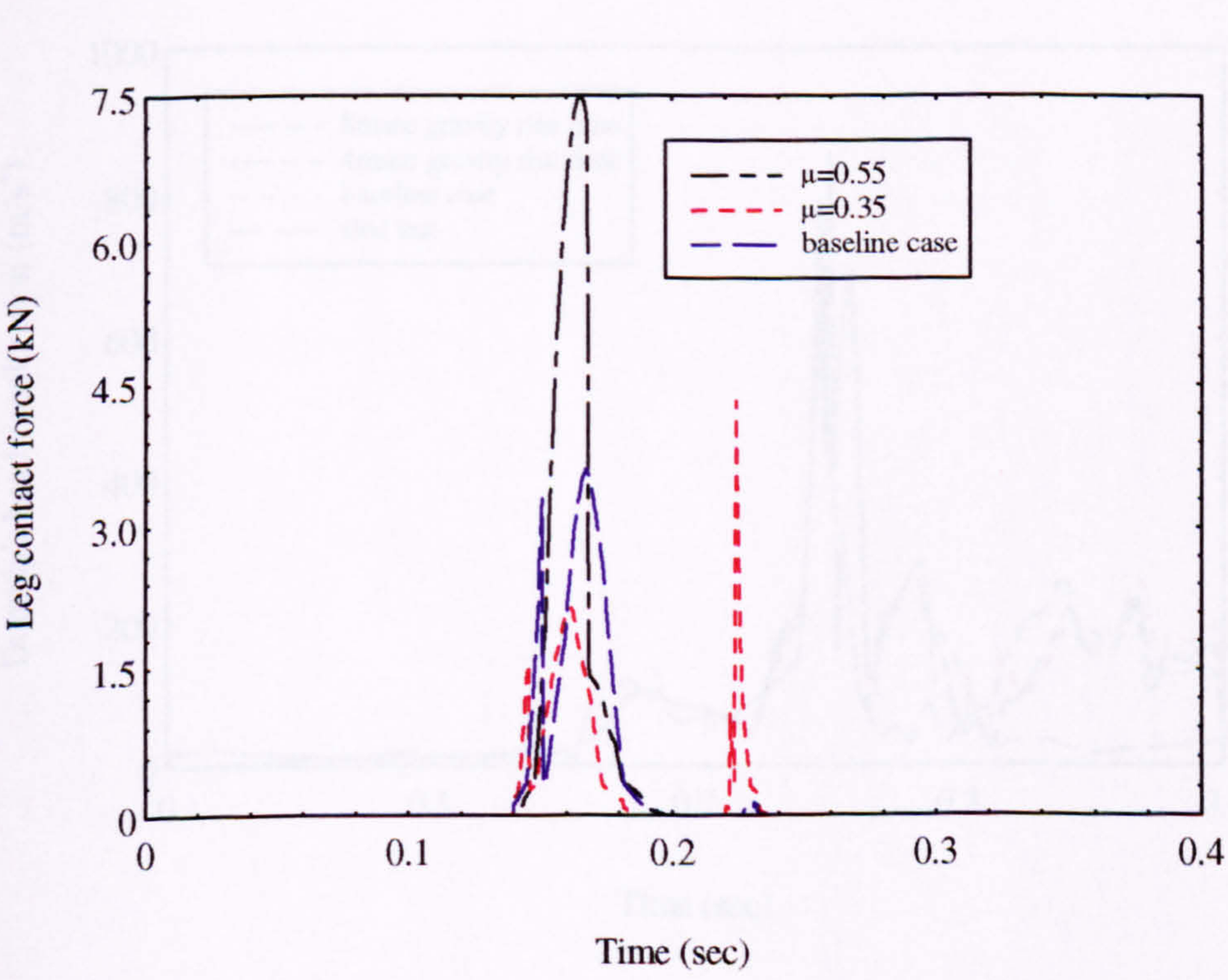

Figure 7.13 : The leg contact force-time history of the models studying contact friction.

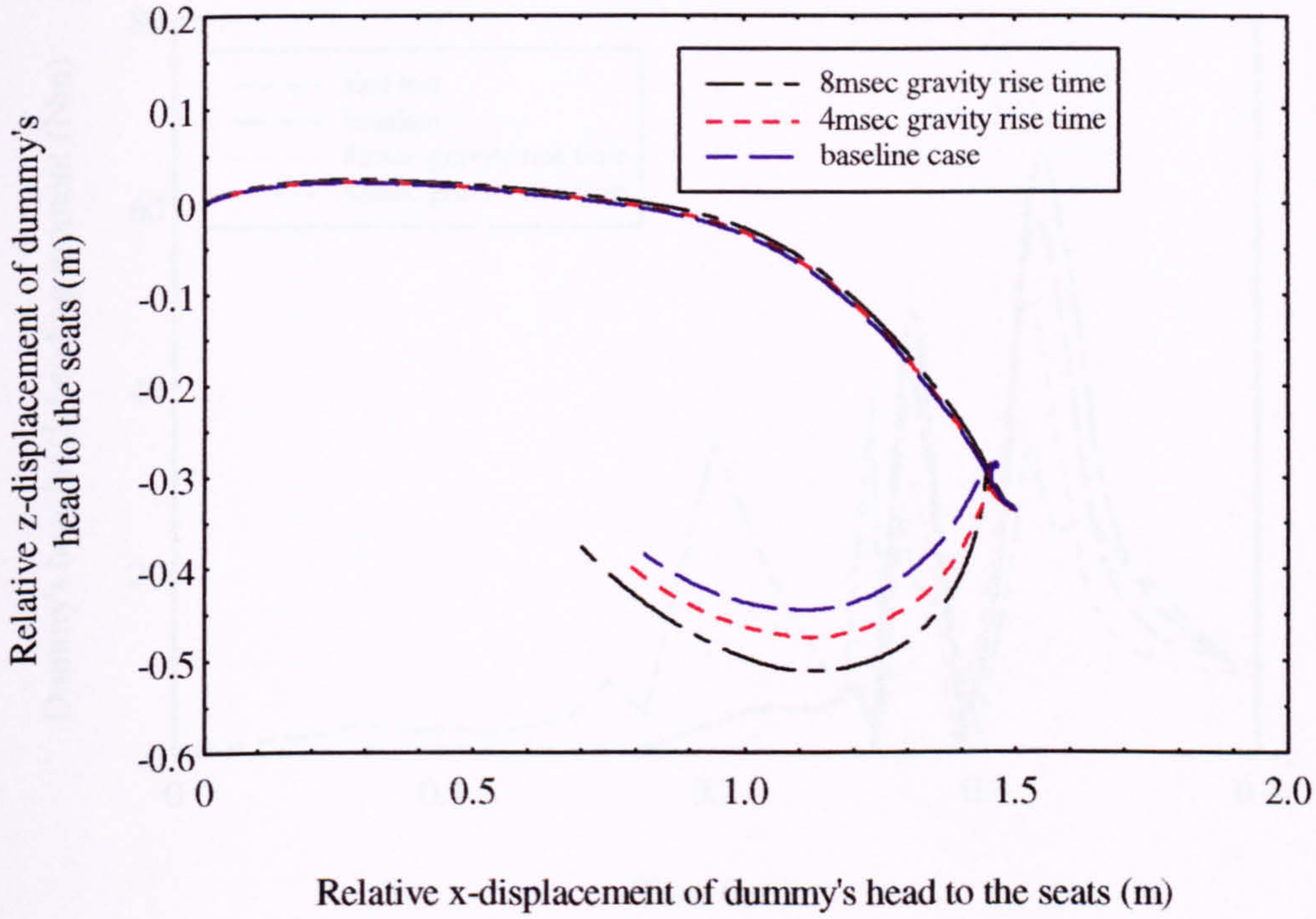

Figure 7.14 : The head's trajectories of the models studying gravity rise time.

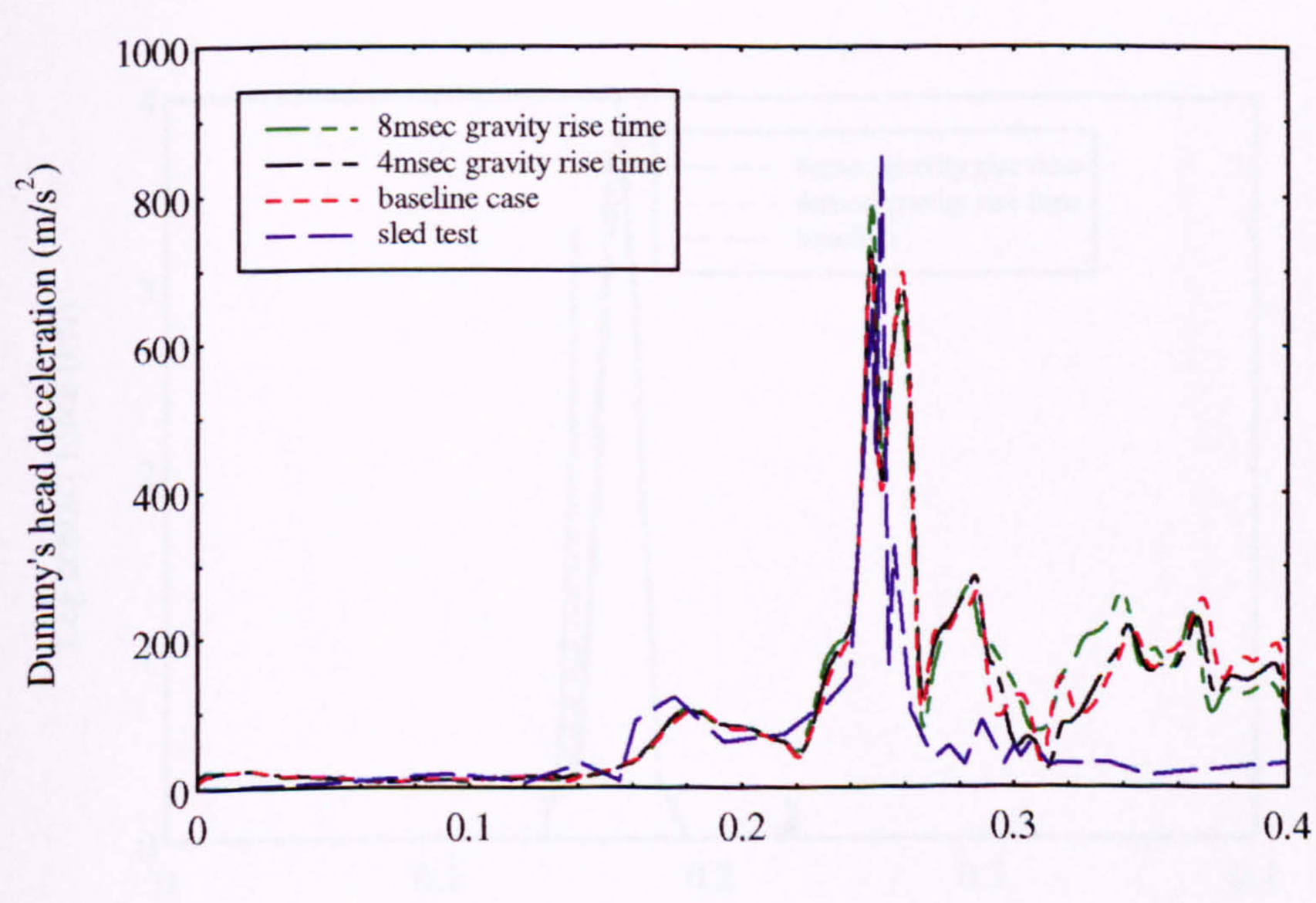

Figure 7.15 : The head's deceleration-time history of the models studying gravity rise time.

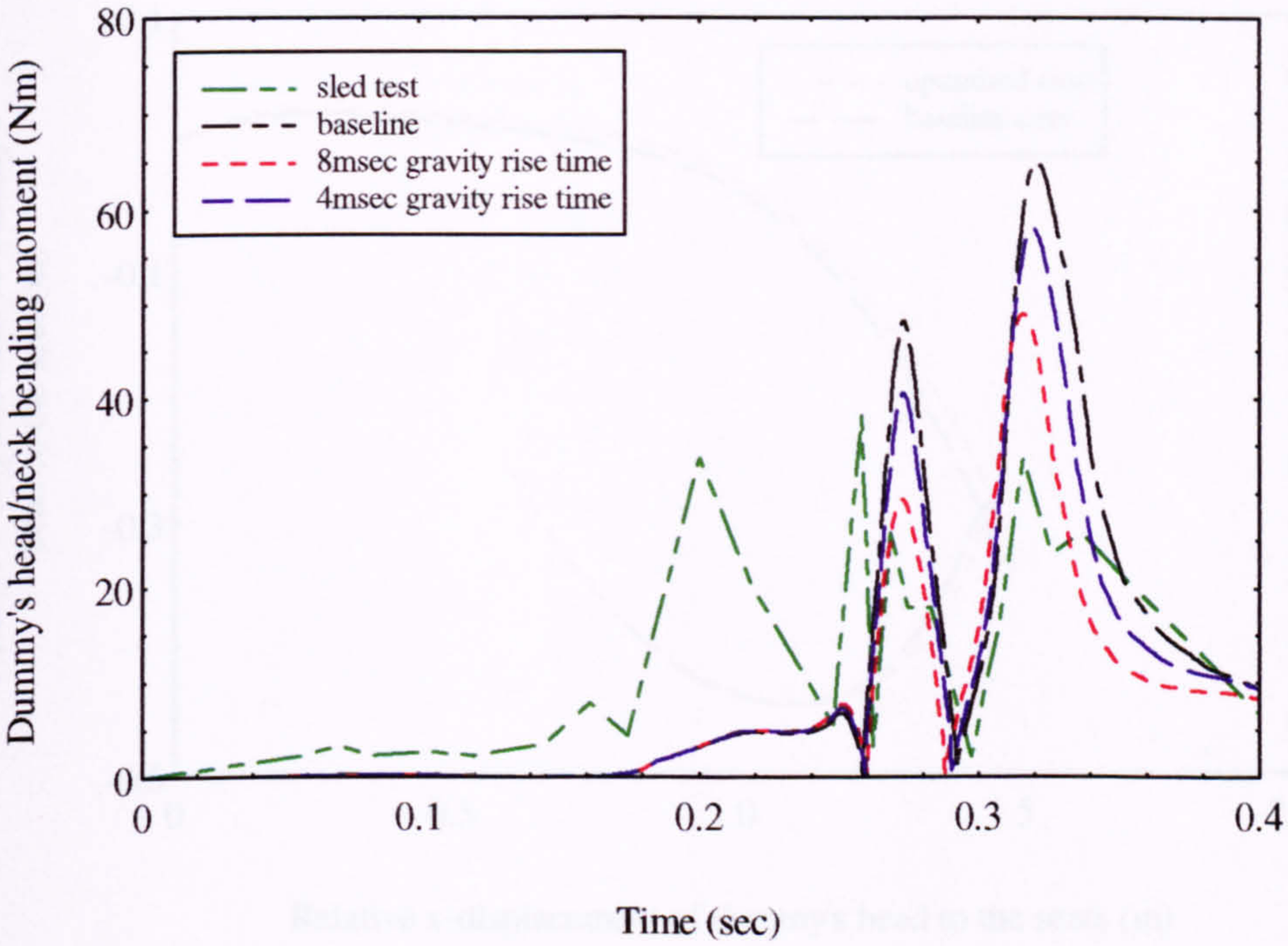

Figure 7.16 : The head/neck moment-time history of the models studying gravity rise time.

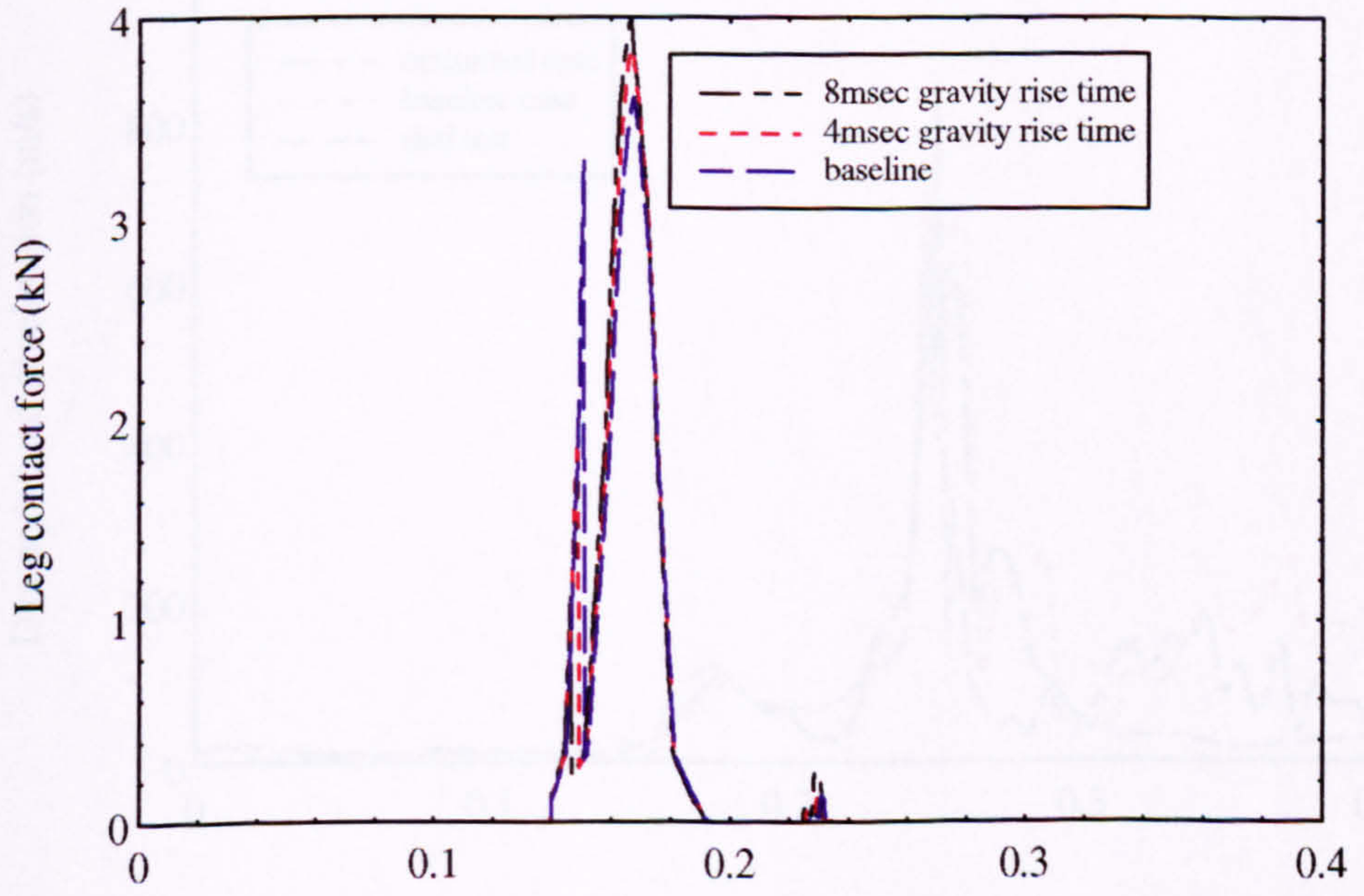

Figure 7.17 : The leg contact force-time history of the models studying gravity rise time.

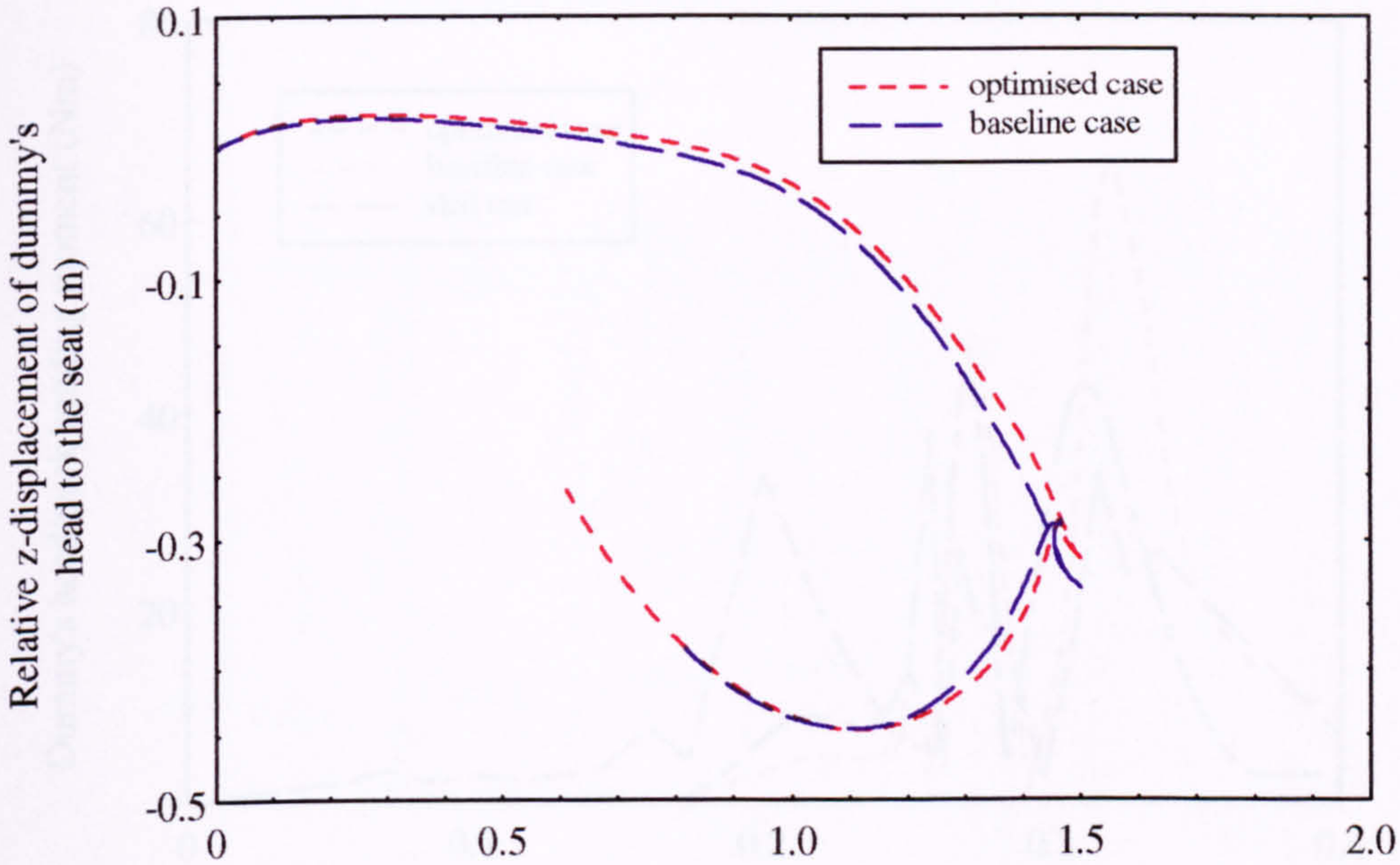

Figure 7.18 : The head's trajectories of the baseline and optimised models.

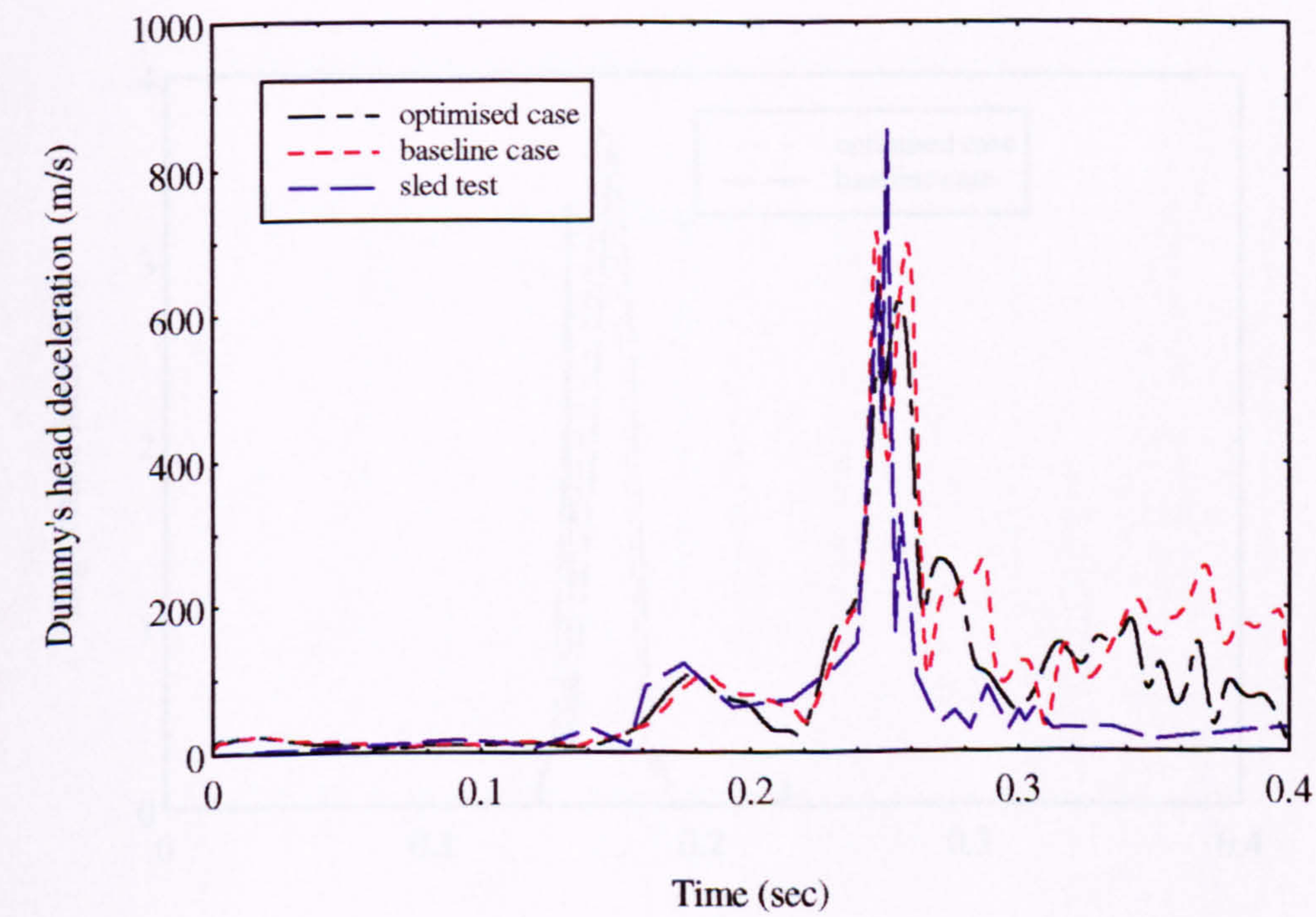

Figure 7.19 : The head's deceleration-time history of the baseline and optimised models.

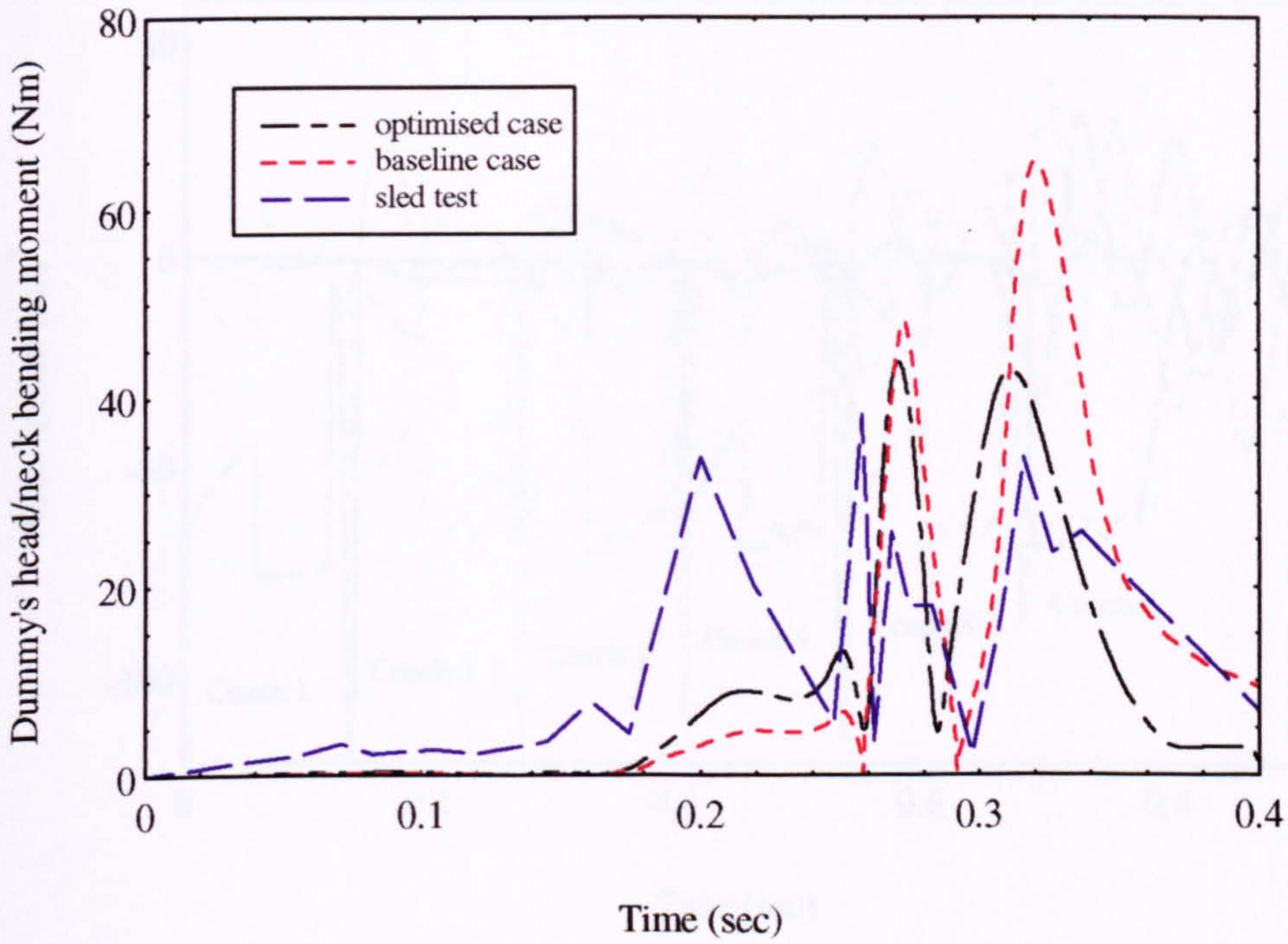

Figure 7.20 : The head/neck moment-time history of the baseline and optimised models.

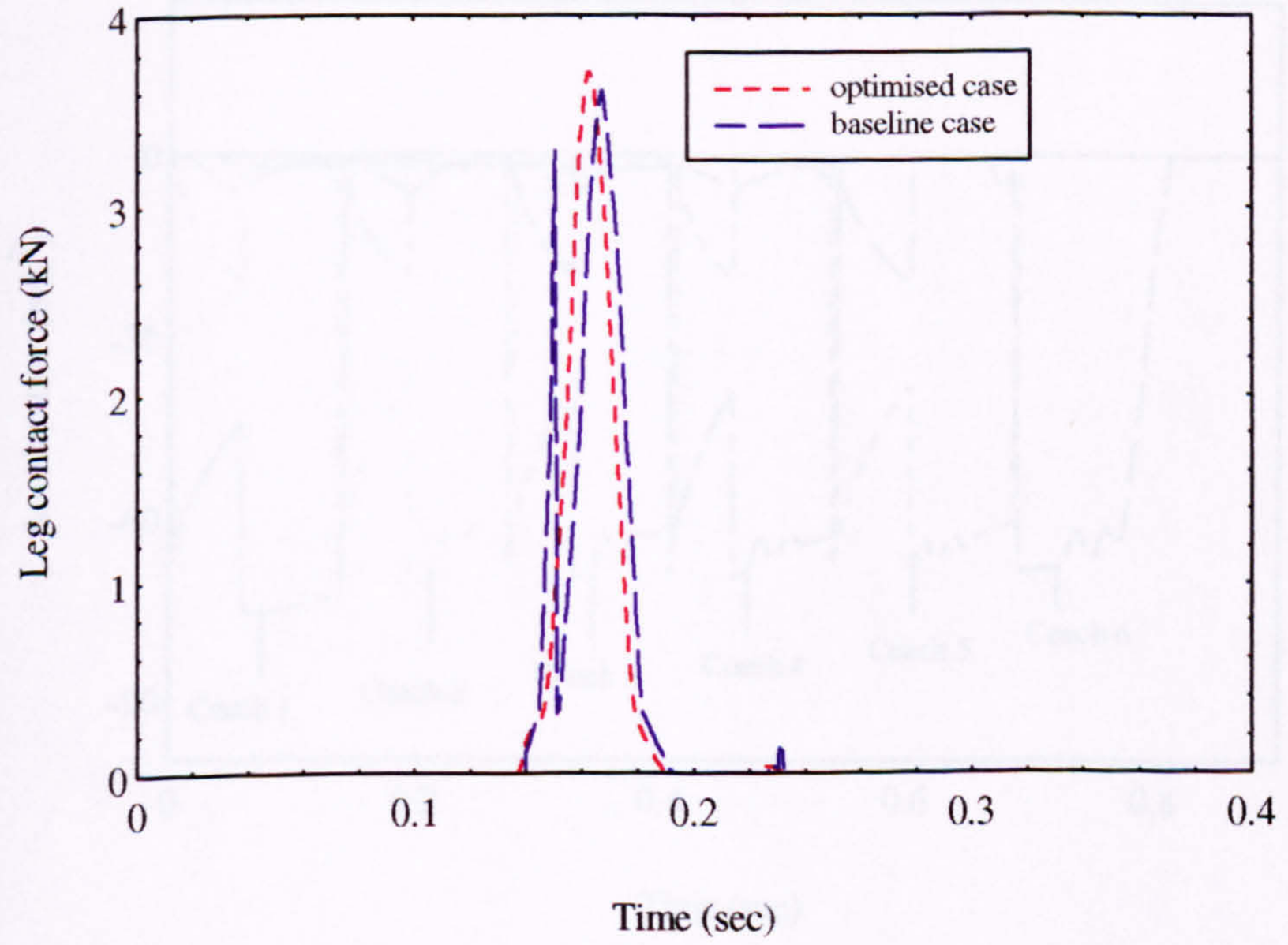

Figure 7.21 : The leg contact force-time history of the baseline and optimised models.

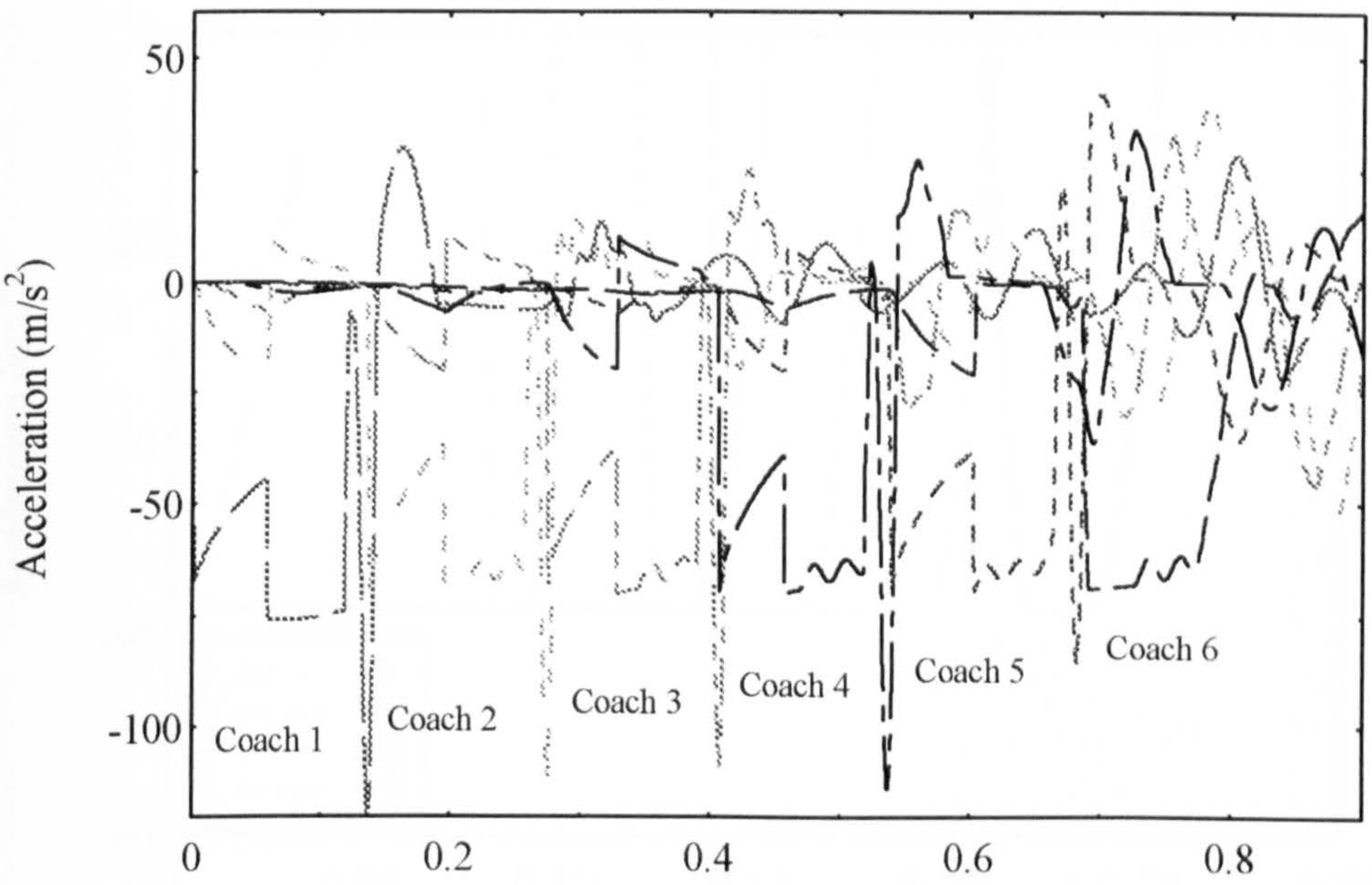

Figure 8.1 : The raw acceleration-time graphs for the coaches in mixn6 (Chapter 4).

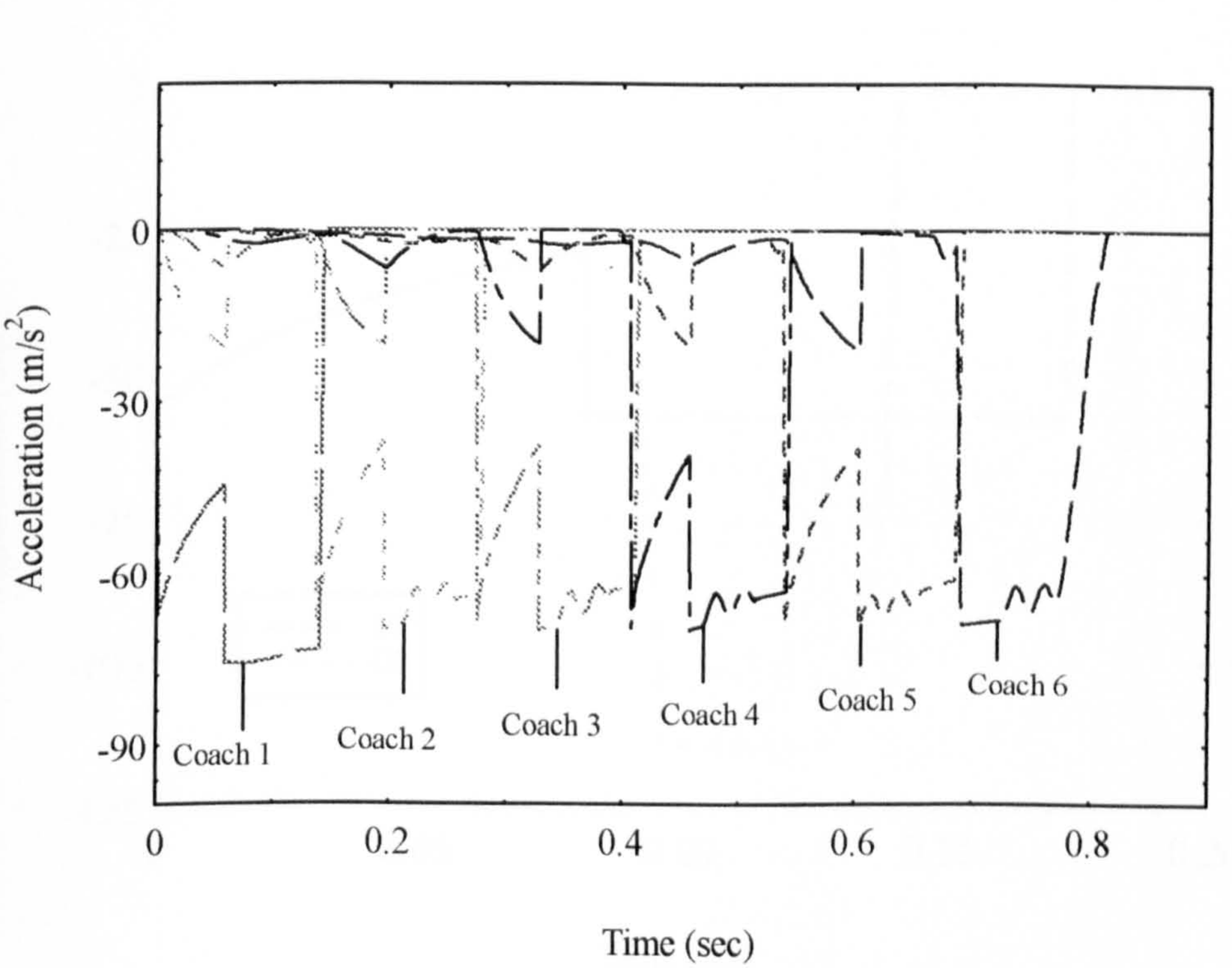

Figure 8.2 : The processed acceleration-time graphs.

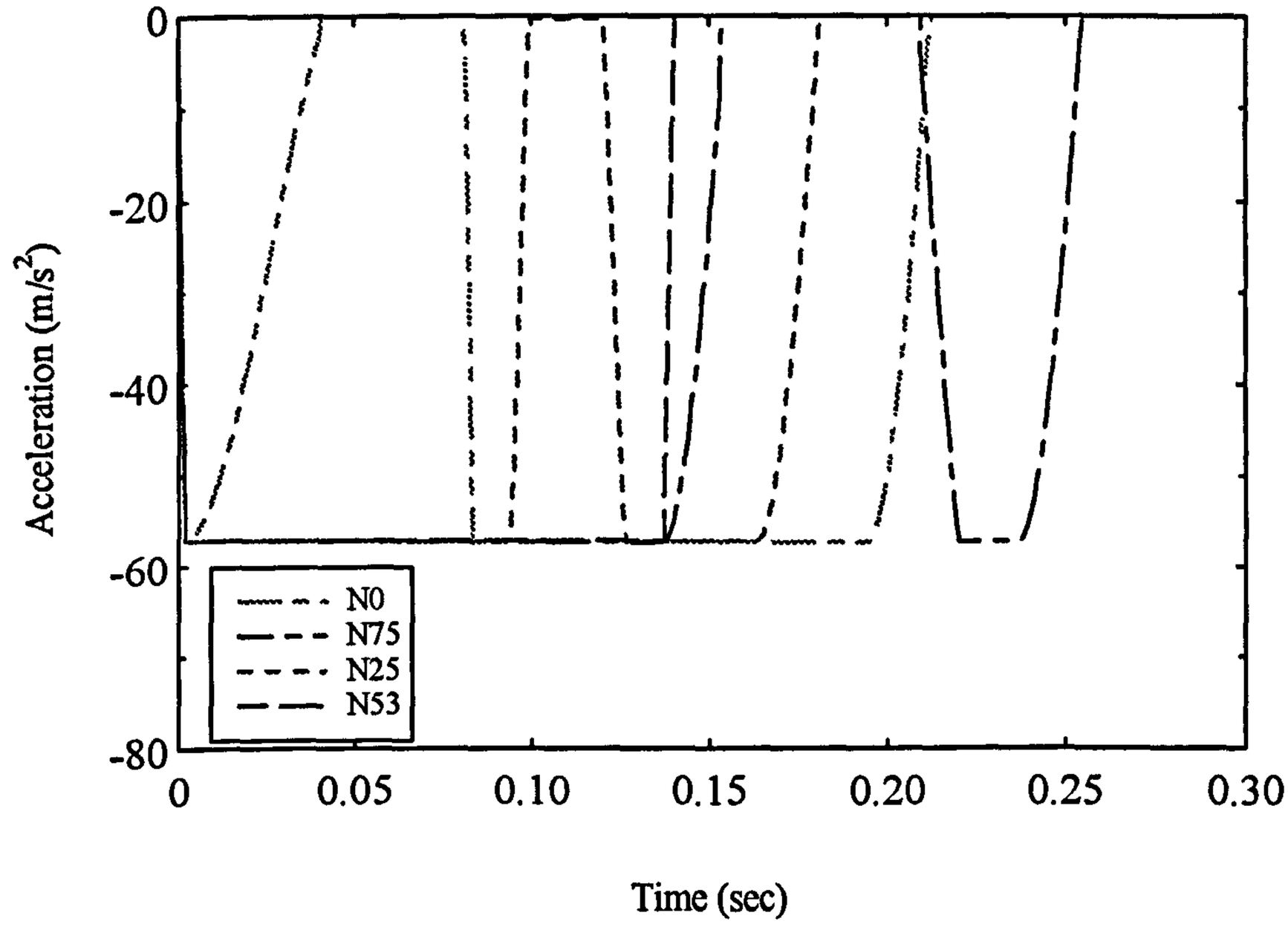

Figure 8.3 : The acceleration pulses in the N-series.

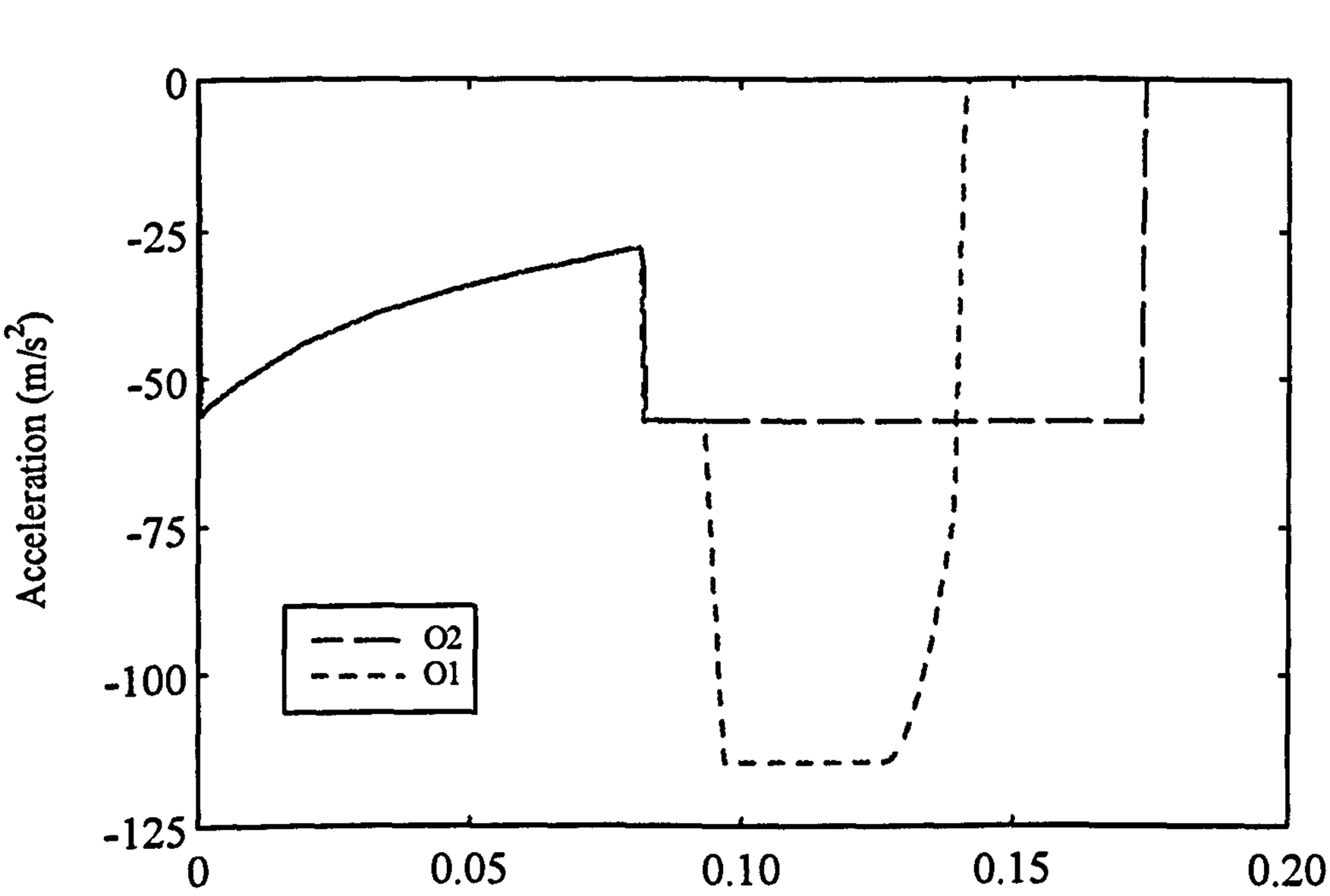

Figure 8.4 : The acceleration pulses in the O-series

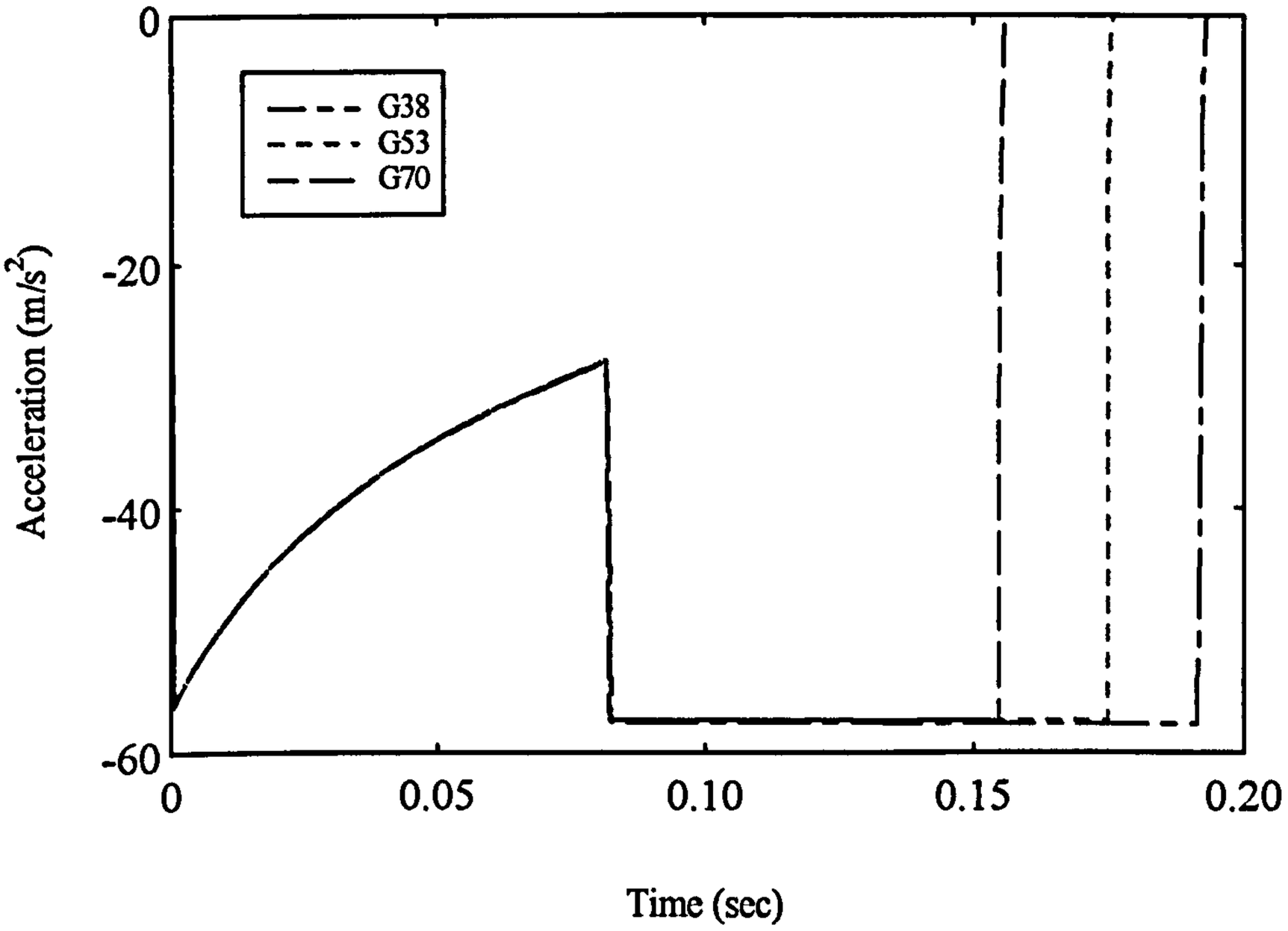

Figure 8.5 : The acceleration pulses in the G-series

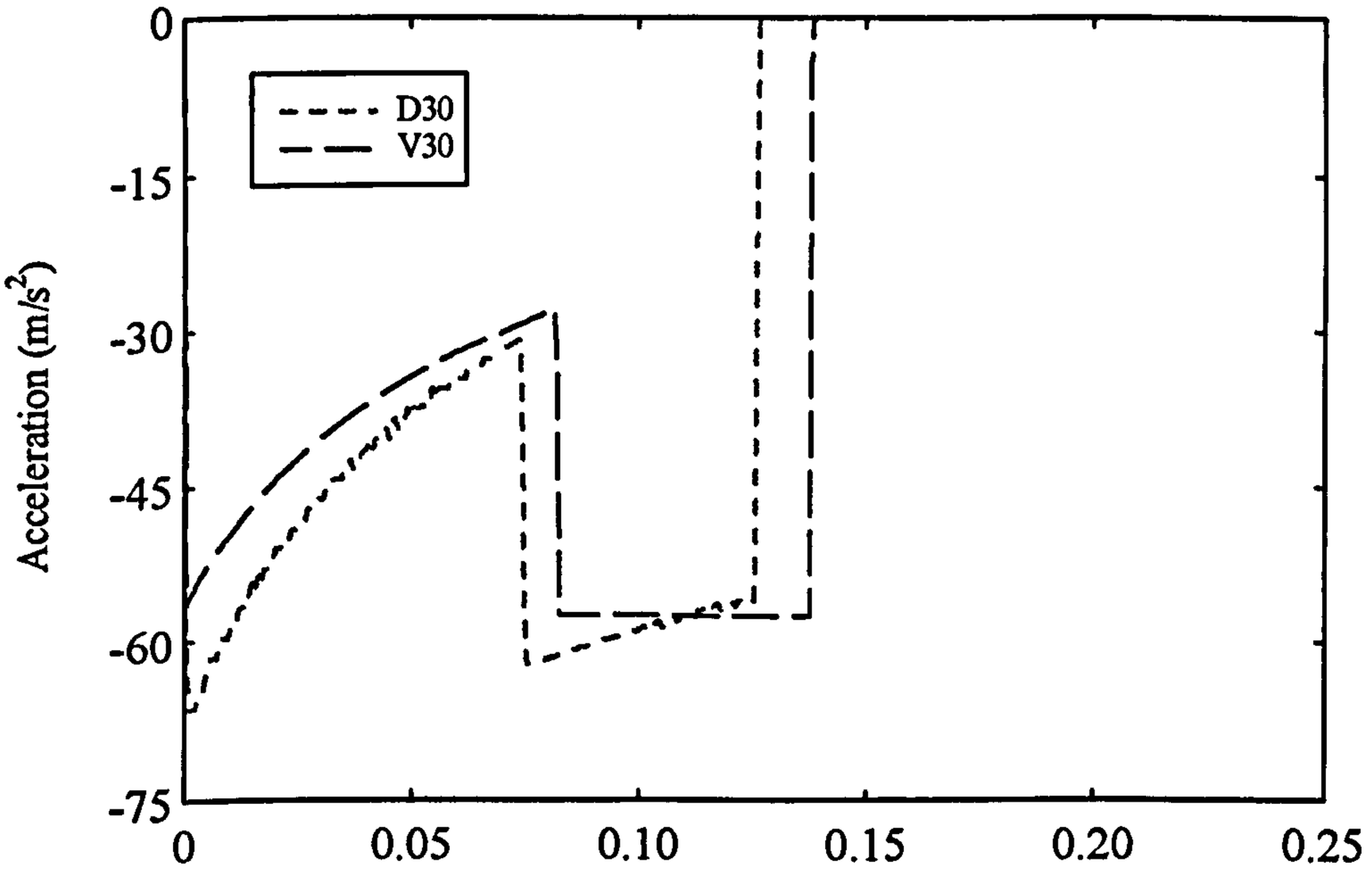

Figure 8.6a : The acceleration pulses in the D-series

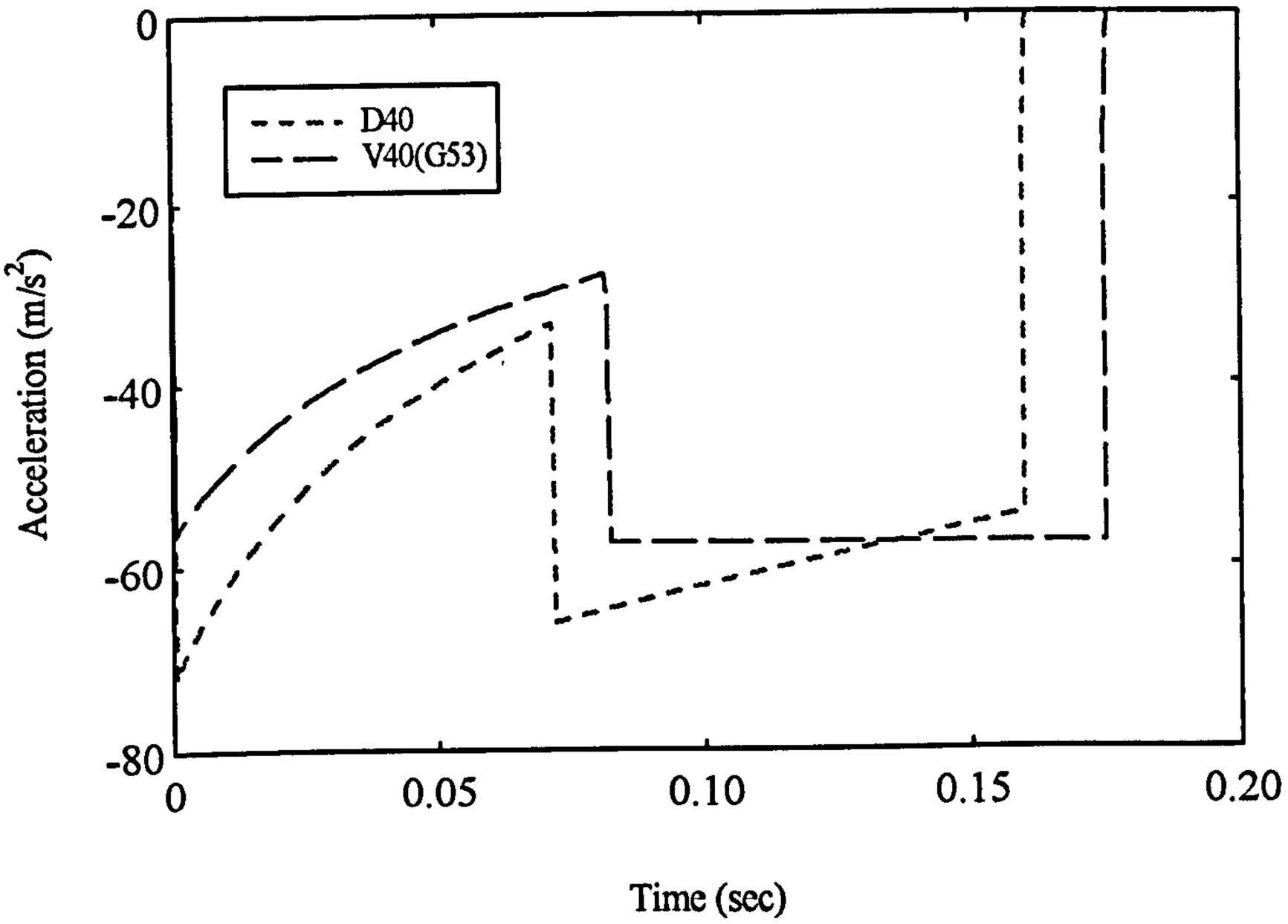

Figure 8.6b : The acceleration pulses in the D-series

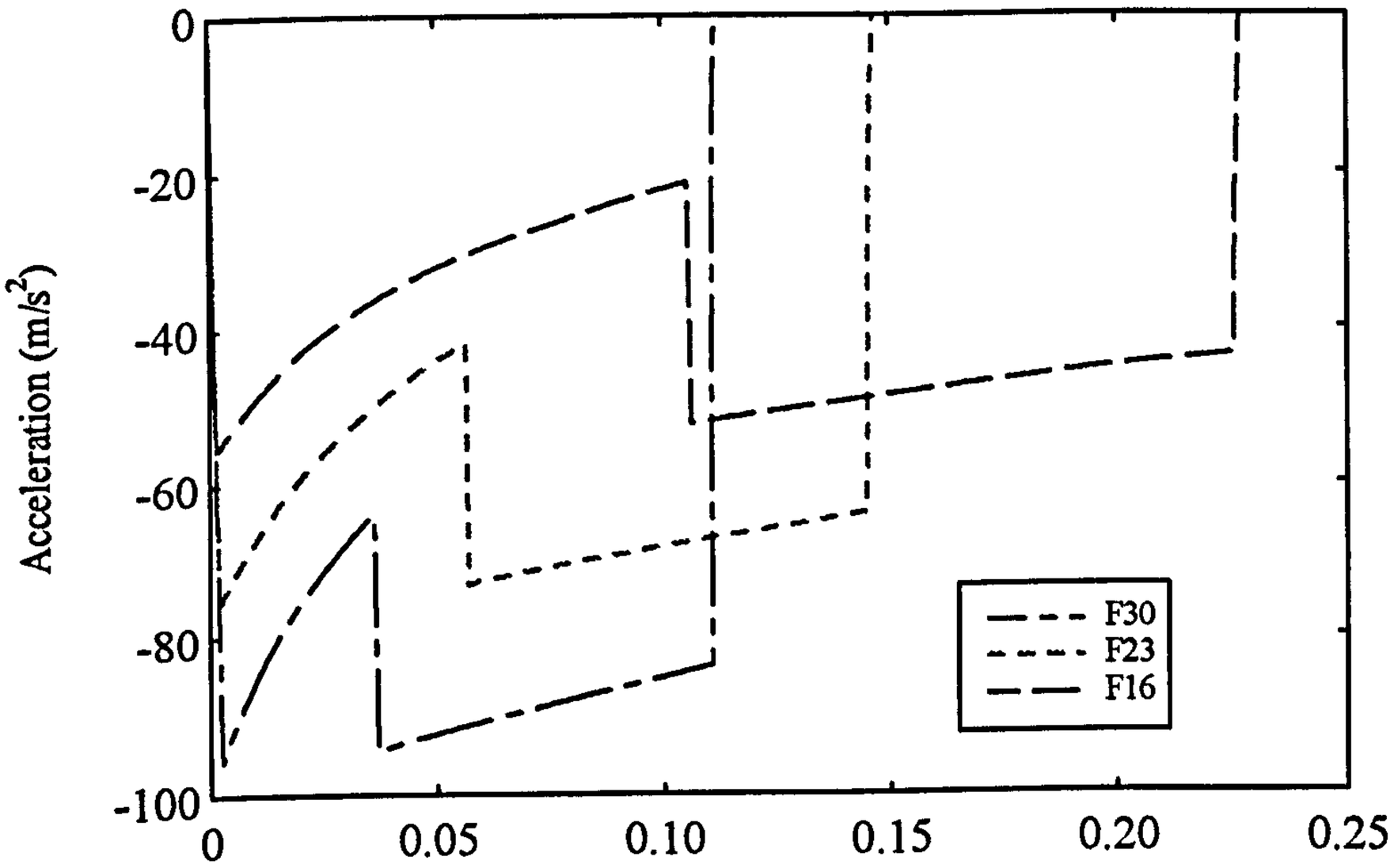

Figure 8.7 : The acceleration pulses in the F-series

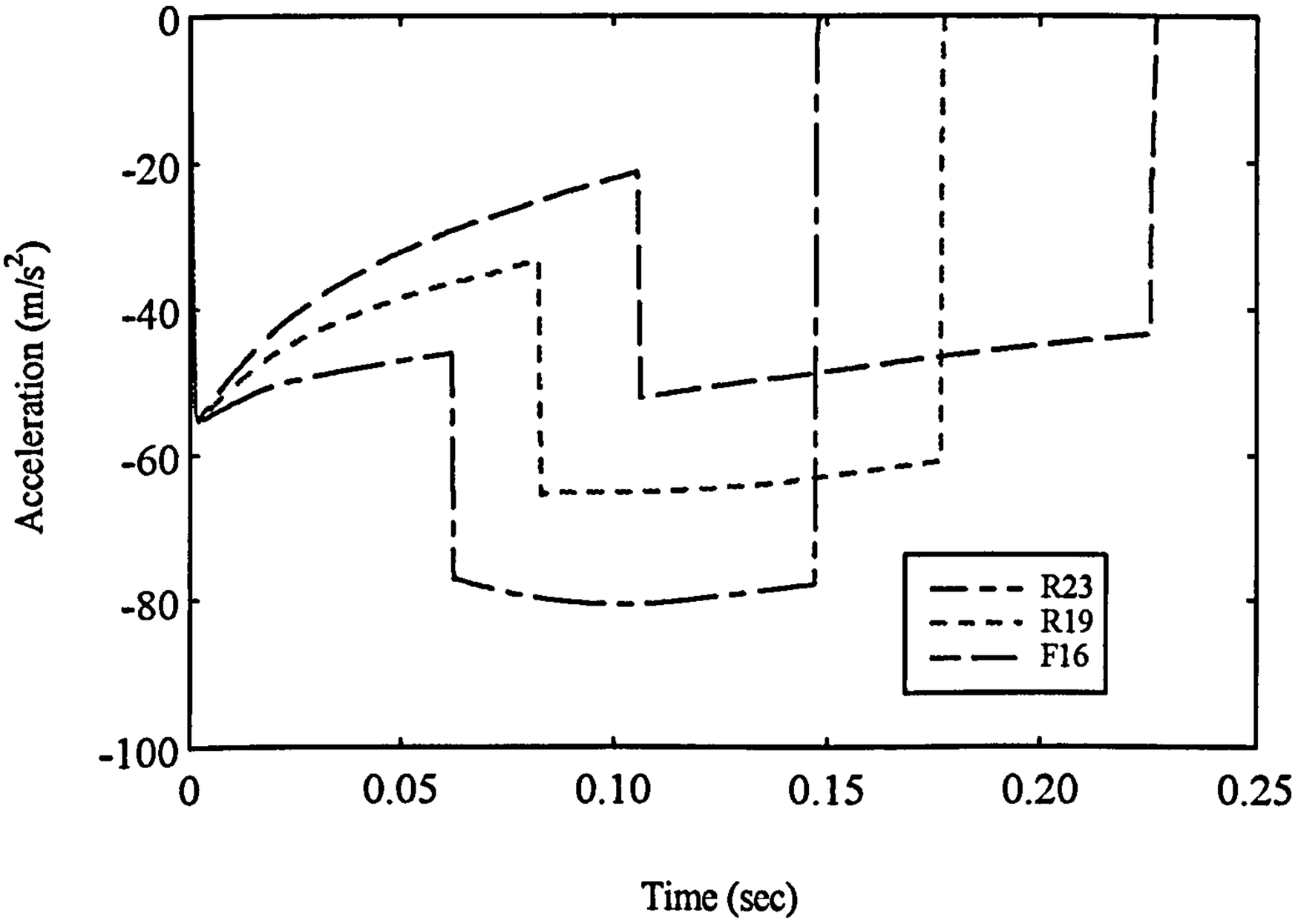

Figure 8.8 : The acceleration pulses in the R-series

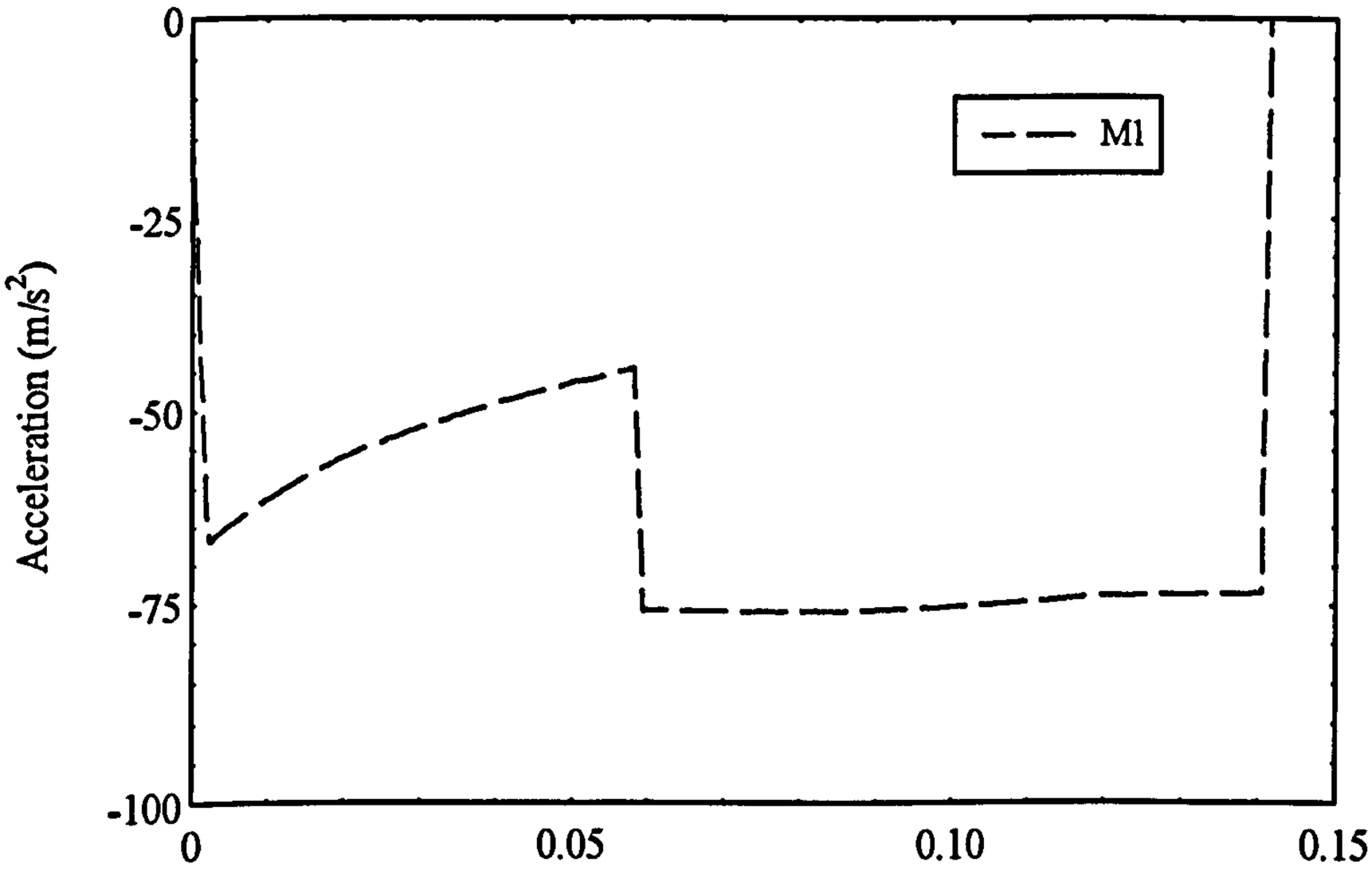

Figure 8.9 : The M1 pulse

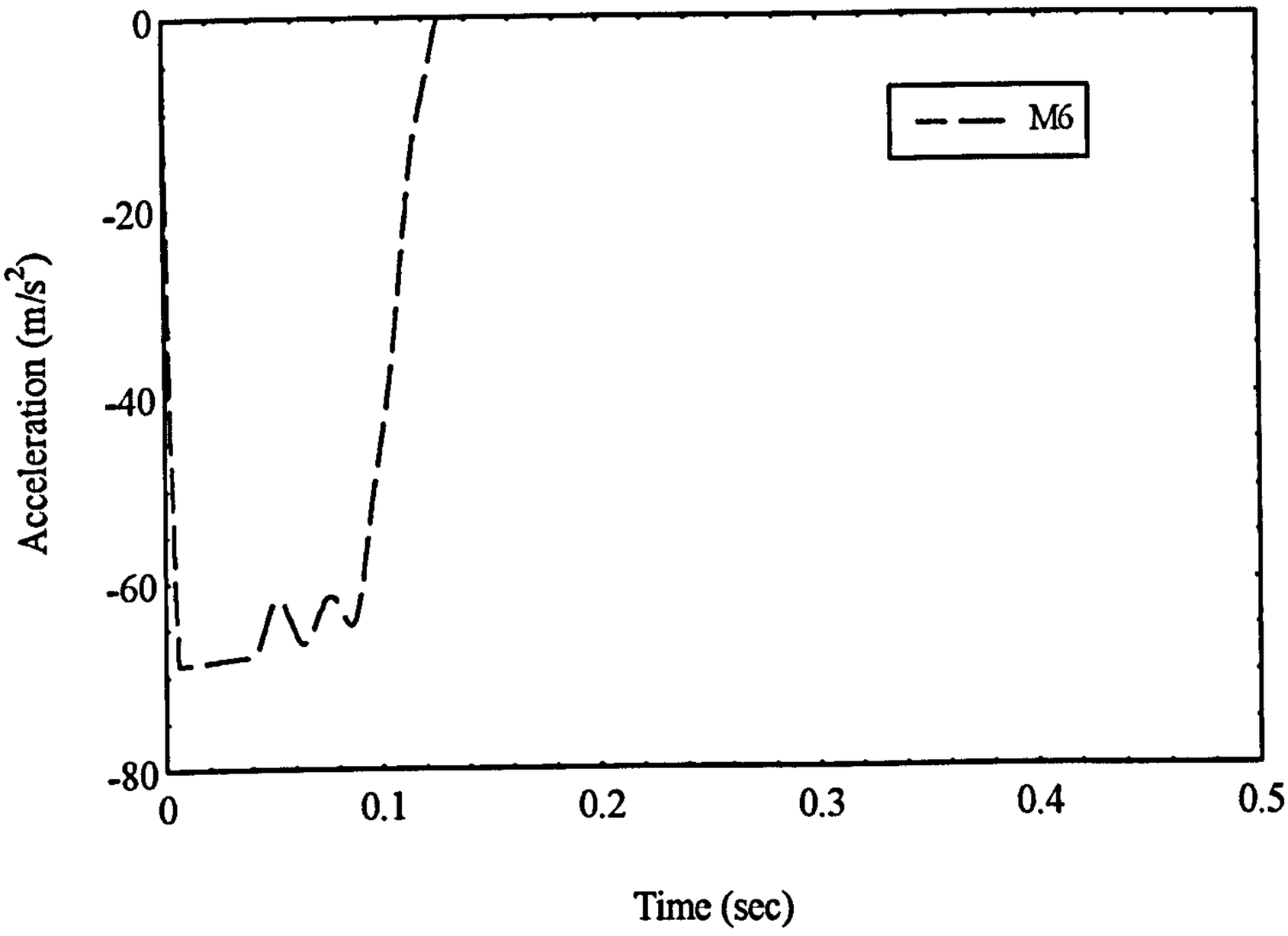

Figure 8.10 : The M6 pulse

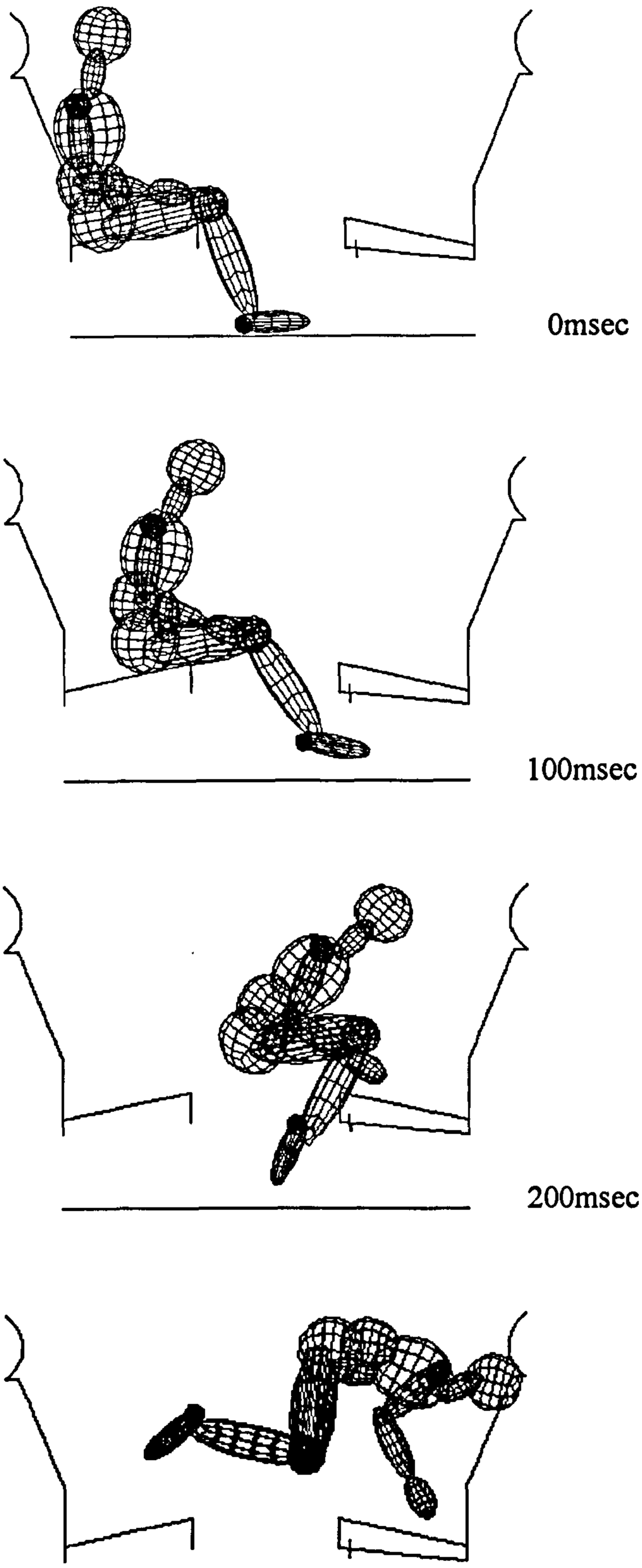

Figure 8.11 : The sequence of animated response in N53.

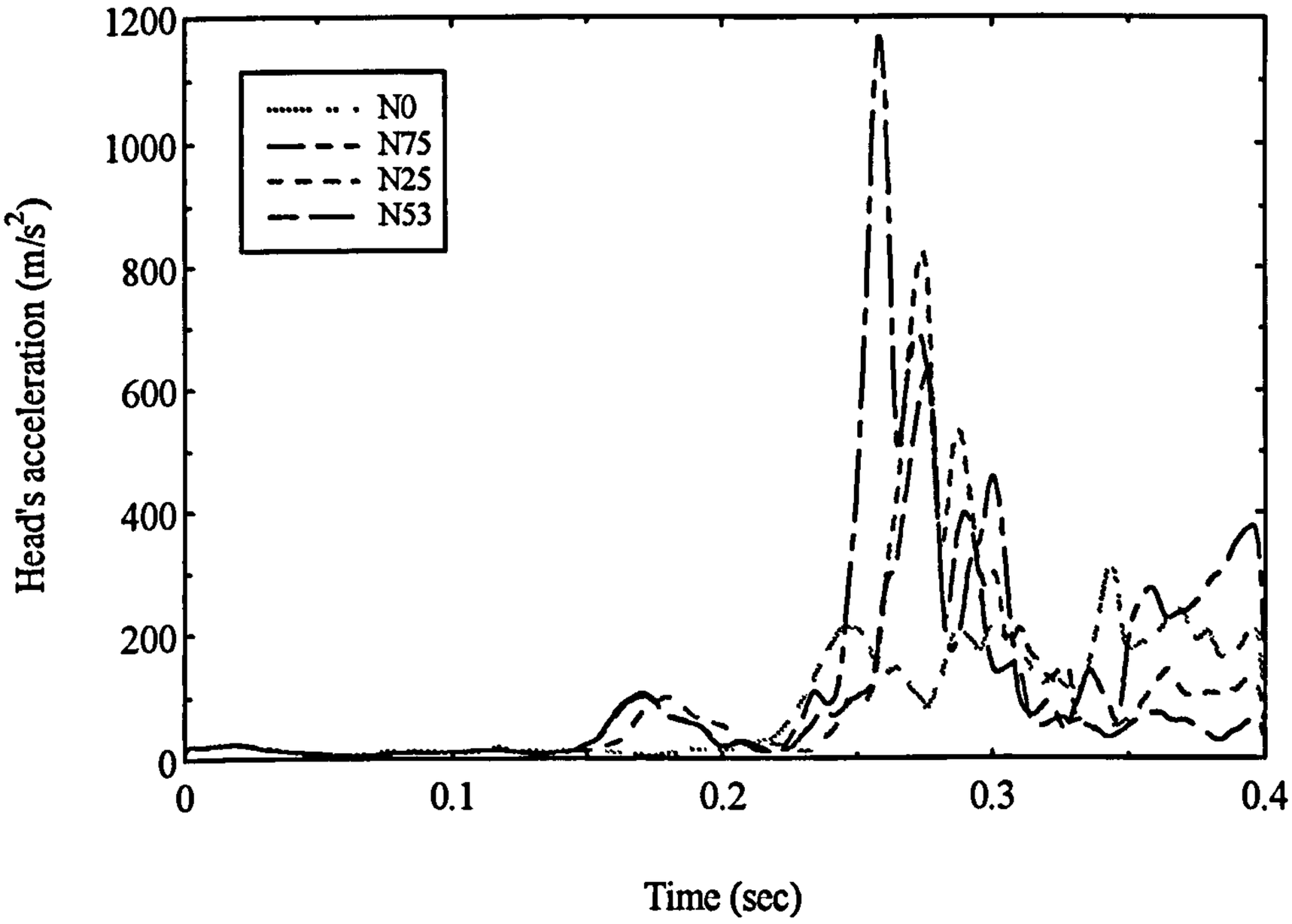

Figure 8.12 : Head acceleration-time history for models in the N-series.

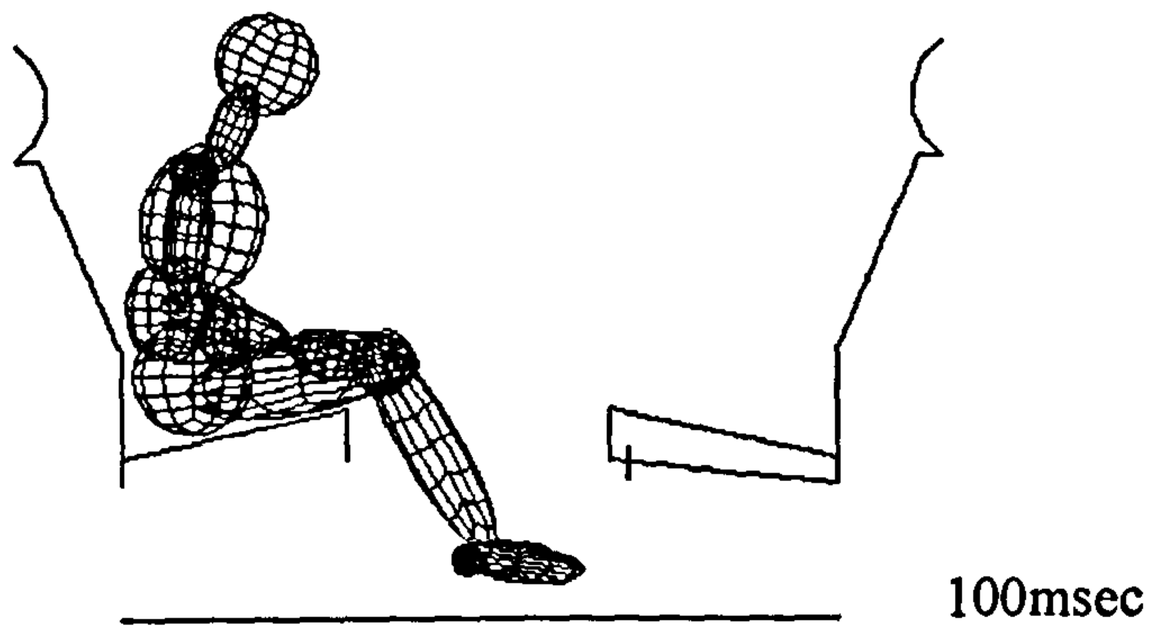

Figure 8.13 : The sequence of animated response in N0.

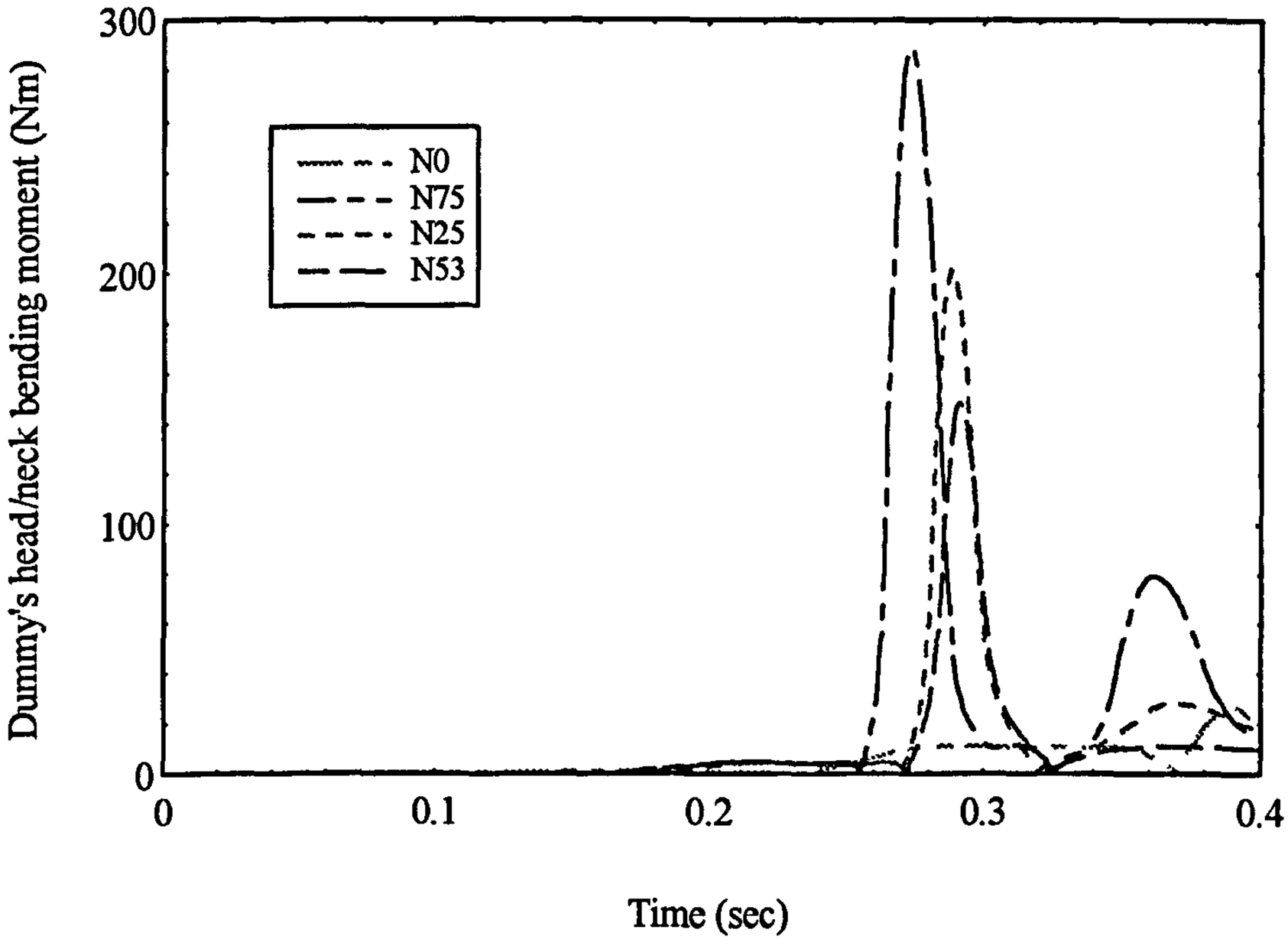

Figure 8.14 : Head/neck bending moment-time history for models in the N-series.

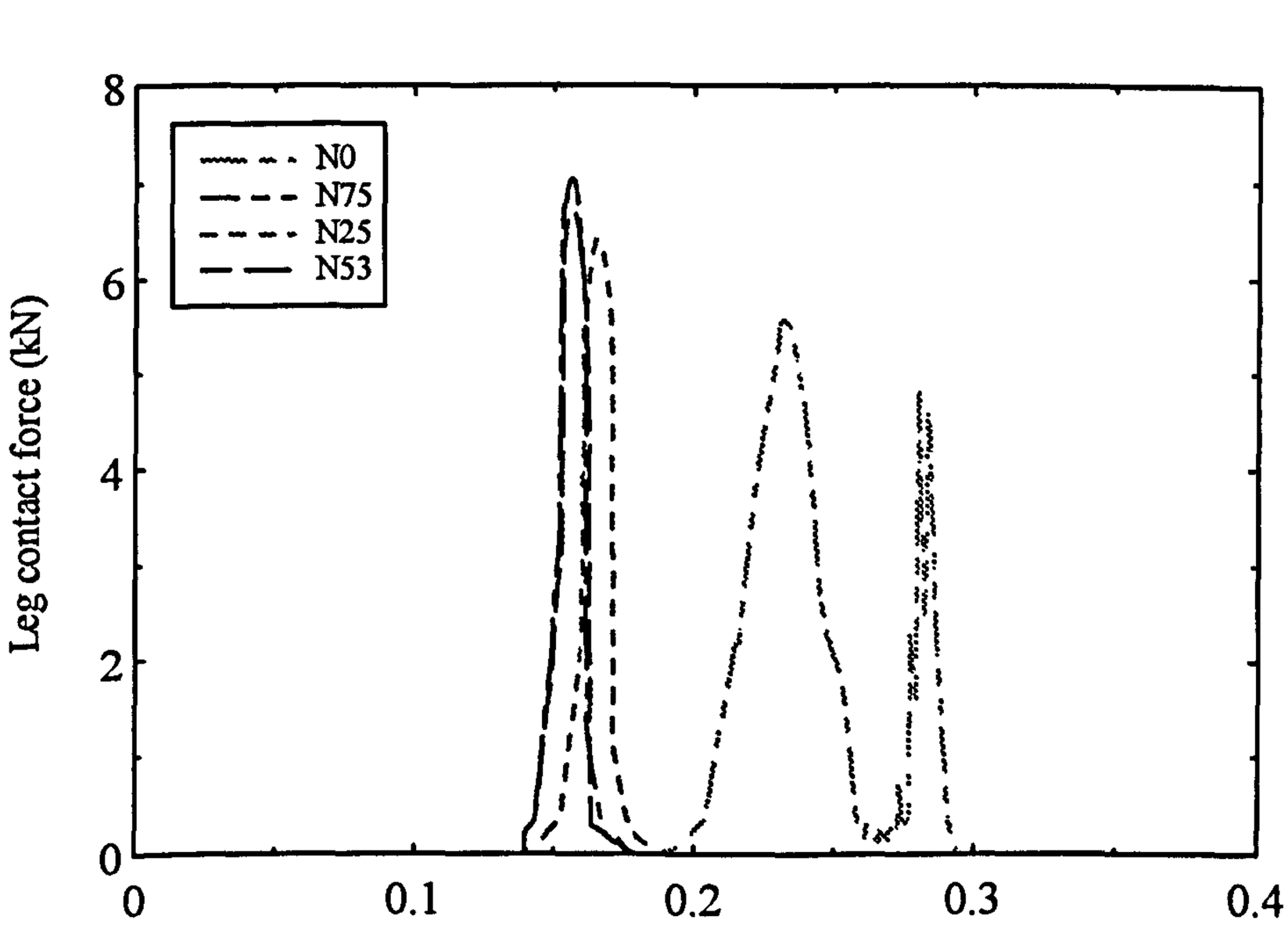

Figure 8.15 : Leg contact force-time history for models in the N-series.

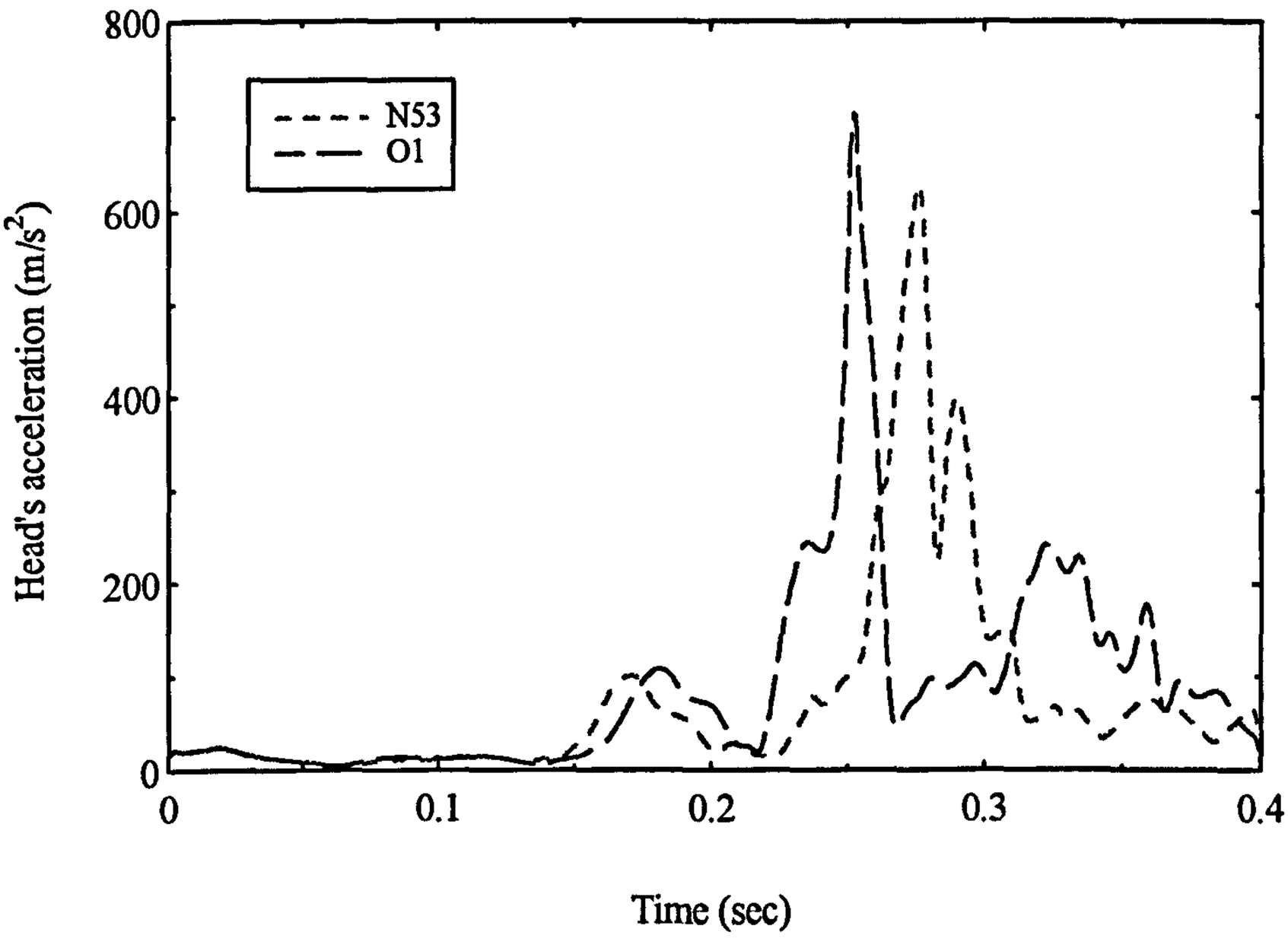

Figure 8.16 : Head acceleration-time history for models in the O-series.

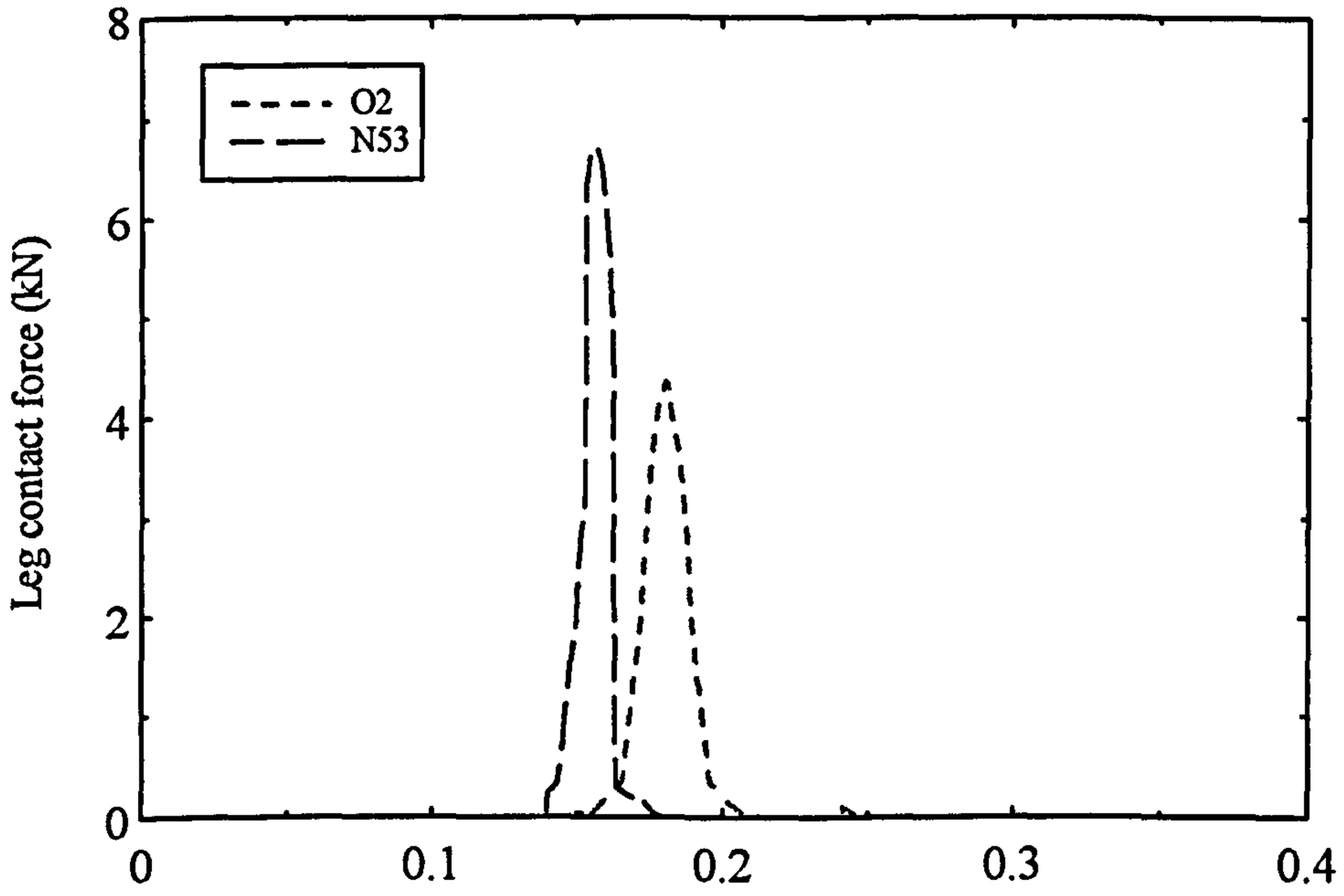

Figure 8.17 : Leg contact force-time history for models in the O-series.

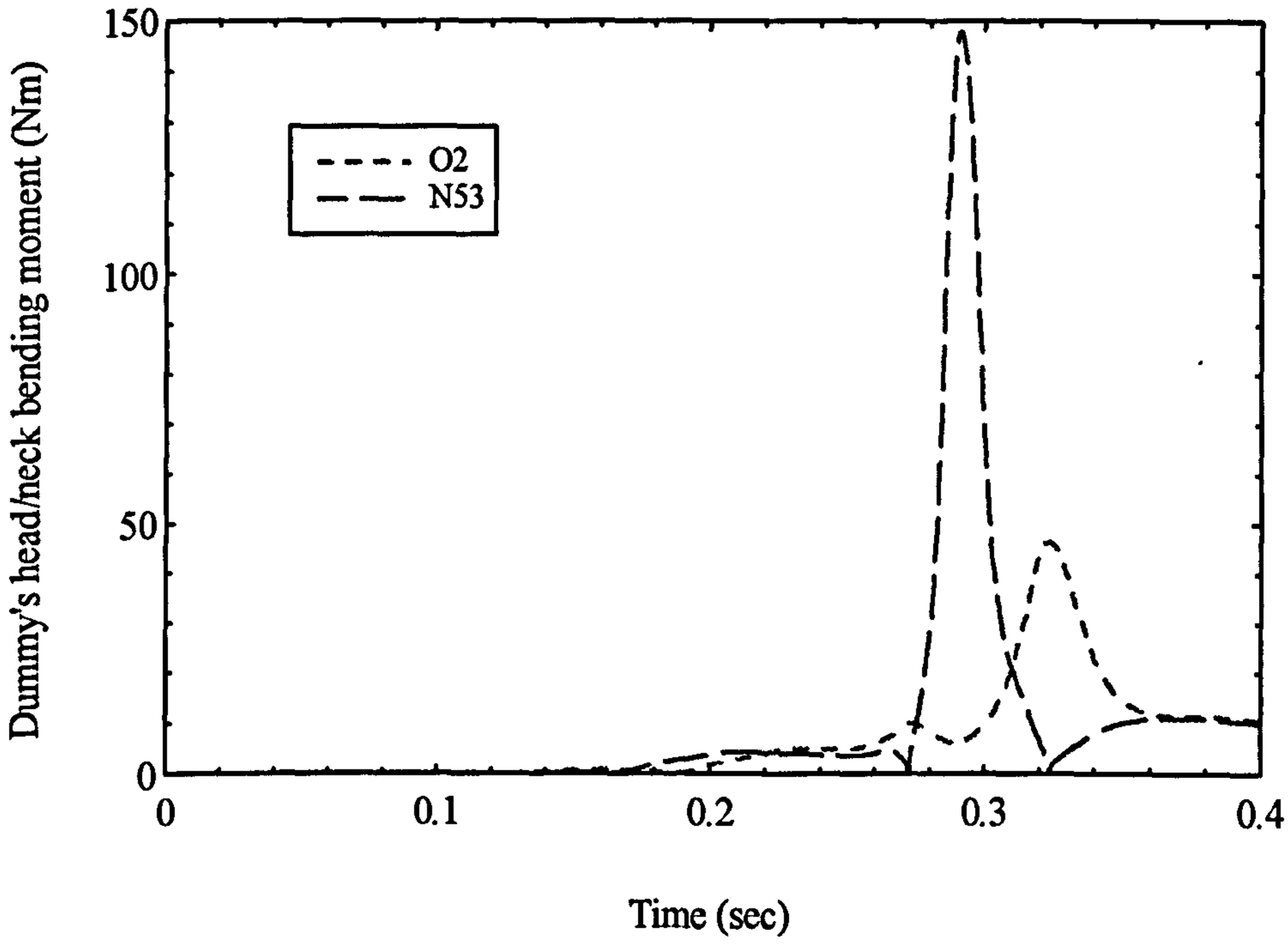

Figure 8.18 : Head/neck bending moment-time history for models in the O-series.

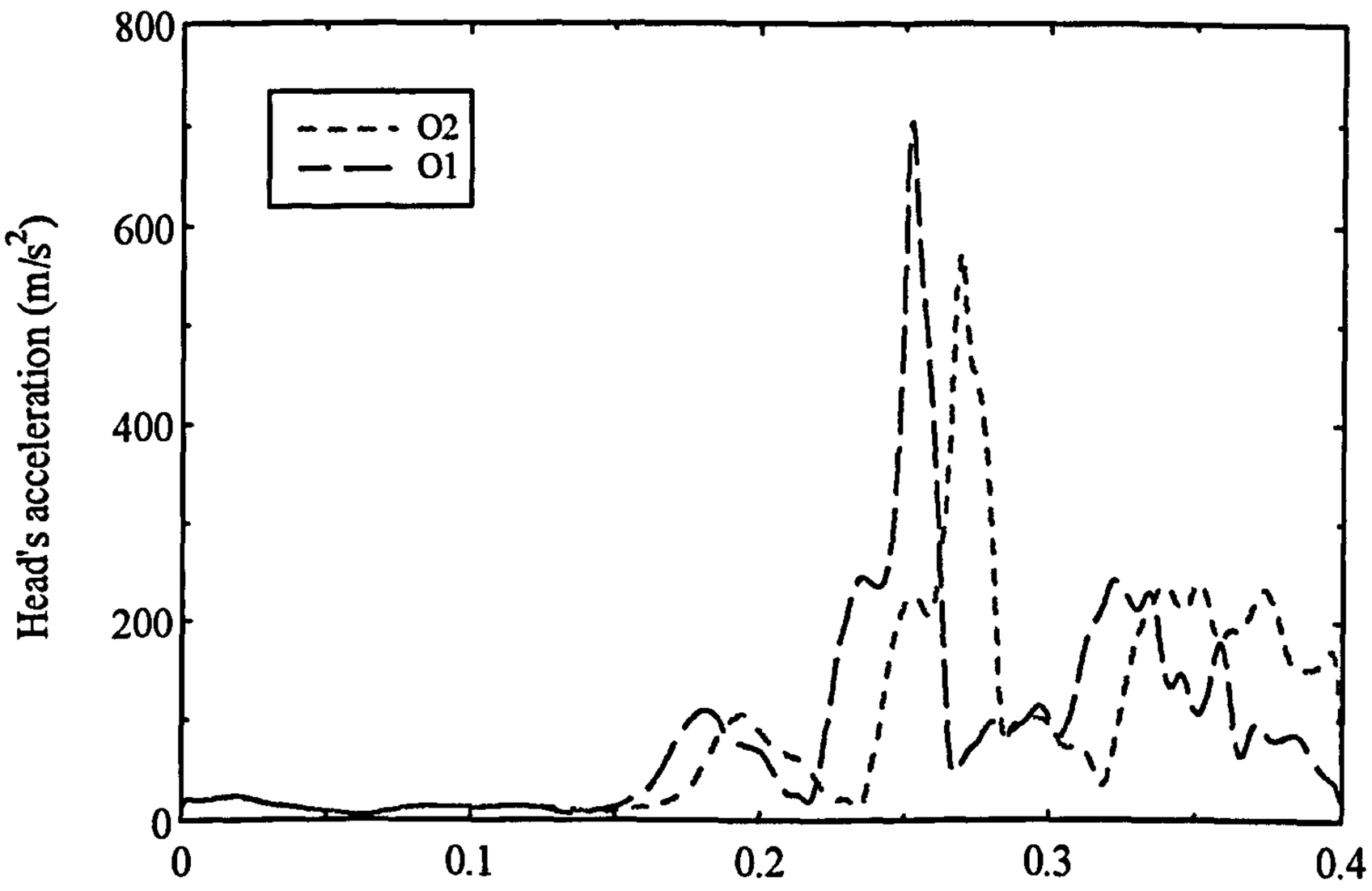

Figure 8.19 : Head acceleration-time history for models in the O-series.

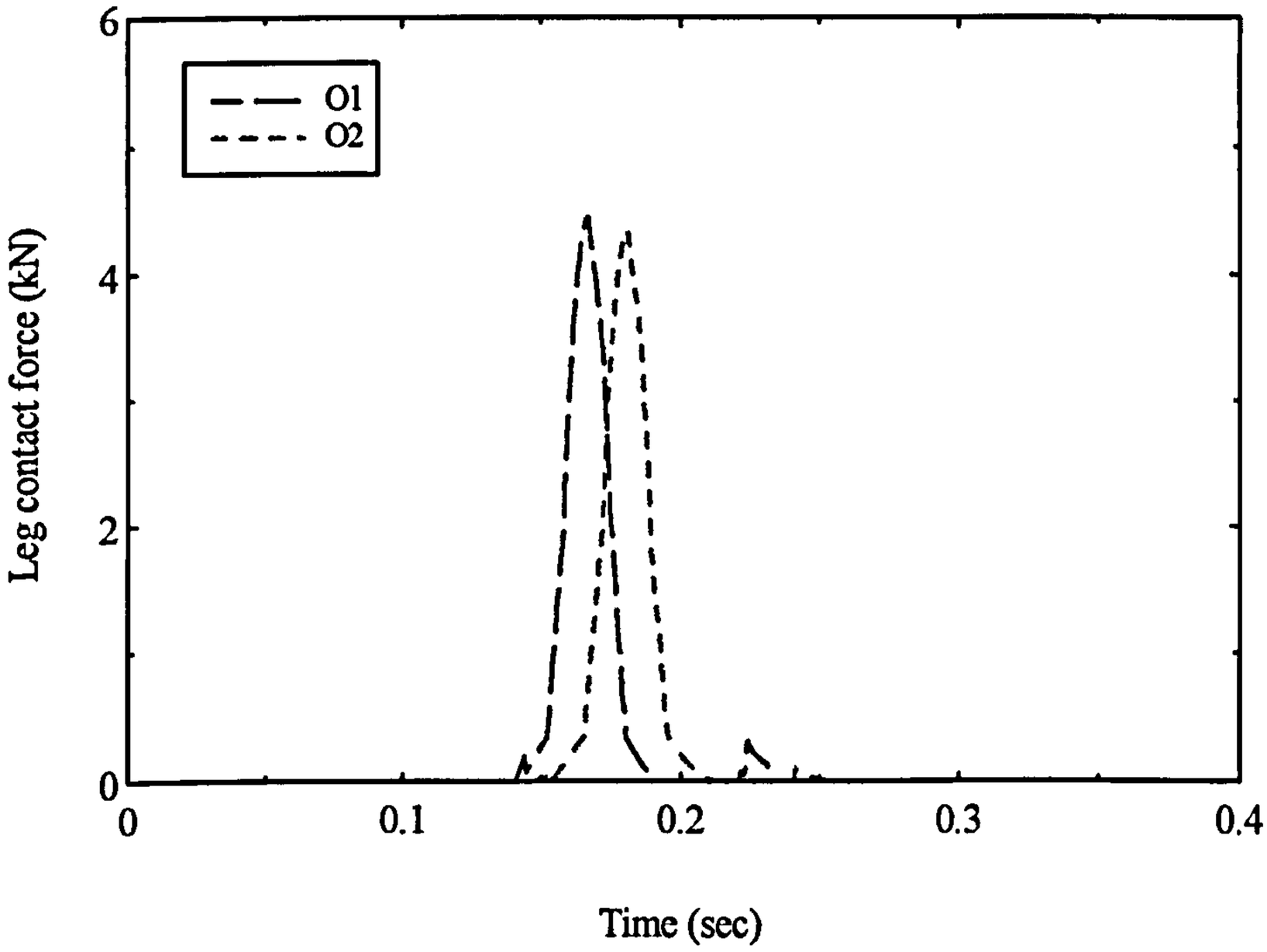

Figure 8.20 : Leg contact force-time history for models in the O-series.

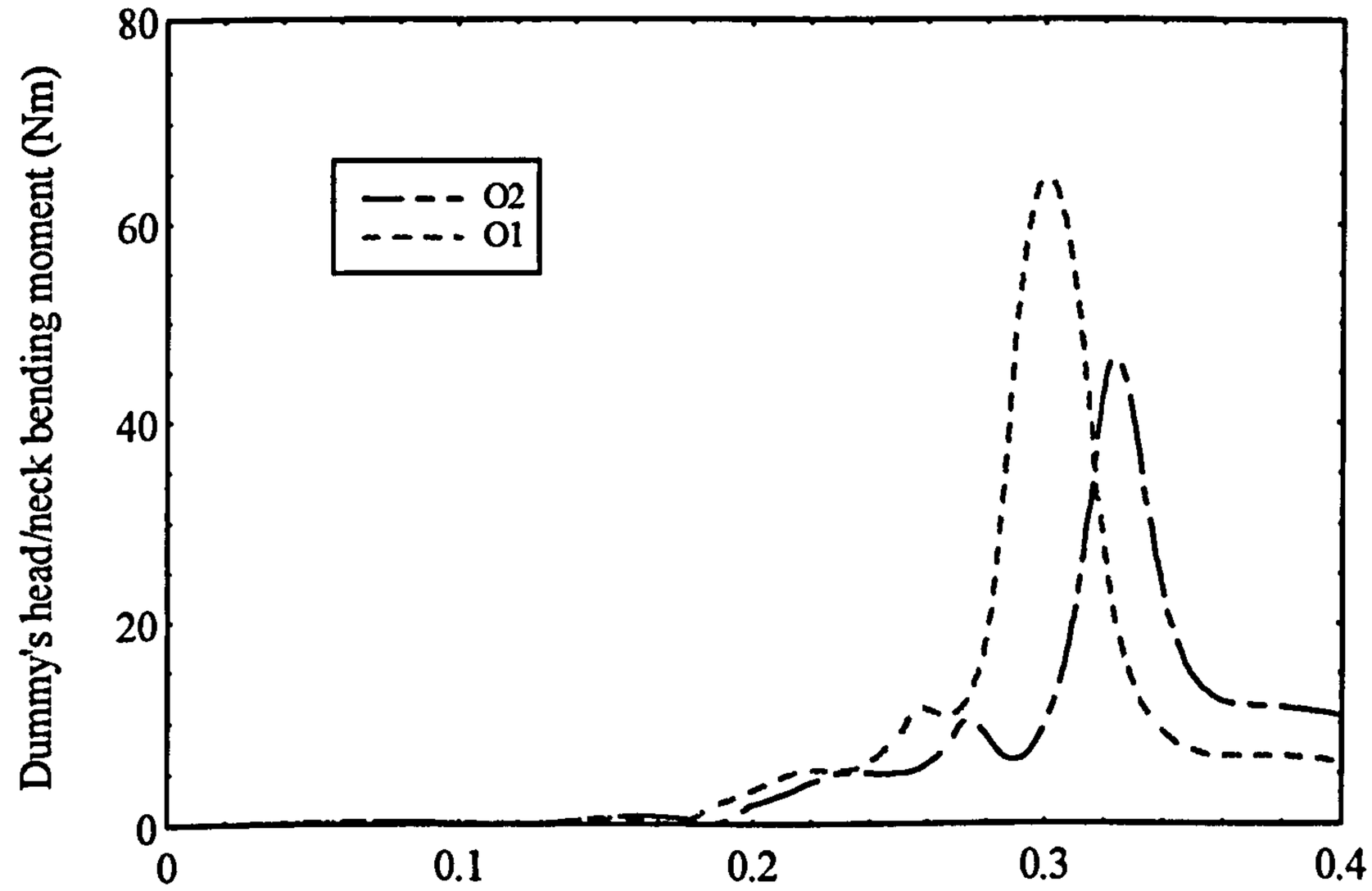

Figure 8.21 : Head/neck bending moment-time history for models in the O-series.

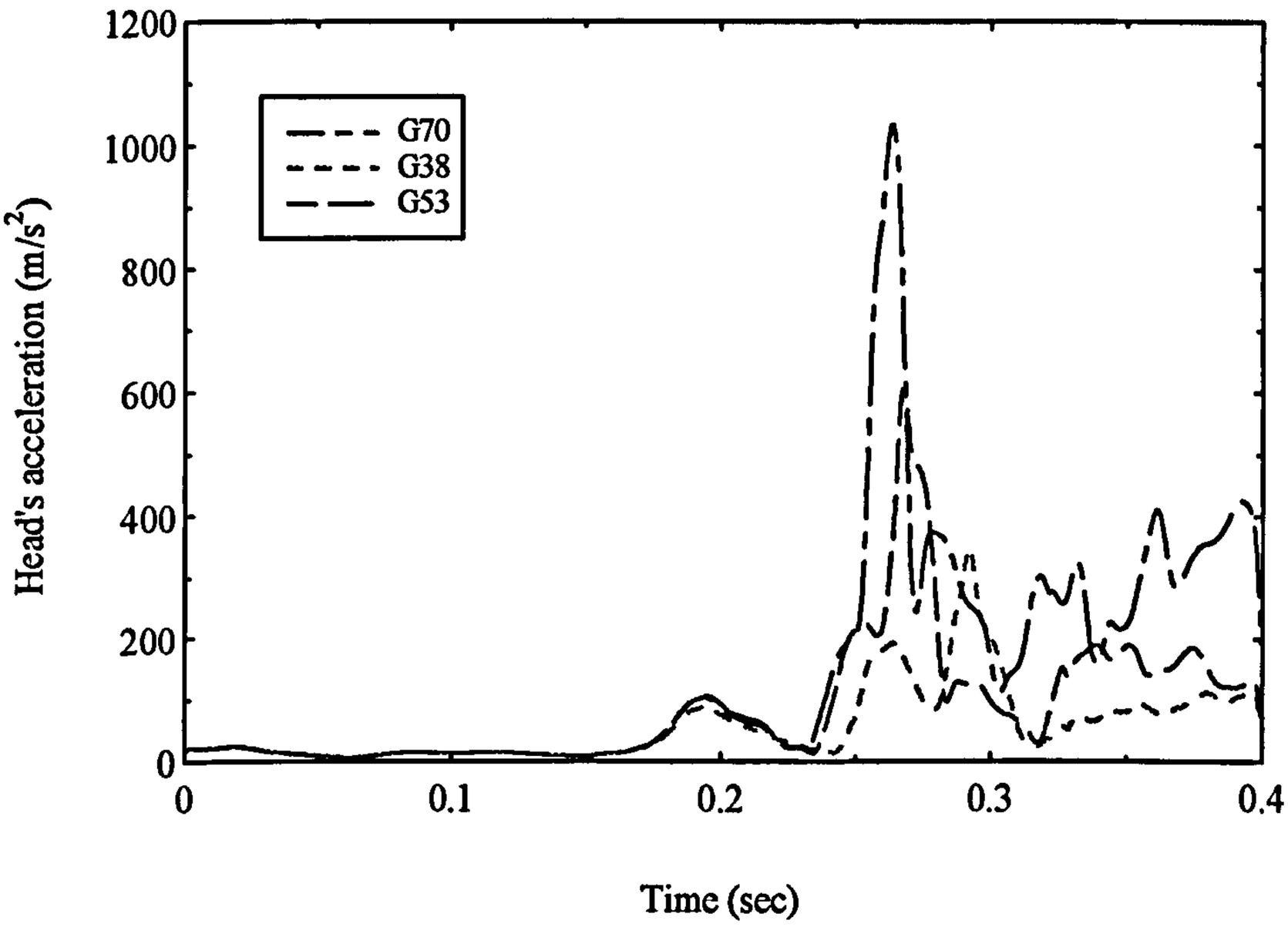

Figure 8.22 : Head acceleration-time history for models in the G-series.

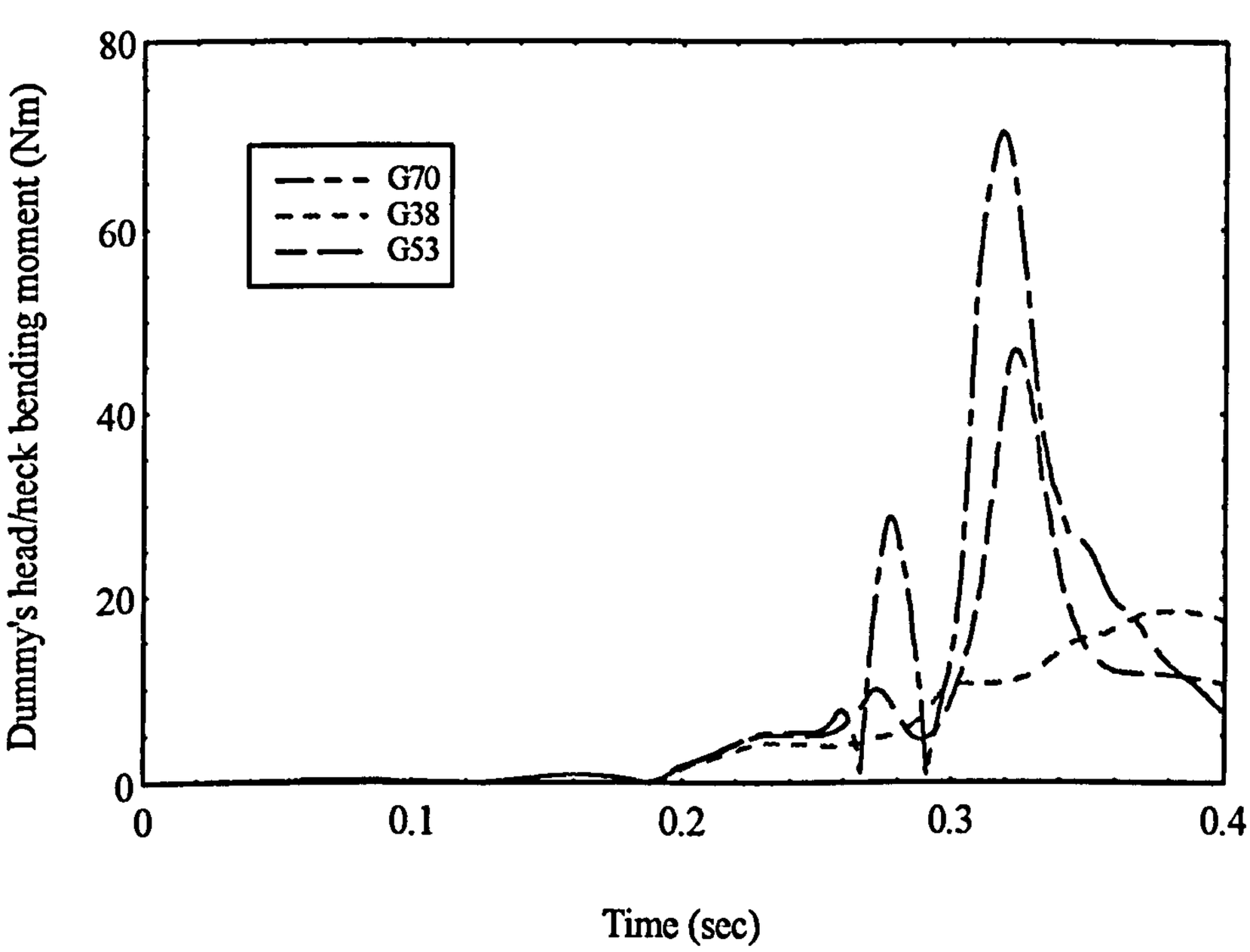

Figure 8.23 : Head/neck bending moment-time history for models in the G-series.

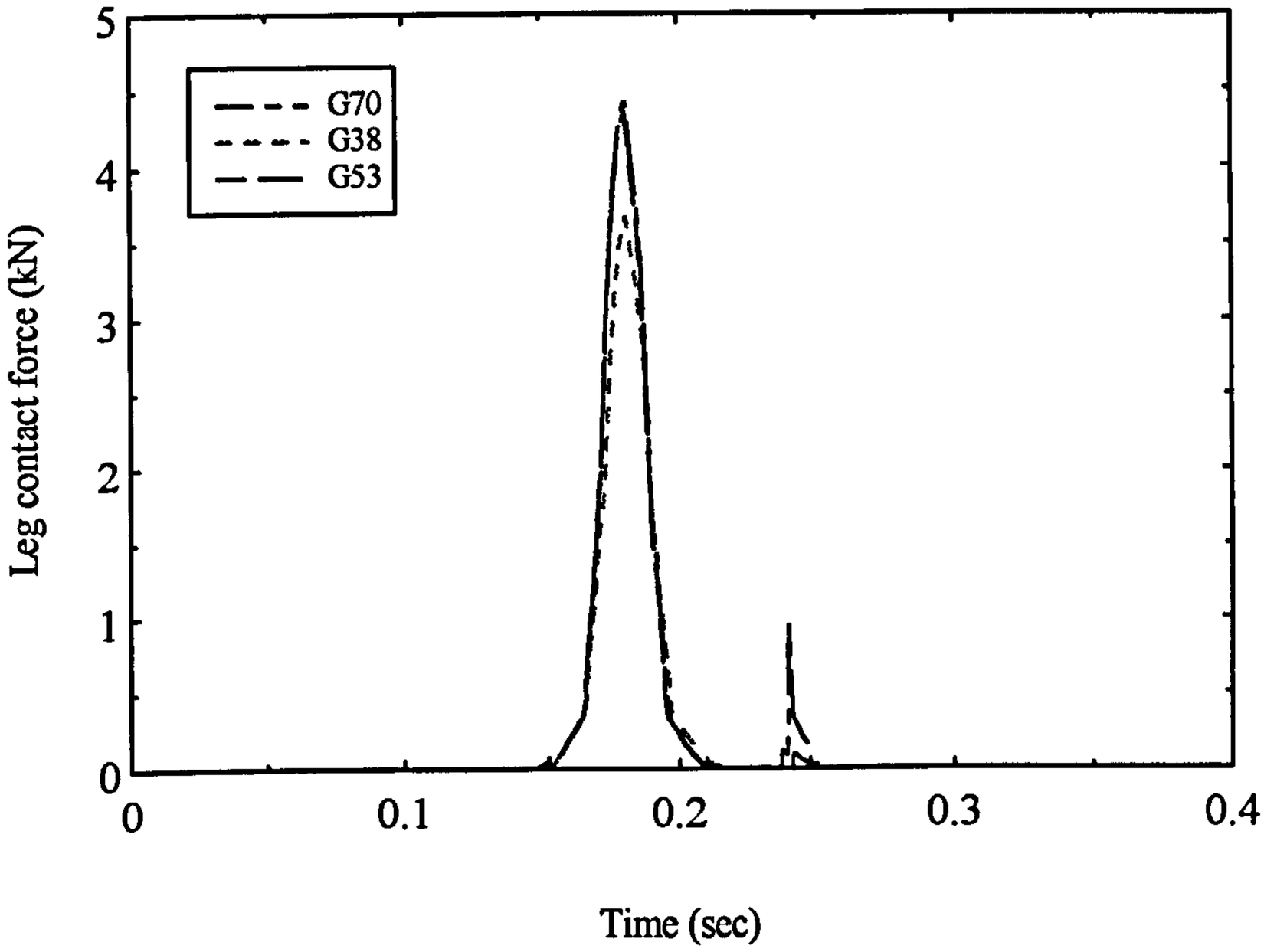

Figure 8.24 : Leg contact force-time history for models in the G-series.

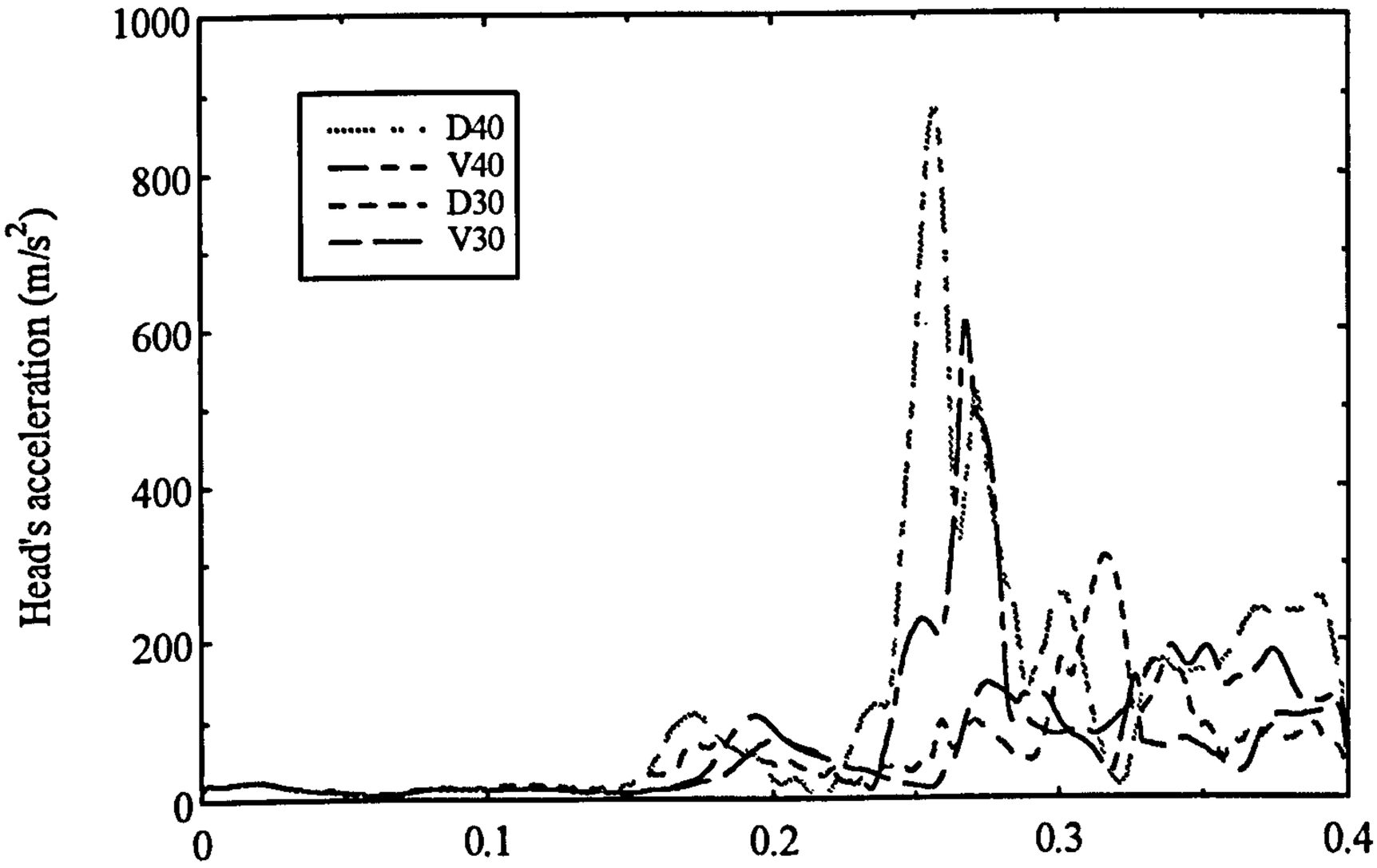

Figure 8.25 : Head acceleration-time history for models in the D-series.

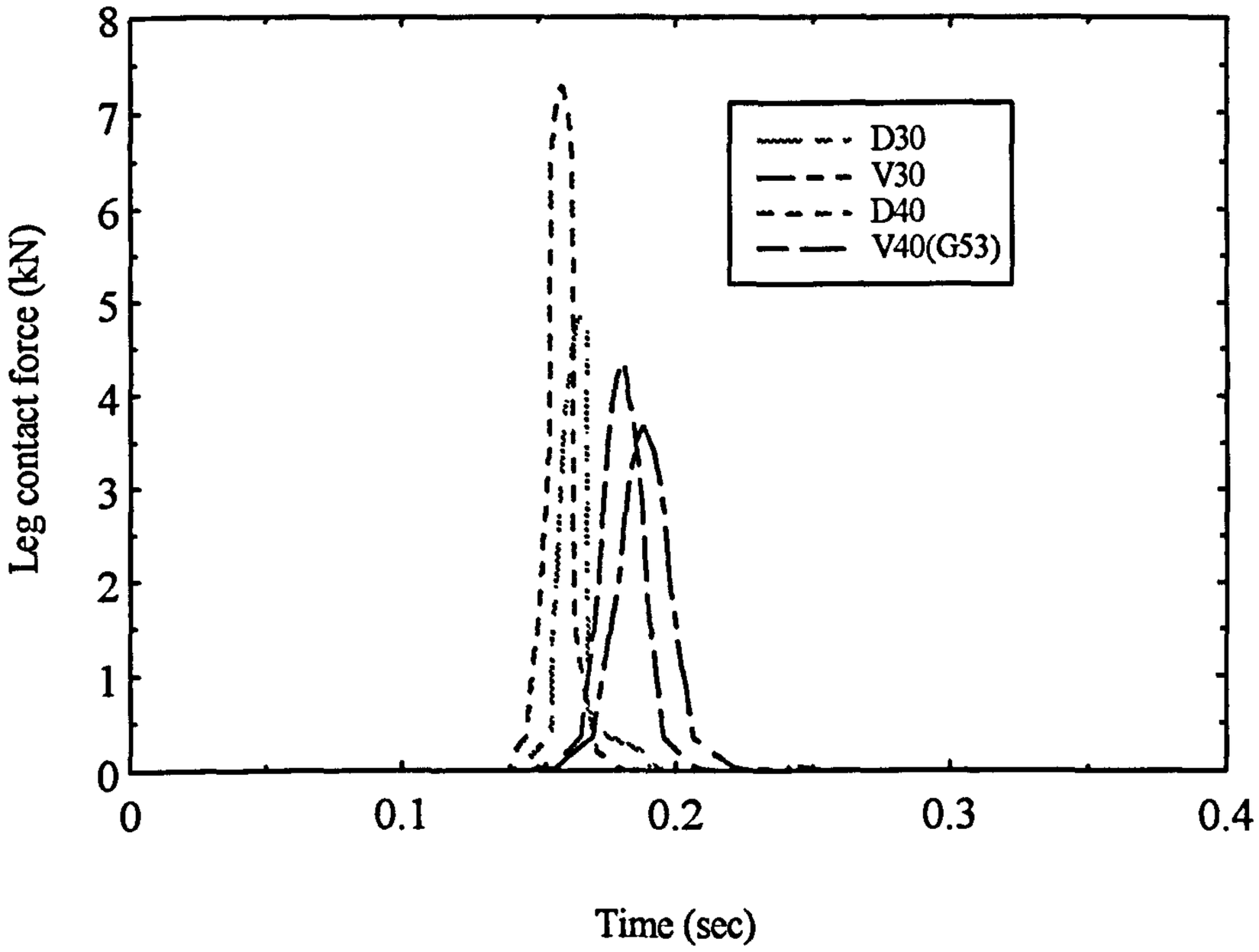

Figure 8.26 : Leg contact force-time history for models in the D-series.

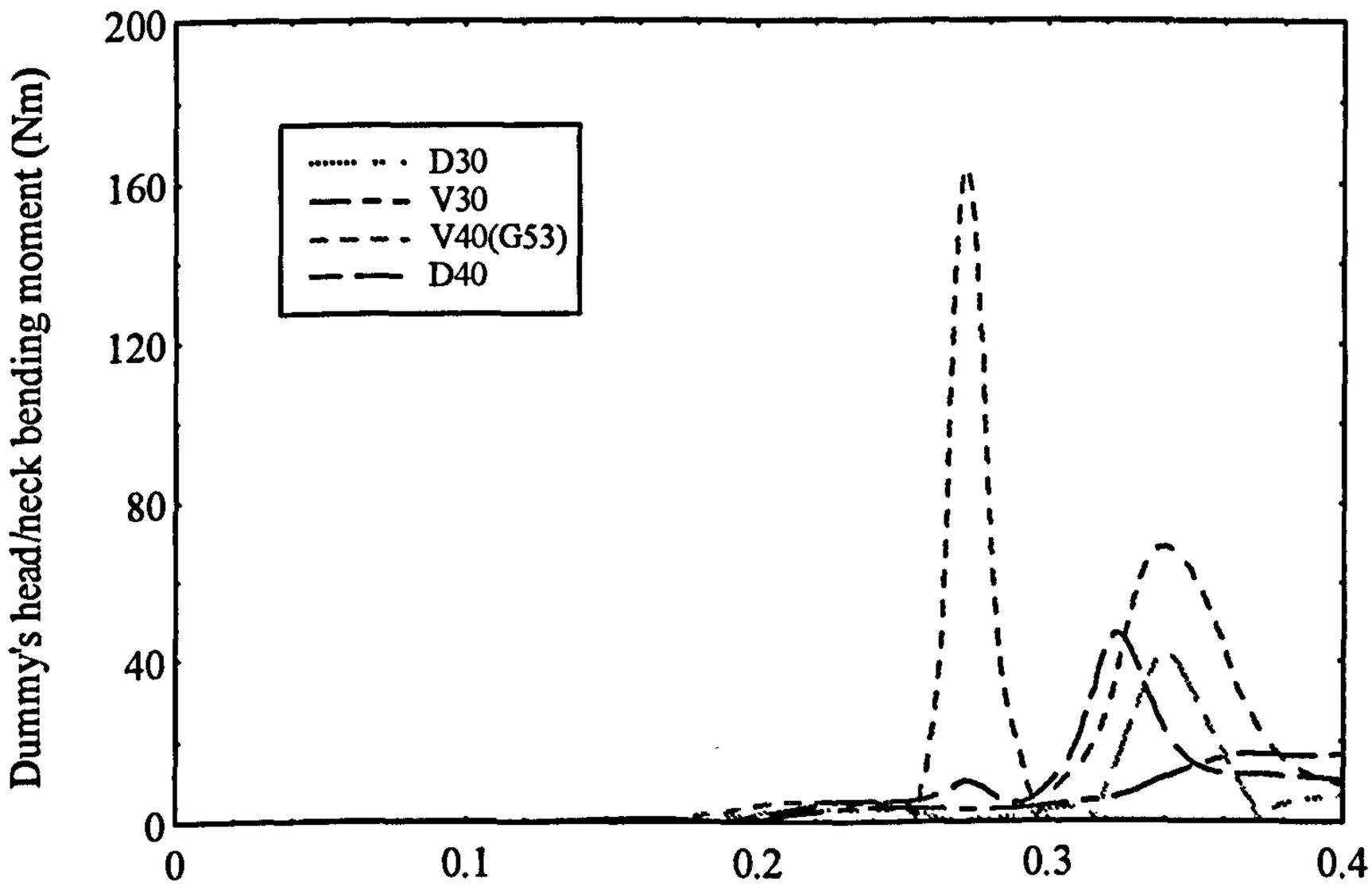

Figure 8.27 : Head/neck bending moment-time history for models in the D-series.

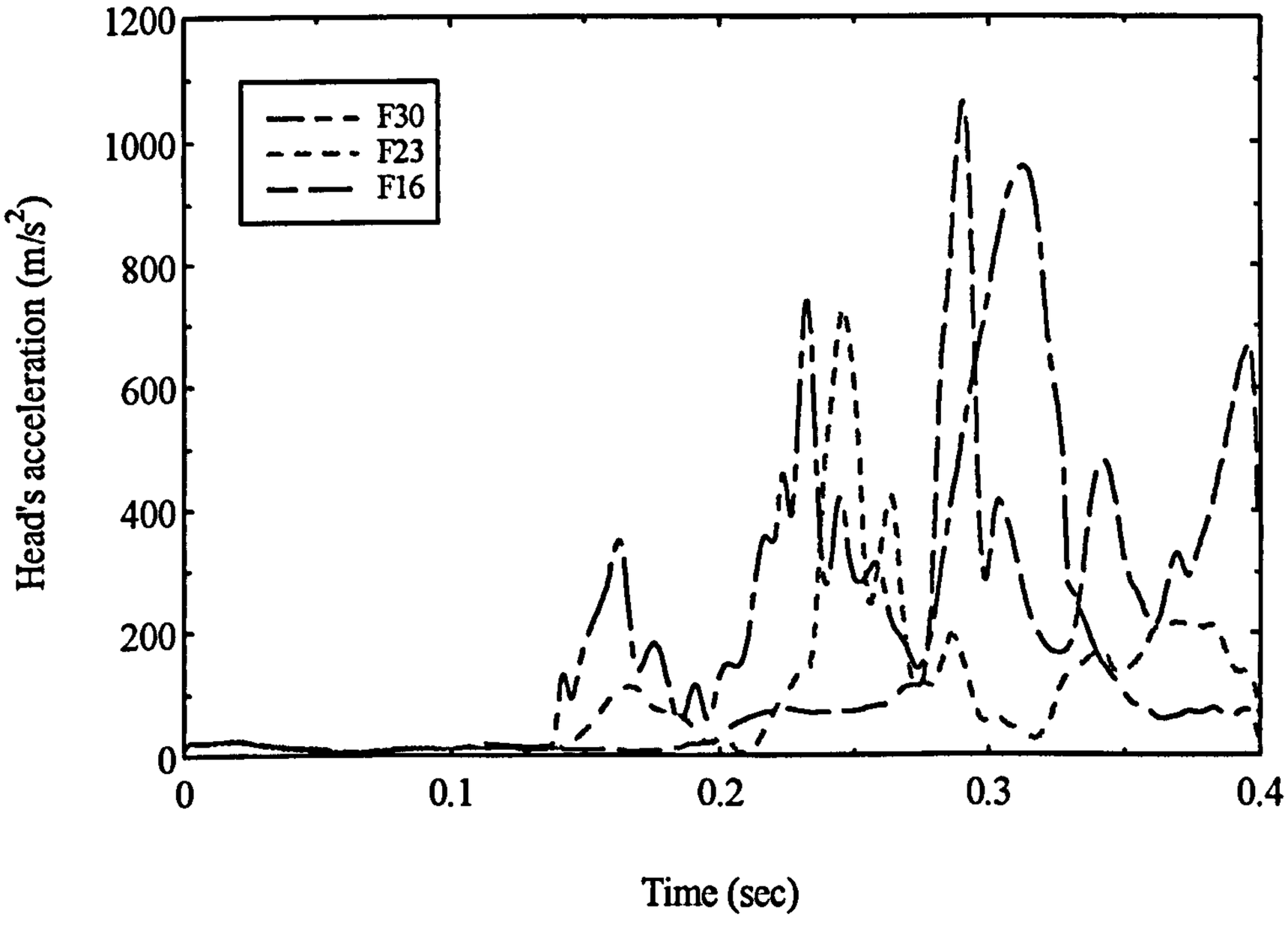

Figure 8.28 : Head acceleration-time history for models in the F-series.

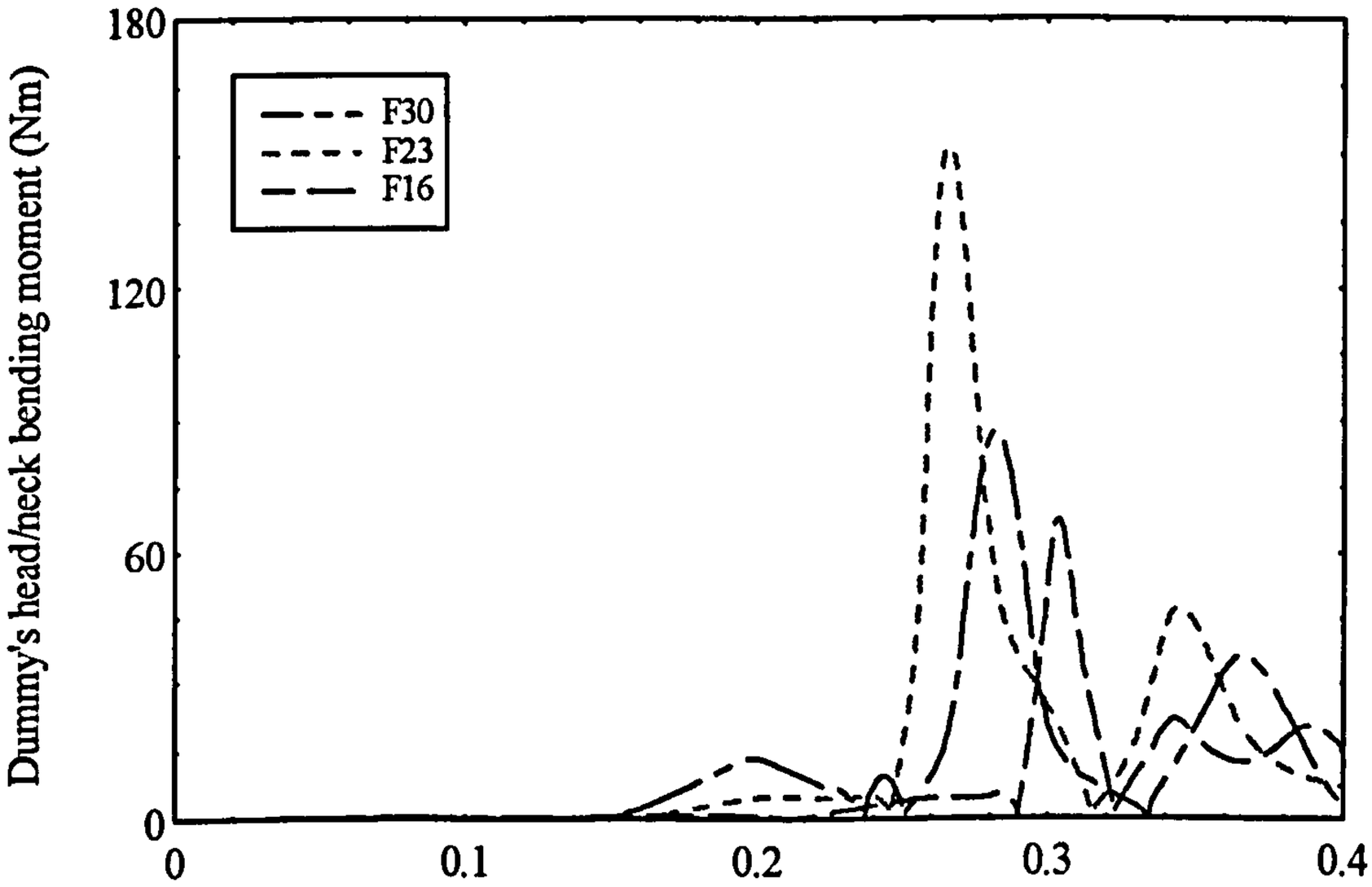

Figure 8.29 : Head/neck bending moment-time history for models in the F-series.

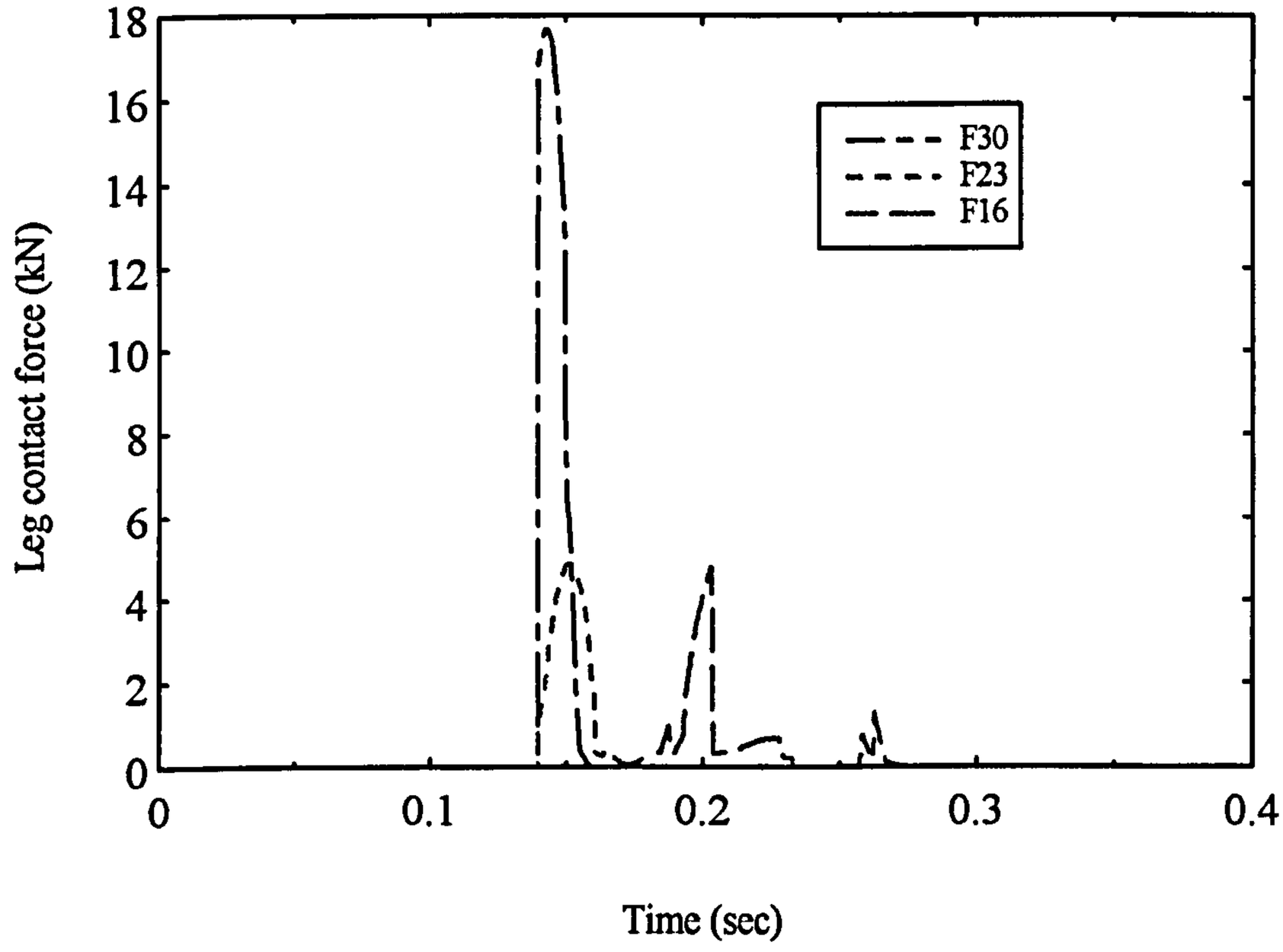

Figure 8.30 : Leg contact force-time history for models in the F-series.

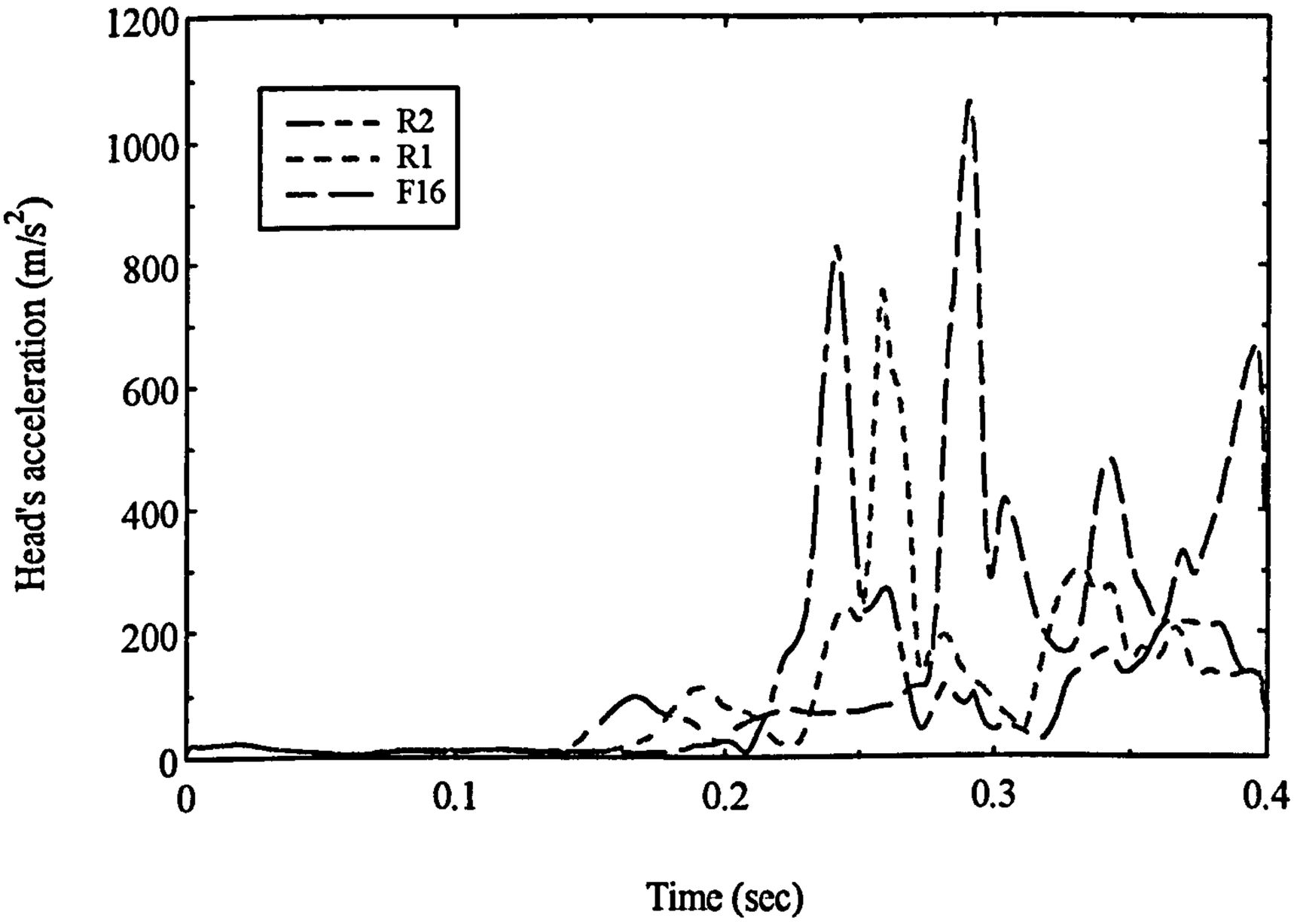

Figure 8.31 : Head acceleration-time history for models in the R-series.

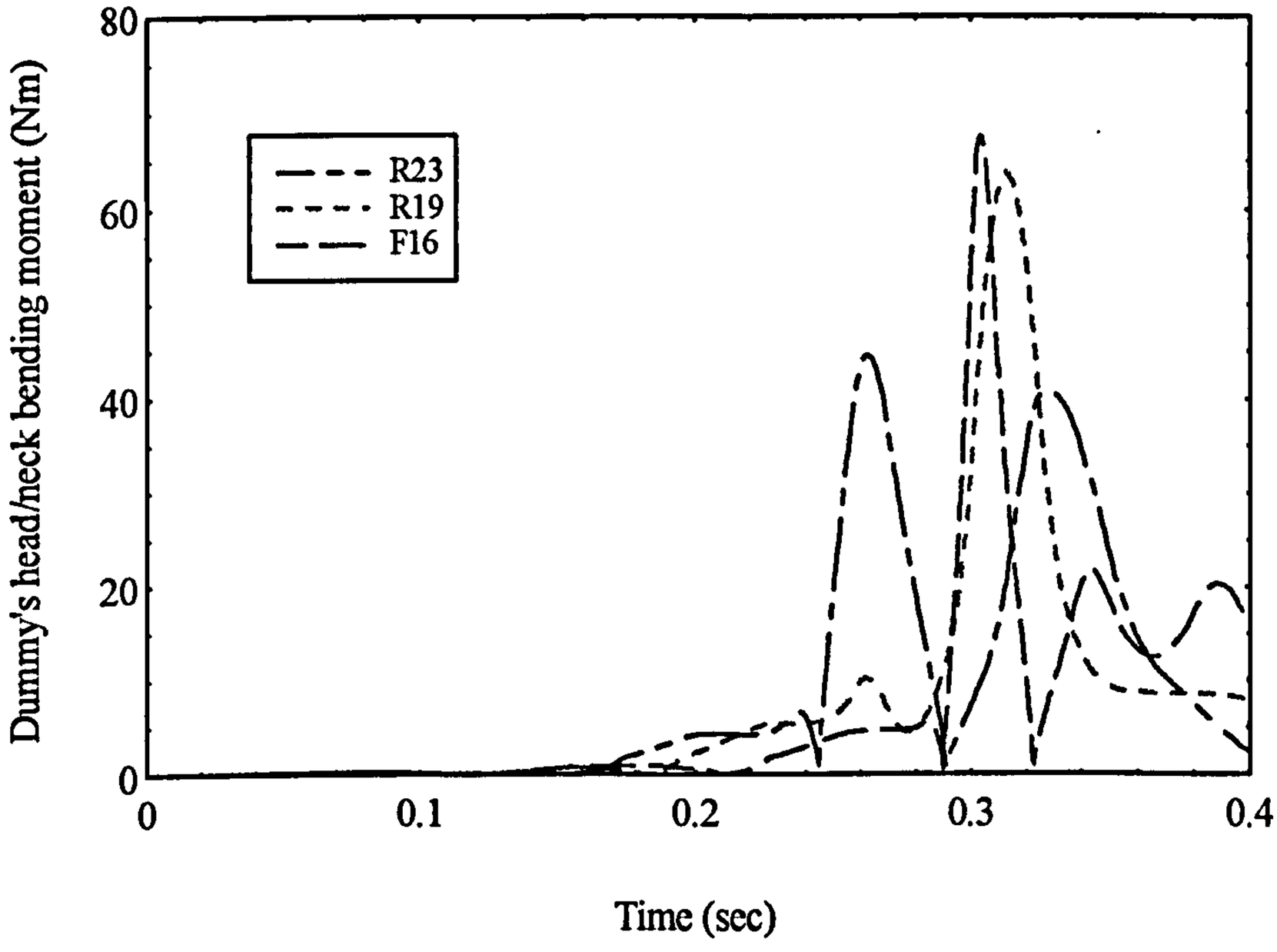

Figure 8.32 : Head/neck bending moment-time history for models in the R-series.

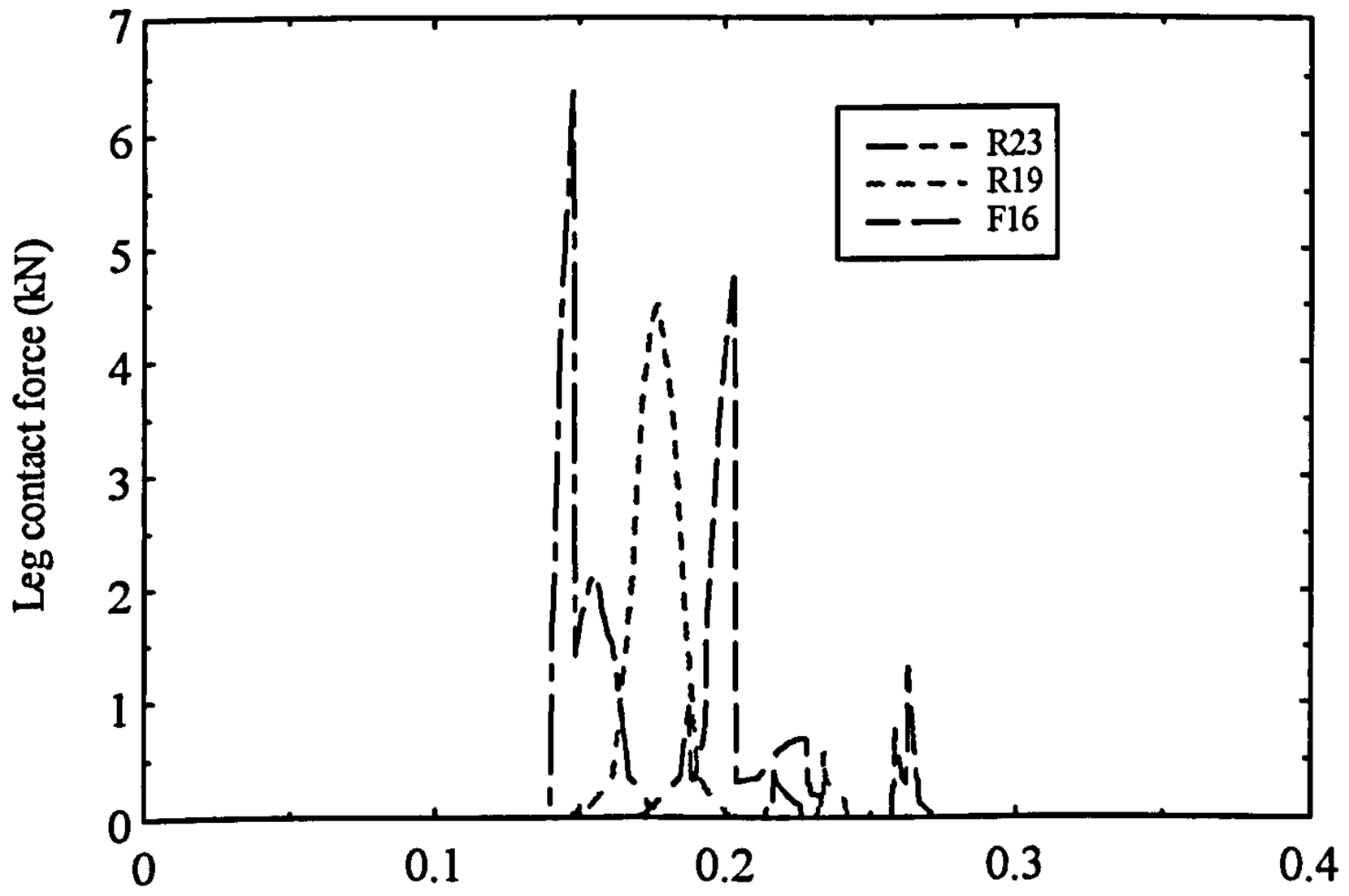

Figure 8.33 : Leg contact force-time history for models in the R-series.

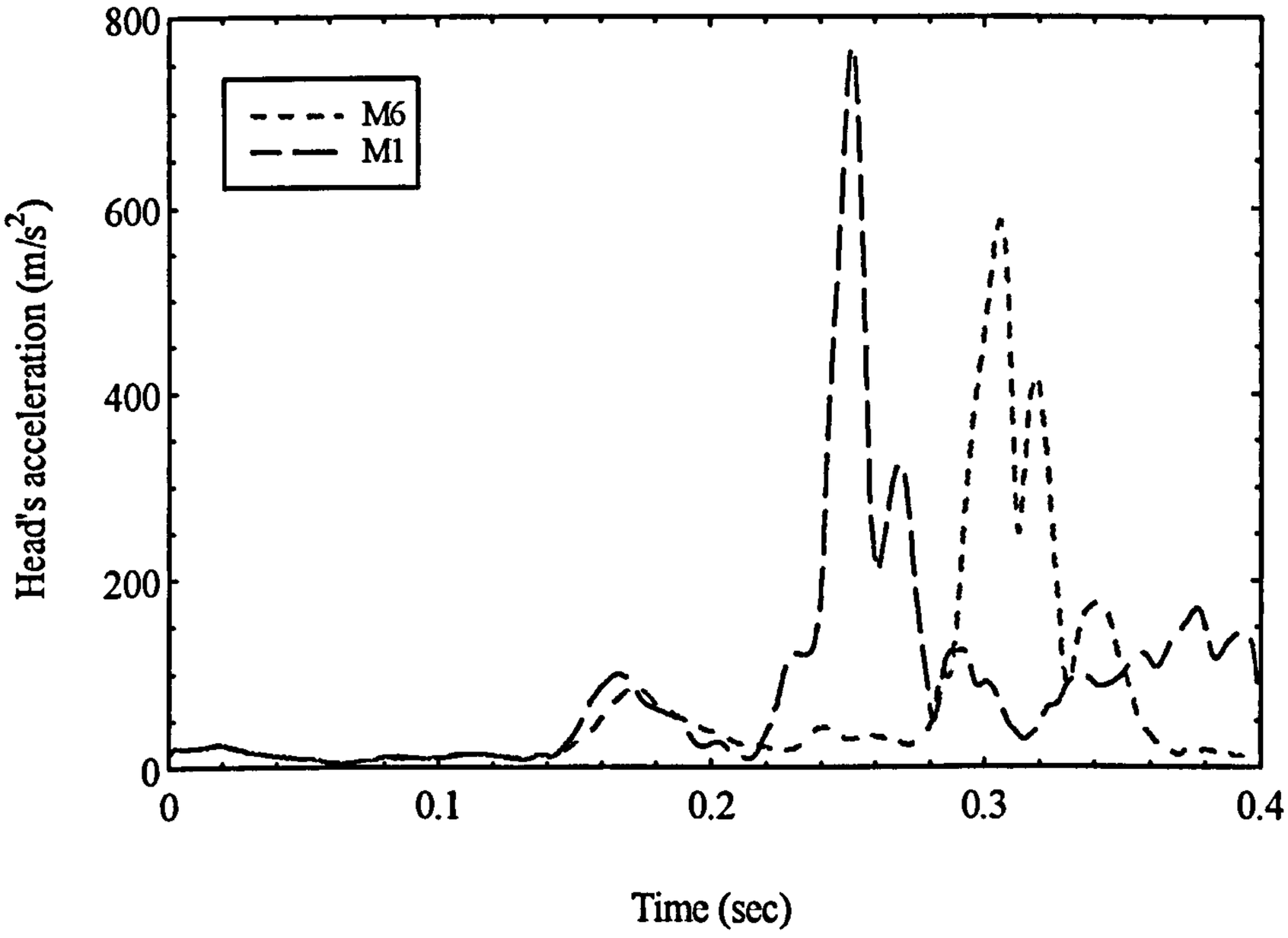

Figure 8.34 : Head acceleration-time history for models in the M-series.

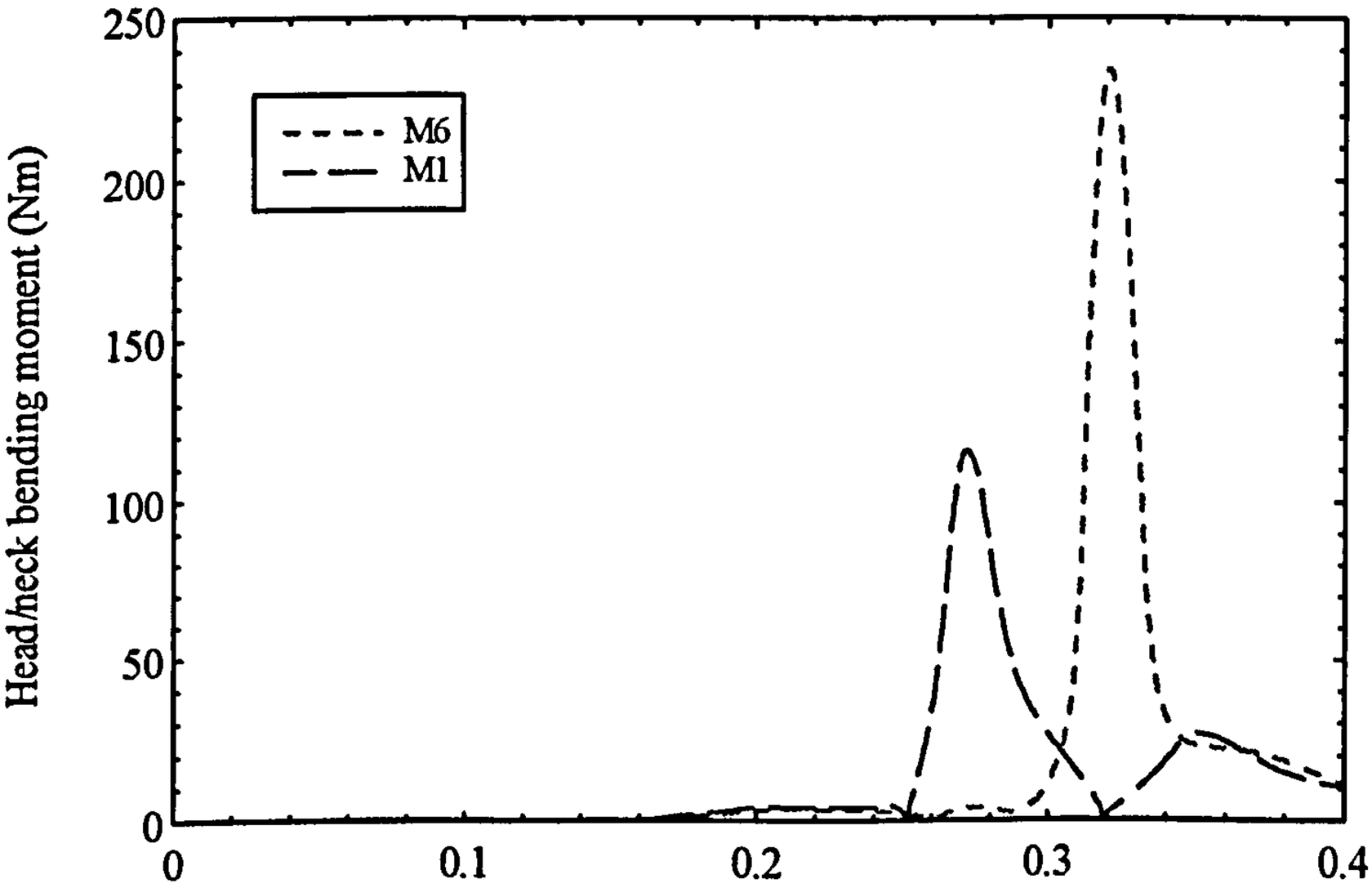

Figure 8.35 : Head/neck bending moment-time history for models in the M-series.

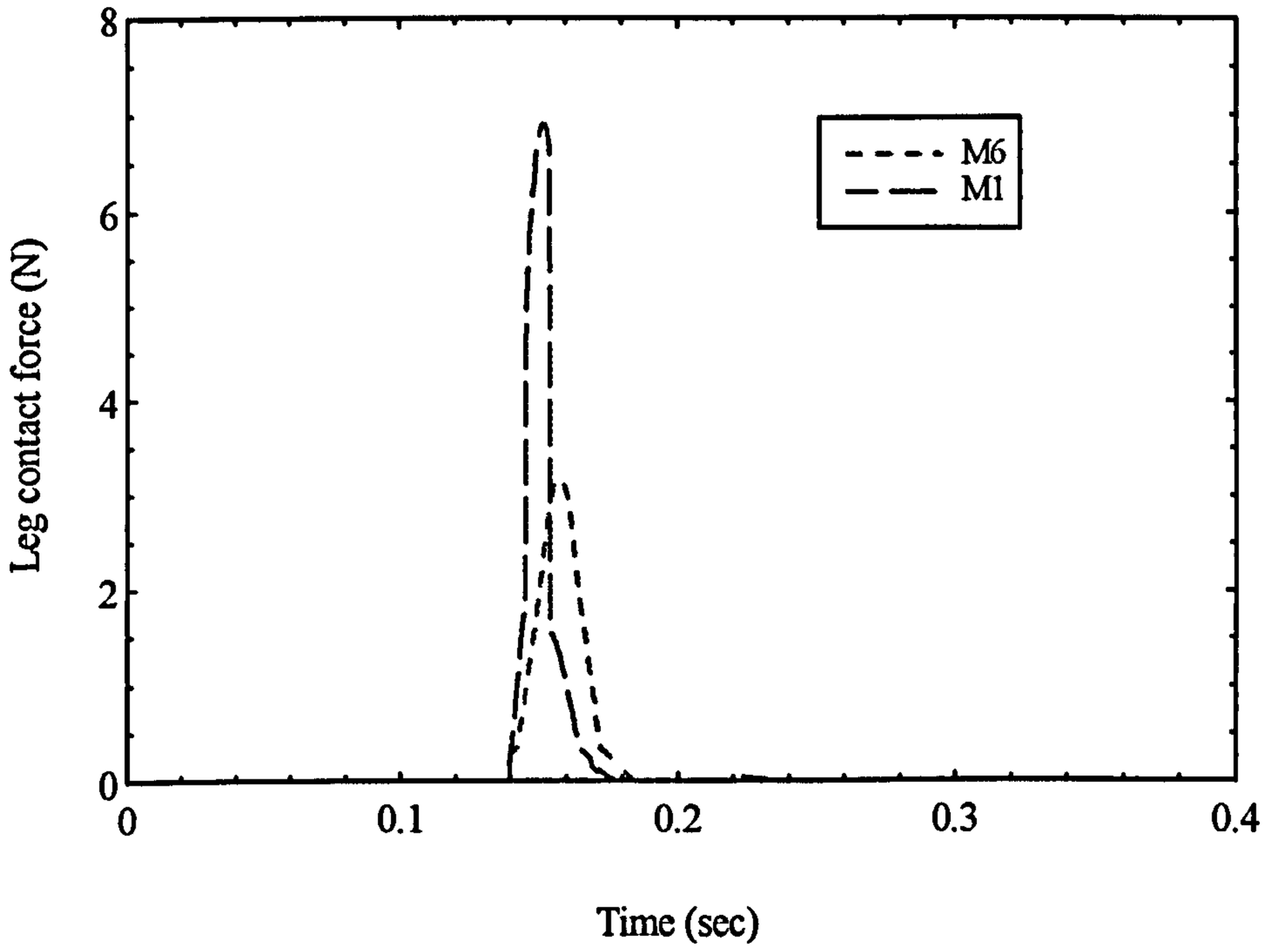

Figure 8.36 : Leg contact force-time history for models in the M-series.

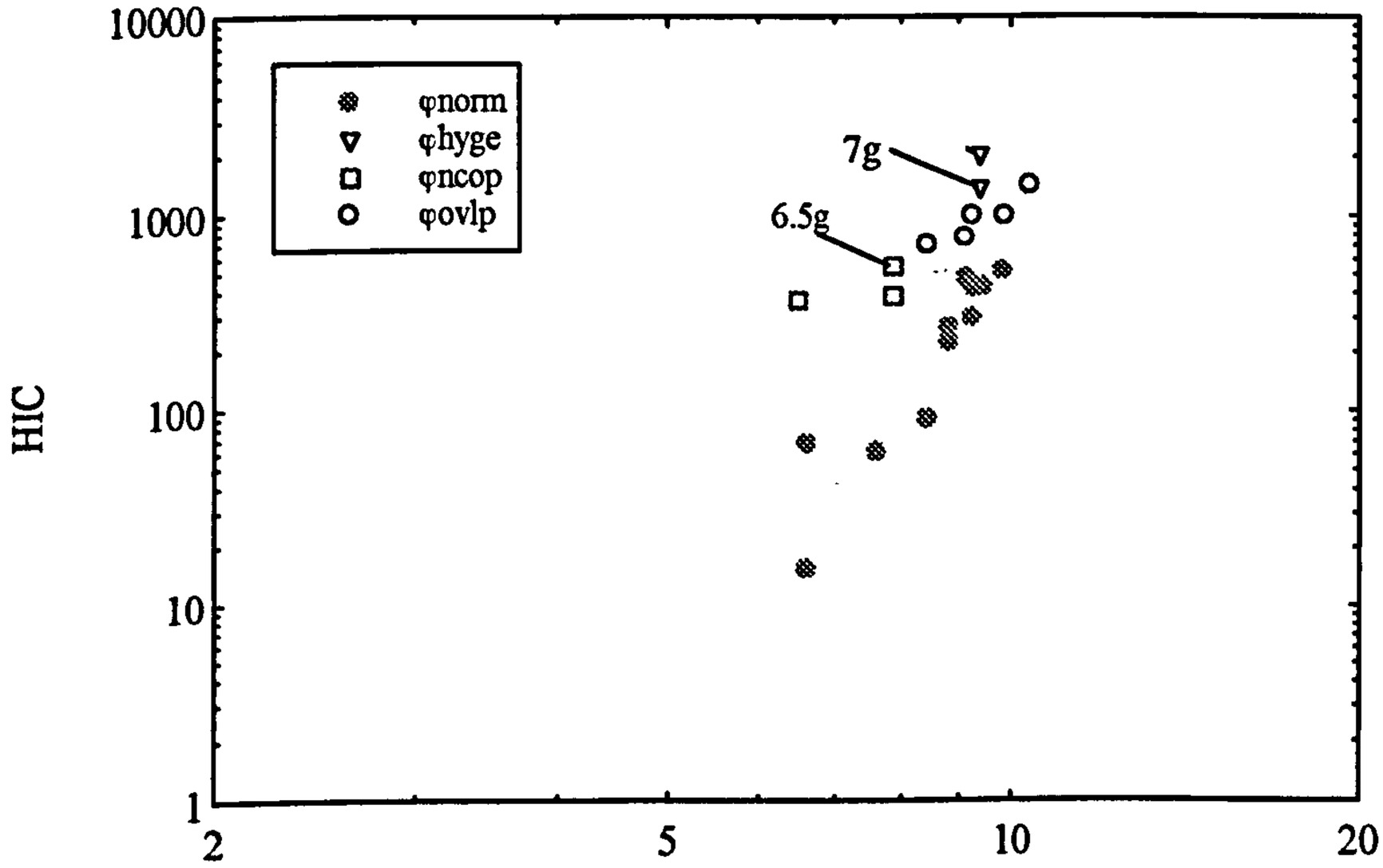

Figure 8.37 : log (HIC) against log (ΔV)

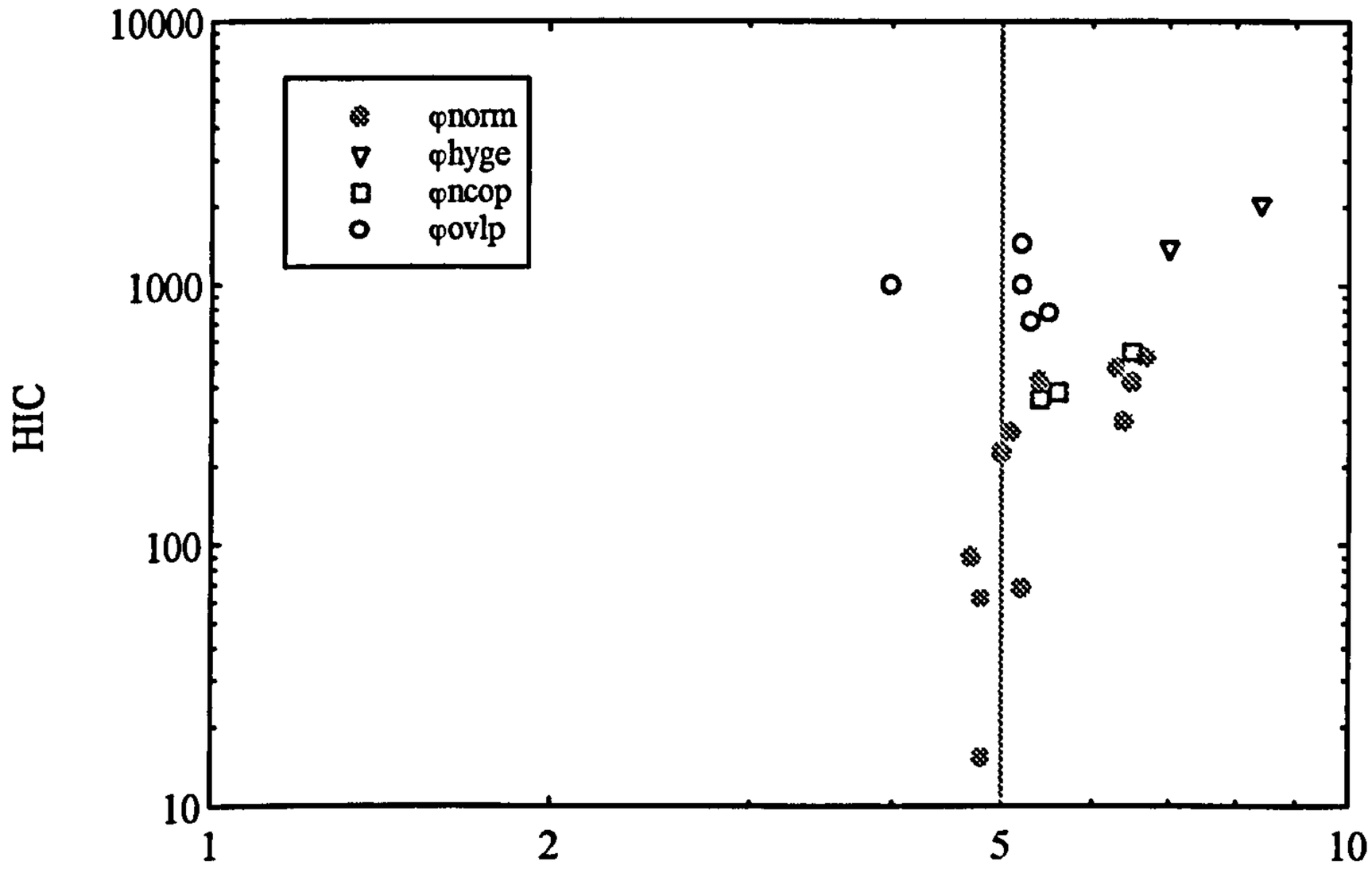

Figure 8.38 : log (HIC) against log (A_m)

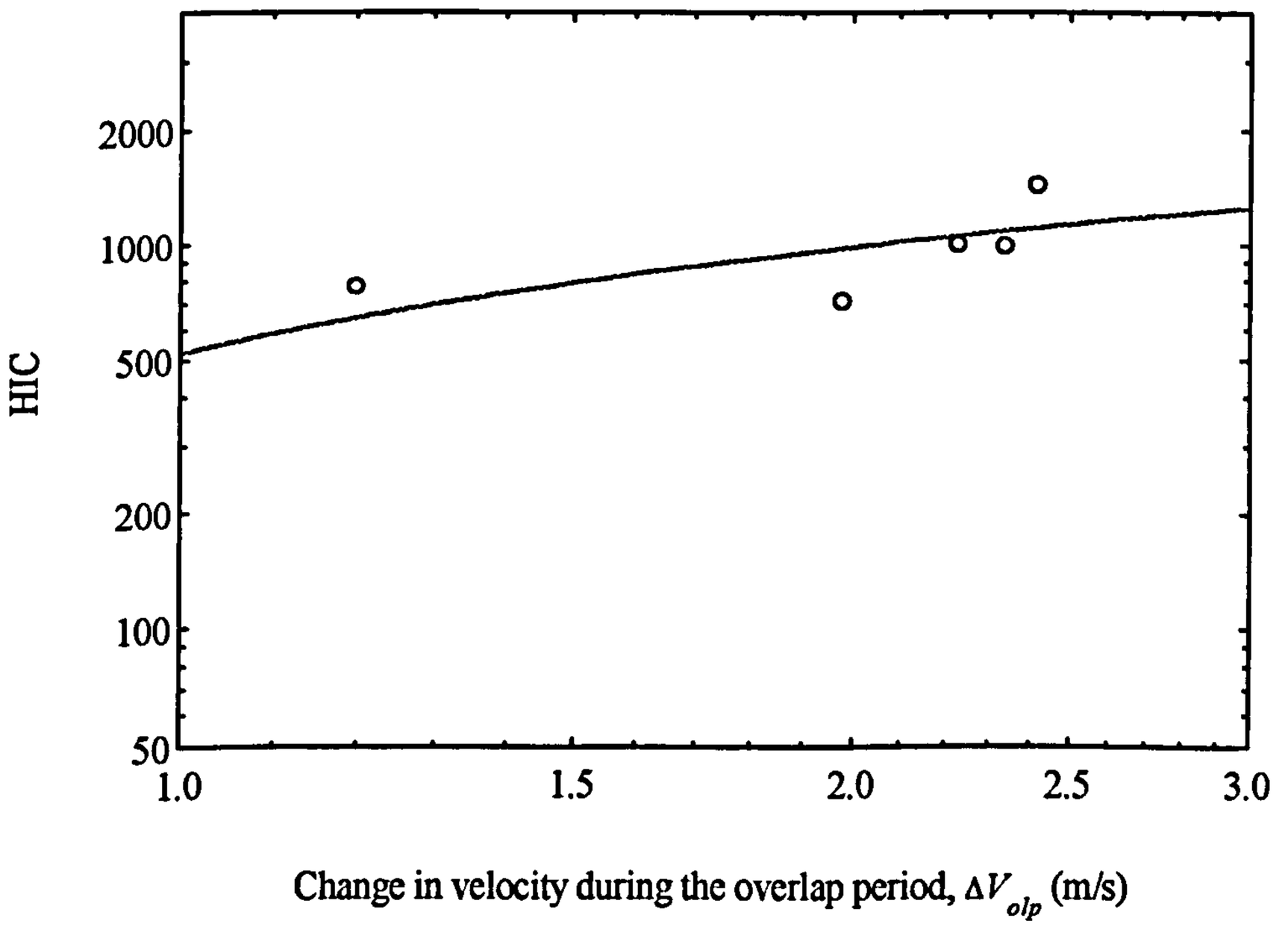

Figure 8.39 : log (HIC) against log (Δv_{olp}) for models in φovlp.

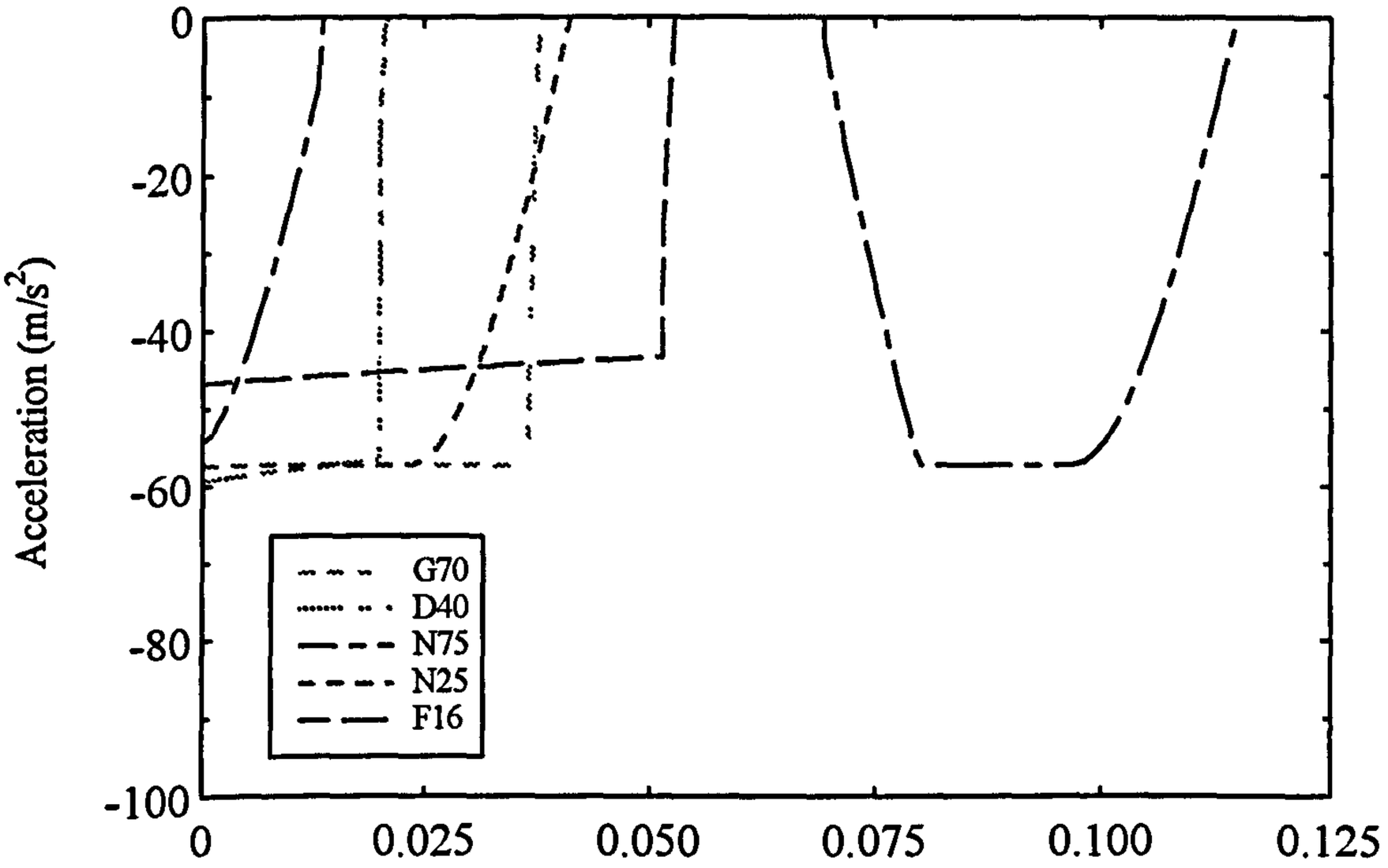

Figure 8.40 : The final portion of the acceleration pulses for models in φovlp during the 'overlapped' period.

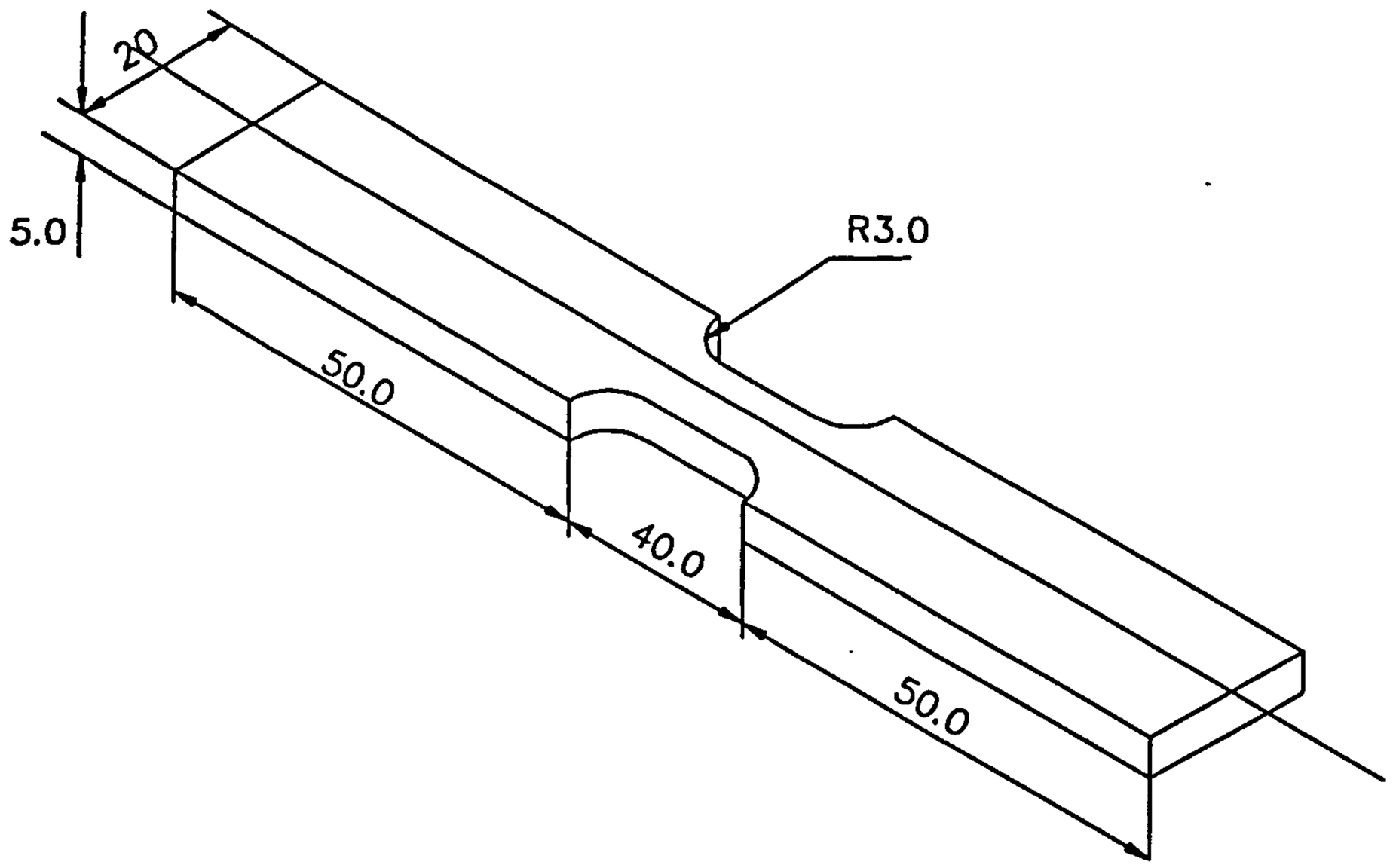

Figure A.1 : The geometry of tensile test specimens (all dimensions in mm).

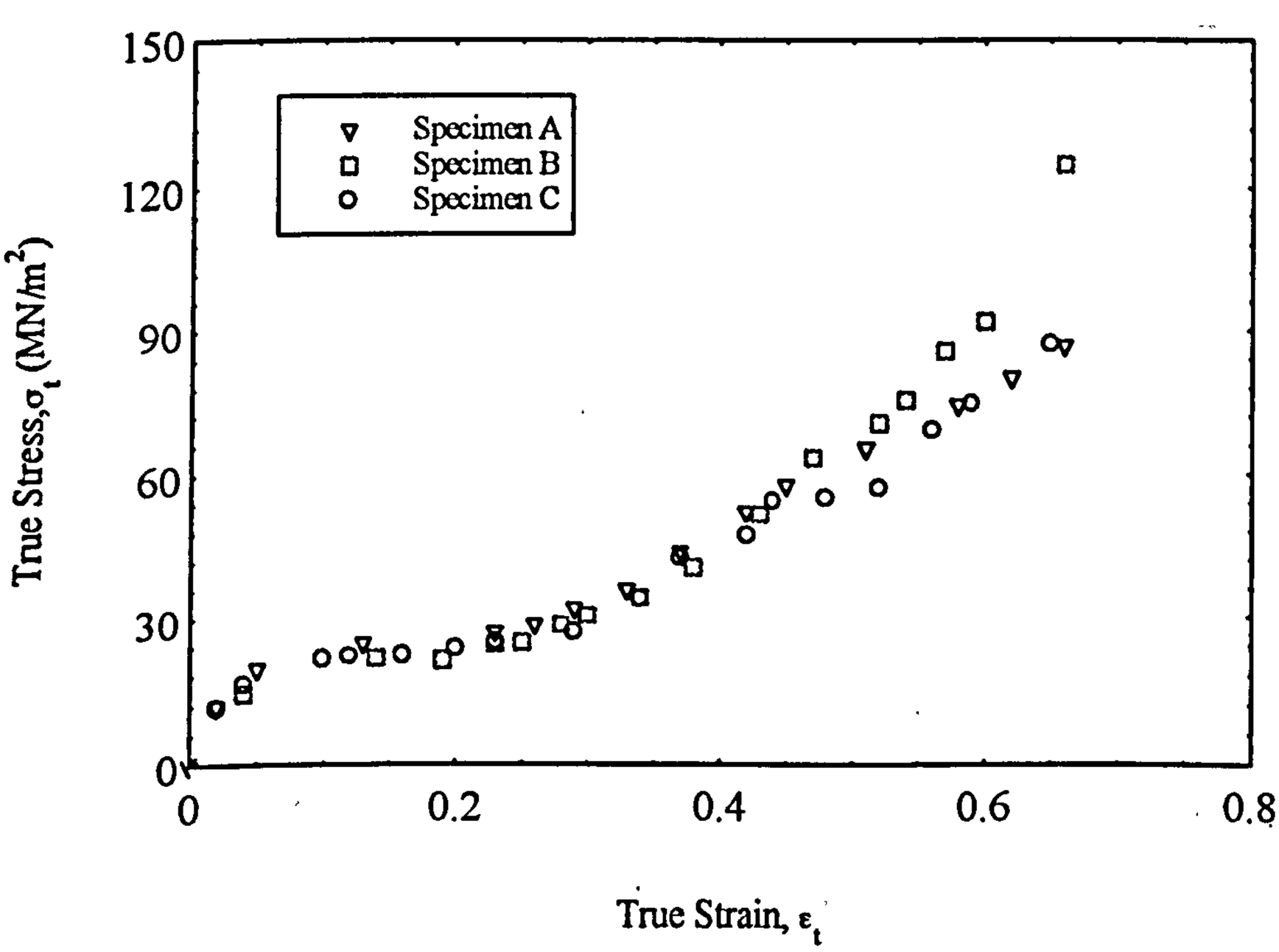

Figure A.2 : The True Stress against True Strain curves for three specimens tested.

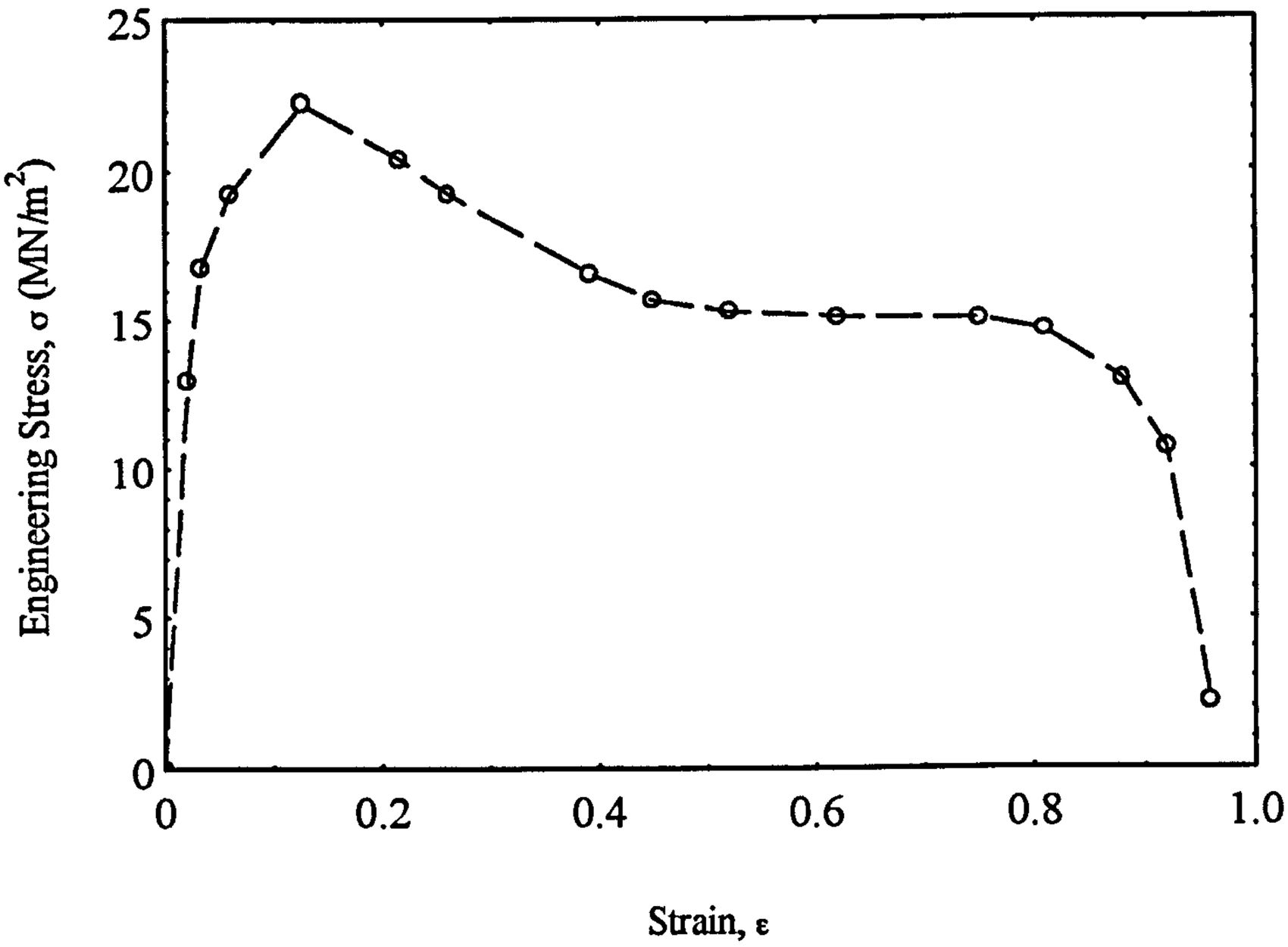

Figure A.3 : The Engineering Stress-Strain Curve for a tested specimen.

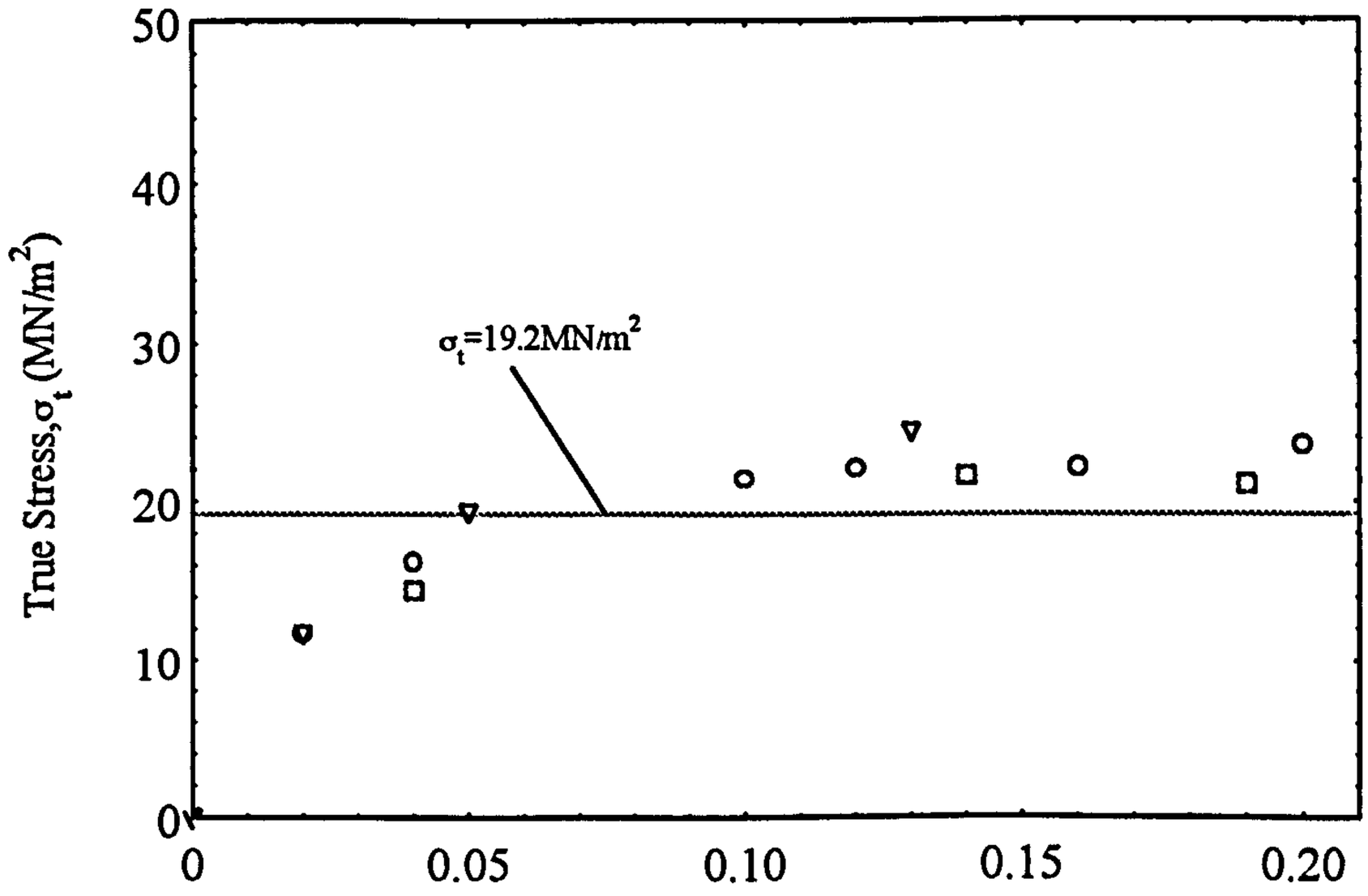

Figure A.4 : The 'plateau' during the early stage of plastic deformation, with a perfectly plastic line fitted as 19.2MN/m^2.

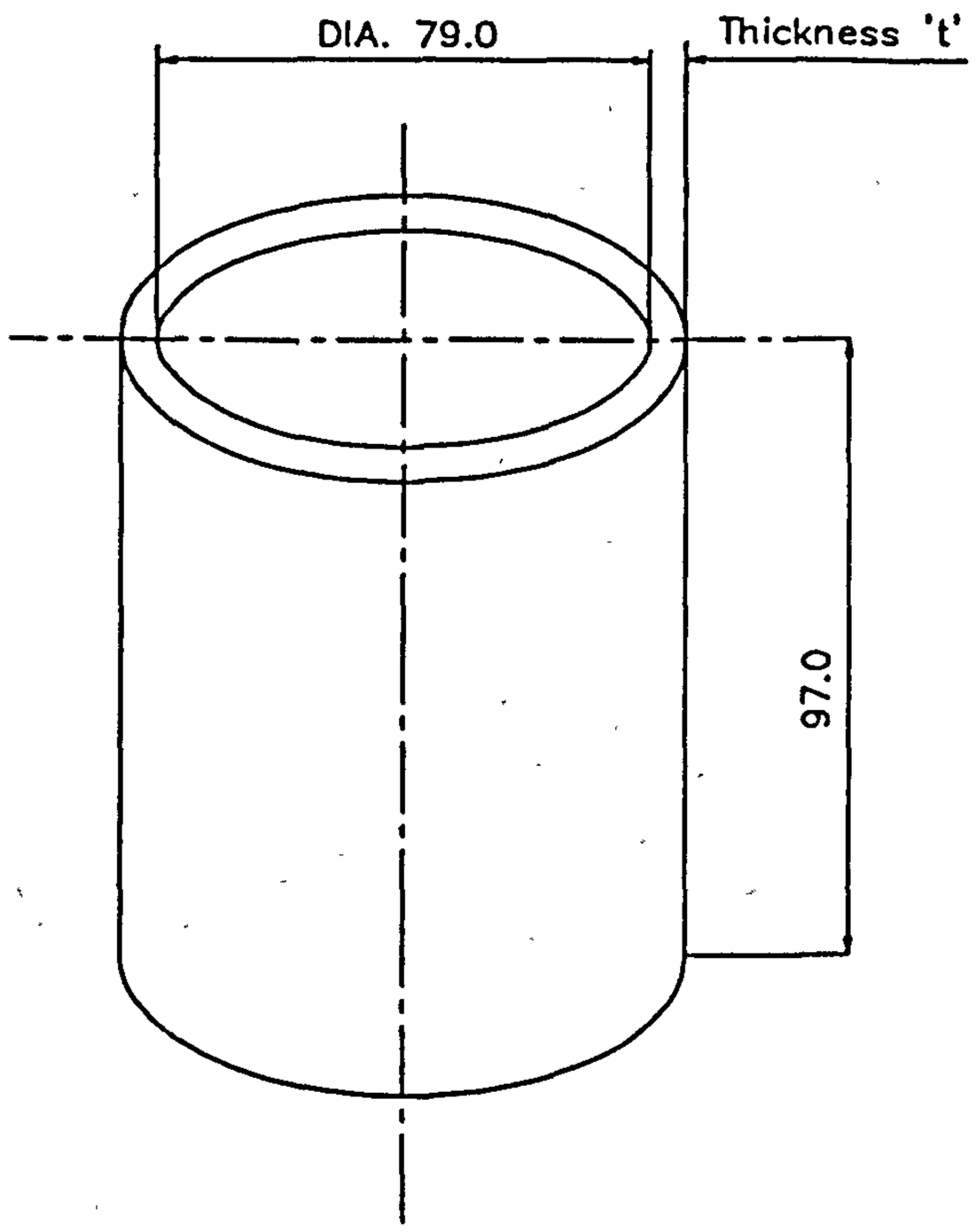

Figure A.5 : The geometry of crush specimens.

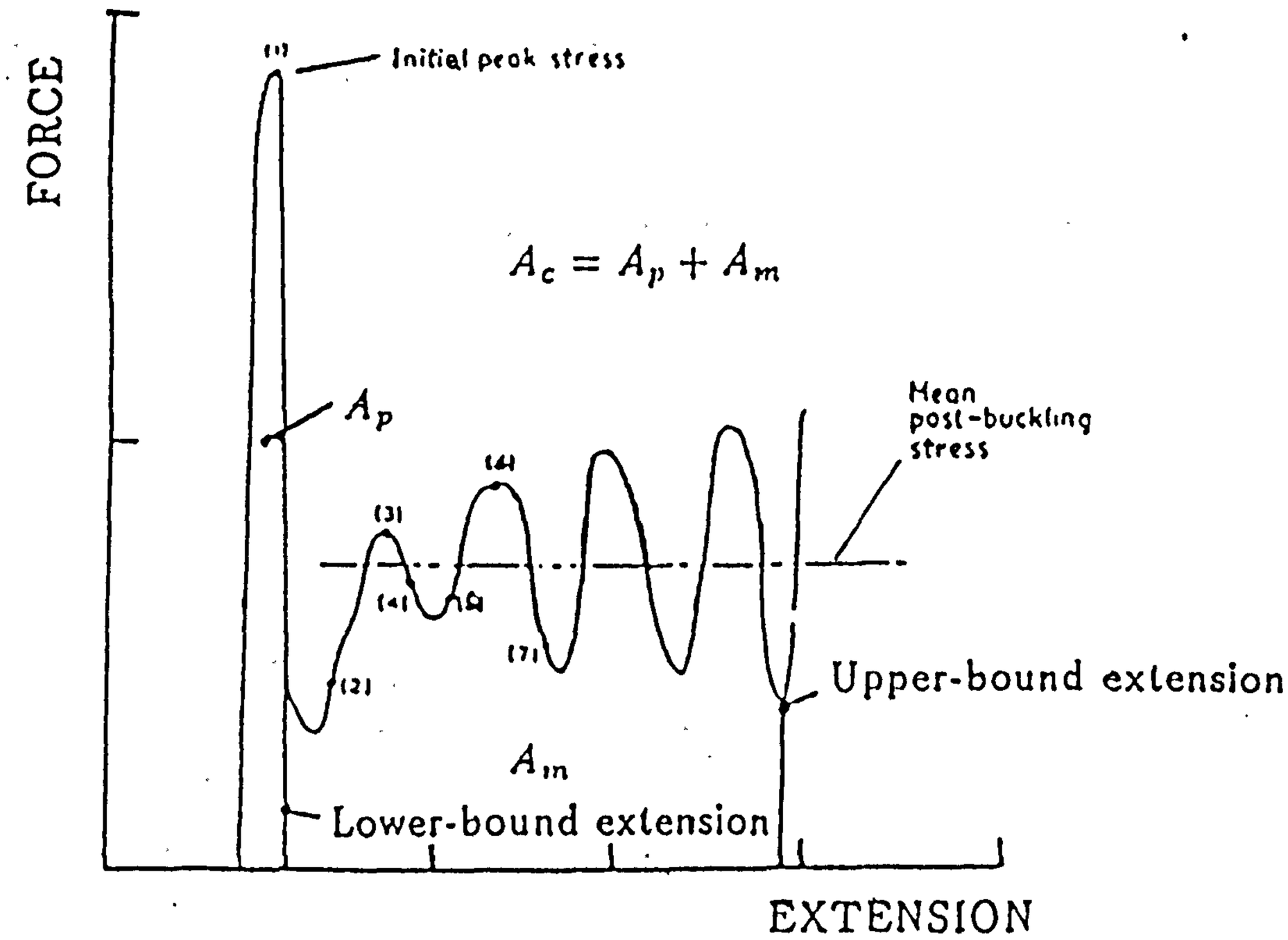

Figure A.6 : The interpretation of mean post buckling load and energy absorbed from an experimental load-deflection graph.

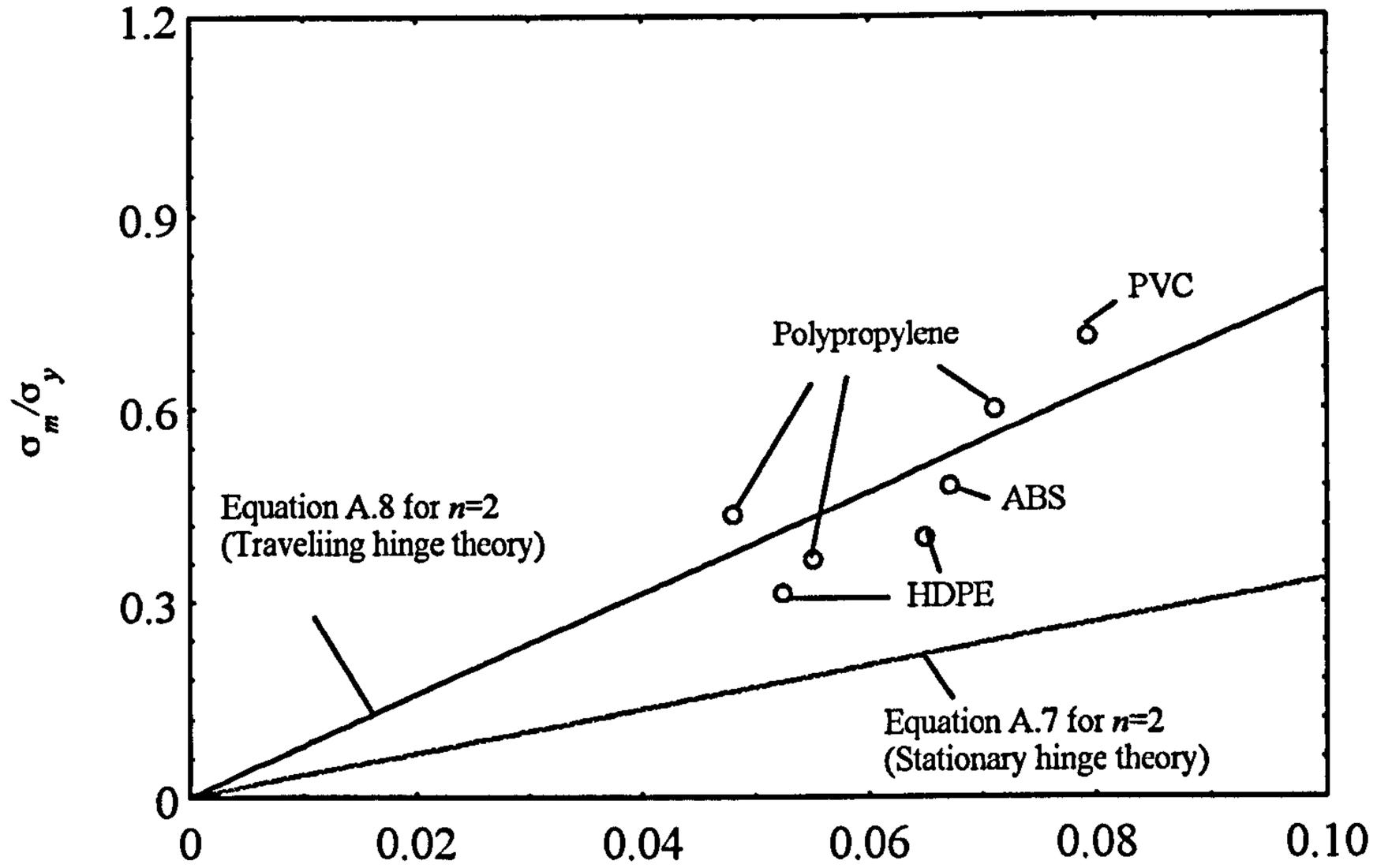

Figure A.7 : Experimental data for various polymeric tubes with n=2, with Johnson *et. al.* theoretical lines superimposed.

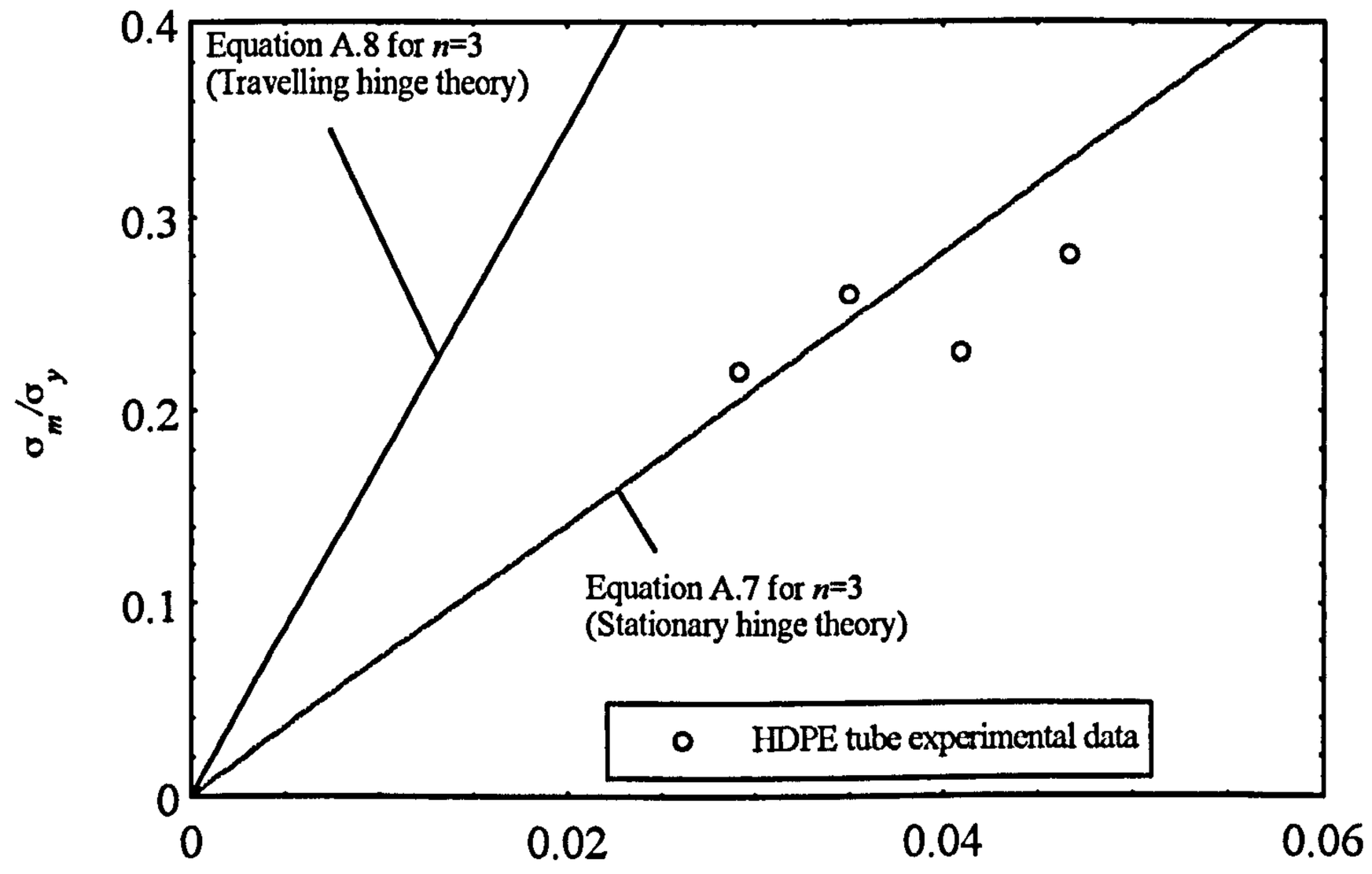

Figure A.8 : Experimental data for HDPE tubes with n=3, with Johnson *et. al.* theoretical lines superimposed.

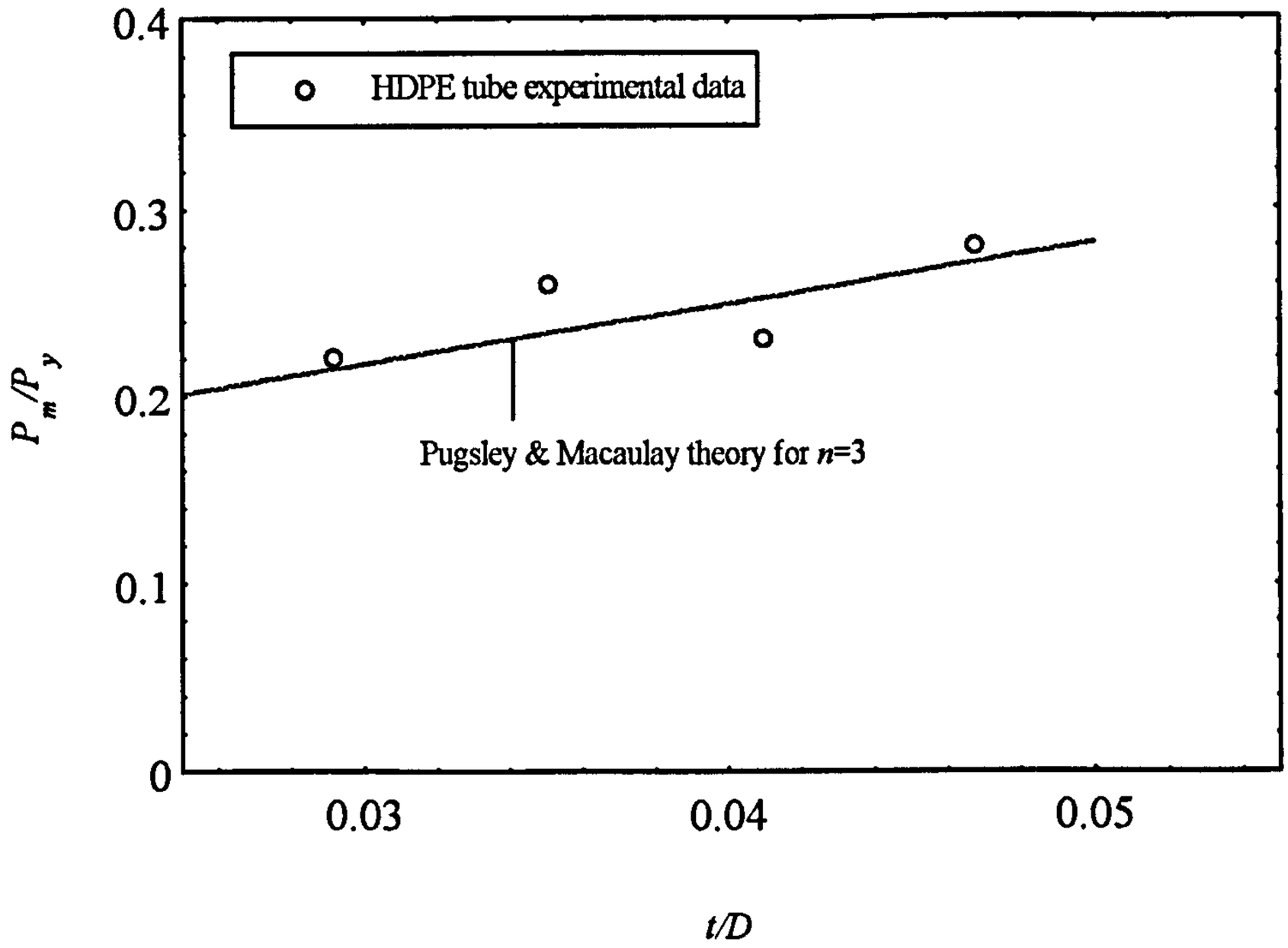

Figure A.9 : Experimental data for HDPE tubes with n=3, with Pugsley and Macaulay theoretical line superimposed.

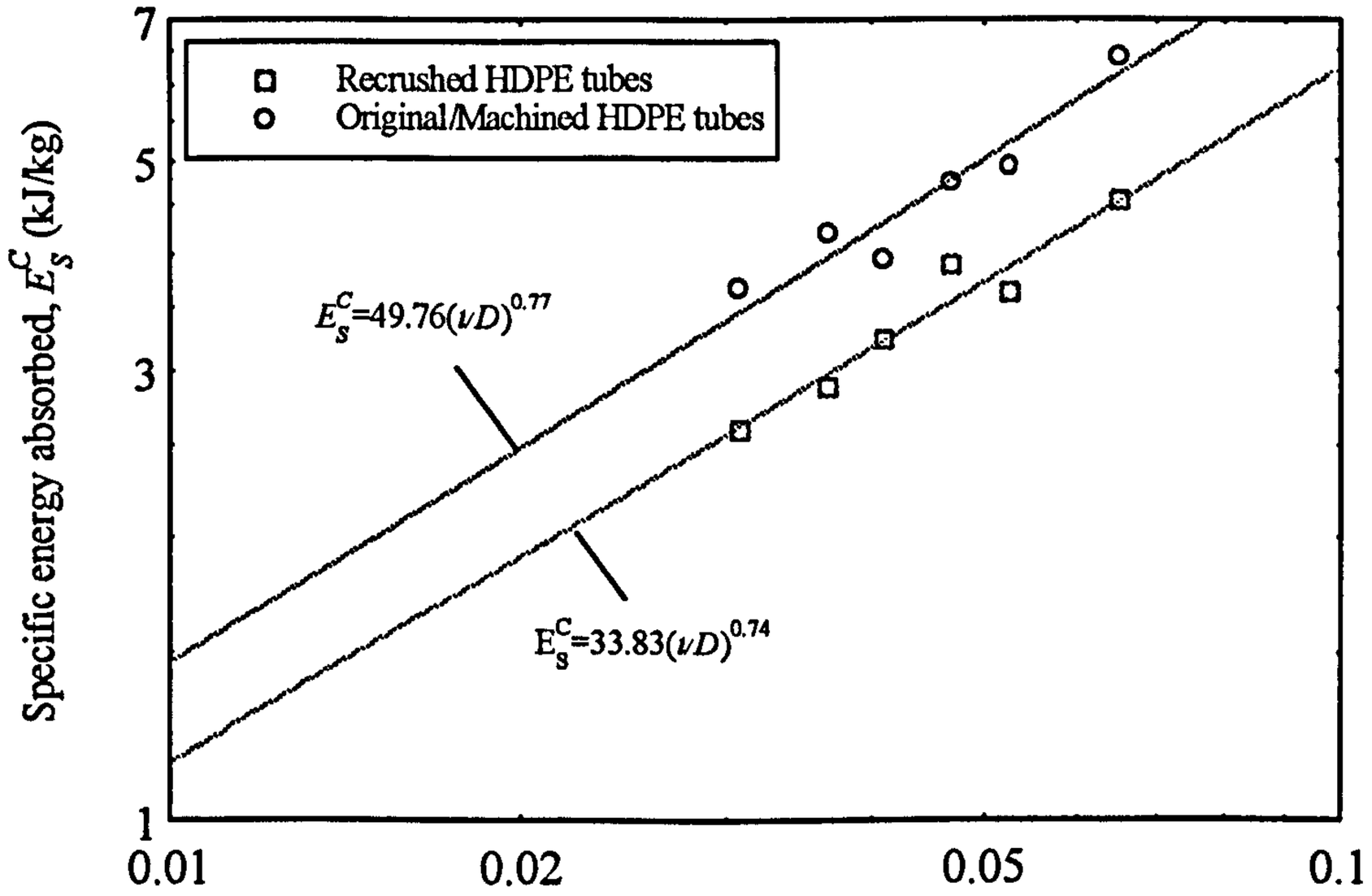

Figure A.10 : The log-log plot of specific energy absorbed against t/D, as recommended by Thornton and Magee [5].

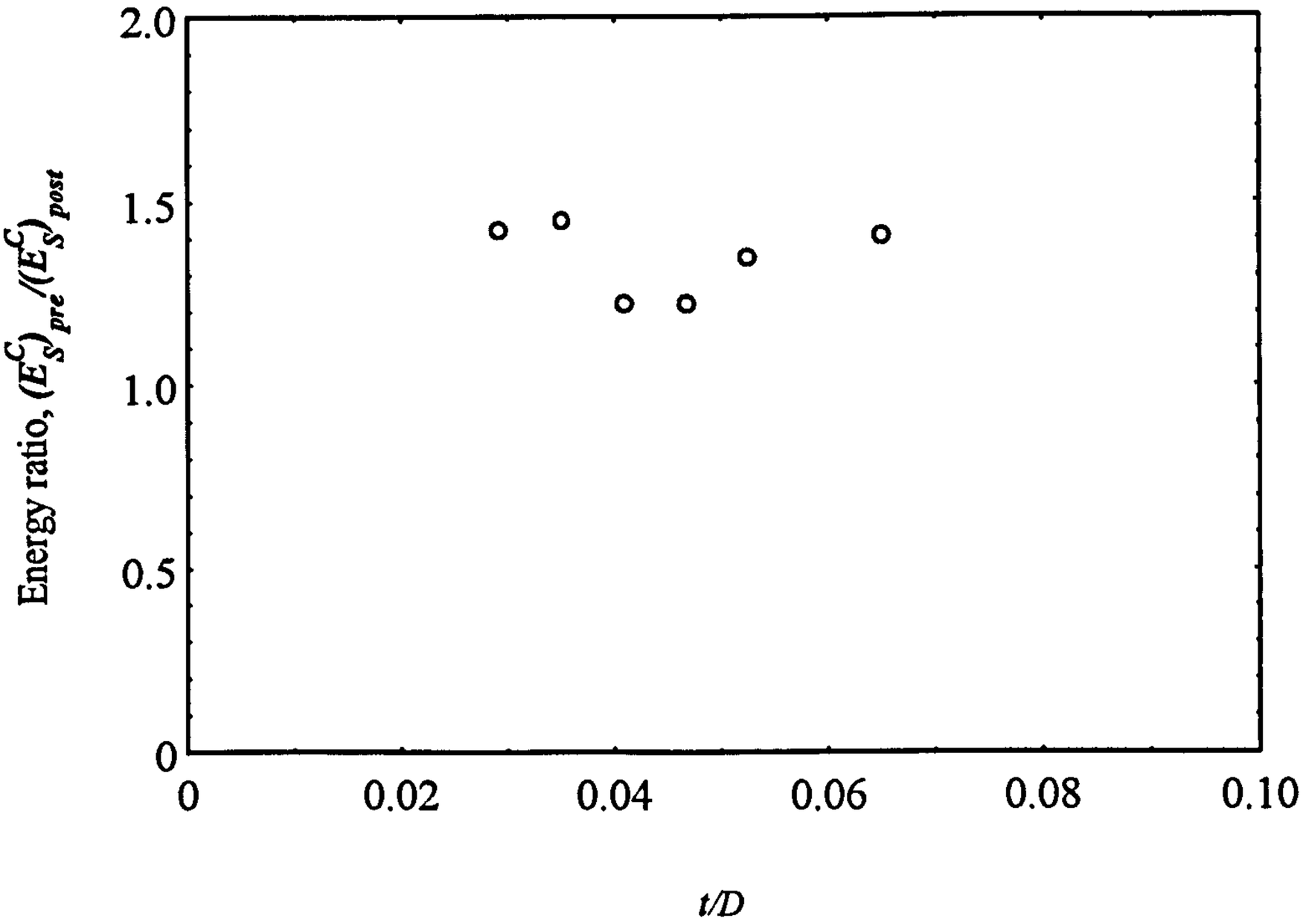

Figure A.11 : Energy ratio against *t/D*. This graph suggests that the loss in energy dissipation for recycled tubes is independent of *t/D* of the tubes.

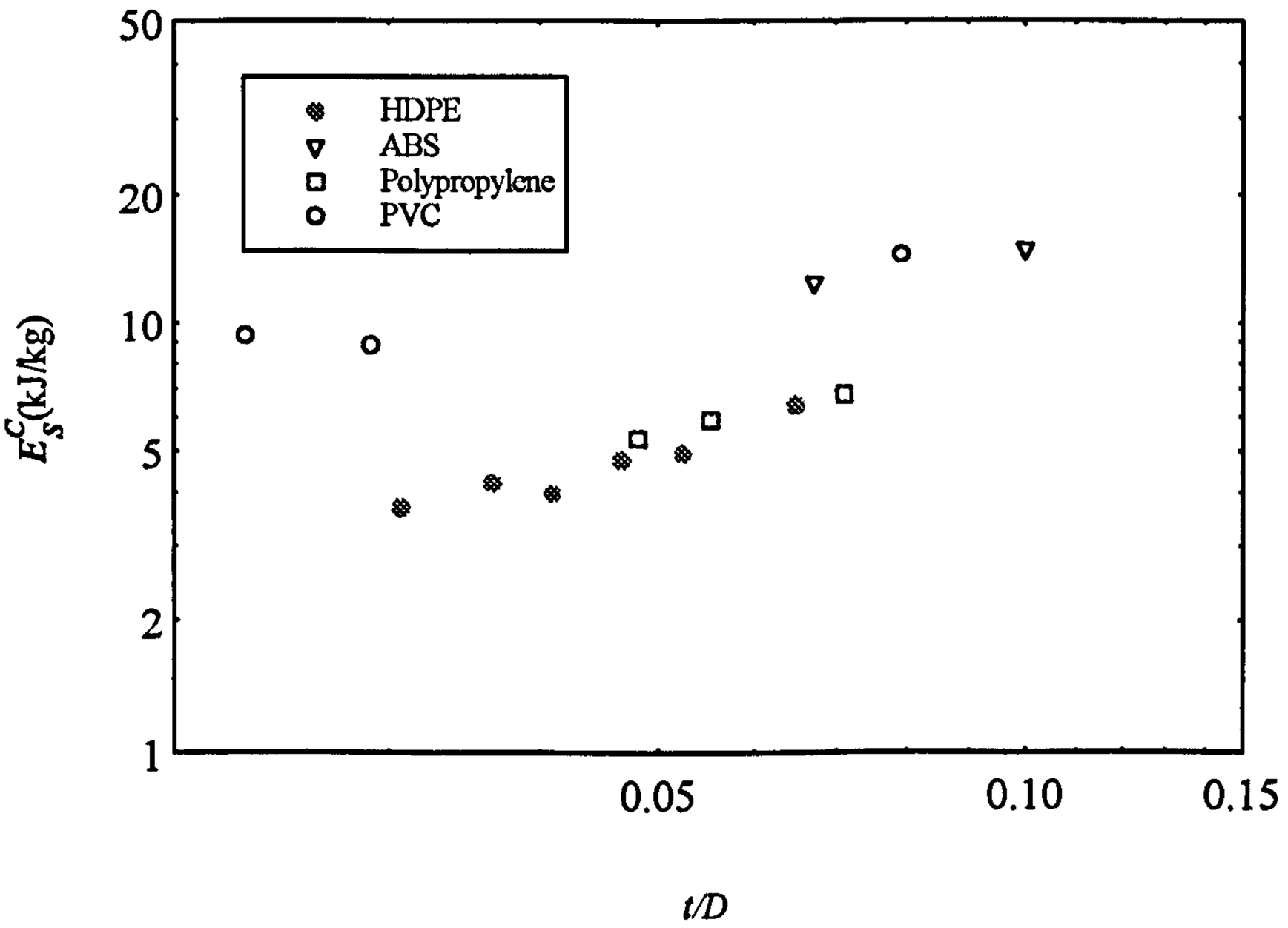

Figure A.12 : The log-log graphs of E_S^C against *t/D* for various polymeric tubes tested by Morgan [1] and the author.

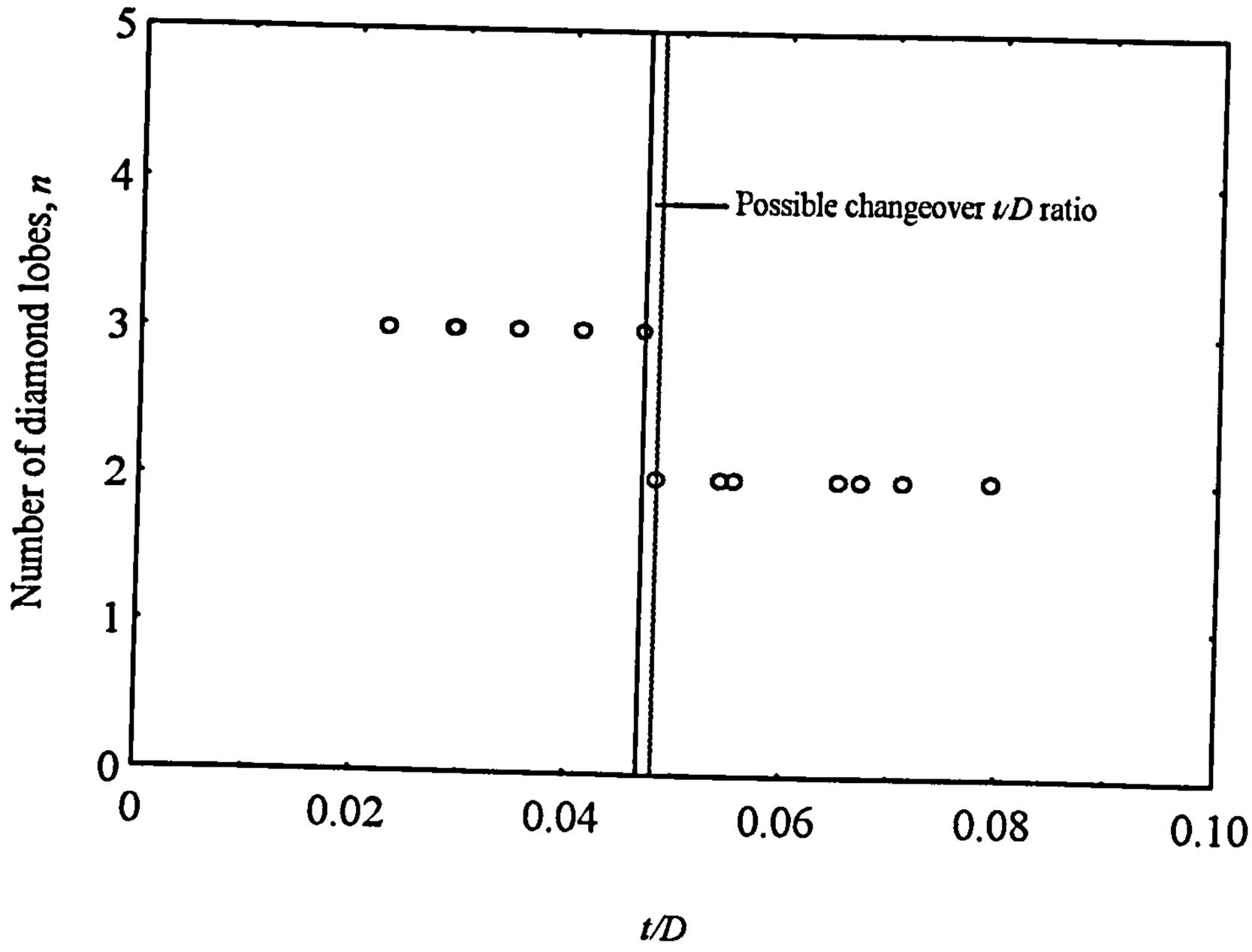

Figure A.13 : Number of diamond lobes against *t/D*.

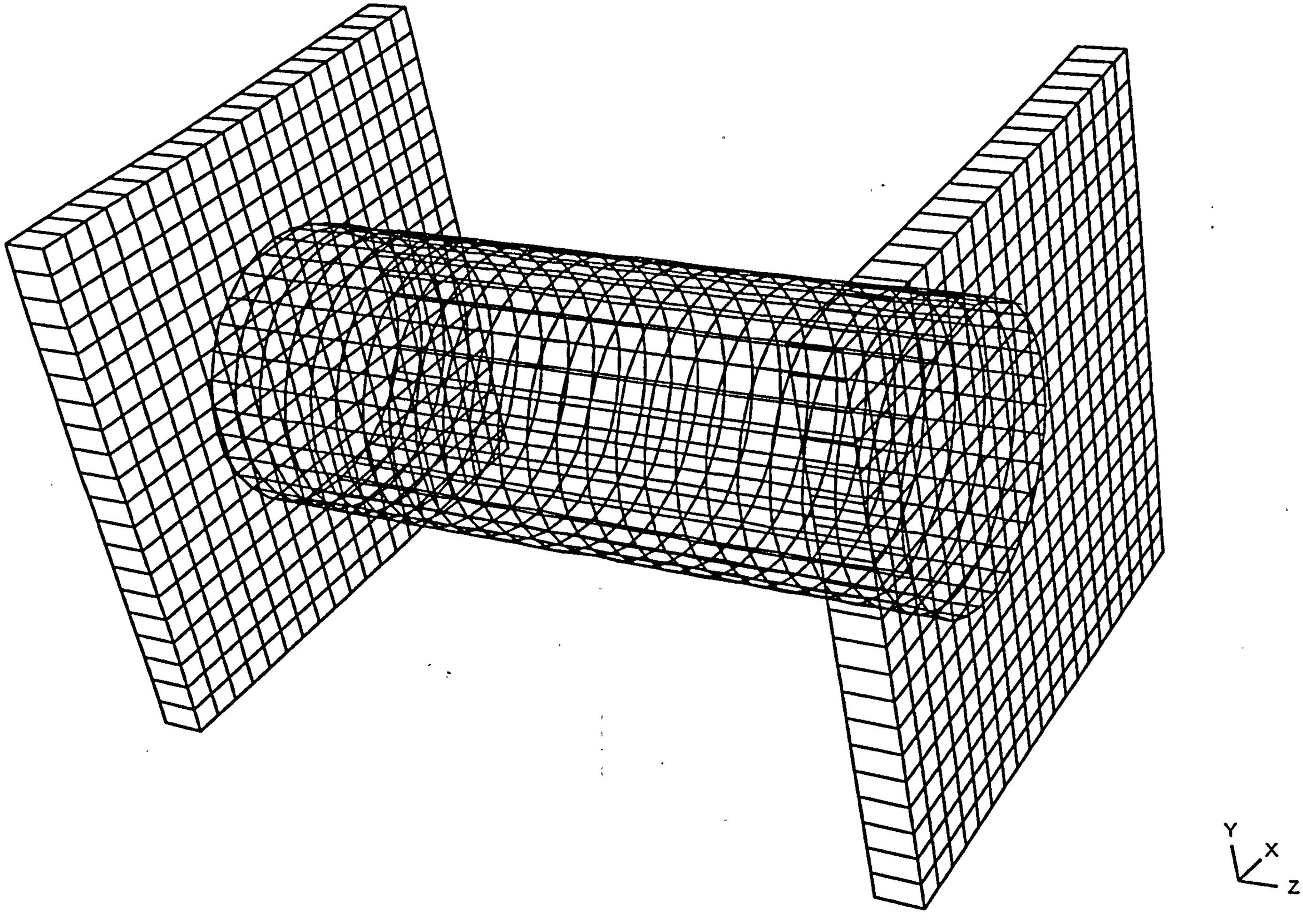

Figure B.1 : The model set-up for HDPE-true and HDPE-bilinear.

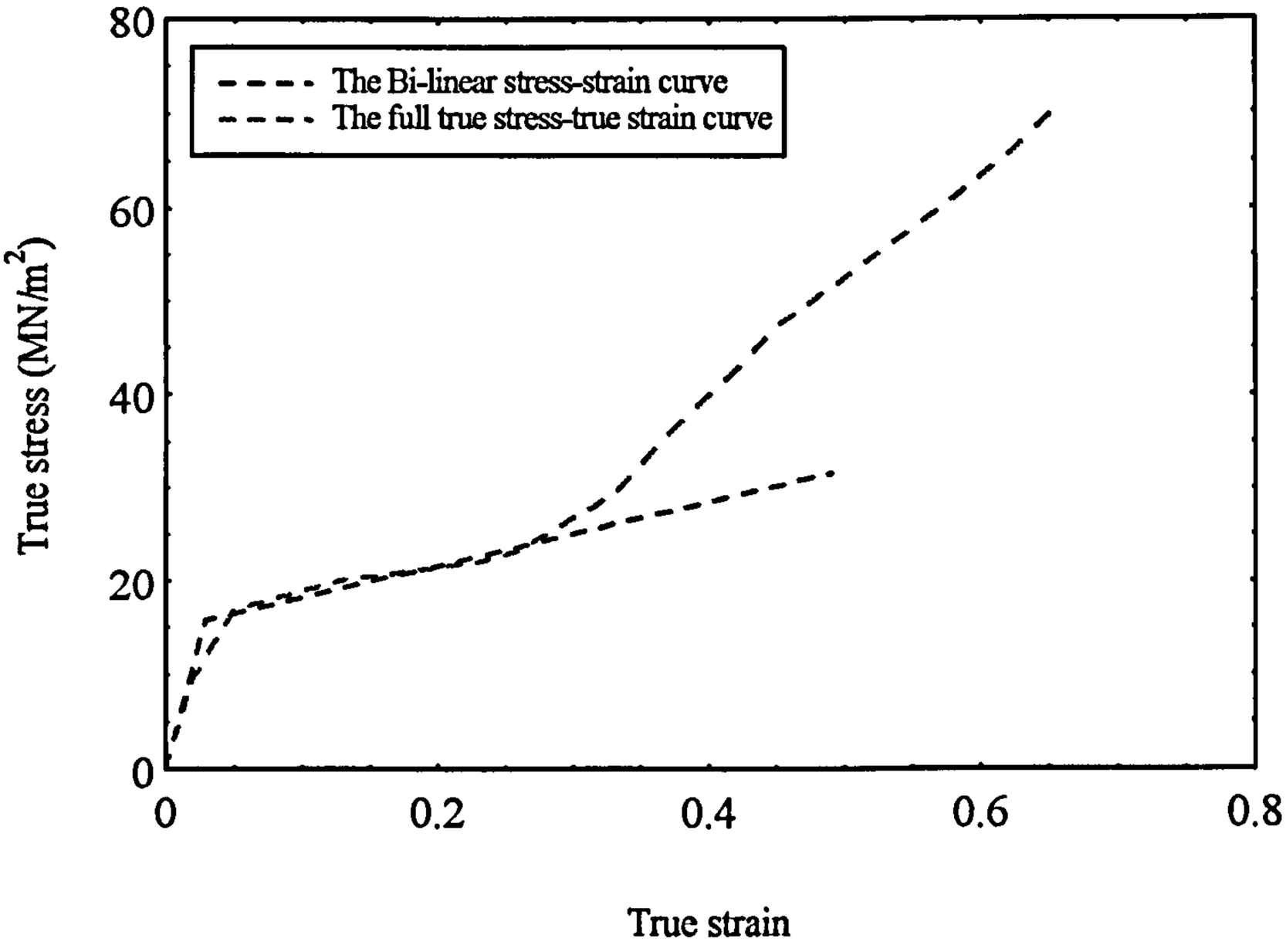

Figure B.2 : The full true stress-true strain curve and its bi-linear simplified curve.

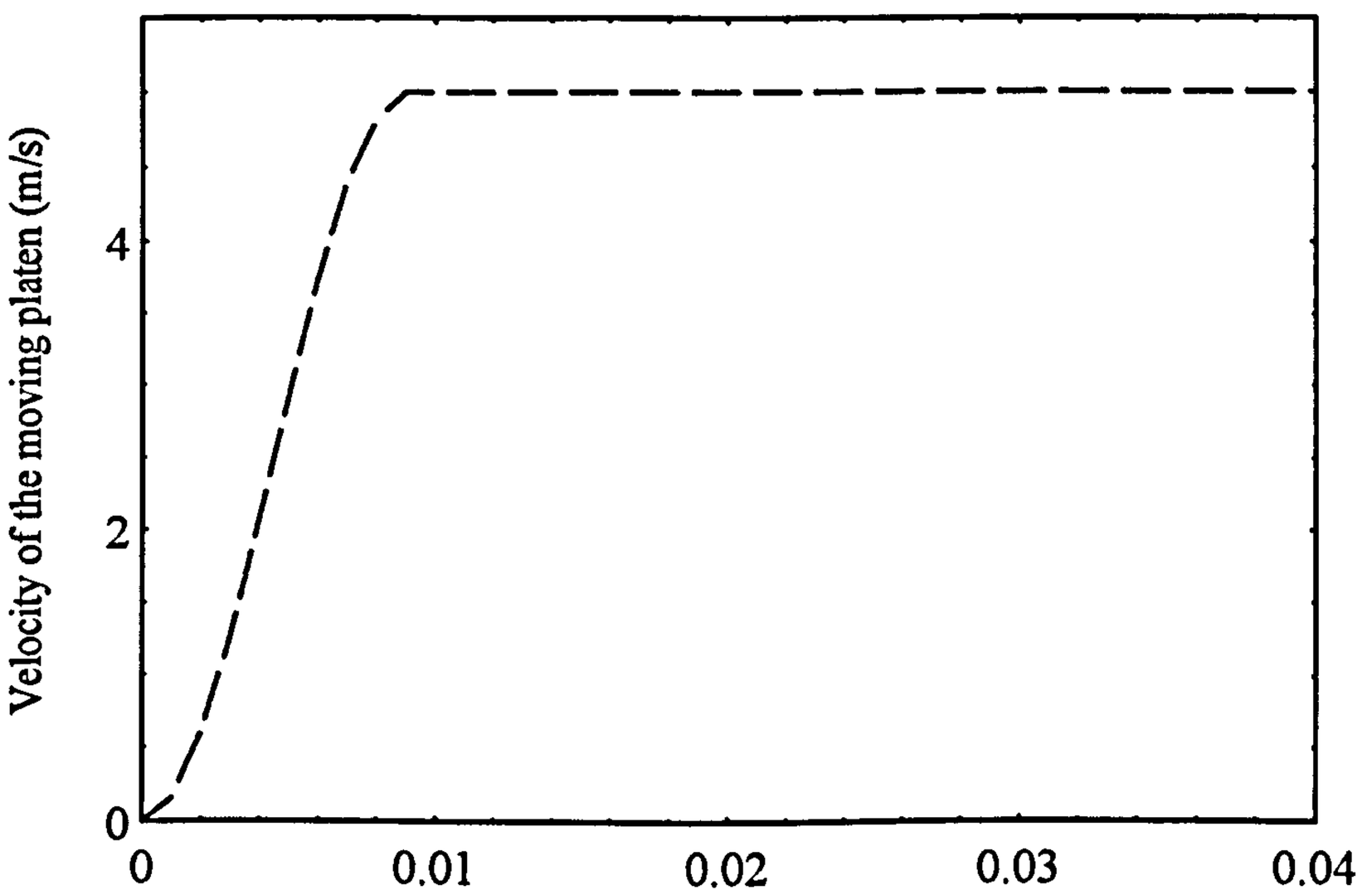

Figure B.3 : The velocity load curve for the moving platen.

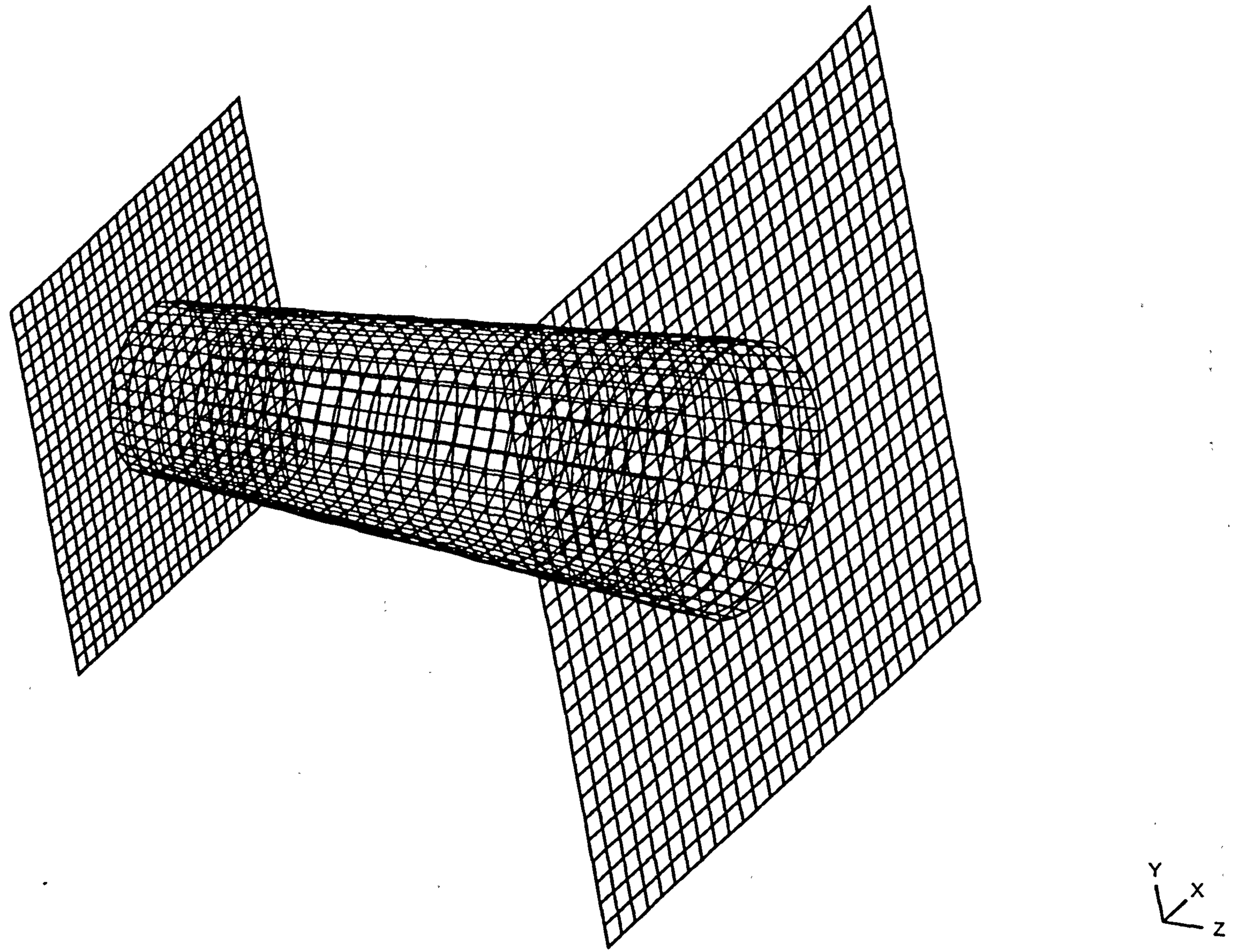

Figure B.4 : The model set-up for PVC-conic.

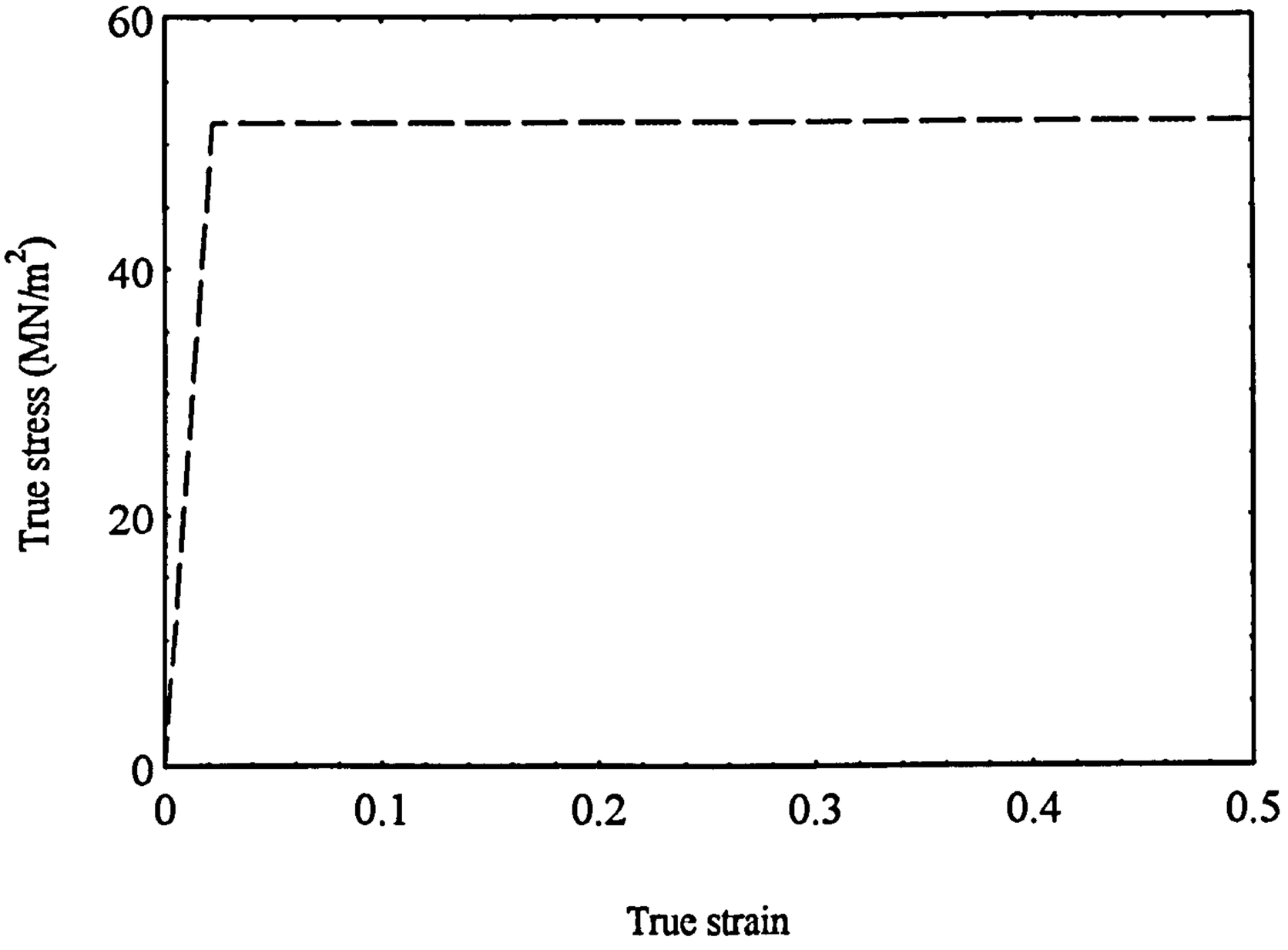

Figure B.5 : The stress-strain curve used in the crushing of the conical PVC model.

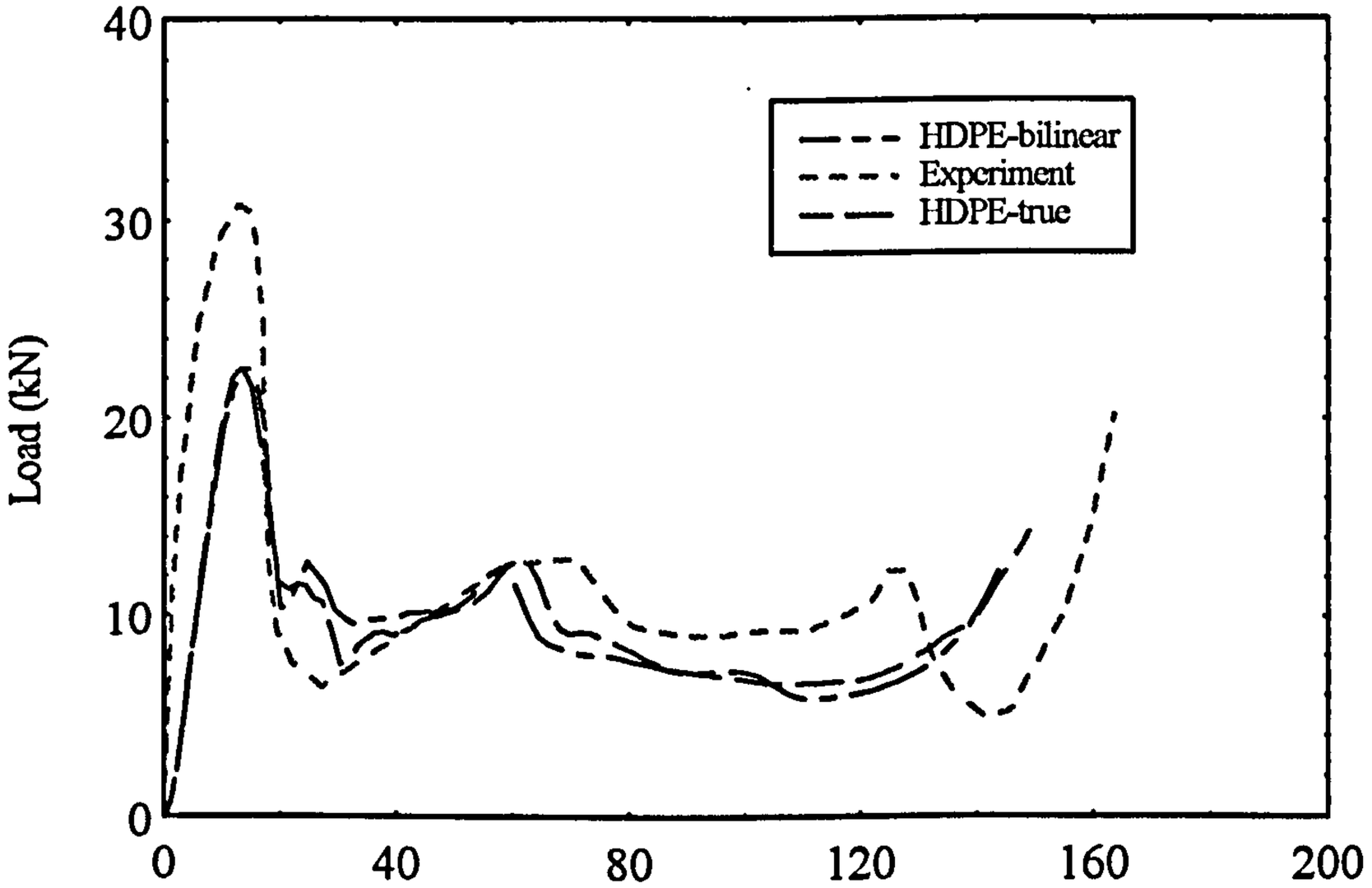

Figure B.6 : The load-deflection results for the crushing of HDPE tubes with t/D=0.0651.

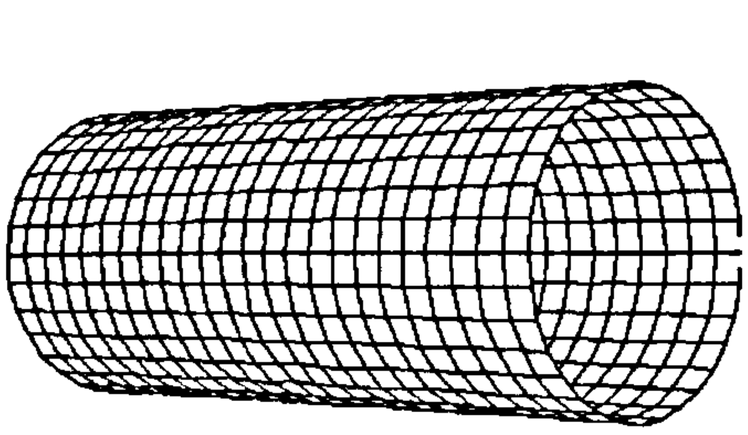

t=0msec

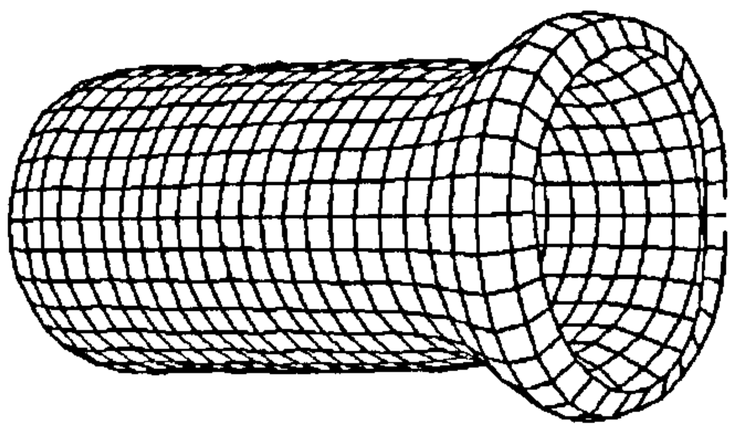

t=10.6msec

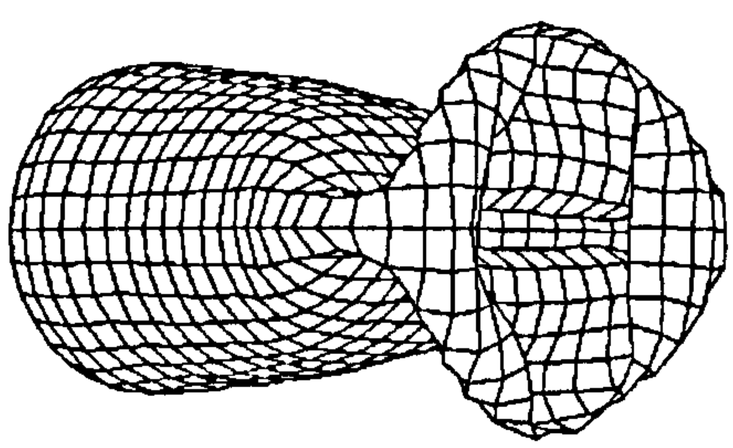

t=21.2msec

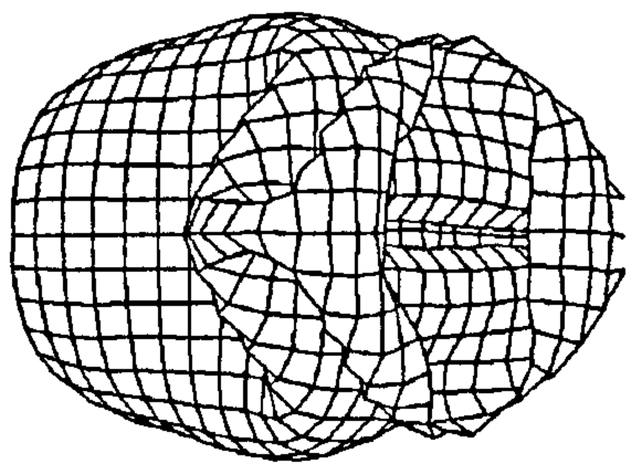

t=31.8msec

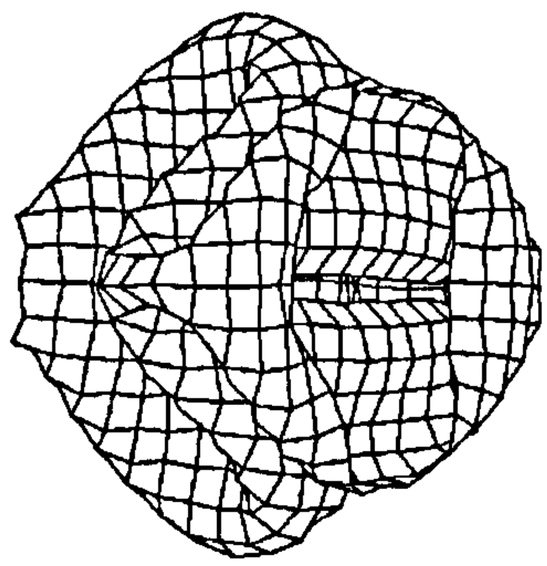

t=47.4msec

Fig. B.7 : The deformation sequence as predicted by the DYNA3D model HDPE-bilinear.

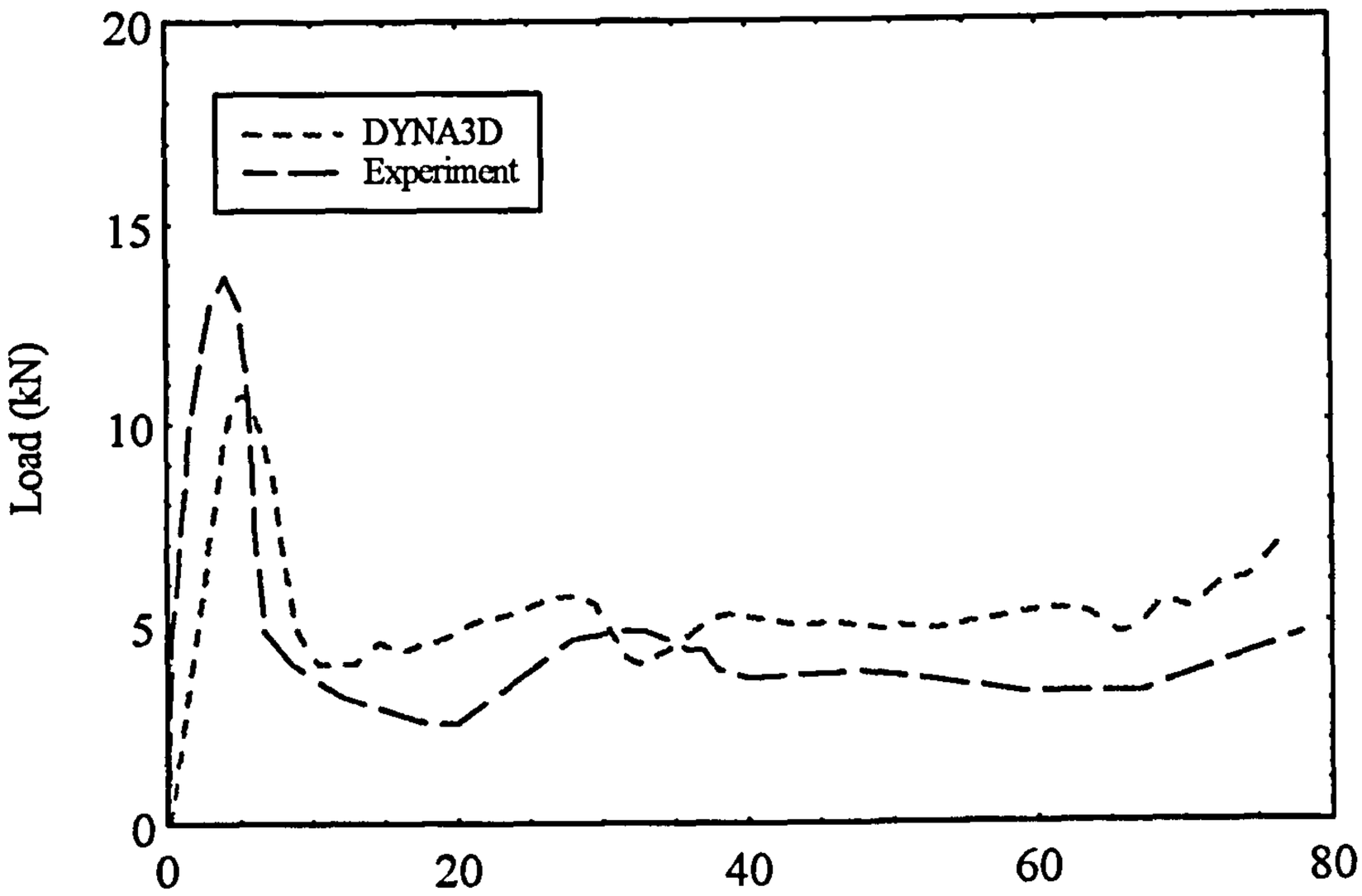

Figure B.8 : The load-deflection results for the crushing of HDPE tubes with t/D=0.0351.

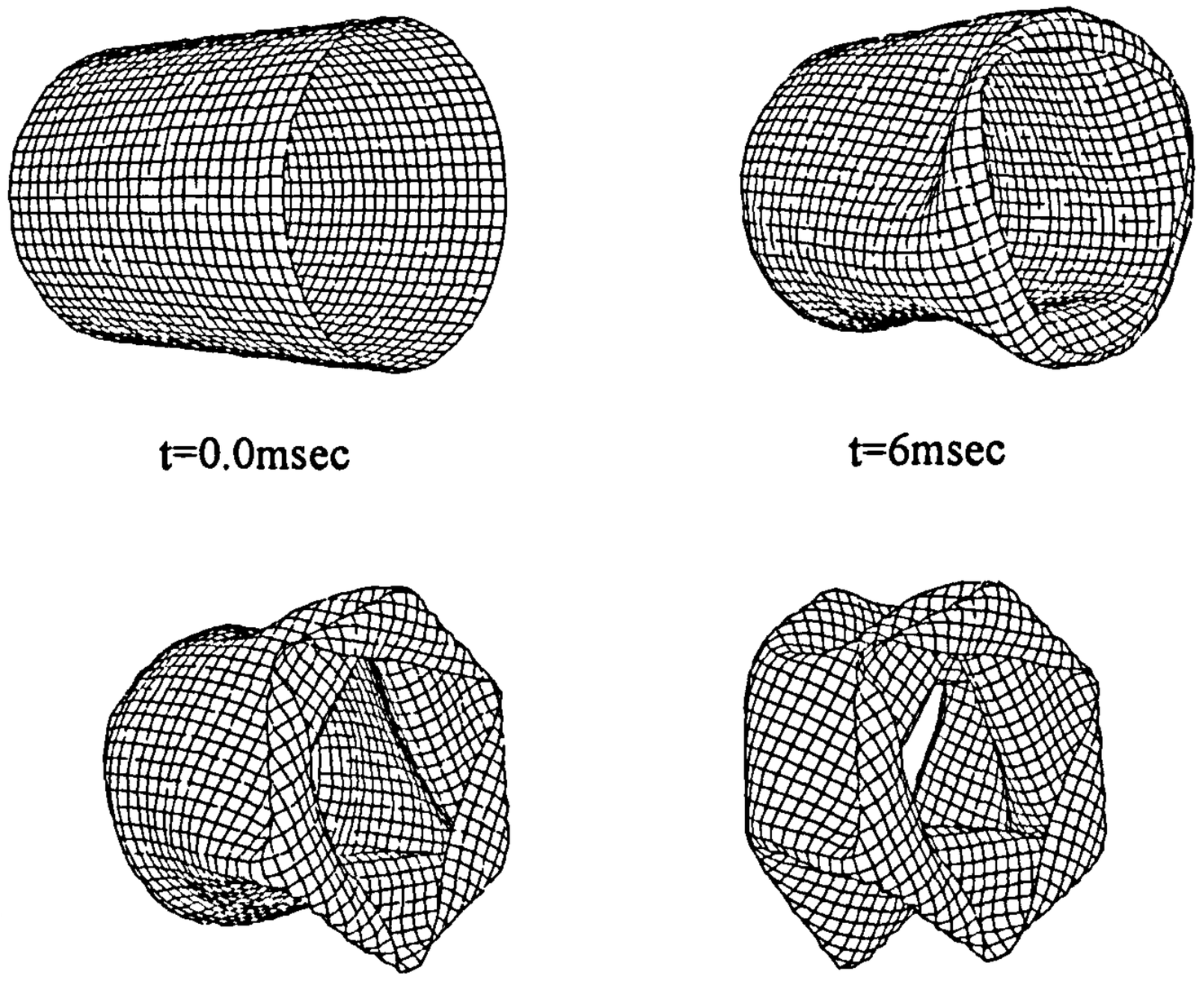

Figure B.9 : The deformation sequence as predicted by the DYNA3D model.

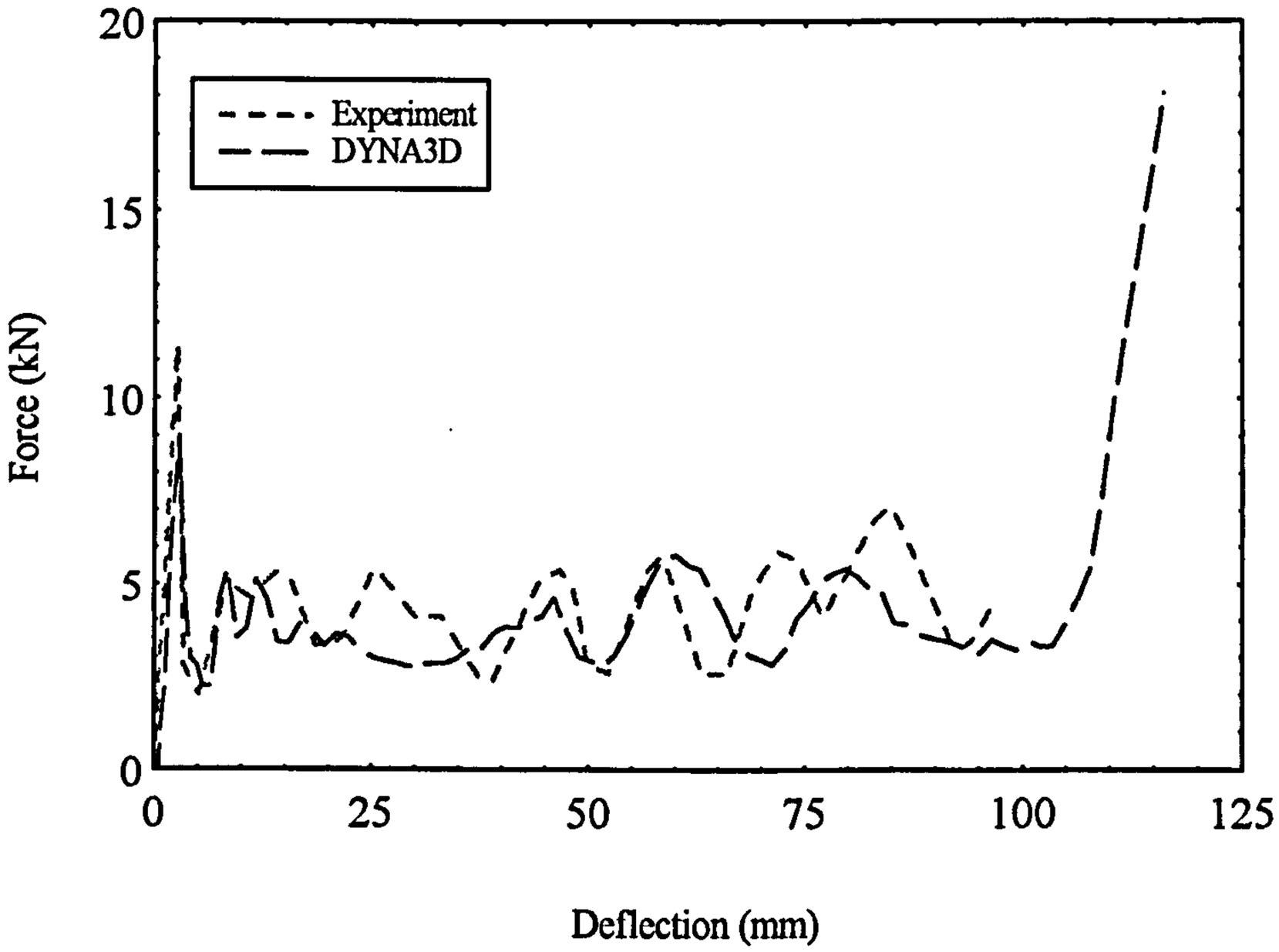

Figure B.10 : The load-deflection results for the crushing of the conical PVC tube.

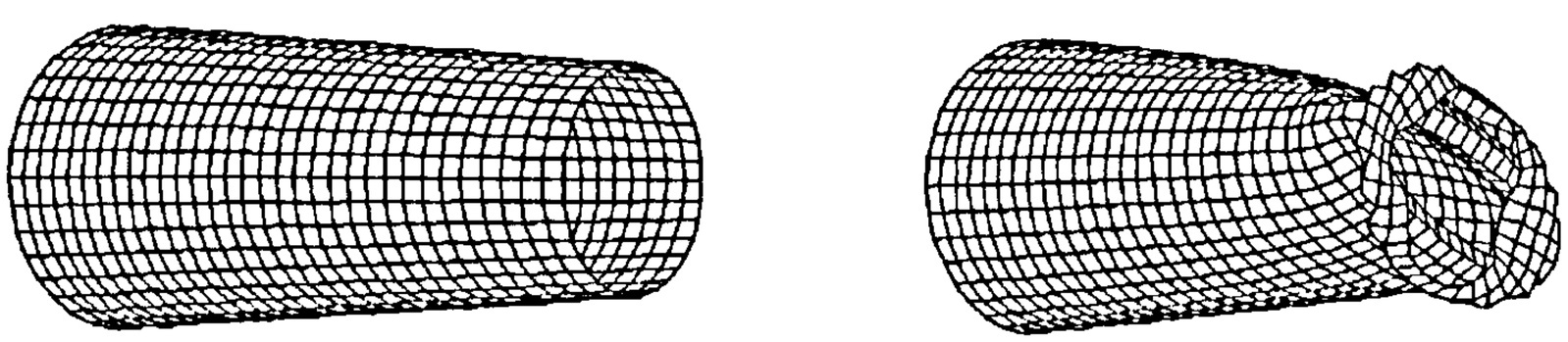

t=0.0msec.

t=8.4msec

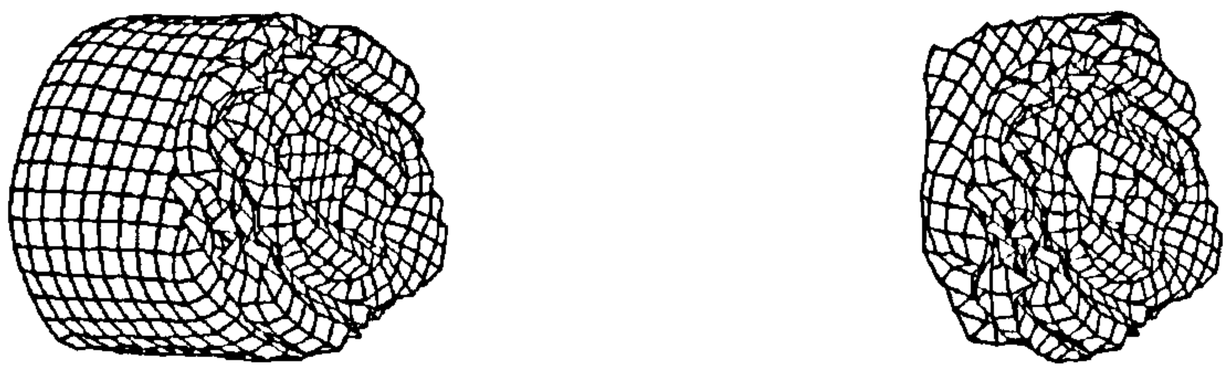

t=19.6msec

t=22.4msec

Figure B.11 : The deformation sequence as predicted by the DYNA3D model PVC-conic.